

# INAUGURAL – DISSERTATION

Zur Erlangung der Doktorwürde  
der  
Naturwissenschaftlich-Mathematischen Gesamtfakultät  
der  
Ruprecht-Karl Universität Heidelberg

vorgelegt von  
M.Sc. Florian Christian Krob  
geboren in Freiburg im Breisgau

Tag der mündlichen Prüfung:  
16.07.2020



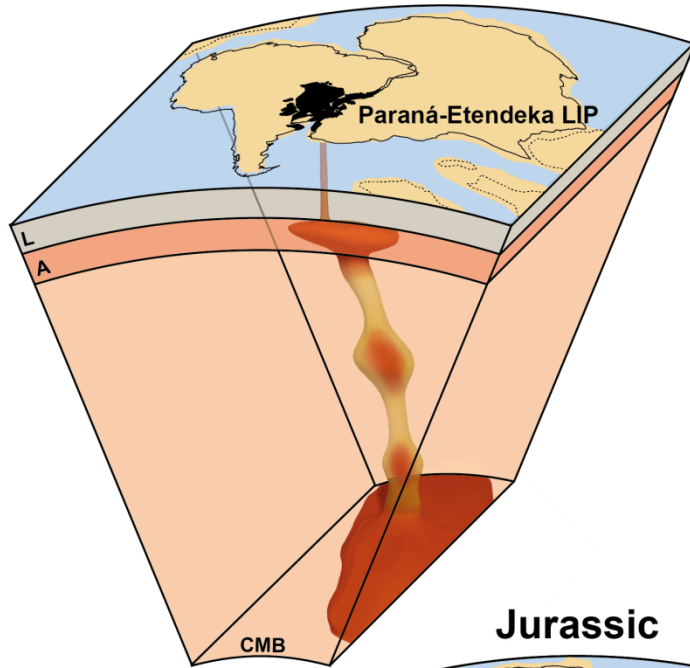
THE NEOPROTEROZOIC TO RECENT EVOLUTION OF  
SW GONDWANA – FROM AN OROGEN TO A PASSIVE  
CONTINENTAL MARGIN ENVIRONMENT INDUCED BY  
THE “PLATE” AND “PLUME MODE”

Gutachter: Prof. Dr. Ulrich A. Glasmacher

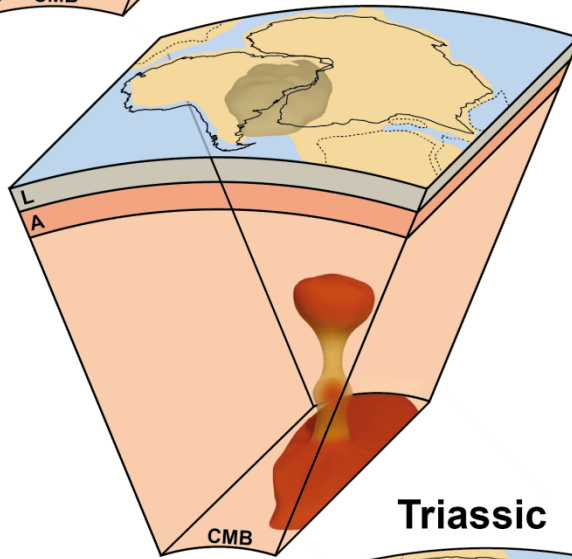
Prof. Dr. Peter A. Kukla



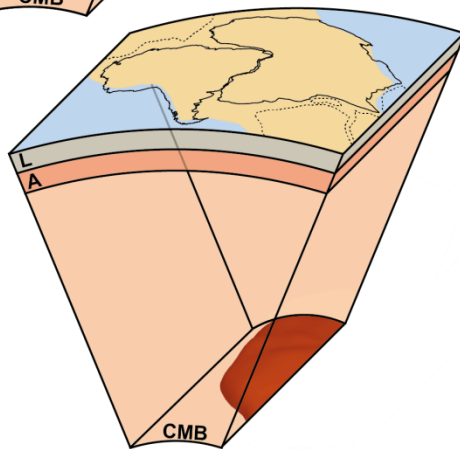
# Early Cretaceous



# Jurassic



# Triassic



“To me a mountain is a Buddha. Think of the patience, hundreds of thousands of years just sittin there bein perfectly perfectly silent and like prayin for all living creatures in that silence and just waitin for us to stop all our frettin and foolin.”

– Jack Kerouac

“An ice age here, million years of mountain building there.  
Geology is the study of pressure and time.  
That’s all it takes really, pressure and time”

– The Shawshank Redemption

# ACKNOWLEDGEMENT

First of all, I would like to thank my supervisor **Prof. Dr. Ulrich A. Glasmacher** for the opportunity to graduate in his research group and develop as a scientist. I am very grateful for the possibility to obtain a doctorate mainly from funds of his personal projects. Of course, I very much appreciated the countless and daily scientific discussions over the years and would like to thank Ulli for sharing his unique knowledge and experience with me. Moreover, I am very thankful for the possibility to have experienced many unforgettable moments during field trips, conference attendances, research travels, and the DAAD exchange program in Rio Claro, Brazil.

I would like to thank **Prof. Dr. Peter Kukla** for his readiness to function as my second assessor of this thesis. In Addition, I would like to thank **Prof. Dr. Oliver Friedrich** and **Prof. Dr. Olaf Bubenzer** for their willingness to complete the board of defence.

Also, I would like to thank **Prof. Dr. Hans-Peter Bunge** for lots of vigorous discussions, and his support on matters related to the general research and publishing process. I very much appreciated the discussions with members of the SPP-1375 SAMPLE and the discussions and logistic support by the research group of **Prof. Dr. Peter C. Hackspacher** and the Geoscience team in Rio Claro, UNESP. Special thanks go to **Prof. Dr. Anke Friedrich** for her ideas and vigorous discussions that led to the improvement of the outcome of CHAPTER 4.

Without the **financial support** provided with grants to Prof. Dr. Ulrich A. Glasmacher by the **German Research Foundation** (Deutsche Forschungsgemeinschaft, DFG, GL182/14-1, 14-2, GL 182/18-1) within the **Priority Program 1375 (SAMPLE)** and the **DAAD** (50753850) this research would not have been possible to carry out.

Special thanks go to my colleagues of the **ThermoArcheo research group** at the Institute of Earth Sciences of the University of Heidelberg for their moral support, scientific and administrative assistance, endless entertainment, and lot of fun we had together during the lunch and coffee breaks. In particular, I would like to thank **Christian Stippich**, **Lucas Holl**, **Dr. Sebastian Kollenz**, **Dr. Sebastian Dederer** and **Dr. Ioannis Tzifas** for their great impact to the last three and a half years.

I am very grateful to the former colleagues **Dr. Melissa Perner**, **Dipl. Geol. Daniel Eldracher**, **Dr. Sebastian Kollenz**, **Dipl. Geol. Markus Karl**, and **Dr. Eric Salomon** for their preparatory contribution concerning the organization of the field trips, the sample collection, sample preparation and processing, and dating analysis during the early phases of the research projects that led to the today's outcome of the research of this thesis.

Furthermore, I would like to thank the former and present Lab-managers **Margit Brückner** and **Tatjana Spilger** for their support in the laboratory and their constantly helpful hands. Also, I appreciated to supervise many Master and Bachelor students over the years and would like to thank them for the experience to guide them during their time in our research group.

I am very grateful to many of the stuff at the Institute of Earth Sciences, in particular, to **Petra Mai**, **Torsten Hoffmann**, and **Francisco Cueto** as I probably would not have gotten this far without their constant help and support.

An dieser Stelle möchte ich ebenfalls all jenen Menschen danken, die mich die letzten zehn Jahre in Heidelberg und in meinem Leben bis zu dieser Stelle begleitet haben:

Ich danke **Benni**, **Zahra**, **Linda** und **Keo** für die Zeit während unseres Bachelorstudiums, all die Partys und Chill-Abende, und dafür, dass ihr all die unvergesslichen und (Fremdschäm)-Momente wegen Benni während und außerhalb der Vorlesungen und Exkursionen mit mir durchgestanden habt.

Ich möchte auch ganz herzlich **Martin** für die Zeit während unseres sehr persönlichen Masterstudiums danken, dass uns wohl erst wegen der Umstände zusammengebracht hat. Wir waren ein exzellentes Zwei-Mann Team und ich war zu jeder Zeit dankbar, dass du mit dabei gewesen bist und habe die lustige Zeit auf den Exkursionen in Neufundland und vor allem Mexiko sehr genossen.

Ganz herzlich danke ich allen Menschen des **TSV Handschuhsheim**, die kamen, gingen oder blieben und mit denen ich zusammen trainieren, spielen, feiern und zusammensitzen durfte. Es sind großartige Freundschaften aus diesen Begegnungen entstanden.

Danken möchte ich auch den Jungs der **KGBGS** Gruppe, für die unvergesslichen Momente des Lachens, des Spielens und des Feierns, für alle die unzähligen und furchtbar unsinnig sinnigen Unterhaltungen und vor allem dafür, dass ich von Anfang an, in eurer Mitte, wie in einer Familie aufgenommen wurde. Ich danke auch **Frédéric Skanda** für seine unermüdliche Hilfe bei der Modellierung des Graphical Abstracts dieser Arbeit.

Ganz herzlich danken möchte ich **Clara**, für die Zeit, die wir zusammen verbringen, und die Freundschaft und Verbindung, die wir haben und teilen.

Ich danke **Marcus** für die letzten zehn Jahre in Heidelberg, die unvergesslichen verplanten Aktionen, Momente, Trips, die (wirklich) unermesslichen vielen Stunden vor der Playstation, und dafür, dass wir den TSV zusammen entdeckt haben.

Ich danke auch herzlich den **Tag-eins-Dudes** aus Freiburg für die mittlerweile 25+ Jahre unzertrennliche Freundschaft und die Möglichkeit, immer wieder nach Hause zurück zu kommen und wieder wie früher zu sein. Es war mir eine Freude, mit euch zusammen aufzuwachsen und durchs Leben zu gehen.



Mein besonderer Dank geht an **Helena** (und Robby) für ihre mentale Unterstützung, ihren Rückhalt und Verständnis, gerade in den letzten und nicht einfachen Monaten. Ich bin sehr dankbar, dass es dich in meinem Leben gibt und genieße unsere gemeinsame Zeit.

Schlussendlich möchte ich mich bei **meiner Schwester und meinen Eltern** für die bedingungslose Liebe und Unterstützung in allen erdenklichen Belangen bedanken. Es tut unfassbar gut, zu wissen, immer jemanden hinter sich zu haben.

Für alles, was ihr mir in meinem Leben ermöglicht habt, möchte ich DANKE sagen.



# EIDESSTATTLICHE VERSICHERUNG / AFFIDAVIT

Eidesstattliche Versicherung gemäß §8 der Promotionsordnung für die Naturwissenschaftlich-Mathematische Gesamtfakultät der Universität Heidelberg / [Sworn Affidavit according to §8 of the doctoral degree regulations of the Combined Faculty of Natural Sciences and Mathematics.](#)

1. Bei der eigenreichten Dissertation zu dem Thema / [The thesis I have submitted entitled](#)

“THE NEOPROTEROZOIC TO RECENT EVOLUTION OF SW GONDWANA - FROM AN OROGEN TO A PASSIVE CONTINENTAL MARGIN ENVIRONMENT INDUCED BY THE “PLATE-“ AND “PLUME-MODE”

handelt es sich um meine eigenständig erbrachte Leistung / [is my own work.](#)

2. Ich habe nur die angegebenen Quellen und Hilfsmittel benutzt und mich keiner unzulässigen Hilfe Dritter bedient. Insbesondere habe ich wörtlich oder sinngemäß aus anderen Werken übernommene Inhalte als solche kenntlich gemacht. / [I have only used the sources indicated and have not made unauthorized use of services of a third party. Where the work of others has been quoted or reproduced, the source is always given.](#)

3. Die Arbeit oder Teile davon habe ich bislang nicht an einer Hochschule des In- oder Auslands als Bestandteil einer Prüfungs- oder Qualifikationsleistung vorgelegt. / [I have not yet presented this thesis or parts thereof to a university as part of an examination or degree.](#)

4. Die Richtigkeit der vorstehenden Erklärungen bestätige ich. / [I confirm that the declarations made above are correct.](#)

5. Die Bedeutung der eidesstattlichen Versicherung und die strafrechtlichen Folgen einer unrichtigen oder unvollständigen eidesstattlichen Versicherung sind mir bekannt. / [I am aware of the importance of a sworn affidavit and the criminal prosecution in case of a false or incomplete affidavit.](#)

Ich versichere an Eide statt, dass ich nach bestem Wissen die reine Wahrheit erklärt und nichts verschwiegen habe. / [I affirm that the above is the absolute truth to the best of my knowledge and that I have not concealed anything.](#)

--- Ort und Datum / [Place and Date](#) ---

----- Unterschrift / [Signature](#) -----



# SELBSTÄNDIGKEITSERKLÄRUNG / DECLARATION OF INDEPENDENCE

Hiermit erkläre ich, die vorliegende Arbeit, und vor allem alle Texte, selbständig verfasst und diese, weder gesamt noch in Teilen, an einer anderen Hochschule des In- oder Auslands als Bestandteil einer Prüfungs- oder Qualifikationsleistung vorgelegt zu haben. / I hereby declare that the thesis, and especially all texts, has been composed by myself and that the work has not been submitted for any other degree or institutional examination.

Ich bestätige, dass es sich bei der eingereichten Arbeit um meine eigenständig erbrachte Leistung handelt, ausgenommen der Teile, die während der Zusammenarbeit der gemeinsam verfassten Veröffentlichungen erarbeitet wurden und als solche in der Arbeit gekennzeichnet sind. Darüber hinaus habe ich nur die angegebenen Quellen und Hilfsmittel benutzt und mich keiner unzulässigen Hilfe Dritter bedient. Insbesondere habe ich wörtlich oder sinngemäß aus anderen Werken übernommene Inhalte als solche kenntlich gemacht. / I confirm that the work submitted is my own, except where work which has formed part of jointly-authored publications has been included. Moreover, I have only used the sources indicated and have not made unauthorized use of services of a third party. Where the work of others has been quoted or reproduced, the source is always given.

Meine eigenen Forschungsbeiträge und diese ferner beteiligter Mitarbeiter und Co-Autoren sind in **KAPITEL 1.5** aufgeführt und genauer erklärt. Des Weiteren sind den jeweiligen Veröffentlichungen explizite **Erklärungen zu den Beiträgen der jeweiligen Autoren** vorangestellt. Damit bestätige ich, dass den Beiträgen anderer die angemessene Anerkennung zu Teil kommt. / My contributions and those of the other workers and authors to this work have been indicated explicitly during **CHAPTER 1.5** and within the respective **CRediT author statements** that are prepended to each of the publications. Thereby, I confirm that appropriate credit has been given within this thesis where reference has been made to the work of others.

Die in **KAPITEL 1** vorgestellte Arbeit umfasst eine Einführung, die Zielstellung, den theoretischen Ansatz sowie eine kurze Zusammenstellung der Ergebnisse und Kernaussagen meiner Forschung und repräsentiert daher ausschließlich meine eigene erbrachte Leistung. Alle direkt oder indirekt verwendeten Quellen sind als Referenzen kenntlich gemacht. / The work presented in **CHAPTER 1** comprises an introduction, objectives, theoretical approach, as well as a short summary of the results and conclusions of the thesis and therefore, consist of my unaided work. All direct or indirect sources used are acknowledged as references.

Die in **KAPITEL 2** vorgestellte Studie wurde zuvor in der Zeitschrift *Journal of South American Earth Sciences*, Volume 92 (2019), 77-94 (<https://doi.org/10.1016/j.jsames.2019.02.012>) unter dem Titel “Multi-chronometer thermochronological modelling of the Late Neoproterozoic to recent *t-T*-evolution of the SE coastal region of Brazil” von mir, **Florian C. Krob**, als korrespondierender Erstautor mit der Hilfe der Co-Autoren Prof. Dr. Ulrich A. Glasmacher\*, Markus Karl, Dr. Melissa Perner, Prof Dr. Peter C. Hackspacher und Dr. Daniel F. Stockli veröffentlicht. Während alle aufgeführten Co-Autoren zur Datenerhebung beitrugen, umfasst mein Anteil die Ausarbeitung des Konzeptes, die Modellierungen, sowie das Verfassen und die Visualisation des ursprünglichen Entwurfes der Veröffentlichung. Prof. Dr. Ulrich A. Glasmachers Anteil umfasst des Weiteren die Überprüfung und Korrektur des Entwurfes. / The research presented in **CHAPTER 2** was previously published in the *Journal of South American Earth Sciences*, Volume 92 (2019), 77-94 (<https://doi.org/10.1016/j.jsames.2019.02.012>) as “Multi-chronometer thermochronological modelling of the Late Neoproterozoic to recent *t-T*-evolution of the SE coastal region of Brazil” by myself, **Florian C. Krob**, as the corresponding author holding the first authorship and co-authored by Prof. Dr. Ulrich A. Glasmacher\*, Markus Karl, Dr. Melissa Perner, Prof Dr. Peter C. Hackspacher, and Dr. Daniel F. Stockli. As all co-authors contributed to the investigation and curation of data, I conceived the conceptualization, modeling results, and the writing and visualisation of the original draft. Prof. Dr. Ulrich A. Glasmacher further contributed to this research during the review and editing process.

Die in **KAPITEL 3** vorgestellte Studie wurde zuvor in der Zeitschrift *International Journal of Earth Sciences* (<https://doi.org/10.1007/s00531-020-01819-7>) unter dem Titel “Late Neoproterozoic-to-recent long-term *t-T*-evolution of the Kaoko and Damara belts in NW Namibia” von mir, **Florian C. Krob**, als korrespondierender Erstautor mit der Hilfe der Co-Autoren Daniel P. Eldracher, Prof. Dr. Ulrich A. Glasmacher\*, Sabine Husch, Dr. Eric Salomon, Prof Dr. Peter C. Hackspacher und Dr. Nortin P. Titus veröffentlicht. Während alle aufgeführten Co-Autoren zur Datenerhebung beitrugen, umfasst mein Anteil die Ausarbeitung des Konzeptes, die Modellierungen, sowie das Verfassen und die Visualisation des ursprünglichen Entwurfes der Veröffentlichung. Prof. Dr. Ulrich A. Glasmachers Anteil umfasst des Weiteren die Überprüfung und Korrektur des Entwurfes. / The research presented in **CHAPTER 3** was previously published in the *International Journal of Earth Sciences* (<https://doi.org/10.1007/s00531-020-01819-7>) as “Late Neoproterozoic-to-recent long-term *t-T*-evolution of the Kaoko and Damara belts in NW Namibia” by myself, **Florian C. Krob**, as the corresponding author holding the first authorship and co-authored by Daniel P. Eldracher, Prof. Dr. Ulrich A. Glasmacher\*, Sabine Husch, Dr. Eric Salomon, Prof Dr. Peter C. Hackspacher, and Dr. Nortin P. Titus. As all co-authors contributed to the investigation and curation of data, I conceived the conceptualization, modeling results, and the writing and visualisation of the original draft. Prof. Dr. Ulrich A. Glasmacher further contributed to the research during the review and editing process.

Die in **KAPITEL 4** vorgestellte Studie wurde zuvor in der Zeitschrift *Gondwana Research*, Volume 84 (2020), 81-110 (<https://doi.org/10.1016/j.gr.2020.02.010>) unter dem Titel “Application of stratigraphic frameworks and thermochronological data on the Mesozoic SW Gondwana intraplate environment to retrieve the Paraná-Etendeka plume movement” von mir, **Florian C. Krob**, als korrespondierender Erstautor mit der Hilfe der Co-Autoren Prof. Dr. Ulrich A. Glasmacher\*, Prof. Dr. Hans-Peter Bunge, Prof. Dr. Anke M. Friedrich und Prof. Dr. Peter C. Hackspacher veröffentlicht. Während alle aufgeführten Co-Autoren an der Konzeptualisierung und der Verbesserung des Entwurfes beteiligt waren, umfasst mein Anteil die Erhebung der Daten, die Modellierungen, sowie das Verfassen und die Visualisation des ursprünglichen Entwurfes der Veröffentlichung. / The research presented in **CHAPTER 4** was previously published in the Journal of *Gondwana Research*, Volume 84 (2020), 81-110 (<https://doi.org/10.1016/j.gr.2020.02.010>) as “Application of stratigraphic frameworks and thermochronological data on the Mesozoic SW Gondwana intraplate environment to retrieve the Paraná-Etendeka plume movement” by myself, **Florian C. Krob**, as the corresponding author holding the first authorship and co-authored by Prof. Dr. Ulrich A. Glasmacher\*, Prof. Dr. Hans-Peter Bunge, Prof. Dr. Anke M. Friedrich, and Prof. Dr. Peter C. Hackspacher. As all co-authors contributed to the conceptualization and during the review and editing process, I conceived the investigation and curation of data, modeling results, and the writing and visualisation of the original draft.

\*Erstgutachter dieser Arbeit / Supervisor of this thesis.

--- Ort und Datum / Place and Date ---

--- Unterschrift / Signature -----

This thesis is produced for the purpose of examination as a doctoral dissertation only and not intended as a permanent scientific record. Presented data should therefore only be cited using the reference of the concerning publication or the author's explicit written approval.

**The Copyrights** of the individual publications that appear in this thesis remain with **Elsevier** and **Springer** that allocate the non-commercial use of the copyrighted material within the official author's rights without the need to obtain specific permission.



## ABSTRACT

The overarching goal of this thesis is the reconstruction of a coherent Late Neoproterozoic to recent time-temperature-evolution to connect individual geological stages (environments) of the *Wilson Cycle*, and consequently, follow the development from an active orogeny to an intraplate and later passive continental margin environment induced by the interaction of the “plate” and “plume mode”.

The research is based on the thermochronological analysis of Neoproterozoic basement rocks along the South Atlantic passive continental margins in SE Brazil and NW Namibia as well as the numerical modeling of the collected data. Moreover, the study combines multiple geological archives, e.g. geo- and thermochronological data from the published geological record and the stratigraphic records of sedimentary basins to constrain the entire time-temperature-evolution.

In addition, the research aims to retrieve signals and traces of the Paraná-Etendeka vertical and horizontal plume movement during the Mesozoic SW Gondwana intraplate environment. It quantifies the possibly plume-induced rock and surface uplift (*dynamic topography*) preceding the Paraná-Etendeka Large Igneous Province integrating all available thermochronological data sets along the South Atlantic passive continental margins and the stratigraphic records of the major sedimentary basins surrounding the Paraná-Etendeka Large Igneous Province.

By combining multiple geological archives, this thesis succeeds to reconstruct a possible and coherent Late Neoproterozoic to recent time-temperature evolution. Thereby, this research quantifies the timing, magnitude and rates of cooling and heating, or rather exhumation and subsidence during the development of the individual geological environments.

The thesis therefore comprises the post-Pan African/Brasiliano orogenic cooling of rocks, the burial and subsidence involving the heating of the Neoproterozoic basement rocks during the Late Paleozoic Gondwana intraplate basin formation, and the thermal overprint caused by the Paraná-Etendeka flood basalt deposition and magmatic activity and following cooling during the post-South Atlantic rift and breakup exhumation. Furthermore, signals and traces of the Paraná-Etendeka plume movement causing large scale rock and surface uplift prior to the emplacement of the Paraná-Etendeka Large Igneous Province are retrieved. As a result, it is possible to determine spatial and temporal ranges for the plume movement-influenced area on the Earth's surface during the Mesozoic SW Gondwana intraplate environment. Thereby, this thesis contributes to the understanding of the complex evolution of the individual yet interconnected geological environments and the dynamic interplay of the driving endo- and exogenous forces.



# KURZFASSUNG

Das übergeordnete Ziel dieser Dissertation ist die zusammenhängende Rekonstruktion der Zeit-Temperatur-Entwicklung seit dem späten Neoproterozoikum, um die einzelnen geologischen Stadien (Environments) des *Wilson Zyklus* zu verknüpfen und somit der gesamtheitlichen Entwicklung von einer aktiven Orogenese, über ein Zwischenplatten-, zu einem passivem Kontinentalrand-Environment, bedingt durch den Einfluss des „*Platten*“ und „*Plume Modes*“ zu folgen.

Um diese Entwicklung zu untersuchen, basiert die Arbeit auf der thermochronologischen Analyse von neoproterozoischen Gesteinen entlang der passiven Kontinentalränder im Südosten Brasiliens und Nordwesten Namibias und der numerischen Modellierung der gewonnenen Daten. Darüber hinaus verbindet diese Arbeit verschiedene geologische Archive, wie z.B. geo- und thermochronologische Daten aus der veröffentlichten geologischen Datenbank und stratigraphische Tabellen der sedimentären Becken, um eine höhere Wahrscheinlichkeit der gesamtheitlichen Zeit-Temperaturentwicklung, auf Basis der Archive, zu gewährleisten.

Ein weiteres Ziel dieser Arbeit ist es, Signale und Spuren der vertikalen und horizontalen Konvektion des aufsteigenden Paraná-Etendeka Plumes während des mesozoischen, südwestlichen Gondwana-Zwischenplatten-Environments in den geologischen Archiven aufzuspüren. Im Zuge dessen quantifiziert diese Arbeit die, der Paraná-Etendeka magmatischen Großprovinz vorausgehende und durch den möglichen Plume Aufstieg beeinflusste, Gesteins- und Oberflächenhebung (*Dynamic Topography*) und integriert dabei alle verfügbaren thermochronologischen Datensätze entlang der südatlantischen Kontinentalränder von Süd Amerika und dem südwestlichen afrikanischen Kontinents und die stratigraphischen Tabellen der wichtigsten, und an die Paraná-Etendeka magmatische Großprovinz angrenzenden, sedimentären Becken.

Durch die Verknüpfung mehrerer geologischer Archive gelingt es dieser Arbeit eine mögliche und zusammenhängende Zeit-Temperaturentwicklung seit dem Neoproterozoikum zu rekonstruieren. Dadurch kann die Forschung die zeitlichen Abschnitte, die Größenordnung und Raten der Abkühlung und Aufheizung, bzw. Exhumation und Subsidenz während der Entwicklung der einzelnen geologischen Stadien quantifizieren.

Somit umfasst diese Dissertation die Abkühlung der Gesteine nach der Pan Afrikanischen/Brasilianischen Orogenese, die Überlagerung und Subsidenz und damit verbundene Aufheizung der Gesteine des neoproterozoischen Grundgebirges während der spät paläozoischen Beckenbildung im Zwischenplattenstadium, und der thermischen Überprägung der Gesteine, ausgelöst durch die Ablagerung der Paraná-Etendeka Flutbasalte und der begleiteten magmatischen Aktivität, und der nachfolgenden Abkühlung während der, dem Aufbrechen des südatlantischen Ozeans folgenden Exhumation. Zusätzlich gelingt es der Studie die Signale und Spuren von der, dem Auftreten der Paraná-Etendeka magmatische Großprovinz hervorgehenden großflächigen Gesteins- und Oberflächenhebung in den geologischen Archiven zu finden. Folglich ist es möglich Grenzen der räumlichen und zeitlichen Dimension der, während des mesozoischen südwestlichen Gondwana Zwischenplatten-Environments und vom Paraná-Etendeka Plume Aufstieg, beeinflussten Fläche auf der

Erdoberfläche zu bestimmen. Durch diese Erkenntnisse kann diese Studie dazu beitragen, das Verständnis der komplexen Entwicklung der einzelnen jedoch verbundenen geologischen Environments und das dynamische Zusammenspiel der treibenden endogenen und exogenen Kräfte zu verbessern.

**Keywords:** low-temperature-thermochronology; long-term time-temperature-evolution; SE Brazil; NW Namibia, Pan African/Brasiliano orogeny; geochronology; Gondwana intraplate environment; South Atlantic continental passive margin; apatite; zircon; fission-track analysis; (U-Th-(Sm))/He analysis; numerical modeling, HeFTy; stratigraphy, sedimentary basins; Paraná-Etendeka large igneous province; plume movement; geodynamics; mantle dynamics.



# TABLE OF CONTENTS

ACKNOWLEDGEMENT	IX
EIDESSTÄTLICHE VERSICHERUNG / AFFIDAVIT	XIII
SELBSTÄNDIGKEITSERKLÄRUNG / DECLARATION OF INDEPENDENCE	XV
ABSTRACT	XIX
KURZFASSUNG	XXI
TABLE OF CONTENTS	XXV
LIST OF FIGURES	XXIX
LIST OF TABLES	XXXIII
<b>CHAPTER 1: INTRODUCTION</b>	<b>1</b>
1.1 STATE-OF-THE-ART	3
1.2 OBJECTIVES	7
1.3 STUDY AREA AND APPROACH	9
1.4 THESIS STRUCTURE	15
1.5 CONTRIBUTIONS	16
1.6 SUMMARY OF RESULTS, AND CONCLUSIONS	17
1.7 FUTURE PERSPECTIVES	32
<b>LIST OF REFERENCES</b>	<b>33</b>
<b>CHAPTER 2: MULTI-CHRONOMETER THERMOCHRONOLOGICAL MODELING OF THE LATE NEOPROTEROZOIC TO RECENT t-T-EVOLUTION OF THE SE COASTAL REGION OF BRAZIL</b>	<b>39</b>
GRAPHICAL ABSTRACT	40
CRediT AUTHOR STATEMENT	41
ABSTRACT	43
INTRODUCTION	43
GEOLOGICAL SETTING	45
PRECAMBRIAN BASEMENT	45
TECTONIC STRUCTURES	46
PARANÁ BASIN SUBSIDENCE	46
POST-BREAKUP EVOLUTION	46

METHODS	47
THERMOCHRONOLOGY	47
THERMAL MODELING: t-T-PATHS AND GEOLOGICAL MODEL	48
EXHUMATION AND SUBSIDENCE RATES	48
RESULTS	48
ZIRCON FISSION-TRACK DATA	48
ZIRCON (U-Th-(Sm))/He DATA	48
APATITE FISSION-TRACK DATA	50
APATITE (U-Th-(Sm))/He DATA	50
THERMAL HISTORY MODELING	50
INTERPRETATION AND DISCUSSION	50
STAGE 1: LATE NEOPROTEROZOIC TO UPPER PALEOZOIC – SYN- TO POST- OROGENIC COOLING, EROSION AND UPLIFT (EXHUMATION)	52
Exhumation rates during the late Neoproterozoic to upper Paleozoic	52
Age and timing of movement along tectonic structures	53
STAGE 2: UPPER PALEOZOIC TO EARLY CRETACEOUS – PARANÁ BASIN FORMATION, PARANÁ-ETENDEKA PLUME ACTIVITY, PRE- TO SYN-BREAKUP PROCESSES	53
Subsidence rates during the Early Paleozoic to Early Cretaceous	53
STAGE 3: EARLY CRETACEOUS TO RECENT – POST-BREAKUP PROCESSES, EROSION AND SURFACE UPLIFT (EXHUMATION)	55
Exhumation and subsidence rates	57
CONCLUSIONS	57
ACKNOWLEDGEMENTS	57
REFERENCES	58
<b>CHAPTER 3: LATE NEOPROTEROZOIC TO RECENT LONG-TERM t-T-EVOLUTION OF THE KAOKO AND DAMARA BELTS IN NW NAMIBIA</b>	<b>63</b>
GRAPHICAL ABSTRACT	64
CRediT AUTHOR STATEMENT	65
ABSTRACT	67
INTRODUCTION	67
GEOLOGICAL SETTING	68
LATE NEOPROTEROZOIC TO EARLY PALEOZOIC – PAN AFRICAN/BRASILIANO OROGENY	68
LATE PALEOZOIC TO JURASSIC EVOLUTION – SW GONDWANA INTRAPLATE FORMATION OF SEDIMENTARY BASINS	68
LATE JURASSIC TO CENOZOIC EVOLUTION – BREAKUP, AND SYN- TO POST-RIFT PROCESSES	70
TECTONIC STRUCTURES	71



METHODS		73
THERMOCHRONOLOGY		73
NUMERICAL MODELING OF CONTINUOUS t-T-PATHS (t-T-EVOLUTION)		73
RECONSTRUCTION OF THE t-T-PATH AND CALCULATION OF RATES		73
RESULTS	5	75
APATITE FISSION-TRACK DATA		75
Kaoko Belt		75
Damara Belt		75
ZIRCON FISSION-TRACK AGES		77
NUMERICAL MODELING OF THE t-T-EVOLUTION		77
INTERPRETATION AND DISCUSSION		77
LATE NEOPROTEROZOIC TO EARLY PALEOZOIC – SYN- TO POST-PAN AFRICAN COOLING AND EXHUMATION		79
LATE PALEOZOIC TO LATE JURASSIC –SW GONDWANA BASIN FORMATIONON		87
LATE JURASSIC TO RECENT – SAPCM SYN- TO POST-RIFT PROCESSES AND THE THERMAL INFLUENCE OF THE PARANÁ-ETENDEKA LIP		89
CONCLUSIONS		93
ACKNOWLEDGEMENTS		93
REFERENCES		93
<b>CHAPTER 4: APPLICATION OF STRATIGRAPHIC FRAMEWORKS AND THERMOCHRONOLOGICAL DATA ON THE MESOZOIC SW GONDWANA INTRAPLATE ENVIRONMENT TO RETRIEVE THE PARANÁ-ETENDEKA PLUME MOVEMENT</b>		<b>99</b>
GRAPHICAL ABSTRACT		100
CRediT AUTHOR STATEMENT		101
ABSTRACT		103
INTRODUCTION		103
THE EVENT-BASED PLUME STRATIGRAPHIC FRAMEWORK (ePSF)		104
FIRST ARCHIVE: STRATIGRAPHIC RECORDS OF THE PALEOZOIC TO MESOZOIC SW GONDWANA INTRAPLATE SEDIMENTARY BASINS		107
PRE-PLUME-EVENT EVOLUTION OF THE MAJOR CONTINENTAL BASINS SURROUNDING THE EARLY CRETACEOUS PARANÁ-ETENDEKA LIP		107
POST-PARANÁ-ETENDEKA PLUME EVENT EVOLUTION OF THE SOUTHERN-CENTRAL SAPCM OFFSHORE BASINS		107
PLUME STRATIGRAPHIC MAPPING OF THE PARANÁ-ETENDEKA LIP		107
RESULTS AND DISCUSSION OF THE STRATIGRAPHIC MAPPING		111
Plume center		111
Plume margin		111
Distal regions		111
Critical view and uncertainty analysis		112

SECOND ARCHIVE: THERMOCHRONOLOGICAL DATA SETS OF THE SW AFRICAN AND NE TO SE SOUTH AMERICAN SAPCM	117
LOW-TEMPERATURE THERMOCHRONOLOGY (LTT) DATA SETS	117
VISUALIZATION OF APATITE FISSION-TRACK DATA SETS	117
RESULTS AND DISCUSSION: THERMOCHRONOLOGICAL DATA SETS IN THE PERSPECTIVE OF THE EVENT-BASED PLUME STRATIGRAPHIC FRAMEWORK (ePSF)	117
CRITICAL VIEW AND UNCERTAINTY ANALYSIS	118
COMBINING BOTH ARCHIVES: STRATIGRAPHIC RECORDS AND LTT DATA SETS	118
INVERSE NUMERICAL MODELING TO RETRIEVE THE t-T-EVOLUTION OF THE PARANÁ-ETENDEKA PLUME CENTRAL AREA	118
GEOLOGICAL EVOLUTION MODEL (GEM)	120
RESULTS OF THE NUMERICAL MODELING OF THE t-T-EVOLUTION	120
3D-VISUALISATION OF THE t-T-EVOLUTION	120
RESULTS OF THE 3D-VISUALISATION: THE THERMAL STRUCTURE OF THE NEOPROTEROZOIC, GONDWANA BASEMENT SURFACE	121
DISCUSSION: STRATIGRAPHIC RECORDS VS. LTT DATA SETS VS. THE ePSF	123
FINAL DISCUSSION AND INTERPRETATION	126
CONCLUSIONS	128
ACKNOWLEDGEMENTS	131
REFERENCES	131
<b>CHAPTER 5: APPENDIX</b>	<b>133</b>
A: SUPPLEMENTARY MATERIAL FOR CHAPTER 2	137
B: SUPPLEMENTARY MATERIAL FOR CHAPTER 3	177
C: SUPPLEMENTARY MATERIAL FOR CHAPTER 4	213
<b>CURRICULUM VITAE</b>	<b>265</b>
<b>LIST OF PUBLICATIONS</b>	<b>267</b>

# LIST OF FIGURES

## CHAPTER 1: INTRODUCTION

Figure 1.1: Geological features on the Earth's surface.	4
Figure 1.2: Visualization of the "plume mode" theory.	5
Figure 1.3: Schematic view of the <i>Wilson Cycle</i> .	10
Figure 1.4: Overview of the specific study areas.	11
Figure 1.5: Area of research in SE Brazil showing topographic transects.	12
Figure 1.6: Area of research in NW Namibia showing topographic transects.	13
Figure 1.7: Paleogeographic reconstruction and thermal basement structure from the Early Ordovician and the Early Devonian.	19
Figure 1.8: Paleogeographic reconstruction and thermal basement structure from the Late Devonian until the Late Carboniferous.	20
Figure 1.9: Paleogeographic reconstruction and thermal basement structure from the Early Permian until the Early Jurassic.	22
Figure 1.10: Possible ranges and limits on the temporal scale.	24
Figure 1.11: Paleogeographic reconstruction and thermal basement structure from the Early Jurassic until the Mid Jurassic.	24
Figure 1.12: Paleogeographic reconstruction and thermal basement structure from the Late Jurassic until the Early Cretaceous.	26
Figure 1.13: Possible ranges and limits of the lateral distribution.	29
Figure 1.14: Paleogeographic reconstruction and thermal basement structure from the Early Cretaceous until the Late Paleogene.	30

## CHAPTER 2: MULTI-CHRONOMETER THERMOCHRONOLOGICAL MODELING OF THE LATE NEOPROTEROZOIC TO RECENT t-T-EVOLUTION OF THE SE COASTAL REGION OF BRAZIL

Graphical Abstract of <i>CHAPTER 2</i> .	40
Figure 1: Simplified geological map of the study area in SE Brazil.	44
Figure 2: Geological units of the study area.	45
Figure 3: Stratigraphy of Paraná basin depositional sequences.	47
Figure 4: All thermochronological data of this study plotted against time.	49
Figure 5: Time (t)-temperature (T)-evolution of the individual blocks in SE Brazil.	51
Figure 6: Late Neoproterozoic to recent temperature evolution.	54
Figure 7: Calculated exhumation and subsidence rates.	55
Figure 8: Modeled interpolation maps of the age distribution.	56

## CHAPTER 3: LATE NEOPROTEROZOIC TO RECENT LONG-TERM t-T-EVOLUTION OF THE KAOKO AND DAMARA BELTS IN NW NAMIBIA

Graphical Abstract of <i>CHAPTER 3</i> .	40
Figure 1: Workflow showing the approach of <i>CHAPTER 3</i> .	69
Figure 2: Geological units of the study area.	70

Figure 3: Simplified geological map of the study area in NW Namibia with corresponding sample locations and numbers.	71
Figure 4: Simplified stratigraphic records of the Huab and Waterberg basins.	72
Figure 5: Numerical modeling set up for samples of the Namibian Damara Sequence.	74
Figure 6: Apatite fission-track (AFT) age distribution in the Kaoko and Damara belts.	76
Figure 7: Modeled interpolation map of apatite fission-track age distribution.	78
Figure 8: Zircon fission-track (ZFT) age distribution in the Kaoko and Damara belts.	79
Figure 9: Modeled interpolation map of zircon fission-track age distribution.	80
Figure 10: Results of the inverse numerical modeling.	81
Figure 11: Long-term time t-T-evolution of the individual areas of the Kaoko and Damara belts in NW Namibia.	82
Figure 12a: Calculated cooling and heating rates.	84
Figure 12b: Calculated cooling and heating rates.	86
Figure 13: Late Neoproterozoic to recent t-T-evolution of the SAPCM in NW Namibia.	88
Figure 14: Detailed interpolation map showing a possible modeled projection of the major apatite fission-track (AFT) data sets from Angola to NW Namibia.	90
Figure 15: Boomerang plots of the Namibian AFT data sets.	91
Figure 16: Lower to Upper Cretaceous SAPCM of Africa and South America modeled projection of the AFT age distribution.	92

#### **CHAPTER 4: APPLICATION OF STRATIGRAPHIC FRAMEWORKS AND THERMOCHRONOLOGICAL DATA ON THE MESOZOIC SW GONDWANA INTRAPLATE ENVIRONMENT TO RETRIEVE THE PARANÁ-ETENDEKA PLUME MOVEMENT**

Graphical Abstract of <i>CHAPTER 4</i> .	100
Figure 1: Geological archives of the Mesozoic SW Gondwana intraplate environment.	105
Figure 2: Workflow of <i>CHAPTER 4</i> .	106
Figure 3: Stratigraphic records of the sedimentary basins of the study area.	108
a: Stratigraphic records of the SW Africa basins.	108
b: Stratigraphic records of South America.	109
c: Stratigraphic records of marine basins along the central SAPCM	110
Figure 4: Plume stratigraphic mapping.	112
a: Plume stratigraphic mapping approach.	112
b: SW African basins.	113
c: South American basins.	114
d: Marine basins along the central SAPCM.	115
Figure 5: Plume stratigraphic mapped, lateral distribution of the Paraná-Etendeka LIP.	116
Figure 6: LTT data sets along the SAPCMs of SW Africa from NW Angola to South Africa and Zimbabwe, and South America from NE Brazil to NE Argentina	117
Figure 7: Apatite fission-track (AFT) age distribution showing all AFT data sets surrounding the Paraná-Etendeka LIP.	119
Figure 8: Histograms of the AFT data sets.	120

Figure 9: Modeled 3D-interpolation maps showing the Neoproterozoic basement, thermal structure of the plume central area.	121
a: Early Triassic to Early Jurassic.	121
b: Early to Late Jurassic.	122
c: Late Jurassic.	123
d: Lower to Upper Cretaceous.	124
Figure 10: Stratigraphic records vs. numerical modeling of LTT data sets vs. ePSF.	126
a: 220 Ma-195 Ma	126
b: 190 Ma-175 Ma.	127
c: 155 Ma-138 Ma.	128
d: 125 Ma-115 Ma.	129
Figure 11: Possible ranges and limits for the Paraná-Etendeka plume lateral distribution and on the temporal scale.	130

## CHAPTER 5: APPENDIX

### A: SUPPLEMENTARY MATERIAL FOR CHAPTER 2

Figure A. 1: 2D-transects of the post-rift- Early Cretaceous to recent geological evolution of the SAPCM in SE Brazil.	158
Figure A. 2: Area of research in SE Brazil showing topographic transects.	159
Figure A. 3: Paleozoic climate reconstruction of the research area.	160
Figure A. 4: Reconstruction of global, average surface temperatures since Carboniferous.	161
Figure A. 5: Age distribution maps for the individual thermochronometers.	162
5.1: Zircon fission-track (ZFT) ages.	162
5.2: Zircon (U-Th-(Sm))/He (ZHe) ages.	163
5.3: Apatite fission-track (AFT) ages.	164
5.4: Apatite (U-Th-(Sm))/He (AHe) ages.	165
Figure A. 6: Time (t)-Temperature (T)-evolution paths modeled with HeFty®.	166
6.1: A) BR10-01, B) BR10-04, C) BR10-05.	167
6.2: A) BR10-07, B) BR10-08, C) BR10-09, D) BR10-11.	168
6.3: A) BR09-01, B) BR10-12, C) BR10-15.	169
6.4: A) BR10-20, B) BR10-21, C) BR10-22.	170
6.5: A) BR10-23, B) BR10-24, C) BR10-25, D) BR10-26.	171
6.6: A) BR10-27, B) BR10-29.	172
6.7: A) BR09-45, B) BR09-46, C) BR09-47, D) BR09-50.	173
6.8: A) BR09-51, B) BR09-52, C) BR09-53, D) BR10-32.	174

### B: SUPPLEMENTARY MATERIAL FOR CHAPTER 3

Figure B. 1: Geo- and Thermochronometers and their effective closure temperatures.	194
Figure B. 2: Apatite fission-track (AFT) real age distribution in the Kaoko and Damara belts.	195
Figure B. 3: Zircon fission-track (ZFT) real age distribution in the Kaoko Belt.	196
Figure B. 4: Time (t)-Temperature (T)-evolution paths modeled with HeFty®.	197
4.1: A) NA11-71, B) NA11-77, C) NA11-84, D) NA11-86.	198
4.2: A) NA11-89, B) NA11-90, C) NA11-91, D) NA11-92.	199
4.3: A) NA11-94, B) NA11-95, C) NA11-96, D) NA11-103.	200

4.4: A) NA11-106, B) NA11-107, C) NA11-109, D) NA11-117	201
4.5: A) NA11-121, B) NA11-123, C) NA11-127, D) NA11-130	202
4.6: A) NA11-140.	203
4.7: A) NA11-09, B) NA11-10, C) NA11-11, D) NA11-42.	204
4.8: A) NA11-43, B) NA11-49, C) NA11-52, D) NA11-70.	205
Figure B. 5: Long-term time t-T-evolution for the individual geological areas with incorporated published geo- and thermochronological data.	206
5.1: Western Kaoko Zone – northern area (green).	206
5.2: Central Kaoko Zone – northern central area (blue).	207
5.3: Western and Central Kaoko Zone – central area (orange).	207
5.4: Southern Kaoko Belt – Ugab Zone (yellow).	208
5.5: Damara Belt – Northern Central Zone (red).	208
5.6: Damara Belt – Southern Zone (red).	209
Figure B. 6: Boomerang plots of the SE Brazilian AFT data sets.	210
Figure B. 7: Detailed interpolation map showing the AFT age distribution of the major data sets from NE to SE Brazil.	211
 C: SUPPLEMENTARY MATERIAL FOR CHAPTER 4	
Figure C. 1: The GEM for the NW Namibian Samples	245
Figure C. 2: The GEM for the SE Brazilian Samples (north)	246
Figure C. 3: The GEM for the SE Brazilian Samples (south)	247
Figure C. 4: Time (t)-Temperature (T)-evolution paths modeled with HeFty®.	248
4.1: A) BR10-01, B) BR10-04, C) BR10-05.	248
4.2: A) BR10-07, B) BR10-08, C) BR10-09, D) BR10-11.	249
4.3: A) BR09-01, B) BR10-12, C) BR10-15.	250
4.4: A) BR10-20, B) BR10-21, C) BR10-22.	251
4.5: A) BR10-23, B) BR10-24, C) BR10-25, D) BR10-26.	252
4.6: A) BR10-27, B) BR10-29.	253
4.7: A) BR09-45, B) BR09-46, C) BR09-47, D) BR09-50.	254
4.8: A) BR09-51, B) BR09-52, C) BR09-53, D) BR10-32.	255

# LIST OF TABLES

## CHAPTER 5: APPENDIX

### A: SUPPLEMENTARY MATERIAL FOR CHAPTER 2

Table A. 1: Sub phases of the syn- to post-rift evolution of the SAPCM.	138
Table A. 2: Overview of t-T-constraints derived from the geological model.	138
Table A. 3: All thermochronological samples with corresponding ages.	139
Table A. 4: Data tables for <i>CHAPTER 2</i> .	141
4.1: Summary of the dated samples in SE Brazil.	141
4.2: Zircon fission-track data of SE Brazil.	142
4.3: Zircon (U-Th-(Sm))/He data of SE Brazil.	143
4.4: Apatite fission-track data of SE Brazil.	144
4.5: Apatite fission-track length and Dpar data of SE Brazil.	145
4.6: Apatite (U-Th-(Sm))/He data of SE Brazil.	146
Table A. 5: Overview of sample data which was used for modeling in SE Brazil.	147
Table A. 6: Paraná Basin deposition sequences.	148
Table A. 7: Published geochronological data for SE Brazil.	149
Table A. 8: Calculated cooling and heating rates.	156

### B: SUPPLEMENTARY MATERIAL FOR CHAPTER 3

Table B. 1: Summary of all samples of the NW Namibian Kaoko and Damara belts.	178
Table B. 2: Apatite fission-track (AFT) data of Kaoko and Damara belt samples.	180
Table B. 3: Apatite fission-track (AFT) length and Dpar <sup>®</sup> data of the Kaoko and Damara belt samples.	182
Table B. 4: Zircon fission-track (ZFT) data of the Kaoko Belt.	184
Table B. 5: Published geochronological data for NW Namibia.	185
5.1: Western Kaoko Zone – northern area (green).	185
5.2: Central Kaoko Zone – northern central area (blue).	185
5.3: Western and Central Kaoko Zone – central area (orange).	186
5.4: Southern Kaoko Belt – Ugab Zone (yellow).	190
5.5: Damara Belt – Northern Central Zone (red).	191
5.6: Damara Belt – Southern Zone (red).	192

### C: SUPPLEMENTARY MATERIAL FOR CHAPTER 4

Table C. 1: Overview of all SAPCM related LTT data sets in SW Africa from NW Angola to South Africa and Zimbabwe, and in South America from NE Brazil to NE Argentina.	214
Table C. 2: All published AFT ages of SW Africa and Zimbabwe.	215
Table C. 3: All published AFT ages of the South American SAPCM.	228





# 1

## INTRODUCTION

---

### CONTENTS

1.1	STATE-OF-THE-ART	3
1.2	OBJECTIVES	7
1.3	STUDY AREA AND APPROACH	9
1.4	THESIS STRUCTURE	15
1.5	CONTRIBUTIONS	16
1.6	SUMMARY OF RESULTS AND DISCUSSION	17
1.7	FUTURE PERSPECTIVES	32
	LIST OF REFERENCES	33

---

„The forces which display continents are the same as those which produce great fold-mountain ranges. Continental drift, faults, and compressions, earthquakes, volcanicity, transgression cycles and polar wandering are undoubtedly connected causally on a grand scale. Their common intensification in certain periods of the Earth's history shows this to be true. However, what is cause and what effect, only the future will unveil.”

– Alfred Wegener, *“The Origins of Continents and Oceans”* (1929).

## 1.1 STATE-OF-THE-ART

Ever since humankind has wandered and inhabited the Earth, the appearance and complexity of geological features observed on the Earth's surface, such as mountain ranges, valleys, peneplains, and fluvial systems have presented a challenge to humans while continuously accompanying and influencing their evolution.

By the beginning of the 21<sup>st</sup> century, we understand these geological observations as expressions of an ever-changing topography that constitutes individual geological environments, e.g. orogenies, intracratonic planes, continental margins, and oceans on the surface of the geological system "Earth". It is understood that these landscape forming environments are connected, driven by endogenous dynamics – such as converging plate tectonics, diverging continental drift and breakup including rifting and sea-floor spreading, and magmatic activity – and affected exogenously by erosion, precipitation, weathering, and transport and deposition of sediment material.

Continuously, geodynamic research has brought forth unifying theories, such as the *Wilson Cycle* (Wilson, 1963, 1965) describing the connections between various plate tectonic stages (environments) and the interplay of endo- and exogenous forces on the Earth's surface (Fig. 1.1).

Consequently, plate tectonics and significant vertical movement on the Earth's surface were linked to the endogenous convection of material flow in the Earth's mantle and geo-dynamicists began to perceive vertical deflections and horizontal plate motion on the Earth's surface as a Lithosphere expression of convective motion in the sublithospheric

mantle (Crough, 1979; Fisher, 1989; Davies and Richards, 1992; Davies, 1999). Based on reconstructions of plate motion (Gordon and Jurdy, 1986; Lithgow-Bertelloni and Richards, 1997) integrating large scale mantle heterogeneities and mantle circulation, theoretical models of a viscous, convecting sublithospheric mantle were factored in potential influences on the dynamics of the asthenosphere, lithosphere and the Earth's surface (Morgan, 1965; McKenzie, 1977; Crough, 1979; Richards and Hager, 1984; Ricard et al., 1984; Hager et al., 1985; Hager and Gurnis, 1987; Fisher, 1889; Richards and Engebretson, 1992; Bunge et al., 1998; Bunge and Glasmacher, 2018).

Earth surface topography resulting from the dynamic motion of the sublithospheric mantle is thus defined as *dynamic topography* (Hager et al., 1985; Hager and Gurnis, 1987; Braun et al., 2010).

Time-dependent changes in *dynamic topography* link to the convective mantle flow regimes, and are caused by horizontal (*plate mode*) and vertical (*plume mode*) material flow, and exogenous climate change (Hager et al., 1985; Griffiths et al., 1989; Davies, 1999; Davies et al., 2019).

The "*plate mode*" refers primarily to cooling of the oceanic lithosphere and its descent into the mantle by subduction but may also appear on large spatial scales ( $\approx 10,000$  km) during long-wavelength mantle convection away from active subduction zones (Bunge et al., 1998). This occurs over long temporal scales ( $\approx 100$  Myr) as it can be interpreted physically as the time needed to overturn the large-scale mantle (Chase and Sprowl, 1983; Bunge et al., 1998; Müller et al., 2019).

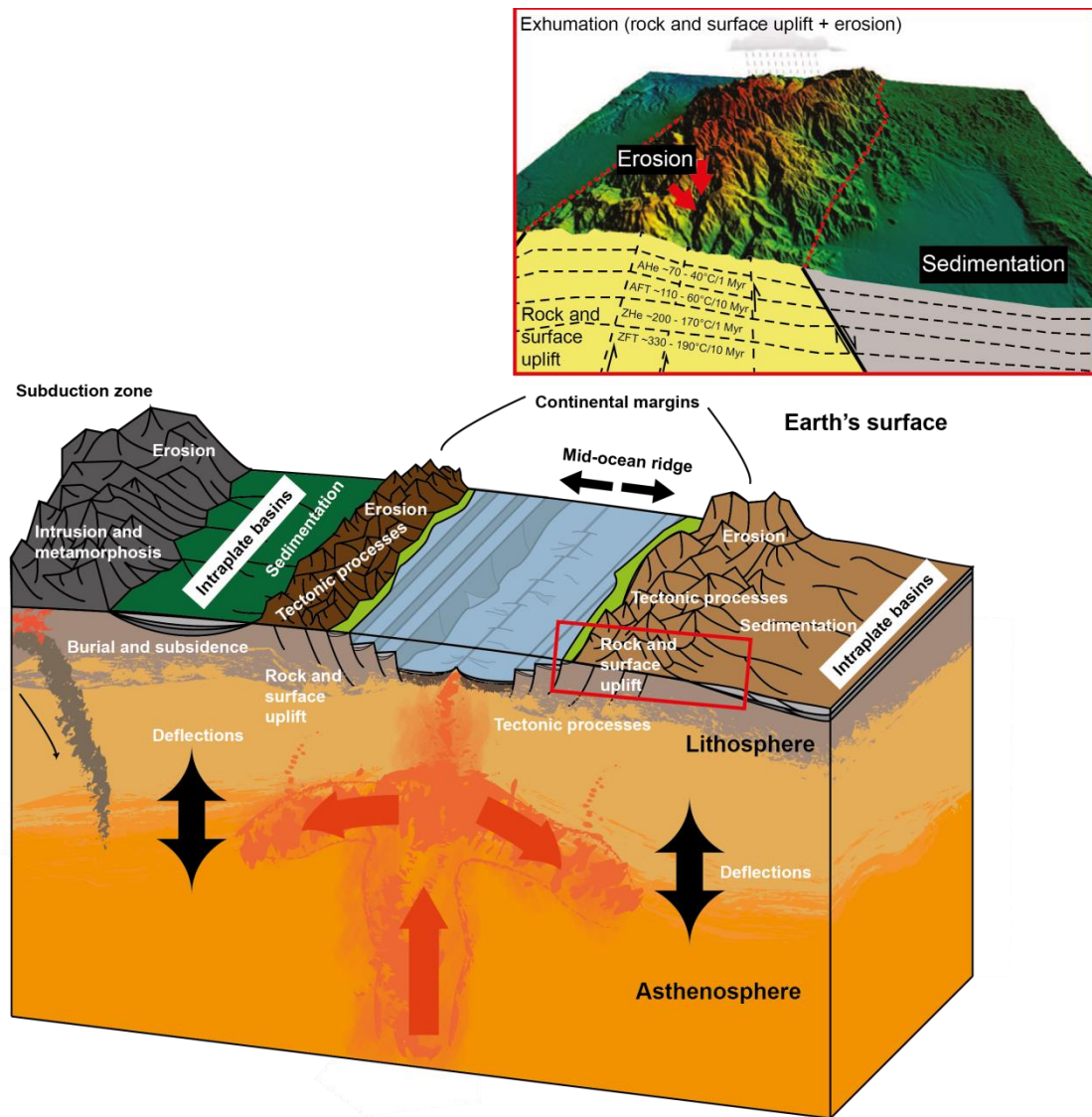


Figure 1.1: Geological features on the Earth’s surface, the upper most lithospheric mantle, and the asthenosphere showing the interaction of the various endo- and exogenous forces on, and near the Earth’s surface that lead to the *dynamic topography* driven long-term landscape forming processes. Red Box: Time-temperature ranges of the individual thermochronological thermochronometers indicating the history of cooling that rocks possibly experience through rock and surface uplift and erosion (exhumation) (modified after Ehlers and Farley, 2003; Bauer et al., 2010).

Whilst geologic evidence is consistent with these scales (Wilson, 1965), *dynamic topography* may also occur in shorter episodes of vertical movement at the Earth’s surface ( $\approx 10$  Myr) and appears at inter-regional scales seemingly unrelated to large-scale mantle convection of the plate mode (Griffiths and Campbell, 1990; Ernst and Buchan, 2001a, b; Şengör, 2001). Instead, the “*plume mode*” links to the rise

of mantle plumes from a hot thermal boundary layer at the *Core Mantle Boundary* (CMB) (Fig. 1.2). Mantle circulation models estimate the total plume heat transport in the range of 10 TW (e.g., Bunge, 2005; Schubert et al., 2009; Simmons et al., 2009), suggesting the plume mode to be responsible for  $\approx 30\%$  of the global mantle heat budget (Davies and Davies, 2020).

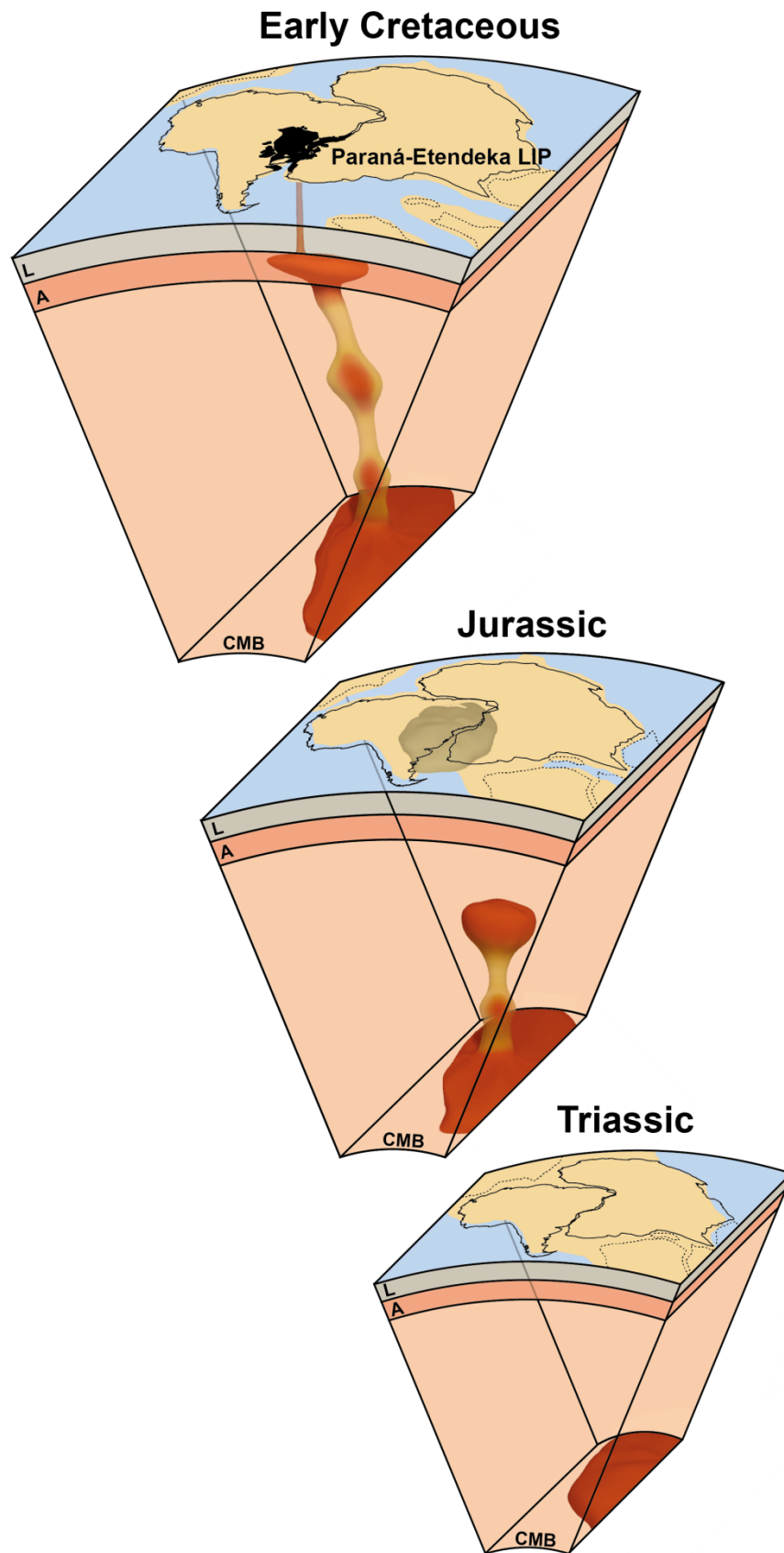


Figure 1.2: Visualization of the “*plume mode*” theory indicating the rise of the Paraná-Etendeka plume from the Core Mantle Boundary through the Earth’s mantle to its surface during the Mesozoic SW Gondwana intraplate environment. L.: Lithosphere; A.: Asthenosphere; CMB: Core Mantle Boundary.

Theoretical considerations based on the *dynamic topography* response of Earth models to internal non-lithospheric mantle loads (e.g., hot rising plumes or cold sinking lithosphere) imply deflections in the order of  $\pm 1$  km (Colli et al., 2016), causing the evolution, reactivation, and horizontal migration of lithospheric structures and transient topography changes on, and near the Earth's surface (Gurnis, 1988). There, long-term landscape forming processes (Fig. 1.1) are expressed by various signals and traces, e.g. extensive and localized tectonic and magmatic activity, rock and surface uplift and erosion (exhumation), burial, subsidence and inversion of sedimentary basins, and affect the tectono-thermal dynamics on the Earth's surface and within its upper crust (Franke, 2013; Müller et al., 2018).

Consequently, important information about the interaction of mantle plume movement and the Earth's surface can be derived from *dynamic topography* signals and traces stored in various geological archives, e.g. igneous, metamorphic, magmatic, and sedimentary rocks near, and on the Earth's surface.

Whereas geochronological analysis provides information about the intrusion, crystallization, and cooling of rocks during magmatic and metamorphic events, stratigraphic records of sedimentary basins convey insights into the evolution of sediments and sedimentary rocks during burial and exhumation.

Temperature sensitive methods, such as low temperature thermochronological (LTT) analysis provide important information about the cooling and heating history of rocks that contribute to the understanding of the long-term time (t)-temperature (T)-evolution of rocks in various geological environments (Fig. 1.1,

red box), i.e. along passive continental margins around the world (e.g., Japsen et al., 2012, 2014; Brown et al., 2014; Green et al., 2015, 2017; Braun, 2018).

However, until recently, most of the research focused on specific geological archives and the geological evolution of individual geological environments of the *Wilson Cycle*, e.g., the intrusion, crystallization and metamorphic deformation with orogens, the syn- to post-rift and breakup evolution of passive continental margins, or the formation and development of intraplate sedimentary basins. Therefore, this thesis also investigates the geological evolution of distinct stages of the *Wilson Cycle* in detail, but further aims to connect these individual geological environments to retrieve a coherent long-term t-T-evolution, i.e. the development from an active orogeny to intraplate and later passive continental margin environment induced by the interaction of "plate" and "plume mode". The study combines multiple geological archives in research areas suitable to address the following research objectives.

## 1.2 OBJECTIVES

This thesis focuses on the reconstruction of the coherent long-term t-T-evolution of the Neoproterozoic rocks along the South Atlantic passive continental margins (SAPCM's) in SE Brazil and NW Namibia. By investigating the tectono-thermal dynamics and long-term landscape forming geological processes on, and near the Earth's surface, the research addresses the following key features accordingly to their chronological order constraint from the Late Neoproterozoic to recent time:

*The Late Neoproterozoic to Early Paleozoic syn- to post-Pan African/Brasiliano orogenic cooling and exhumation of the basement rocks.*

Thermochronological data sets including those presented in this thesis, only record the cooling of rocks of the upper most crust covering temperature ranges of <300°C (Reiners and Brandon, 2006; Reiners and Shuster, 2009). However, the stratigraphic records of the sedimentary basins in the study areas show the onset of sedimentation during Mid Paleozoic time (Johnson et al., 1996; Stollhofen et al., 1999; Milani et al., 2007) indicating that rocks must have been below 300°C at the time. Therefore, the thermochronological data sets of this study only allow tracing back the cooling of the rocks since the Late Paleozoic.

Yet, this thesis intends to capitalize on the connection of different geological stages leading to the long-term landscape and t-T-evolution covering the entire thermo-dynamic processes, such as the crystallization and intrusion of rocks, followed by post-orogenic cooling, and exhumation to the Earth's surface. Thus,

this research adds geo- and thermo-chronological data close to the presented sample locations covering temperature ranges of >300°C to connect information of the preceding thermo-dynamic processes to the modeled t-T-evolution constrained by the thermo-chronological data of this research.

Through this reconstruction and coupling of the thermodynamic processes, the thesis aims to address the timing and magnitude, and rates of the Late Neoproterozoic to Early Paleozoic syn- to post-Pan African/Brasiliano orogenic cooling and exhumation of the individual crustal segments of the Neoproterozoic basement.

*The quantification of timing and rates of subsidence during the major SW Gondwana intracratonic sedimentary basin formation.*

Following the Pan-African/Brasiliano orogeny, the SW Gondwana intraplate environment experienced rock and surface uplift and erosion caused by post-orogenic denudation of the Neoproterozoic mobile belts during the Early to Mid Paleozoic and Carboniferous to Permian syn- to post Gondwana Ice Age processes (Frimmel et al., 1998; Goscombe et al., 2003a, b; Goscombe and Gray, 2007; Miller et al., 2008; Basei et al., 2010). This mobilization, transport and deposition of sedimentary material led to the development of the major SW Gondwana intraplate basins (Stollhofen et al., 1999; Milani et al., 2007; Basei et al., 2010). The research focuses on the timing, magnitude, and rates of subsidence during the major SW Gondwana intraplate sedimentary basin formation in order to quantify the role of basin inversion and sediment column, and their effects on the thermochronological

data of the study areas. Consequently, the research also provides a method to verify the stratigraphic data in the published geological record.

*The timing and causes, and rates of exhumation during the pre- to syn-rift South Atlantic breakup processes, the interaction of plume movement, and the magmatic activity of the Paraná-Etendeka LIP.*

This time window that comprises the pre- to syn-rift South Atlantic breakup processes is characterized by different geological features that shall be addressed explicitly within this thesis. The research focusses on the Early Mesozoic transition from the SW Gondwana intraplate basin formation to the pre-South Atlantic breakup possibly plume-influenced rock and surface uplift and erosion leading to the inversion of sedimentary basins within the study area.

By applying theoretical models, such as the event-based plume stratigraphic framework (ePSF, Friedrich et al., 2008), the study aims to quantify the impact of plume movement on the intraplate, tectono-thermal evolution of the upper crust and its sedimentary basins surrounding the Early Cretaceous Paraná-Etendeka LIP. To this end, two comprehensive geological archives are used, the stratigraphic records of the SW Gondwana intraplate sedimentary basins, and all available thermochronological data sets surrounding the Paraná-Etendeka LIP area to retrieve signals and traces of the vertical and horizontal material flow preceding the Paraná-Etendeka flood basalt event (Krob et al., 2020b).

In this context, questions arise whether, and in what way, such geological archives

can retrieve plume event preceding rock and surface uplift, and what uncertainties have to be dealt with. The research sets out to determine ranges for the influence of plume movement on the Earth's surface on the spatial and temporal scales. Furthermore, it intends to precisely quantify the thermal influence of the Paraná-Etendeka magmatic activity on the Neoproterozoic basement rocks of the study areas.

*Post-South Atlantic breakup and rift evolution, surface uplift and erosion, and tectonic activity.*

The thesis integrates new thermochronological data into the previously published geological record for both sides of the SAPCM's, e.g. Green (1986), Gallagher et al. (1994, 1995, 1998), Raab et al. (2002), Brown, et al. (2014), and Engelmann de Oliveira et al. (2016a, b) that on the one hand can help to verify the observations made by the published research, and on the other hand provides new insights into the complex development of the rift-stages during the South Atlantic breakup. Therefore, this thesis concentrates on the post-breakup cooling of the Neo-proterozoic basement rocks and investigates a possible reactivation of the predominant tectonic structures (Franco-Magalhaes et al., 2010; Karl et al., 2013; Salomon et al., 2015).

The study tests the possibility of an earlier exhumation of the Late Cretaceous Neoproterozoic basement to the Earth's surface and addresses the role, extension, and thermal influence derived from subsidence by the tectonic reactivation of the Cenozoic onshore graben systems on the Neoproterozoic basement rocks in SE Brazil.



Their role and thickness during the geological evolution of the margin will be discussed and comparisons drawn to the post-rift evolution in NW Namibia.

*Quantification of timing and duration of single geological environments and the connection of different geological stages of the Wilson Cycle.*

The connection of different geological stages of the *Wilson Cycle* remains complex and up to the present most of the research along the South Atlantic passive continental margin (SAPCM) in SE Brazil and NW Namibia was either focused on the Precambrian deformation, the Paleozoic to Mesozoic intraplate development, or the syn- to post-rift evolution (e.g., Goscombe et al. 2003a, b, 2007, 2017; Foster et al., 2009; Raab et al., 2002, 2005; Catuneanu et al., 2005; Miller et al, 2008; Brown et al., 2014). For the first time, this research aims to reconstruct an entire t-T-evolution connecting these individual geological stages beginning with the Late Neoproterozoic to Early Paleozoic syn- to post-Pan African/Brasiliano orogenic, followed by the Late Paleozoic to Mesozoic intracratonic basin formation within the SW Gondwana intraplate environment, to the syn- to post-South Atlantic breakup and rifting evolution (Krob et al., 2019, 2020a).

This approach shall enable the detailed quantification of the timing and duration of individual stages of the Wilson Cycle and connects those stages to retrieve a coherent long-term t-T-evolution providing insights into the development from an active orogeny to a intraplate and later passive continental margin environment.

### 1.3 STUDY AREA AND APPROACH

The present SAPCM's of South America and SW Africa, as part of the formerly connected SW Gondwana intraplate environment, constitute an excellent key area and geological setting for understanding and reconstructing various plate tectonic stages of the *Wilson Cycle* (Fig 1.3).

Beginning in the Late Neoproterozoic to Early Paleozoic, the contemporary SAPCMs were part of the large-scale Pan African/Brasiliano orogeny leading to the formation of the Gondwana supercontinent. During the Palaeozoic and Lower Mesozoic (stage 1), the intracratonic environment was characterized by erosion, denudation of the Neoproterozoic mobile belts, and large basin formation (stage 2, Krob et al., 2019, 2020). Pre- to syn-rift (embryonic), ocean spreading (juvenile) and post-breakup (mature) processes enabled the evolution from the intraplate to the recent SAPCM environment since the Upper Mesozoic (stage 3, Krob et al., 2019, 2020a).

Furthermore, the study areas (Fig. 1.4) provide several geological archives having stored field and laboratory observations of the geological evolution since the Late Neoproterozoic, i.e. the Paraná-Etendeka related dike swarms and flood basalt depositions of the Paraná-Etendeka Large Igneous Province (LIP) showing a geochemical signature of lithospheric- and asthenospheric mantle source (Trumbull et al., 2004, 2007). Therefore, it is very convenient to investigate the SAPCM of SE Brazil and NW Namibia using the available geological archives (Krob et al., 2019, 2020a).

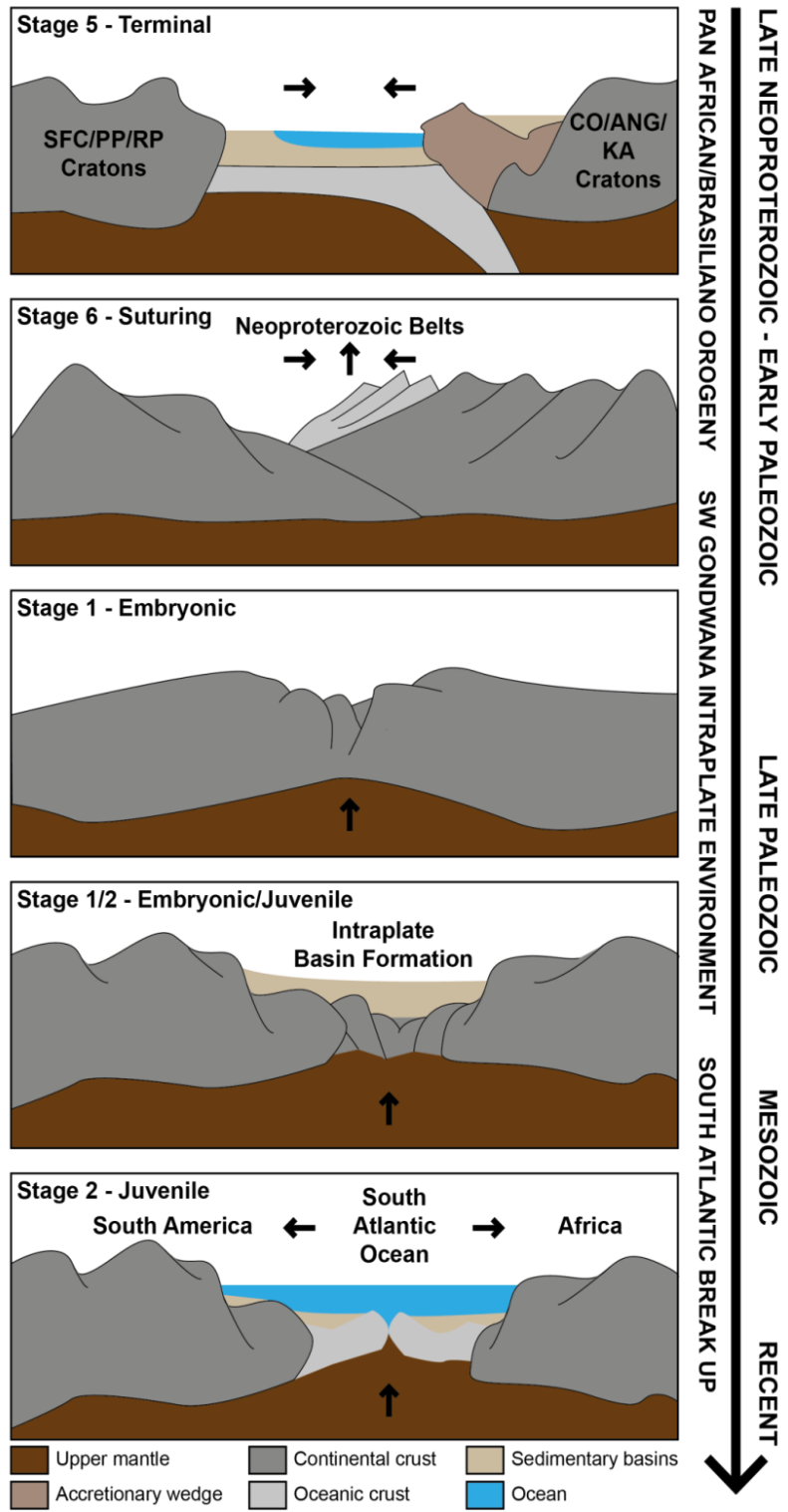


Figure 1.3: Schematic view of the *Wilson Cycle* (Wilson, 1965, 1966) showing the single stages that affected the geological evolution of the study areas since the Late Neoproterozoic (modified and redrawn from Pearson Prentice Hall, Inc., 2008). SFC: São Francisco Craton; PP: Paranapanema Cratons; RP: Rio de la Plata Craton; CO: Congo Craton; ANG: Angola Craton; KA: Kalahari Craton.

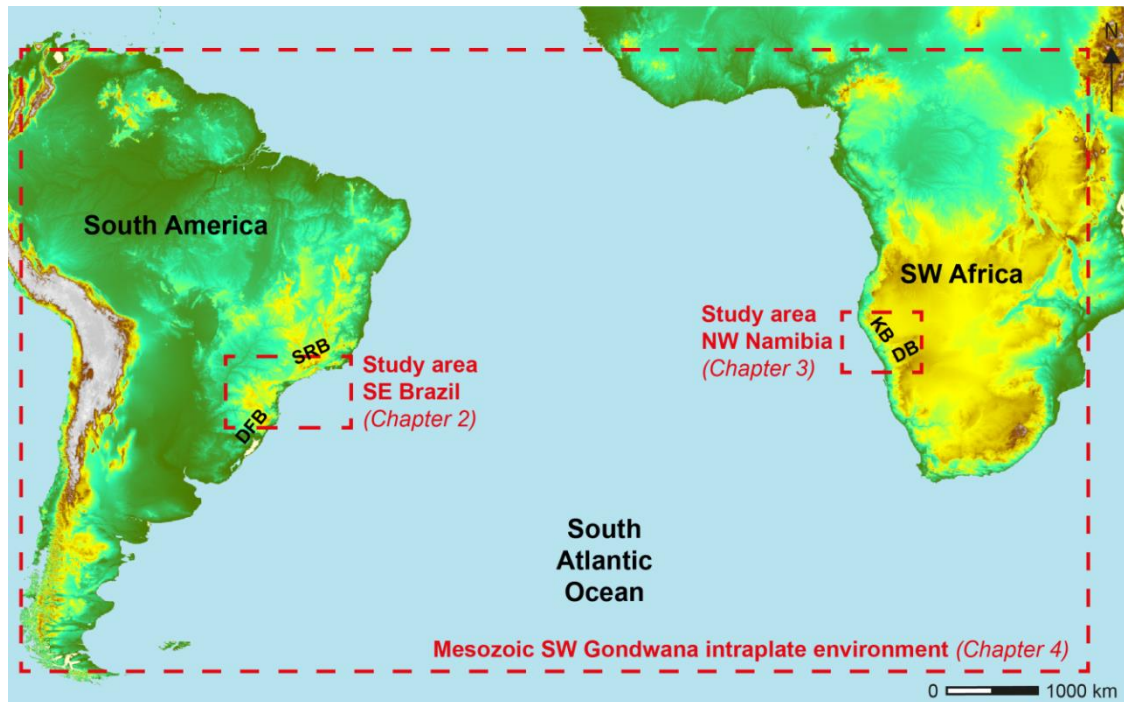


Figure 1.4: Overview of the specific study areas (red boxes) approached in the individual chapters of this thesis. While the present South Atlantic continental margins of SE Brazil in South America and NW Namibia in SW Africa served as the base for the CHAPTERS 2 and 3, the former Mesozoic SW Gondwana intraplate environment, contemporarily represented by the South American and SW African continents including the transition to the offshore basins of the South Atlantic Ocean provided the bedrock for the research of CHAPTER 4. SRB: Southern Ribeira Belt; DFB: Dom Feliciano Belt; KB; Kaoko Belt; DB: Damara Belt.

Whereas the regional geology in SE Brazil provides the basement rocks of the ( $\approx$ margin parallel) southern Ribeira and Dom Feliciano Neoproterozoic orogenic belts, basement rocks of the ( $\approx$ margin parallel) Kaoko and the ( $\approx$ margin perpendicular) Damara Neoproterozoic orogenic belts characterize the regional geology of the NW Namibian SAPCM. Both sides display Paleozoic and Mesozoic sedimentary and volcanic rocks covering the orogenic Neoproterozoic basement. Therefore, this geological setting provides a unique natural laboratory to study in detail sole parts of the *Wilson Cycle* (Wilson, 1963, 1965) and beyond that allows combining individual geological

sections to retrieve a long-term landscape and t-T-evolution (Krob et al., 2019, 2020a). In SE Brazil, the study area (Fig. 1.5) reaches from north of the city of Rio de Janeiro to south of the city of Florianópolis, and from the coast to the inland Ponta Grossa Arc (PGA, Fig. 1,5). The topography of the SE Brazilian SAPCM can be divided into three distinct areas as follows. Beginning in the north, the two mountain ranges of the inland Serra da Mantiqueira (SdaM) and the coastal Serra do Mar (SdoM) extend from south of the city of São Paulo, in the São Paulo state to the NE of the Rio de Janeiro state, just north of its eponymous capital.

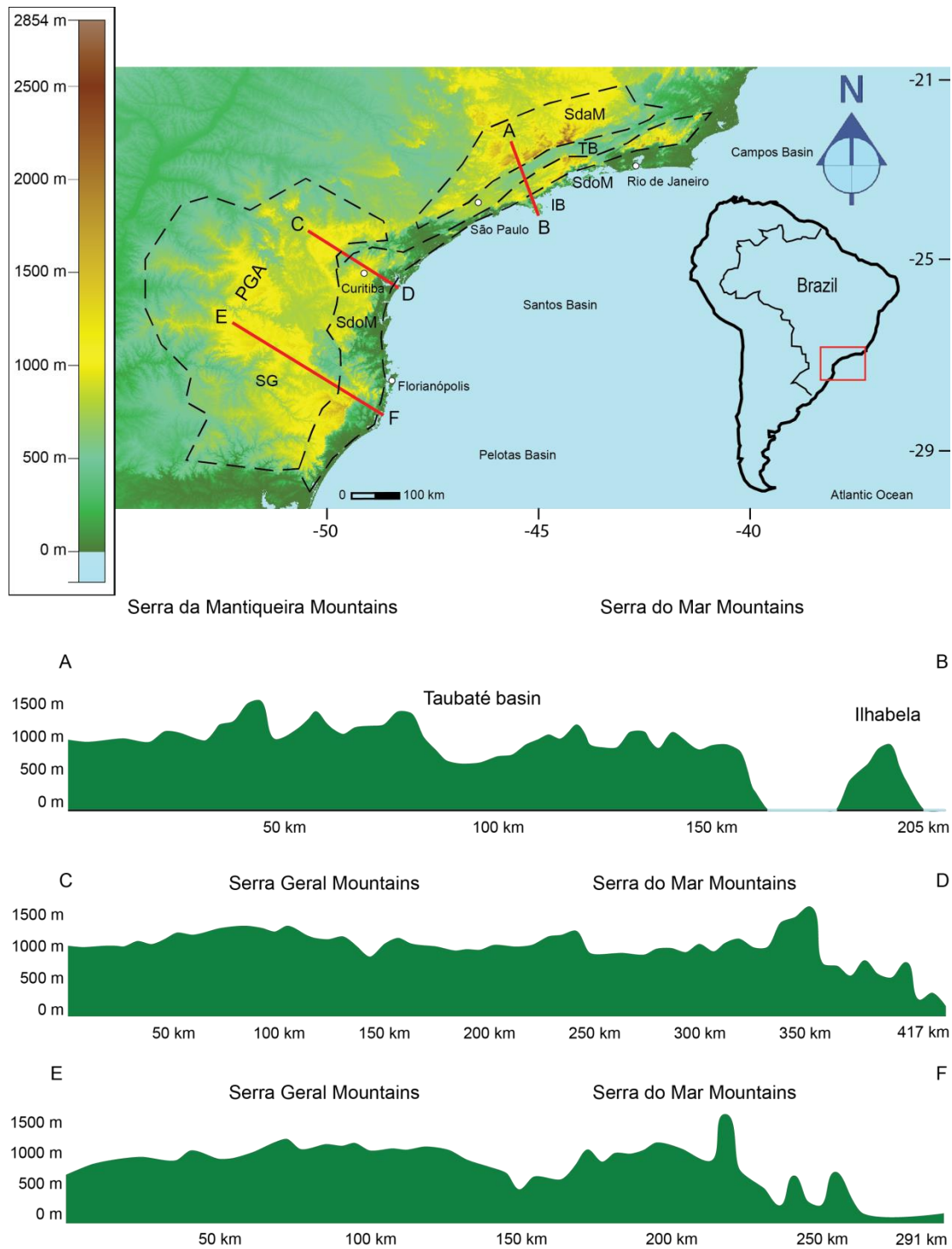


Figure 1.5: Area of research in SE Brazil showing topographic transects (A-B, C-D, and E-F) within the study area of CHAPTER 2. PGA: Ponta Grossa Arc; SG: Serra Geral, SdoM: Serra do Mar, SdaM: Serra da Mantiqueira, TB: Taubaté Basin, IB: Ilhabela (São Sebastião Island) (Stippich, in prep).

Both NE-SW trending mountain ranges are separated by the Taubaté Basin (TB). The escarpment (Fig. 1.5; A-B) reaches elevations of  $\approx 1000$ - $1500$  m a.s.l. in the inland Serra da Mantiqueira mountain range, is interrupted by the Taubaté Basin where elevations drop down to  $\approx 500$  m a.s.l., and rise again within the Serra do Mar mountains lying approximately around 1000 m above sea level (a.s.l.).

This topography can also be observed further south in the surroundings of the city of Curitiba in the Paraná state. There,

the southern tip of the Taubaté Basin graben system separates the inland Serra Geral (SG) mountains from the coastal Serra do Mar. Generally, elevations are slightly lower ( $\approx 1000$  m a.s.l.), only reaching  $\approx 1500$  m a.s.l. in the Serra do Mar mountain range (Fig. 1.5; C-D) and correlate with those obtained in transect south of the city of Florianópolis in the Santa Catarina state (Fig. 1.5; E-F). In the south, the elevation drops from more than  $\approx 1250$  m a.s.l. down to the coastal lowlands of  $\approx 60$  m a.s.l.

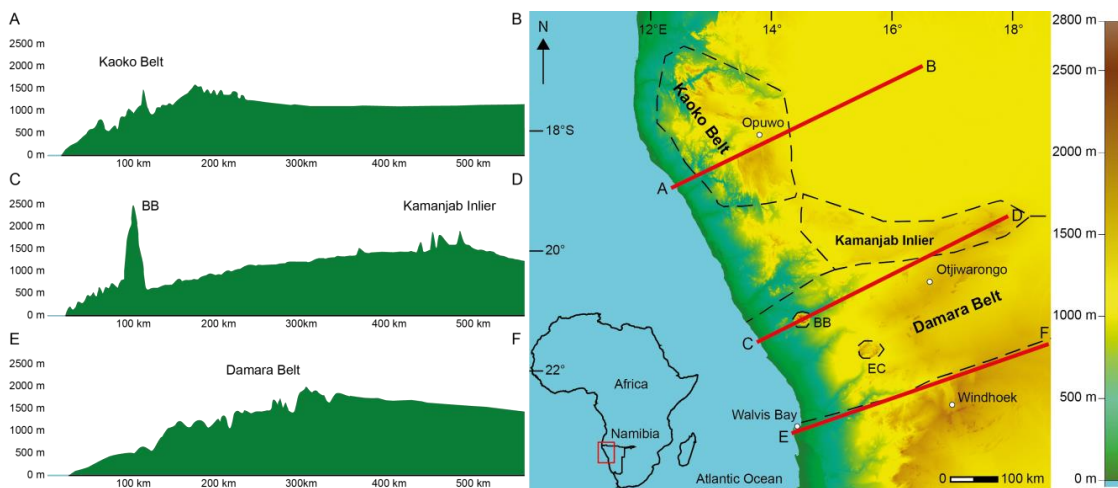


Figure 1.6: Area of research in NW Namibia showing topographic transects (A-B, C-D, and E-F) within the study area of CHAPTER 3. BB: Brandberg; EC: Erongo Complex.

In NW Namibia, the study area extends from the Angolan border in the north to the area around Walvis Bay in the Erongo State and the City of Windhoek, in the Khomas State and from the coast to the inner highlands of the Omaheke and Kunene states. The topography reaches similar extension as the escarpment in SE Brazil. In the northern Kaoko Belt, elevation increases from sea level to  $\approx 1500$  m a.s.l., just south of the city of Opuwo and continues indicating a plateau towards the inland of  $\approx 1000$  m a.s.l. (Fig. 1.6; A-B). Further south, the second transect (Fig. 1.6; C-D) shows a slowly increasing

topography interrupted by the volcanic Brandberg (BB) that reaches almost  $\approx 2500$  m a.s.l. Then the topography increases continuously from  $\approx 500$  m to  $\approx 1500$  m a.s.l. towards the Kamanjab Inlier further inland, just north of the city of Otjiwarongo, in the Otjozondjupa state. South of the Brandberg, the Erongo Complex (EC) also reaches similar elevations interrupting the interregional topography. In the south of the Erongo state, the topography rises from sea level around Walvis Bay to over 1500 m a.s.l. north of Windhoek (Fig. 1.6; E-F).

While *CHAPTER 2* and *3* are limited to the Neoproterozoic rocks of the onshore SAPCM of SE Brazil and NW Namibia, *CHAPTER 4* widens the study area to encompass the Mesozoic SW Gondwana intraplate environment (Fig. 1.4). This allows for the integration of the comprehensive geological record, including stratigraphic records of continental and offshore basins, and thermochronological datasets, both having stored field and laboratory observations of the sedimentological, thermal, and magmatic evolution of both, the South American and SW African continent. Building on this, the systematic approach of this research shall be outlined in the following.

Based mainly on field work, sample preparation, and fission-track analyses, this study provides thermochronological data derived from apatite and zircon fission-track (AFT and ZFT, respectively), and apatite and zircon (U-Th-(Sm))/He dating (AHe and ZHe, respectively) that were performed on Neoproterozoic metamorphic rocks along the SAPCM's of SE Brazil and NW Namibia. Sample preparation and analyses followed the same protocol as, e.g. Karl et al., 2013, and Kollenz, 2015. Whenever possible all four thermochronometry dating techniques were applied to the samples, allowing for a more robust evaluation of the spatial and temporal cooling of the sampled rocks.

This thesis presents and processes the thermochronological data including the numerical modeling of the t-T-evolution using the software code HeFTy (Ketcham et al., 2005, 2007a, b), the calculation of exhumation and subsidence rates, and the visualization of the thermochronological data and the modeled t-T-evolution. Furthermore, existing geo- and thermochronological data derived from the

published geological record was integrated and attached to the modeled t-T-evolution to reconstruct a possible coherent Late Neoproterozoic to recent t-T-evolution including pre- to syn-Pan African/Brasiliano intrusion and crystallization, post-orogenic rock cooling and exhumation, intraplate basin formation and subsidence, plume influenced pre- to syn-South Atlantic breakup, and post-South Atlantic rifting processes. Hence, this study uses published geochronological data of Neoproterozoic basement samples such as U-Pb, Sm-Nd and Rb-Sr analyses, and low temperature thermochronology (LTT) data revealed by K/Ar,  $^{40}\text{Ar}/^{39}\text{Ar}$  analyses. Based on the entirety of geological data, the research proposes a possible t-T-evolution of the Neoproterozoic basement showing its thermal structure at specific time steps since the Late Neoproterozoic.

Finally, this research focuses on the application of stratigraphic frameworks and thermochronological data on the Mesozoic SW Gondwana intraplate environment by combining the two geological archives, stratigraphic records of sedimentary basins, and thermochronological data to retrieve a possible t-T-evolution influenced by the Paraná-Etendeka plume movement.

However, each publication provides a detailed description of the approach and methodology, as well as further information on the regional geological setting of the individual study areas.

## 1.4 THESIS STRUCTURE

This thesis comprises three publications that have already been released in peer-reviewed international journals and focus on the reconstruction of the t-T-evolution of the Neoproterozoic rocks along the contemporary SAPCM's of SE Brazil and NW Namibia. All publications were composed with the contribution of several co-authors that have been acknowledged explicitly in the *DECLARATION OF INDEPENDENCE*, in the following *CHAPTER 1.5*, and during the *CRedit author statements* prepended to each publication. Moreover, each publication is self-containing, incorporating abstract, introduction, geology, methodology, results, discussion and conclusion subchapters:

*CHAPTER 2* presents a new multi-thermochronometer data set including AFT, ZFT, AHe, and ZHe data to reconstruct a detailed t-T-evolution of the SE Brazilian SAPCM from the Late Neoproterozoic to recent, and therefore, integrates the published geo- and thermochronological record of SE Brazil. Thereby, it combines the existing data with the numerical modeling of new thermochronological data presented within this study. Through this reconstruction, the study addresses the timing and magnitude of the Late Neoproterozoic to recent thermodynamic processes near and on the Earth's surface, and of the upper most crust. This chapter is already published in the *Journal of South American Earth Sciences, Volume 92 (2019), 77-94*, <https://doi.org/10.1016/j.jsames.2019.02.012>.

*CHAPTER 3* focuses on the Late Neoproterozoic to recent long-term t-T-evolution of the Kaoko and Damara belts in NW Namibia, and therefore, acts as the counterpart to *CHAPTER 2*. The study combines numerical modeling of new thermochronological data with previously published geo- and thermochronological data reconstructing a coherent long-term t-T-evolution of the Neoproterozoic basement rocks including the discussion of thermo-dynamic processes on the Earth's surface, and of the upper most crust. Moreover, the study highlights possible t-T-paths, introduces differentiated exhumation rates and draws a comparison to the t-T-evolution of other areas along the SAPCM's of South America and SW Africa, including the opposite part, the SE Brazilian SAPCM. This chapter is already published in the *International Journal of Earth Sciences*.

<https://doi.org/10.1007/s00531-020-01819-7>.

*CHAPTER 4* follows a new approach applying stratigraphic frameworks and thermo-chronological data to the Mesozoic SW Gondwana intraplate environment to retrieve the Paraná-Etendeka plume movement. Therefore, this study provides a comprehensive overview of existing geological archives, namely the stratigraphic records of the continental and marine basins of the Mesozoic SW Gondwana intraplate environment and all published thermo-chronological data along the SAPCM's of South America and SW Africa. The study aims to identify signals and traces of plume movement in the geological archives using a theoretical model to define spatial and temporal ranges of plume movement-influenced areas near and on the Earth's surface.

Thereby, the study combines both archives to numerically model a possible t-T-evolution of the SE Brazilian and NW Namibian key areas. This chapter is already published in the journal of *Gondwana Research*, <https://doi.org/10.1016/j.gr.2020.02.010>.

## 1.5 CONTRIBUTIONS

The presented chapters have benefited from the input of several researches and students which shall be acknowledged in the following:

The involvement of Dipl. Geol. Markus Karl, Dr. Sebastian Kollenz, and Dr. Melissa Perner has contributed to *CHAPTER 2* including the field trip organization, sampling, sample preparation, and dating analyses.

My contribution comprises the dating analyses of the Laguna Block samples during the work for my Bachelor thesis, the processing of the collected data, the numerical modeling, the compilation of geo- and thermochronological data from the published geological record, and the discussion. Moreover, I authored the original manuscript, figures, and tables that served for the publication of the findings. Furthermore, Prof. Dr. Ulrich A. Glasmacher and Prof. Dr. Peter Hackspacher have contributed through their support during field trip, in data processing, and vigorous discussions. Lastly, five unknown reviewers were involved in the critical reading and constructive revisions of the accepted manuscripts.

Dipl. Geol. Markus Karl, Dr. Melissa Perner and Dr. Eric Salomon were involved in the field trip organization and sampling for *CHAPTER 3*. Dipl. Geol. Daniel Eldracher (former Menges) conducted sample preparation and the dating analyses.

My input concerns data processing, numerical modeling, the compilation of the geo- and thermochronological data from the published geological record, and discussion. Moreover, I authored the original manuscript, figures, and tables that served for the successful publication of the findings. Furthermore, Prof. Dr. Ulrich A. Glasmacher and Prof. Dr. Peter Hackspacher contributed through supervision of the field trips and support in data processing, and vigorous discussions. Lastly, Prof. Dr. Paul Green, Prof. Dr. Peter Kukla and two unknown reviewers were involved in the critical reading and constructive revisions during the successful publishing process.

My involvement in *CHAPTER 4* includes the compilation of the data of the geological archives, the data processing, numerical modeling, and discussion. Moreover, I authored the original manuscript writing, figures, and tables that served for the successful publication of the findings. Prof. Dr. Ulrich A. Glasmacher, Prof. Dr. Hans-Peter Bunge, and Prof. Dr. Anke M. Friedrich provided the idea to this work and were involved in the discussions and critical reading. Lastly, two unknown reviewers were involved in the critical reading and constructive revisions of the accepted manuscript.



## 1.6 SUMMARY OF RESULTS, AND CONCLUSIONS

For the first time, this thesis succeeds to model a coherent long-term t-T-evolution following the geological evolution of SW Gondwana from a Late Neoproterozoic active orogen to an intraplate, and later passive continental margin environment under the influence of the “plate” and “plume mode” using various combined geological archives.

Through this reconstruction, the thesis proves Precambrian metamorphic and magmatic, and Paleozoic to Mesozoic sedimentary and volcanic rocks to be important geological archives storing temperature-sensitive information about the upper mantle and crustal tectono-thermal dynamics. Thereby, the research allows assumptions related to the long-term landscape forming processes on the Earth’s surface, e.g. extensive and localized tectonic and volcanic activity, exhumation (rock and surface uplift and erosion), and burial and crustal scale subsidence.

Summarizing, the thesis presents new thermochronological data from fission-track and (U-Th-(Sm))/He analysis on apatite and zircon derived from Neoproterozoic basement rocks of SE Brazil and NW Namibia.

Furthermore, the study integrates over 35 previously published thermochronological data sets meaning >1300 apatite fission-track ages alone, along the SAPCM’s of South America and SW Africa.

Moreover, the research compiled comprehensive geo- and thermo-

chronological data sets derived from U-Pb, Sm-Nd, Rb-Sr, and K/Ar and  $^{40}\text{Ar}/^{39}\text{Ar}$  analysis to provide information about the tectono-thermal processes, such as the intrusion, crystallization, metamorphism, and cooling of rocks in deeper temperature ranges over 300°C of the upper most crust. Additionally, the compilation of 18 stratigraphic records of the major continental and marine sedimentary basins of the Mesozoic SW Gondwana intraplate environment permits interpretations of the sedimentary processes, e.g. deposition and burial of sedimentary rocks, and their exhumation on the Earth’s surface.

Where the thermochronological data of this study covering temperature ranges below 300°C lack in constraining coherent t-T-paths, the research benefits from the combination of geo- and thermo-chronological data and sedimentological knowledge from the published geological record, and therefore, guarantees a viable t-T-evolution of the Neoproterozoic rocks of the study areas. Possible exhumation and subsidence rates derived from calculated cooling and heating rates provide new insights in the geological processes on the Earth’s surface.

Consequently, this research contributes significantly to the understanding of the interplay of the “plate” and “plume mode”-driven endo- and exogenous dynamics and their influences on the *dynamic topography* of the Earth’s surface.

In the following, the thesis addresses the key objectives accordingly to their chronological order constraint from the Late Neoproterozoic to recent time:

*The Late Neoproterozoic to Early Paleozoic syn- to post-Pan African/Brasiliano orogenic cooling and exhumation of the basement rocks.*

The Late Neoproterozoic to Early Paleozoic evolution of SW Gondwana is characterized by the Pan African/Brasiliano orogeny under the driving forces of the “plate mode”. The thesis succeeds to capitalize on the combination of the geo- and thermochronological data to retrieve the syn- to post-orogenic evolution of the different crustal segments within the study areas, and therefore, connects the individual thermodynamic processes, such as the intrusion, crystallization, and metamorphism of rocks, and their post-orogenic cooling, and exhumation to the Earth’s surface.

The syn- to post-Late Neoproterozoic to Early Paleozoic t-T-evolution of the SAPCM in SE Brazil is shown to be very complex. While the results of the northern, northern inland (Ponta Grossa Arc, PGA), and the southern areas led assume a rather fast cooling and direct exhumation to the Earth’s surface, the central part of the SAPCM, the Pan African/Brasiliano post-orogenic cooling and exhumation of Neoproterozoic rocks occur to be threefold (Krob et al., 2019):

(1) A rapid Late Neoproterozoic exhumation of the basement rocks is followed by (2) a phase of relatively thermal stability where rocks are kept within the crust (at temperatures of about 300-200°C) from the Early Cambrian to the Devonian, and (3) a second fast

exhumation moving Neoproterozoic rocks to the surface until the Late Devonian (Krob et al., 2019). The northern and southern parts indicate a distinct syn- to post-orogenic exhumation to the surface implying a faster cooling, and erosion from the Late Neoproterozoic to Devonian/Carboniferous.

Generally, the central areas are better constrained by the published record, and therefore, allow the assumption of the proposed threefold evolution. In addition, the lack of available data in the northern, PGA, and southern areas results in the revealed perpetual cooling and exhumation.

Nevertheless, those observations correlate with the revealed t-T-evolution of the NW Namibian crustal segments that also show three phases of exhumation with an almost stable period in between two phases of rapid exhumation (Krob et al., 2020a).

However, the published record of SE Brazil infers that syn- to late orogenic intrusion and crystallization of the rocks set in earlier than on the NW Namibian side (Krob et al., 2019; Krob et al., 2020a). Consequently, syn- to post orogenic cooling indicates to have set in earlier on the SE Brazilian side.

This is reflected by the interpolation maps of the modeled thermal Neoproterozoic basement structure showing lower temperatures in near surface areas reached earlier by the rocks in SE Brazil than by the NW Namibian rocks (Fig. 1.7, Early Ordovician). In general, the thermal structure on the Namibian indicates that the crustal segments cooled down rather evenly showing a rather homogenous temperature distribution.

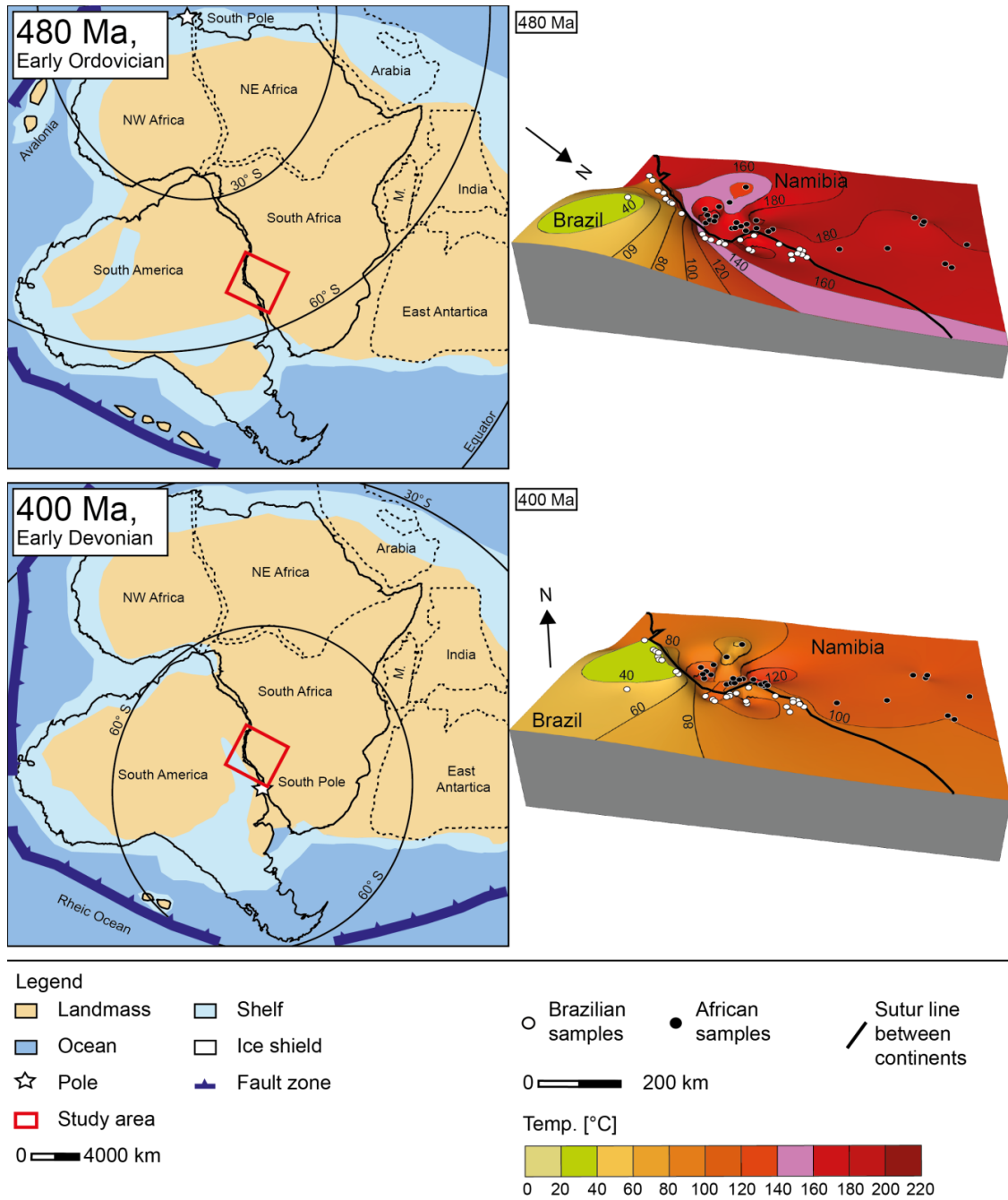


Figure 1.7: Left panel: Paleogeographic reconstruction of the Gondwana intraplate environment during the Early Ordovician and the Early Devonian (redrawn after Torsvik and Cocks, 2017). Red box shows the study area of SE Brazil and NW Namibia. Right Panel: Modeled 3D-interpolation maps showing the Neoproterozoic basement thermal structure of the SE Brazilian-NW Namibian study at the corresponding time. The maps are based on paleotemperatures taken at specific time steps and were derived from the “weighted-mean” paths of the modeled t-T evolution of each modeled sample (black and white dots). Red colors indicate higher temperatures and therefore, are generally assumed to lie deeper within the upper crust. Light colors rather show near surface areas (y-axis shows temperature). Purple area: 160-140°C; Green area: 40-20°C. The black thick line indicates the former suture line between the continents. The geographical reconstruction and graphical extraction were done after Torsvik et al. (2009, 2013).

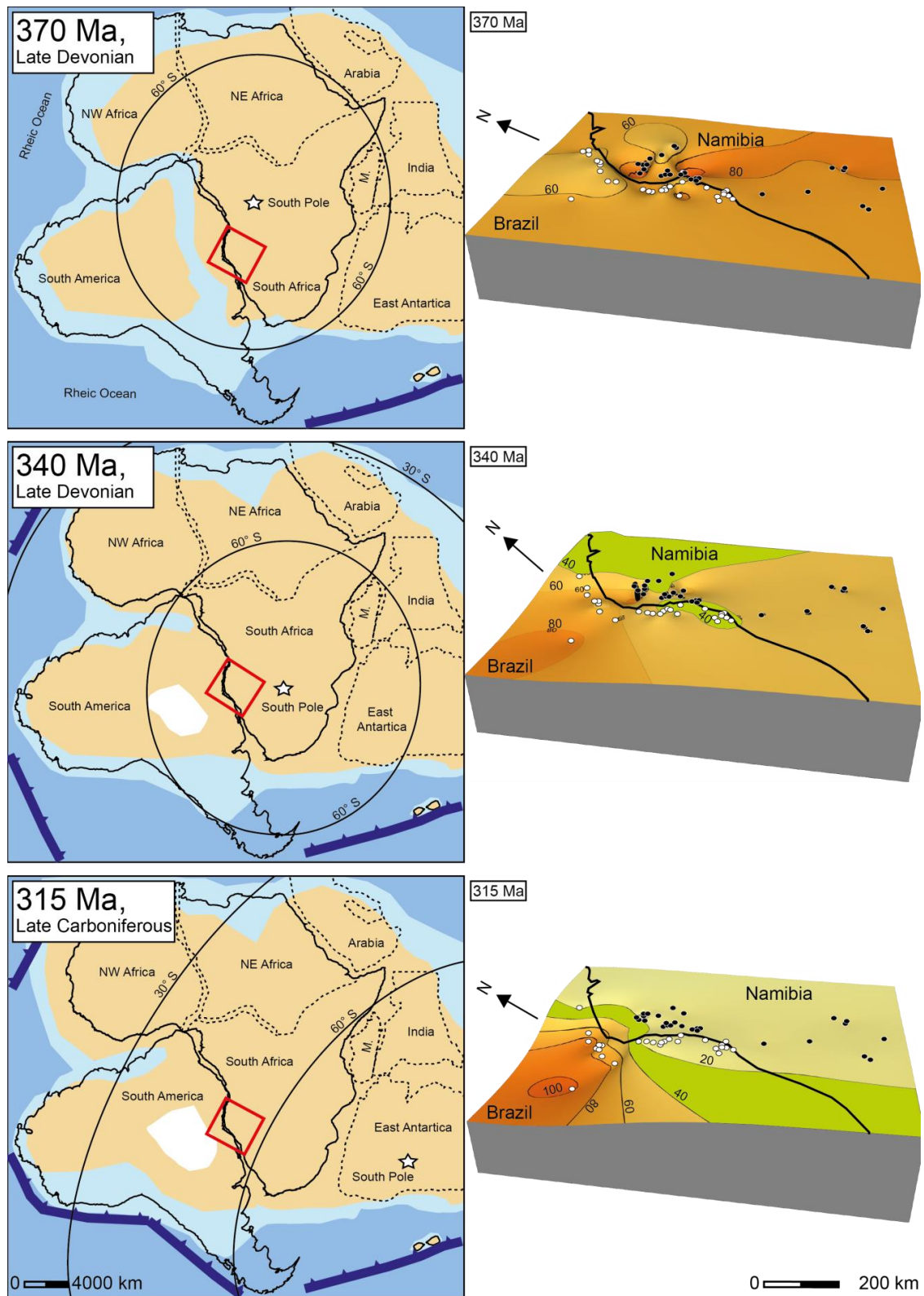


Figure 1.8: (Previous page) Left panel: Paleogeographic reconstruction of the Gondwana intraplate environment from the Late Devonian until the Late Carboniferous (redrawn after Torsvik and Cocks, 2017). Red box shows the study area of SE Brazil and NW Namibia. Right Panel: Modeled 3D-interpolation maps showing the Neoproterozoic basement thermal structure of the SE Brazilian-NW Namibian study at the corresponding time. For further information, please see Figure 1.7.

Nonetheless, the comprehensive compilation of geo- and thermochronological data available in NW Namibia reveals much differentiated cooling paths within the different geological venues that shall not be disregarded but altogether are assumed less relevant for the presentative cooling history of the entire crustal segments.

The final cooling and surface uplift of the Neoproterozoic basement rocks is most likely triggered by significant tectonic and surface uplift, and erosion during the Devonian (SE Brazil) and Late Devonian/Early Carboniferous (NW Namibia). Changes in climate and direction of erosion and transport of sediments during the Late Paleozoic Gondwana glaciation (Montañez and Poulsen, 2013), and later, far-field effects of the Gondwanide orogeny (Zalán et al., 1991; Trouw & De Wit, 1999) also may have provoked the transition of the predominant tectonic structures. Therefore, this thesis expects glacial erosion and transport of sedimentary material combined with a temporally lower geothermal gradient during the Late Paleozoic Gondwana Ice House (Montañez and Poulsen, 2013) to have caused the displayed Mid to Late Paleozoic ZFT and AFT age distribution (Montañez and Poulsen, 2013; Krob et al., 2020a, b).

During this period, both areas indicate a more homogeneous thermal structure before the Paraná Basin subsidence sets in (Fig. 1.8).

However, the thermal structure indicates that rocks in SE Brazil already experienced subsidence while the NW Namibian rocks were kept close to the Earth's surface in temperatures ranges of  $\approx 40\text{-}20^\circ\text{C}$ . Montañez and Poulsen, 2013 also assume significant amounts of sediment material transported to the southern and western parts of the Gondwana intraplate environment that support the displayed thermal structure.

*The quantification of timing and rates of subsidence during the major SW Gondwana intracratonic sedimentary basin formation.*

The Late Paleozoic t-T-evolution marks a transition on the predominant geological conditions and is characterized by the intraplate basin formation of the major continental sedimentary basin of the Paleozoic to Mesozoic SW Gondwana intraplate environment (Fig. 1.9).

In SE Brazil, the t-T-evolution of the rocks show trends of ongoing subsidence during depositional sequences of the Paraná Basin from Mid to Late Paleozoic.

However, thermochronological data are unable to constrain high temperatures corresponding to the accumulation of expected overlying sediment thicknesses suggested by the existing stratigraphy (Milani et al., 2007). In general, the Namibian rocks did not experience as much subsidence as the SE Brazilian rocks, which sets in later towards the end of the Paleozoic.

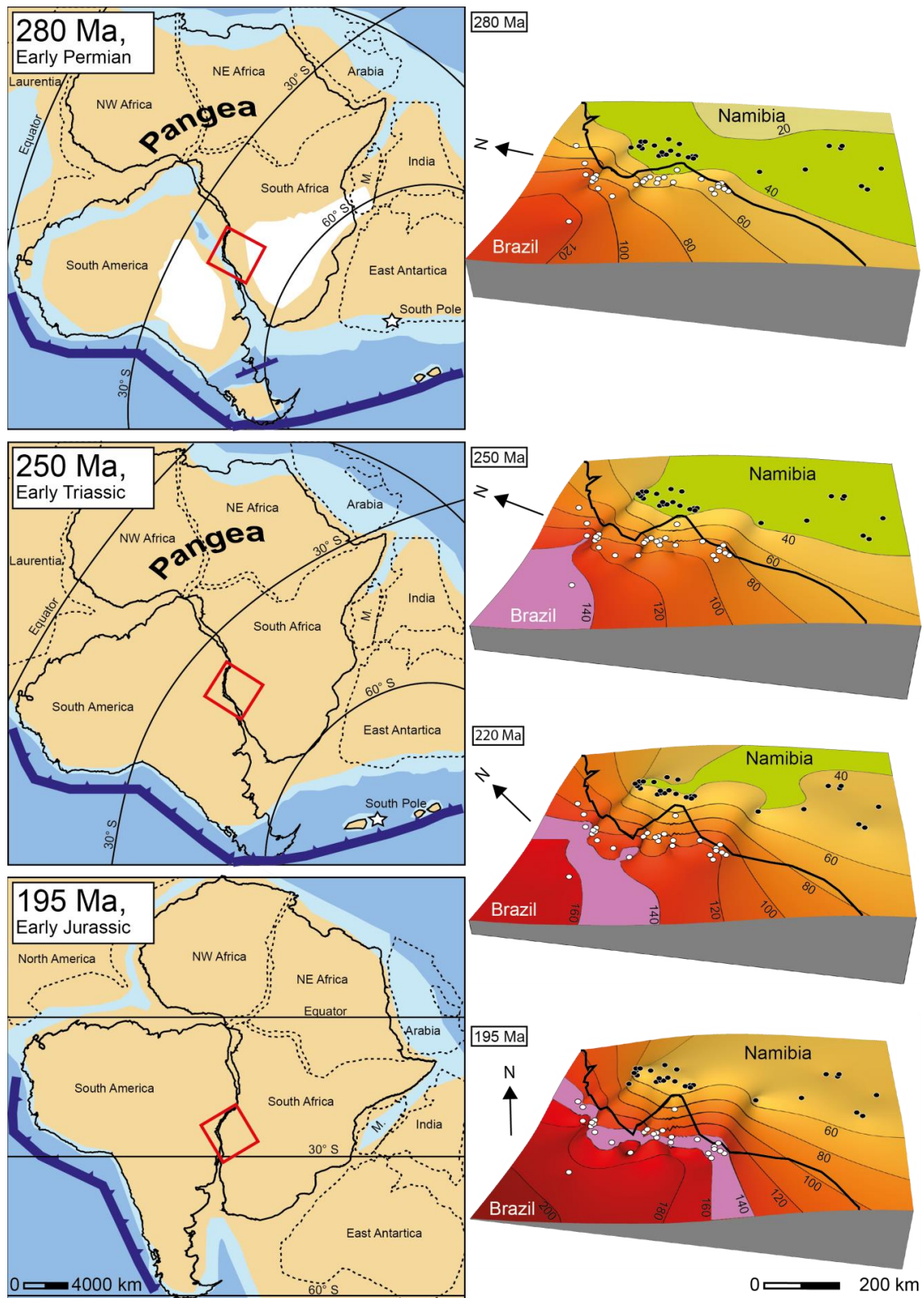


Figure 1.9: (Previous page) Left panel: Paleogeographic reconstruction of the Gondwana intraplate environment from the Early Permian until the Early Jurassic (redrawn after Torsvik and Cocks, 2017). Red box shows the study area of SE Brazil and NW Namibia. Right Panel: Modeled 3D-interpolation maps showing the Neoproterozoic basement thermal structure of the SE Brazilian-NW Namibian study at the corresponding time. For further information, please see Figure 1.7.

Whereas the Brazilian rocks reach temperatures of between  $\approx 100^{\circ}\text{C}$  and  $\approx 200^{\circ}\text{C}$ , the basement surface on the Namibian side only reaches maximum temperatures of  $\approx 100^{\circ}\text{C}$  by the end of the Triassic meaning a difference of  $\approx 3$  km of overlying sediments. Unfortunately, the thermochronological ages of this research do not store further evidence to better constrain overlying sediment thicknesses as most of the data experienced thermal overprint by the later Paraná-Etendeka event. Nonetheless, most of the ZFT and ZHe data of both study areas prove that rocks most likely did not experience temperatures  $>180^{\circ}\text{C}$  since the post-orogenic cooling, and therefore do not permit sediment overburden as described in the published literature (Milani et al., 2007). However, the modeled interpolation maps of the thermal structure of the basement rocks indicate that rocks could have reached temperature of up to  $\approx 160^{\circ}\text{C}$  implying almost 5000 m of overlying sediments by the beginning of the Mesozoic at least for the SE Brazilian area.

Summarizing, the results of this research leave the question whether rocks store the influences of the Late Paleozoic to Mesozoic SW Gondwana intraplate basin formation partly unanswered. Whereas AFT and AHe data do not allow any assumptions, ZFT and ZHe data can at least constrain the upper limits of the reached temperatures by the accumulated overlying sediment material.

*The timing and causes, and rates of exhumation during the pre- to syn-rift South Atlantic breakup processes induced by the “plume mode” and influence of the magmatic activity of the Paraná-Etendeka LIP.*

The investigation of the Paraná-Etendeka plume induced pre- to syn-rift South Atlantic breakup processes took centre stage during this thesis (CHAPTER 4). The research proved that both archives reveal significant signals and traces well in advance of the flood basalt eruptions on the Earth's surface and it is possible to recognize the timing of events and distinct patterns of flood basalt event preceding rock and surface uplift consistent with those expected by theoretical models of mantle plume movement (Krob et al., 2020b).

Thermochronological data from the SAPCMs of SW Africa from NW Angola to South Africa, and of South America, from NE Brazil to northern Argentina expose centers of thermally overprinted AFT ages ( $<135$  Ma) that overlap with the Paraná-Etendeka related dike swarms and flood basalt depositions indicating a significant thermal influence by the volcanic activity of the Paraná-Etendeka LIP. Combined with the timing of hiatuses and unconformities in the stratigraphy records, the AFT data permits to define permissible ranges on the temporal scale (Fig. 1.10).

Krob et al., 2020b propose a viable transit time range prior the Paraná-Etendeka LIP event between  $\sim 85$  Ma and  $\sim 30$  Ma leading to a permissible event horizon between  $\sim 220$  Ma and  $\sim 165$  Ma.

The interpolation maps of the modeled thermal basement structure visualize the t-T-evolution under the influence of the “plume mode” showing a halt of the ongoing subsidence during the Paraná and NW Namibian basin formation by the end of the Triassic/Early Jurassic as a signal of the first plume movement (Figs. 1.9, 1.11).

# Possible ranges on the temporal scale

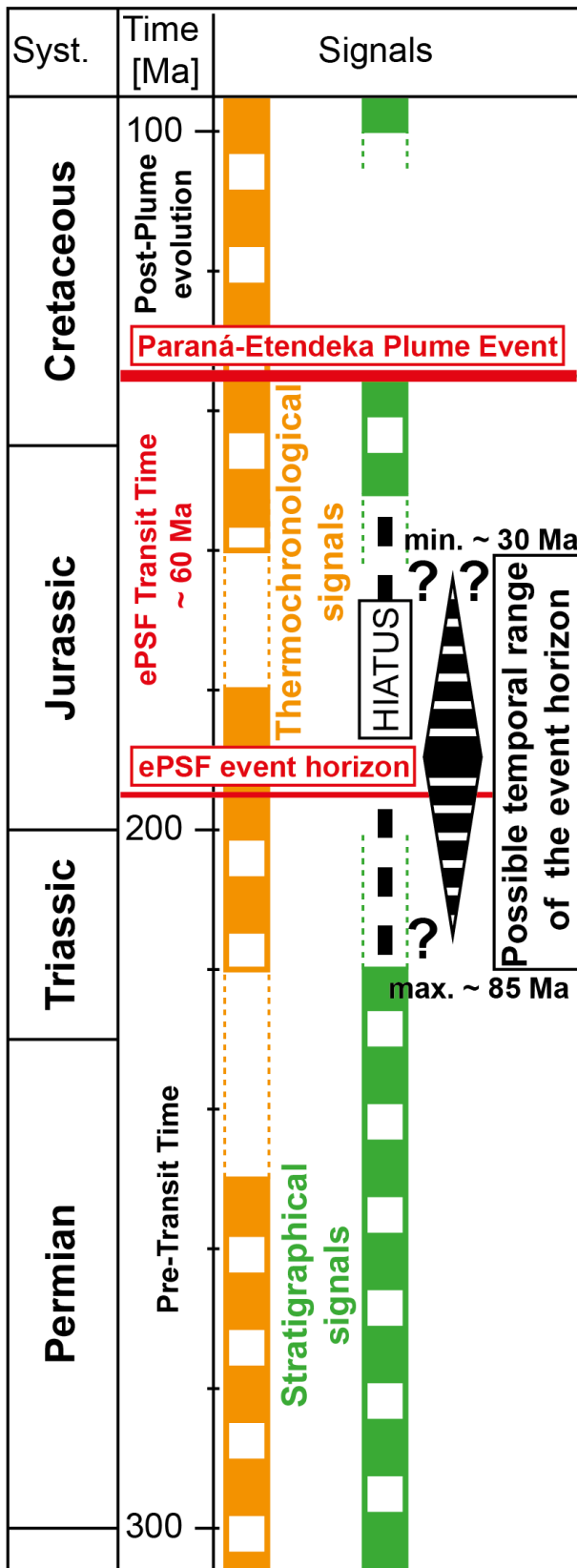
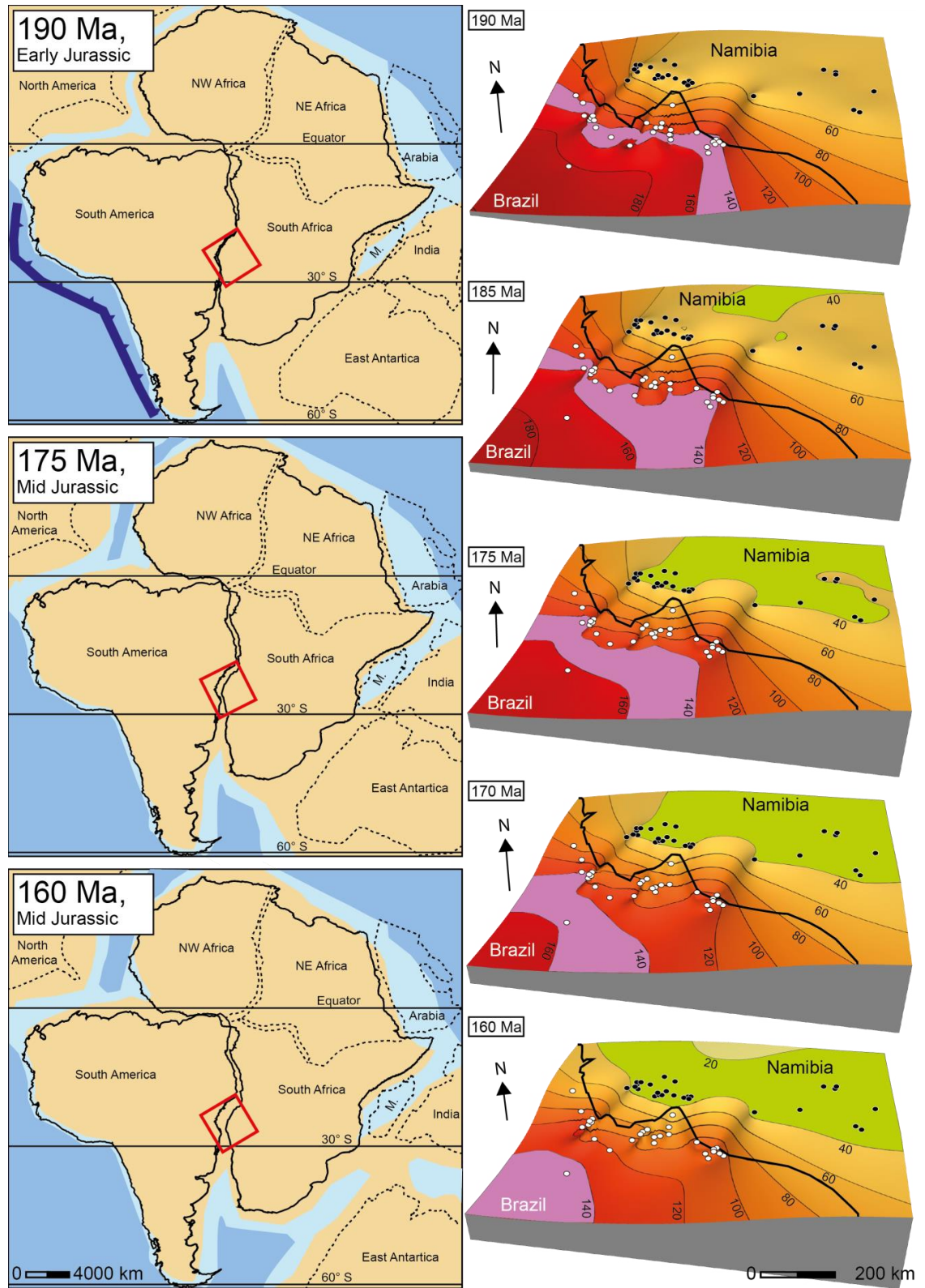


Figure 1.10: (Left) Possible ranges and temporal limits of the Paraná-Etendeka plume transit time during the plume ascent (modified after Krob et al., 2020b). The temporal scale includes the Paraná-Etendeka plume event ( $\approx 135$  Ma), and the event horizon ( $\approx 195$  Ma) and transit time ( $\approx 60$  Ma) predicted by the ePSF (red bars). Orange bars illustrate the thermochronological signals indicating the age peaks of all published AFT cooling ages. Green bars signify the depositional sequences recorded in the stratigraphic records of the central basins (Paraná, Huab, and Waterberg). Black dashed line: maximum hiatuses in the stratigraphic records. Black rhombus indicates the possible temporal ranges of the event horizon assuming a decreasing probability towards the poorly constrained upper and lower limits. Both archives leave room for a possible event horizon between  $\approx 220$  Ma and  $\approx 165$  Ma, and a Paraná-Etendeka transit time between  $\approx 30$  Ma and  $\approx 85$  Ma.

Figure 1.11: (Next page) Left panel: Paleogeographic reconstruction of the Gondwana intraplate environment from the Early Jurassic until the Mid Jurassic (redrawn after Torsvik and Cocks, 2017). Red box shows the study area of SE Brazil and NW Namibia. Right Panel: Modeled 3D-interpolation maps showing the Neoproterozoic basement thermal structure of the SE Brazilian-NW Namibian study at the corresponding time. For further information, please see Figure 1.7.





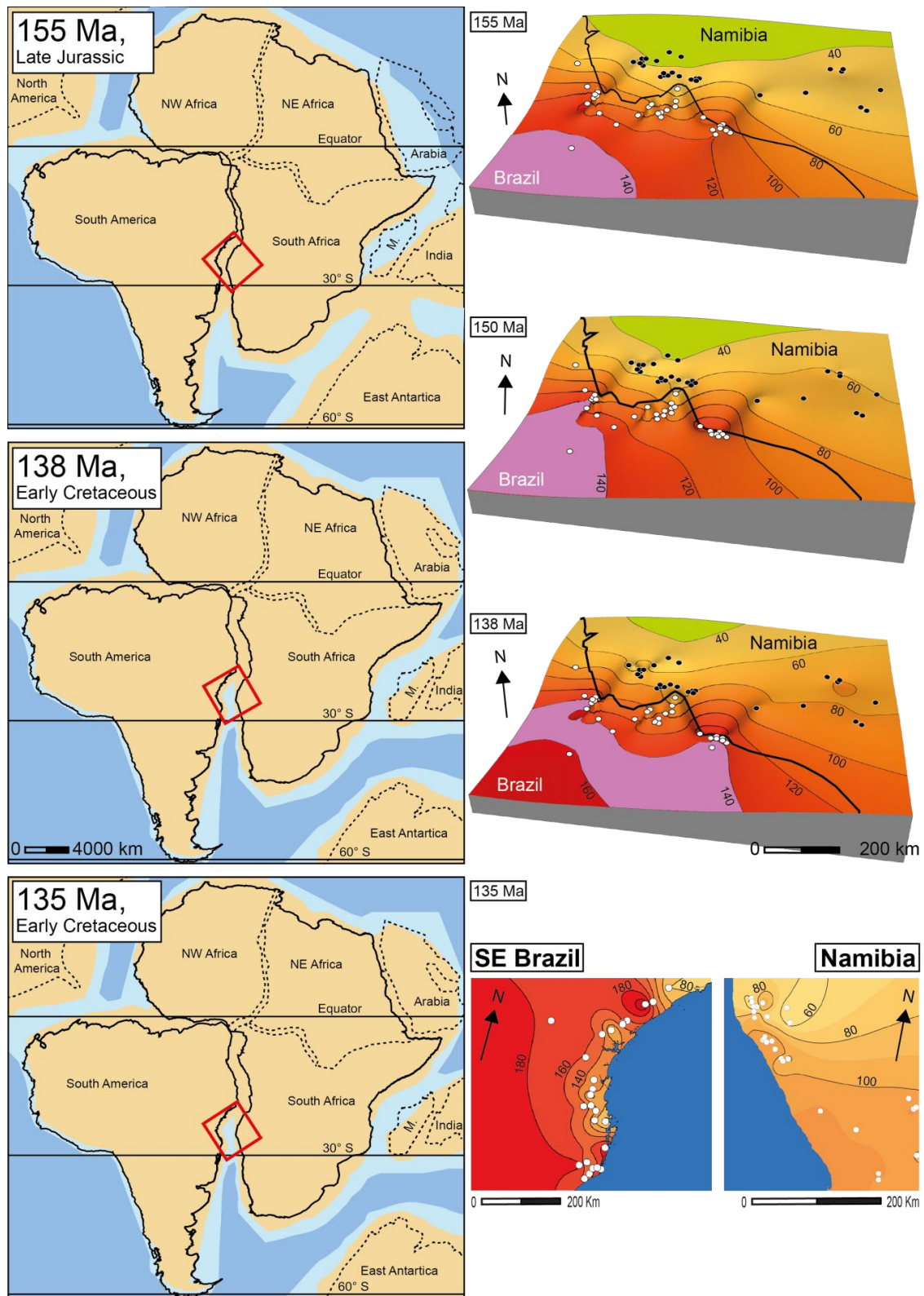


Figure 1.12: (Previous page) Left panel: Paleogeographic reconstruction of the Gondwana intraplate environment from the Late Jurassic until the Early Cretaceous (redrawn after Torsvik and Cocks, 2017). Red box shows the study area of SE Brazil and NW Namibia. Right Panel: Modeled 3D-interpolation maps showing the Neoproterozoic basement thermal structure of the SE Brazilian-NW Namibian study at the corresponding time. For further information, please see Figure 1.7.

Following, this short phase of rock and surface uplift, a renewed increase of temperatures is caused by the thermal influence of the Paraná-Etendeka plume head at the base of the lithosphere and the emplacement of dike swarms within the upper most crust (Fig. 1.12).

Consequently, the emplacement of Paraná-Etendeka related dike swarms causing local volcanic activity, and the eruption of flood basalts characterize the Late Jurassic to Early Cretaceous t-T-evolution of the SW Gondwana intraplate environment.

Whereas maximum temperatures on the SE Brazilian side range between  $\approx 80$ - $160^\circ\text{C}$  in the northern regions and exceed  $200^\circ\text{C}$  in the southern region (Krob et al., 2019), the basement rocks of NW Namibia only range between  $\approx 60$ - $120^\circ\text{C}$  at the time (Krob et al. 2020a, b).

It can be assumed that rocks were either locally influenced for a relatively short time by the convective heat flow (geothermal gradient) caused by the crosscutting dike swarms and accompanied local volcanic activity, and/or reheated due to the overburden thicknesses of the erupted flood basalts (Krob et al., 2020b).

Furthermore, the plume stratigraphic mapping, using the stratigraphic records is suitable to demark a possible plume center, plume margins and distal regions (Friedrich et al., 2018). In addition, the compiled thermochronological data expose centers showing a significant thermal Paraná-Etendeka plume influence. Together, both geological archives allow this research to map permissible spatial dimensions of a Paraná-Etendeka plume movement-influenced area (Fig. 1.12).

However, this research critically analysed the revealed uncertainties, such as the lateral significance and reliability of

stratigraphic records, or the overprint of AFT age information, that occur in both contemporary geological archives.

Therefore, the studies draw the conclusions that temporarily both data sets lack in sensitivity to determine a precise spatial dimension on the Earth's surface, and exact transit time and timing of initial plume movement preceding the Paraná-Etendeka flood basalt eruptions (Krob et al., 2020b). Consequently, the research does not commit itself to neglect the high uncertainty concerning the very outer limits of the permissible ranges.

Nevertheless, the combined data is able to validate the ePSF approach providing an excellent fit to retrieve the possible Paraná-Etendeka plume movement when applied to the Mesozoic SW Gondwana intraplate environment. The combined data proposes an asymmetric central area that ranges from  $\sim 2.3$  Mio km<sup>2</sup> (Fig. 1.12, (1)) to  $\sim 2.75$  Mio km<sup>2</sup> (Fig. 1.12, (2)) consistent with the predicted geological patterns of a possible plume center.

This area allows diameters between  $\approx 2000$  km (horizontally, E-W) and  $\approx 2200$  km (vertically, N-S) leading to a viable plume center expanding over both contemporary continental plates. Building on these conclusions, a possible plume marginal area can be defined extending from a minimum of  $\sim 4$  Mio km<sup>2</sup> to a maximum of between  $\sim 9.3$  Mio km<sup>2</sup> and  $\sim 10.6$  Mio km<sup>2</sup> meaning a long-range Paraná-Etendeka plume movement-influenced area in the SW Gondwana intraplate environment with permissible diameters between  $\approx 2200$  km and  $\approx 3000$ - $4100$  km (horizontally, E-W), and between  $\approx 2800$  km and  $\approx 5100$  km (vertically, N-S).

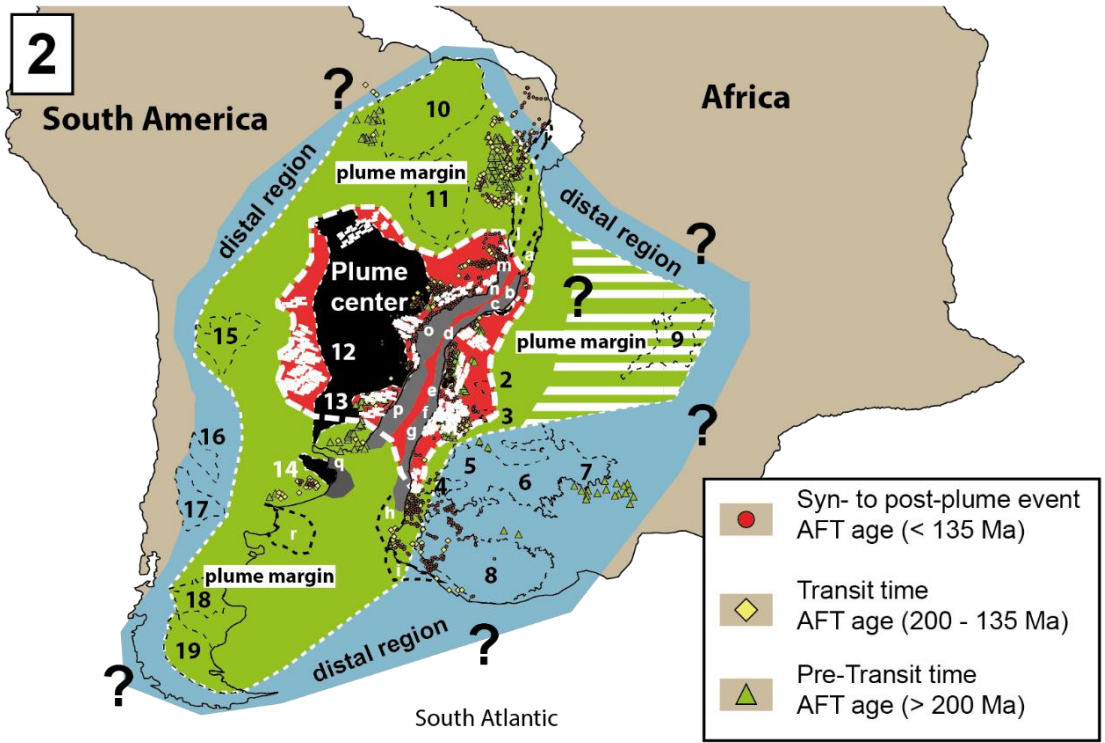
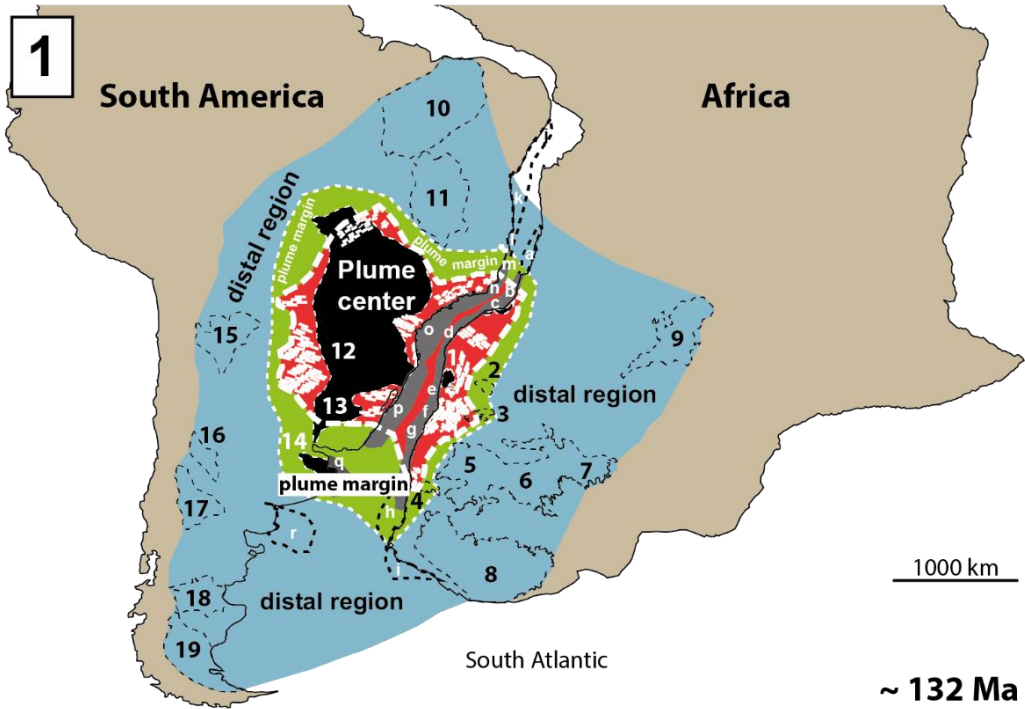


Figure 1.13: (Previous page) Possible ranges and limits for the spatial distribution of the Paraná-Etendeka LIP influenced area on the Earth's surface during a possible plume ascent (modified after Krob et al., 2020b). (1): Possible spatial distribution when followed strictly the outlines of the ePSF (Friedrich et al., 2019). (2) Spatial distribution showing a possible deviation in the spatial range including a critical uncertainty analysis regarding the geological archives and the ePSF.

*Post-South Atlantic breakup and rifting evolution, surface uplift and erosion, and tectonic activity.*

The Post-South Atlantic breakup and rift t-T-evolution is dominated by continuous rifting, continental breakup, and sea floor spreading that led to the surface uplift of the basement rocks and intense erosion on the Earth's surface (Fig. 1.14). The Neoproterozoic basement shows relatively slow, post-eruption, thermal recovering and rock cooling during the Early Cretaceous that infers a thermal reestablished upper crust following the Paraná-Etendeka event (Hu et al., 2018; Krob et al., 2020b).

The rocks probably experienced different amounts of cooling that indicate a complex multi-stage rift evolution (Gallagher et al., 1998). Thermochronological data presented in this study support the cooling history revealing major post-Paraná-Etendeka cooling events during the Early to Mid-Cretaceous accompanied by long and complex and/or sequential and transient denudation processes and tectonic activity following the South Atlantic breakup (Green, 1986; Gallagher et al., 1998; Raab et al., 2002; Brown, et al., 2014).

The modeled thermal structure implies a differentiated t-T-evolution of the SAPCM of SW Africa and South America (Courtilot et al., 1999; Torsvik et al., 2009, 2013; Hu et al., 2018; Andrés-Martinez et al., 2019). Continental breakup is assumed to have taken place along the old Pan African/Brasiliano orogeny suture line (Buiter and Torsvik, 2014) dividing the

investigated area. Consequently, the research considers both thermal structures of the Neoproterozoic basement individually (Fig. 1.14). The t-T-evolution of the Neoproterozoic basement thermal structure indicates a similar t-T-history for both, SE Brazil and NW Namibia. However, the temperature distribution remains inhomogeneous showing significantly higher temperatures on the southern SE Brazil side throughout the entire Mesozoic SW Gondwana intraplate environment (Krob et al., 2019, 2020a, b). In general, the research records higher experienced temperatures in the southern regions on both side of the plume central area that infer a stronger thermal overprint by the Paraná-Etendeka flood basalts.

Moreover, the study concludes that pre-plume movement thermal structures and conditions probably already existed and were not totally reset or overprinted by the effect of the Paraná-Etendeka plume movement (Krob et al., 2019, 2020a, b).

While the course of isolines illustrates the significant age increase towards the inland and different age spectra exist in the subdivided longitudinal Eastern, Central and Western (Kaoko) zones in NW Namibia, isolines in SE Brazil also follow the younger NW-SE trending structures during the Early Cretaceous. This supports a possible reactivation and movement of the Precambrian shear zones and change in the predominant tectonic activity during the South Atlantic breakup, and syn-to post rift stages (Brown et al., 2014; Salomon et al., 2015, 2017).

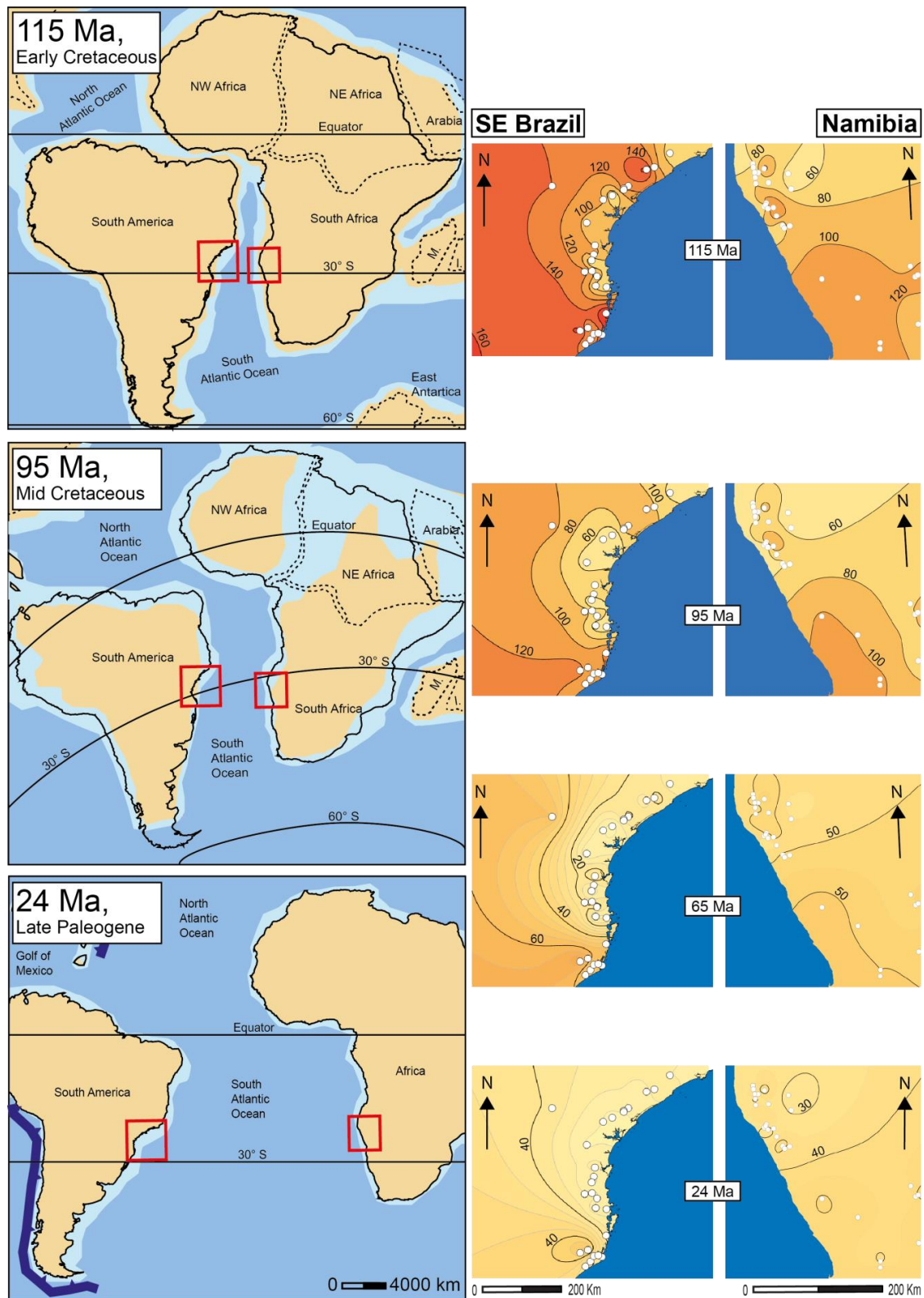


Figure 1.14: (Previous page) Left panel: Paleogeographic reconstruction of the Gondwana intraplate environment from the Early Cretaceous until the Late Paleogene (redrawn after Torsvik and Cocks, 2017). Red box shows the study area of SE Brazil and NW Namibia. Right Panel: Modeled 3D-interpolation maps showing the Neoproterozoic basement thermal structure of the SE Brazilian-NW Namibian study at the corresponding time. For further information, please see Figure 1.7.

Whereas in SE Brazil, regional tectonic and volcanic activity, and local graben sedimentation indicates that the basement rocks most likely reached the Earth's surface at the end of the Cretaceous, evidence supporting a similar geological evolution lacks for the NW Namibian counterpart. However, NW Namibian rocks also show a relatively homogeneous Late Cretaceous to recent cooling correlating with the SE Brazilian SAPCM. Generally, the northern areas indicate to have cooled down fast whereas the southern regions of the Laguna Block in SE Brazil and the Damara Belt in NW Namibia cooled down slower reaching the Earth's surface within the last  $\approx 24$  Myr (Fig. 1.14).

*Quantification of timing and duration of single geological environments and the connection of different geological stages of the Wilson Cycle.*

By the reconstruction of the possible t-T-evolution of the Neoproterozoic basement rocks in SE Brazil and NE Namibia, the research allows only few assumptions towards the timing and duration of single geological environments and the possible connection of different geological stage of the *Wilson Cycle*.

Beginning in the Late Neoproterozoic to Early Paleozoic, published geo- and thermo-chronological data permit the quantification of the timing of the syn-to post-orogenic intrusion, and crystallization and metamorphic processes. Furthermore, the new ZFT and ZHe data of this research can be assumed to constrain the transition from syn-to post-orogenic magmatic and metamorphic processes in the upper crust to the tectonic and sedimentological dynamics near, and on the Earth's surface. Following, by the combination of

thermochronological and stratigraphic data, the thesis succeeds to retrieve a viable t-T-evolution as described by theoretical models. The research clearly reveals signals and traces induced by the *dynamic topography* of the "plume mode". Nevertheless, the transition from intraplate environment dominated by interregional basin formation to significant vertical deflections leading to the inversion of the predominant sedimentary basins remains less constrained. This also yields for the post-South Atlantic breakup evolution as the data rather exposes a long-time multi-stage rift and persistent post-break up evolution.

Concluding, the data shows that the Late Neoproterozoic to Early and Mid Paleozoic t-T-history might not be necessarily connected with the Upper Paleozoic to Late Mesozoic, and Cenozoic evolution.

However, the repeated movement of the predominant tectonic structures imply to have been active during different geological stages and may have survived individual plate tectonics environments, supporting the differentiated movement of the individual crustal blocks that mirrored by the t-T-evolution of the Neoproterozoic basement structure. Nevertheless, the research does not commit it selves to make assumptions about the duration of single geological environments as the geological archives often lack in sensitivity to better constrain the timing of the individual plate tectonic stages. Moreover, the outcome of this research reveals that the transition between different geological environments and its driving forces present itself to be very complex and occur rather fluently. Therefore, it remains very uncertain to determine temporal ranges of the predominant "plate" and "plume mode" phases.

## 1.7 FUTURE PERSPECTIVES

This thesis carries forward a new approach by combining various geological archives to retrieve the coherent t-T-evolution connecting different geological environments since the Late Neoproterozoic. Thereby, the research recognizes *dynamic topography* signals and traces on the Earth's surface induced by the respective predominant driving forces ("plate" and "plume mode"). However, geological archives, such as thermochronological data and stratigraphic records showed to often lack in sensitivity and revealed uncertainties that can lead to significant error strings when combined.

Nevertheless, the thesis perfectly proved the approach as possible to validate theoretical models, and further on, verify the geodynamic research.

Therefore, it would be highly interesting to apply the approach to other geological environments, i.e. intraplate environments and Large Igneous Provinces as size and volume of vertical material flow, the composition and viscosity of mantle and the Earth's crust, and the nature of the Earth's surface differ from plume ascent to plume ascent and will surely effect the timing of events and spatial distributions. Thus, the southernmost African Karoo plume event and the Afar plume in NE Africa would be highly suitable to investigate the effects of the "plume mode" induced *dynamic topography* on the respective geological environments.

Consequently, this thesis proposes the systematic extension of geological archives, i.e. thermochronological data sets over wider areas also covering transitional regions to better constrain, and therefore, understand the t-T-evolution from the Late Neoproterozoic SW Gondwana orogen to the South Atlantic passive continental

margin environment induced by the "plate" and "plume mode".



## LIST OF REFERENCES

- Basei, M.A.S., Brito Neves, B.B., Siga Junior, O., Babinski, M., Pimentel, M.M., Tassinari, C.C.G., Hollanda, M.H.B., Nutmaan, A., Cordani, U.G., 2010.** Contribution of SHRIMP U-Pb geochronology to unravelling the evolution of Brazilian Neoproterozoic fold belts. *Precambrian Research* 183, 112-155.  
<https://doi.org/10.1016/j.precamres.2010.07.015>
- Bauer, F.U., Glasmacher, U.A., Malikwisha, M., Mambo, V.S., Mutete, B.V., 2010.** The Eastern Congo – a beauty spot, rediscovered from a geological point of view. *The Geologists' Association & the Geological Society of London, Geology Today* 26, 55-64.  
<https://doi.org/10.1111/j.1365-2451.2010.00747.x>
- Brand, A., Allen, L., Altman, M., Hlava, M., Scott, J., 2015.** Beyond authorship: attribution, contribution, collaboration, and credit. *Learned Publishing* 28:151-155.  
<https://doi.org/10.1087/20150211>
- Braun, J., 2010.** The many expressions of mantle dynamics. *Nature Geoscience* 3, 825-833.  
<https://doi.org/10.1038/ngeo1020>
- Braun, J., 2018.** A review of numerical modeling studies of passive margin escarpments leading to a new analytical expression for the rate of escarpment migration velocity. *Gondwana Research* 53, 209-224.  
<https://doi.org/10.1016/j.gr.2017.04.012>
- Brown, R., Summerfield, M., Gleadow, A., Gallagher, K., Carter, A., Beucher, R., Wildman, M., 2014.** Intracontinental deformation in southern Africa during the Late Cretaceous. *Journal of African Earth Sciences* 100, 20-41.  
<https://doi.org/10.1016/j.jafrearsci.2014.05.014>
- Buiter, S.J.H., Torsvik, T.H., 2014.** A review of Wilson Cycle plate margins: A role for mantle plumes in continental break-up along sutures? *Gondwana Research* 26, 627-653.  
<https://doi.org/10.1016/j.gr.2014.02.007>
- Bunge, H.-P., Richards, M.A., Lithgow-Bertelloni, C., Baumgardner, J.R., Grand, S.P., Romanowicz, B.A., 1998.** Time scales and heterogeneous structure in geodynamic earth models. *Science* 280:91-95. [10.1126/science.280.5360.91](https://doi.org/10.1126/science.280.5360.91)
- Bunge, H.-P., 2005.** Low plume excess temperature and high core heat flux inferred from non-adiabatic geotherms in internally heated mantle circulation models. *Physics of the Earth and Planetary Interiors* 153, 3-10.  
<https://doi.org/10.1016/j.pepi.2005.03.017>
- Bunge, H.P., Glasmacher, U.A.** Models and observations of vertical motion (MoveOn) associated with rifting to passive margins: Preface. *Gondwana Research*, Vol. 53, January 2018, 1-8. [10.1016/j.gr.2017.07.005](https://doi.org/10.1016/j.gr.2017.07.005)
- Catuneanu, O., Wopfner, H., Eriksson, P.G., Cairncross, B., Rubidge, B.S., Smith, R.M.H., Hancox, P.J., 2005.** The Karoo basins of south-central Africa. *Journal of African Earth Sciences* 43, 211-253.  
<https://doi.org/10.1016/j.jafrearsci.2005.07.007>
- Chase, C.G., Sprowl, D.R., 1983.** The modern geoid and ancient plate boundaries. *Earth and Planetary Science Letters* 82, 314-320.  
[https://doi.org/10.1016/0012-821X\(83\)90002-X](https://doi.org/10.1016/0012-821X(83)90002-X)
- Colli, L., Ghelichkhan S., Bunge, H.-P., 2016.** On the ratio of dynamic topography and gravity anomalies in a dynamic Earth. *Geophysical Research Letters* 43, 2510-2516.  
<https://doi.org/10.1002/2016GL067929>
- Courtillot, V., Jaupart, C., Manighetti, I., Tapponnier, P., Besse, J., 1999.** On causal links between flood basalts and continental breakup. *Earth and Planetary Science Letters* 166, 77-195.  
[https://doi.org/10.1016/S0012-821X\(98\)00282-9](https://doi.org/10.1016/S0012-821X(98)00282-9)
- Crough, S.T., 1979.** Hotspot epeirogeny. *Tectonophysics* 61, 321-333.  
[https://doi.org/10.1016/0040-1951\(79\)90304-4](https://doi.org/10.1016/0040-1951(79)90304-4)
- Davies, G.F., Richards, M.A., 1992.** Mantle convection. *The Journal of Geology* 100: 151–206.  
<http://dx.doi.org/10.1086/629582>

## LIST OF REFERENCES

- Davies, G.F.**, 1999. *Dynamic Earth: Plates, Plumes & Mantle Convection*. Cambridge University Press.  
<http://dx.doi.org/10.1017/CBO9780511605802>.
- Davies, J.H.**, Davies, D.R., 2010, Earth's surface heat flux. *Solid Earth* 1, 5-24.  
<https://doi.org/10.5194/se-1-5-2010>
- Davies, J.H.**, Valentine, A.P., Kramer, S.C., Rawlinson, N., Hoggard, M.J., Eakin, C.M., Wilson, C.R., 2019. Earth's multi-scale topographic response to global mantle flow. *Nature Geoscience* 12, 845-850.  
<https://doi.org/10.1038/s41561-019-0441-4>
- Engelmann de Oliveira, C.H.**, Jelinek, A.R., Chemale Jr., F., Bernet, M., 2016a. Evidence of post-Gondwana breakup in Southern Brazilian Shield: Insights from apatite and zircon fission track thermochronology. *Tectonophysics* 666, 173-187.  
<https://doi.org/10.1016/j.tecto.2015.11.005>
- Engelmann de Oliveira, C.H.**, Jelinek, A.R., Chemale Jr., Cupertino, J.A., 2016b. Thermotectonic history of the southeastern Brazilian margin: Evidence from apatite fission track data of the offshore Santos Basin and continental basement. *Tectonophysics* 685, 21-34.  
<https://doi.org/10.1016/j.tecto.2016.07.012>
- Ernst, R.E.**, Buchan, K.L., 2001a. *Mantle Plumes: Their Identification Through Time*. Geological Society of America Special Paper 593 pp.
- Fisher, O.**, 1889. *Physics of the Earth's Crust*. The Macmillan Company, New York.
- Foster, D.A.**, Goscombe, B.D., Gray, D.R., 2009. Rapid exhumation of deep crust in an obliquely convergent orogeny: The Kaoko Belt of the Damara Orogen. *Tectonics*, Vol. 28, TC4002.  
<https://doi.org/10.1029/2008TC002317>
- Franco-Magalhães, A.O.B.**, Hackspacher, P.C., Glasmacher, U.A., Saad, A.R., 2010. Rift to post-rift evolution of a "passive" continental margin: The Ponta Grossa Arch, SE Brazil. *International Journal of Earth Sciences (Geologische Rundschau)* 99, 1599-1613.  
<https://doi.org/10.1007/s00531-010-0556-8>
- Franke, D.**, 2013. Rifting, lithosphere breakup and volcanism: Comparison of magma-poor and volcanic rifted margins. *Marine and Petroleum Geology* 43, 63-87.  
<https://doi.org/10.1016/j.marpetgeo.2012.11.003>
- Friedrich, A.M.**, Bunge, H.-P., Rieger, S.M., Colli, L., Ghelichkhan, S., Nerlich, R., 2018. Stratigraphic framework for the plume mode of mantle convection and the analysis of interregional unconformities on geological maps. *Gondwana Research* 53, 159-188.  
<https://doi.org/10.1016/j.jgr.2017.06.003>
- Frimmel, H.E.**, Frank, W., 1998. Neoproterozoic tectono-thermal evolution of the Gariep Belt and its basement, Namibia and South Africa. *Precambrian Research* 90, 1-28.  
[https://doi.org/10.1016/S0301-9268\(98\)00029-1](https://doi.org/10.1016/S0301-9268(98)00029-1)
- Gallagher, K.**, Hawkesworth, C.J., Mantovani, M.S.M., 1994. The denudation history of the offshore continental margin of SE Brazil inferred from apatite fission-track data. *Journal of Geophysical Research* 99, 18117-18145.  
<https://doi.org/10.1029/94JB00661>
- Gallagher, K.**, Hawkesworth, C.J., Mantovani, M.S.M., 1995. Denudation, fission track analysis and the long-term evolution of passive margin topography: application to the southeast Brazilian margin. *Journal of South American Earth Sciences* 8, 65-77.  
[https://doi.org/10.1016/0895-9811\(94\)00042-Z](https://doi.org/10.1016/0895-9811(94)00042-Z)
- Gallagher, K.**, Brown, R., Johnson, C., 1998. Fission track analysis and its applications to geological problems. *Annual Reviews of Planetary Science* 26, 519-572.  
<https://doi.org/10.1146/annurev.earth.26.1.519>
- Gordon, R.G.**, Jurdy, D.M., 1986. Cenozoic global plate motions. *Journal of Geophysical Research-Solid Earth* 91, 12389-12406.  
<https://doi.org/10.1029/JB091iB12p12389>
- Goscombe, B.D.**, Hand, M., Gray, D., 2003a. Structure of the Kaoko Belt, Namibia: progressive evolution of a classic transpressional orogen. *Journal of Structural Geology* 25, 1049-1081.  
[https://doi.org/10.1016/S0191-8141\(02\)00150-5](https://doi.org/10.1016/S0191-8141(02)00150-5)

- Goscombe, B.D., Hand, M., Gray, D., Mawby, J., 2003b.** The metamorphic architecture of a transpressional orogen: the Kaoko Belt, Namibia. *Journal of Petrology* 44, 679-711.  
<https://doi.org/10.1093/petrology/44.4.679>
- Goscombe, B.D., Gray, D., 2007.** The Coastal Terrane of the Kaoko Belt, Namibia: outboard arc-terrane and tectonic significance. *Precambrian Research* 155, 139–158.  
<https://doi.org/10.1016/j.precamres.2007.01.008>
- Goscombe, B.D., Foster, D.A., Gray, D.R., Wade, B., 2017.** Metamorphic response and crustal architecture in a classic collisional orogeny: The Damara Belt, Namibia. *Gondwana Research* 52, 80-124.  
<https://doi.org/10.1016/j.gr.2017.07.006>
- Gray, D.R., Foster, D.A., Goscombe, B., Passchier, C.W., Trouw, R.A.J., 2006.**  $^{40}\text{Ar}/^{39}\text{Ar}$  thermochronology of the Pan-African Damara Orogen, Namibia, with implications for tectono-thermal and geodynamic evolution. *Precambrian Research* 150, 49-72.  
<https://doi.org/10.1016/j.precamres.2006.07.003>
- Green, P.F., 1986.** On the thermo-tectonic evolution of Northern England: evidence from fission track analysis. *Geological Magazine* 123, 493-506.  
<https://doi.org/10.1017/S0016756800035081>
- Green, P.F., Machado, V., 2015.** Pre-rift and syn-rift exhumation. Post-rift subsidence and exhumation of the onshore Namibe Margin of Angola revealed from apatite fission track analysis. *Geological Society, London, Special Publications* 438, 20 p.  
<https://doi.org/10.1144/SP438.2>
- Green, P.F., Duddy, I.R., Japsen, P., Bonow, J.M., Malan, J.A., 2017.** Post-breakup burial and exhumation of the southern margin of Africa. *Basin Research* 29, 96-127.  
<https://doi.org/10.1016/j.j.gr.2017.03.007>
- Griffiths, R.W., Gurnis, M., Eitelberg, G., 1989.** Holographic measurements of surface topography in laboratory models of mantle hotspots. *Geophysical Journal International* 96:477-495.  
<https://doi.org/10.1111/j.1365-246X.1989.tb06009.x>
- Griffiths, R.W., Campbell, I.H., 1990.** Stirring and structure in mantle starting plumes. *Earth and Planetary Science Letters* 99:66–78.  
[https://doi.org/10.1016/0012-821X\(90\)90071-5](https://doi.org/10.1016/0012-821X(90)90071-5)
- Gurnis, M., 1988.** Large-scale mantle convection and the aggregation and dispersal of supercontinents. *Nature* 332, 695-699.  
<https://doi.org/10.1038/332695a0>
- Hackspacher, P.C., Ribeiro, L.F.B., Ribeiro, M.C.S., Fetter, A.H., Hadler, N.J.C., Tello Saenz, C.A., Dantas, E.L., 2004.** Consolidation and break-up of the South American Platform in south-eastern Brazil: tectono-thermal and denudation histories. *Gondwana Research* 1, 91-101.  
[https://doi.org/10.1016/S1342-937X\(05\)70308-7](https://doi.org/10.1016/S1342-937X(05)70308-7)
- Haddon, I.G., 2005.** The sub-Kalahari geology and tectonic evolution of the Kalahari Basin, Southern Africa. Dissertation. University of the Witwatersrand, Johannesburg, South Africa.
- Hager, B.H., Clayton, R.W., Richards, M.A., Comer, R.P., Dziewonski, A.M., 1985.** Lower mantle heterogeneity, dynamic topography and the geoid. *Nature* 313, 541-545.  
<https://doi.org/10.1038/313541a0>
- Hager, B.H., Gurnis, M., 1987.** Mantle convection and the state of the Earth's interior. *Reviews of Geophysics* 25, 1277-1285.  
<https://doi.org/10.1029/RG025i006p01277>
- Hu, J., Liu, L., Faccenda, M., Zhou, Q., Fischer, K.M., Marshak, S., Lundstrom, C., 2018.** Modification of the Western Gondwana craton by plume-lithosphere interaction. *Nature Geoscience* 11, 203-210.  
<https://doi.org/10.1038/s41561-018-0064-1>
- Japsen, P., Bonow, J.M., Green, P.F., Cobbold, P.R., Chioffi, D., Lilletveit, R., Magnavita, L.P., Pedreira, A., 2012.** Episodic burial and exhumation in BE Brazil after opening of the South Atlantic. *Geological Society of America Bulletin*, 124, 800-816.  
<https://doi.org/10.1130/B30515.1>
- Japsen, P., Green, P.F., Bonow, J.M., Nielsen, T.F.D., Chalmers, J.A., 2014.** From volcanic plains to glaciated peaks: Burial, uplift and exhumation history of Southern East Greenland after opening of the NE Atlantic. *Global and Planetary Change*, 116, 91-114.  
<https://doi.org/10.1016/j.gloplacha.2014.01.012>

## LIST OF REFERENCES

- Johnson, M.R., Van Vuuren, C.J., Hegenberger, W.F., Key, R., Shoko, U., 1996.** Stratigraphy of the Karoo Supergroup in southern Africa: an overview. *Journal of African Earth Sciences* 23, 3-15.  
[https://doi.org/10.1016/S0899-5362\(96\)00048-6](https://doi.org/10.1016/S0899-5362(96)00048-6)
- Karl, M., Glasmacher, U.A., Kollenz, S., Franco-Magalhaes, A.O.B., Stockli, D.F., Hackspacher, P.C., 2013.** Evolution of the South Atlantic passive continental margin in southern Brazil derived from zircon and apatite (U–Th–Sm)/He and fission-track data. *Tectonophysics*, 604, 224-244.  
<https://doi.org/10.1016/j.tecto.2013.06.017>
- Ketcham, R.A., 2005.** Forward and Inverse Modelling of low-temperature thermochronometry data. *Rev. Min. Geoch.* 58, 275-314.  
<https://doi.org/10.2138/rmg.2005.58.11>
- Ketcham, R.A., Carter, A., Donelick, R.A., Barbarand, J., Hurford, A.J., 2007 a.** Improved measurements of fission-track annealing in apatite. *Am. Mineral* 92, 789-798.  
<https://doi.org/10.2138/am.2007.2280>
- Ketcham, R.A., Carter, A., Donelick, R.A., Barbarand, J., Hurford, A.J., 2007 b.** Improved modelling of fission-track annealing in apatite. *Am. Mineral* 92, 799-810.  
<https://doi.org/10.2138/am.2007.2281>
- Kollenz, S., 2015.** Long-term landscape evolution, cooling and exhumation history of the South American passive continental margin in NE Argentina & SW Uruguay. Ph.D. thesis, Institute of Earth Sciences, Heidelberg University.
- Krob, F.C., Glasmacher, U.A., Karl, M., Perner, M., Hackspacher, P., Stockli, D.F., 2019.** Multi-chronometer thermochronological modelling of the Late Neoproterozoic to recent t-T-evolution of the SE coastal region of Brazil. *Journal of South American Earth Sciences* 92, 77-94.  
<https://doi.org/10.1016/j.isames.2019.02.012>
- Krob, F.C., Eldracher, D.P., Glasmacher, U.A., Husch, S., Salomon, E., Hackspacher, P.C., Titus, N.P., 2020a.** Late Neoproterozoic-to-recent long- t-T-evolution of the Kaoko and Damara belts in NW Namibia. *International Journal of Earth Sciences (Geologische Rundschau)*.  
<https://doi.org/10.1007/s00531-020-01819-7>
- Krob, F.C., Glasmacher, U.A., Friedrich, A.M., Bunge, H.P., Hackspacher, P.C., 2020b.** Application of stratigraphic frameworks and thermochronological data on the Mesozoic SW Gondwana intraplate environment to retrieve the Paraná-Etendeka plume movement. *Gondwana Research* 84, 81-110.  
<https://doi.org/10.1016/j.jgr.2020.02.010>
- Lithgow-Bertelloni, C., and Gurnis, M., 1997.** Cenozoic subsidence and uplift of continents from time-varying dynamic topography. *Geology* 25, 735-738.  
[https://doi.org/10.1130/0091-7613\(1997\)025<0735:CSAUOC>2.3.CO;2](https://doi.org/10.1130/0091-7613(1997)025<0735:CSAUOC>2.3.CO;2)
- McKenzie, D., 1977.** Surface deformation, gravity anomalies and convection. *Geophysical Journal International* 48, 211-238.  
<https://doi.org/10.1111/j.1365-246X.1977.tb01297.x>
- Milani, E.J., de Melo, J.H.G., de Souza, P.A., Fernandes, L.A., França, A.B., 2007.** Bacia do Paraná. *B. Geociências Petrobras, Rio de Janeiro*, 15, 265-287.  
<https://doi.org/10.1016/j.gr.2014.08.007>
- Milani, L., Kinnaird, J.A., Lehmann, J., Naydenov, K.V., Saalman, K., Frei, D., Gerdes, A., 2015.** Role of crustal contribution in the early stage of the Damara Orogen, Namibia: New constraints from combined U-Pb and Lu-Hf isotopes from the Goas Magmatic Complex. *Gondwana Research* 28, 961-986.  
<https://doi.org/10.1016/j.jgr.2014.08.007>
- Miller, R.M., 2008.** The geology of Namibia. Geological Survey of Namibia, Windhoek (2008).
- Montañez, I.P., Poulsen, C.J., 2013.** The Late Paleozoic Ice Age: An Evolving Paradigm. *Annual Review of Earth and Planetary Sciences* 41, 629-656.  
<https://doi.org/10.1146/annurev.earth.031208.100118>
- Morgan, J.W., 1965.** Gravity anomalies and convection currents: 1. A sphere and cylinder sinking beneath the surface of a viscous fluid. *Journal of Geophysical Research* 70, 6175-6187.  
<https://doi.org/10.1029/JZ070i024p06175>

- Moulin, M., Aslanian, D., Unternehr, P., 2010.** A new starting point for the South and Equatorial Atlantic Ocean. *Earth Science Reviews* 98, 1-37.  
[doi:10.1016/j.earscirev.2009.08.001](https://doi.org/10.1016/j.earscirev.2009.08.001)
- Müller, D.R., Zahirovic, S., Williams, S.E., Cannon, J., Seton, M., Bower, D.J., Tetley, M.G., Heine, C., Le Breton, E., Liu, S., Russell, S.H.J., Yang, T., Leonard, J., Gurnis, M., 2019.** A Global Plate Model Including Lithospheric Deformation Along Major Rifts and Orogens Since the Triassic. *Tectonics* 38, 24 p.  
<https://doi.org/10.1029/2018TC005462>
- Müller, D.R., Hassan, R., Gurnis, M., Flament, N., Williams, S.E., 2019.** Dynamic topography of passive continental margins and their hinterlands since the Cretaceous. *Gondwana Research* 53, 225-251.  
<http://dx.doi.org/10.1016/j.gr.2017.04.028>
- Navarrete, C., Gianni, G., Encinas, A., Márquez, M., Kamerbeek, Y., Valle, M., Folguera, A., 2019.** Triassic to Middle Jurassic geodynamic evolution of southwestern Gondwana: From a large flat-slab to mantle plume suction in a rollback subduction setting. *Earth Science Reviews* 194, 125-159.  
<https://doi.org/10.1016/j.earscirev.2019.05.002>
- Raab, M.J., Brown, R.W., Gallagher, K., Carter, A., Weber, K., 2002.** Late Cretaceous reactivation of major crustal shear zones in northern Namibia: constraints from apatite fission track analysis. *Tectonophysics* 349, 75-92.  
[https://doi.org/10.1016/S0040-1951\(02\)00047-1](https://doi.org/10.1016/S0040-1951(02)00047-1)
- Raab, M.J., Brown, R.W., Gallagher, K., Weber, K., Gleadow, A.J.W., 2005.** Denudational and thermal history of the Early Cretaceous Brandberg and Kenyena igneous complexes on Namibia's Atlantic passive margin. *Tectonics* 24, 15 p.  
<https://doi.org/10.1029/2004TC001688>
- Reiners, P.W., Brandon, M.T. 2006.** Using thermochronology to understand orogenic erosion. *Annual Review of Earth Planetary Sciences* 34, 419-66.  
<https://doi.org/10.1146/annurev.earth.34.031405.125202>
- Reiners, P.W., Shuster, D.L., 2009.** Thermochronology and landscape evolution. *Physics Today* 62, 31 p.  
<https://doi.org/10.1063/1.3226750>
- Richards, M.A., Hager, B.H., 1984.** Geoid Anomalies in a Dynamic Earth. *Journal of Geophysical Research* 89, 5987-6002.  
<https://doi.org/10.1029/JB089iB07p05987>
- Richards, M.A., Engbretson, D.C., 1992.** Large-scale mantle convection and the history of subduction. *Nature* 355, 437-440.  
<https://doi.org/10.1038/355437a0>
- Salomon, E., Koehn, D., Passchier, C., 2015.** Brittle reactivation of ductile shear zones in NW Namibia in relation to South Atlantic rifting. *Tectonics*, 34, 70-85.  
<https://doi.org/10.1002/2014TC003728>
- Salomon, E., Passchier, C., Koehn, D., 2017.** Asymmetric continental deformation during South Atlantic rifting along southern Brazil and Namibia. *Gondwana Research* 51, 170-176.  
<https://doi.org/10.1016/j.gr.2017.08.001>
- Schuberth, B.S.A., Bunge, H.-P., Steinle-Neumann, G., Moder, C., Oeser, J., 2009.** Thermal versus elastic heterogeneity in high-resolution mantle circulation models with pyrolite composition: High plume excess temperatures in the lowermost mantle. *Geochemistry, Geophysics, Geosystems* 10, 1-24.  
<https://doi.org/10.1029/2008GC002235>
- Şengör, A.M.C., 2001.** Elevation as indicator of mantle-plume activity. In: Ernst, R.E., Buchan, K.L. (Eds.), *Mantle Plumes: Their Identification Through Time*. Geological Society of America Special Papers Vol. 352:pp. 183-225.
- Simmons, N.A., Forte, A.M., Grand, S.P., 2009.** Joint seismic, geodynamic and mineral physical constraints on three-dimensional mantle heterogeneity: Implications for the relative importance of thermal versus compositional heterogeneity. *Geophysical Journal International* 177, 1284-1304.  
<https://doi.org/10.1111/j.1365-246X.2009.04133.x>

## LIST OF REFERENCES

- Stollhofen, H.**, 1999. Karoo Synrift-Sedimentation und ihre tektonische Kontrolle am entstehenden Kontinentalrand Namibia. *Zeitschrift der deutschen geologischen Gesellschaft* 149, 519-632.
- Tello Saenz, C.A.**, Hackspacher, P.C., Hadler Neto, J.C., Lunes, P.J., Guedes, S., Ribeiro, L.F.B., Paulo, S.R., 2003. Recognition of Cretaceous, Paleocene, and Neogene tectonic reactivation through apatite fission-track analysis in Precambrian areas of southeast Brazil: association with the opening of the South Atlantic Ocean. *Journal of South American Earth Sciences* 15, 765-774.  
[https://doi.org/10.1016/S0895-9811\(02\)00131-1](https://doi.org/10.1016/S0895-9811(02)00131-1)
- Torsvik, T.H.**, Rouse, S., Labails, C., Smethurst, M.A., 2009. A new scheme for the opening of the South Atlantic Ocean and the dissection of an Aptian salt basin. *Geophysical Journal International* 177, 1315-1333.  
<https://doi.org/10.1111/j.1365-246X.2009.04137.x>
- Torsvik, T.H.**, Cocks, L.R.M., 2013. Gondwana from top to base in space and time. *Gondwana Research* 24, 999-1030.  
<https://doi.org/10.1016/j.gr.2013.06.012>
- Torsvik, T.H.**, Cocks, L.R.M., 2017. *Earth History and Palaeogeography*. Cambridge University Press, Cambridge, p. 317.
- Trumbull, R.B.**, Vietor, T., Hahne, K., Wackerle, R., Ledru, P., 2004. Aeromagnetic mapping and reconnaissance geochemistry of the Early Cretaceous Henties Bay-Outjo dike swarm, Etendeka Igneous Province, Namibia. *Journal of African Earth Sciences* 40, 17-29.  
<https://doi.org/10.1016/j.jafrearsci.2004.07.006>
- Trumbull, R.B.**, Reid, D.L., de Beer, C., van Acken, D., Romer, R.L., 2007. Magmatism and continental breakup at the west margin of southern Africa: A geochemical comparison of dolerite dikes from northwestern Namibia and the Western Cape. *South African Journal of Geology* 110, 477-502.  
<https://doi.org/10.2113/gssaig.110.2-3.477>
- Wilson, J.T.**, 1963. A possible origin of the Hawaiian islands. *Canadian Journal of Physics* 41 (6):863-870. <https://doi.org/10.1139/p63-094>
- Wilson, J.T.**, 1965. A new class of faults and their bearing on continental drift. *Nature* 207, 343-347.  
<https://doi.org/10.1038/207343a0>

# 2

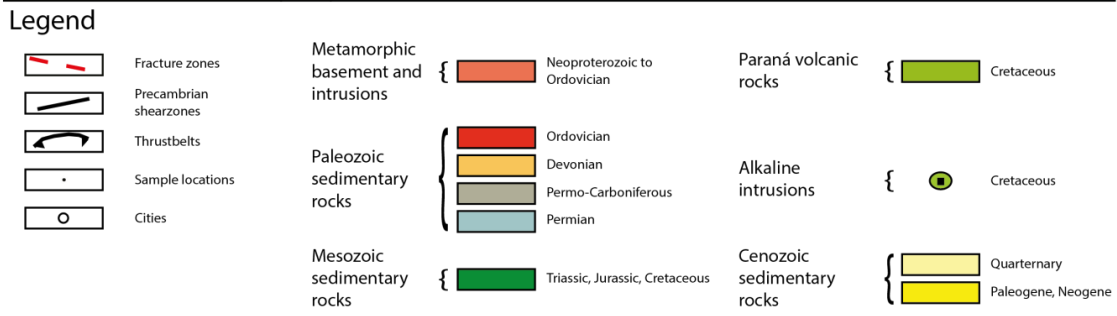
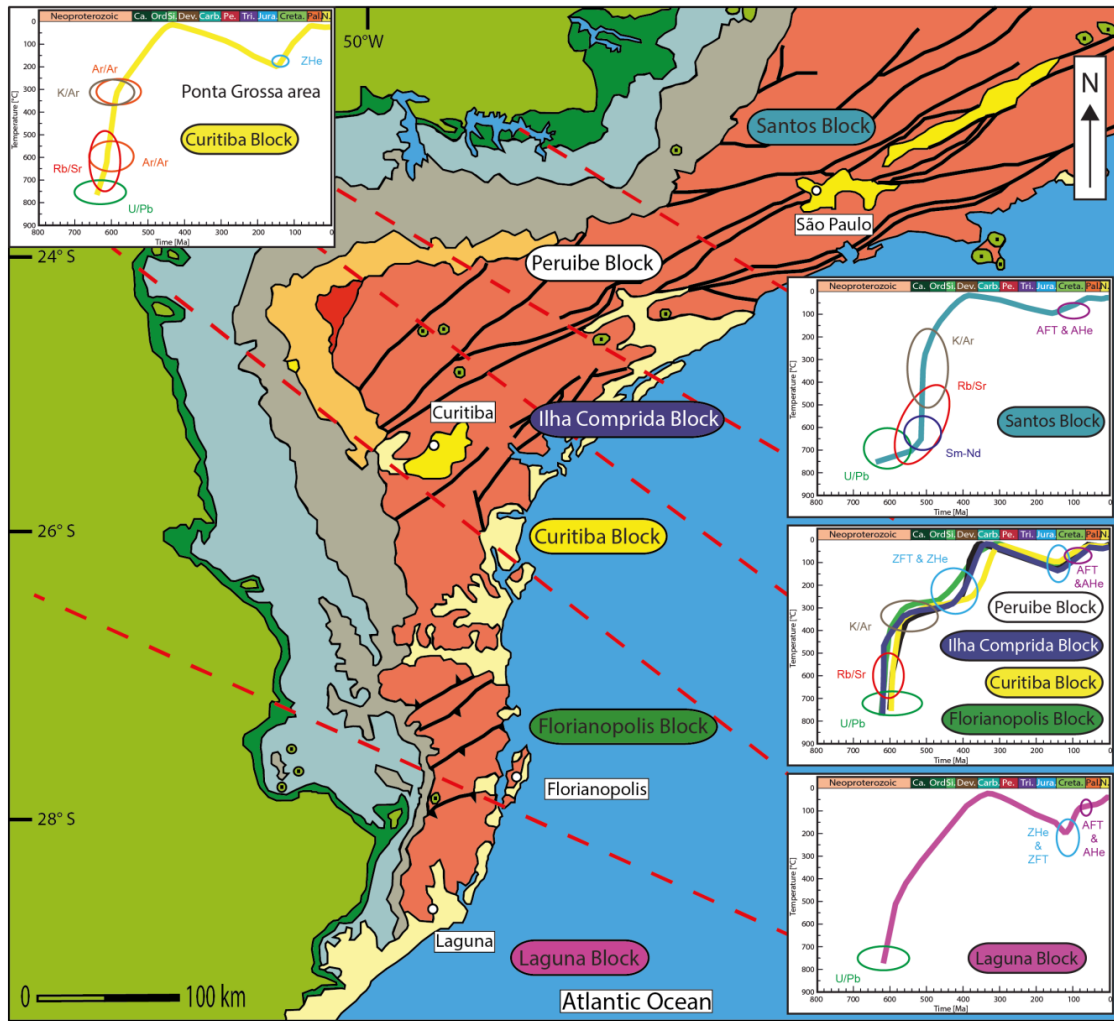
## MULTI-CHRONOMETER THERMOCHRONOLOGICAL MODELING OF THE LATE NEOPROTEROZOIC TO RECENT t-T- EVOLUTION OF THE SE COASTAL REGION OF BRAZIL

---

### CONTENTS

GRAPHICAL ABSTRACT	40
CRediT AUTHOR STATEMENT	41
ABSTRACT	43
INTRODUCTION	43
GEOLOGICAL SETTING	45
METHODS	47
RESULTS	48
INTERPRETATION AND DISCUSSION	50
CONCLUSIONS	57
ACKNOWLEDGEMENTS	57
REFERENCES	58

---



Graphical Abstract of CHAPTER 2.



## CRedit author statement

**Publication title:** Multi-chronometer thermochronological modelling of the Late Neoproterozoic to recent t-T-evolution of the SE coastal region of Brazil.

**Authors:** Florian C. Krob, Ulrich A. Glasmacher, Markus Karl, Melissa Perner, Peter C. Hackspacher, Daniel F. Stockli.

### Author contributions\*:

<b>Florian C. Krob:</b>	Conceptualization, methodology, software, validation, formal analysis, investigation, data curation, writing – original draft, visualization, project administration ( <b>≈80%</b> ).
<b>Prof. Dr. Ulrich A. Glasmacher:</b>	Conceptualization, methodology, validation, resources, writing – review & editing, supervision, project administration, funding acquisition ( <b>≈10%</b> ).
<b>Markus Karl:</b>	Investigation, formal analysis, data curation ( <b>≈7.5%</b> ).
<b>Dr. Melissa Perner:</b>	Investigation, formal analysis, data curation ( <b>≈1%</b> ).
<b>Prof. Dr. Peter C. Hackspacher:</b>	Resources, writing - review & editing ( <b>≈1%</b> ).
<b>Dr. Daniel F. Stockli:</b>	Resources ( <b>≈0.5%</b> ).

*\*Reproduced from Brand et al. (2015)*

Heidelberg, 15.04.2020

Florian Krob – Corresponding author

Ulrich A. Glasmacher – Supervisor

Peter C. Hackspacher – Deputy Co-Author





Contents lists available at ScienceDirect

## Journal of South American Earth Sciences

journal homepage: [www.elsevier.com/locate/jsames](http://www.elsevier.com/locate/jsames)

## Multi-chronometer thermochronological modelling of the Late Neoproterozoic to recent t-T-evolution of the SE coastal region of Brazil



Florian C. Krob<sup>a,\*</sup>, Ulrich A. Glasmacher<sup>a</sup>, Markus Karl<sup>a</sup>, Melissa Perner<sup>a</sup>, Peter C. Hackspacher<sup>b</sup>, Daniel F. Stockli<sup>c</sup>

<sup>a</sup> Institute of Earth Sciences, Heidelberg University, Im Neuenheimer Feld 234, 69120, Heidelberg, Germany

<sup>b</sup> Departamento de Petrologia e Metalogenia, Instituto de Geociências e Ciências Exatas, Universidade Estadual Paulista, Av. 24-A, 1515, Bela Vista, 13506-900, Rio Claro, SP, Brazil

<sup>c</sup> Department of Geological Sciences, University of Texas, Austin, 1 University Station C9000, Austin, TX, 78712-0254, USA

### ABSTRACT

South-eastern Brazil is as an important geological archive for understanding and reconstructing various plate tectonic stages of the Wilson Cycle. In the Neoproterozoic, the area of the today's South Atlantic passive continental margin (SAPCM: e.g. between São Paulo and Laguna) of south-eastern Brazil underwent subduction, followed by the collision of the contemporary plates of South America and Africa creating a Neoproterozoic orogeny within the supercontinent Gondwana. During the Palaeozoic and Lower Mesozoic (stage 1), the future SAPCM, as an intracratonic area, experienced erosion, denudation of the Neoproterozoic mobile belts (Pan African/Brasiliano orogeny), and large basin formation (Paraná Basin) (stage 2). Possibly plume-driven pre-to syn-rift (embryonic), ocean spreading (juvenile), and post-break up (mature) processes led to the recent evolution of the SAPCM since the Upper Mesozoic (stage 3).

For the first time, this research aims to reconstruct the syn-to post-orogenic t-T-evolution of Neoproterozoic basement rocks of the SE coastal region of Brazil covering the entire geological evolution since the Late Neoproterozoic. Therefore, this study uses geochronological and thermochronological data combined with numerical modelling. This includes published geochronological data of Neoproterozoic basement samples such as U-Pb, Sm-Nd and Rb-Sr analyses, and low temperature thermochronology (LTT) data revealed by K/Ar, <sup>40</sup>Ar/<sup>39</sup>Ar analyses. To this existing LTT data set, we report new apatite (AFT) and zircon (ZFT) fission-track, and (U-Th-Sm)/He (AHe, ZHe) data. Numerical modelling of that LTT data attached to the existing geochronological data indicates the following evolution:

- Stage 1: In the central part of the future SAPCM, the Pan African/Brasiliano post-orogenic cooling and exhumation (uplift and erosion of Neoproterozoic rocks to the surface) history occurs in three phases: (i) rapid Late Neoproterozoic exhumation, (ii) a period of relative thermal stability (temperatures of about 200–300 °C) in which rocks reside at upper crust levels during the Early Cambrian to Devonian, and (iii) a second rapid exhumation phase moving the Neoproterozoic basement rocks to the surface during the Devonian. The northern and southern parts indicate a distinct post-orogenic exhumation suggesting faster cooling and exhumation from the Late Neoproterozoic to Devonian/Carboniferous than in the central section.

- Stage 2: A phase of subsidence leading to the formation of the Paraná Basin followed by pre-to syn-rift processes and the emplacement of the Paraná-Etendeka flood basalts.

- Stage 3: Post-South Atlantic break up processes, such as erosion and exhumation.

### 1. Introduction

“Passive” continental margins are “first-order” archives of the Earth's surface documenting information from the interplay of endogene and exogene forces. The South Atlantic passive continental margin (SAPCM) in south-eastern Brazil not only provides information related to continental rifting, syn-to post-break up dynamics, and climate changes, but also stores the syn-to post-Late Neoproterozoic evolution since the assembly of West Gondwana. The large scale Pan African/Brasiliano orogeny (Pimentel et al., 1999) included the amalgamation of several cratons and microplates around the São Francisco-Congo (SFC) Craton. During the Early Palaeozoic post-orogenic regional

uplift and erosion triggered cooling and denudation of the Neoproterozoic mobile belts (Soares et al., 2001, 2008; Santos et al., 2015; Valeriano et al., 2008; Florisbal et al., 2012). Deposition of the material eroded at that time caused subsidence of the Paraná Basin (Basei et al., 2010). Since the Upper Mesozoic, the SAPCM in south-eastern Brazil was subject of pre-to syn-rift, ocean spreading, and post-break up processes.

Neoproterozoic metamorphic and magmatic rocks characterize the exposed geology between São Paulo and Florianópolis (Fig. 1). The Neoproterozoic basement is cut by mafic dykes of Lower Cretaceous, and alkaline to carbonatite intrusions of Early and Late Cretaceous age. To the West, the basement is overlain by Palaeozoic and Mesozoic

\* Corresponding author.

E-mail address: [florian.krob@geow.uni-heidelberg.de](mailto:florian.krob@geow.uni-heidelberg.de) (F.C. Krob).

<https://doi.org/10.1016/j.jsames.2019.02.012>

Received 18 June 2018; Received in revised form 15 February 2019; Accepted 20 February 2019

Available online 07 March 2019

0895-9811/ © 2019 Elsevier Ltd. All rights reserved.

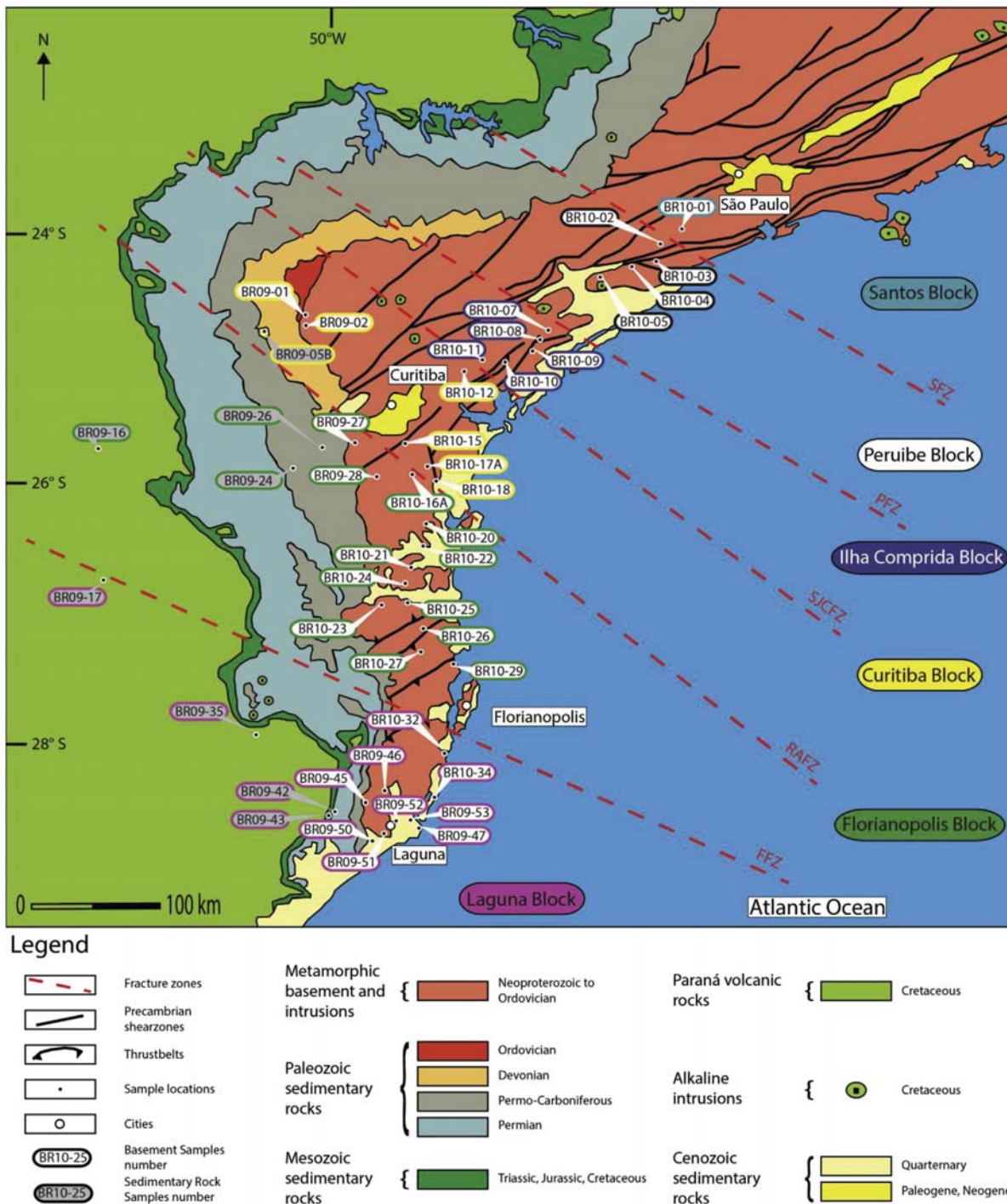


**Fig. 1.** Simplified geological map of the study area with sample locations (modified after the geological map of South America, from CPRM and DNPM, Brazil). Positions and directions of fracture zones were taken from Cobbold et al. (2001), Meisling et al. (2001), Riccomini et al. (2005), Strugale et al. (2007), Franco-Magalhaes et al. (2010), and Karl et al. (2013). Onshore extensions only show tendencies, and are not confirmed trends. SFZ: Santos fracture zones; PFZ: Peruipe fracture zone; SJCFZ: São Jerônimo-Curiúva fracture zone; RAFZ: Rio Alonzo fracture zone; FFZ: Florianópolis fracture zone.

siliciclastic and carbonate sequences of the Paraná Basin. Lower Cretaceous Paraná-Etendeka flood basalts and rhyolites cover the Jurassic siliciclastic sedimentary rocks. In some areas, the Lower Cretaceous Paraná-Etendeka sequence is overlain by siliciclastic rocks of Upper Cretaceous age. Locally, thin Eocene to Miocene siliciclastic sediments overlay the Neoproterozoic basement.

The research presented here focuses on the reconstruction of the

syn- to post-orogenic thermal evolution of Neoproterozoic rocks as part of the Southern Ribeira and Dom Feliciano belts. Through this reconstruction we aim to address the timing and magnitude of syn- to post-Late Neoproterozoic cooling and surface uplift, and erosion (exhumation), the timing and rate of subsidence, exhumation, and erosion during the formation of the Paraná Basin, the thermal influence of the Paraná-Etendeka flood basalts, and the extent and tectonic influence of

Cenozoic onshore graben systems such as the Taubaté Basin.

To answer these outstanding questions, the research uses published geochronological data of Neoproterozoic basement samples, such as U-Pb, Sm-Nd and Rb-Sr analyses, and low temperature thermochronology (LTT) data revealed by the K/Ar,  $^{40}\text{Ar}/^{39}\text{Ar}$  analyses. To this existing data set, this study presents new information on the time (t)-temperature (T)-evolution of rocks in low temperature ranges derived from dating techniques, such as fission-track (FT) and (U-Th-Sm)/He (He) dating on apatite and zircon. We use the numerical modelling software code HeFty (Ketcham et al., 2007a, b) to obtain thermal history information from the LTT data. We use current fission track annealing models and helium diffusion kinetics combined with geological constraints from previous work to determine the t-T-evolution of crustal segments. By assuming a geothermal gradient and surface temperatures over time, we are able to calculate rates of exhumation, erosion, and subsidence.

## 2. Geological setting

### 2.1. Precambrian basement

The formation of the Neoproterozoic basement in south-eastern Brazil (Fig. 2) was part of a succession of several thermo-tectonic events during the consolidation of the Gondwana supercontinent in the Late Neoproterozoic-Early Palaeozoic (ca. 650–490 Ma). This series of collisional processes is referred to as the Pan African/Brasiliano orogeny (Pimentel et al., 1999; Hackspacher and Godoy, 1999; Cordani et al., 2000; Alkmim et al., 2001; Schmitt et al., 2004). During the Late Neoproterozoic, the Paranapanema Craton and the Goiás Massif were transported towards the East, and amalgamated with the W-SW margin of the SFC Craton (0.64–0.61 Ga) (Pimentel et al., 1999; Almeida et al., 2000; Alkmim et al., 2001; Valeriano et al., 2008; Heilbron et al., 2008). This early phase of collision, involved subduction of oceanic lithosphere, smaller terranes and magmatic arcs, followed by folding and thrusting along former continental margins, and led to the formation of the Brasília Belt. The complex orogenic domain is dominated by high-grade metamorphic rocks that reached their metamorphic peak in the southern part around 0.65–0.63 Ga, and magmatic intrusions (Pimentel et al., 2000; Valeriano et al., 2008).

Ongoing subduction and progressive rotation of the continental blocks (0.6–0.5 Ga, Valeriano et al., 2008) involving several microplates, drove convergence of the São Francisco, Congo, and Angola cratons and formed two compressional, metamorphic, and magmatic fold belts (Campos Neto, 2000; Heilbron et al., 2000, 2017;

Hackspacher et al., 2000; Alkmim et al., 2001). In the North, the Araçuaí Belt merges into the Central and Southern Ribeira Belt in the South. Both complex orogenic belts stretch along the S-SE margin of the São Francisco Craton, show the same structural trend, and indicate a common Neoproterozoic collisional history (Heilbron et al., 2000). The Ribeira Belt has its metamorphic climax between 600 and 560 Ma (Machado et al., 1996; Brueckner et al., 2000). It roughly coincides with the Araçuaí Belt (peak metamorphism: ~580–560 Ma, Soares et al., 2008, 2011; Alkmim et al., 2017), and thus, belongs to the younger orogens of the Pan African/Brasiliano orogeny (Heilbron et al., 2000).

The NE-trending Ribeira Belt (Fig. 2) is the largest geo-tectonic unit of the West Gondwana Assembly, extending over 1400 km along the SAPCM of Brazil (Brito Neves et al., 1999; Heilbron et al., 2000; Silva et al., 2005). Its geology is characterized by Palaeo-to Neoproterozoic, high amphibolite to granulite-facies metasedimentary, and magmatic rocks. They represent a long term generation of different marine-to continental arc complexes (860–620 Ma), that continuously collided with several microcontinents against the passive margin of the São Francisco Craton (620–510 Ma) (Machado et al., 1996; Schmitt et al., 2004; Trouw et al., 2013; Valeriano et al., 2016). The Southern Ribeira Belt mainly contains Palaeo-to Neoproterozoic, metavolcano-sedimentary, and metasedimentary rocks (Faleiros et al., 2011; Valeriano et al., 2016).

Continuous movement of the southern cratonic blocks of the Gondwana Assembly led to further collisional events in the Late Precambrian to Early Cambrian. The converging Rio de la Plata and Kalahari cratons pressed into the Northern Luis Alves, Paranapanema, and Angola cratons, creating orogenic belts along the south-western margin of the Angola Craton (Kaoko Belt), and between the Angola and Kalahari cratons (Damara Belt). The Dom Feliciano Belt (Fig. 2), as the western counterpart, stretches over 1200 km along the eastern margin of the Rio de la Plata Craton (Alkmim et al., 2001; Oyhantcabal et al., 2007; Basei et al., 2008; Bruno et al., 2018). The orogenic belt reaches from the state of Santa Catarina in south-eastern Brazil to southern Uruguay. Its Brazilian geology is dominated by calc-alkaline to alkaline granitoid rocks of the Eastern Granitoid Belt, low grade metavolcano-sedimentary rocks (greenschist and amphibolite facies) of the supra-crustal Schist Belt, and metamorphic sedimentary and volcanic rocks of the Foreland Basins (Basei et al., 2008). However, these rocks are less affected by deformation and metamorphism (Hartmann et al., 2003; Passarelli et al., 2010; Basei et al., 2000, 2008, 2011).

The Ribeira and Dom Feliciano belts are separated by continental fragments of the Luis Alves (LAC) microplate (Fig. 2). These granitic-

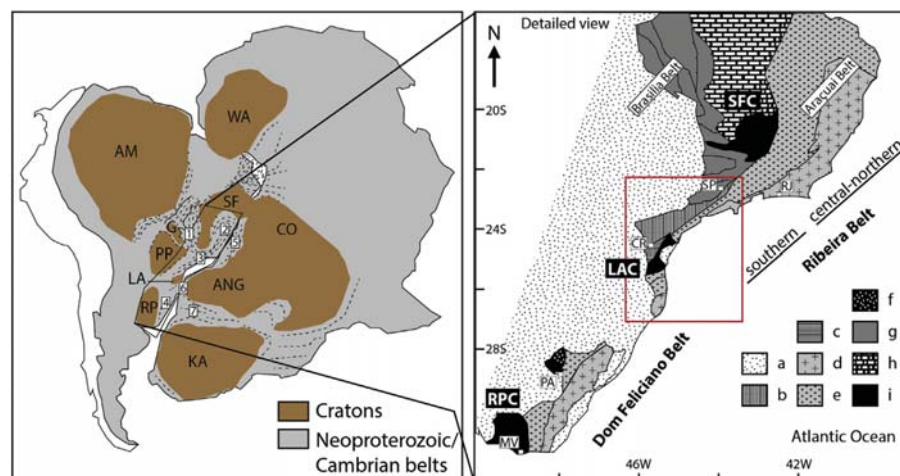


Fig. 2. Left: Location of Neoproterozoic mobile belts and cratons in South America and Africa (Western Gondwana) modified after Heilbron et al. (2008). Neoproterozoic belts: 1. Brasília Belt; 2. Araçuaí Belt and Central Ribeira Belt; 3. Southern Ribeira Belt; 4. Dom Feliciano Belt; 5. West Congo Belt; 6. Kaoko Belt; 7. Damara Belt. Major Cratons: AM: Amazonia; SF: São Francisco; LA: Luis Alves; RP: Rio de la Plata; WA: West Africa; CO: Congo; ANG: Angola; KA: Kalahari. Right: Tectonic units of the Dom Feliciano and Ribeira belts modified after Heilbron et al. (2008). Cratonic fragments: SFC: São Francisco-Congo; LAC: Luis Alves; RPC: Rio de la Plata. Tectonic units: a: post-Cambrian sedimentary rocks of the Paraná Basin; Ribeira Belt: b: Apiaí Terrane; c: Curitiba Terrane; d: Oriental Terrane; e: Occidental, Paraíba do Sul and Embú terranes; f: São Gabriel Belt; g: Brasília Belt; h: cratonic cover; i: São Francisco basement. Major cities: RJ: Rio de Janeiro; SP: São Paulo; CR: Curitiba; PA: Porto Alegre; MV: Montevideo.

magmatic dyke swarms crosscut the metamorphic basement and extend into the Paraná Basin sequence (Franco-Magalhaes et al., 2010; Florisbal et al., 2014). Chemical and isotopic composition of these dykes correlate with those of the flood basalts, implying that the dyke swarms could have acted as feeder channels for the volcanic rocks. Ages of lenticular alkaline to carbonatitic magmatic bodies occurring within the Jurassic siliciclastic rocks, range between  $138.4 \pm 1.3$  and  $127.6 \pm 1.2$  Ma ( $^{40}\text{Ar}/^{39}\text{Ar}$ ) (Amaral et al., 1967; Gomes et al., 1987; Sonoki and Garda, 1988; Renne et al., 1996). Riccomini et al. (2005) published slightly younger ages of 101–105 Ma (K-Ar).

The post-orogenic processes started during the Early Cambrian (~530 Ma) and most likely continued until the Early Ordovician (~490–480 Ma) (Soares et al., 2001, 2008; Florisbal et al., 2012; Santos et al., 2015). They were characterized by intense post-collisional magmatism along old major shear zones (Florisbal et al., 2012; Bento dos Santos et al., 2010, 2014; Bruno et al., 2018). Erosion and surface uplift, due to the collapse and denudation of Neoproterozoic mobile belts, generated an enormous supply of sediment material for the Palaeozoic to Mesozoic development of the major basins (Basei et al., 2010).

## 2.2. Tectonic structures

The study area comprises two predominant tectonic systems (Fig. 1). On the one hand, NE-SW trending shear zones and thrust belts crosscut the Neoproterozoic basement. Those tectonic structures are of Precambrian age and have proven to be important lineaments for the regional geological evolution (Basei et al., 1995, 1999, 2008, 2010, 2011; Bruno et al., 2018). While Hiruma et al. (2010) reported repeated reactivation of the Precambrian tectonic structures further north, such knowledge about similar structures in the south is uncertain.

On the other hand, seismic offshore data revealed large NW-SE trending fracture zones (Fig. 1) dominating the younger geological evolution of the study area (Santos Fracture Zone (SFZ), Peruipe Fracture Zone (PFZ), São Jerônimo-Curiuva Fracture Zone (SJCFZ), Rio Alonzo Fracture Zone (FFZ) and Florianópolis Fracture Zone (FFZ)) They extend onshore, and subdivide the region in different crustal blocks (Santos, Peruipe, Ilha Comprida, Curitiba, Florianópolis and Laguna) (Petrobras, partly unpublished, Cobbold et al., 2001, Meisling et al., 2001; Riccomini et al., 2005; Strugale et al., 2007, Franco-Magalhaes et al., 2010; Karl et al., 2013). Those tectonic features are interpreted as Paleozoic to Mesozoic transfer zones and have been probably reactivated repeatedly (Cobbold et al., 2001; Karl et al., 2013). However, their age and timing of movement and possible reactivation over time is still uncertain and its influence on the evolution of the individual blocks needs further investigation (Cobbold et al., 2001; Meisling et al., 2001; Riccomini et al., 2005; Strugale et al., 2007; Torsvik et al., 2009; Franco-Magalhaes et al., 2010; Karl et al., 2013; Salomon et al., 2015).

## 2.3. Paraná Basin subsidence

According to the published stratigraphy by Milani et al. (2007) (Fig. 3), the Paraná Basin subsidence initiated during the Ordovician (Rio Ivaí), followed by a second depositional sequence (Paraná) from Early to Late Devonian. Subsequent to a significant hiatus, sedimentation evidently continued in the Late Carboniferous/Early Permian (Gondwana I), and progressed during the Early to Late Triassic (Gondwana II). There is no evidence of further deposition leading to an hiatus from Late Triassic to Late Jurassic, followed by aeolian sands of the Botucatu Formation (Gondwana III), and the occurrence of the Paraná-Etendeka flood basalts (Gondwana III, Serra Geral Formation). These continental flood basalts (~1700 m), and acid volcanic rocks overlay discordantly the sedimentary sequence in the southern and western part of the Paraná Basin. The Paraná-Etendeka flood basalts are dated at  $133.0 \pm 1.0$  Ma ( $^{40}\text{Ar}/^{39}\text{Ar}$ ) (Renne et al., 1992, 1996), and correlate with the syn-rift stage of the South Atlantic rift evolution (Torsvik et al., 2006) (Tab. S1, see supplementary data). Within the Ponta Grossa Arch (PGA), two large NW-SE trending Early Cretaceous

magmatic dyke swarms crosscut the metamorphic basement and extend into the Paraná Basin sequence (Franco-Magalhaes et al., 2010; Florisbal et al., 2014). Chemical and isotopic composition of these dykes correlate with those of the flood basalts, implying that the dyke swarms could have acted as feeder channels for the volcanic rocks. Ages of lenticular alkaline to carbonatitic magmatic bodies occurring within the Jurassic siliciclastic rocks, range between  $138.4 \pm 1.3$  and  $127.6 \pm 1.2$  Ma ( $^{40}\text{Ar}/^{39}\text{Ar}$ ) (Amaral et al., 1967; Gomes et al., 1987; Sonoki and Garda, 1988; Renne et al., 1996). Riccomini et al. (2005) published slightly younger ages of 101–105 Ma (K-Ar).

## 2.4. Post-break up evolution

Based on onshore and offshore data, the post-rift evolution of the SAPCM in south-eastern Brazil is not continuous but described as separate events which took place during the Late Cretaceous, the Paleogene, and the Neogene to Quaternary (Tab. S1, Fig S1). Thermochronological ages around 90 Ma indicate the exhumation and tectonic denudation of high-elevated areas occurred during the Late Cretaceous as a response to the drifting of the South American Platform over a thermal anomaly (Trindade hotspot) (Gallagher et al., 1994, 1995; Tello et al., 2003; Hackspacher et al., 2004, 2007; Engelmann de Oliveira et al., 2016). This rock and surface uplift, and exhumation were accompanied by intense alkaline magmatism (90–80 Ma).

During the Early Palaeogene, tectonic activation of onshore graben systems along the coast most likely caused the onset of subsidence within onshore basins such as Resende, Taubaté, São Paulo, Pariqueraçu and Curitiba (from NE to SW) (Salamuni et al., 2003; Hiruma et al., 2010). Additionally, Cobbold et al. (2001) discuss a significant decrease of sediment supply for the central Santos Basin in Early Eocene indicating a change in transport direction of sediment.

In the Taubaté Basin (Fig. S1), Palaeocene to Eocene sediments overlie unconformably crystalline Neoproterozoic rocks (Cogné et al., 2011, 2012, 2013) leading to the assumption that the basement had reached the surface before the activation of onshore graben systems in the Early Cenozoic. Palaeocene to Eocene thermochronological ages indicating reactivation of the SAPCM in south-eastern Brazil are related to block faulting and exhumation. These are associated to the formation of the NE-SW continental rift basins and consequent exhumation of the flanks along both sides of the Palaeogene rifts (Franco-Magalhaes et al., 2010). Contemporaneously, the SE border of the Paraná Basin was uplifted to the surface, tilted, and eroded (Zalán et al., 1990).

Inversion of the graben system took place during the Neogene (Riccomini, 1989; Riccomini et al., 2004), and was caused by right-lateral transpression (Cobbold et al., 2001). Post-Miocene, the proto-Serra do Mar experienced block faulting and exhumation, while transpression inverted the continental rift basins (Almeida and Carneiro, 1998; Salamuni et al., 2003; Franco-Magalhaes et al., 2010), leading to a surface uplift of the Serra do Mar (Fig. S2) (Almeida et al., 1998; Hiruma et al., 2010). The onshore supply of sediments for the offshore basins during the Oligocene and Miocene occurred from the SW of the study area towards the Santos Basin (unpublished data by Petrobras; Cobbold et al., 2001).

During the Miocene, the transport direction changed and sediments were supplied from the NE as well. Recent thermochronological data support this change in the direction of the sediment supply (Franco-Magalhaes et al., 2010). Furthermore, thermochronological data indicate movement along NW-SE trending fault zones (e.g. São Jerônimo-Curiuva and Rio Alonzo Fault Zones) leading to a distinct exhumation in the NE of the PGA (Franco-Magalhaes et al., 2010; Karl et al., 2013). Early Cretaceous flood basalts and Late Cretaceous sedimentary rocks are tilted with a dip to the NW.

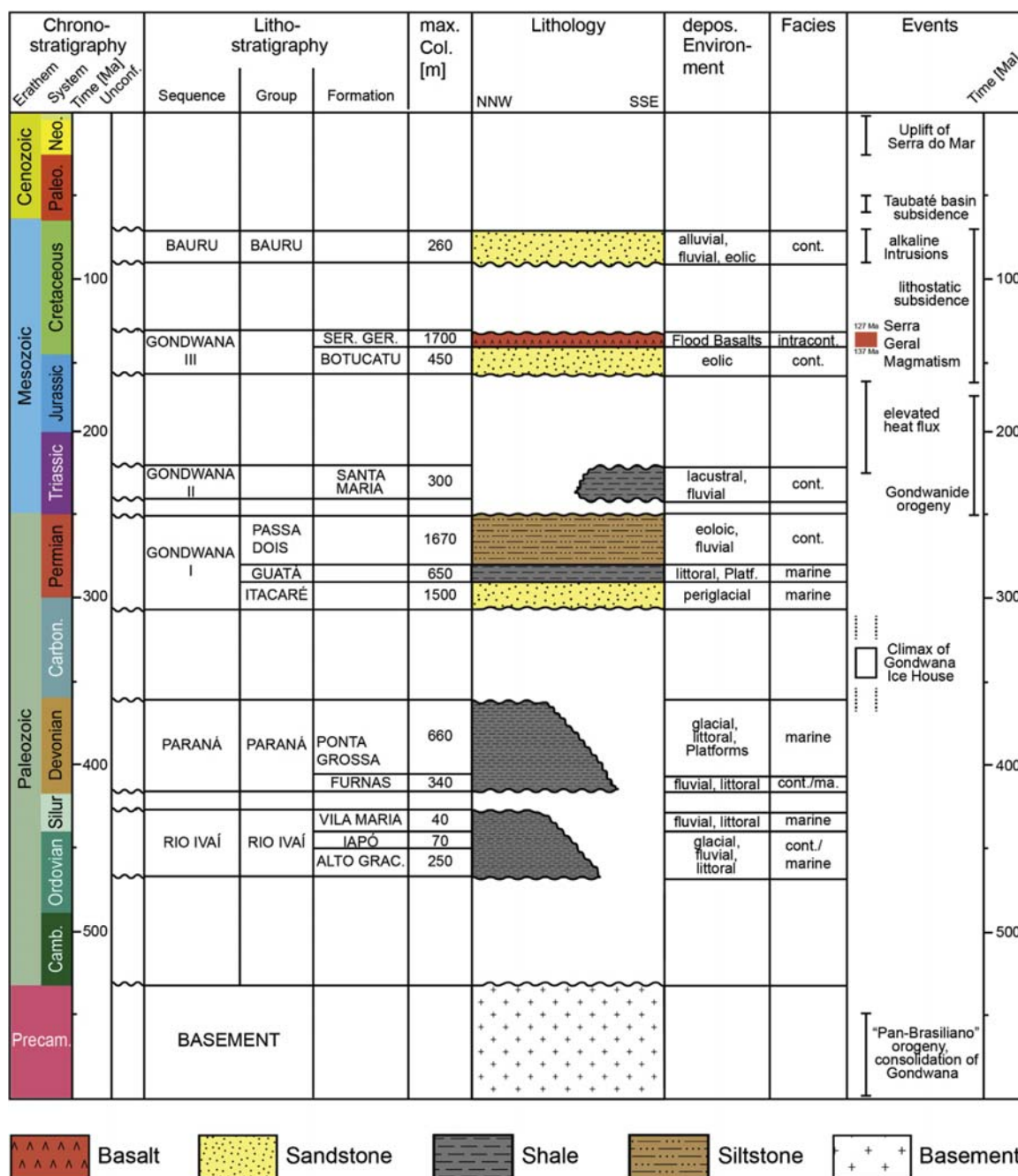


Fig. 3. Stratigraphy of Paraná basin depositional sequences. Chronostratigraphy, Lithostratigraphy, max. Column deposited, Lithology, depositional Environment, Facies, Events (modified after Milani et al., 2007).

3. Methods

3.1. Thermochronology

Thermochronology is based on the accumulation and thermally controlled retention of isotopic daughter products and linear crystal defects produced during the radioactive decay of parent. Due to the temperature sensitivity of the thermochronometers, ages provide information about the cooling history of the rock, rather than mineral crystallization ages (although in some cases they do record crystallization ages as well).

For this research, apatite and zircon fission-track (AFT and ZFT,

respectively), and apatite and zircon (U-Th-Sm)/He dating (AHe and ZHe, respectively) were performed on Neoproterozoic metamorphic rocks along the coast between São Paulo in the north and Laguna in the south (BR10-XX, Fig. 1). Samples preparation and analyses followed the same protocol as, e.g. Karl et al. (2013). Whenever possible all four thermochronometry dating techniques were applied to the samples, allowing a more robust evaluation of the spatial and temporal cooling of the sampled rocks. Twenty-seven samples contained apatite and/or zircon grains in quantities, to allow AFT/ZFT, and AHe/ZHe dating (Fig. S5.1-S5.4; Tables 3.1-3.6). For the results and interpretation, we applied the critical use of AHe and ZHe data. In this context, we chose the crystal size and form as the selection criterion for zircon and apatite

grains for the (U-Th-Sm)/He system as it is used in such data (Brown et al., 2013; Beucher et al., 2013; Green and Duddy, 2018), as well as their homogeneity in grain size and chemical content (U, Th, Sm, low radiation damage (eU)). Therefore, we only present clear grains for apatite and clear, light coloured grains for zircon, respectively when the requirement for a full morphology was fulfilled.

Mineral dating technique corresponds to a specific closure temperature (T(c)) and total annealing temperature (T (an)). When temperatures exceed T(c) and T (an) over certain time, the chronometer is reset. Partial annealing or rather retention occurs when temperatures or required time did not fulfil the conditions for a total annealing/retention. For further interpretations the following temperatures were used for T(c), and partial annealing (PAZ), or rather partial retention (PRZ) zones, respectively for apatites and zircons, performed during this research:

- AFT (PAZ): between 110 °C/10 Myr and 60 °C/10 Myr (Gleadow and Duddy, 1981).
- AHe: T(c): ~75 °C/1 Myr (Dodson, 1973) and PRZ: between 70 °C/1 Myr and 40 °C/1 Myr (Wolf et al., 1996, 1998; Farley, 1996, 2000; Stockli et al., 2000).
- ZFT (PAZ): between 330 °C/10 Myr and 190 °C/10 Myr (Garver and Kamp, 2002; Garver, 2003; Hurford, 1986; Rahn et al., 2004; Reiners and Brandon, 2006).
- ZHe: T(c): ~180 °C/1 Myr and PRZ: between 200 °C/1 Myr and 170 °C/1 Myr (Reiners et al., 2002, 2004)

### 3.2. Thermal modelling: time-temperature (t-T) paths and geological model

Thermal modelling of thermochronological data allows us to reconstruct the cooling history for several crustal segments. HeFTy<sup>®</sup> (v.1.9.3.) (Ketcham, 2005; Ketcham et al., 2007a, b; 2009) was used to test time-temperature (t-T) paths against the thermochronological data set. The software code runs paths through t-T-constraints to find possible solutions for a t-T-history considering the input data. When possible, all available thermochronometers were combined and jointly modelled (supplementary data, table S5). For the first time, HeFTy<sup>®</sup> Version 1.9.3 permits to combine several zircon and apatite grains from the (U-Th-Sm)/He system.

The thermochronological data sets used for the numerical modelling are:

- AFT: single grain ages, confined spontaneous fission-track length distribution (> 50 individual length) corrected for c-axis related angle (Donelick et al., 1999; Ketcham, 2017, 5.5M, 2009), etch pit size ( $D_{par}$ ), annealing kinetics of Ketcham et al. (2007a,b)
- AHe: U-, Th-, and Sm concentration, radius of the single grains, uncorrected single grain ages, diffusion kinetics of Flowers et al. (2007, 2009).
- ZFT: only the central age, implemented as external t-T-constraints when necessary to improve thermal modelling
- ZHe: U-, Th-, and Sm concentration, radius of the single grains, uncorrected single grain ages, diffusion kinetics of Guenther et al. (2013).

To define a possible t-T-evolution we tested our thermochronological data against a geological evolution model and an inverse, numerical model was performed. The geological evolution model is determined by t-T-constraints and based on published knowledge of the geological history (Milani et al., 2007). Therefore, Specific t-T-constraints (Tab. S2, with a range corresponding to their uncertainty) were set corresponding to assumed geological events. For all geological t-T-constraints we applied the same coordinates to guarantee a better comparability of the t-T-histories for the modelled samples in their respective blocks (Tab. S2). However, fixed t-T-coordinates may vary slightly from each other in exceptional cases, e.g. t-T-histories of the

samples during the last exhumation in Late Cenozoic.

Palaeo-geothermal gradients published by Hamza et al. (2005) were used for the interpretation of the t-T-models and the calculation of exhumation, and subsidence rates, respectively. We decided to work with a homogenous and arithmetical mean palaeo-geothermal gradient of 30 °C/km for the entire modelled time. The palaeo-geographical reconstruction of the research area was taken from Scotese et al. (1992, 1999) (Fig. S3, S4) and leads to palaeo-surface temperatures of an average of 10 °C for Precambrian to Palaeozoic time, and an mean of 25 °C since Mesozoic time.

Interpolation maps showing the thermal structure of Neoproterozoic basement surface of the study area were generated using the Golden Software Surfer<sup>®</sup>. Palaeotemperatures at specific time steps were taken directly from the “weighted-mean” paths of the modelled t-T-evolution.

### 3.3. Exhumation and subsidence rates

The change in temperature ( $\Delta T$ ) over time ( $\Delta t$ ) was used to determine the cooling or heating rate ( $\Delta T/\Delta t$ ) using the “weighted-mean” paths of the modelled t-T-models. The cooling and heating rates were divided by a fixed geothermal gradient (30°/km) to obtain an exhumation and subsidence rate, respectively. All rates are expressed as positive rates, and relate to exhumation or subsidence according to the decrease and increase of temperature over time.

## 4. Results

All ages obtained (Fig. 4, Tab. S3) are younger than their stratigraphic age. Also, the ages from each thermochronometer conform to an expected relationship given their decreasing closure temperature (i.e. ZFT > ZHe > AFT > AHe age). The elevations of the samples range from almost sea level up to around 1000 m a.s.l. These results were combined with published LTT data from Karl et al. (2013) (nineteen samples, BR09-XX, 11 from basement, 8 sedimentary rocks, Fig. S5.1-S5.4; Tables 3.1-3.6).

### 4.1. Zircon fission-track data

Zircon fission-track analyses was performed on 22 samples (Fig. S5.1; Fig. S6.1, S6.2; Tab. S4.2). The results can be divided into three distinctive regions, beginning with relatively homogenous ages in the northern blocks (Santos, Peruipe, Ilha Comprida, and Curitiba). In these blocks, ages range between  $387.8 \pm 57.0$  Ma and  $255.1 \pm 33$  Ma. Only two ages ( $188.8 \pm 27.6$  Ma for BR10-05 and  $145.5 \pm 16.8$  Ma for BR10-02) do not lie in the general age range. Further to the south, samples from the Florianopolis Block yielded older ages that range from  $539.9 \pm 68.4$  Ma to  $314.1 \pm 39.8$  Ma. Those ages show an increasing trend from the far north to the middle block. The Laguna Block in the south differs in age from the other blocks, showing relatively young ages between  $230.8 \pm 32.1$  Ma and  $108.4 \pm 15.0$  Ma. All single grain age distributions fulfilled the requirement of the  $\chi^2$ -test with values > 5% indicating a homogenous distribution with respect to 1 $\sigma$ -error of the single grain ages (Galbraith, 1981).

### 4.2. Zircon (U-Th-Sm)/He data

Twenty-five samples could be dated using ZHe analyses. 16 of these samples have also been dated using ZFT (Fig. S5.2, Tab. S4.3). Their age distribution is consistent with the ZFT age distribution. ZHe ages range between  $414.2 \pm 33.1$  Ma and  $207.3 \pm 16.6$  Ma in the northern blocks (Santos, Peruipe, Ilha Comprida and Curitiba) with the exception of BR10-05, which was collected at the coast and yielded an age of  $119.9 \pm 9.6$  Ma. This younger age correlates with a significantly younger ZFT age at this location. Further inland, a ZHe age of  $129.7 \pm 10.4$  Ma for BR09-01 is also anomalously younger than the surrounding ZHe ages. The Florianopolis Block reveals an age spectra



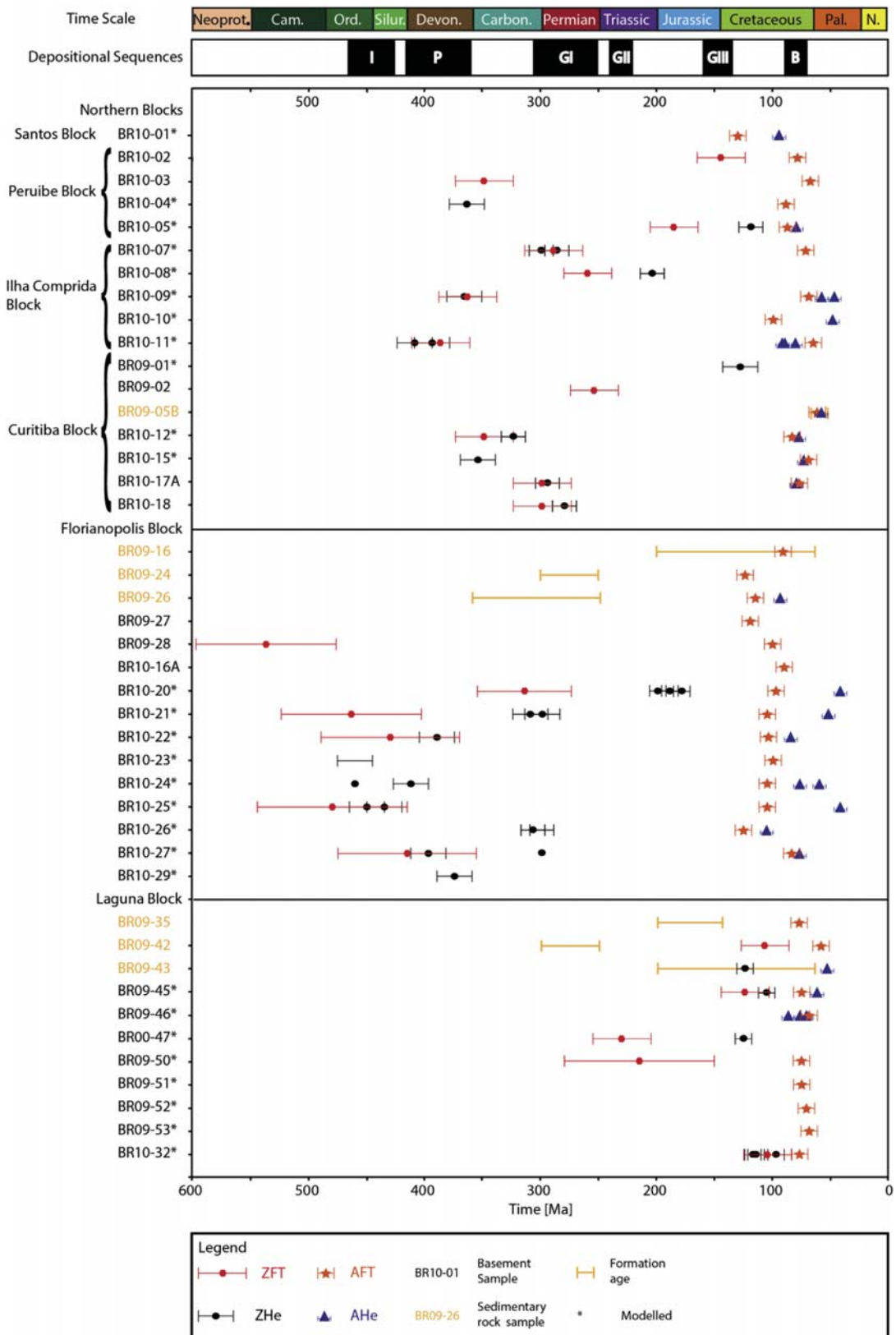


Fig. 4. All thermochronological data of this study plotted against time [Ma]. Orange bars signify age of deposition for sedimentary rock samples.

varying from  $459.9 \pm 36.8$  Ma to  $270.0 \pm 21.6$  Ma except BR10-20 with three grain ages between  $203.3 \pm 16.3$  Ma and  $182.5 \pm 14.6$  Ma. In the south, as observed in the ZFT data, the Laguna Block shows distinctively younger ages with a tight range from  $124.9 \pm 0.6$  Ma to  $98.5 \pm 7.9$  Ma.

#### 4.3. Apatite fission-track data

For thirty-nine samples, at least 18 grains could be dated with AFT analysis except for BR10-07 (12 grains), BR09-17 and BR09-35 (5 grains each) (Fig. S5.3; Fig. S6.3-S6.6; Tab. S4.4, S4.5). All ages are significantly younger than the zircon ages (ZFT and ZHe). All single grain age distributions passed the  $\chi^2$ -test with values between 58 and 100% indicating a heterogeneous distribution with respect to  $1\sigma$ -error of the single grain ages (Galbraith, 1981). Only the Palaeocene sediment sample (BR09-05b,  $\chi^2$ : 5.2%) and a Jurassic sandstone (BR09-42,  $\chi^2$ : 1.0%) failed  $\chi^2$ -test with lower values probably representing two different populations.

The Florianopolis Block represents the oldest ages between  $125.8 \pm 8.9$  Ma and  $85.2 \pm 5.3$  Ma. A trend of younger ages is observed to the north where AFT ages range from  $102.9 \pm 9.8$  Ma to  $63.0 \pm 6.1$  Ma. There is only one sample in the Santos Block that reveals a significant older age of  $130.7 \pm 8.8$  Ma. Figure S5.3 shows AFT ages published by Franco-Magalhaes et al. (2010) which generally show younger ages between 70 and 40 Ma, and some very young ages below 10 Ma.

The Laguna Block shows anomalously younger ages between  $78.0 \pm 5.8$  Ma and  $59.5 \pm 5.2$  Ma along the coast. Also, the AFT ages form a trend of old ages in the north and younger ages in the south that is consistent the trend in ZFT and ZHe data. There is one Jurassic sandstone sample that fits that range with  $79.7 \pm 10.9$  Ma further inland. Further to the west, a Cretaceous basalt sample (Paraná volcanic suite) revealed a younger AFT-age of  $47.7 \pm 11.0$  Ma.

Apatite fission-track length and etch pit size ( $D_{\text{par}}^*$ ) data 36 was acquired for samples. In average, 5.8  $D_{\text{par}}^*/\text{grain}$ , and 123.2  $D_{\text{par}}^*/\text{sample}$ , respectively were counted meaning a total of 4682 etch pit sizes for all apatite grains (Tab S4.5). The mean  $D_{\text{par}}^*$  value for each sample ranges between 1.0 and 2.1  $\mu\text{m}$  with an average  $D_{\text{par}}^*$  value of 1.4  $\mu\text{m}$ . This wide range indicates a relatively inhomogeneous composition concerning the fluorine and chlorine content of apatite. We measured 40.6 track lengths per sample, meaning 1504 track lengths of confined fission-tracks for all samples. Sixteen samples obtained between 52 and 101 measured confined fission-track lengths (75 confined track lengths/grain) that could be used for numerical modelling of the thermal history. Mean track lengths vary between 9.3  $\mu\text{m}$  and 15.8  $\mu\text{m}$ . The correction of the confined track lengths for their crystallographic orientation led to a slightly different distribution between 9.8 and 16.3  $\mu\text{m}$ .

#### 4.4. Apatite (U-Th-Sm)/He data

Twenty apatite grains were analysed with (U-Th-Sm)/He dating (Fig. S5.4; Tab. S4.6). The  $\alpha$ -ejection corrected single grain AHe ages mostly range between  $107.3 \pm 8.6$  Ma and  $59.5 \pm 2.0$  Ma showing no obvious trends in age for the individual blocks. Also, no correlation between grain size and single grain age could be observed. Younger ages between  $58.9 \pm 3.5$  Ma and  $43.0 \pm 2.8$  Ma were also obtained, often along faults.

#### 4.5. Thermal history modelling

Using HeFty<sup>®</sup>, thermal histories for 27 basement samples were modelled. By combining multiple thermochronometers when possible and imposing known geological constraints we find t-T-paths consistent with both the thermochronological data (Tab. S3) and geological history (Tab. S1; S2). For 16 samples, the high number of measured fission

tracks in apatite (> 52) allow robust constraints on the t-T path through 60–110 °C, with ZHe and AHe providing thermal information over hotter and colder temperatures, respectively. Even when the number of track lengths is low, combining AFT with ZHe and AHe still provides a detailed dataset to model. For the first time, HeFty<sup>®</sup> v. 1.9.3 allowed to model successfully multiple combined grains for zircon and apatite, for those samples where grains ages are equal within error. Despite the lack of measured confined fission-track lengths, eleven samples could be modelled combining ZHe and AHe data (Tab. S5). Combining ZHe data, which constrains temperatures between 170 and 200 °C (Reiners et al., 2002, 2004) with AHe data covering temperatures between 40 °C and 70 °C (Wolf et al., 1996, 1998; Farley, 1996, 2000; 2002; Stockli et al., 2000) still guarantees a solid dataset behind the t-T-models. To improve thermal modelling, ZFT ages were implemented as external t-T-constraints for eleven samples.

All models show the t-T-evolution since Late Neoproterozoic time over temperatures below 300 °C (Fig. S7.1-7.8). The geological model derived from Milani et al. (2007) assumes an exhumation to the surface of Neoproterozoic basement rocks after the Pan African/Brasiliano orogeny, followed by the onset of sedimentation and therefore ongoing formation and subsidence of the Paraná Basin mainly during the Devonian. Though, for some localities sedimentation started earlier during the Ordovician or later during the Permian. To test how the samples were influenced thermally in time by the overlying sediment column of the Paraná Basin depositional sequences, t-T-models have been permitted to run mainly unconstrained covering wide temperature intervals. The constraint boundaries for those temperature intervals have been assumed for either none sediments deposited, or calculated maximum thicknesses of deposited sediments during depositional sequences (Tab. S6). From Late Mesozoic, the t-T-evolution is dominated by the syn- and post-rift evolution of the SAPCM including possible exhumation to the surface during the Early Cenozoic. A possible thermal influence triggered by the Palaeogene evolution of the onshore graben systems parallel to the recent coast was tested subsequently against the data set before the final exhumation to the surface occurred.

For all samples (Fig. S7.1-7.8), 50 000 t-T-paths have been tested against the data set. In general, thermal modelling yielded for a high goodness of fit (G.O.F.). However, to provide comparability of the modelled samples we accepted lower values of the G.O.F. without omitting thermochronometers or t-T-constraints to gain better values. Therefore, t-T-models passed our requirements when good fits were found. Altogether, t-T-models reveal between 8 and 6952 good, and between 87 and 12345 acceptable t-T-paths, while the majority shows results > 120 good and > 350 acceptable t-T-paths. The AFT age and confined fission-track length distribution for 14 samples reproduced with an excellent goodness of fit (G.O.F.) > 81%, and for 11 samples a GOF > 85%. Only two samples revealed a G.O.F. of 19 and 79% for the AFT age, and five samples between 22 and 79% for the confined fission-track length distribution. For the ZHe data, the obtained t-T-models of 19 samples indicate a G.O.F. > 75% whereas three samples provide 31–55%. While eight modelled samples show a G.O.F. > 82% for the AHe data, six samples could be reproduced between 19 and 59%. One possibility to explain lower values of the G.O.F. can be traced back to the difficulty of finding t-T-models capable of satisfying the complex data of different thermochronometers from multiple grains. The more thermochronological data combined in HeFty<sup>®</sup> resulted in thermal histories with a poorer G.O.F. to the individual thermochronometers.

### 5. Interpretation and discussion

For discussion and interpretation of the t-T-evolution of the Neoproterozoic basement, published geochronological data (Tab. S7) were directly incorporated into the modelled t-T-histories (Fig. 5) to cover the entire syn-to post-Late Neoproterozoic evolution of the SE coastal region of Brazil along the SAPCM (stages 1–3). Thermal modelling histories were used to make estimates on exhumation and

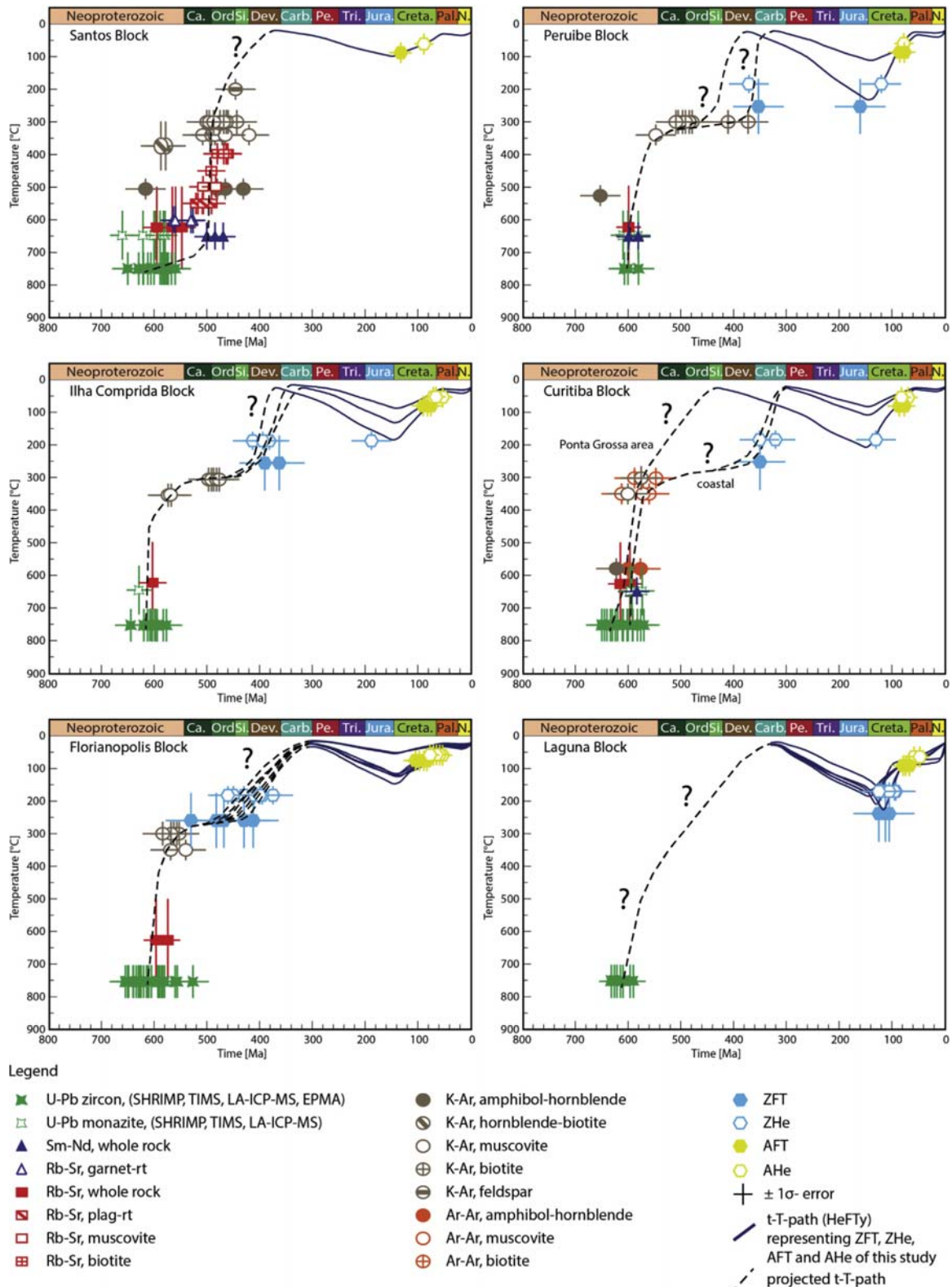


Fig. 5. Time (t)-temperature (T)-evolution of the individual blocks of the SAPCM in south-eastern Brazil. Published geochronological data were directly incorporated into the “weighted-mean” t-T-paths of the samples modelled with the software code HeFTy<sup>®</sup> (Ketcham et al., 2007a,b) to reconstruct the entire syn- to post-Neoproterozoic t-T-evolution of the SAPCM in south-eastern Brazil.

subsidence rates.

### 5.1. Stage 1: Late Neoproterozoic to Upper Palaeozoic – syn- to post-orogenic cooling, erosion and uplift (exhumation)

The Neoproterozoic basement in south-eastern Brazil was formed during the Pan African/Brasiliano orogeny (Machado et al., 1996; Töpfer, 1996; Hackspacher and Godoy, 1999; Cordani et al., 2000; Alkmim et al., 2001). Therefore, the Late Neoproterozoic to Upper Palaeozoic is characterized by post-orogenic cooling of the rocks and exhumation. Published geochronological data combined with thermochronological data of this study indicate a very complex and distinct geological evolution of the different crustal blocks along the south-eastern coast of Brazil (Fig. 5; 6, A-E).

Previously published geochronological data (Tab. S7) from the Ponta Grossa Arch (PGA, inland Curitiba Block) implies initial cooling (from 700 to 800 °C) of the Neoproterozoic basement during the Late Neoproterozoic (~650–580 Ma; U-Pb, Sm-Nd, Rb-Sr) (Siga et al., 1995, 2003; 2007, 2009; Prazeres Filho et al., 2003, 2005; Faleiros, 2008; Tassinari et al., 2008; Salazar et al., 2008). The possible cooling path of the metamorphic rocks in this area continues through the latest Ediacaran to Early Palaeozoic (550–500 Ma; Ar-Ar, K-Ar) (Siga et al., 1995; Campagnoli, 1996; Machado et al., 2007; Faleiros, 2008; Kaulfuss, 2011). Due to the lack of further data and the first occurrence of sedimentary rocks close to the samples (Fig. 1; 3, Rio Ivaí, Milani et al., 2007) the exhumation of the basement in the PGA can be assumed until the end of the Ordovician.

The exhumation history of the northern Santos Block (Fig. 5; 6, A-E; Tab. S7) correlates with the exhumation history of the PGA showing a relatively fast exhumation to the surface until the end of the Devonian. Initial cooling of the metamorphic basement took place between ~650 and ~570 Ma (U-Pb) north and south of the City of São Paulo (Hackspacher et al., 2000; Dias Neto, 2001; Tassinari, 2008; Passarelli et al., 2008; Alves et al., 2013). Sm-Nd, Rb-Sr, and K-Ar-ages (Dias Neto, 2001; Hackspacher et al., 2001) between ~560 and ~460 Ma indicate an initial period of slower cooling. This is followed by fast exhumation during the Early Palaeozoic. The occurrence of Paraná sediments (Milani et al., 2007) constrains the exhumation of the Neoproterozoic basement during the Devonian (Fig. 3).

Further south, post-orogenic cooling of the central blocks of Peruibe, Ilha Comprida, Curitiba (coastal), and Florianópolis differs clearly from the northern area and the PGA (Fig. 5; 6, A-E; Tab. S7). The post-orogenic cooling and exhumation of Neoproterozoic rocks indicate to be threefold.

- (1) Geochronological data (Tab. S7) showing ages between ~650 and 530 Ma (U-Pb, Sm-Nd, Rb-Sr) imply that initial rock uplift and rapid cooling took place during the Late Neoproterozoic. Ar-Ar ages between ~600 and ~570 Ma (Machado et al., 2007; Kaulfuss, 2011) support the described cooling (Fig. 5).
- (2) Younger K-Ar ages covering lower temperatures of 300–400 °C range between ~550 and ~490 Ma for the Peruibe Block (Passarelli et al., 2001, 2008), and around 575, and between ~505 and ~490 Ma in the Ilha Comprida Block (Passarelli et al., 2001, 2006) indicating a decrease in cooling rate and rock uplift velocity (Fig. 5). In the Curitiba Block (coastal) K-Ar ages range between ~620–600, and ~550–500 Ma (Siga et al., 1995; Campagnoli, 1996; Kaulfuss, 2011). This data is supported by Ar-Ar ages around 615 Ma and between ~590 and ~550 Ma (Siga Jr. et al., 1995; Faleiros, 2008; Kaulfuss, 2011). K-Ar ages between ~585 and 540 Ma (Passarelli et al., 2010) continue the cooling path for the Florianópolis Block. In this Early Cambrian to Devonian period, rocks remained at middle to upper crustal levels at temperatures of about 200–300 °C (Fig. 5; 6, D, E). Florisbal et al. (2012) and Bento dos Santos et al. (2010, 2014) also described a relatively long period (> 80 Ma) with higher temperature conditions, and slow

cooling within the middle and lower crust due to intense post-collisional magmatism along the major shear zones.

New ZFT and ZHe ages of this study (Fig. 8A and B) are consistent with the t-T-evolution of the Neoproterozoic basement rocks and support the assumption of a stable period as thermochronological data do not allow an earlier and faster rock uplift to the surface. In the Peruibe, Ilha Comprida, and Curitiba Block, ZFT and ZHe ages range between ~440 and ~220 Ma, and ~450 and ~260 Ma, respectively (Fig. 4; 8; Tab. S3). ZFT ages imply a stable and old Florianópolis Block in the centre of the study area with ages between ~500 and ~300 Ma. Valeriano et al. (2016) describe post-collisional magmatism possibly caused by break-off of the subducted lithospheric slab following the Pan African/Brasiliano orogeny during the Early Palaeozoic, leading to intrusions of post-collisional granites into the Precambrian basement within the Ribeira Belt in the North (City of Santos up to the state of Espírito Santo). Hence, ZFT and ZHe ages between ~500 and ~300 Ma may also represent cooling ages of post-collisional activities.

The interpolation maps of the age distribution of the Neoproterozoic basement (Fig. 8A and B) clearly indicate how the Florianópolis Block is bordered by the Florianópolis fracture zone (FFZ) and Rio Alonzo fracture zone (RAFZ). Siga Jr. et al. (1995) also refer to K-Ar hornblende and biotite ages of 2.1–1.7 Ga within the Luís Alves Terrane as an indication for stable crustal segments during the Pan African/Brasiliano orogeny within the Florianópolis Block. This evolution can also be seen in the ZHe data that range between ~400 and ~300 Ma.

- (3) Sedimentary rocks of the Upper Palaeozoic close to the sampled rocks of this study infer a rapid exhumation moving the Neoproterozoic rocks to the surface during the Late Devonian (Peruibe, Ilha Comprida, Curitiba) and the Carboniferous/Early Permian (Florianópolis).

In the far South, there only exist few geochronological data for the Laguna Block (Fig. 5; 6, A-E, Tab. S7). Initial post-orogenic cooling is stored in U-Pb data (zircon) ranging between ~640 Ma and ~580 Ma (Silva et al., 1997 and unpublished; Hartmann et al., 2003; Jelinek et al., 2005). Due to Permo-Carboniferous sedimentary rocks close to the samples, exhumation to the surface can be assumed from Late Carboniferous to the Early Permian. However, the t-T-evolution of the Laguna Block from the Late Neoproterozoic to the Upper Palaeozoic remains uncertain. We suggest the Paleozoic tectonic exhumation of the mobile belts and deposition of the lower sequences of the Paraná Basin to cause the major contrast in the t-T-evolution of the different blocks.

#### 5.1.1. Exhumation rates during the Late Neoproterozoic to Upper Palaeozoic

Results of our thermal modelling of the combined geo- and thermochronological data can be used to determine exhumation rates for the distinct t-T-evolution of the individual blocks.

The PGA area (Curitiba Block) and the Santos Block, in the north, show an initial exhumation rate of ~0.25 mm/a (640–580 Ma), and ~0.03 mm/a (640–510 Ma) respectively (Fig. 7; Tab. S8). This relatively fast exhumation continued with rates of ~0.07 mm/a (580–430 Ma) for the PGA and ~1.23 mm/a (510–500 Ma), and ~0.07 mm/a (500–380 Ma) for the Santos Block (Fig. 7; Tab. S8).

- (1) During the initial cooling and rock uplift of the middle blocks, exhumation rates are similar at ~0.27 mm/a (600–550 Ma, Peruibe), 0.23 mm/a (620–560 Ma, Ilha Comprida), 0.33 mm/a (600–560 Ma, Curitiba (coastal)), and 0.37 mm/a (600–560 Ma, Florianópolis) (Fig. 7; Tab. S8).
- (2) During the relatively long and stable period from the Early Cambrian to the Devonian where rocks remained at upper crust levels, exhumation rates slow down to ~0.02 mm/a (550–400 Ma, Peruibe), ~0.01 mm/a (560–430 Ma, Ilha Comprida), ~0.02 mm/a

(560–370 Ma, Curitiba (coastal)), and  $\sim 0.01$  mm/a (560–430, Florianópolis) (Fig. 7; Tab. S8). These rates are consistent with observations made by Florisbal et al. (2012) and Bento dos Santos et al. (2010, 2014) who describe low cooling rates ( $\sim 1$  °C/Ma) within the middle and lower crust due to intense post-collisional magmatism along the major shear zones.

- (3) The final Palaeozoic uplift to the surface reveals exhumation rates of  $\sim 0.22$  mm/a (400–360 Ma, Peruibe),  $\sim 0.09$  mm/a (430–330 Ma, Ilha Comprida),  $\sim 0.11$  mm/a (370–300 Ma, Curitiba (coastal)), and  $\sim 0.05$  mm/a (460–310 Ma, Florianópolis) (Fig. 7; Tab. S8).

The southern Laguna Block shows Late Neoproterozoic to Upper Palaeozoic exhumation rates of  $\sim 0.13$  mm/a (620–530 Ma) and  $\sim 0.07$  mm/a (530–330 Ma) (Fig. 7; Tab. S8).

### 5.1.2. Age and timing of movement along tectonic structures

The age and timing of movement along the predominant tectonic systems of the SE Brazilian coastal region is part of a major debate in Brazil (Basei et al., 1995, 1999; 2008, 2010; 2011; Cobbold et al., 2001; Meisling et al., 2001; Torsvik et al., 2009; Franco-Magalhaes et al., 2010; Hiruma et al., 2010; Karl et al., 2013; Bruno et al., 2018). However, our thermochronological data and its t-T-evolution models do not permit us to make any suggestion concerning the formation age and possible reactivation of the Precambrian NE-SW trending shear zones and thrust belts. The interpolation maps of the thermal basement structure also indicate light N-S trends for the Late Neoproterozoic to Upper Palaeozoic t-T-evolution (Fig. 6, A–D).

This N-S trends shifts during the Devonian/Carboniferous (Fig. 6E and F), and the course of temperature isolines indicates to follow more similar NW-SE trends of the younger Paleozoic fracture zones. Therefore, our data support a distinct thermal evolution along the future SAPCM and infer possible movement along fracture zones separating the different blocks (Figs. 5 and 6). Similar large W-E trending structures exist in the Damara Belt on the African side and have been dated back to the Precambrian (Coward and Daly, 1984; Raab et al., 2002; Goscombe and Gray, 2008; Foster et al., 2009; Brown et al., 2014; Goscombe et al., 2017). Still, our results do not permit any reasonable prediction about the formation age of the NW-SE trending fracture zones in south-eastern Brazil. However, the distinct t-T-evolution allows the assumption that repeated reactivation and movement along the Paleozoic fracture zones could have possibly played a role over time. Such trends in the thermal structure of the Neoproterozoic basement cannot be observed before the Devonian and therefore, leaves the question about a more accurate age unanswered.

Furthermore, we suggest changes in climate and direction of erosion induced by the upcoming Gondwana glacial period (Montañez and Poulsen, 2013), and later, far-field effects of the Gondwanide orogeny (Zalán et al., 1991; Trouw and de Wit, 1999) that may have provoked the transition of the predominant tectonic structures, and therefore, the transition of the temperature isoline orientation.

### 5.2. Stage 2: Upper Palaeozoic to Early Cretaceous – Paraná Basin formation and the Paraná–Etendeka plume activity, pre-to syn-break up processes

The Upper Palaeozoic to Early Cretaceous t-T-evolution of the Neoproterozoic basement rocks (Fig. 1; Fig. 5.2, F–J) along the SAPCM is characterized by formation of the Paraná Basin. According to Milani et al. (2007), subsidence of the Paraná Basin started during the Ordovician (PGA), the Devonian (Santos, Peruibe, Ilha Comprida), or rather the Permo-Carboniferous (Curitiba, Florianópolis, Laguna). Ongoing sedimentation of five second order depositional sequences occurred in the centre of the basin until syn-rift stage in Early Cretaceous. Stratigraphic records revealed a total accumulation thickness of sedimentary rock of  $\sim 5500$ – $\sim 5900$  m (Fig. 3; Tab. S6) overlying the Neoproterozoic basement rocks until the Early Cretaceous. By using already

described palaeo-parameters (surface temperatures:  $\sim 10$ – $\sim 25$  °C (Figs. S3; S4); geothermal gradient: 30 °C/km), these columns would have heated the basement to temperatures between  $\sim 200$  and  $\sim 220$  °C. Adding 1700 m (Serra Geral Formation) of Paraná–Etendeka flood basalts during syn-rift stage would imply  $> 7600$  m of sediment column ( $> 275$  °C) by the end of Gondwana III depositional sequence in the northern blocks. In the South, accumulated sedimentary rocks starting in the Carboniferous/Permian (Gondwana I) would have reached an overlying thickness of  $> 4500$  m ( $> 170$  °C) until the Botucatu Formation (Gondwana III) just before syn-rift stage, or rather  $> 6200$  m ( $> 230$  °C) of sediment column adding Paraná–Etendeka flood basalts during syn-rift stage. The assumed overlying thicknesses, and therefore elevated temperatures would have had reset the entire ZFT and ZHe thermochronometers and resulted in the homogeneous ages of Early to Mid-Cretaceous. This thermal overprint cannot be found in most of the thermochronological data (Fig. 8A–D), old zircon ages ( $\sim 500$  and  $\sim 300$  Ma, Florianópolis Block) indicate that temperatures did not exceed  $\sim 185$ – $160$  °C/1Myr since the post-orogenic cooling of the Neoproterozoic basement. This evolution continues further to the North, as the Curitiba and Ilha Comprida blocks can be interpreted as transition zones also showing old zircon ages between  $\sim 400$  and  $\sim 300$  Ma. Thermal modelling (Fig. 5) also supports this, by not exceeding maximum temperatures of 160 °C since the exhumation during Early to Late Palaeozoic for the northern blocks. Results show homogeneous and lower temperature t-T-evolution histories with a few exceptions (BR10-05, BR09-01 and BR10-20) that could have been thermally influenced by intrusions during the syn- and post-rift stage causing partly younger zircon ages. The Laguna Block shows a distinct thermal evolution reaching temperatures from 160 to 220 °C (Fig. 6, J) by the end of the syn-rift stage.

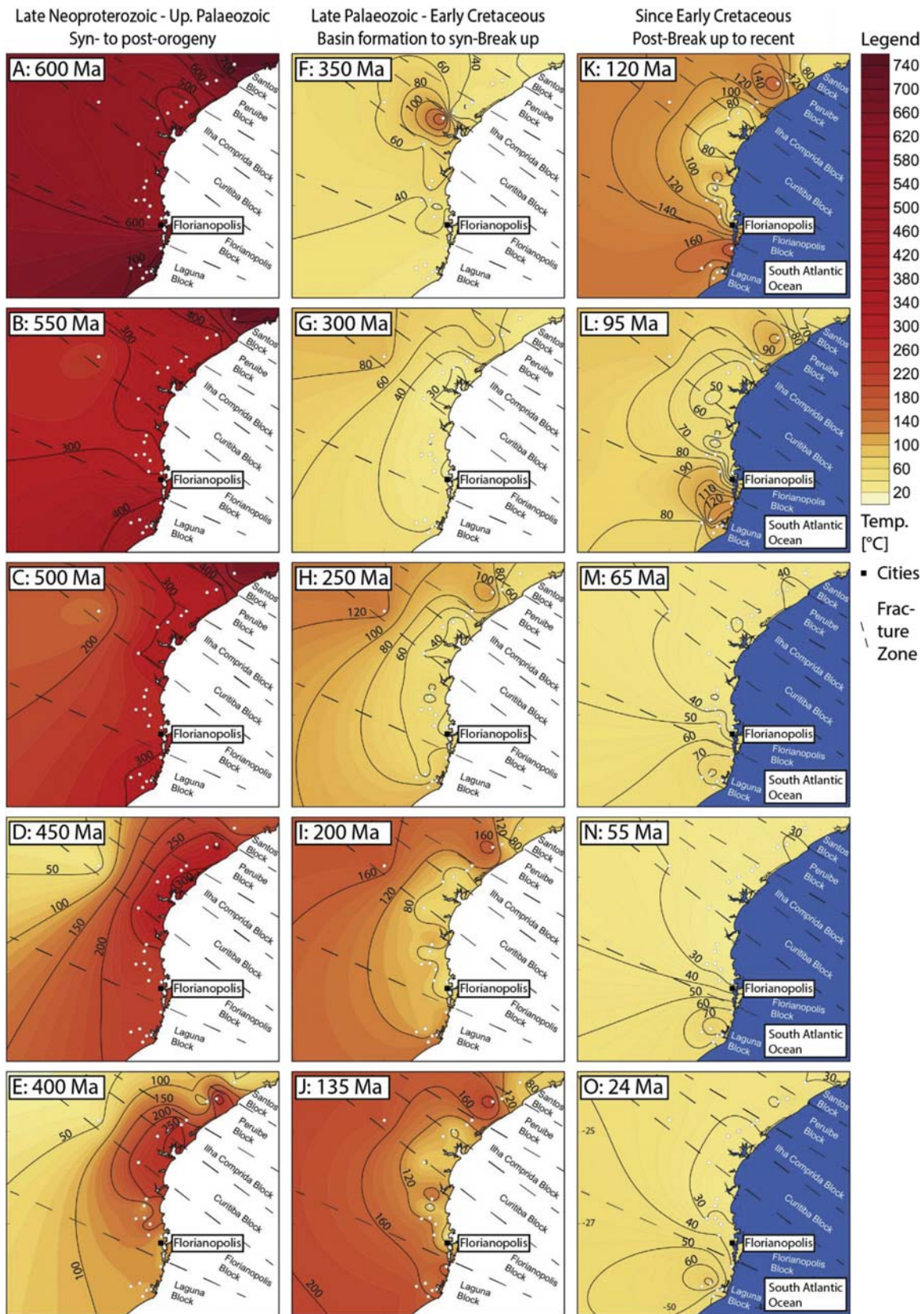
### 5.3. Two possible scenarios are presented

- (1) Thermal modelling shows maximum temperatures between 80 and 160 °C (Fig. 6H–J) that would correspond to a column of 2000–4600 m of overlying Paraná Basin sedimentary rocks until syn-rift stage in the northern blocks. Cogné et al. (2011, 2012, and 2013) also indicate sediment thicknesses between 2000 and 5000 m eroded during post-rift stage for the northern coastal area between São Paulo and Rio de Janeiro. For the southern Laguna Block (Fig. 6, J), maximum temperatures between 160 and 220 °C indicate a column of 4600–6600 m of overlying rocks. Following the assumption of homogeneous sedimentation in the study area, the Laguna block could have been covered by  $\sim 2000$  m of flood basalts during syn-rift stage. This scenario does not allow any deposition of Paraná–Etendeka flood basalts north of the Laguna block.
- (2) The research area is located far from the Paraná basin centre where the stratigraphic record by Milani et al. (2007) was taken and might be an outer part where significantly less to almost no sedimentary rocks were deposited during second order deposition sequences in Palaeozoic and Mesozoic time. This would imply temperatures between 80 and 160 °C in the North (Fig. 6H–J), and  $> 200$  °C in the Laguna Block (Fig. 6, J) were caused exclusively by the thermal influence of the Paraná–Etendeka magmatic activity.

However, thermochronological data and thermal modelling show distinct thermal evolution of the study area (Fig. 6, F–J). All thermochronological evidence indicates much less sediments deposited and almost no recognized thermal overprint for ZFT and ZHe ages, neither caused by subsidence, nor thermal influence by the Paraná–Etendeka Large Igneous Province for the northern blocks.

#### 5.3.1. Subsidence rates during the Upper Palaeozoic to Early Cretaceous

Thermal history models suggest subsidence rates (Fig. 7; Tab. S8) between  $\sim 0.01$  (Santos) and  $\sim 0.02$  mm/a (Curitiba, PGA) for the northern blocks. In the Laguna Block, t-T-evolution paths provide



(caption on next page)

**Fig. 6.** Late Neoproterozoic to recent temperature evolution. Maps show the temperature distribution of the old Neoproterozoic surface at specific time steps based on the t-T-paths obtained from modelling our thermochronological data. Red colours signify that the Neoproterozoic basement was in depth at high temperatures. Whereas lighter colours indicate temperatures of the Neoproterozoic surface near the surface. Isolines show temperatures. No data were available for the white area (western African part of Gondwana (before 135 Ma). Positions and directions of fracture zones were taken from [Cobbold et al. \(2001\)](#), [Meisling et al. \(2001\)](#), [Riccomini et al. \(2005\)](#), [Strugale et al. \(2007\)](#), [Franco-Magalhaes et al. \(2010\)](#), and [Karl et al. \(2013\)](#). Onshore extensions only show tendencies, and are not confirmed trends.

subsidence rates of ~0.03 mm/a (330-145 Ma), followed by ~0.05 mm/a (145-120 Ma).

**5.4. Stage 3: Early Cretaceous to recent – post-break up processes, erosion and surface uplift (exhumation)**

The Early Cretaceous to recent t-T-evolution (Fig. 5; 6, K-O) of the SAPCM in south-eastern Brazil is characterized by post-break up processes, such as cooling, erosion and surface uplift (exhumation). The t-T-history in the blocks of Florianopolis and those in the North evolved as follows. While ZFT and ZHe data have been mostly unaffected thermally during the syn- and post-rift tectonic evolution, AFT and AHe data were completely reset during the formation of dike swarms and the emplacement of the Paraná-Etendeka flood basalts. Most samples cool down from temperatures between 80 and 120 °C (~2800 m) to 60–80 °C (~1300 m) around 95 Ma (Fig. 6; K, L). The timing of cooling, and exhumation, respectively, correlates with observations by [Cogné et al. \(2011, 2012, and 2013\)](#). However, the AFT and AHe age distribution (Fig. 8; C, D) is very complex. As already observed for the zircon ages (ZFT and ZHe), the Florianopolis Block also shows the oldest ages for the AFT (~120-100 Ma) and AHe (~90-70 Ma) data. Combined thermochronological data lead to the interpretation that the old and stable Florianopolis Block exhumed earlier along FFZ and RAFZ than the other blocks indicating the reactivation of these large fracture zones during syn- and post-rift evolution of the SAPCM. NE-SW trending isolines for ZFT, AFT and AHe data also correlate with NE-SW trending fracture zones (Fig. 8). To the North, AFT ages are around ~80 Ma. This implies an event causing young reset AFT ages during the

post-rift stage. The thermal overprint can also be seen in the AHe data as ages varying between ~90 and ~70 Ma, due to a thermal anomaly induced by the Trinidade hot spot during the Late Cretaceous and Early Palaeogene ([Thompson et al., 1998](#); [Ernst and Buchan, 2001](#); [Meisling et al., 2001](#), [Storey et al., 2001](#); [Tello et al., 2003](#); [Hackspacher et al., 2004, 2007](#)). Further inland, published AFT data by [Franco-Magalhaes et al. \(2010\)](#) show very young ages (< 70 Ma) indicating a thermal overprint caused by post-rift reactivation of the old Precambrian shear zones due to the evolution of continental rift basins ([Franco-Magalhaes et al., 2010](#)). Young AHe ages from 60 to 50 Ma along the coast might also be related to the activation of onshore structures. AFT ages in this area are comparable with published data by [Hackspacher et al. \(2004\)](#) and [Engelmann de Oliveira et al. \(2016\)](#) and indicate a trend of increased ages to the North, which correlate with published AFT-ages by [Gallagher et al. \(1994\)](#).

Cooling since the Early Cretaceous (Fig. 5; 6, K-O) implies three phases of surface uplift and erosion during the post-rift evolution for the blocks north of the City of Florianopolis. Stratigraphic records show Early Cenozoic sedimentary rocks overlying the Neoproterozoic basement rocks in several onshore basins along the south-eastern Brazilian coast ([Salamuni et al., 2003](#); [Hiruma et al., 2010](#); [Cogné et al., 2011, 2012, and 2013](#)). This indicates that basement rocks were already exhumed to the surface by the end of the Cretaceous/Early Cenozoic.

The second post-rift phase began during Early Cenozoic. Tectonic and volcanic activity within onshore graben systems such as the Taubaté Basin led to erosion and sedimentation into onshore and offshore basins. The thermochronological data set was tested against such a possible thermal influence initiated during onshore graben system

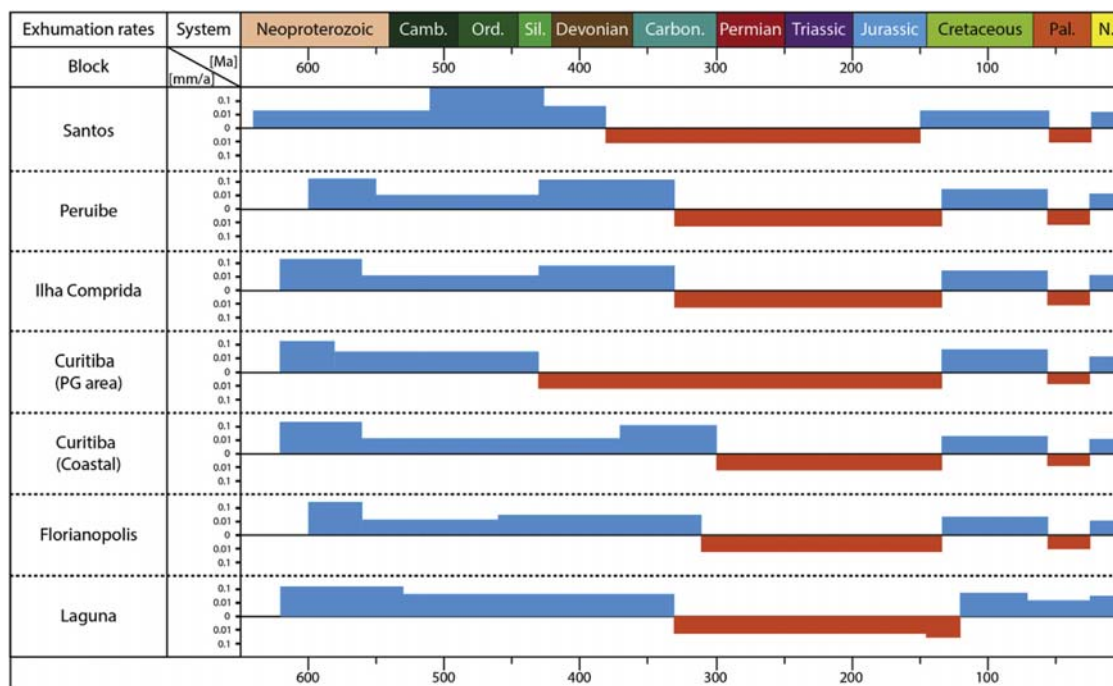


**Fig. 7.** Calculated exhumation and subsidence rates, derived from combined geochronological and thermochronological t-T-modelling of the thermal evolution of the individual blocks of the SAPCM in south-eastern Brazil (Fig. 5). For further information see methods, chapter 3.4. Blue bars indicate exhumation (derived from cooling rates), red bars signify subsidence (derived from heating rates). The thickness of the bars implies higher/lower rates.

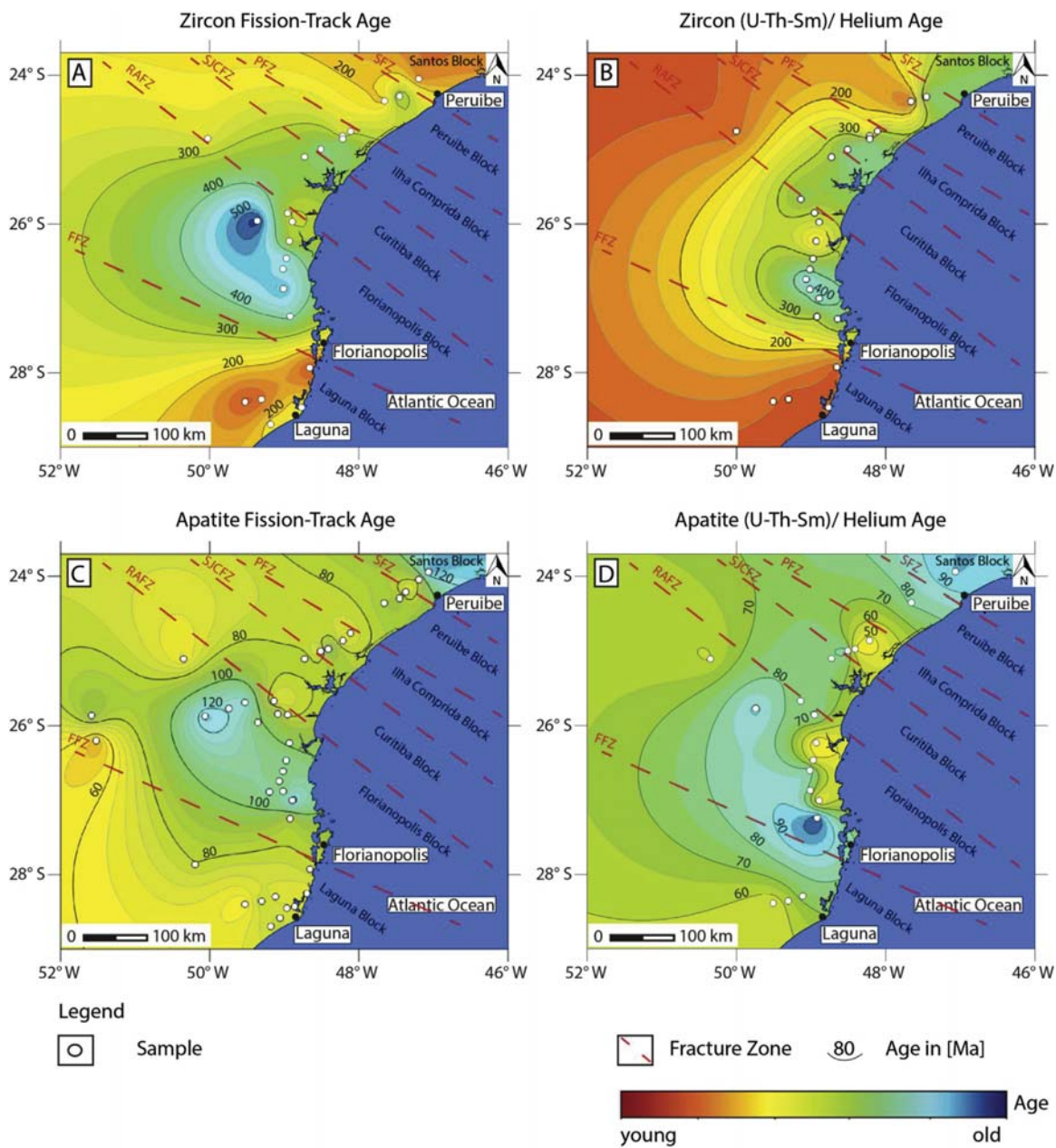


**Fig. 8.** Modelled interpolation maps of the age distribution of the samples of this study for the individual thermochronometers using the Golden Software Surfer®. Yellow to red colours indicate younger ages. Green to blue colours imply older ages. Isolines show age in [Ma] without error. White dots show samples locations. Positions and directions of fracture zones were taken from [Cobbold et al. \(2001\)](#), [Meisling et al. \(2001\)](#), [Riccomini et al. \(2005\)](#), [Strugale et al. \(2007\)](#), [Franco-Magalhaes et al. \(2010\)](#), and [Karl et al. \(2013\)](#). Onshore extensions only show tendencies, and are not confirmed trends.

activity (Palaeogene to Neogene) leading to regional heating, or rather subsidence of several onshore basins along the coast. The t-T-models allow possible heating with subsidence reaching temperatures between 20 and 45 °C meaning less than 800 m of sedimentary rocks deposited (Fig. 5; 6, M, N) as thermochronological data shows no thermal overprint for the corresponding time interval. Still, thermal modelling indicates possible extended onshore basins along the coast from the North as far as the Florianópolis Block. The third phase of the post-rift evolution is characterized by the final exhumation within the Neogene.

In the South, the Laguna Block stands out significantly from the other blocks. Zircon ages (ZFT and ZHe) are fully reset showing ages of < 140 Ma during the syn- and post-rift evolution of the SAPCM. This block reached the highest temperatures (160–220 °C, Fig. 5; 6, J, K)

during syn- and post-rift stage. Therefore, we assume that the Laguna block was kept in higher temperatures until the end of the Lower Cretaceous and then later experienced exhumation driven cooling. Higher temperatures could be either attributed to a thicker column of overlying sedimentary rocks and/or Paraná-Etendeka flood basalts. Also, a temporally increased geothermal gradient caused during volcanic activity (flood basalts and dyke swarms) could have played a role. Nevertheless, thermochronological data shows that the Neoproterozoic basement underwent a significant thermal overprint within the Laguna Block. AFT and AHe ages range between ~80 and ~60 Ma and show a homogenous age distribution for this block (Fig. 8C and D). Steady cooling and exhumation to the surface characterized the t-T-evolution of the Southern Laguna Block. Thermal modelling does not permit any



reheating during the onset of the onshore graben system activity in the Early Cenozoic (Salamuni et al., 2003; Hiruma et al., 2010; Cogné et al., 2011, 2012, and 2013). Therefore, we suggest that rocks experienced higher temperatures for longer time, and exhumation occurred later than in the northern blocks. Thermal history models and the interpolation maps of the thermal structure of the Neoproterozoic basement indicate that the Neoproterozoic basement rocks of the Laguna block were kept in temperatures between  $\sim 60$  and  $\sim 80$  °C (1300–2000 m) (Fig. 5; 6, M, N).

During Serra do Mar uplift in the south (Almeida et al., 1998; Hiruma et al., 2010), thermal modelling indicates rapid cooling leading to the assumption that the final exhumation of the Neoproterozoic basement took place within the last 20 Myr. The Laguna Block appears to have cooled down slower having experienced more time at higher temperatures. Distinct, ongoing erosion from the north to the south could have also played a role for the individual exhumation.

#### 5.4.1. Exhumation and subsidence rates

Three phases of cooling and exhumation of Neoproterozoic rocks during the post-rift evolution occurred for the blocks north of Florianópolis. (1) From Early Cretaceous ( $\sim 135$  Ma) to Early Cenozoic ( $\sim 55$  Ma) t-T-models reveal exhumation rates of  $\sim 0.03$  mm/a (Santos),  $\sim 0.05$  mm/a (Peruibe),  $\sim 0.05$  mm/a (Ilha Comprida),  $\sim 0.03$  mm/a (Curitiba, coastal),  $\sim 0.07$  mm/a (Curitiba, PGA), and  $\sim 0.04$  mm/a (Florianópolis) (Fig. 7; Tab. S8). (2) A second phase is characterized by possible erosion and sedimentation into onshore and offshore basins. Possible subsidence reveals rates of  $\sim 0.01$ . (3) Within the Neogene, t-T-models for these blocks provide rates of  $\sim 0.02$  mm/a for the final exhumation (Fig. 7; Tab. S8).

The Laguna block shows distinct exhumation rates for its different exhumation history since the Early Cretaceous. From Early ( $\sim 120$  Ma) to Late ( $\sim 70$  Ma) Cretaceous, cooling, or rather exhumation set in with rates  $\sim 2.30$  °C/Ma and  $\sim 0.08$  mm/a, respectively. During the Early Cenozoic, exhumation slows down to  $\sim 0.025$  mm/a (70–24 Ma). The final exhumation within the last 20 Myr reveals rates of  $\sim 0.056$  mm/a (Fig. 7; Tab. S8).

## 6. Conclusions

We present an extensive new multi-thermochronometer dataset to reconstruct a detail t-T-evolution of the Brazilian SAPCM. To cover the entire temperature range from post-orogenic cooling to near-surface processes published geochronological data were directly integrated into the thermochronological data of this study to reconstruct the syn-to post-Late Neoproterozoic t-T-evolution of the SE coastal region of Brazil.

The syn-to post-Late Neoproterozoic to Upper Palaeozoic t-T-evolution of the SAPCM in south-eastern Brazilian margin is shown to be very complex. In the central part of the SAPCM, the Pan African/Brasiliano post-orogenic cooling and exhumation of Neoproterozoic rocks occurs in three stages: (1) A first rapid, Late Neoproterozoic exhumation of the basement; (2) a phase where rocks are kept within the crust (at temperatures of about 200–300 °C) from the Early Cambrian to the Devonian; (3) and a second rapid exhumation moving Neoproterozoic rocks to the surface occurred in the Late Devonian. The northern and southern parts indicate a distinct syn-to post-orogenic exhumation to the surface implying a faster cooling, and erosion from Late Neoproterozoic to Devonian/Carboniferous.

Quantification of timing and rates of subsidence, exhumation, and erosion is possible using numerical modelling. From the Upper Palaeozoic, the t-T-evolution of the SAPCM in south-eastern Brazil is characterized by ongoing subsidence during the formation of the Paraná Basin. The t-T-evolution of the samples show trends of on-going subsidence during depositional sequences of the Paraná Basin. However, thermochronological data are unable to constrain high temperatures corresponding to the accumulation of overlying sediment

thicknesses suggested by from existing stratigraphy (Milani et al., 2007). Maximum temperatures of the thermal modelling are reached during syn- and early post-South Atlantic rift stage, which has been described by Engelmann de Oliveira et al. (2016). While ZFT and ZHe ages north of Florianópolis Block have not been affected thermally since the formation of the basement during the Late Neoproterozoic, most of the zircon and apatite ages have been completely reset thermally by syn- and post-South Atlantic rift processes. Numerical modelling also indicates a distinct evolution of the study area with a significant thermal overprint in the southern Laguna Block (reset ZFT and ZHe data) most likely caused by the Paraná-Etendeka flood basalt volcanism. The Florianópolis and northern blocks indicate less to almost no thermal overprint experienced during syn- and post-rift stage of the South Atlantic. The role of dyke swarms in the Curitiba and Ilha Comprida blocks remains still unclear though AFT and AHe ages indicate thermal overprint in the North. Nevertheless, it is clear that temperatures never exceeded  $\sim 160$  °C though ZFT and ZHe ages have not been reset in the North during Paraná-Etendeka magmatic activity.

Cooling and exhumation of the Neoproterozoic basement rocks began during post-rift stage and continued until surface uplift during Early Cenozoic in the north. However, thermal modelling allows low reheating, corresponding to subsidence for the Florianópolis and the northern blocks during Early Cenozoic. This indicates a possible thermal influence coeval with the onset of tectonic and volcanic activity in onshore graben systems including erosion and sedimentation into onshore and offshore basins. In the south, the Laguna Block shows a distinct exhumation evolution reaching the surface within the last 24 Myr, which also correlates with observations made by Engelmann de Oliveira et al. (2016).

Finally, geo- and thermochronological data shows that the Late Neoproterozoic to Early Paleozoic t-T-history might not be necessarily connected with the Upper Paleozoic to Cenozoic geological evolution. From the Upper Paleozoic, NW-SE trending structures predominate the SE coastal region of Brazil. There may have been several movements along NW-SE trending Paleozoic fracture zones and distinct exhumation between the several blocks over time. Especially, exhumation in the northern blocks differs from the Laguna Block in the south. The Florianópolis Block stands out as the coolest and most stable block showing the oldest ages for zircon and apatite. It directly faces the younger Laguna Block in the South, just separated by the large Florianópolis fracture zone that has possibly been reactivated several times since the Paleozoic.

## Acknowledgements

Special thanks goes to Markus Karl and Sebastian Kollenz as they did their contribution to this study concerning field work, sample preparation, and dating analyses during their time in our research group. Also we appreciate very much the discussions with members of the SPP-1375 SAMPLE and the discussions and logistic support by the research group of Peter C. Hackspacher and the Geoscience team in Rio Claro, UNESP. Furthermore, we like to thank Danny Stockli's team for the analytical assistance, Richard A. Ketcham and Raymond A. Donelick for providing the computer code HeFTy, Raymond A. Donelick allowing us to use  $D_{\text{par}}$  as a kinetic factor, and Istvan Dunkl for providing the software code TrackKey.

In addition, we appreciate very much the technical support given by the Forschungs-Neutronenquelle FRM II at Garching, TU München, Germany organized by Dr. Gerstenberg.

Finally, without the financial support provided with grants to Ulrich A. Glasmacher by the German Research Foundation (Deutsche Forschungsgemeinschaft, DFG, GL182/14–1, 14–2) within the Priority Program 1375 (SAMPLE) and the DAAD (50753850) we would not be able to perform the research.

## Appendix A. Supplementary data

Supplementary data related to this article can be found at <https://doi.org/10.1016/j.jsames.2019.02.012>.

## References

- Alkmim, F.F., Marshak, S., Fonseca, M.A., 2001. Assembling western Gondwana in the neoproterozoic: clues from the São Francisco craton region, Brazil. *Geology* 29, 319–322.
- Alkmim, F.F., Teixeira, W., 2017. The paleoproterozoic mineiro belt and the quadrilátero ferrífero. In: Heilbron, M., Cordani, U., Alkmim, F. (Eds.), *São Francisco Craton, Eastern Brazil. Regional Geology Reviews*. Springer, Cham.
- Almeida, F.F.M., Carneiro, C.D.R., 1998. Origem e evolução da Serra do Mar. *Rev. Bras. Geociências* 28 (2), 135–150.
- Almeida, F.F.M., Brito Neves, B.B., Carneiro, C.D.R., 2000. The origin and evolution of the South American Platform. *Earth Sci. Rev.* 50, 77–111.
- Alves, A., Janasi, V., Campos Neto, M., Heaman, L., Simonetti, A., 2013. U-Pb geochronology of the granite magmatism in the embu terrane: implications for the evolution of the central Ribeira belt, Brazil. *Precambrian Res.* 230, 1–12.
- Amaral, G., Bushee, J., Cordani, U.G., Kawashita, K., Reynolds, J.H., 1967. Potassium-argon ages of alkaline rocks from southern Brazil. *Geochem. Cosmochim. Acta* 31, 117–142.
- Basei, M.A.S., Ahrendt, H., Wemme, K., Passarelli, C.R., 1995. Evolução policíclica de Zona de Cisalhamento de Major gercindo, Santa Catarina, Brasil. In: *Simpósio Nacional de Estudos Tectônicos 5, Gramado. Anais da Academia Brasileira de Ciências*, pp. 371–373.
- Basei, M.A.S., Siga Jr., O., Reis Neto, J.M., Passarelli, C.R., Prazeres, H.J., Kaulfuss, G., Sato, K., Limsa, O.S., 1999. Paleoproterozoic granulitic belts of the Brazilian southern region (PR-SC). In: *II South American Symposium on Isotope Geology, Cordoba, Argentina, Short Papers*, vol. 1, pp. 291–294.
- Basei, M.A.S., Siga Jr., O., Masquelin, H., Harara, O., Reis Neto, J., Preciozzi, F., 2000. The Dom Feliciano Belt of Brazil and Uruguay and its foreland domain, the Rio de la Plata Craton: framework, tectonic evolution and correlations with similar terranes of southwestern Africa. *Tectonic Evolution of South America, Rio de Janeiro*, pp. 311–534.
- Basei, M.A.S., Frimmel, H.E., Nutman, A.P., Preciozzi, F., 2008. West Gondwana amalgamation based on detrital zircon ages from Neoproterozoic Ribeira and Dom Feliciano belts of South America and comparison with coeval sequences from SW Africa. *Geological Society, London, Special Publications* 294, 239–256.
- Basei, M.A.S., Brito Neves, B.B., Siga Junior, O., Babinski, M., Pimentel, M.M., Tassinari, C.C.G., Hollanda, M.H.B., Nutman, A., Cordani, U.G., 2010. Contribution of SHRIMP U-Pb geochronology to unravelling the evolution of Brazilian Neoproterozoic fold belts. *Precambrian Res.* 183, 112–155.
- Basei, M.A.S., Campos Neto, M.C., Castro, N.A., Nutman, A.P., Wemmer, K., Yamamoto, M.T., Hueck, M., Osako, L., Siga Jr., O., Passarelli, C.R., 2011. Tectonic evolution of the brusque group, Dom Feliciano belt, Santa Catarina, southern Brazil. *J. South Am. Earth Sci.* 32, 324–350.
- Bento dos Santos, T.M., Munha, J.M., Tassinari, C.G., Fonseca, P.E., Dias Neto, C., 2010. Thermochronology of central Ribeira fold belt, SE Brazil: petrological and geochronological evidence for long-term high temperature maintenance during western Gondwana amalgamation. *Precambrian Res.* 180, 285–298.
- Bento dos Santos, T.M., Tassinari, C.G., Fonseca, P.E., 2014. Garnet-biotite diffusion mechanism in granulite from Ribeira fold belt (SE Brazil). *Community Geology* 99 (2), 101–105.
- Beucher, R., Roderick, W., Brown, R.W., Roper, S., Stuart, F., Persano, C., 2013. Natural age dispersion arising from the analysis of broken crystals: Part II. Practical application to apatite (U–Th)/He thermochronometry. *Geochem. Cosmochim. Acta* 120, 395–416.
- Brito Neves, B.B., Campos Neto, M., Fuck, R.A., 1999. From rodinia to western Gondwana: an approach to the brasiliano-Pan african cycle and orogenic collage. *Journal of International Geosciences* 22 (3), 155–165.
- Brown, R.W., Beucher, R., Roper, S., Persano, C., Stuart, F., Fitzgerald, P., 2013. Natural age dispersion arising from the analysis of broken crystals: Part I. Theoretical basis and implications for the apatite (U–Th)/He thermochronometer. *Geochemica et Cosmochimica Acta* 121, 478–497.
- Brown, R.W., Summerfield, M., Gleadow, A., Gallagher, K., Carter, A., Beucher, R., Wildman, M., 2014. Intracontinental deformation in southern Africa during the late cretaceous. *J. Afr. Earth Sci.* 100, 20–41.
- Brueckner, H.K., Cunningham, D., Alkmim, F.F., Marshak, S., 2000. Tectonic implications of precambrian Sm–Nd dates from the southern São Francisco craton and adjacent Araçuaí and Ribeira belts, Brazil. *Precambrian Res.* 99, 255–269.
- Bruno, H., Almeida, J., Heilbron, M., Salomão, Cury, L., 2018. Architecture of major precambrian tectonic boundaries in the northern part of the Dom Feliciano Orogen, southern Brazil: implications for the West Gondwana amalgamation. *J. South Am. Earth Sci.* 86, 301–317.
- Campagnoli, F., 1996. Considerações sobre a geologia da Sequência Turvo-Cajati, na região do Alto Rio Jacupranguinha. SP. MSc Dissertation, Institute of Geosciences – University of São Paulo, pp. 96.
- Campos Neto, M.C., 2000. Orogenic systems from southwestern Gondwana: an approach to brasiliano-Pan african cycle and orogenic collage in southeastern Brazil. In: *Tectonic Evolution of South America*, pp. 335–365.
- Cobbold, P.R., Meisling, K.E., Mount, V.S., 2001. Reactivation of an obliquely rifted margin, Campos and Santos basins, southern Brazil. *Am. Assoc. Petrol. Geol. Bull.* 85 (11), 1925–1944.
- Cogné, N., Gallagher, K., Cobbold, P.R., 2011. Post-rift reactivation of the onshore margin of southeast Brazil: evidence from apatite (U–Th)/He and fission-track data. *Earth Planet. Sci. Lett.* 309, 118–130.
- Cogné, N., Gallagher, K., Cobbold, P.R., Riccomini, C., Gautheron, C., 2012. Post break-up tectonics in southeast Brazil from thermochronological data and combined inverse forward thermal history modelling. *J. Geophys. Res.* 117, 11413.
- Cogné, N., Cobbold, P.R., Riccomini, C., Gallagher, K., 2013. Tectonic setting of Taubaté Basin (south-eastern Brazil): insights from regional seismic profiles and outcrop data. *J. South Am. Earth Sci.* 42, 195–204.
- Cordani, U.G., Sato, K., Teixeira, W., Tassinari, C.C.G., Basei, M.A.S., 2000. Crustal evolution of the south American Platform. In: Cordani, U., Milani, E.J., Thomaz Filho, A., Campos, D.A. (Eds.), *Tectonic Evolution of South America Platform*, 31st International Geological Congress, Rio de Janeiro, pp. 19–40.
- Coward, M.P., Daly, M.C., 1984. Crustal lineaments and shear zones in Africa: their relationship to plate movements. *Precambrian Res.* 24, 27–45.
- Dias Neto, C.M., 2001. Evolução tectono-thermal do complexo Costeiro (faixa de dobramentos Ribeira) em São Paulo. Ph.D. Thesis. Instituto de Geociências, University of São Paulo, pp. 189.
- Dodson, M.H., 1973. Closure Temperature in Cooling Geochronological and Petrological Systems: Contributions to Mineralogy and Petrology, vol. 40. pp. 259–274.
- Donelick, R.A., Ketcham, R.A., Carlson, W.D., 1999. Variability of apatite fission-track annealing kinetics II: crystallographic orientation effects. *Am. Miner.* 84, 1224–1234.
- Engelmann de Oliveira, C.H., Jelinek, A.R., Chemale, F., Cupertino, J.A., 2016. Thermotectonic history of the south eastern Brazilian margin: evidence from apatite fission-track data of the offshore Santos Basin and continental basement. *Tectonophysics* 685, 21–34.
- Ernst, R.E., Buchan, K.L., 2001. The use of mafic dike swarms in identifying and locating mantle plumes. In: In: Ernst, R.E., Buchan, K.L. (Eds.), *Mantle Plumes: Their Identification through Time*, vol. 352. Geological Society, America Spec. Paper, pp. 247–265.
- Faleiros, F.M., 2008. Evolução de terrenos tectono-metamórficos da Serrania do Ribeira e Planalto Alto Turco (SP, PR). Doctor of Science Thesis. Geosciences Institute. University of Sao Paulo, pp. 306.
- Faleiros, M.F., Campanha, G.A., Martins, L., Vlach, S.R.F., Vasconcelos, P.M., 2011. Edicaran high-pressure collision metamorphism and tectonics of the Southern Ribeira Belt (SE Brazil): evidence for terrane accretion and dispersion during Gondwana assembly. *Precambrian Res.* 189, 263–291.
- Farley, K.A., Wolf, R.A., Silver, L.T., 1996. The effects of long alpha-stopping distances on (U–Th)/He ages. *Geochem. Cosmochim. Acta* 60, 4223–4229.
- Farley, K.A., 2000. Helium diffusion from apatite: general behaviour as illustrated by Durango fluorapatite. *Journal of Geophysics* 105, 2903–2914.
- Farley, K.A., 2002. U–Th/He dating: techniques, calibrations and applications. In: In: Porcelli, P.D., Ballentine, C.J., Wieler, R. (Eds.), *Noble Gas Geochemistry*, vol. 47. *Rev. Min. Geoch.*, pp. 819–843.
- Flowers, R.M., Shuster, D.L., Wernicke, B.P., Farley, K.A., 2007. Radiation damage control on apatite (U–Th)/He dates from the Grand Canyon region, Colorado Plateau. *Geology* 35, 447–450.
- Flowers, R.M., Bowring, S.A., Reiners, P.W., 2009. Low long-term erosion rates and extreme continental stability documented by ancient (U–Th)/He dates. *Geology* 34, 925–928.
- Florisbal, L.M., de Assis Janasi, V., Bitencourt, M.F., Heaman, L.M., 2012. Space-time relation of post-collisional granitic magmatism in Santa Catarina, southern Brazil: U–Pb LA-MC-ICP-MS zircon geochronology of coeval mafic-felsic magmatism related to the Major Gercino Shear Zone. *Precambrian Res.* 216–219, 132–151.
- Florisbal, L.M., Heaman, L.M., de Assis Janasi, V., Bitencourt, M.F., 2014. Tectonic significance of the Florianópolis dyke swarm, paraná-etendeka magmatic province: a reappraisal based on precise U–Pb dating. *J. Volcanol. Geotherm. Res.* 289, 140–150.
- Foster, D.A., Goscombe, B.D., Gray, D.R., 2009. Rapid exhumation of deep crust in an obliquely convergent orogeny: the Kaoko Belt of the Damara Orogen. *Tectonics* 28, TC4002.
- Franco-Magalhães, A.O.B., Hackspacher, P.C., Glasmacher, U.A., Saad, A.R., 2010. Rift to post-rift evolution of a “passive” continental margin: the Ponta Grossa Arch, SE Brazil. *Int. J. Earth Sci.* 99, 1599–1613.
- Galbraith, R.F., 1981. On statistical models for fission-track counts. *Math. Geol.* 13 (6), 471–478.
- Gallagher, K., Hawkesworth, C.J., Mantovani, M.S.M., 1994. The denudation history of the offshore continental margin of SE Brazil inferred from apatite fission-track data. *J. Geophys. Res.* 99, 18117–18145.
- Gallagher, K., Hawkesworth, C.J., Mantovani, M.S.M., 1995. Denudation, fission track analysis and the long-term evolution of passive margin topography: application to the southeast Brazilian margin. *J. South Am. Earth Sci.* 8 (1), 65–77.
- Garver, J.I., Kamp, P.J.J., 2002. Integration of zircon color and zircon fission track zonation patterns in Orogenic belts: application of the Southern Alps, New Zealand. *Tectonophysics* 349 (1–4), 203–219.
- Garver, J.I., 2003. Discussion: “Metamictization of natural zircon: accumulation versus thermal annealing of radioactivity-induced damage. *Contrib. Mineral. Petrol.* 143, 756–757.
- Gleadow, A.J.W., 1981. Fission-track dating methods: what are the real alternatives? *Nucl. Tracks* 5 (1–2), 3–14.
- Gomes, C.B., Barbieri, M., Beccaluva, L., Brotzu, P., Conte, A., Gabarino, C., Macciotta, G., Melusso, L., Morbidelli, L., Ruberti, E., Scheibe, L.F., Tamura, R.M., Travessa, G., 1987. Petrological and geochemical studies alkaline rocks from continental Brazil. 2. The Tunas massif, State of Paraná. *Geochem Brasiliensis* 1, 201–234.
- Goscombe, B.D., Gray, D.R., 2008. Structure and strain variation at mid-crustal levels in a transpressional orogeny: a review of Kaoko Belt structure and the character of West

- Gondwana amalgamation and dispersal. *Gondwana Res.* 12, 45–85.
- Goscombe, B.D., Foster, D.A., Gray, D.R., Wade, B., 2017. Metamorphic response and crustal architecture in a classic collisional orogeny: the Damara Belt, Namibia. *Gondwana Res.* 52, 80–124.
- Guenther, W.R., Reiners, P.W., Ketchum, R.A., Nasdala, L., Giester, G., 2013. Helium diffusion in natural zircon: radiation damage, anisotropy, and the interpretation of zircon (U-Th)/He thermochronology. *Am. J. Sci.* 313, 145–198.
- Green, P., Duddy, I., 2018. Apatite (U-Th-Sm)/He thermochronology on the wrong side of the tracks. *Chem. Geol.* 488, 21–33.
- Hackspacher, P.C., Godoy, A.M., 1999. Vertical displacement during late collisional escape tectonics (brasiliiano orogeny) in the Ribeira belt, São Paulo state, Brazil. *J. Afr. Earth Sci.* 29 (1), 25–32.
- Hackspacher, P.C., Dantas, E.L., Spoladore, A., Fetter, A.H., Oliveira, M.A.F., 2000. Evidence for neoproterozoic backarc basin development in the central Ribeira belt, South-eastern Brazil: new geochronological and geochemical constraints from the São Roque-açungui groups. *Rev. Bras. Geociências* 30 (1), 110–114.
- Hackspacher, P.C., Juliani, C., Fetter, A., Dantas, E.L., 2001. Evolution of the central Ribeira belt, Brazil: implications for the assembly of West Gondwana. *Gondwana Res.* 4 (4), 626–627.
- Hackspacher, P.C., Ribeiro, L.F.B., Ribeiro, M.C.S., Fetter, A.H., Hadler, N.J.C., Tello Saenz, C.A., Dantas, E.L., 2004. Consolidation and break-up of the South American Platform in south-eastern Brazil: tectono-thermal and denudation histories. *Gondwana Res.* 1, 91–101.
- Hackspacher, P.C., Godoy, D.F., Ribeiro, L.F.B., Hadler, N.J.C., Franco, A.O.B., 2007. Modelagem tectônica e geomorfológica da borda sul do cráton do São Francisco: termocronologia por traços de fissão em apatita. *Rev. Bras. Geociências* 37, 928–938.
- Hamza, V.M., Cardoso, R.A., Gomes, A.J.L., 2005. Gradiente e fluxo geotérmico na região sudeste: índices de calor residual do magmatismo alcalino e implicações para maturação térmica de sedimentos na plataforma continental. 3rd Simpósio de Vulcanismo e Ambientes Associados, Cabo Frio, SBG. *Anais* 1, 319–324.
- Hartmann, L.A., Bitencourt, M.F., Santos, J.O.S., McNaughton, N.J., Riveira, C.B., Bettiolo, L., 2003. Prolonged paleoproterozoic magmatic participation in the neoproterozoic Dom Feliciano belt, Santa Catarina, Brazil, based on zircon U-Pb SHRIMP geochronology. *J. South Am. Earth Sci.* 16, 477–492.
- Heilbron, M., Mohriak, W.U., Valeriano, C.M., Milani, E.J., Almeida, J., Tupinambá, M., 2000. From Collision to Extension: the Roots of the South-Eastern Continental Margin of Brazil. *American Geophysical Union. Geophysical Monograph Series*, vol. 115.
- Heilbron, M., Valeriano, C.M., Tassinari, C.C.G., Almeida, J.C.H., Tupinambá, M., Siga, O., Trouw, R.A.J., 2008. Correlation of Neoproterozoic terranes between the Ribeira Belt, SE Brazil and its African counterpart: comparative tectonic evolution and open questions. *Geological Society, London, Special Publications* 294, 211–237.
- Heilbron, M., Cordani, U.G., Alkmim, F.F., 2017. The São Francisco craton and its margins. In: Heilbron, M., Cordani, U., Alkmim, F. (Eds.), *São Francisco Craton, Eastern Brazil*. Regional Geology Reviews. Springer, Cham.
- Hiruma, S.T., Riccomini, C., Modenesi-Gauttieri, M.C., Hackspacher, P.C., Neto, J.C.H., Franco-Magalhaes, A.O.B., 2010. Denudation history of the Bocaina Plateau, Serra do Mar, south-eastern Brazil: relationships to Gondwana break-up and passive margin development. *Gondwana Res.* 18, 674–687.
- Hurfurd, A.J., 1986. Standardization of fission-track dating calibration: results of questionnaire distributed by International Union of Geosciences Subcommittee on Geochronology. *Nucl. Tracks* 11, 329–333.
- Jelinek, A.R., Bastos-Neto, A.C., Leite, J.A.D., Hartmann, L.A., McNaughton, N.J., 2005. SHRIMP U-Pb zircon dating of pedras grandes suite, southern Santa Catarina state, Brazil. *An. Acad. Bras. Cienc.* 77 (1), 125–135.
- Karl, M., Glasmacher, U.A., Kollenz, S., Franco-Magalhaes, A.O.B., Stockli, D.F., Hackspacher, P.C., 2013. Evolution of the South Atlantic passive continental margin in southern Brazil derived from zircon and apatite (U-Th-Sm)/He and fission-track data. *Tectonophysics* 604, 224–244.
- Kaulfuss, G.A., 2011. Geocronologia dos Núcleos de Embasamento Setuva, Betara e Tigre, Norte de Curitiba, Paraná. Dissertação (Mestrado) - Instituto de Geociências, de Geociências, Universidade de São Paulo, pp. 115.
- Ketchum, R.A., 2005. Forward and Inverse Modelling of low-temperature thermochronometry data. *Rev. Mineral. Geochem.* 58, 275–314.
- Ketchum, R.A., Carter, A., Donelick, R.A., Barbarand, J., Hurfurd, A.J., 2007 a a. Improved measurements of fission-track annealing in apatite. *Am. Mineral.* 92, 789–798.
- Ketchum, R.A., Carter, A., Donelick, R.A., Barbarand, J., Hurfurd, A.J., 2007 b b. Improved modelling of fission-track annealing in apatite. *Am. Mineral.* 92, 799–810.
- Ketchum, R.A., Donelick, R.A., Balestrieri, M.L., Zattin, M., 2009. Reproducibility of apatite fission-track length data and thermal history reconstruction. *Earth Planet. Sci. Lett.* 284, 504–515.
- Ketchum, R.A., 2017. HeFTy Version 1.9.3, Manual.
- Machado, N., Heilbron, M., Valeriano, C., 1996. U-Pb geochronology of the central Ribeira Belt (Brazil) and implications for the evolution of the Brazilian orogeny. *Precambrian Res.* 79 (3–4), 347–361.
- Machado, N., Dehler, N.M., Vasconcelos, P., 2007. <sup>40</sup>Ar/<sup>39</sup>Ar ages (600–570 Ma) of the Serra do Azeite transtensional shear zone: evidence for syncontractional extension in the Cajati Area, southern Ribeira Belt. *An. Acadêmica Brasileiras Ciências* 79 (4), 713–723.
- Meisling, K.E., Cobbold, P.R., Mount, V.S., 2001. Segmentation of an obliquely rifted margin, Campos and Santos basins, south-eastern Brazil. *American Association Petroleum Geological Bulletin* 85 (11), 1903–1924.
- Milani, E.J., de Melo, J.H.G., de Souza, P.A., Fernandes, L.A., França, A.B., 2007. Bacia do Paraná. B. Geociências Petrobras. *Rio de Janeiro* 15 (2), 265–287.
- Montañez, I.P., Poulsen, C.J., 2013. The late paleozoic ice age: an evolving paradigm. *Annu. Rev. Earth Planet Sci.* 41, 629–656.
- Oyhantcabal, P., Siegesmund, S., Wemmer, K., Frei, R., Layer, P., 2007. Post-collisional transition from calc-alkaline to alkaline magmatism during transcurrent deformation in the southernmost Dom Feliciano Belt (Brazilian-Pan-African, Uruguay). *Lithos* 98, 141–159.
- Passarelli, C.R., 2001. Caracterização estrutural e geocronológica dos domínios tectônicos da porção sul-oriental do Estado de São Paulo. Ph.D. Thesis. IGC-USP, São Paulo, SP, Brasil, pp. 254.
- Passarelli, C.R., Basei, M.A.S., Prazeres Filho, H.J., Szabó, G.A.J., Marco-Neto, J., 2006. Structural and geochronological constraints on the evolution of the juréia massif, registro domain, state of São Paulo, Brazil. *An. Acad. Bras. Ciências* 79 (3), 441–455.
- Passarelli, C.R., Wemmer, K., Basei, M.A.S., Siga Jr., O., 2008. Tecton-thermal evolution of the SE São Paulo state precambrian terranes. In: VI South American Symposium on Isotope Geology. Bariloche, Argentina.
- Passarelli, C.R., Basei, M.A.S., Siga Jr., O., Mc Reath, I., Campos Neto, M., 2010. Deformation and geochronology of syntectonic granitoids emplaced in the Major Gercino Shear Zone, south eastern South America. *Gondwana Res.* 17, 688–703.
- Pimentel, M.M., Fuck, R.A., Botelho, N.F., 1999. Granites and the geodynamic history of the neoproterozoic brasílica belt, central Brazil: a review. *Lithos* 46, 463–483.
- Pimentel, M.M., Fuck, R.A., Jost, H., Ferreira Filho, C.F., Araújo, S.M., 2000. The basement of the brasílica fold belt and the goiás magmatic arc. In: Cordani, U.G., Milani, E.J., Thomaz Filho, A., Campos, D.A. (Eds.), *Tectonic Evolution of South America*. Rio de Janeiro, 31<sup>st</sup> International Geological Congress, pp. 195–230.
- Prazeres Filho, H.J., Harara, O.M., Basei, M.A.S., Passarelli, C.R., Siga Jr., O., 2003. Litoquímica, geocronologia U-Pb, e geologia isotópica (Sr-Nd-Pb) das rochas graníticas dos Batólitos Cunhaporanga e Três Córregos na Porção Sul do Cinturão Ribeira, Estado de Paraná, vol. 3. *Revista do Instituto de Geociências - University of São Paulo*, pp. 51–70.
- Prazeres Filho, H., 2005. Caracterização geológica e petrogenética do Batólito Granítico Três Córregos (PR-SP): Geoquímica isotópica (Nd-Sr-Pb, idades ID-TIMS/SHRIMP e O18 em zirção). University of São Paulo, São Paulo, SP, pp. 207 Unpublished thesis submitted for the degree of Doctor of Philosophy.
- Raab, M.J., Brown, R.W., Gallagher, K., Carter, A., Weber, K., 2002. Late Cretaceous reactivation of major crustal shear zones in northern Namibia: constraints from apatite fission track analysis. *Tectonophysics* 349, 75–92.
- Rahn, M.K., Brandon, M.T., Batt, G.E., Garver, J.I., 2004. A zero-damage model for fission-track annealing in zircon. *Am. Mineral.* 89, 473–484.
- Reiners, P.W., Farley, K.A., Hickes, H.J., 2002. He diffusion and (U-Th)/He thermochronometry of zircon: initial results from fish canyon tuff and gold butte, Nevada. *Tectonophysics* 349, 297–308.
- Reiners, P.W., Spell, T.L., Nicolescu, S., Zanetti, K.A., 2004. Zircon (U-Th)/He thermochronometry: He diffusion and comparisons with <sup>40</sup>Ar/<sup>39</sup>Ar dating. *Geochem. Cosmochim. Acta* 68, 1857–1887.
- Reiners, P.W., Brandon, M.T., 2006. Using thermochronology to understand orogenic erosion. *Annu. Rev. Earth Planet Sci.* 34, 419–466.
- Renne, P.R., Ernesto, M., Pacca, I.I.G., Coe, R.S., Glen, J.M., Prévot, M., Perrin, M., 1992. The age of Paraná flood volcanism, rifting of Gondwanaland, and the Jurassic-Cretaceous boundary. *Science* 258, 975–979.
- Renne, P.R., Deckart, K., Ernesto, M., Féraud, G., Piccirillo, E.M., 1996. Age of Ponta Grossa dike swarm (Brazil), and implications to Paraná flood volcanism. *Earth Planet. Sci. Lett.* 144, 199–211.
- Riccomini, C., Pelloggia, A.U.G., Saloni, J.C.L., Kohnk, M.W., Figueira, R.M., 1989. Neotectonic activity in the Serra do Mar rift system (south eastern Brazil). *J. South Am. Earth Sci.* 2 (2), 191–197.
- Riccomini, C., Santa Anna, L.G., Ferrari, A.L., 2004. Evolução geológica do rift continental do sudeste do Brasil. In: Mantesso Neto, V., Bartorelli, A., Carneiro, C.D.R., Neves, B.B.B. (Eds.), *Geologia do continente Sul-Americano: evolução da Obra de Fernando Flávio Marques de Almeida*. Editora Beca, São Paulo, pp. 383–405.
- Riccomini, C., Velázquez, V.F., Gomes, C.B., 2005. Tectonic controls of the Mesozoic and Cenozoic alkaline magmatism in central south-eastern Brazilian Platform. In: Comin-Chiaromonti, P., Gomes, C.B. (Eds.), *Zircon from Cenozoic Alkaline Magmatism in the Brazilian Platform*. São Paulo, Edusp/Fapesp, pp. 31–55.
- Salamuni, E., Ebert, H.D., Borges, M.S., Hasui, Y., Costa, J.B.S., Salamuni, R., 2003. Tectonics and sedimentation in the Curitiba basin, south of Brazil. *J. South Am. Earth Sci.* 15, 901–910.
- Salazar, C.A., Archanjo, C.J., Babinski, M., Liu, D., 2008. Magnetic fabric and zircon U-Pb geochronology of the itaoca pluton: implications for the brasiliiano deformation of the southern Ribeira belt (SE Brazil). *J. South Am. Earth Sci.* 26, 286–299.
- Salomon, E., Koehn, D., Passchier, C., Hackspacher, P.C., Glasmacher, U.A., 2015. Contrasting stress fields on correlation margins of the South Atlantic. *Gondwana Res.* 28, 1152–1167.
- Santos, T.M.B., Tassinari, C.C.G., Fonseca, P.E., 2015. Diachronic collision, slab, break-off and long-term high thermal flux in the Brasiliiano-Pan African orogeny: implications for the geodynamic evolution of the Mantiqueira Province. *Precambrian Res.* 260, 1–22.
- Schmitt, R.S., Trouw, R.A.J., Van Schmus, W.R., Pimentel, M.M., 2004. Late amalgamation in the central part of West Gondwana: new geochronological data and the characterization of a Cambrian collisional orogeny in the Ribeira Belt (SE Brazil). *Precambrian Res.* 133, 29–61.
- Scotese, C.R., Golonka, J., 1992. Paleogeographic Atlas. Paleomap Projekt. Department of Geology, U. Texas at Arlington.
- Scotese, C.R., Boucot, A.J., McKerrow, W.S., 1999. Gondwanan paleogeography and paleoclimatology. *J. Afr. Earth Sci.* 28 (1), 99–114.
- Siga Jr., O., Basei, M.A.S., Reis Neto, J.M., Machiavelli, A., Harara, O.M., 1995. O complexo atuba: um cinturão neoproterozoico intensamente retrabalhado no neoproterozoico. *Bol. IG-USP Ser. Cient.* 26, 69–98.
- Siga Jr., O., Basei, M.A.S., Sato, K., Prazeres Filho, H.J., Cury, L.F., Weber, W., Passarelli,

- C.R., Harara, O.M., Reis Neto, J.M., 2003. U–pb (Zircon) Ages of Metavolcanic Rocks from the Itaiacoca Group: Tectonic Implications, vol. 3. *Revista do Instituto de Geociências – University of São Paulo*, pp. 39–49.
- Siga Jr., O., Basei, M.A.S., Passarelli, C.R., Harara, O.M., Sato, K., Cury, L.F., Prazeres Filho, H.J., 2007. Geochronologia de rochas gnáissico-migmatíticas e sienograníticas do Núcleo Setuva (PR): implicações tectônicas. *Revista Brasileira de Geociências* 37 (1), 114–128.
- Siga Jr., O., Basei, M.A.S., Passarelli, C.R., Sato, K., Cury, L.F., McReath, I., 2009. Lower and upper neoproterozoic magmatic records in itaiacoca belt (Paraná-Brazil): zircon ages and lithostratigraphy studies. *Gondwana Res.* 15, 197–208.
- Silva, L.C., McNaughton, N.J., Hartmann, L.A., Fletcher, I.R., Gresse, P., Scheepers, R., 1997. UP-b (SHRIMP) isotopic constraints for the evolution of Southern Brazilian Granitic Province, and some correlated South African, Pan-African plutons. In: *International Symposium on Granites and Associated Mineralisations 2*, Salvador, Anais da Academia Brasileira de Ciências, pp. 276–277.
- Silva, L.C., McNaughton, N.J., Armstrong, R., Hartmann, L.A., Fletcher, I.R., 2005. The Neoproterozoic Mantiqueira Province and its African connections: a zircon-based U–Pb geochronological subdivision for the Brasiliano/Pan-African systems of orogens. *Precambrian Res.* 136, 203–240.
- Soares, P.C., Noce, C.M., Wiedemann, C.M., Pinto, C.P., 2001. The Arçuaí-West-Congo Orogen in Brazil: an overview of a confined orogen formed during Gondwanaland assembly. *Precambrian Res.* 110, 307–323.
- Soares, P.C., Alkmim, F.F., Tack, L., Noce, C.M., Babinski, M., Silva, L.C., Martins-Neto, M.A., 2008. Similarities and differences between the Brazilian and african counterparts of the neoproterozoic arçuaí-west Congo orogen. *Geological Society, London, Special Publications* 294, 153–172.
- Soares, P.C., Riffel, S.B., Fiori, A.P., 2011. Geomorphological and geophysical evidences for neotectonics, central and southern Brazil. 13. *Simposio Nacional Estudos Tectônicos (SNET) e VII International Symposium on Tectonics*. Campinas (São Paulo) Anais da Academia Brasileira de Ciências, pp. 401–404.
- Sonoki, I.K., Garda, G.M., 1988. Idades K–Ar de rochas alcalinas do Brasil meridional e Paraguai oriental: compilação e adaptação as novas constantes de decaimento, vol. 19. *Boletim do Instituto de Geociências da USP Série Científica*, pp. 63–85.
- Storey, B.C., Leat, P.T., Ferris, J.K., 2001. The location of mantle-plume centres during the initial stages of Gondwana break-up. In: *Ernst, R.E., Buchan, K.L. (Eds.), Mantle Plumes: Their Identification through Time*, vol. 352. Geological Society of America, Boulder, Colorado, Special Paper, pp. 71–80.
- Stockli, D.F., Farley, K.A., Dumitru, T.A., 2000. Calibration of the apatite (U–Th)/He thermochronometer on an exhumed fault block, White Mountains, California. *Geology* 28 (11), 983–986.
- Strugale, M., Rostirola, S.P., Mancini, F., Portela Filho, C.V., Fonseca Ferreira, F.J., de Freitas, R.C., 2007. Structural framework and mesozoic-cenozoic evolution of Ponta Grossa Arch, Paraná basin, southern Brazil. *J. South Am. Earth Sci.* 24, 203–227.
- Tassinari, C.C.G., Munha, J.M.U., Dias Neto, C., Santos, T., Cordani, U.G., Nutman, A.P., Fonseca, P., 2008. SHRIMP U–Pb zircon geochronology, Rb–Sr and Sm–Nd isotope geochemistry of Ribeira Belt charnockites and associated granitoids. In: *VI South American Symposium on Isotope Geology, 2008, Bariloche, Argentina. SSAGI 2008 (Abstract)*.
- Tello, C.A.S., Hackspacher, P.C., Hadler, N.J.C., Iunes, P.J., Guedes, S., Paulo, S.R., Ribeiro, L.F.B., 2003. Recognition of cretaceous, paleocene and Neogene tectonic reactivation, through apatite fission-track analysis in precambrian areas of the southeast Brazil: association with the south atlantic ocean opening. *J. South Am. Earth Sci.* 15, 137–142.
- Thompson, R.N., Gibson, S.A., Mitchell, J.G., Dickin, A.P., Leonardos, O.H., Brod, J.A., Greenwood, J.C., 1998. Migrating Cretaceous-Eocene magmatism in the Serra do Mar alkaline province, SE Brazil: melts from the deflected Trindade mantle plume? *J. Petrol.* 39, 1493–1526.
- Töpfer, C., 1996. Brasiliano-Granitoide in den Bundesstaaten São Paulo und Minas Gerais, eine vergleichende Studie. *Münchner Geologische Hefte, Reihe A* 17, 258.
- Torsvik, T.H., Smethurst, M.A., Burke, K., Steinberger, B., 2006. Large igneous provinces generated from the margins of the large low velocity provinces in the deep mantle. *Geophys. J. Int.* 167, 1447–1460.
- Torsvik, T.H., Rouse, S., Labails, C., Smethurst, M.A., 2009. A new scheme for the opening of the South Atlantic Ocean and the dissection of an Aptian salt basin. *Geophys. J. Int.* 177, 1315–1333.
- Trouw, R.A.J., de Wit, M.J., 1999. Relation between the Gondwanide Orogen and contemporaneous intracratonic deformation. *J. Afr. Earth Sci.* 28, 203–213.
- Trouw, R.A.J., Petemel, R., Ribeiro, A., Heilbron, M., Vinagre, R., Duffles, P., Trouw, C.C., Fontainha, M., 2013. A new interpretation for the interference zone between the southern Brasília Belt and the Central Ribeira Belt, SE Brazil. *J. South Am. Earth Sci.* 48, 43–57.
- Valeriano, C.M., Pimentel, M.M., Heilbron, M., Almeida, J.C.H., Trouw, R.A.J., 2008. Tectonic Evolution of the Brasília Belt, Central Brazil, and Early Assembly of Gondwana, vol. 294. Geological Society, London, Special Publications, pp. 197–210.
- Valeriano, C.M., Mendes, J.C., Tupinambá, M., Bongioiolo, E., Heilbron, M., do Carmo Bustamante Junho, M., 2016. Cambro-Ordovician post-collisional granites of the Ribeira Belt SE-Brazil: a case of terminal magmatism of a hot orogeny. *J. South Am. Earth Sci.* 68, 269–281.
- Wolf, R.A., Farley, K.A., Silver, L.T., 1996. Helium diffusion and low-temperature thermochronometry of apatite. *Geochem. Cosmochim. Acta* 60, 4231–4240.
- Wolf, R.A., Farley, K.A., Kass, D.M., 1998. Modelling of the temperature sensitivity of the apatite (U–Th)/He thermochronometer. *Chem. Geol.* 148 (1–5), 105–144.
- Zalán, P.V., Wolff, S., Astolfi, M.A.M., Vieira, I.S., Conceição, J.C.J., Appi, V.T., Neto, E.V.S., Cerqueira, J.R., Marques, A., 1990. The Paraná basin, Brazil. In: *Leighton, M.W., Kolata, D.R., Oltz, D.F., Eidel, J.J. (Eds.), Interior Cratonic Basins*, vol. 51. AAPG Memoir, pp. 681–708.
- Zalán, P.V., 1991. Influence of pre-Andean orogenies on the Paleozoic intracratonic basins of South America. *IV Simp. Bolivariano, Memorias Tomo*, vol. 1, 22.





# 3

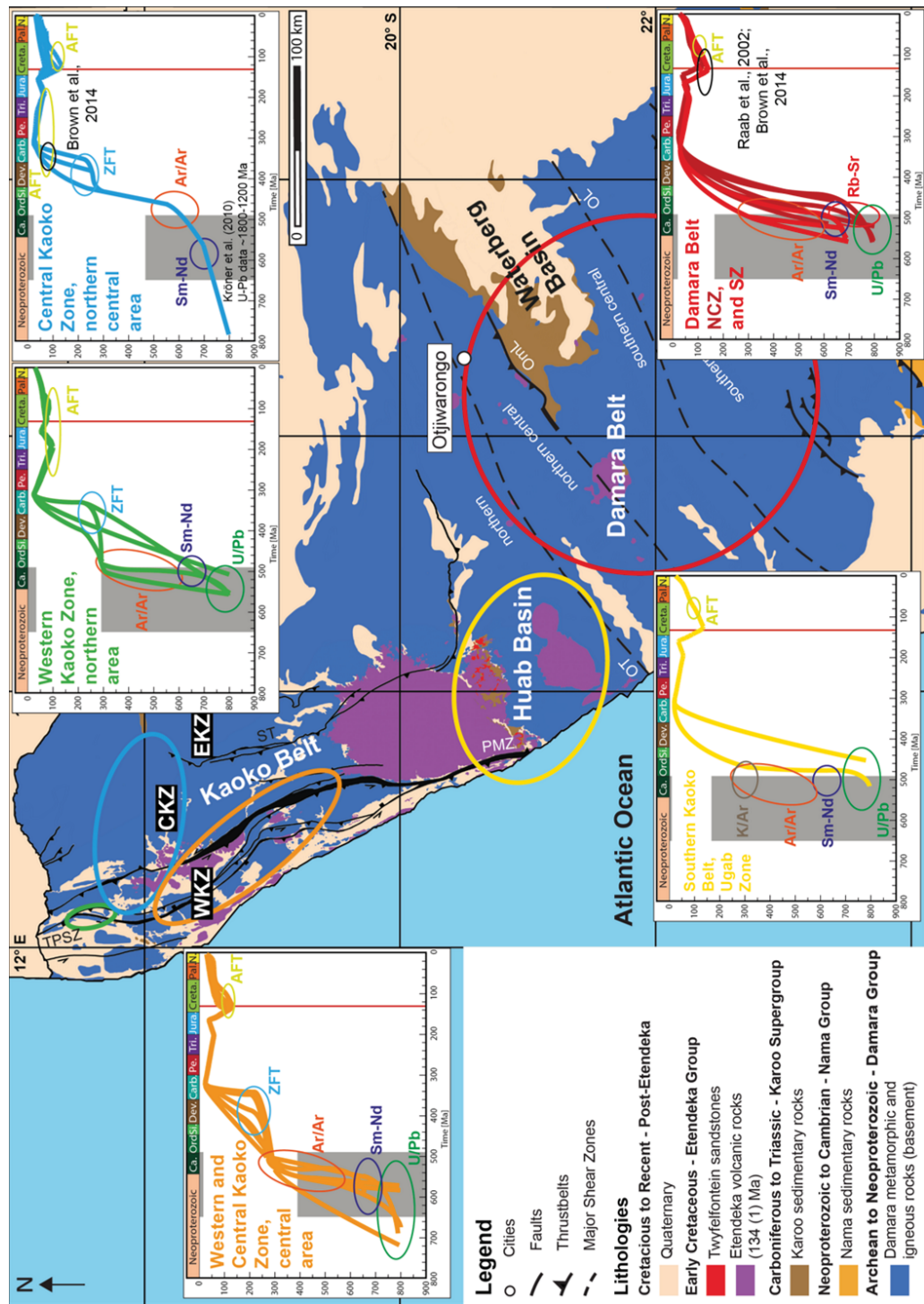
## LATE NEOPROTEROZOIC-TO-RECENT LONG- TERM t-T-EVOLUTION OF THE KAOKO AND DAMARA BELTS IN NW NAMIBIA

---

### CONTENTS

GRAPHICAL ABSTRACT	64
CRediT AUTHOR STATEMENT	65
ABSTRACT	67
INTRODUCTION	67
GEOLOGICAL SETTING	68
METHODS	73
RESULTS	75
INTERPRETATION AND DISCUSSION	77
CONCLUSIONS	93
ACKOWLEGDEMENTS	93
REFERENCES	93

---



Graphical Abstract for CHAPTER 3.



### CRedit author statement

**Publication title:** Late Neoproterozoic-to-recent long-term t-T-evolution of the Kaoko and Damara belts in NW Namibia.

**Authors:** Florian C. Krob, Daniel P. Eldracher, Ulrich A. Glasmacher, Sabine Husch, Eric Salomon, Peter C. Hackspacher, Nordin P. Titus.

#### Author contributions\*:

<b>Florian C. Krob:</b>	Conceptualization, methodology, software, validation, formal analysis, investigation, data curation, writing – original draft, visualization, project administration ( <b>≈75%</b> ).
<b>Daniel P. Eldracher:</b>	Investigation, formal analysis, data curation ( <b>≈12%</b> ).
<b>Prof. Dr. Ulrich A. Glasmacher:</b>	Conceptualization, methodology, validation, resources, writing – review & editing, supervision, project administration, funding acquisition ( <b>≈10%</b> ).
<b>Sabine Husch:</b>	Visualization ( <b>≈0.5%</b> ).
<b>Dr. Eric Salomon:</b>	Investigation, writing – review & editing ( <b>≈1%</b> ).
<b>Prof. Dr. Peter C. Hackspacher:</b>	Resources, writing – review & editing ( <b>≈1%</b> ).
<b>Dr. Nordin P. Titus:</b>	Resources ( <b>≈0.5%</b> ).

\*Reproduced from Brand et al. (2015)

Heidelberg, 15.04.2020



Florian Krob – Corresponding author



Ulrich A. Glasmacher – Supervisor



Peter C. Hackspacher – Deputy Co-Author





# Late Neoproterozoic-to-recent long-term $t$ – $T$ -evolution of the Kaoko and Damara belts in NW Namibia

Florian C. Krob<sup>1</sup> · Daniel P. Eldracher<sup>1</sup> · Ulrich A. Glasmacher<sup>1</sup> · Sabine Husch<sup>1</sup> · Eric Salomon<sup>2</sup> · Peter C. Hackspacher<sup>3</sup> · Nordin P. Titus<sup>4</sup>

Received: 29 August 2019 / Accepted: 8 January 2020  
© Geologische Vereinigung e.V. (GV) 2020

## Abstract

This research aims to reconstruct the Late Neoproterozoic-to-recent long-term time–temperature–evolution of the NW Namibian Kaoko and Damara belts combining numerical modeling of new thermochronological data with previously published geochronological data, i.e., U–Pb, Sm–Nd, and Rb–Sr analyses, and K/Ar, <sup>40</sup>Ar/<sup>39</sup>Ar low-temperature thermochronology. Consequently, we retrieve a coherent long-term time–temperature–evolution of the NW Namibian Neoproterozoic basement rocks including rates of exhumation and subsidence periods over the last ~ 500 Myr. Neoproterozoic basement rocks indicate fast post-Pan African/Brasiliano cooling and exhumation, reheating, or rather subsidence during the development of the Paleozoic-to-Mesozoic SW Gondwana intraplate environment and a significant thermal overprint of the rocks during South Atlantic syn- to post-rift processes, and therefore, resemble the opposite SE Brazilian time–temperature–evolution. We provide an overview of thermochronological data including new apatite and zircon fission-track data derived from Neoproterozoic, Late Paleozoic, and Lower Cretaceous rocks. Apatite fission-track ages range from 390.9 ± 17.9 Ma to 80.8 ± 6.0 Ma in the NW Kaoko Belt with youngest ages confined to the coastal area and significant age increase towards the inland. New zircon apatite fission-track data reveal ages between 429.5 ± 47.8 and 313.9 ± 53.4 Ma for the rocks of the Kaoko Belt. In the central Damara Belt, new apatite fission-track ages range between 138.5 ± 25.3 Ma to 63.8 ± 4.8 Ma. Combined apatite fission-track age distributions from Angola to Namibia and SE Brazil correlate for both sides of the South Atlantic passive continental margin and the reset AFT ages overlap with the lateral Paran–Etendeka dike swarm distribution.

**Keywords** Long-term  $t$ – $T$ -evolution · Thermochronology · Numerical modeling · South Atlantic passive continental margin of NW Namibia

Florian C. Krob and Daniel P. Eldracher have contributed equally to this study.

**Electronic supplementary material** The online version of this article (<https://doi.org/10.1007/s00531-020-01819-7>) contains supplementary material, which is available to authorized users.

✉ Florian C. Krob  
florian.krob@geow.uni-heidelberg.de

- <sup>1</sup> Institute of Earth Sciences, Heidelberg University, Im Neuenheimer Feld 234, 69120 Heidelberg, Germany
- <sup>2</sup> Department of Earth Sciences, University of Bergen, Realfagbygget, Allgt. 41, 5020 Bergen, Norway
- <sup>3</sup> Departamento de Petrologia e Metalogenia, Instituto de Geoscincias e Cincias Exatas, Universidade Estadual Paulista, Av. 24-A, 1515, Bela Vista, Rio Claro, SP 13506-900, Brazil
- <sup>4</sup> Ministry of Mines and Energy, Geological Survey of Namibia, Private Bag 13297, Winhoek, Namibia

## Introduction

Precambrian metamorphic and magmatic rocks are important archives that have stored information about long-term landscape forming processes, e.g., extensive and localized tectonic and volcanic activity, surface uplift and erosion (exhumation), and crustal scale subsidence. These long-term landscape forming processes are related to upper mantle and crustal tectono-thermal dynamics, which can be reconstructed from the long-term time ( $t$ )–temperature ( $T$ )–evolution of rocks in specific geological environments, i.e., along passive continental margins around the world (e.g., Brown et al. 2014; Green et al. 2015, 2018; Japsen et al. 2012, 2014; Braun 2018).

Until recently, most of the research along the South Atlantic passive continental margin (SAPCM) in NW Namibia was either focused on the Precambrian deformation, the

Paleozoic-to-Mesozoic intraplate development, or the syn- to post-rift evolution (e.g., Goscombe et al. 2003a, b, 2007, 2017; Foster et al. 2009; Raab et al. 2002, 2005; Catuneanu et al. 2005; Miller 2008; Brown et al. 2014; Milani et al. 2015). Moreover, this area provides a unique natural laboratory to study in detail sole stages of the Wilson cycle (Wilson 1963, 1965; Stanistreet et al. 1991) and beyond that allows connecting those individual geological stages to retrieve a coherent long-term  $t$ - $T$ -evolution, i.e., the development from an orogeny to a passive continental margin environment.

In a recent study, Krob et al. (2019) published a coherent long-term  $t$ - $T$ -evolution including rates of exhumation and subsidence periods over the last ~500 Myr of the western side of the SAPCM, the SE Brazilian passive continental margin. Consequently, this research focusses on the long-term  $t$ - $T$ -evolution of the eastern counterpart, the NW Namibian passive continental margin. We present a large number of thermochronological data including new apatite and zircon fission-track (AFT, ZFT) data, integrate them to published AFT data sets along the Angolan-to-Namibian SAPCM (Silva et al. 2019; Green and Machado 2015; Raab et al. 2002, 2005; Brown et al. 2014), and provide a comparison of AFT data sets from both the Angolan-to-Namibian, and SE Brazilian SAPCM.

We combine numerical modeling of our data set with geo- and thermochronological data (U–Pb, Sm–Nd and Rb–Sr, and K/Ar,  $^{40}\text{Ar}/^{39}\text{Ar}$ , AFT) from previous work (e.g., Seth et al. 1998; Goscombe et al. 2003a, b, 2005a, b; Kröner et al. 2004; Gray et al. 2006; Foster et al. 2009; Milani et al. 2015) to reconstruct the coherent long-term  $t$ - $T$ -evolution of the Neoproterozoic basement rocks along the NW Namibian Kaoko and Damara belts (Fig. 1). Through this reconstruction, we retrieve the timing and rates of (a) the syn- to post-Pan African cooling and exhumation, (b) the heating, or rather subsidence during the intraplate basin formation of the Karoo Supergroup, and (c) the thermal influence of the Lower Cretaceous Paraná–Etendeka Large Igneous Province (LIP) event, and the SAPCM syn- to post-rift evolution.

## Geological setting

### Late Neoproterozoic-to-early Paleozoic evolution—Pan African/Brasiliano orogeny

From the Late Neoproterozoic to Early Paleozoic (ca. 650–490 Ma), the Pan African/Brasiliano Orogeny took place during the large-scale consolidation of the Gondwana supercontinent (Fig. 2) (e.g., Stanistreet et al. 1991; Goscombe and Gray 2008; Foster et al. 2009; Frimmel et al. 2011; Nascimento et al. 2016). Following an early phase of collisional events in the northern parts of the Gondwana

Assembly (Amazonia, Paranapanema, Goiás, São Francisco, and Congo cratons), continuous movement of the cratonic blocks (Rio de la Plata, Luis Alves, Angola, and Kalahari cratons) in the southern part led to the amalgamation of the SE Brazilian Dom Feliciano, and the NW Namibian Kaoko and Damara Neoproterozoic mobile belts (ca. 560–490 Ma) (e.g., Goscombe et al. 2003a, b, 2007; Gray et al. 2006; Miller 2008; Oyhantcabal et al. 2011; Schmitt et al. 2012).

The coastal, NW-trending Kaoko Belt extends from northern Namibia to the Huab Basin in the south (Fig. 3). The basement consists of the Archean and Paleo- to Mesoproterozoic rocks of the Congo Craton that are overlain by more than 1000 m of Neoproterozoic para-metamorphic (sedimentation age: 770–600 Ma) and igneous rocks of the Damara Sequence (Miller 1983; Frimmel et al. 1998, 2011; Hoffman et al. 1998; Goscombe et al. 2003a, b, 2007; Goscombe and Gray 2008; Nascimento et al. 2016). The Kaoko Belt is subdivided into three individual zones that comprise several tectonic domains. The Western Kaoko Zone (WKZ) involves the Coastal Terrane representing a transpressive magmatic arc, and the Orogen Core (Fig. 2c, d) that both obducted onto the Congo Craton (Fig. 2e, f; Central Kaoko Zone, CKZ). The Eastern Kaoko Zone (EKZ) contains the Northern Platform and the Epupa Metamorphic Complex in the north (Fig. 2g, EMC) (Goscombe et al. 2007). Finally, the Ugab Zone (Fig. 2h) as part of the Orogen Core represents the most southern part of the Kaoko Belt (Goscombe et al. 2007; Miller 2008, 2013).

The EW-trending Damara Belt stretches from the coast to the Waterberg Basin further inland and comprises Precambrian basement rocks of the Kalahari Craton also overlain by Neoproterozoic para-metamorphic and igneous rocks of the Damara Sequence (Fig. 3) (Miller 1983). Several tectonic zones subdivide the Damara Belt in the Northern (NZ, Outjo Zone), Northern and Southern Central (NCZ and SCZ, Swakop Zone), and Southern (SZ, Khomas Zone) zones (Fig. 2). In the south, the Southern Margin Zone (Hakos Zone) and the Southern Nama Foreland border the southern Damara Belt and represent the transition towards the southern Kalahari Craton (Miller 2008).

### Late Paleozoic-to-Jurassic evolution—SW Gondwana intraplate formation of sedimentary basins

Following the Pan African Orogeny, the SW Gondwana intraplate environment experienced a long period of predominantly surface uplift, and erosion caused by post-orogenic denudation of the Neoproterozoic mobile belts during the Early-to-Middle Paleozoic, and Carboniferous-to-Permian syn- to post-Gondwana Ice Age processes (Frimmel et al. 1998; Goscombe et al. 2003a, b; Goscombe and Gray 2008; Miller 2008). Subsequently, geological conditions changed

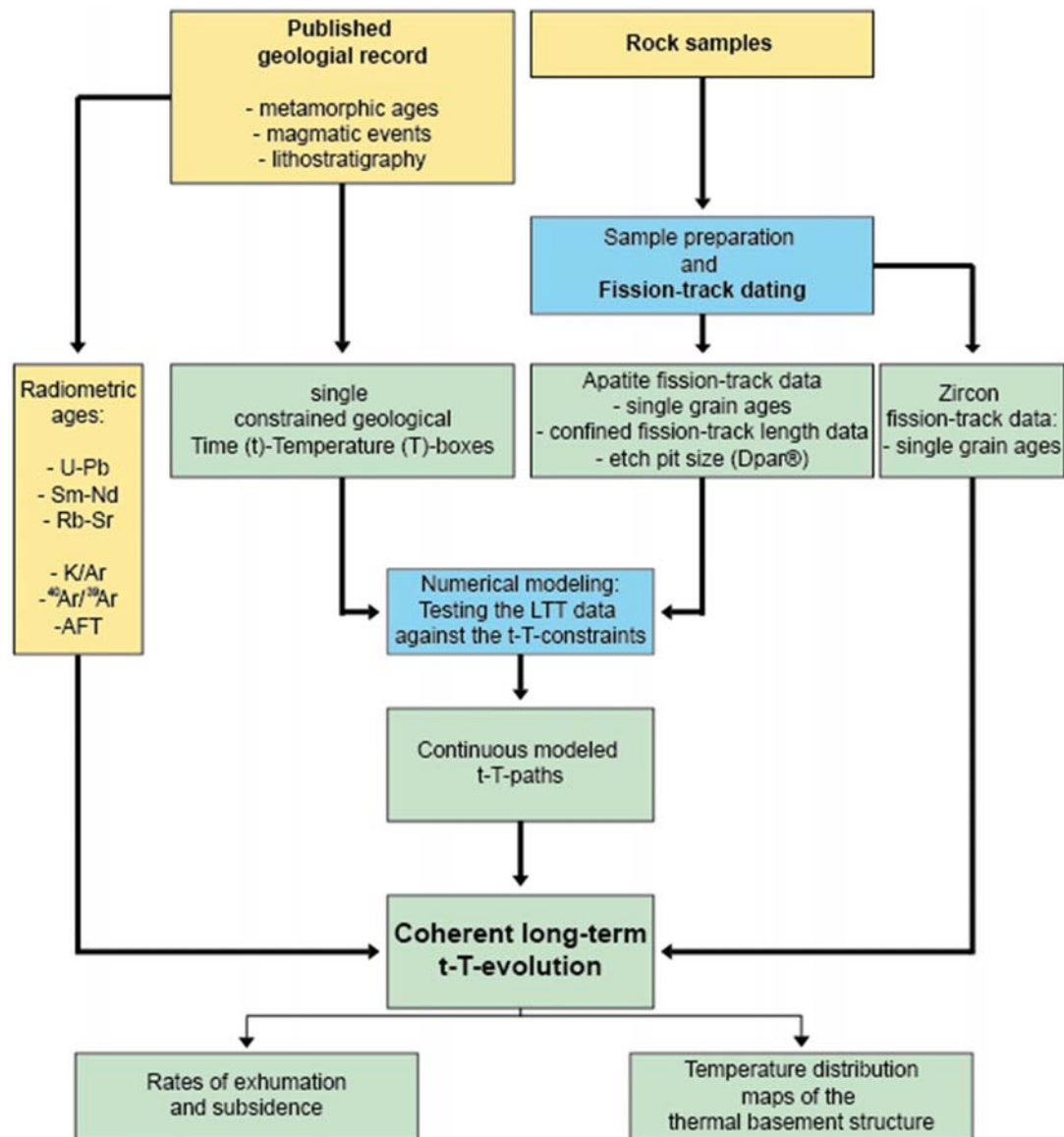


**Fig. 1** Schematic workflow showing the approach of this research study. Sample preparation of Neoproterozoic rock samples from the NW Namibian Kaoko and Damara belts were performed at the institute of Earth sciences, Heidelberg University (right panel). Fission-track dating on apatite and zircon provided apatite and zircon single grain ages, apatite confined fission-track length, and etch pit size (Dpar<sup>®</sup>) data (Eldracher, in prep.). We used the published geological record to generate a numerical modeling set-up by transferring single geological events into time (*t*)-temperature (*T*)-constrained

boxes (left panel). By testing our thermochronological data against the modeling set-up, we derived continuous *t-T*-paths that were combined with previous geo- and thermochronological data to reconstruct a possible coherent long-term *t-T*-evolution for the Neoproterozoic basement rocks in NW Namibia. Thereby, we are able to make estimations on exhumation and subsidence rates and generate interpolation maps of the Neoproterozoic basement thermal structure. Colors of boxes: yellow: data compilation; blue: methods and approach; green: results

towards the Late Paleozoic and renewed transport and deposition of sediments led to the development of the major SW Gondwana intraplate basins, e.g., the southern African Karoo and the SE Brazilian Paraná basins (Stollhofen et al. 1999).

In the NW Namibian Huab (southern Kaoko Belt) and the Waterberg (eastern Damara Belt) basins, localized sedimentation of the Karoo Supergroup started during the Late Carboniferous discordantly onto Damara orogen rocks (Fig. 4). Siliciclastic rocks of the Carboniferous-to-Permian Dwyka Group were deposited during the Gondwana Ice Age,

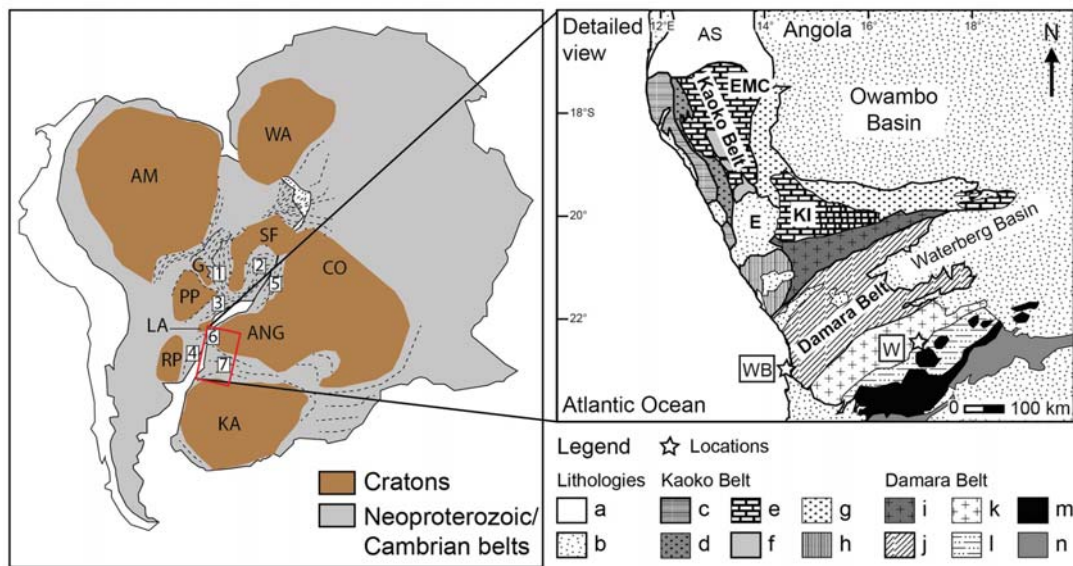


**Fig. 2** Left: Neoproterozoic mobile belts and cratons in South America and Africa (SW Gondwana) modified after Heilbron et al. (2008). Red rectangle shows study area. Neoproterozoic belts: 1: Brasilia Belt; 2: Araçuaí Belt and Central Ribeira Belt; 3: Southern Ribeira Belt; 4: Dom Feliciano Belt; 5: West Congo Belt; 6: Kaoko Belt; 7: Damara Belt. Major Cratons: AM Amazonia, SF São Francisco, LA Luis Alves, RP Rio de la Plata, WA West Africa, CO Congo, ANG Angola, KA Kalahari, PP Paranapanema. Right: Tectonic units of the NW Namibian Kaoko and Damara belts (modified after Goscombe et al. 2003a, b; Hoffmann et al. 2004; Miller 2008; Jung et al. 2014): a Bangweulo shield; b Mesozoic sedimentary and volcanic rocks

and Cenozoic cover; Kaoko Belt: Western Kaoko Zone: c Coastal Terrane; d Orogen Core; Central Kaoko Zone: e Pre-Damara Congo Craton; f Central Kaoko Zone; Eastern Kaoko Zone: g Northern Platform; Southern Kaoko Belt: h Ugab Zone. Damara Belt: i Outjo Zone (Northern Zone); j Swakop Zone (Northern and Southern Central Zone); k Khomas Zone (Southern Zone); l Hakos Zone (Southern Margin Zone); m Pre-Damara Kalahari Craton; n Southern Nama Foreland. AS Angola shield, EMC Epupa Metamorphic Complex, E Etendeka flood basalts, KI Kamanjab Inlier, W Windhoek, WB walvis bay

whereas Ecça and Drakensberg sedimentary and volcanic rocks indicate that the climate became progressively more arid changing from tropical and subtropical to more desert-like depositional environments (Miller 2008). In the Huab Basin, post-glacial sediments (Ecça and Beaufort Group) consist of siliciclastic units intercalated with coal seams and carbonate rocks. In contrast, these sedimentary sections are lacking within the Waterberg Basin where sedimentation resumed with mainly siliciclastic rocks (Dwyka-to-Stromberg Group) with only minor intercalation of carbonate units (Ecça Group) until the Early Jurassic. These sedimentary rocks (<750 m) are overlain by a siliciclastic section (Etjo Fm) interfingering with basaltic flows (5 m, Rooival Fm) that are correlated to the Karoo LIP event of Early Jurassic time ( $\sim 183 \pm 1$  Ma, Johnson et al. 1996; Duncan et al. 1997; Catuneanu et al. 2005).

### Late Jurassic-to-Cenozoic evolution-break-up, and syn- to post-rift processes.

The Late Jurassic-to-Early Cretaceous evolution of the Namibian SAPCM was dominated by continuous pre- to post-rift processes, e.g., tectonic and surface uplift, erosion,

subsidence, and sedimentation, as well as the emplacement of dike swarms and flood basalts caused by the Paraná–Etendeka plume movement (e.g., Courtillot et al. 1999; Sengör 2001; Ernst and Buchan 2001a; Trumbull et al. 2007; Hu et al. 2018).

In the western Huab Basin, this geological evolution is recorded by Etendeka volcanic rocks overlying Upper Jurassic-to-Lower Cretaceous eolian sediments (Twyfelfontein Formation) (Fig. 4) (Miller 2008). These sedimentary rocks interfinger with the overlying volcanic rocks (Jerram et al. 1999; Salomon et al. 2016), and both sections correlate with its Brazilian counterparts, the sedimentary Botucatu, and volcanic Serra Geral formations (Milner 1986; Stollhofen et al. 2000; Miller 2008). Together with these Brazilian Paraná basin volcanic rocks, the Etendeka flood basalts form the Lower Cretaceous Paraná–Etendeka LIP that emplaced during the South Atlantic syn-rift stage. In Africa, the Etendeka volcanic suite covers more than 78,000 km<sup>2</sup> (Fig. 3), and maximum preserved thicknesses reach  $\sim 900$  m (Milner et al. 1992; Peate 1997; Stollhofen et al. 1999). However, Etendeka dike swarms indicate a wider area of originally lava covered area reaching as far north as the Angolan border and as far west as the southern Waterberg Basin area within

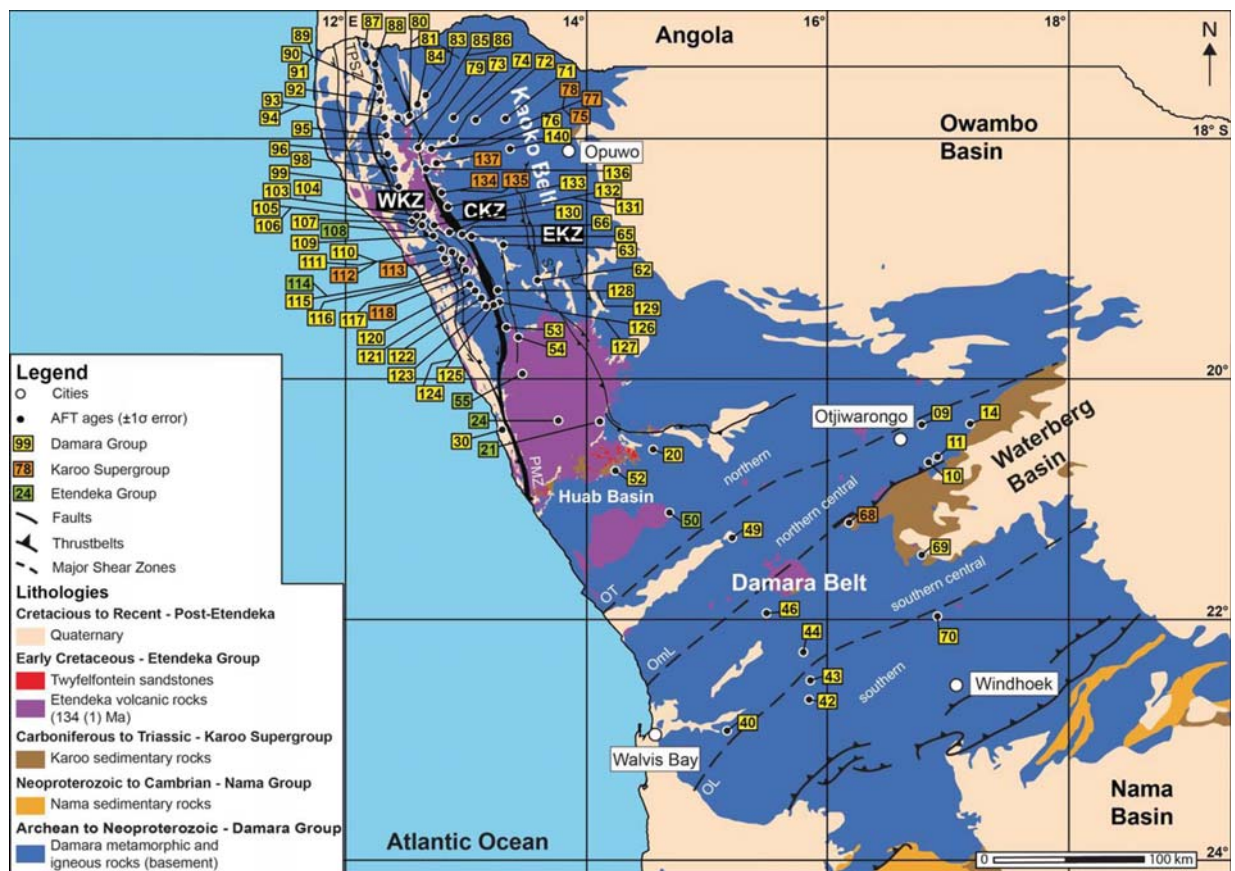


**Fig. 3** Simplified geological map of the study area in NW Namibia with the corresponding sample locations and numbers (NA11-xx) (modified after Frimmel et al. 2011; locations of shear zones after Foster et al. 2009; Salomon 2015). WKZ Western Kaoko Zone, CKZ

Central Kaoko Zone, EKZ Eastern Kaoko Zone, ST Sesfontein thrust, PMZ Purros mylonite zone, TPSZ Tree palms shear zones, OT Otjohorong thrust, OmL Omaruru lineament, OL Okahandja lineament. For further information, see supplementary material, table S1

the Damara Belt (Peate 1997; Trumbull et al. 2004, 2007; Torsvik et al. 2009, 2014). The dike swarms have most likely acted as feeder channels for the volcanic rocks and follow the Kaoko (~margin parallel) and the Damara (~margin perpendicular) belt structures (Trumbull et al. 2004, 2007; Salomon et al. 2017). Radiometric ages for the volcanic rocks range from ~135 to ~127 Ma (Trumbull et al. 2004, 2007; Baksi 2018) indicating ongoing magmatic activities along the Namibian SAPCM for approximately up to 10 Myr (Milner et al. 1995).

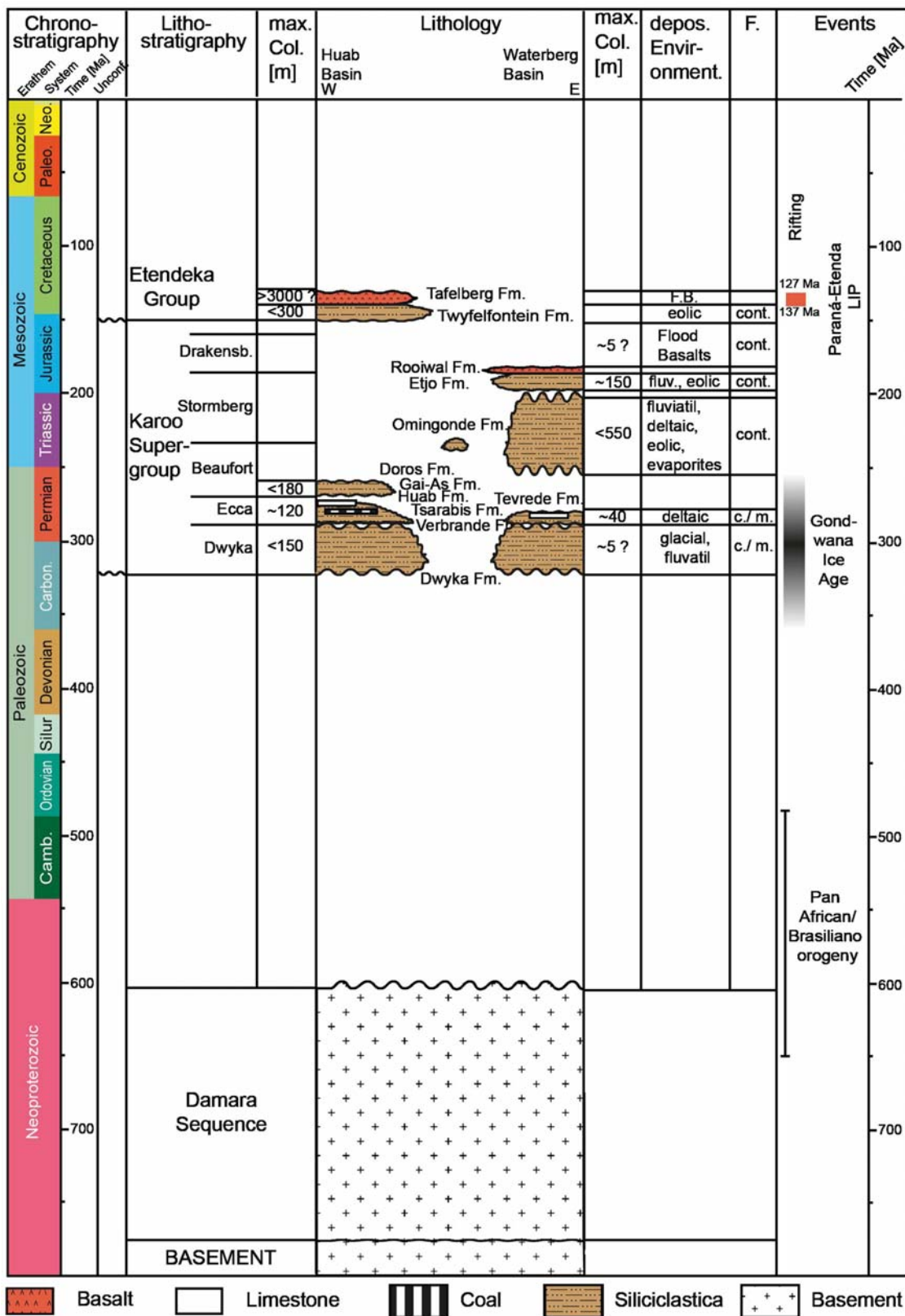
Following the Paraná–Etendeka magmatic activity, the NW Namibian SAPCM rocks experienced post-rift cooling and exhumation. In the NW Kaoko Belt, published AFT ages range from ~80 to ~50 Ma along the coast and from ~330 to ~260 Ma further inland (Brown et al. 2014). In the Damara Belt, published AFT data revealed age from ~120 to ~70 Ma. Further south (Windhoek area), AFT ages range between ~550 and ~200 Ma (Raab 2001; Raab et al. 2002, 2005; Brown et al. 2014). Brown et al. (1990) proposed

cooling of the coastal rocks during the Early Cretaceous-to-Cenozoic post-rift processes due to erosion of up to 3.5 km of sediments and transport to the offshore basins.

### Tectonic structures

In the Kaoko Belt, predominant tectonic zones are of Neoproterozoic age [Sesfontein Thrust (ST), Purros Mylonite Zone (PMZ), and Tree Palms Shear Zone (TPSZ)], and follow the ~NW trend dividing the mobile belt into the longitudinal Eastern, Central, and Western (Kaoko) Zones (Fig. 3) (Goscombe et al. 2003a, b). Salomon et al. (2015) assume partial reactivation of the tectonic structures during the South Atlantic opening, with estimated normal offsets < 1200 m. Kukulius (2004) also assumes major post-flood basalt deposition tectonic activity due to the offset of tilted basal Etendeka volcanic rocks.

South of the Kaoko Belt (Fig. 3), major margin perpendicular lineaments [Otjohorong Thrust (OT), Omaruru





◀**Fig. 4** Simplified stratigraphic W–E transect through the NW Namibian sedimentary Huab and Waterberg basins with corresponding chronostratigraphy, lithostratigraphy, max. column deposited, lithology, depositional environment, facies (F.), and events (after Johnson et al. 1996; Stollhofen et al. 1999; Catuneanu et al. 2005). For locations of the basins, see Fig. 3

Lineament (OmL), and Okahandja Lineament (OL)] extend across the EW-trending Damara Belt following the pre-Damara metamorphic basement structures of the intracontinental branch and also have probably been reactivated during the break-up processes (Raab et al. 2002, 2005; Brown et al. 2014; Salomon et al. 2015, 2017).

## Methods

### Thermochronology

Thermochronology is based on the accumulation and thermally controlled retention of isotopic daughter products and linear crystal defects produced during the radioactive decay of a parent. Due to the temperature sensitivity of thermochronometers, ages provide information about the thermal history of the rock, rather than mineral crystallization ages (although in fast cooled volcanic rocks, they do record crystallization ages).

For this research, apatite and zircon fission-track (AFT and ZFT, respectively) analyses were performed on 89 samples of Neoproterozoic metamorphic, and magmatic, Carboniferous-to-Permian sedimentary, and Lower Cretaceous volcanic rocks along the NW Namibian Kaoko and Damara belts (Fig. 3, Tab. S1). Sample preparation and analyses followed the same protocol as, e.g., Karl et al. (2013). Whenever possible, two thermochronometry dating techniques were applied to the samples, allowing a more robust evaluation of the spatial and temporal cooling of the sampled rocks. However, only a few samples (25) contained apatite and zircon grains in quantities, to allow AFT and ZFT analyses.

Fission-track dating techniques correspond to a specific total annealing temperature [ $T$  (an)]. When temperatures exceed  $T$  (an) over a certain time, the chronometer is totally reset. Partial annealing occurs when temperatures or required time did not fulfil conditions for total annealing. For further interpretations, this research uses temperatures between 110 °C/10 Myr and 60 °C/10 Myr for the partial annealing zone (PAZ) for the AFT analysis (Gleadow and Duddy 1981), and between 330 °C/10 Myr and 190 °C/10 Myr for ZFT analysis (Garver and Kamp 2002; Garver 2003; Hurford 1986; Rahn et al. 2004; Reiners and Brandon 2006).

### Numerical modeling of continuous $t$ – $T$ -paths ( $t$ – $T$ -evolution)

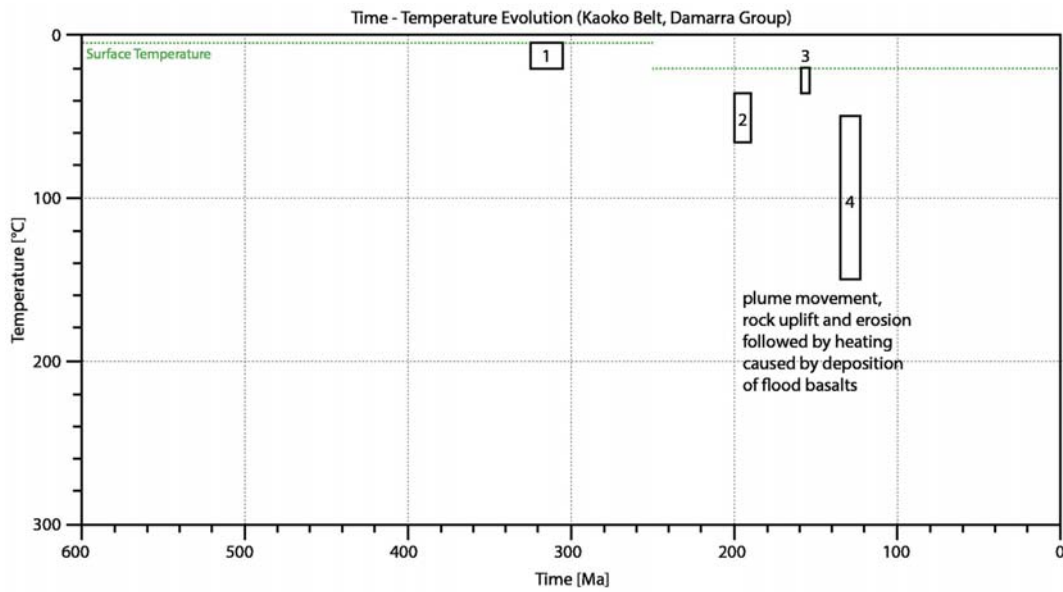
Thermal modeling of thermochronological data was used to determine continuous cooling and heating histories ( $t$ – $T$ -evolution) of individual samples (Fig. 1). The numerical modeling software code HeFTy<sup>®</sup> (v.1.9.3.) (Ketcham 2005; Ketcham et al. 2007a, b, 2009, 2017) allows for reconstruction of the  $t$ – $T$ -evolution of the Neoproterozoic basement to quantify the exhumation and subsidence history of several crustal segments of the upper crust.

Therefore, we used the existing information derived from the published geological record, such as metamorphic ages, magmatic events, and lithostratigraphic data that were transferred into single constrained  $t$ – $T$ -boxes and embedded into the modeling software (Fig. 5). The  $t$ – $T$ -constraints differ across sample locations within the key area. However, the same  $t$ – $T$ -coordinates were applied strictly to samples of the same geological area to guarantee a better comparability of the  $t$ – $T$ -histories of the modeled samples in their respective regions.

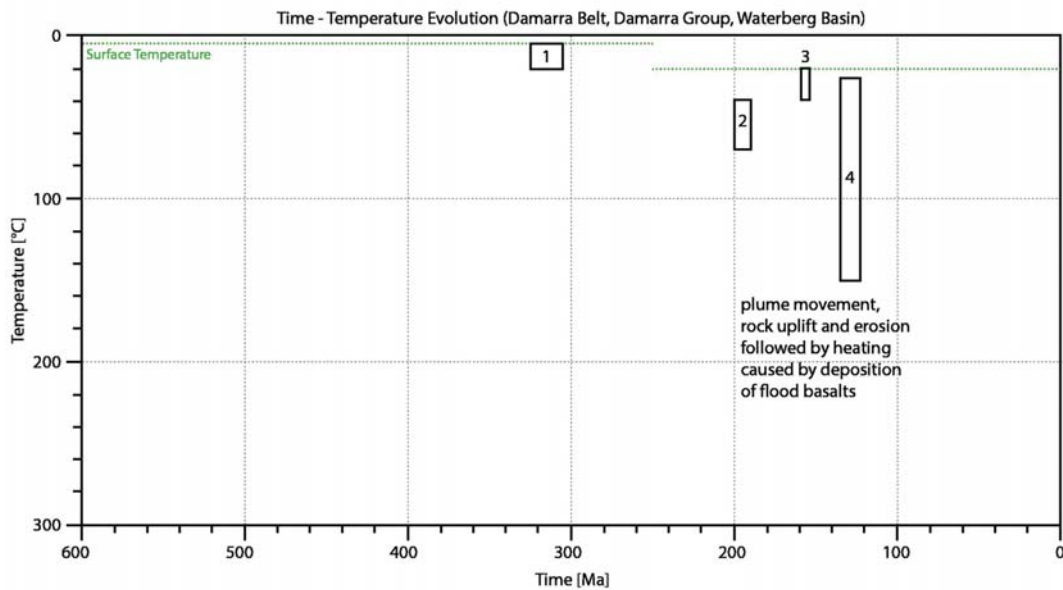
Then, HeFTy<sup>®</sup> performs a so-called inverse model and seeks paths that fit through the  $t$ – $T$ -constraints considering the input thermochronological data. Thereby, we test our thermochronological data against specific  $t$ – $T$ -constraints derived from the published geological record to retrieve continuous long-term  $t$ – $T$ -paths since the Late Paleozoic. The thermochronological data sets used for the numerical modelling are: AFT single grain ages, confined spontaneous fission-track length distribution (> 50 individual length) corrected for  $c$ -axis related angle (Donelick et al. 1999; Ketcham et al. 2007a, b, 2009), etch pit size ( $D_{\text{par}}^{\text{®}}$ ), and annealing kinetics of Ketcham et al. (2007a, b).

### Reconstruction of the $t$ – $T$ -paths and calculation of rates

Thermochronological data presented in this study only cover the last ~400–300 Ma and we, therefore, integrated published geo- and thermochronological data (U–Pb, Sm–Nd and Rb–Sr, and K/Ar, <sup>40</sup>Ar/<sup>39</sup>Ar, AFT) to our own data set to reconstruct a coherent  $t$ – $T$ -path over more than 500 Ma. Most of the geo- and thermochronological data are confined to specific geological regions or only describe local geological phenomena, i.e., intrusions or contact metamorphism that do not provide information of the  $t$ – $T$ -evolution of entire crustal blocks and segments. Therefore, we chose published data, which we consider relevant for our study locations. Consequently, the published geochronological data reflect the main intrusion, crystallization, metamorphic, and cooling processes, and constrain the presented  $t$ – $T$ -evolution. Published ages were transferred to specific temperature areas according to their effective closure, and/



No.	Time [Ma]	Temperature [°C]	Event
1	325 - 305	20 - 5	Onset of Paraná Basin sedimentation
2	200 - 190	65 - 35	Possible initial plume rise and surface uplift based on stratigraphic records
3	160 - 155	35 - 20	Possible climax and collapse of plume head based on renewed sedimentation
4	140 - 125	150 - 50	Twyfelfontein Sedimentation, Paraná-Etendeka flood basalts (Tafelberg Fm)



No.	Time [Ma]	Temperature [°C]	Event
1	325 - 305	20 - 5	Onset of sedimentation
2	200 - 190	70 - 40	Possible Initial plume rise and surface uplift based on stratigraphic records
3	160 - 155	40 - 20	Possible climax and collapse of plume head based on renewed sedimentation
4	140 - 125	150 - 25	Deposition of Paraná-Etendeka flood basalts (Etjo Formation, Rooiwal Fm)

◀**Fig. 5** Numerical modeling set-up for samples of the Namibian Damara Sequence located in the Kaoko Belt (upper), and Damara Belt (lower). The set-up was generated from previous work and uses field observations and published stratigraphic (Johnson et al. 1996; Duncan et al. 1997; Catuneanu et al. 2005; Miller 2008), paleo-geographic (Scotese et al. 1992, 1999; Torsvik et al. 2009, 2014), and -climatic knowledge (Wygrala 1989; Brown et al. 1990). We took single geological events from the published geological record, i.e., metamorphic ages, magmatic events, and lithostratigraphic data and transferred the given information into specific  $t$ - $T$ -constraints applied to the numerical modeling software code HeFTy<sup>®</sup> (v.1.9.3.) (Ketcham 2005; Ketcham et al. 2007a, b, 2009, 2017). The connected tables below the  $t$ - $T$ -evolution show further explanations for the applied  $t$ - $T$ -constraints

or annealing temperatures including wide ranges of errors, both in time, and temperature (Fig. S1; Pollard et al. 2002). In a further step, we drew average  $t$ - $T$ -paths connecting the existing data taking into account that uncertainties related to the time, temperature, locations, and the probability of the reconstructed cooling paths often entail the generation of error strings, and should not be disregarded.

This critical view also holds for the calculation of exhumation and subsidence rate that directly base on the course of the differentiated  $t$ - $T$ -path and do not reflect the timing of geological events, e.g., single intrusion and/or metamorphism ages. The intervals were also constrained by the different cooling paths and describe the distance from tipping point to tipping point. The change in temperature ( $\Delta T$ ) over time ( $\Delta t$ ) was used to determine the cooling or heating rate ( $\Delta T/\Delta t$ ) using the “weighted-mean” paths of the models  $t$ - $T$ -histories. The cooling and heating rates were divided by an assumed geothermal gradient to obtain an exhumation and subsidence rate, respectively.

Geothermal gradients depend on the predominant average heat flow over long-term periods including the heat generation and thermal conductivity of rocks, metamorphic reactions, and descendent waters (Barker et al. 1986; Rybach et al. 1988; Yağın et al. 1997; Burov 2009). There exist short-term periods with anomalously high or low geothermal gradients, e.g., in direct surrounding of intrusions or during Ice House periods. However, quantitative research of the thermal influence in relation to distance or depth (e.g. intrusions, dikes, or ice shields), and the effect and duration of those anomalous periods (e.g., intrusion or magmatic activity in LIP environments) is lacking (Barker et al. 1986; Rybach et al. 1988; Yağın et al. 1997; Burov 2009). Therefore, we decided to work with a homogenous and arithmetical mean paleo-geothermal gradient of 30 °C/km for the entire modeled time (Brown et al. 1990). The paleo-geographical reconstruction of the research area was taken from Scotese et al. (1992, 1999) and leads to paleo-surface temperatures of an average of 10 °C for Precambrian-to-Late Paleozoic time, and an mean of 25 °C since Mesozoic time (Wygrala 1989). All rates are expressed as positive rates and

are related to exhumation or subsidence according to the decrease and increase of temperature over time.

## Results

### Apatite fission-track data

#### Kaoko belt

For the Kaoko belt igneous and sedimentary rocks, altogether 72 samples, revealed at least between 10 and 29 grains that could be dated with AFT analysis (Figs. 6; S1; Table S2). Six samples revealed only between 3 and 9 grains, and therefore, their age information remain less certain. Except for 8 samples (all 0%), all single grain age distributions (of 64 samples) passed the Chi-square test with values > 5% indicating a homogeneous distribution with respect to 1 $\sigma$ -error of the single grain ages (Galbraith 1981).

AFT ages of the Precambrian Damara Sequence (58 samples) range between  $390.9 \pm 17.9$  Ma and  $81.3 \pm 4.2$  Ma. In general, AFT ages are younger along the coast and ages increase systematically inland within the Central and Eastern zones (Figs. 6, 7; S1). Sedimentary rocks of the Karoo Supergroup (9) revealed ages between  $342.2 \pm 18.3$  Ma and  $96.5 \pm 8.4$  Ma. Magmatic rocks of the Etendeka Group (5) provided ages between  $125.6 \pm 23.6$  Ma and  $103.5 \pm 4.9$  Ma.

Confined spontaneous fission-track length and etch pit size ( $D_{\text{par}}^{\text{®}}$ ) data were acquired for all 72 Kaoko Belt samples (Table S3) showing  $D_{\text{par}}^{\text{®}}$  values between 0.8 and 1.8  $\mu\text{m}$  (average: 1.2  $\mu\text{m}$ ). This range indicates a relatively inhomogeneous composition concerning the fluorine and chlorine content of apatite. We measured altogether 2529 lengths of confined spontaneous fission tracks for all 72 Kaoko Belt samples. For 24 samples, between 50 and 152 confined spontaneous fission-track lengths could be measured and were integrated to the software code HeFTy<sup>®</sup> to model the  $t$ - $T$ -evolution. Mean track lengths vary between 7.9 and 14.8  $\mu\text{m}$ . The  $c$ -axes correction of the confined track lengths led to a length distribution between 9.8 and 15.4  $\mu\text{m}$ .

#### Damara Belt

For 17 Damara Belt rock samples (Figs. 6; S2; Table S2), at least 15 grains could be dated with AFT analysis except for NA11-69B (five grains). All single grain age distributions passed the Chi-square test with values > 5% indicating a homogeneous distribution with respect to 1 $\sigma$ -error of the single grain ages (Galbraith 1981).

AFT ages of the Precambrian Damara Sequence (15) range between  $138.5 \pm 25.3$  and  $63.8 \pm 4.8$  Ma. In general, AFT ages are younger along the coast and ages increase systematically inland towards the Waterberg Basin

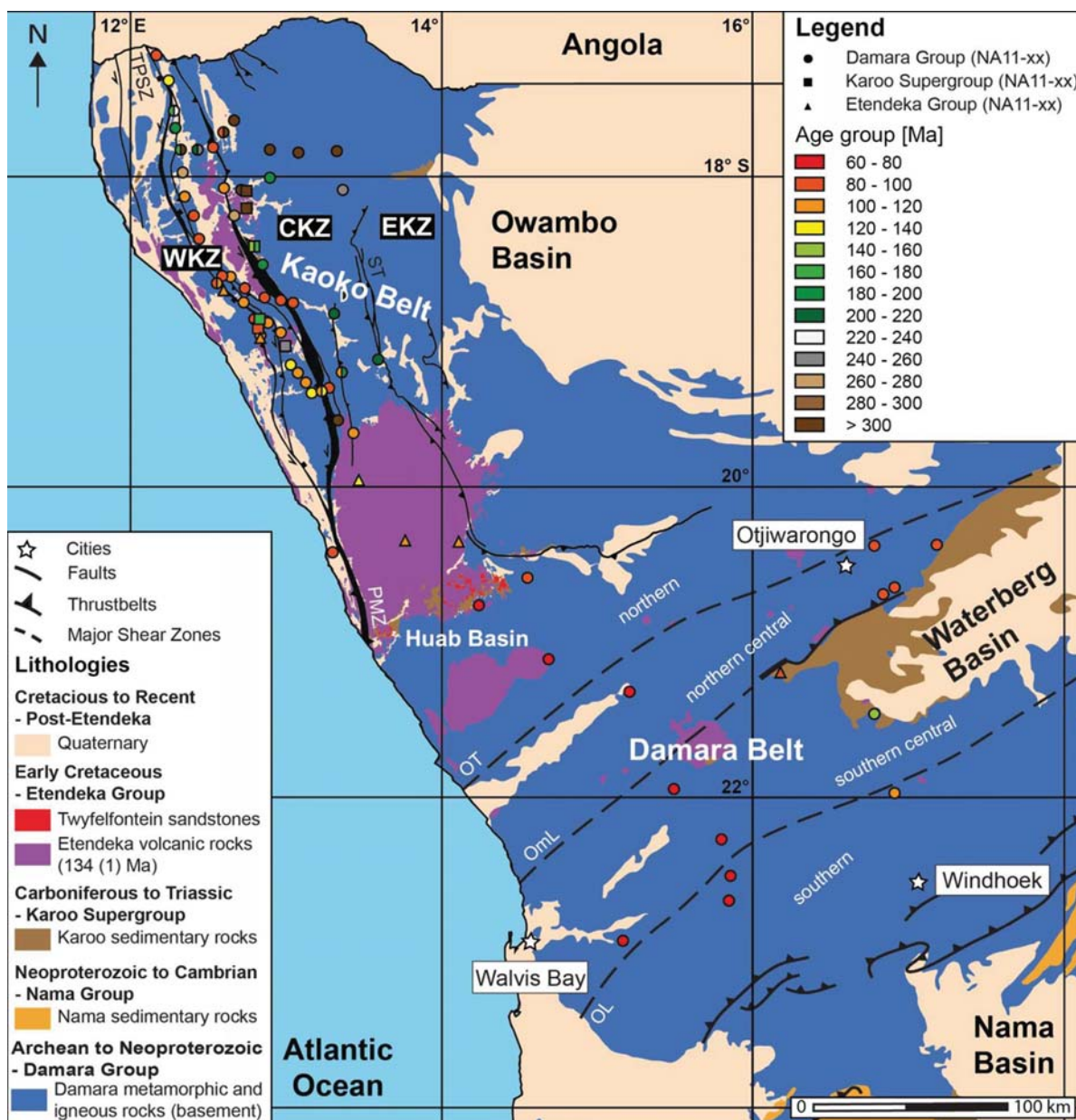


**Fig. 6** Simplified geological map of the study area in NW Namibia showing the regional apatite fission-track (AFT) age distribution in the Kaoko and Damara belts (modified after Frimmel et al. 2011; locations of shear zones after Foster et al. 2009; Salomon 2015). Dots: Neoproterozoic samples; rectangles: Paleozoic-to-Mesozoic Karoo samples; triangles: Late Jurassic-to-Early Cretaceous Etendeka samples. WKZ Western Kaoko Zone, CKZ Central Kaoko Zone, EKZ Eastern Kaoko Zone, ST Sesfontein thrust, PMZ Purros mylonite zone, TPSZ Tree palms shear zones, OT Otjohorongo thrust, Oml Omaruru lineament, OL Okahandja lineament. For further information, see supplementary material, tables S1 and S2

(Figs. 6, 7; S2). AFT analysis revealed only one age for a Karoo conglomerate ( $88.4 \pm 7.2$  Ma) and Etendeka granite ( $71.6 \pm 5.2$  Ma).

Confined spontaneous fission-track length and etch pit size ( $D_{\text{par}}^{\text{®}}$ ) data were acquired for all Damara Belt samples (Table S3). We measured 1963 etch pit sizes for all

apatite grains. The mean  $D_{\text{par}}^{\text{®}}$  value for each sample ranges between 1.1 and 1.6  $\mu\text{m}$  with an average  $D_{\text{par}}^{\text{®}}$  value of 1.3  $\mu\text{m}$ . This narrow range indicates a homogeneous composition concerning the fluorine and chlorine content of apatite. We measured 736 confined spontaneous fission-track lengths for all Damara Belt samples. Eight samples obtained

between 51 and 111 measured confined spontaneous fission-track lengths that were applied to the software code HeFty<sup>®</sup> for the numerical modeling of the  $t$ - $T$ -evolution. Mean track lengths vary between 8.6 and 13.5  $\mu\text{m}$ . The  $c$ -axes correction of the confined track lengths led to a distribution between 11.9 and 14.5  $\mu\text{m}$ .

### Zircon fission-track ages

ZFT analyses were performed on 29 rock samples of the Kaoko Belt (Figs. 8; S3; Tab. S4). All ages obtained for the Precambrian Damara Sequence (26 samples) are younger than their stratigraphic age. ZFT ages range between  $429.5 \pm 67.8$  and  $313.9 \pm 53.4$  Ma. Only two samples, NA11-89G ( $118.2 \pm 25.1$  Ma) and NA11-91 ( $233.5 \pm 43.5$  Ma) in the north, show younger ages and do not lie in the general age trend (Fig. 9). However, both samples revealed only two grains to perform FT analysis and therefore, the reliability of the age information remains uncertain. Furthermore, both samples have abnormal high uranium contents in relation to the other samples. This also holds for only three measured grains of the gneiss sample NA11-126 ( $316.3 \pm 70.7$  Ma). Nevertheless, all single grain age distributions fulfilled the requirement of the  $\chi^2$ -test with values  $> 5\%$  indicating a homogenous distribution with respect to  $1\sigma$ -error of the single grain ages (Galbraith 1981) with the exception of NA11-106 ( $436.8 \pm 45.9$  Ma) that fails the  $\chi^2$ -test (0.01%).

Three sedimentary rock samples (NA11-118, NA11-135GO, NA11-135R) of the Karoo Supergroup revealed ZFT ages between  $365.6 \pm 30.6$  Ma and  $377.2 \pm 30.4$  Ma and, therefore, represent detrital ages.

### Numerical modeling of the $t$ - $T$ -evolution

Using the software code HeFty<sup>®</sup> (v.1.9.3.; Ketcham 2005; Ketcham et al. 2007a, b, 2009, 2017), the inverse numerical modeling of the  $t$ - $T$ -evolution of the Neoproterozoic basement rocks within the NW Namibian Kaoko and Damara belts was applied to test the thermochronological data set against single geological events ( $t$ - $T$ -constraints) described in the published geological record (Fig. 5).

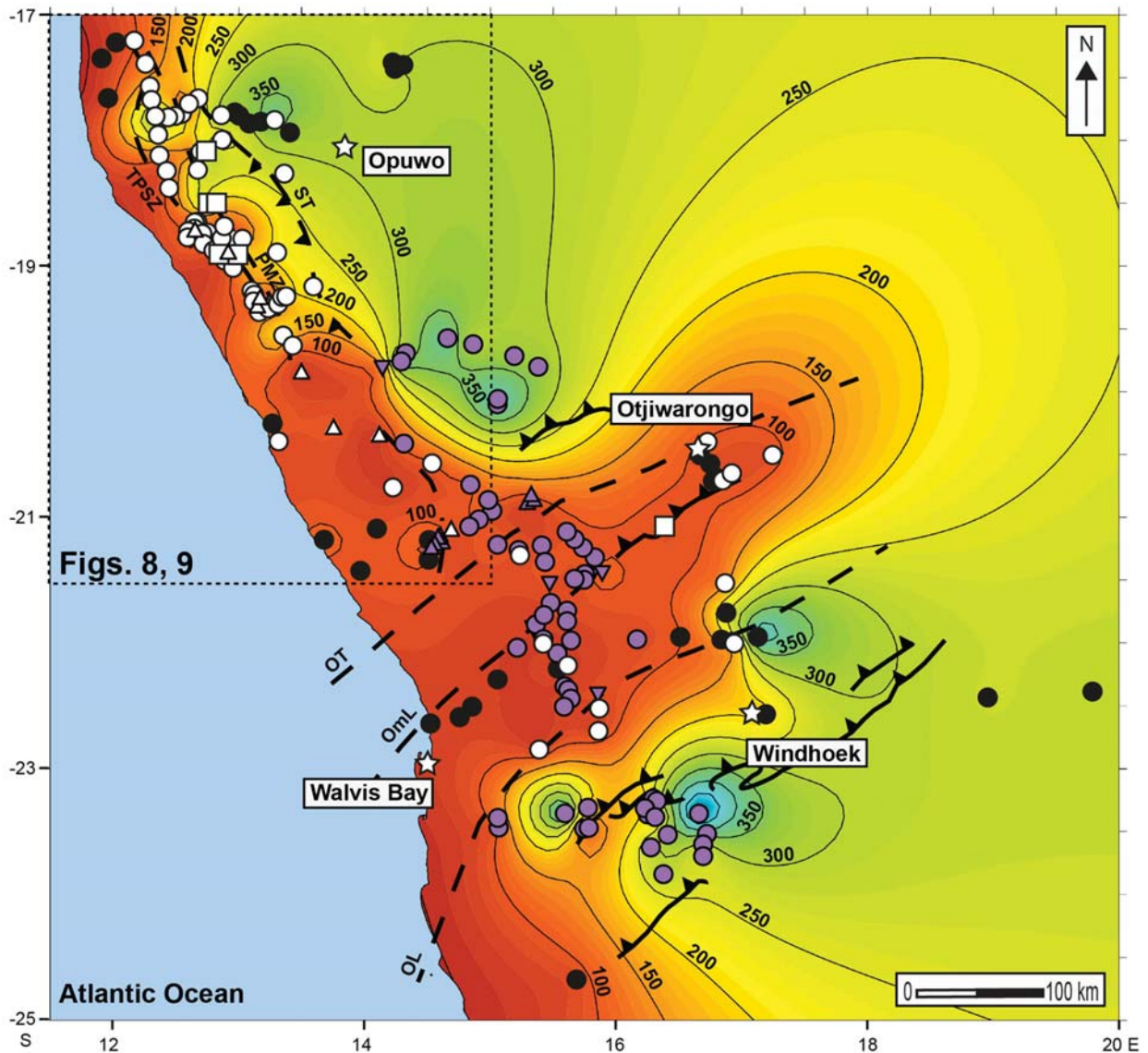
For 29 samples (Tab. S3), a high number of measured fission tracks in apatite ( $> 51$ ) allow robust constraints on the  $t$ - $T$ -path through 60–110 °C. In general, 50 000  $t$ - $T$ -paths have been tested against the data set and yielded a high goodness of fit (G.O.F.) (Figs. S4.1–S4.8) (Ketcham et al. 2007a, b). However, to provide comparability of the modeled samples, lower G.O.F. values were also accepted without omitting  $t$ - $T$ -constraints to gain better results. Therefore,  $t$ - $T$ -models passed our requirements when good fits were found. Altogether,  $t$ - $T$ -models reveal between 1 and 519 good, and between 3 and 2681 acceptable  $t$ - $T$ -paths, while 34% of the models show  $> 100$  good paths, and 58%  $> 30$ .

More than 1000 acceptable paths could be reproduced by 38% of the models, and  $> 100$  by 93%. The AFT age and confined fission-track length distribution for 86%, or rather 55% of the samples were reproduced with an excellent G.O.F. of  $> 80\%$ . Therefore, we find sufficient  $t$ - $T$ -paths consistent with both the thermochronological data and geological history.

The sole numerical modeling of our thermochronological data focusses on the  $t$ - $T$ -evolution since Carboniferous time over temperatures below 300 °C (Fig. 10). The published record suggests that Neoproterozoic basement rocks had reached the surface before the onset of the Karoo sedimentation during the Early-to-Late Paleozoic SW Gondwana intraplate environment (Johnson et al. 1996; Stollhofen et al. 2000; Catuneanu et al. 2005; Milani et al. 2007). During the Triassic, the models show coherent heating of the samples showing the ongoing subsidence of the Paleozoic-to-Mesozoic basins (Huab and Waterberg). From Early Jurassic,  $t$ - $T$ -models allow cooling inferred from possible initial plume movement during pre-rift-processes (Şengör 2001). All models show a possible cooling to temperatures near or at the Earth's surface. The evolution is followed by a reheating during the Early Cretaceous that reflects the thermal influence caused by the emplacement of dike swarms and accompanied volcanic activity, and the deposition of the Etendeka flood basalts. Maximum temperatures are reached especially in the southern Damara Belt ( $\sim 120$  °C). Then, renewed cooling sets in during the Early Cretaceous and continues until the Cenozoic.

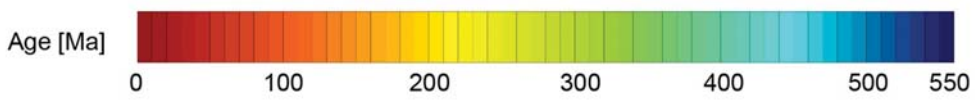
### Interpretation and discussion

For discussion and interpretation of the proposed  $t$ - $T$ -evolution of the Neoproterozoic basement, published geo- and thermochronological data (Tables S5.1–S5.6) were directly incorporated into the modeled  $t$ - $T$ -histories to retrieve a coherent syn- to post-Late Neoproterozoic evolution of the NW Namibian Kaoko and Damara belts (Fig. 11). The projected  $t$ - $T$ -paths were used to make estimates on exhumation and subsidence rates (Fig. 12a, b) and reflect an average and/or “weighted”-mean  $t$ - $T$ -path of the modeled  $t$ - $T$ -histories including wide error ranges for temperatures as well as on the temporal scale related to each dating method. We are well aware of the uncertainties and the generated error string entailed by the calculation of long-term exhumation and subsidence rates covering large areas over long-time periods. Nevertheless, we would like to propose these long-term rates as an approximation approaching the long-term temperature processes. Finally, temperature interpolation maps of the Neoproterozoic basement surface were used to approach a visualization of the  $t$ - $T$ -evolution of the SW Gondwana intraplate thermal structure (Fig. 13).



**Legend**

- ☆ Cities
- ↗ Thrust belts
- - - Fault zones



Sample locations

- |                         |                                       |                    |                  |
|-------------------------|---------------------------------------|--------------------|------------------|
| This study              | ○ Damara Group                        | □ Karoo Supergroup | △ Etendeka Group |
| Raab et al., 2002, 2005 | ● Proterozoic Basement & Damara Group |                    | ▲ Etendeka Group |
| Brown et al., 2014      | ● Proterozoic Basement & Damara Group |                    |                  |

◀**Fig. 7** Detailed interpolation map showing a possible modeled projection of the regional AFT age distribution of the NW Namibian Kaoko and Damara belts. Samples of this study (white) are integrated to published AFT data by Brown et al. (2014) (black), and Raab et al. (2002, 2005) (purple) using the Golden Software Surfer®. Whereas yellow-to-red colors indicate younger ages, green-to-blue colors imply older ages. Isolines show age in [Ma] without error. Colored dots (Neoproterozoic Damara basement rocks), rectangles (Late Paleozoic-to-Mesozoic Karoo sedimentary rocks), and triangles (Lower Cretaceous Etendeka sedimentary and volcanic rocks) show sample locations according to the references. Isolines show age in [Ma] without error. *ST* Sesfontein thrust, *PMZ* Purros mylonite zone, *TPSZ* Tree palms shear zones, *OT* Otjohorong thrust, *OmL* Omaruru lineament, *OL* Okahandja lineament. Dashed box: locations of ZFT data see Figs. 8 and 9

### Late Neoproterozoic-to-Early Paleozoic— syn-Pan-to-post-Pan African cooling and exhumation

The Late Neoproterozoic-to-Early Paleozoic is characterized by post-Pan African cooling and exhumation of the Neoproterozoic basement rocks. The published geochronological data indicate a very complex and distinct geological evolution of the different crustal segments (Figs. 10, 11). We assume individual cooling paths within each crustal segment based on the published data. Therefore, we propose cooling paths reflecting the cooling of pre-Pan African deformation

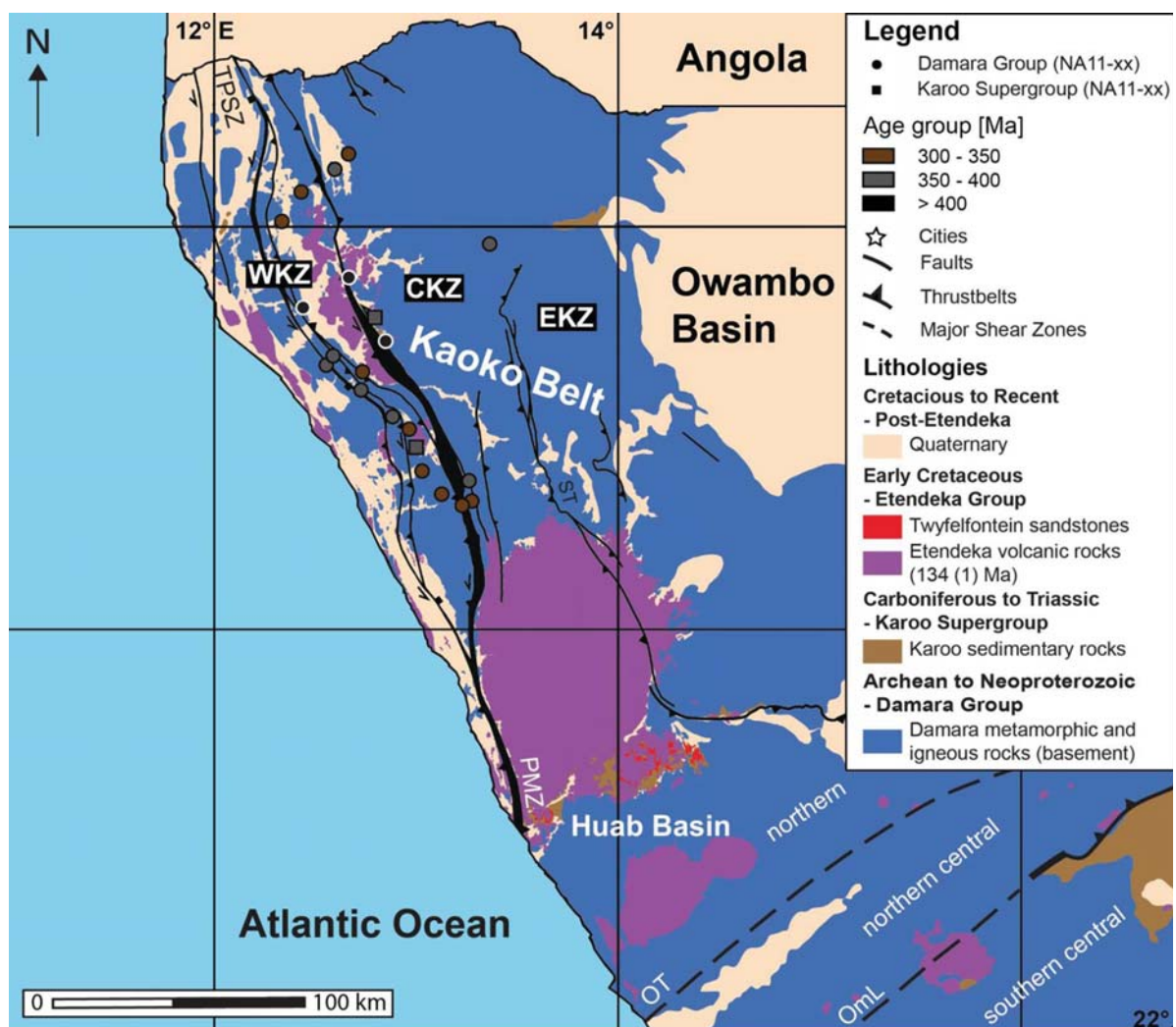
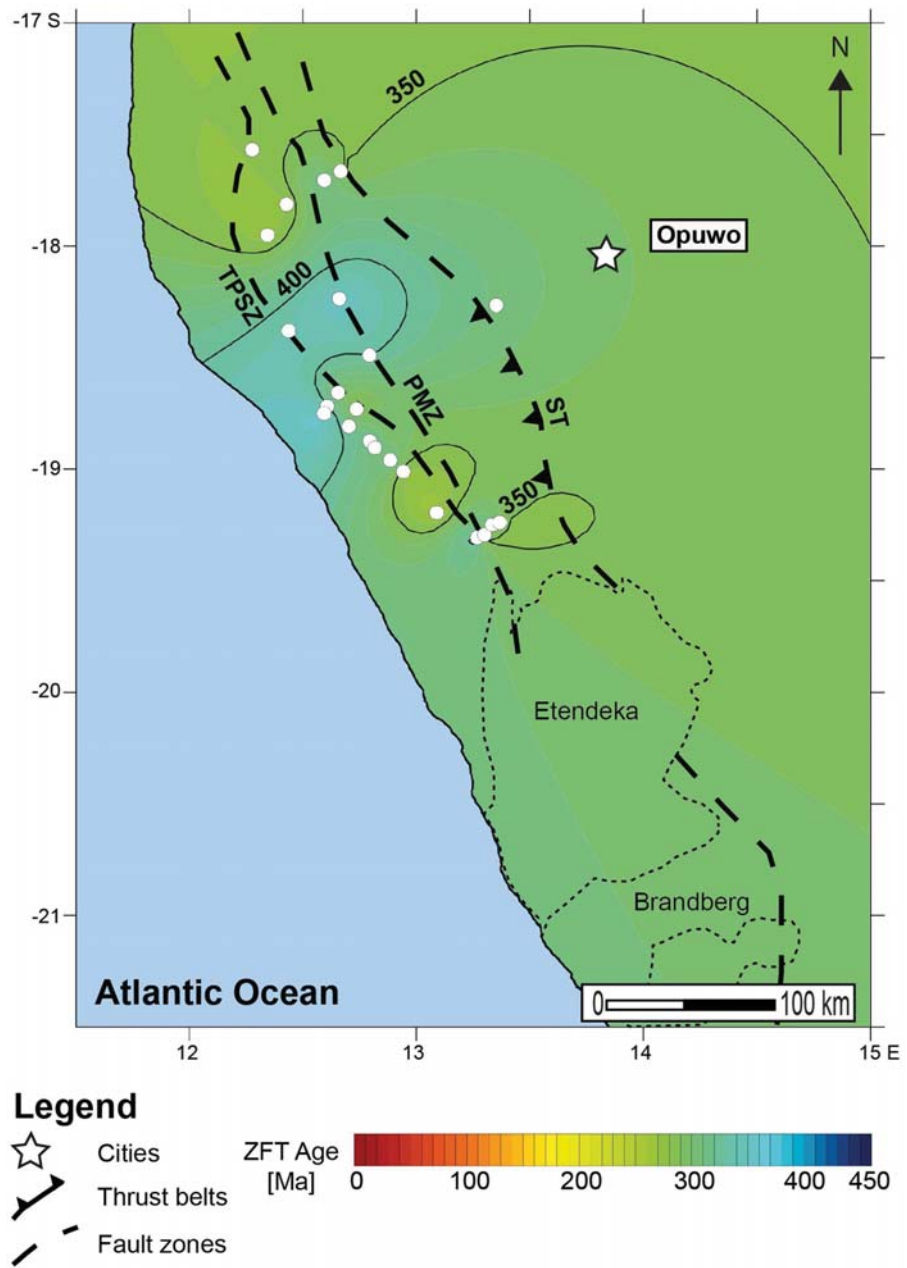


**Fig. 8** Simplified geological map of the study area in NW Namibia showing the regional zircon fission-track (ZFT) age distribution in the Kaoko and Damara belts (modified after Frimmel et al. 2011; locations of shear zones after Foster et al. 2009; Salomon 2015). Dots: Neoproterozoic samples; rectangles: Paleozoic-to-Mesozoic Karoo samples; triangles: Late Jurassic-to-Early Cretaceous Etendeka sam-

ples. WKZ Western Kaoko Zone, CKZ Central Kaoko Zone, EKZ Eastern Kaoko Zone, *ST* Sesfontein thrust, *PMZ* Purros mylonite zone, *TPSZ* Tree palms shear zones, *OT* Otjohorong thrust, *OmL* Omaruru lineament, *OL* Okahandja lineament. For further information, see supplementary material, tables S1 and S4

**Fig. 9** Detailed interpolation map showing a possible modeled projection of the regional ZFT age distribution of the NW Namibian Kaoko Belt using the Golden Software Surfer®. For orientation, see Fig. 7 (dashed box). Whereas yellow-to-red colors indicate younger ages, green-to-blue colors imply older ages. White dots show sample locations of the Neoproterozoic Damara basement rocks. Isolines show age in [Ma] without error. *ST* Sesfontein thrust, *PMZ* Purros mylonite zone, *TPSZ* Tree palms shear zones, *OT* Otjohorong thrust, *OmL* Omaruru lineament, *OL* Okahandja lineament



intrusion and crystallization of rocks, the evolution most likely representing the syn-Pan African intrusion/crystallization, main metamorphism and subsequent cooling of the area, as well as the cooling of post-Pan African deformation intrusion and crystallization of rocks. These cooling paths connect the individual published data that often stem from different locations and, thus, are not linked to each other. Nevertheless, we consider the projected cooling paths to represent a possible *t*-*T*-evolution of the crustal segments along the contemporary SAPCM of NW Namibia.

In the northern Kaoko Belt, geochronological data from the northern WKZ (Figs. 10, 11, green (1); Table S5.1) show U-Pb crystallizations and metamorphic ages of the Neoproterozoic basement rocks between ~575 and ~540 Ma (Goscombe et al. 2005a, b). We suggest three individual cooling paths for the Orogen Core (Fig. 11, dark blue dashed lines) in the northern area of the WKZ: the first and second cooling path describes syn-orogenic cooling either connecting the U-Pb ages and <sup>40</sup>Ar/<sup>39</sup>Ar hornblende cooling ages around 540 Ma (Gray et al. 2006), or the Sm-Nd metamorphic age of ~506 Ma by Goscombe et al. (2005a, b).



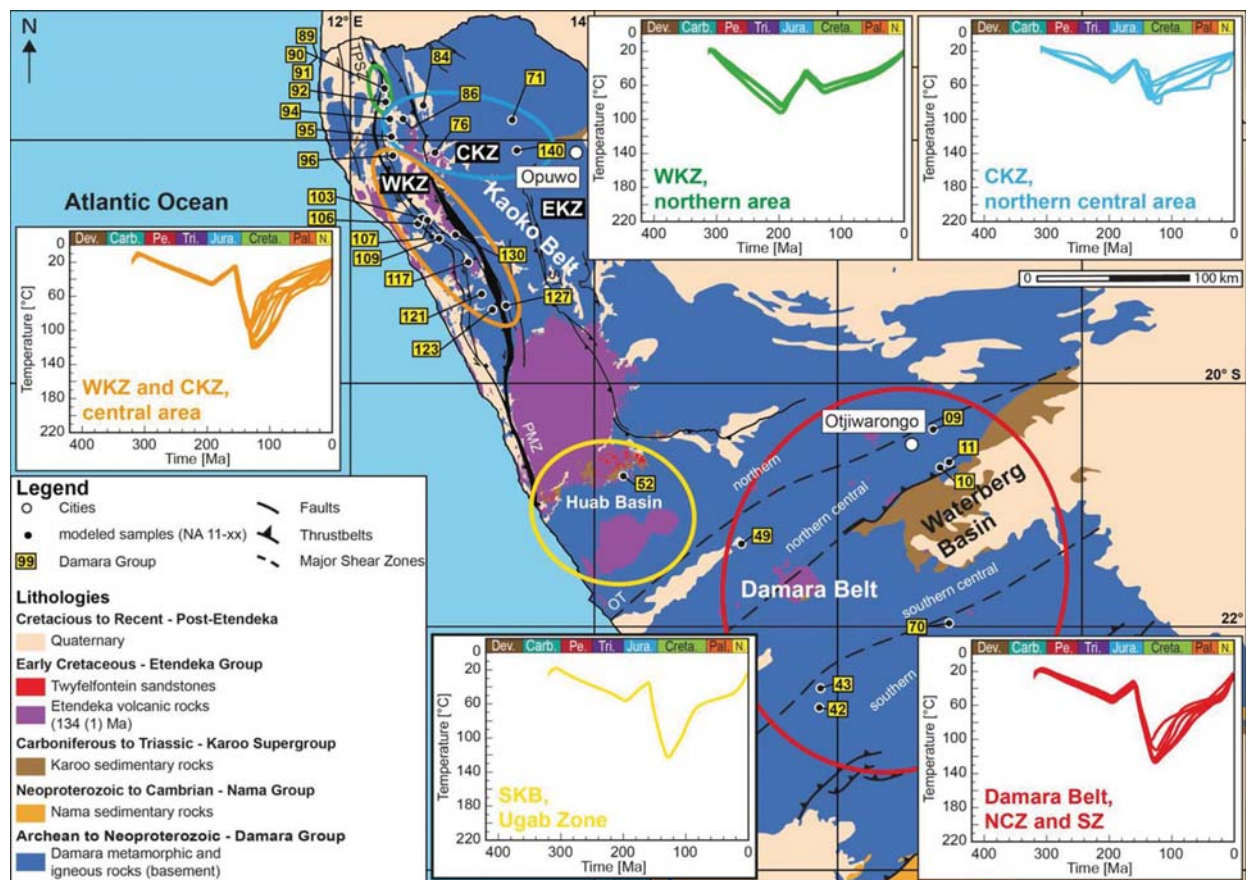


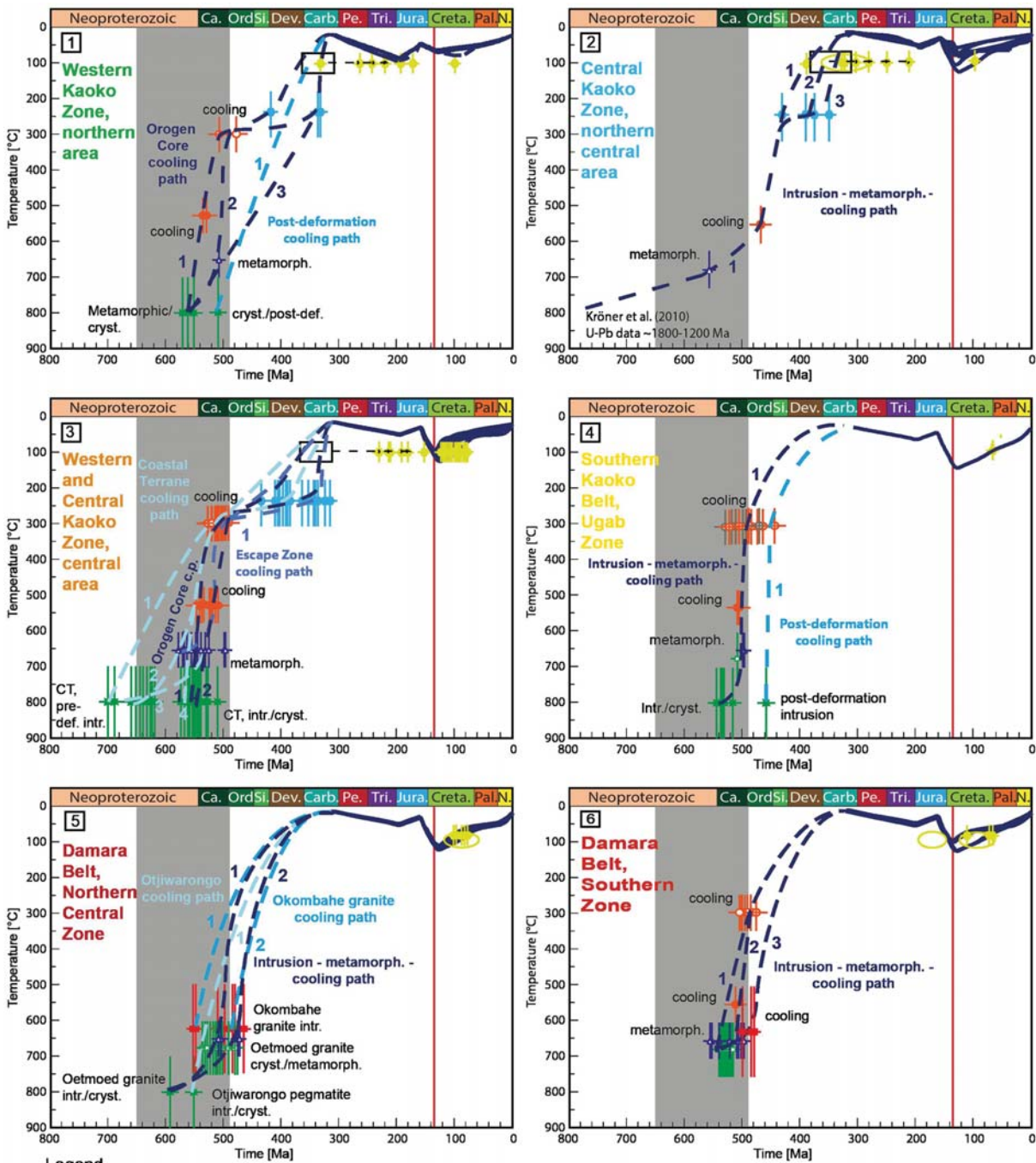
**Fig. 10** Simplified geological map of the study area in NW Namibia showing the results of the inverse numerical modeling in different areas of the Kaoko and Damara belts (modified after Frimmel et al. 2011; locations of shear zones after Foster et al. 2009, Salomon 2015). Windows show the continuous “weighted-mean”  $t$ - $T$ -paths of the samples since the Late Carboniferous modeled with the software code HeFty® (Ketcham et al. 2007a, b; 2017). Samples were subdivided in individual areas of the northern area of the Western Kaoko Zone (WKZ, green), the northern central area of the Central Kaoko

Zone (CKZ, blue), the central area of the Western and Central Kaoko Zone (orange), and the Ugab Zone of the Southern Kaoko Belt (SKB, yellow) within the Kaoko Belt, and the northern central and southern zones (red) of the Damara Belt. WKZ Western Kaoko Zone, CKZ Central Kaoko Zone, EKZ Eastern Kaoko Zone, ST Sesfontein thrust, PMZ Purros mylonite zone, TPSZ Tree palms shear zones, OT Otjiwarongo thrust, OmL Omaruru lineament, OL Okahandja lineament. For further information, see supplementary material figures S6.1–S6.8

We propose relatively fast cooling with exhumation rates between  $\sim 0.3$  mm/a (path 1) and  $\sim 0.1$  mm/a followed by very fast exhumation with  $\sim 1.17$  mm/a (path 2) (Fig. 12a, WKZ, Orogen Core). Both  $t$ - $T$ -paths most likely show homogeneous cooling from  $\sim 500$  Ma on ( $^{40}\text{Ar}/^{39}\text{Ar}$ , Gray et al. 2006), and therefore, we propose ongoing cooling connecting ZFT ages of this study of either Early Devonian, or Carboniferous age. Consequently, post-orogenic cooling initially decreased showing exhumation rates between  $\sim 0.02$  and  $\sim 0.01$  mm/a, and therefore, we assume that rocks have been kept at middle-to-upper crustal levels at temperatures of about  $\sim 300$ – $200$  °C. However, we assume both scenarios probable to reflect the syn- to post-orogenic cooling based on the most constrained cooling path for the northern Orogen Core.

A third possible path (3) describes syn- to post-orogenic cooling from  $\sim 540$  Ma onwards connecting U–Pb, Sm–Nd (Goscombe et al. 2005a, b; Gray et al. 2006) and Carboniferous ZFT ages of this study showing exhumation rates of  $\sim 0.08$  mm/a until the Early Carboniferous. There exists one younger U–Pb post-kinematic age by Goscombe et al. (2005a, b) around  $\sim 505$  Ma that reflects differentiated late- or post-deformation cooling from Early Paleozoic to Carboniferous, and we propose a homogeneous long-term exhumation rate of  $\sim 0.3$  mm/a due to the lack of further data constraining this post-deformation cooling path.

Towards the east, the northern central area of the CKZ (Figs. 10, 11, blue (2); Table S5.2) shows a different syn- to post-orogenic cooling. However, less data were available within this area leaving the possible cooling less constrained



**Legend**

**Intrusion/crystallization/metamorphism**

- U-Pb zircon, (SHRIMP, TIMS, LA-ICP-MS, EPMA)
- ▣ U-Pb monazite, (SHRIMP, TIMS, LA-ICP-MS)
- ▲ Sm-Nd, whole rock
- △ Sm-Nd, garnet-rt
- ▴ Rb-Sr, garnet-rt
- Rb-Sr, whole rock
- ▣ Rb-Sr, plag-rt
- ▣ Rb-Sr, muscovite
- ▣ Rb-Sr, biotite

**Cooling**

- K-Ar, amphibol-hornblende
- K-Ar, hornblende-biotite
- K-Ar, muscovite
- K-Ar, biotite
- K-Ar, feldspar
- Ar-Ar, amphibol-hornblende
- Ar-Ar, muscovite
- Ar-Ar, biotite

- ZFT } of this study
- AFT } of this study
- AFT ages from Brown et al., 2014 and Raab et al., 2002
- ± 1σ error
- t-T-path (HeFTy) representing AFT ages of this study
- projected t-T-path

◀**Fig. 11** Coherent long-term time ( $t$ )–temperature ( $T$ )-evolution of the individual areas of the Kaoko and Damara belts in NW Namibia. Published geochronological data were directly incorporated into the “weighted-mean”  $t$ – $T$ -paths (Fig. 10) of the samples modeled with the software code HeFty® (Ketcham et al. 2007a, b) to reconstruct the entire syn-to post-Late Neoproterozoic  $t$ – $T$ -evolution of the SAPCM in NW Namibia. Dashed blue lines show possible  $t$ – $T$ -paths for the published geochronological data. Numbers show the differentiated  $t$ – $T$ -paths for the individual area that were used for the calculation of cooling and heating, and exhumation and subsidence rates, respectively. Grey bar: Pan African/Brasiliano orogeny (e.g., Goscombe and Gray 2008; Foster et al. 2009; Frimmel et al. 2011; Nascimento et al. 2016); red line: Paraná–Etendeka event Trumbull et al. 2004, 2007; Baksi 2018). For further information of the geochronological data, see supplementary material, tables S5.1–S5.6 and figures S7.1–7.6

(Table S5.2). Kröner et al. (2010) describe old U–Pb ages between ~1800 and ~1200 Ma that represent pre-Pan African deformation crystallization of the Pre-Damara rocks of the Congo Craton. However, our proposed cooling path sets in during syn-Pan African cooling recorded by a metamorphic Sm–Nd age by Goscombe et al. (2003b) followed by an  $^{40}\text{Ar}/^{39}\text{Ar}$  age of ~470 Ma (Gray et al. 2006). Therefore, we present only one average cooling path including the intrusion, metamorphism, and post-orogenic cooling for the northern central area of the CKZ. Consequently, exhumation initially occurred from Late Neoproterozoic with rates of ~0.06 mm/a, and probably increased during the Ordovician/Silurian to 0.2 mm/a (Fig. 12a, CKZ, northern central area). The post-Pan African cooling can be better constrained by ZFT ages of this study, and thus, we assume differentiated cooling from the Silurian to Carboniferous. Whilst a ZFT range of ~429 Ma that allows a relatively homogeneous exhumation (0.1 mm/a) directly to near surface temperatures (~15 °C), we propose individual cooling paths including the ZFT data of Devonian to Carboniferous age with possible exhumation rates between ~0.3 and ~0.1 mm/a. Therefore, post-Pan African cooling of the northern central area of the CKZ permits a similar stable phase showing very slow cooling of <0.5 °C/Ma until the Late Devonian/Early Carboniferous.

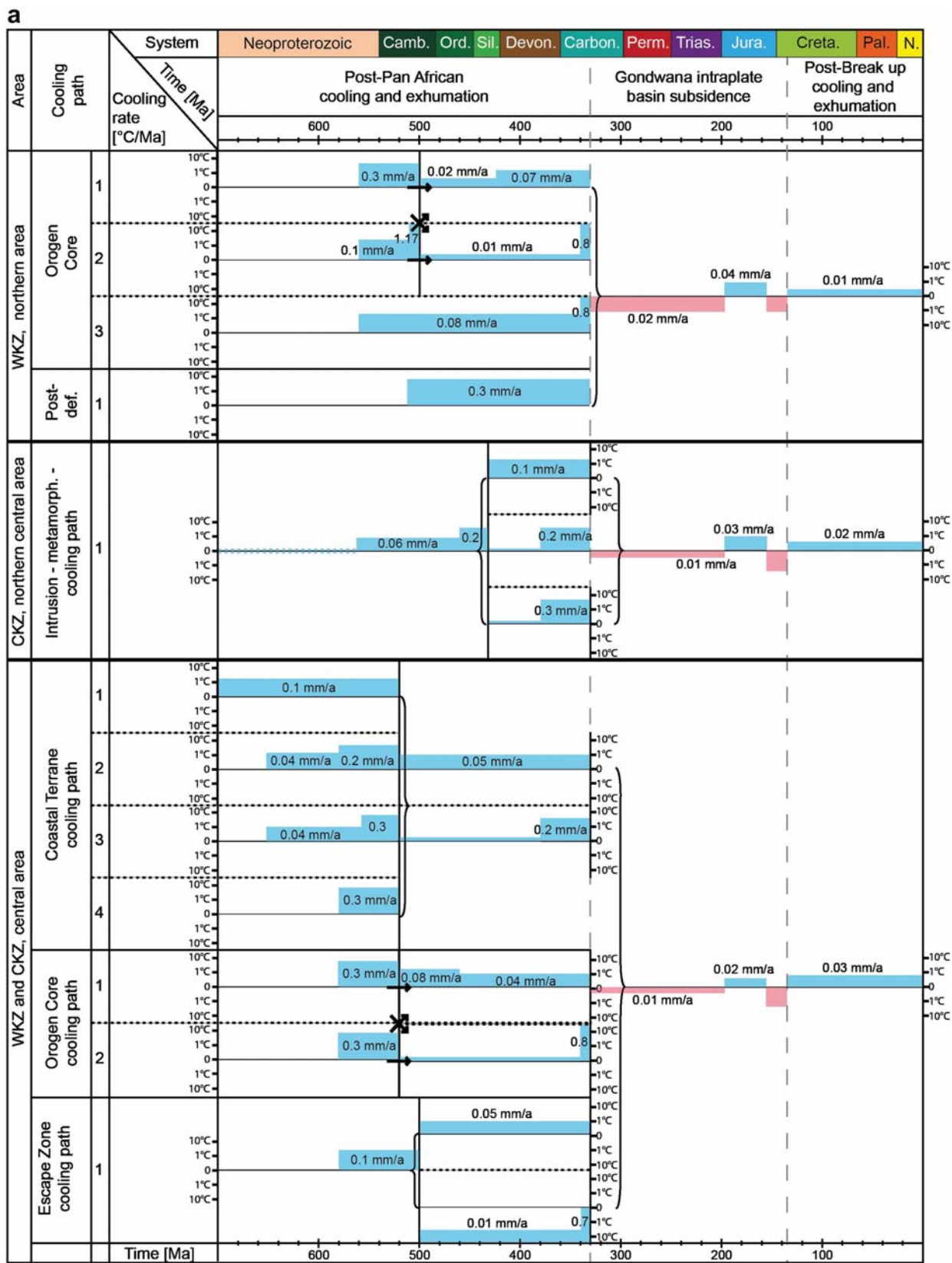
Further south in the central area of the WKZ and CKZ [Figs. 10, 11, orange (3); Table S5.3], the geological record comprises a large set of solid geochronological data that allow constraining the differentiated cooling paths for the individual crustal segments. Based on the data, we suggest four individual cooling paths for the western Coastal Terrane during the syn-to-post-Pan African  $t$ – $T$ -evolution (Fig. 11, orange (3), sky blue lines) that join together from the Late Cambrian on for the post-Pan African exhumation. U–Pb ages between ~705 and ~690 Ma indicate pre-Pan African deformation crystallization (Seth et al. 1998; Kröner et al. 2004) that are combined with  $^{40}\text{Ar}/^{39}\text{Ar}$  ages between ~540 and ~520 Ma (Foster et al. (2009) and constrain this separate pre-deformation cooling path (1) from ~700 to ~520 Ma.

Due to the lack of further data, we assume a homogeneous cooling with exhumation rates of ~0.1 mm/a (1) (Fig. 12a, WKZ and CKZ, Coastal Terrane). Younger U–Pb zircon and monazite ages indicate syn-Pan African crystallization between ~660 and ~620 Ma, and from ~580 to ~510 Ma (Seth et al. 1998; Goscombe et al. 2005a, b; Konopásek et al. 2008) that either can be combined with a Sm–Nd age of ~534 Ma (path 2) (Jung et al. 2014), or an  $^{40}\text{Ar}/^{39}\text{Ar}$  hornblende age of ~546 Ma (path 3) (Foster et al. 2009) to provide two distinct cooling paths. In both cases, the cooling shows a relatively slow initial cooling with exhumation rates of ~0.04 mm/a that is followed by faster exhumation with rates between ~0.3 and ~0.2 mm/a until the Early Paleozoic (Fig. 12a, WKZ and CKZ, Coastal Terrane, 2, 3, and 4).

In the Orogen Core (Figs. 10, 11, orange (3), dark blue lines), syn-Pan African crystallization is recorded by U–Pb ages ranging between ~580 and ~540 Ma (Seth et al. 1998; Goscombe et al. 2005a, b) that correlate with Sm–Nd metamorphic ages between ~580 and ~570 Ma (Goscombe et al. 2003a, b). Syn-Pan African cooling set in with Sm–Nd cooling ages between ~550 and ~500 Ma (Goscombe et al. 2005a, b; Foster et al. 2009; Jung et al. 2014) followed by  $^{40}\text{Ar}/^{39}\text{Ar}$  ages on hornblende, and on muscovite and biotite around 530 Ma, and between ~530 and ~500 Ma, respectively (Goscombe et al. 2005a, b; Gray et al. 2006; Foster et al. 2009). Therefore, we suggest two relatively homogeneous  $t$ – $T$ -paths including the syn-Pan African intrusion, metamorphism, and cooling of the rocks within the Orogen Core from Late Neoproterozoic to Early Cambrian showing both an average exhumation rate of ~0.3 mm/a (Fig. 12a, WKZ and CKZ, Orogen Core cooling path).

In the Escape Zone [Figs. 10, 11, orange (3), purple line], only one Sm–Nd age of ~574 Ma indicates syn-Pan African metamorphism in the CKZ (Goscombe et al. 2003b). The cooling of the Escape zone is recorded by  $^{40}\text{Ar}/^{39}\text{Ar}$  hornblende data between ~530 and ~520 Ma (Foster et al. 2009) correlating with the data of the Orogen Core that also yields for the  $^{40}\text{Ar}/^{39}\text{Ar}$  data on muscovite and biotite (~527–519 Ma, Gray et al. 2006). Consequently, we suggest a single average cooling path representing the syn-Pan African metamorphism and cooling of the Escape Zone rocks from the Late Neoproterozoic to Late Cambrian (0.1 mm/a).

For all three crustal segments (Coastal Terrane, Orogen Core, Escape Zone),  $^{40}\text{Ar}/^{39}\text{Ar}$  data on muscovite and biotite show Cambrian Age, and therefore, we assume relatively simultaneous post-Pan African cooling from the Late Cambrian to Early Carboniferous for the central area of the WKZ and CKZ (orange). We suggest the cooling paths for the crustal segments connecting either ZFT data > 380 Ma, or between ~360 and ~310 Ma, while segments of the WKZ generally tend to be older. Consequently, the cooling paths connecting ages > 380 Ma allow a more direct exhumation to low-temperature areas with rates of ~0.05 mm/a. When



◀ **Fig. 12 a** Calculated cooling and heating rates, derived from combined geochronological and thermochronological  $t$ - $T$ -modeling of the thermal evolution in the individual areas of the Western-to-Eastern Kaoko Zones. The differentiated cooling paths refer to the individual  $t$ - $T$ -paths of Fig. 11. For further information, see text, chapter 3.3. Blue and red bars indicate cooling and heating [ $^{\circ}\text{C}/\text{Ma}$ ]. The thickness of the bars implies higher/lower rates. Black numbers [ $\text{mm}/\text{a}$ ] indicate calculated exhumation and subsidence rates derived from the cooling and heating rates. **b** Calculated cooling and heating rates, derived from combined geochronological and thermochronological  $t$ - $T$ -modeling of the thermal evolution in the individual areas of the Southern Kaoko and Damara belts. The differentiated cooling paths refer to the individual  $t$ - $T$ -paths of Fig. 11. For further information, see text, chapter 3.3. Blue and red bars indicate cooling and heating [ $^{\circ}\text{C}/\text{Ma}$ ]. The thickness of the bars implies higher/lower rates. Black numbers [ $\text{mm}/\text{a}$ ] indicate calculated exhumation and subsidence rates derived from the cooling and heating rates

combined with the younger ZFT ages, the individual cooling paths rather correlate with the northern areas of the WKZ and CKZ (green and blue), also indicating a stable phase at temperatures between 300–200  $^{\circ}\text{C}$  with exhumation rates of  $<0.01$   $\text{mm}/\text{a}$ .

In the SKB [Figs. 10, 11, yellow (4), Table S5.4], U–Pb crystallization ages on zircon and monazite are recorded between  $\sim 550$  and  $\sim 500$  Ma (Van de Flierdt et al. 2003; Schmitt et al. 2012; Milani et al. 2015; Goscombe et al. 2017) followed by Sm–Nd metamorphic ages around  $\sim 491$  Ma that can be connected to K/Ar and  $^{40}\text{Ar}/^{39}\text{Ar}$  data between  $\sim 515$  and  $\sim 490$  Ma (Gray et al. 2006; Goscombe et al. 2007, 2017). We suggest a  $t$ - $T$ -path including intrusion/crystallization, metamorphism, and cooling of the Orogen Core rocks in the Ugab Zone. Syn-Pan African cooling set in from Late Neoproterozoic/Early Cambrian with rates of  $\sim 0.1$   $\text{mm}/\text{a}$ . Then, exhumation rates increased to  $\sim 1.2$   $\text{mm}/\text{a}$  during the Late Cambrian, and dropped again to  $0.06$   $\text{mm}/\text{a}$  during the Early Ordovician (Fig. 12b, SKB, Ugab Zone, Intr.-met.-cooling path). Seth et al. (2000) recorded a single U–Pb around  $\sim 456$  Ma of a Voetspoor syenite that represents a post-Pan African deformation intrusion within the Ugab Zone. This age can be connected to  $^{40}\text{Ar}/^{39}\text{Ar}$  ages of  $\sim 496$  Ma and  $\sim 438$  Ma for the same location (Voetspoor contact aureole schist, Gray et al. 2006). Therefore, we suggest a post-deformation  $t$ - $T$ -path for the Voetspoor intrusion with cooling rates  $>20$   $^{\circ}\text{C}/\text{Ma}$  for the first  $\sim 20$ – $30$  Ma followed by slower cooling with exhumation rates of  $\sim 0.07$   $\text{mm}/\text{a}$  (Fig. 12b, SKB, Ugab Zone, post-def. path). Nevertheless, we assume the first intrusion-metamorphism-cooling path as more probable representing the  $t$ - $T$ -evolution of the Ugab Zone. We propose exhumation rates of  $\sim 0.06$   $\text{mm}/\text{a}$ , and  $0.07$   $\text{mm}/\text{a}$  (post-def. path) that indicate relatively simultaneous cooling of the entire area from Silurian to Late Carboniferous.

In the NCZ of the southern Damara Belt, crystallization and cooling of rocks are recorded for three individual locations (Figs. 10, 11, dark red (5); Tab. S5.5). At the Salem granitic suite, Miller and Burger (1983) record a U–Pb crystallization and metamorphic age for the Oetmoed granite around  $\sim 590$  Ma (Milani et al. 2015). U–Pb crystallization and metamorphic ages on monazite range between  $\sim 538$  and  $\sim 470$  Ma, and is backed with Sm–Nd metamorphic ages of  $\sim 510$  Ma and  $\sim 473$  Ma (Jung et al. 2000a, b). Unfortunately, there do not exist any ZFT ages and the existing AFT data are thermally overprinted by younger events. We suggest two separate intrusion–metamorphism–cooling paths (Fig. 12b, Damara Belt, NCZ, intrusion-met.-cooling path) for the entire syn- and post-Pan African period until the final exhumation to the surface during the Late Carboniferous (Miller 2008). In both cases, the cooling path sets in during the Late Neoproterozoic with rates of  $\sim 0.07$   $\text{mm}/\text{a}$  (1) and  $\sim 0.05$   $\text{mm}/\text{a}$  (2), and rocks experienced the final exhumation with rates of  $\sim 0.1$   $\text{mm}/\text{a}$  until the Late Carboniferous.

A second intrusion is recorded for the Okombahe granite showing Rb–Sr ages between  $\sim 553$  and  $\sim 514$  Ma, and from  $\sim 495$  to  $\sim 465$  Ma (Haack and Martin 1983). Unfortunately, there are no data to further constrain the Okombahe granite cooling path, and therefore, we propose average cooling paths beginning either with the Rb–Sr ages  $>514$  Ma, or the Rb–Sr ages  $<495$  Ma and present long-time cooling to surface near areas during the Late Carboniferous with long-term exhumation rates between  $\sim 0.1$  and  $\sim 0.08$   $\text{mm}/\text{a}$  [Fig. 12b, Damara Belt, Okombahe granite cooling path (1 and 2)].

For our samples close to the Waterberg Basin east of Otjiwarongo (NA11-09, -10, -11), we would like to introduce an Otjiwarongo area cooling path that is only recorded by a U–Pb age of  $\sim 550$  Ma (Lobo-Guerrero Sanz 2005), and, therefore, is poorly constrained. However, we present a long-term exhumation rate from the Late Neoproterozoic to the Late Carboniferous with an average rate of  $\sim 0.1$   $\text{mm}/\text{a}$  (Fig. 12b, Damara Belt, NCZ, Otjiwarongo cooling path).

In the SZ of the Damara Belt (Figs. 10, 11, red (6), Tab. S5.6), published U–Pb crystallization and metamorphic ages on monazite range between  $\sim 527$  and  $\sim 505$  Ma (Kukla et al. 1991) followed either by syn-Pan African Sm–Nd cooling ages between  $\sim 545$  to  $\sim 511$  Ma, or late- to post-Pan African cooling Sm–Nd and Rb–Sr ages between  $\sim 500$  and  $488$  Ma, and  $\sim 490$  and  $\sim 470$  Ma, respectively (Jung and Mezger 2001). The cooling path is continued by  $^{40}\text{Ar}/^{39}\text{Ar}$  ages on hornblende ( $\sim 505$  Ma), and muscovite and biotite ( $\sim 496$ – $482$  Ma, Gray et al. 2006). Therefore, we suggest three individual syn- to post-Pan African cooling paths from the Late Neoproterozoic to Late Carboniferous. The first path includes the first Sm–Nd ages ( $\sim 545$ – $511$  Ma) and connects

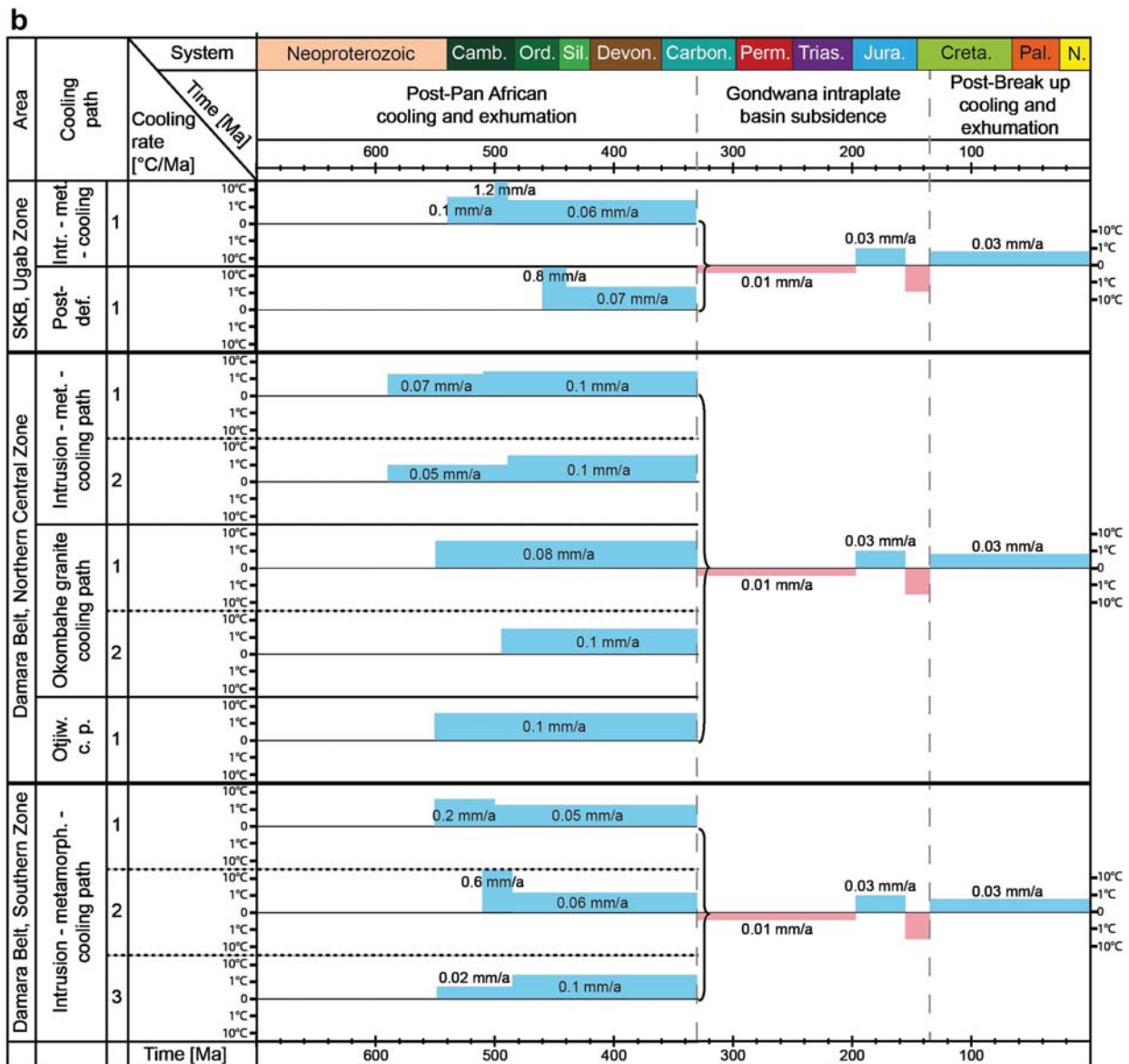


Fig. 12 (continued)

to the  $^{40}\text{Ar}/^{39}\text{Ar}$  ages showing an exhumation rate until the Late Cambrian of initially  $\sim 0.2$  mm/a, and then 0.05 mm/a for the post-orogenic period [Fig. 12b, Damarara Belt, SZ, (1)]. A second possible cooling path connects to the group of younger Sm–Nd ages ( $< 500$  Ma), and combines the Rb–Sr cooling ages with the  $^{40}\text{Ar}/^{39}\text{Ar}$  ages that result in a differentiated cooling with exhumation rates of  $\sim 0.6$  mm/a followed by post-orogenic exhumation with rates of  $\sim 0.06$  mm/a [Fig. 12b, Damarara Belt, SZ (2)]. The third possible  $t$ – $T$ -path follows the post-Pan African Rb–Sr cooling ages showing exhumation rates of initially  $\sim 0.02$  mm/a, and then continues with  $\sim 0.1$  mm/a [Fig. 12b, Damarara Belt, SZ (3)].

In general, syn-to post-Pan African crustal cooling and exhumation correlates for the northern Kaoko Belt within in the WKZ and CKZ [Figs. 10, 11, green (1), orange(3)]. While intrusion and crystallization occurred earlier in the Coastal Terrane, syn-Pan African cooling coincides with cooling paths of the northern and central Orogen Core showing fast cooling until the end of the Cambrian. This also yields for the Ugab Zone [Fig. 11, yellow (4)], as part of the Orogen Core in the SKB where rocks experienced fast Early Cambrian syn-Pan African cooling to temperatures around 300–200 °C. Within the northern Kaoko Belt, ZFT data allow constraining the post-orogenic  $t$ – $T$ -paths that

show decreasing cooling rates from the Late Cambrian on indicating an almost thermally stable period during the Early Paleozoic (~Late Cambrian to ~Early Carboniferous). This correlates with the  $t$ - $T$ -evolution for the SE Brazilian Florianopolis, Peruibe, Curitiba, and Ilha Comprida blocks. Krob et al. (2019) revealed high exhumation rates between ~0.4 and ~0.2 mm/a during the Late Neoproterozoic, followed by an almost stable phase with exhumation rates between ~0.02 and ~0.01 mm/a reaching from the Early Cambrian to the Devonian.

Unfortunately, ZFT data lack for the Ugab Zone, and therefore, the post-Pan African cooling during the Early-to-Late Paleozoic is less constrained. Nevertheless, a similar  $t$ - $T$ -evolution showing an almost stable period without a decrease in temperature during the post-Pan African cooling as for the northern Kaoko Belt and in SE Brazil cannot be ruled out. However, we propose to enlarge the thermochronological data set, especially the ZFT data to better constrain the post-orogenic cooling as such data would provide the transition from high rock temperatures involved during syn-orogenic processes to lower temperature areas (<300 °C) of the upper crust and near the Earth's surface providing more information about the post-orogenic evolution.

Consequently, the  $t$ - $T$ -evolution of the northern central CKZ [Figs. 10, 11, blue (2)] remains less constrained due to the lack of geochronological and thermochronological data. We present a poorly constrained cooling path that differs from the WKZ and CKZ in the northern Kaoko Belt indicating the main crustal cooling during the Early Paleozoic.

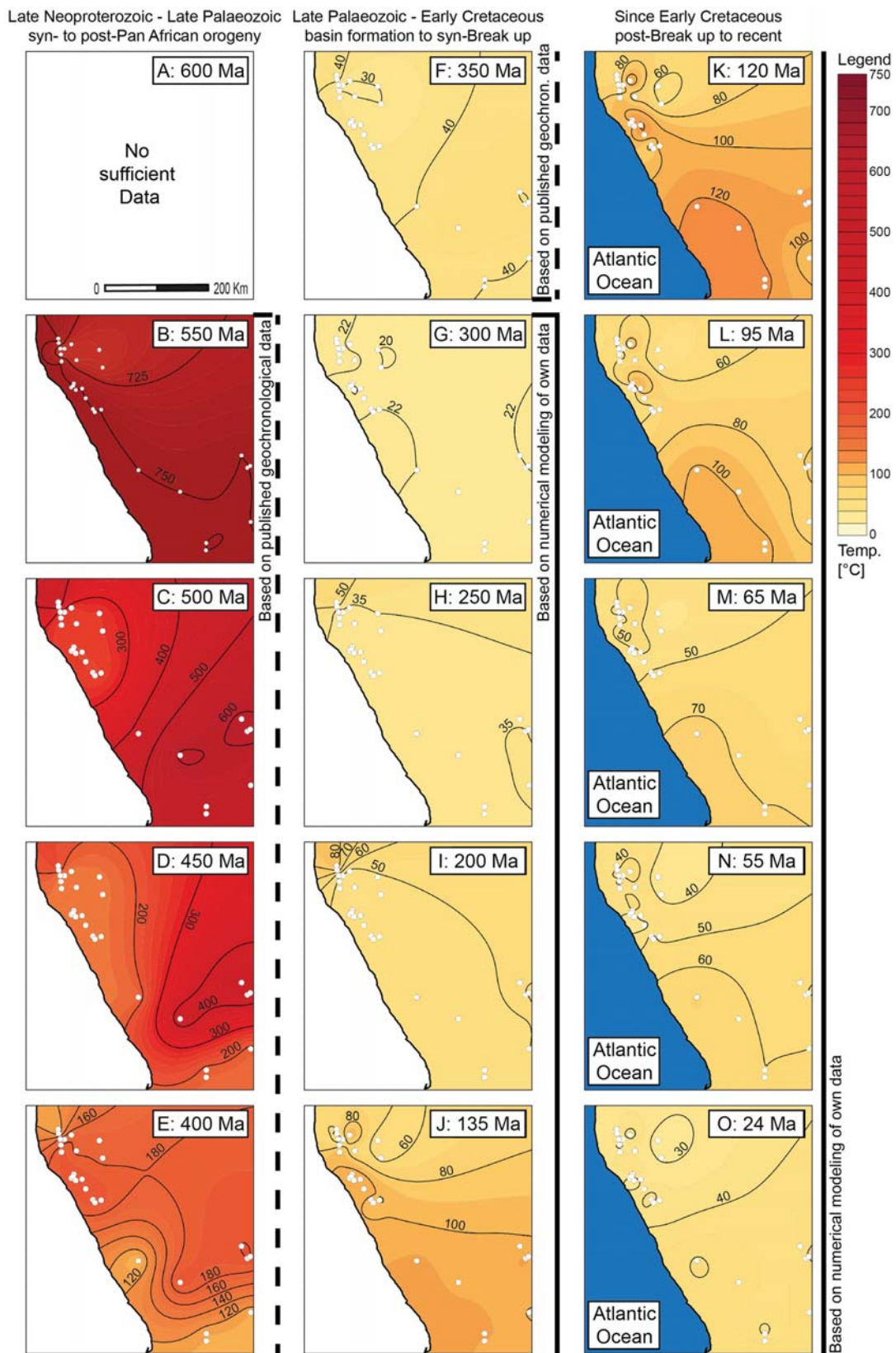
All locations within the southern Damara Belt show similar syn- and post-Pan African crustal cooling and exhumation. Generally, geo- and thermochronological ages are slightly younger as in the Kaoko Belt indicating that crustal cooling set in later, and therefore, rocks stayed longer in high temperature ranges (>300 °C). This  $t$ - $T$ -evolution is also illustrated by the interpolation maps that provide a possible visualization of the Neoproterozoic basement thermal structure. During the Ediacaran-to-Early Cambrian  $t$ - $T$ -evolution, basement rocks show a relatively homogeneous thermal structure (Fig. 13b). Basement temperatures of the southern Damara Belt correlate with those of the Kaoko Belt showing high temperatures (~750–600 °C) for the entire study area. The visualized  $t$ - $T$ -evolution of the thermal structure implies that basement rocks in the northern Kaoko Belt cooled down earlier than within the SKB and Damara Belt showing a trend of decreasing temperature within the study area beginning in the north and followed by the south (Fig. 13b–d). We assume that an inner core of the Damara Belt remained in high temperatures the longest (Fig. 13d), and then cooled down faster than the Kaoko Belt until the Devonian (Fig. 13e) showing a more inhomogeneous temperature distribution of the basement surface.

### Late Paleozoic-to-Late Jurassic—SW Gondwana intraplate basin formation, subsidence, and South Atlantic pre- to syn-rift processes

Following the post-Pan African denudation processes rock cooling, and surface uplift and erosion continued during the Late Paleozoic-to-Mesozoic Gondwana intraplate environment. The  $t$ - $T$ -paths show exhumation of all samples to areas close to the surface by the end of the Carboniferous. Therefore, temperatures of the basement thermal structure range in near surface areas between ~25 and 20 °C. We assume that all crustal segments of the Kaoko and Damara belts experienced a relatively homogeneous  $t$ - $T$ -evolution from the Late Paleozoic, and, therefore, describe a continued  $t$ - $T$ -evolution including exhumation and subsidence rates for the individual areas regardless the different Pan African crustal segments.

ZFT ages and old AFT ages of this study (Figs. 6, 8) range between ~430 and 310 Ma, and ~390 and 280 Ma, respectively, indicating significant tectonic and surface uplift, and erosion during the Devonian-to-Permian. We assume glacial erosion and transport of sedimentary material, and a temporally lower geothermal gradient during the Late Paleozoic Gondwana Ice House (Montañez and Poulsen 2013) to have triggered the final Paleozoic cooling and surface uplift of the Neoproterozoic basement resulting in the displayed ZFT and AFT age distribution. This correlates with the increase of sedimentation and continuous formation of the surrounding sedimentary basins. Montañez and Poulsen (2013) observed significant amounts of sediments transported towards the southern and the western parts of the Gondwana intraplate environment. Stratigraphic records of the major African and South American basins indicate deposition of Upper Paleozoic-to-Lower Mesozoic glacial and siliciclastic sedimentary rocks (Stollhofen et al. 1999; Catuneanu et al. 2005; Milani et al. 2007; Uliana et al. 2014; Krob et al. 2019) supporting the removal of enormous amounts of sediments. Before the Gondwana Ice House, the thermal structure of the Neoproterozoic basement (Fig. 13e) reveals temperatures between ~180 and ~120 °C suggesting an overburden thickness between ~3.5 and ~5.5 km that would have been removed by the glacial erosion until the end of the Carboniferous. However, precise calculations of removed sediment thicknesses which might have been even larger due to the temporally decreased geothermal gradient during the glacial period are still lacking.

Nevertheless, most likely glacial driven cooling, surface uplift, and erosion are recorded by renewed fast exhumation rates between ~0.8 and ~0.2 mm/a in the WKZ and CKZ of the northern Kaoko Belt during the Early-to-Late Carboniferous (Fig. 12a, b). Thus, wide areas of the Kaoko Belt show a threefold division of Paleozoic exhumation that is





◀**Fig. 13** Coherent Late Neoproterozoic-to-recent  $t$ - $T$ -evolution of the SAPCM in NW Namibia showing the interpolated thermal structure of the Neoproterozoic basement surface at specific time steps (a–o) based on the  $t$ - $T$ -paths obtained from modeling of our own thermochronological (black line) and published geochronological data (dashed black line). Red colors signify that the Neoproterozoic basement was in depth at higher temperatures, whereas lighter colors indicate lower temperatures. No data were available for the white areas

also observed in the Late Neoproterozoic-to-Late Paleozoic  $t$ - $T$ -evolution of the SE coastal region of Brazil (Krob et al. 2019).

Sedimentation and intraplate subsidence recommenced in the Kaoko and Damara belts during the Late Carboniferous to Late Permian with the formation of the major SW Gondwana intraplate basins (Stollhofen et al. 1999; Catuneanu et al. 2005; Milani et al. 2007). Increasing temperatures of the Neoproterozoic basement rocks reflect the deposition of sedimentary material (Fig. 13f–h). Slow subsidence occurred with rates between  $\sim 0.02$  and  $\sim 0.01$  mm/a ( $\sim 330/310$ – $195$  Ma) until the Early Jurassic (Fig. 12a, b). The ongoing subsidence stopped during the Early Jurassic recorded by a hiatuses in the stratigraphic records. We assume predominant pre- to syn-rift, possibly plume-driven, surface uplift, and erosion during this period (Courtillot et al. 1999; Şengör 2001; Hu et al. 2018; Krob et al. 2019). Exhumation rates range between  $\sim 0.04$  and  $\sim 0.02$  mm/a ( $\sim 155$ – $135$  Ma).

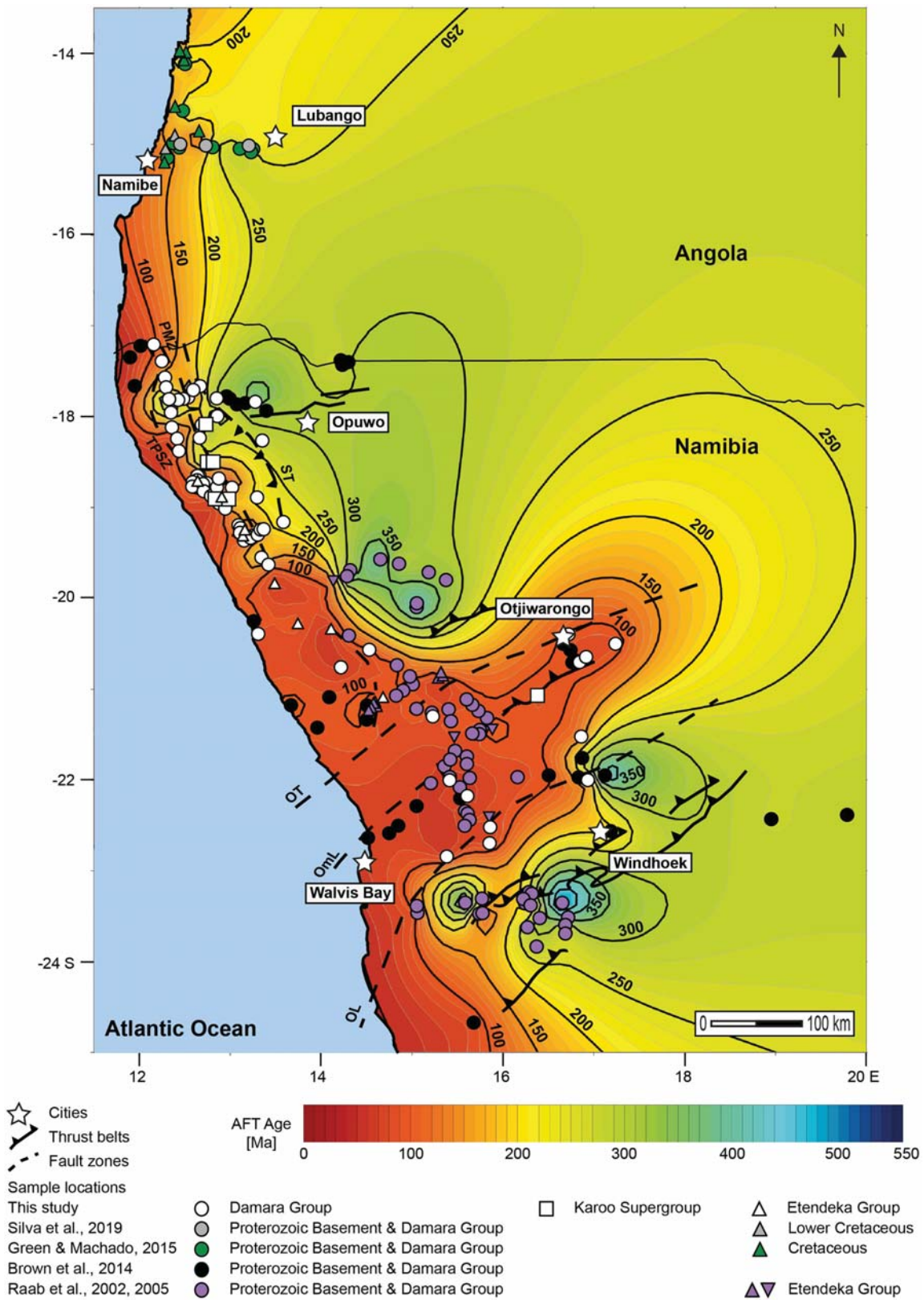
### Late Jurassic to recent—SAPCM syn- to post-rift processes, and the thermal influence of the Paraná–Etendeka LIP

The emplacement of Paraná–Etendeka dike swarms, local volcanic activity, and the eruption of flood basalts dominate the Late Jurassic-to-Early Cretaceous  $t$ - $T$ -evolution of the SW Gondwana intraplate environment. We assume that rocks were either locally influenced for a relatively short time by the convective heat flow (geothermal gradient) caused by the crosscutting dike swarms and accompanied local volcanic activity, and/or reheated due to the overburden thicknesses of the erupted flood basalts. Thus, the calculation of subsidence rates remains uncertain. However, Neoproterozoic rocks show heating rates between  $\sim 1.2$  and  $\sim 4.5$  °C/Ma ( $\sim 155$ – $135$  Ma) during pre- to syn-rift processes indicating higher rates towards the south, and in direct proximity to contemporary Etendeka flood basalt depositions. The thermal basement structure reveals maximum temperatures of  $\sim 80$ – $120$  °C between  $\sim 135$  and  $\sim 120$  Ma reaching higher temperatures in the southern Damara Belt (Fig. 13j, k) (Brown et al. 2014). However, maximum temperatures for NW Namibia do not reach temperatures as high as on the SE Brazilian side where the basement rocks range between  $\sim 80$  and  $160$  °C in the northern regions and over

$200$  °C in the southern region (Krob et al. 2019). Consequently, the Neoproterozoic basement shows relatively slow, post-eruption, thermal recovering, and rock cooling during the Early Cretaceous indicating a thermally reestablished upper crust that also has been observed in SE Brazil (Hu et al. 2018; Krob et al. 2019).

The ZFT and inland AFT ages (Fig. 14), although younger than their stratigraphic age, did not experience any thermal overprint caused by volcanic activity during the Early Cretaceous Paraná–Etendeka Large Igneous Province and, therefore, correlate with observations of earlier studies (Raab et al. 2002, 2005; Brown et al. 2014). Nevertheless, we assume that AFT ages of intermediate age ( $\sim 300$ – $200$  Ma) might have been partially influenced by the Paraná–Etendeka event and probably would have been older originally ( $> 300$  Ma). However, those ages reveal a medium track length distribution when plotted against their corrected mean confined track lengths (Fig. 15a, c) and accordingly indicate a mixture of pre- and post-cooling track accumulation (Green 1986; Lewis et al. 1992; Gallagher et al. 1997, 1998; Green et al. 1998). The youngest AFT ages along the coast (Fig. 15a, c), and within the Damara Belt (b, d) are fully reset showing relatively long mean track lengths and reflect a significant Paraná–Etendeka thermal influence (Fig. 15a, b). However, the so-called boomerang plots (Green 1986; Gallagher et al. 1998) do not confirm an idealized pattern and indicate that the rocks experienced different amounts of cooling and a denudation history more complex than a single-stage rift elevated event (Gallagher et al. 1998). Nevertheless, we are able to recognize a major post-Paraná–Etendeka cooling event during the Cretaceous, but also assume long and complex and/or sequential and transient denudation processes following the South Atlantic break-up due to a wide range of mean track lengths (Green 1986; Gallagher et al. 1998; Raab et al. 2002; Brown et al. 2014). On the SE Brazilian side, boomerang plots (Fig. S6) reveal results that allow assumptions of a similar complex multi-stage rift evolution for the Early-to-Middle Cretaceous ( $100$ – $80$  Ma) (Gallagher et al. 1988; Krob et al. 2019). Whereas in SE Brazil, regional tectonic and volcanic activity, and local graben sedimentation indicates that the basement rocks most likely reached the Earth's surface at the end of the Cretaceous, evidence supporting a similar geological evolution lacks for the NW Namibian counterpart. Therefore, we only provide exhumation rates for the entire post-rift to recent phase with rates ranging between  $\sim 0.01$  and  $\sim 0.03$  mm/a (Fig. 12a, b).

Subsequently, results of this study add to previously published observations and contribute significantly to the general understanding of the AFT data showing most of the totally reset ages with long mean track lengths congruent with the Paraná–Etendeka dike swarm distribution in the southern Damara Belt (Figs. 14, 15c, d). Furthermore,



◀**Fig. 14** Detailed interpolation map showing a possible modeled projection of the major apatite fission-track (AFT) data sets from Angola to NW Namibia using the Golden Software Surfer®. Whereas yellow-to-red colors indicate younger ages, green-to-blue colors imply older ages. Isolines show age in [Ma] without error. Colored dots (Archean-to-Early Paleozoic basement rocks), squares (Karoo sedimentary rocks), and triangles (Lower Cretaceous sedimentary and volcanic rocks) show sample locations colored according to the references. *ST* Sesfontein thrust, *PMZ* Purros mylonite zone, *TPSZ* Tree palms shear zones, *OT* Otjohorong thrust, *Oml* Omaruru lineament, *OL* Okahandja lineament

results show that the projected temperature isolines reflect the major cratonic boundaries in NW Namibia. Therefore, we propose that the old cratonic structures and individual crustal segments are still stable. Whereas the isolines do not point out any differences across the major lineament zones and, therefore, do not allow any interpretation of regional movement or reactivation along the NE-SW trending shear zones in the Damara Belt, isolines in the Kaoko Belt follow significantly the NW-SE-trending shear zones, i.e., the ST,

PMZ, and the TPSZ (Fig. 14, and Fig. 7 in detail). Moreover, the course of isolines illustrates the significant age increase towards the inland and different existing age spectra in the subdivided longitudinal Eastern, Central, and Western (Kaoko) zones. This supports the possible reactivation and movement of the Precambrian shear zones during the South Atlantic break-up, and syn- to post-rift stages (Brown et al. 2014; Salomon et al. 2015, 2017).

Concluding, the modeled projection of our AFT data combined with previous AFT studies along the Angolan-to-Namibian and SE Brazilian SAPCM (Fig. 16; for further details, see Fig. 14 and supplementary material, Fig. S7) outline areas showing high thermal overprint by the Paraná-Etendeka LIP (ages < Paraná-Etendeka age) that coincide with the lateral Paraná-Etendeka dike swarm distribution indicating a highly asymmetric plume central area (Torsvik et al. 2009, 2014; Franke 2013) with possibly two different eruption sources (black circles): (1) the Ponta Grossa Arc (PGA) together with the area north of the NW Namibian Etendeka flood basalt depositions,

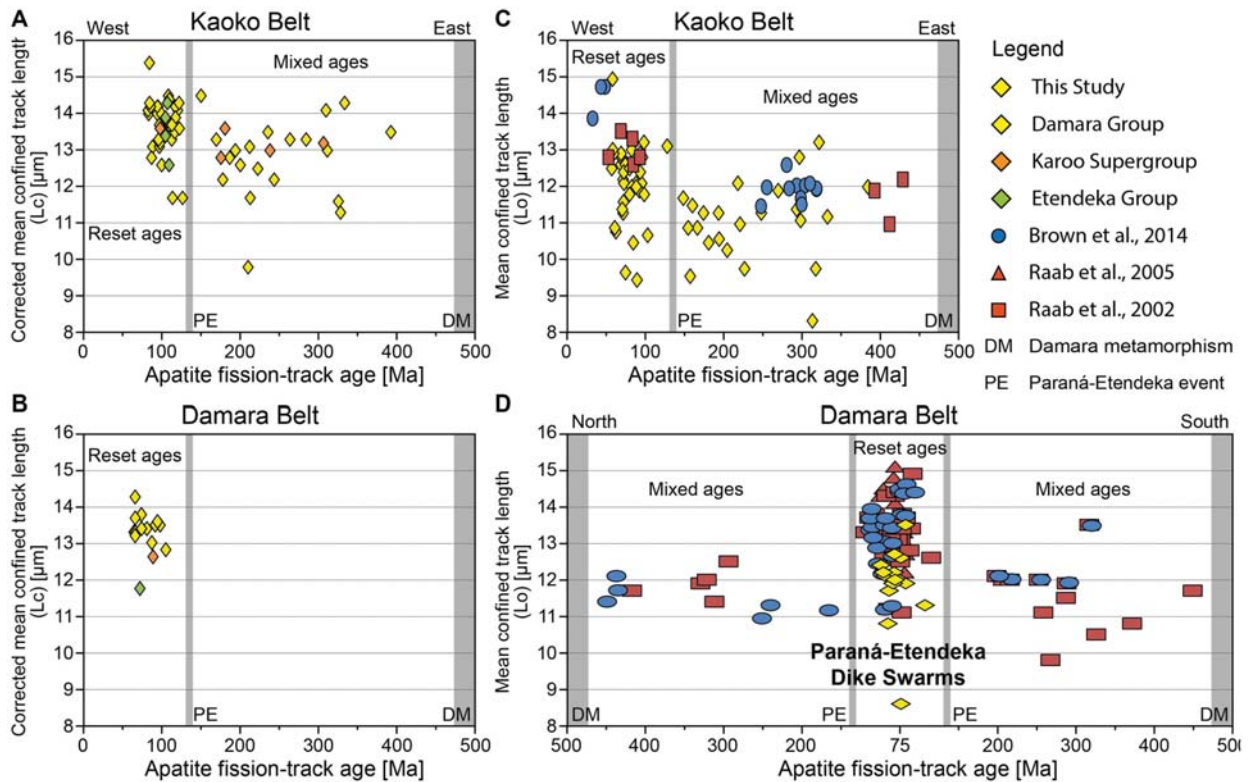


**Fig. 15** Boomerang plots showing (a, b) the apatite fission-track (AFT) data set of this research study plotted against their corrected mean confined track lengths ( $L_c$ ) for the NW Namibian Kaoko and Damara belts, and c, d the integration of our AFT data to results of previous AFT data from NW Namibia by Raab et al. (2002, 2005) and Brown et al. (2014) (right). For the integration, we plotted the AFT ages against their (uncorrected) mean confined track lengths

( $L_0$ ). While old ages with long track lengths most likely reflect “source” ages that have not reached high post-depositional annealing temperatures, young ages having long track lengths reflect totally reset cooling ages. Samples showing both intermediate AFT ages and mean confined track lengths possibly represent “mixed” ages having a mixture of pre- and post-cooling track lengths accumulation (Green 1986, Lewis et al. 1992; Gallagher et al. 1997, 1998)

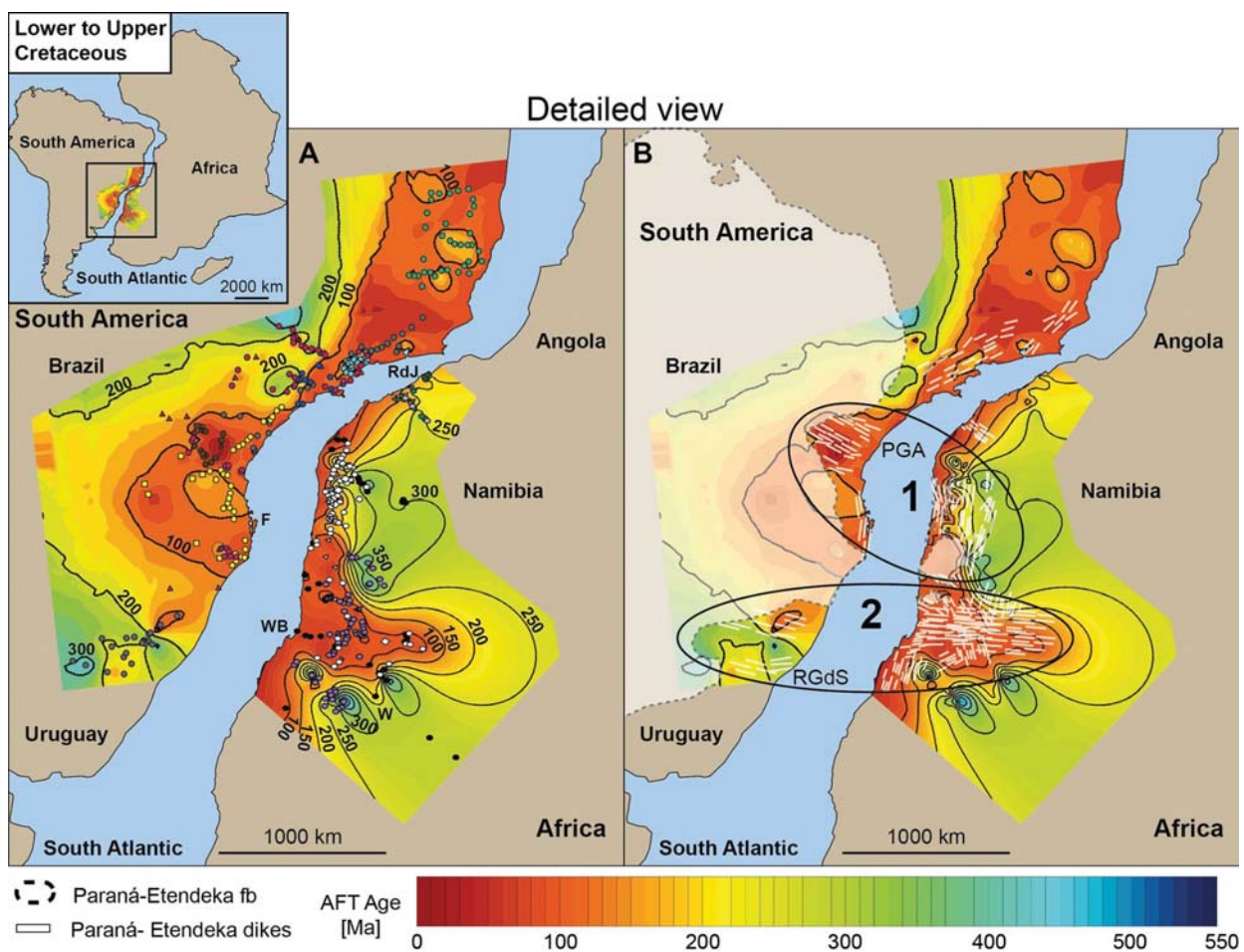


**Fig. 16** Detailed view of the Lower-to-Upper Cretaceous SAPCM of Africa and South America (top left corner): **a** Comparison of the interpolation maps showing the modeled projection of the AFT age distribution of the major thermochronological data sets along the SAPCM in SE Brazil [Gallagher et al. 1994, 1995 (red); Tello Saenz et al. 2003 (blue); Hiruma et al. 2010 (turquoise); Franco Magalhaes et al. 2010 (brown); Jelinek et al. 2014 (light green); Engelmann de Oliveira et al. 2016a, b (anthracite); Karl et al. 2013; Krob et al. 2019 (yellow)]; Angola [Green and Machado 2015 (green); Silva et al. 2019 (light grey)], and Namibia (Raab et al. 2002, 2005 (purple); Brown et al. 2014 (black); and this study (white)]. Circles: Archean-to-Early Paleozoic basement rocks; squares: Upper Paleozoic-to-Lower Mesozoic sedimentary rocks; triangles: Lower Cretaceous sedimentary and volcanic rocks. Paleo-geographic recon-

structions were taken from Torsvik et al. (2009, 2014). For a more detailed view of the separated margins and individual sample locations, see Fig. 14, and supplementary material, figure S3. The modeled interpolation maps were generated using the Golden Software Surfer®. Whereas yellow-to-red colors indicate younger ages, green-to-blue colors imply older ages. Isolines show age in [Ma] without error. Colored dots show samples locations. **b** Regional Paraná-Etendeka related dike swarm distribution (white bars) and contemporary flood basalt depositions (white areas) (after Renne et al. 1996; Peate et al. 1997; Marzioli et al. 1999; Thompson et al. 2001; Trumbull et al. 2004, 2007; Gibson et al. 2006; Franco Magalhaes et al. 2010; Travasso 2014; Florisbal et al. 2014; Guedes et al. 2016; Hartmann et al. 2016) combined with the AFT age distribution along the SAPCM in SE Brazil, and Angola to NW Namibia

and (2) the Rio Grande do Sul (RGdS) dikes together with Damara Belt dike swarms in the south. On the South American side, large parts of the flood basalts are still preserved. Where volcanic rocks are eroded, dike swarms appear crosscutting the basement and its overlying sedimentary rocks. Generally, the AFT ages reflect these geological observations on the Earth's surface reaching further inland on the South American SAPCM. A wide area of young ages occurs north of Rio de Janeiro (RdJ)

where no evidence of erupted flood basalts and/or dike swarms exists and rocks rather experienced a period of intensified post-rift surface uplift and erosion than a thermally induced overprint (Jelinek et al. 2014). Milani et al. (2007) also describe large amounts of sedimentary material within the offshore records that support periods of enormous exhumation for the northern SE Brazilian SAPCM. On the opposite continental margin, only a few published data exist along the central-to-northern

Angolan continental margin, and volcanic remnants of the Paran-Etendeka LIP are missing. Therefore, the contemporary data set does not allow further interpretation. In general, thermochronological data provide an excellent archive to better understand the thermal influence caused by the Paran-Etendeka LIP. More data covering a wider range especially in the north (Angola), and the south would be needed to support assumptions of a greater lateral sphere of originally lava covered area (Jackson et al. 2000; Torsvik et al. 2009, 2014).

## Conclusions

This research study focused on the coherent long-term  $t$ - $T$ -evolution of the Neoproterozoic basement rocks of the NW Namibian Kaoko and Damara belts. We presented an overview of new thermochronological data and combined them with the existing geochronological data, such as U-Pb, Sm-Nd, and Rb-Sr analyses, and low-temperature thermochronology (LTT) data from K/Ar,  $^{40}\text{Ar}/^{39}\text{Ar}$  analysis. Thereby, we propose a possible coherent long-term  $t$ - $T$ -evolution of the Neoproterozoic basement rocks compatible with both, the published geological record, i.e., stratigraphic sections and geochronological ages, and our new thermochronological data.

Modeled  $t$ - $T$ -histories correlate with the  $t$ - $T$ -evolution of the Neoproterozoic basement rocks of the SE coastal region in Brazil. Models show fast syn-to-post-Pan African orogenic cooling and exhumation of the basement rocks during the Late Neoproterozoic-to-Early Paleozoic. New ZFT data range between  $\sim 430$  and  $\sim 310$  Ma for the rocks of the Precambrian Kaoko Belt and likely indicate a period of intense erosion during the Late Paleozoic Gondwana glaciation. The Late Paleozoic-to-Late Jurassic  $t$ - $T$ -evolution is characterized by major intraplate basin formation and the most likely plume interacted pre-to syn-rift, and South Atlantic break-up processes, such as rock and surface uplift, and erosion. During the Paran-Etendeka volcanic activity, the Neoproterozoic basement in NW Namibia reached maximum temperatures between  $\sim 80$  and  $\sim 120$  °C, and, therefore, experienced less thermal influence as the SE Brazilian counterpart (up to  $> 200$  °C). Following, the  $t$ - $T$ -reconstruction indicates a relatively slow, post-eruption thermal recovering and rock cooling during the Lower Cretaceous.

AFT ages along the coast and within the Damara Belt are fully reset by the Paran-Etendeka volcanic event and, mostly range between  $\sim 150$  and  $\sim 60$  Ma, which correlates with the previous studies showing a long and complex post-rift cooling phase. Further inland ages increase significantly, and older AFT data may represent partially reset ages. AFT age distributions extending from Angola to Namibia and

from eastern to south-eastern Brazil correlate for the African and South American SAPCM and coincide with the lateral Paran-Etendeka dike swarm distribution. Finally, we also suggest a greater lateral sphere of originally lava covered area. However, more data covering a wider range in the north, and the south would be needed to fully understand the thermal influence caused by the Paran-Etendeka LIP.

**Acknowledgements** Special thanks go to PhD Melissa Perner and dipl. geol. Markus Karl who did the field work during their stay at our research group. We also very much appreciate the discussions with members of the SPP-1375 SAMPLE. Furthermore, we like to thank Richard A. Ketcham and Raymond A. Donelick for providing the computer code HeFTy, Raymond A. Donelick allowing us to use  $D_{\text{par}}^{\otimes}$  as a kinetic factor, and Istvn Dunkl for providing the software code TrackKey. We would like to thank Prof. Dr. Paul Green, Prof. Dr. Peter Kukla, and two unknown reviewers for their critical reading and constructive comments on earlier versions of the manuscripts that led to significant improvements. In addition, we very much appreciate the technical support given by the Forschungs-Neutronenquelle FRM II at Garching, TU Mnchen, Germany organized by Dr. Gerstenberg.

**Funding** Financial support provided with grants to Ulrich A. Glasmacher by the German Research Foundation (Deutsche Forschungsgemeinschaft, DFG, GL182/14-1, 14-2, GL 182/18-1) within the Priority Program 1375 (SAMPLE) and the DAAD (50753850) gratefully acknowledged.

## References

- Baksi AK (2018) Paran flood basalt volcanism primarily limited to  $\sim 1$  Myr beginning at 135 Ma: new  $^{40}\text{Ar}/^{39}\text{Ar}$  ages for rocks from Rio Grande do Sul, and critical evaluation of published radiometric data. *J Volcanol Geoth Res* 355:66–77. <https://doi.org/10.1016/j.jvolgeores.2017.02.016>
- Barker CE, Pawlewicz MJ (1986) The correlation of vitrinite reflectance with maximum temperature in humic organic matter. In: Buntebarth G, Stegena L (eds) *Paleogeothermics*. Springer, Berlin, pp 79–93
- Braun J (2018) A review of numerical modeling studies of passive margin escarpments leading to a new analytical expression for the rate of escarpment migration velocity. *Gondwana Res* 53:209–224. <https://doi.org/10.1016/j.gr.2017.04.012>
- Brown RW, Rust DJ, Summerfield MA, Gleadow AJW, de Wit MCJ (1990) An early Cretaceous phase of accelerated erosion on the south-western margin of Africa: evidence from apatite fission track analysis and the offshore sedimentary record. *Nucl Tracks Radiat Meas* 17:339–350. [https://doi.org/10.1016/1359-0189\(90\)90056-4](https://doi.org/10.1016/1359-0189(90)90056-4)
- Brown R, Summerfield MA, Gleadow AJW, Gallagher K, Carter A, Beucher R, Wildman M (2014) Intracontinental deformation in southern Africa during the Late Cretaceous. *J Afr Earth Sci* 100:20–41. <https://doi.org/10.1016/j.jafrearsci.2014.05.014>
- Bhn B, Hussinger H, Kramm U, Kukla C, Kukla PA (1994) Tectonometamorphic patterns developed during Pan-African continental collision in the Damara inland Belt, Namibia. *Chem Erde* 54:1–25
- Burov E (2009) Thermo-mechanical models for coupled lithosphere-surface processes: applications to continental convergence and mountain building processes. In: Cloetingh S, Negendank J (eds) *New Frontiers in integrated solid earth sciences*. International

- year of planet earth. Springer, Dordrecht, pp 103–143. [https://doi.org/10.1007/978-90-481-2737-5\\_4](https://doi.org/10.1007/978-90-481-2737-5_4)
- Catuneanu O, Wopfner H, Eriksson PG, Cairncross B, Rubidge BS, Smith RMH, Hancox PJ (2005) The Karoo basins of south-central Africa. *J Afr Earth Sci* 43:211–253. <https://doi.org/10.1016/j.jafrearsci.2005.07.007>
- Courtillot V, Jaupart C, Manighetti I, Tapponnier P, Besse J (1999) On causal links between flood basalts and continental breakup. *Earth Planet Sci Lett* 166:177–195. [https://doi.org/10.1016/S0012-821X\(98\)00282-9](https://doi.org/10.1016/S0012-821X(98)00282-9)
- Donelick R, Ketcham RA, Carlson WD (1999) Variability of fission-track annealing kinetics: II Crystallographic orientation effects. *Am Mineral* 84:1224–1234. <https://doi.org/10.2138/am-1999-0902>
- Duncan RA, Hooper PR, Rehacek J, Marsh JS, Duncan AR (1997) The timing and duration of the Karoo igneous event, southern Gondwana. *J Geophys Res* 102:18127–18138. <https://doi.org/10.1029/97JB00972>
- Engelmann de Oliveira CH, Jelinek AR, Chemale F Jr, Bernet M (2016a) Evidence of post-Gondwana breakup in Southern Brazilian shield: insights from apatite and zircon fission track thermochronology. *Tectonophysics* 666:173–187. <https://doi.org/10.1016/j.tecto.2015.11.005>
- Engelmann de Oliveira CH, Jelinek AR, Chemale F Jr, Cupertino JA (2016b) Thermotectonic history of the southeastern Brazilian margin: evidence from apatite fission track data of the offshore Santos Basin and continental basement. *Tectonophysics* 685:21–34. <https://doi.org/10.1016/j.tecto.2016.07.012>
- Ernst RE, Buchan KL (2001) Mantle plumes: their identification through time. *Geol Soc Am Spec Pap* 352:593
- Florisbal LM, Heaman LM, de Assis JV, Bitencourt MF (2014) Tectonic significance of the Florianópolis dyke Swarm, Paraná–Etendeka magmatic province: a reappraisal based on precise U–Pb dating. *J Volcanol Geoth Res* 289:140–150. <https://doi.org/10.1016/j.jvolgeores.2014.11.007>
- Foster DA, Goscombe BD, Gray DR (2009) Rapid exhumation of deep crust in an obliquely convergent orogeny: the Kaoko Belt of the Damara Orogen. *Tectonics* 28(TC4002):24. <https://doi.org/10.1029/2008TC002317>
- Franco-Magalhães AOB, Hackspacher PC, Glasmacher UA, Saad AR (2010) Rift to post-rift evolution of a “passive” continental margin: the Ponta Grossa Arch, SE Brazil. *Int J Earth Sci (Geologische Rundschau)* 99:1599–1613. <https://doi.org/10.1007/s00531-010-0556-8>
- Franke D (2013) Rifting, lithosphere breakup and volcanism: comparison of magma-poor and volcanic rifted margins. *Mar Pet Geol* 43:63–87. <https://doi.org/10.1016/j.marpetgeo.2012.11.003>
- Frimmel HE, Frank W (1998) Neoproterozoic tectono-thermal evolution of the Gariep Belt and its basement, Namibia and South Africa. *Precamb Res* 90:1–28. [https://doi.org/10.1016/S0301-9268\(98\)00029-1](https://doi.org/10.1016/S0301-9268(98)00029-1)
- Frimmel HE, Basei MS, Gaucher C (2011) Neoproterozoic geodynamic evolution of SW-Gondwana: a southern African perspective. *Int J Earth Sci (Geologische Rundschau)* 100:323–354. <https://doi.org/10.1007/s00531-010-0571-9>
- Galbraith RF (1981) On statistical models for fission-track counts. *Math Geol* 13:471–478. <https://doi.org/10.1007/BF01034498>
- Gallagher K, Brown R (1997) The onshore record of passive margin evolution. *J Geol Soc Lond* 154:451–457. <https://doi.org/10.1144/gsjgs.154.3.0451>
- Gallagher K, Hawkesworth CJ, Mantovani MSM (1994) The denudation history of the offshore continental margin of SE Brazil inferred from apatite fission-track data. *J Geophys Res* 99:18117–18145. <https://doi.org/10.1029/94JB00661>
- Gallagher K, Hawkesworth CJ, Mantovani MSM (1995) Denudation, fission track analysis and the long-term evolution of passive margin topography: application to the southeast Brazilian margin. *J S Am Earth Sci* 8:65–77. [https://doi.org/10.1016/0895-9811\(94\)00042-Z](https://doi.org/10.1016/0895-9811(94)00042-Z)
- Gallagher K, Brown R, Johnson C (1998) Fission track analysis and its applications to geological problems. *Annu Rev Earth Planet Sci* 26:519–572. <https://doi.org/10.1146/annurev.earth.26.1.519>
- Garver JI (2003). Discussion: “Metamictization of natural zircon: accumulation versus thermal annealing of radioactivity-induced damage”. by Nasdala et al. (2001) *Contributions to Mineralogy and Petrology* 143:756–757. <https://doi.org/10.1007/s00410-002-0379-0>
- Garver JI, Kamp PJJ (2002) Integration of zircon color and zircon fission track zonation patterns in Orogenic belts: application of the Southern Alps, New Zealand. *Tectonophysics* 349:203–219. [https://doi.org/10.1016/S0040-1951\(02\)00054-9](https://doi.org/10.1016/S0040-1951(02)00054-9)
- Gibson SA, Thompson RN, Day JA (2006) Timescales and mechanism of plume-lithosphere interactions:  $^{40}\text{Ar}/^{39}\text{Ar}$  geochronology and geochemistry of alkaline igneous rocks from the Paraná–Etendeka large igneous province. *Earth Planet Sci Lett* 251:1–17. <https://doi.org/10.1016/j.epsl.2006.08.004>
- Gleadow AJW (1981) Fission-track dating methods: What are the real alternatives? *Nuclear Tracks* 5:3–14. [https://doi.org/10.1016/0191-278X\(81\)90021-4](https://doi.org/10.1016/0191-278X(81)90021-4)
- Goscombe BD, Gray DR (2007) The coastal Terrane of the Kaoko Belt, Namibia: outboard arc-terranes and tectonic significance. *Precamb Res* 155:139–158. <https://doi.org/10.1016/j.precamres.2007.01.008>
- Goscombe BD, Gray DR (2008) Structure and strain variation at mid-crustal levels in a transpressional orogeny: a review of Kaoko belt structure and the character of West Gondwana amalgamation and dispersal. *Gondwana Res* 12:45–85. <https://doi.org/10.1016/j.gr.2007.07.002>
- Goscombe BD, Hand M, Gray DR (2003a) Structure of the Kaoko Belt, Namibia: progressive evolution of a classic transpressional orogen. *J Struct Geol* 25:1049–1081. [https://doi.org/10.1016/S0191-8141\(02\)00150-5](https://doi.org/10.1016/S0191-8141(02)00150-5)
- Goscombe BD, Hand M, Gray DR, Mawby J (2003b) The metamorphic architecture of a transpressional orogen: the Kaoko Belt, Namibia. *J Petrol* 44:679–711. <https://doi.org/10.1093/petrology/44.4.679>
- Goscombe BD, Gray DR, Armstrong RA, Foster DA, Vogl J (2005a) Event geochronology of the Pan-African Kaoko Belt, Namibia. *Precamb Res* 140:1–41. <https://doi.org/10.1016/j.precamres.2005.07.003>
- Goscombe BD, Gray DR, Hand M (2005b) Extrusional tectonics in the core of a transpressional orogen, the Kaoko Belt, Namibia. *J Petrol* 46:1203–1241. <https://doi.org/10.1093/petrology/egi014>
- Goscombe BD, Gray DR, Hand M (2006) Crustal architecture of the Himalayan metamorphic front in eastern Nepal. *Gondwana Res* 10:232–255. <https://doi.org/10.1016/j.gr.2006.05.003>
- Goscombe BD, Foster DA, Gray DR, Wade B (2017) Metamorphic response and crustal architecture in a classic collisional orogeny: the Damara Belt, Namibia. *Gondwana Res* 52:80–124. <https://doi.org/10.1016/j.gr.2017.07.006>
- Gray DR, Foster DA, Goscombe BD, Passchier CW, Trouw RAJ (2006)  $^{40}\text{Ar}/^{39}\text{Ar}$  thermochronology of the Pan-African Damara Orogen, Namibia, with implications for tectono-thermal and geodynamic evolution. *Precamb Res* 150:49–72. <https://doi.org/10.1016/j.precamres.2006.07.003>
- Green PF (1986) On the thermo-tectonic evolution of Northern England: evidence from fission track analysis. *Geol Mag* 123:493–506. <https://doi.org/10.1017/S0016756800035081>
- Green PF, Machado V (2015) Pre-rift and syn-rift exhumation, post-rift subsidence and exhumation of the onshore Namibe Margin of Angola revealed from apatite fission track analysis. *Geol Soc Lond Spec Publ* 438:99–118. <https://doi.org/10.1144/SP438.2>

- Green PF, Duddy IR, Laslett GM, Hegarty KA, Gleadow AJW, Lovering JF (1998) Thermal annealing of fission tracks in apatite. 4. Quantitative modelling techniques and extension to geological timescales. *Chem Geol (Isotope Geosci Sect)* 79:155–182. [https://doi.org/10.1016/0168-9622\(89\)90018-3](https://doi.org/10.1016/0168-9622(89)90018-3)
- Green PF, Japsen P, Chalmers JA, Bonow JM, Duddy IR (2018) Post-breakup burial and exhumation of passive continental margins: seven propositions to inform geodynamic models. *Gondwana Res* 53:58–81. <https://doi.org/10.1016/j.gr.2017.03.007>
- Guedes E, Heilbron M, Valeriano CM, Almeida JCH, Szatmari P (2016) Evidence of Gondwana early rifting process recorded by Resende-Ilha Grande Dike Swarm, southern Rio de Janeiro, Brazil. *J S Am Earth Sci* 67:11–24. <https://doi.org/10.1016/j.jsames.2016.01.004>
- Haack U, Martin H (1983). Geochronology of the Damara Orogen—a review. In: Martin H, Eder FW (eds) *Intracontinental fold belts*. Springer, Berlin, pp 839–846. [https://doi.org/10.1007/978-3-642-69124-9\\_36](https://doi.org/10.1007/978-3-642-69124-9_36)
- Hartmann LA, Lopes WR, Savian JF (2016) Integrated evaluation of the geology, aerogammaspectrometry and aeromagnetometry of the Sul-Riograndense Shield, southernmost Brazil. *Anais da Academia Brasileira de Ciencias* 88:75–92. <https://doi.org/10.1590/0001-3765201520140495>
- Heilbron M, Valeriano CM, Tassinari CCG, Almeida JCH, Tupinamba M, Siga O, Trouw RAJ (2008) Correlation of Neoproterozoic terranes between the Ribeira Belt, SE Brazil and its African counterpart: comparative tectonic evolution and open questions. *Geol Soc Lond Spec Publ* 294:211–237. <https://doi.org/10.1144/SP294.12>
- Hiruma ST, Riccomini C, Modenesi-Gauttieri MC, Hackspacher PC, Neto JCH, Franco-Magalhaes AOB (2010) Denudation history of the Bocaina Plateau, Serra do Mar, south-eastern Brazil: relationships to Gondwana break-up and passive margin development. *Gondwana Res* 18:674–687. <https://doi.org/10.1016/j.gr.2010.03.001>
- Hoffman PF, Kaufman AJ, Halverson GP, Schrag DP (1998) A Neoproterozoic snowball earth. *Science* 281:1342–1346. <https://doi.org/10.1126/science.281.5381.1342>
- Hoffmann KH, Condon DJ, Bowring SA, Crowley JL (2004) U-Pb zircon date from the Neoproterozoic Ghaub Formation, Namibia: constraints on Marinoan glaciation. *Geology* 32(9):817
- Hu J, Liu L, Faccenda M, Zhou Q, Fischer KM, Marshak S, Lundstrom C (2018) Modification of the Western Gondwana craton by plume-lithosphere interaction. *Nat Geosci* 11:203–210. <https://doi.org/10.1038/s41561-018-0064-1>
- Hurford AJ (1986) Standardization of fission-track dating calibration: results of questionnaire distributed by International Union of Geosciences Sub commission on geochronology. *Nucl Tracks* 11:329–333. [https://doi.org/10.1016/1359-0189\(86\)90061-0](https://doi.org/10.1016/1359-0189(86)90061-0)
- Jackson MPA, Cramez C, Fonck JM (2000) Role of subaerial volcanic rocks and mantle plumes in creation of South Atlantic margins: implications for salt tectonics and source rocks. *Mar Pet Geol* 17:477–498. [https://doi.org/10.1016/S0264-8172\(00\)00006-4](https://doi.org/10.1016/S0264-8172(00)00006-4)
- Japsen P, Bonow JM, Green PF, Cobbold PR, Chiassi D, Lilletveit R, Magnavita LP, Pedreira A (2012) Episodic burial and exhumation in BE Brazil after opening of the South Atlantic. *Geol Soc Am Bull* 124:800–816. <https://doi.org/10.1130/B30515.1>
- Japsen P, Green PF, Bonow JM, Nielsen TFD, Chalmers JA (2014) From volcanic plains to glaciated peaks: burial, uplift and exhumation history of Southern East Greenland after opening of the NE Atlantic. *Glob Planet Change* 116:91–114. <https://doi.org/10.1016/j.gloplacha.2014.01.012>
- Jelinek AR, Chemale F Jr, van der Beek PA, Guadagnin F, Cupertino JA, Viana A (2014) Denudation history and landscape evolution of the northern East-Brazilian continental margin from apatite fission-track thermochronology. *J S Am Earth Sci* 54:158–181. <https://doi.org/10.1016/j.jsames.2014.06.001>
- Jerram D, Moutney N, Holzförster F, Stollhofen H (1999) Internal stratigraphic relationships in the Etendeka group in the Huab Basin, NW Namibia: understanding the onset of flood volcanism. *J Geodyn* 28:393–418. [https://doi.org/10.1016/S0264-3707\(99\)00018-6](https://doi.org/10.1016/S0264-3707(99)00018-6)
- Johnson MR, Van Vuuren CJ, Hegenberger WF, Key R, Shoko U (1996) Stratigraphy of the Karoo Supergroup in southern Africa: an overview. *J Afr Earth Sc* 23:3–15. [https://doi.org/10.1016/S0899-5362\(96\)00048-6](https://doi.org/10.1016/S0899-5362(96)00048-6)
- Jung S, Mezger K (2001) Geochronology in migmatites—a Sm-Nd, U-Pb, and Rb-Sr study from the Proterozoic Damara belt (Namibia): implications for polyphase development of migmatites in high-grade terranes. *J Metamorph Geol* 19:77–97. <https://doi.org/10.1046/j.0263-4929.2000.00297.x>
- Jung S, Hoernes S, Mezger K (2000a) Geochronology and petrogenesis of Pan African syn-tectonic S-type and post-tectonic A-type granite (Namibia)—products of melting of crustal sources, fractional crystallization and wall rock entrainment. *Lithos* 50:259–287. [https://doi.org/10.1016/S0024-4937\(99\)00059-6](https://doi.org/10.1016/S0024-4937(99)00059-6)
- Jung S, Hoernes S, Mezger K (2000b) Geochronology and petrology of migmatites from the Proterozoic Damara Belt—importance of episodic fluid-present disequilibrium melting and consequences for granite petrology. *Lithos* 51:153–179. [https://doi.org/10.1016/S0024-4937\(99\)00062-6](https://doi.org/10.1016/S0024-4937(99)00062-6)
- Jung S, Brandt S, Nebel O, Hellebrand E, Seth B, Jung C (2014) The P-T-t paths of high-grade gneisses, Kaoko Belt, Namibia: constraints from mineral data, U–Pb allanite and monazite and Sm–Nd/Lu–Hf garnet ages and garnet ion probe data. *Gondwana Res* 25:775–796. <https://doi.org/10.1016/j.gr.2013.05.017>
- Karl M, Glasmacher UA, Kollenz S, Franco-Magalhaes AOB, Stockli DF, Hackspacher PC (2013) Evolution of the South Atlantic passive continental margin in southern Brazil derived from zircon and apatite (U–Th–Sm)/He and fission-track data. *Tectonophysics* 604:224–244. <https://doi.org/10.1016/j.tecto.2013.06.017>
- Ketcham RA (2005) Forward and Inverse Modelling of low-temperature thermochronometry data. *Rev Mineral Geochem* 58:275–314. <https://doi.org/10.2138/rmg.2005.58.11>
- Ketcham RA (2017) HeFTy version 1.9.3, Manual
- Ketcham RA, Carter A, Donelick RA, Barbarand J, Hurford AJ (2007a) Improved measurements of fission-track annealing in apatite using *c*-axis projection. *Am Miner* 92:789–798. <https://doi.org/10.2138/am.2007.2280>
- Ketcham RA, Carter A, Donelick RA, Barbarand J, Hurford AJ (2007b) Improved modelling of fission-track annealing in apatite. *Am Miner* 92:799–810. <https://doi.org/10.2138/am.2007.2281>
- Ketcham RA, Donelick RA, Balestrieri ML, Zattin M (2009) Reproducibility of apatite fission-track length data and thermal history reconstruction. *Earth Planet Sci Lett* 284:504–515. <https://doi.org/10.1016/j.epsl.2009.05.015>
- Konopásek J, Kosler J, Tajcmanove L, Ulrich S, Kitt SL (2008) Neoproterozoic igneous complex emplaced along major tectonic boundary in the Kaoko Belt (NW Namibia): ion probe and LA-ICP-MS dating of magmatic and metamorphic zircons. *J Geol Soc Lond* 165:153–165. <https://doi.org/10.1144/0016-76492006-192>
- Krob FC, Glasmacher UA, Karl M, Perner M, Hackspacher PC, Stockli DF (2019) Multi-chronometer thermochronological modelling of the Late Neoproterozoic to recent t–T-evolution of the SE coastal region of Brazil. *J S Am Earth Sci* 92:77–94. <https://doi.org/10.1016/j.jsames.2019.02.012>
- Kröner S, Konopásek J, Kröner A, Passchier CW (2004) U–Pb and Pb–Pb zircon ages for metamorphic rocks in the Kaoko belt of Northwestern Namibia: a Palaeo- to Mesoproterozoic basement

- reworked during the Pan-African orogeny. *S Afr J Geol* 107:455–476. <https://doi.org/10.2113/107.3.455>
- Kröner S, Rojas-Agramonte Y, Hegner E, Hoffmann K-H, Wingate MTD (2010) SHRIMP zircon dating and Nd isotopic systematics of Palaeoproterozoic migmatitic orthogneisses in the Epupa Metamorphic Complex of northwestern Namibia. *Precamb Res* 183:50–69. <https://doi.org/10.1016/j.precamres.2010.06.018>
- Kukla C (1993) Strontium isotope heterogeneities in amphibolite facies, banded metasediments: a case study from the Late Proterozoic Kuiseb formation of the Southern Damara orogen, Central Namibia. *Commun Geol Surv Namib Mem* 15:139
- Kukla C, Kramm U, Kukla PA, Okrusch M (1991) U-Pb monazite data relating to metamorphism and granite intrusion in the northwestern Khomas Trough, Damara Orogen, central Namibia. *Commun Geol Surv Namib* 7:49–54
- Kukulius M (2004) A quantitative approach to the evolution of the Walvis Basin offshore NW-Namibia: structure, mass balancing, and hydrocarbon potential. Dissertation, Julius-Maximilians-Universität Würzburg, Germany.
- Lewis CLE, Green PF, Carter A, Hurford AJ (1992) Elevated K/T palaeotemperatures throughout Northwest England: three kilometers of Tertiary erosion? *Earth Planet Sci Lett* 112:131–145. [https://doi.org/10.1016/0012-821X\(92\)90012-K](https://doi.org/10.1016/0012-821X(92)90012-K)
- Lobo-Guerrero Sanz A (2005) Pre- and Post-Katangan Granitoids of the greater Lufilian Arc—geology, geochemistry, geochronology and metallogenic significance. Dissertation, University of the Witwatersrand, Johannesburg, South Africa
- Marzioli A, Melluso VM, Renne PR, Sgrosso I, D'Antonio M, Morais LD, Morais EAA, Ricci G (1999) Geochronology and petrology of Cretaceous basaltic magmatism in the Kwanza basin (western Angola), and relationships with the Paraná–Etendeka continental flood basalt province. *J Geodyn* 28:341–356. [https://doi.org/10.1016/S0264-3707\(99\)00014-9](https://doi.org/10.1016/S0264-3707(99)00014-9)
- Milani EJ, de Melo JHG, de Souza PA, Fernandes LA, França AB (2007) Bacia do Paraná. *Boletim de Geociências - Petrobras, Rio de Janeiro* 15:265–287
- Milani L, Kinnaird JA, Lehmann J, Naydenov KV, Saalman K, Frei D, Gerdes A (2015) Role of crustal contribution in the early stage of the Damara Orogen, Namibia: new constraints from combined U–Pb and Lu–Hf isotopes from the Goas Magmatic complex. *Gondwana Res* 28:961–986. <https://doi.org/10.1016/j.gr.2014.08.007>
- Miller RMG (1983) The Pan-African Damara orogen of Namibia. In: Miller RMG (ed) *Evolution of the Damara Orogen of South West Africa/Namibia*. *Spec Publ Geol Soc S Afr* 11:431–515.
- Miller RMG (2008) Neoproterozoic and early Palaeozoic rocks of the Damara Orogen. In: Miller RM (ed) *The geology of Namibia*. Geological Survey of Namibia, Windhoek
- Miller RMG (2013) Comparative stratigraphic and geochronological evolution of the Northern Damara Supergroup in Namibia and the Katanga Supergroup in the Lufilian Arc of Central Africa. *Geosci Can* 40(2):118
- Miller RMG, Burger AJ (1983) U-Pb zircon ages of members of the Salem Granitic Suite along the northern edge of the central Damara granite belt. In: Miller RMG (ed) *Evolution of the Damara Orogen of South West Africa/Namibia*. *Spec Publ Geol Soc South Afr* 11:273–280
- Milner SC (1986) The geological and volcanological features of the quartz latites of the Etendeka formation. *Commun Geol Surv Southwest Africa/Namibia* 2:109–116
- Milner SC, Duncan AR, Ewart A (1992) Quartz latite rheoignimbrite flows of the Etendeka Formation, north-western Namibia. *Bull Volcanol* 54:200–219. <https://doi.org/10.1007/BF00278389>
- Milner SC, Le Roex AP, O'Conner JM (1995) Age of Mesozoic igneous rocks in northwestern Namibia, and their relationship to continental breakup. *J Geol Soc* 152:97–104. <https://doi.org/10.1144/gsjgs.152.1.0097>
- Montañez IP, Poulsen CJ (2013) The late Paleozoic ice age: an evolving paradigm. *Annu Rev Earth Planet Sci* 41:629–656. <https://doi.org/10.1146/annurev.earth.031208.100118>
- Nascimento DB, Ribeiro A, Trouw RAJ, Schmitt RS, Passchier CW (2016) Stratigraphy of the Neoproterozoic Damara Sequence in northwest Namibia: slope to basin sub-marine mass-transport deposits and olistolith fields. *Precamb Res* 278:108–125. <https://doi.org/10.1016/j.precamres.2016.03.005>
- Oyhantcabal P, Siegesmund S, Wemmer K, Passchier CW (2011) The transpressional connection between Dom Feliciano and Kaoko Belt at 580–550 Ma. *Int J Earth Sci (Geologische Rundschau)* 100:379–390. <https://doi.org/10.1007/s00531-010-0577-3>
- Peate DW (1997) The Paraná–Etendeka Province. In: Mahoney JJ, Coffin MF (eds) *Large Igneous Provinces: continental, oceanic, and planetary flood volcanism*. Geophysical Monograph 100. Washington, DC: American Geophysical Union, pp 217–245.
- Pollard S (2002) Temperature range of thermochronometers: temperatures that are in current use, and their effective closure temperatures (adapted from Fitzgerald P, Baldwin S, Gehrels G, Reiners P, Duca M). <https://pangea.standard.edu/~dpollard/NSF/main.html>.
- Raab MJ (2001) The geomorphic response of the passive continental margin of Northern Namibia to Gondwana break-up and global scale tectonics. Dissertation, Georg-August-University, Göttingen, Germany
- Raab MJ, Brown RW, Gallagher K, Carter A, Weber K (2002) Late Cretaceous reactivation of major crustal shear zones in northern Namibia: constraints from apatite fission track analysis. *Tectonophysics* 349:75–92. [https://doi.org/10.1016/S0040-1951\(02\)00047-1](https://doi.org/10.1016/S0040-1951(02)00047-1)
- Raab MJ, Brown RW, Gallagher K, Weber K, Gleadow AJW (2005) Denudational and thermal history of the Early Cretaceous Brandberg and Kenyena igneous complexes on Namibia's Atlantic passive margin. *Tectonics* 24(TC3006):15. <https://doi.org/10.1029/2004TC001688>
- Rahn MK, Brandon MT, Batt GE, Garver JI (2004) A zero-damage model for fission-track annealing in zircon. *Am Miner* 89:473–484. <https://doi.org/10.2138/am-2004-0401>
- Reiners PW, Brandon MT (2006) Using thermochronology to understand orogenic erosion. *Annu Rev Earth Planet Sci* 34:419–466. <https://doi.org/10.1146/annurev.earth.34.031405.125202>
- Renne PR, Deckart K, Ernesto M, Féraud G, Piccirillo EM (1996) Age of Ponta Grossa dike swarm (Brazil), and implications to Parana flood volcanism. *Earth Planet Sci Lett* 144:199–221. [https://doi.org/10.1016/0012-821X\(96\)00155-0](https://doi.org/10.1016/0012-821X(96)00155-0)
- Rybach L (1988) Determination of heat production rate. In: Haenel R, Rybach L, Stegena L (eds) *Handbook of terrestrial heat flow density determination*. Kluwer Academic Publishers, Dordrecht, pp 125–142
- Salomon E, Koehn D, Passchier CW (2015) Brittle reactivation of ductile shear zones in NW Namibia in relation to South Atlantic rifting. *Tectonics* 34:70–85. <https://doi.org/10.1002/2014TC003728>
- Salomon E, Koehn D, Passchier CW, Chung P, Häger T, Salvona A, Davis J (2016) Deformation and fluid flow in the Huab Basin and Etendeka Plateau, NW Namibia. *J Struct Geol* 88:46–62. <https://doi.org/10.1016/j.jsg.2016.05.001>
- Salomon E, Passchier CW, Koehn D (2017) Asymmetric continental deformation during South Atlantic rifting along southern Brazil and Namibia. *Gondwana Res* 51:170–176. <https://doi.org/10.1016/j.gr.2017.08.001>
- Schmitt RS, Trouw RAJ, Passchier CW, Medeiros SR, Armstrong R (2012) 530 Ma syntectonic and granites in NW Namibia—their relation with collision along the junction of the Damara



- and Kaoko belts. *Gondwana Res* 21:362–377. <https://doi.org/10.1016/j.gr.2011.08.006>
- Scotese CR, Golonka J (1992) PALEOMAP paleogeographic atlas. PALEOMAP Progress Report 20, Department of Geology, University of Texas, Arlington, Texas, p 34
- Scotese CR, Boucot AJ, McKerrow WS (1999) Gondwanan paleogeography and paleoclimatology. *J Afr Earth Sc* 28:99–114. [https://doi.org/10.1016/S0899-5362\(98\)00084-0](https://doi.org/10.1016/S0899-5362(98)00084-0)
- Şengör AMC (2001) Elevation as indicator of mantle-plume activity. In: Ernst RE, Buchan KL (eds) *Mantle plumes: their identification through time*. *Geol Soc Am Spec Pap* 352:183–225
- Seth B, Kröner A, Mezger K, Nemchin AA, Pidgeon RT, Okrusch M (1998) Archaean to Neoproterozoic magmatic events in the Kaoko belt of NW Namibia and their geodynamic significance. *Precambr Res* 92:341–363. [https://doi.org/10.1016/S0301-9268\(98\)00086-2](https://doi.org/10.1016/S0301-9268(98)00086-2)
- Seth B, Okrusch M, Wilde M, Hoffmann KH (2000) The Voetspoor Intrusion, Southern Kaoko Zone, Namibia: mineralogical, geochemical and isotopic constraints for the origin of a syenitic magma. *Commun Geol Surv Namib* 12:143–156
- Silva BV, Hackspacher PC, Ribeiro MCS, Glasmacher UA, Gonçalves AO, Doranti-Tiritan C, Godoy DF, Constantino RR (2019) Evolution of the Southwestern Angolan Margin: episodic burial and exhumation is more realistic than long-term denudation. *Int J Earth Sci (Geologische Rundschau)* 108:89–113. <https://doi.org/10.1007/s00531-018-1644-4>
- Stanisstreet IG, Kukla PA, Henry G (1991) Sedimentary basinal responses to Late Precambrian Wilson cycles; the Damara Orogen and Nama Foreland, Namibia. *J Afr Earth Sc* 13:141–156. [https://doi.org/10.1016/0899-5362\(91\)90048-4](https://doi.org/10.1016/0899-5362(91)90048-4)
- Stollhofen H (1999) Karoo Synrift-Sedimentation und ihre tektonische Kontrolle am entstehenden Kontinentalrand Namibia. *Zeitschrift der deutschen geologischen Gesellschaft* 149:519–632
- Stollhofen H, Stanisstreet IG, Bangert B, Grill H (2000) Tuffs, tectonism and glacially related sea-level changes, Carboniferous-Permian, southern Namibia. *Palaeogeogr Palaeoclimatol Palaeoecol* 161:127–150. [https://doi.org/10.1016/S0031-0182\(00\)00120-6](https://doi.org/10.1016/S0031-0182(00)00120-6)
- Tello Saenz CA, Hackspacher PC, Hadler Neto JC, Lunes PJ, Guedes S, Ribeiro LFB, Paulo SR (2003) Recognition of Cretaceous, Paleocene, and Neogene tectonic reactivation through apatite fission-track analysis in Precambrian areas of southeast Brazil: association with the opening of the south Atlantic Ocean. *J S Am Earth Sci* 15:765–774. [https://doi.org/10.1016/S0895-9811\(02\)00131-1](https://doi.org/10.1016/S0895-9811(02)00131-1)
- Thompson RN, Gibson SA, Dicking AP, Smith PM (2001) Early Cretaceous Basalt and Picrite dykes of the Southern Etendeka Region, NW Namibia: windows into the role of the Tristan Mantle plume in Paraná–Etendeka magmatism. *J Petrol* 42:2049–2081. <https://doi.org/10.1093/petrology/42.11.2049>
- Torsvik TH, Rousse S, Labails C, Smethurst MA (2009) A new scheme for the opening of the South Atlantic ocean and the dissection of an Aptian salt basin. *Geophys J Int* 177:1315–1333. <https://doi.org/10.1111/j.1365-246X.2009.04137.x>
- Torsvik TH, von der Voo R, Doubrovine PV, Burke K, Steinberger B, Ashwal LD, Trønnes RG, Webb SJ, Bull AL (2014) Deep mantle structures as a reference frame for movements in and on the Earth. *Proc Natl Acad Sci USA* 111:8735–8740. <https://doi.org/10.1073/pnas.1318135111>
- Travassos RP (2014) *Interpretação estrutural regional do escudo Sul-Rio-Grandense -Rio Grande do Sul, Brasil, com base em aeromagnetometria*. Dissertation. Instituto de Geociências, Universidade de Brasília, Brazil
- Trumbull RB, Vietor T, Hahne K, Wackerle R, Ledru P (2004) Aeromagnetic mapping and reconnaissance geochemistry of the Early Cretaceous Henties Bay-Outjo dike swarm, Etendeka Igneous Province, Namibia. *J Afr Earth Sc* 40:17–29. <https://doi.org/10.1016/j.jafrearsci.2004.07.006>
- Trumbull RB, Reid DL, de Beer C, van Acken D, Romer RL (2007) Magmatism and continental breakup at the west margin of southern Africa: a geochemical comparison of dolerite dikes from northwestern Namibia and the Western Cape. *S Afr J Geol* 110:477–502. <https://doi.org/10.2113/gssajg.110.2-3.477>
- Uliana MA, Legarreta L, Laffitte GA, Villar HJ (2014) Estratigrafía y Geoquímica de la facies generadoras de hidrocarburos en la cuencas petrolíferas de Argentina. IV Congreso de Exploración y Desarrollo de Hidrocarburos (Mar del Plata). *Actas* 1:1–63
- Van de Flierdt T, Hoernes S, Jung S, Masberg P, Hoffer E, Schaltegger U, Friedrichsen H (2003) Lower crustal melting and the role of open-system processes in the genesis of syn-orogenic quartz diorite–granite–leucogranite associations: constraints from Sr–Nd–O isotopes from the Bandombaai complex, Namibia. *Lithos* 67:205–226. [https://doi.org/10.1016/S0024-4937\(03\)00016-1](https://doi.org/10.1016/S0024-4937(03)00016-1)
- Wilson JT (1963) A possible origin of the Hawaiian islands. *Can J Phys* 41:863–870. <https://doi.org/10.1139/p63-094>
- Wilson JT (1965) A new class of faults and their bearing on continental drift. *Nature* 207:343–347. <https://doi.org/10.1038/207343a0>
- Wygrala BP (1989) *Integrated Study of an oil field in the southern Po Basin, northern Italy*. KFA-Jülich 2313, 328 p. <https://hdl.handle.net/2128/6740>
- Yalçın MN, Littke R, Sachsenhofer RF (1997) Thermal history of sedimentary basins. In: Welte DH, Horsfield B, Baker DR (eds) *Petroleum and basin evolution*. Springer, Berlin, pp 71–167. [https://doi.org/10.1007/978-3-642-60423-2\\_3](https://doi.org/10.1007/978-3-642-60423-2_3)



# 4

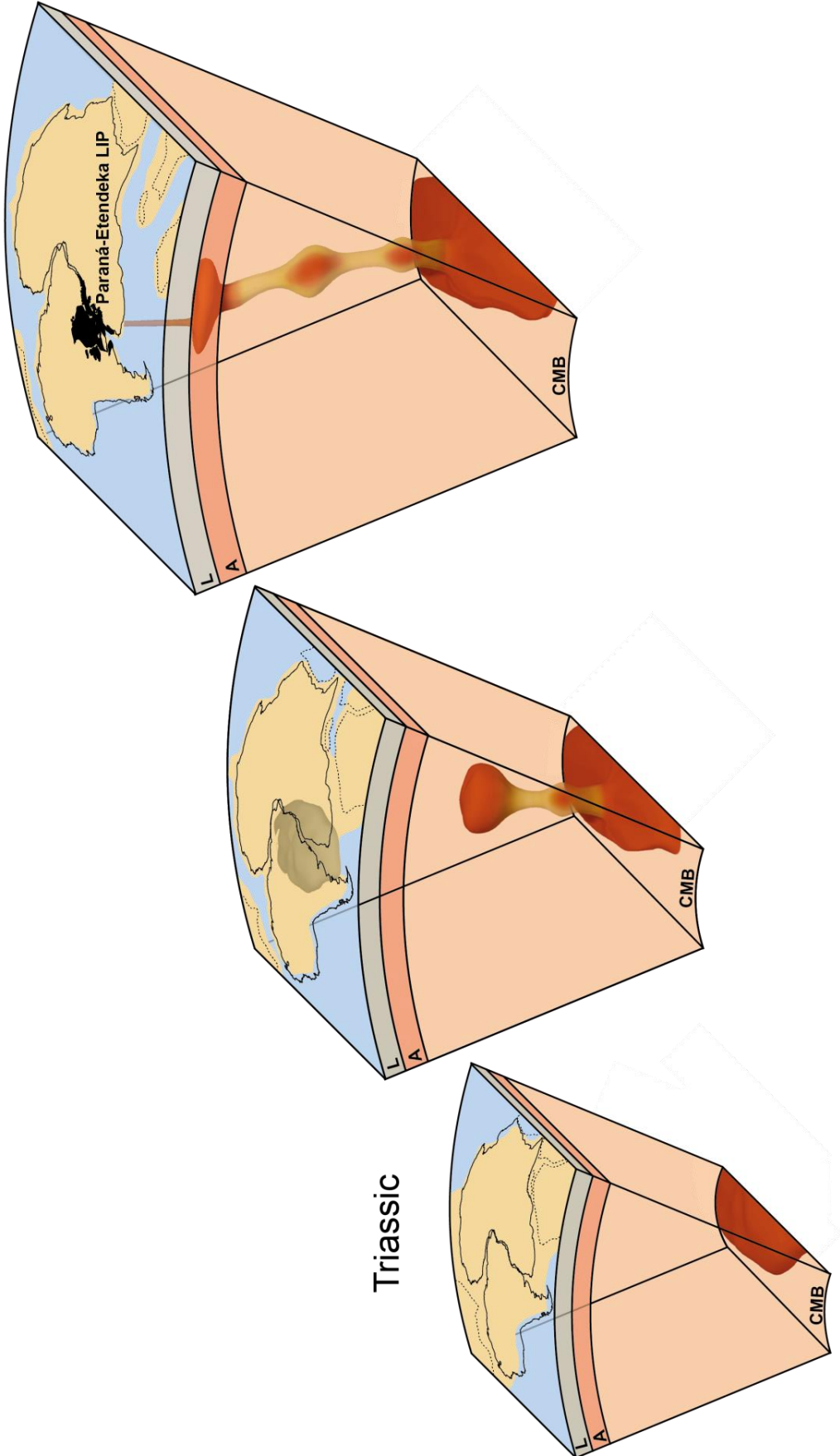
## APPLICATION OF STRATIGRAPHIC FRAMEWORKS AND THERMOCHRONOLOGICAL DATA ON THE MESOZOIC SW GONDWANA INTRAPLATE ENVIRONMENT TO RETRIEVE THE PARANÁ- ETENDEKA PLUME MOVEMENT

---

### CONTENTS

GRAPHICAL ABSTRACT	100
CREDIT AUTHOR STATEMENT	101
ABSTRACT	103
INTRODUCTION	103
THE EVENT-BASED PLUME STRATIGRAPHIC FRAMEWORK (EPSF)	104
FIRST ARCHIVE: STRATIGRAPHIC RECORDS	107
SECOND ARCHIVE: THERMOCHRONOLOGICAL DATA SETS	117
COMBINING BOTH ARCHIVES: STRATIGRAPHIC RECORDS AND LTT DATA SETS	118
FINAL DISCUSSION AND INTERPRETATION	126
CONCLUSIONS	128
ACKNOWLEDGEMENTS	131
REFERENCES	131

---



Graphical Abstract for CHAPTER 4.

### CRediT author statement

**Publication title:** Application of stratigraphic frameworks and thermochronological data on the Meozoic SW Gondwana intraplate environment to retrieve the Paraná-Etendeka plume movement.

**Authors:** Florian C. Krob, Ulrich A. Glasmacher, Hans-Peter Bunge, Anke M. Friedrich, Peter C. Hackspacher.

#### Author contributions\*:

<b>Florian C. Krob:</b>	Conceptualization, methodology, software, validation, formal analysis, investigation, data curation, writing – original draft, visualization, project administration ( <b>≈77%</b> ).
<b>Prof. Dr. Ulrich A. Glasmacher:</b>	Conceptualization, methodology, validation, resources, writing – review & editing, supervision, project administration, funding acquisition ( <b>≈10%</b> ).
<b>Prof. Dr. Hans-Peter Bunge:</b> ( <b>≈10%</b> ).	Validation, resources, writing – review & editing
<b>Prof. Dr. Anke M. Friedrich:</b> ( <b>≈2.5%</b> ).	Validation, resources, writing – review & editing
<b>Prof. Dr. Peter C. Hackspacher:</b>	Resources, writing – review & editing ( <b>≈0.5%</b> ).

\*Reproduced from Brand et al. (2015)

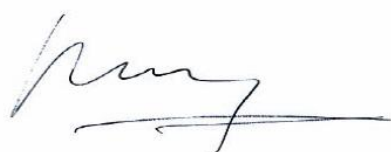
Heidelberg, 15.04.2020



Florian Krob – Corresponding author



Ulrich A. Glasmacher – Supervisor



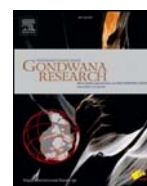
Hans-Peter Bunge – Deputy Co-Author





Contents lists available at ScienceDirect

Gondwana Research

journal homepage: [www.elsevier.com/locate/gr](http://www.elsevier.com/locate/gr)

# Application of stratigraphic frameworks and thermochronological data on the Mesozoic SW Gondwana intraplate environment to retrieve the Paraná-Etendeka plume movement



Florian C. Krob<sup>a,\*</sup>, Ulrich A. Glasmacher<sup>a</sup>, Hans-Peter Bunge<sup>b</sup>, Anke M. Friedrich<sup>c</sup>, Peter C. Hackspacher<sup>d</sup>

<sup>a</sup> Institute of Earth Sciences, Heidelberg University, Im Neuenheimer Feld 234, 69120 Heidelberg, Germany

<sup>b</sup> Department of Earth and Environmental Sciences, Geophysics, LMU, Theresienstraße 41, 80333 Munich, Germany

<sup>c</sup> Department of Earth and Environmental Sciences, Geology, LMU, Luisenstraße 37, 80333 Munich, Germany

<sup>d</sup> Departamento de Petrologia e Metalogenia, Instituto de Geociências e Ciências Exatas, Universidade Estadual Paulista, Av. 24-A, 1515, Bela Vista, 13506-900 Rio Claro, SP, Brazil

## ARTICLE INFO

### Article history:

Received 26 July 2019

Received in revised form 17 February 2020

Accepted 18 February 2020

Available online xxx

Handling Editor: R.D. Nance

## ABSTRACT

Since plate tectonics has been linked to material flow in the Earth's mantle, it is commonly accepted that convective motion in the sublithospheric mantle results in vertical deflections and horizontal plate motion on the Earth's surface. Those mantle flow-driven vertical deflections are recognized through significant signals and traces in the sedimentary records (unconformities and missing sections). Recently, Friedrich et al. (2018) introduced an event-based plume stratigraphic framework that uses such signals in the stratigraphic record to detect the geological evolution near, and on the Earth's surface in areas of interregional scale caused by mantle plume movement. Information about these dynamic processes is stored in geological archives, such as (1) stratigraphic records of sedimentary basins and (2) thermochronological data sets of igneous, metamorphic, and sedimentary rocks.

For the first time, this research combines these two geological archives and applies them to the Mesozoic SW Gondwana intraplate environment to retrieve the Paraná-Etendeka plume movement prior to the Paraná-Etendeka LIP. We compiled 18 stratigraphic records of the major continental and marine sedimentary basins and over 35 thermochronological data sets including >1300 apatite fission-track ages surrounding the Paraná-Etendeka Large Igneous Province to test the event-based plume stratigraphic framework and its plume stratigraphic mapping to retrieve the timing and spatial distribution of the Paraná-Etendeka plume.

The plume stratigraphic mapping, using the stratigraphic records is suitable to demark a possible plume center, plume margins and distal regions (Friedrich et al., 2018). Thermochronological data reveal centers of a significant thermal Paraná-Etendeka plume influence. Both archives show significant signals and traces of mantle plume movement well in advance of the flood basalt eruptions. Our LTT data combined with stratigraphic records are modeled successfully with respect to a viable mantle plume driven thermal evolution and therefore, we suggest that thermochronological data, in combination with stratigraphy records have the potential to retrieve the Paraná-Etendeka plume movement.

© 2020 International Association for Gondwana Research. Published by Elsevier B.V. All rights reserved.

## 1. Introduction

Ever since plate tectonics has been linked to material flow in the Earth's mantle (Wilson, 1963, 1965; Davies and Richards, 1992), it is commonly accepted that convective motion in the sublithospheric mantle results in vertical deflections and horizontal plate motion on the Earth's surface (Davies, 1999; Davies et al., 2019). Those mantle flow-driven vertical deflections, known as 'dynamic topography' (Hager et al., 1985; Braun, 2010), have attracted considerable attention

lately (Bunge and Glasmacher, 2018). Evidence for dynamic topography changes over geologic time comes from passive continental margins, in particular in the South Atlantic region (Paton et al., 2008; Guillocheau et al., 2012; Autin et al., 2013; Dressel et al., 2015), where spreading rate changes appear to correlate with uplift events, presumably owing to variations of upper mantle flow (Colli et al., 2013; Colli et al., 2014; Brune et al., 2016). Dynamic topography thus links to the convective mantle flow regime. Theoretical considerations based on the dynamic topography response of Earth models to internal loads (e.g., hot rising plumes or cold sinking lithosphere) imply that the Earth's surface sustains deflections on the order of  $\pm 1$  km (Colli et al., 2016), resulting in significant signals and traces in the sedimentary records (unconformities and missing sections, e.g., Stille, 1919).

\* Corresponding author.

E-mail address: [florian.krob@geow.uni-heidelberg.de](mailto:florian.krob@geow.uni-heidelberg.de) (F.C. Krob).

Geodynamicists explore mantle convection in terms of the so-called *plate* and *plume* mode (Davies, 1999; Davies et al., 2019; Heron, 2018). The former refers to cooling of the oceanic lithosphere and its descent into the mantle by subduction. The latter links to the rise of mantle plumes from a hot thermal boundary layer at the Core Mantle Boundary (CMB). A strong plume mode is inferred from mantle circulation models. These place the total plume heat transport into the range of 10 TW (e.g., Bunge, 2005; Schuberth et al., 2009; Simmons et al., 2009), suggesting that the plume mode may account for ~30% of the global mantle heat budget (e.g., Davies and Davies, 2010). This makes it important to explore dynamic topography signals that link to the plume mode.

Recently, Friedrich et al. (2018) introduced an event-based plume stratigraphic framework (ePSF) that predicts the existence of such signals in the stratigraphic record to describe the geological evolution near, and on the Earth's surface in areas of interregional scale. The ePSF, which follows plume scaling proposed by Campbell and Griffiths (1990) predicts that vertical mantle plume movement produces distinct temporal and spatial patterns of episodic rock and surface uplift accompanied by crustal deformation, the evolution, reactivation, and horizontal migration of tectonic structures, subsidence and inversion of sedimentary basins, and the emplacement of dike swarms and flood basalts. Depending on the location above the ascending plume head, either one or two episode of broad uplift and subsidence result in formation of regional-scale unconformities, i.e., hiatuses.

However, quantitative research connecting vertical material flow in the Earth's mantle and crust with structural, topographic, and magmatic surface expressions in intraplate environments remains elusive and is highly dependent on the properties of the assumed Earth model (Bunge et al., 1998; Bunge and Glasmacher, 2018). Therefore, less is known about the timing and rates of such dynamic processes and their spatial distribution prior to the flood basalt eruptions. Nevertheless, information about these dynamic processes is stored in geological archives, such as stratigraphic records of sedimentary basins and thermochronological data sets of igneous, metamorphic, and sedimentary rocks.

The contemporary continents of SW Africa and South America, as part of the former Mesozoic SW Gondwana intraplate environment provide excellent data of both, stratigraphic records and thermochronological data sets, having stored the sedimentological, thermal, and magmatic evolution surrounding the Paraná-Etendeka Large Igneous Province (LIP) (Fig. 1). Furthermore, the geochemical signature of its Lower Cretaceous flood basalts was linked to those of lithos- and asthenospheric mantle source in the past (Trumbull et al., 2007; Keiding et al., 2013; Will et al., 2016; Stronck et al., 2017; Owen-Smith et al., 2017, 2019; Hartmann et al., 2019).

Hence, for the first time, this research combines these two geological archives and applies them to the Mesozoic SW Gondwana intraplate environment to retrieve the Paraná-Etendeka plume movement prior to the Paraná-Etendeka LIP flood basalt eruptions (Fig. 2). Together, these two archives provide excellent data to quantify the temporal scale and spatial distributions of the Paraná-Etendeka plume-driven surface deflections during the Mesozoic SW Gondwana intraplate environment along the present South Atlantic passive continental margins (SAPCM) of SW Africa and South America.

## 2. The event-based plume stratigraphic framework (ePSF)

The ePSF (Friedrich et al., 2018) transcribes ascending mantle plume-related surface modifications that result in successive topographic and sedimentological responses recognized through distinct signals and traceable patterns in the stratigraphic records. Those stratigraphic responses are expressed by unconformities, hiatuses, and the inversion of basins, and allow systematic and testable predictions about the evolution of an ascending mantle plume. In the

following, we provide a short comprehensive description of the various phases of the ePSF (see supplementary material, Fig. S1):

### 2.1. Phase A – incipient plume head

The initiation of the plume movement at the CMB is defined as event horizon in the stratigraphic records. Colli et al. (2018) estimate ascent velocities of the rising plume head around 25–50 km/Myr. Friedrich et al. (2018) considered an exemplary ascent velocity of about 50 km/Myr leading to an event horizon at about 60 Myr prior to the eruption of plume derived flood basalts at the Earth's surface.

### 2.2. Phases B, C, and D – rising Plume head and impact at base of lithosphere

As the plume head ascends through the non-lithospheric mantle the Earth's surface successively responds to the transient vertical movement with continuous vertical deflection (doming). This primary large wavelength structural doming mirrors the vertical material flow in the non-lithospheric mantle and appears to be limited to an amplitude of 0.5 to 2 km of surface uplift over a radius of about 1000 km (Griffiths et al., 1989; Griffiths and Campbell, 1990; Ernst and Buchan, 2001; Şengör, 2001; Guillocheau et al., 2018). With decreasing plume head depth the radius of the evolving dome above the plume axis shrinks simultaneously leading to the development of a fast and narrow uplifting center, and slower uplifting peripheral regions (plume margin). Regional scale erosion pattern (Cox, 1989) dominate above the plume head prior to the plume arrival at the base of the lithosphere, and radial transport and deposition of sediments shifts from the plume center towards the marginal and distal regions. Continuously, the plume margin experiences decreased relative rock and surface uplift and the decrease of the uplifting dome's diameter entails the subsidence of the margin.

### 2.3. Phases E, F – climax and collapse of plume head

When the plume head reaches the base of the lithosphere, it flattens out and a large volume of the vertically transported material is directed horizontally (~10<sup>6</sup> km<sup>3</sup>; Duncan and Richards, 1991). On the Earth's surface, this deflection of vertical material flow results in the extensional collapse of the previously uplifted central dome. The inversion of topography triggers other endogenic processes, such as narrow rifting that may lead to oceanic spreading and the emplacement of dike swarms (Courtilot et al., 1999). Only little of the excess mantle material (~10%) reaches the Earth's surface probably using the dike swarms as feeder channels and results in the deposition of flood basalts (Burke and Wilson, 1972; Burke and Dewey, 1973; Cox, 1989; Campbell and Griffiths, 1990; Şengör, 1995; Ernst and Buchan, 2001).

Concurrently, the majority of mantle material is deflected horizontally beneath the lithosphere where it may spread laterally, preferably under regions of thinned lithosphere (Courtilot et al., 1999; ~10<sup>6</sup> km<sup>3</sup>, Duncan and Richards, 1991). Thicker lithosphere, such as cratonic roots, probably diverts the lateral asthenospheric material flow (Sleep, 1997; Ebinger and Sleep, 1998) leading to highly asymmetric rock and surface uplift, and erosion as the marginal areas experience a lateral extension >2000 km (Campbell and Griffiths, 1990; Campbell, 2007).

### 2.4. Phases F, G – lateral spreading, crustal deformation, rifting and thermal relaxation

Following the flood basalt eruptions, lateral spreading and crustal deformation continue causing broad lithospheric-scale rifting and ongoing horizontal plate motion. Crustal segments eventually experience slow thermal relaxation. Erosion of the uplifted margins leads to renewed in- and outward directed transport and deposition of sediments, forming incipient successor basins.



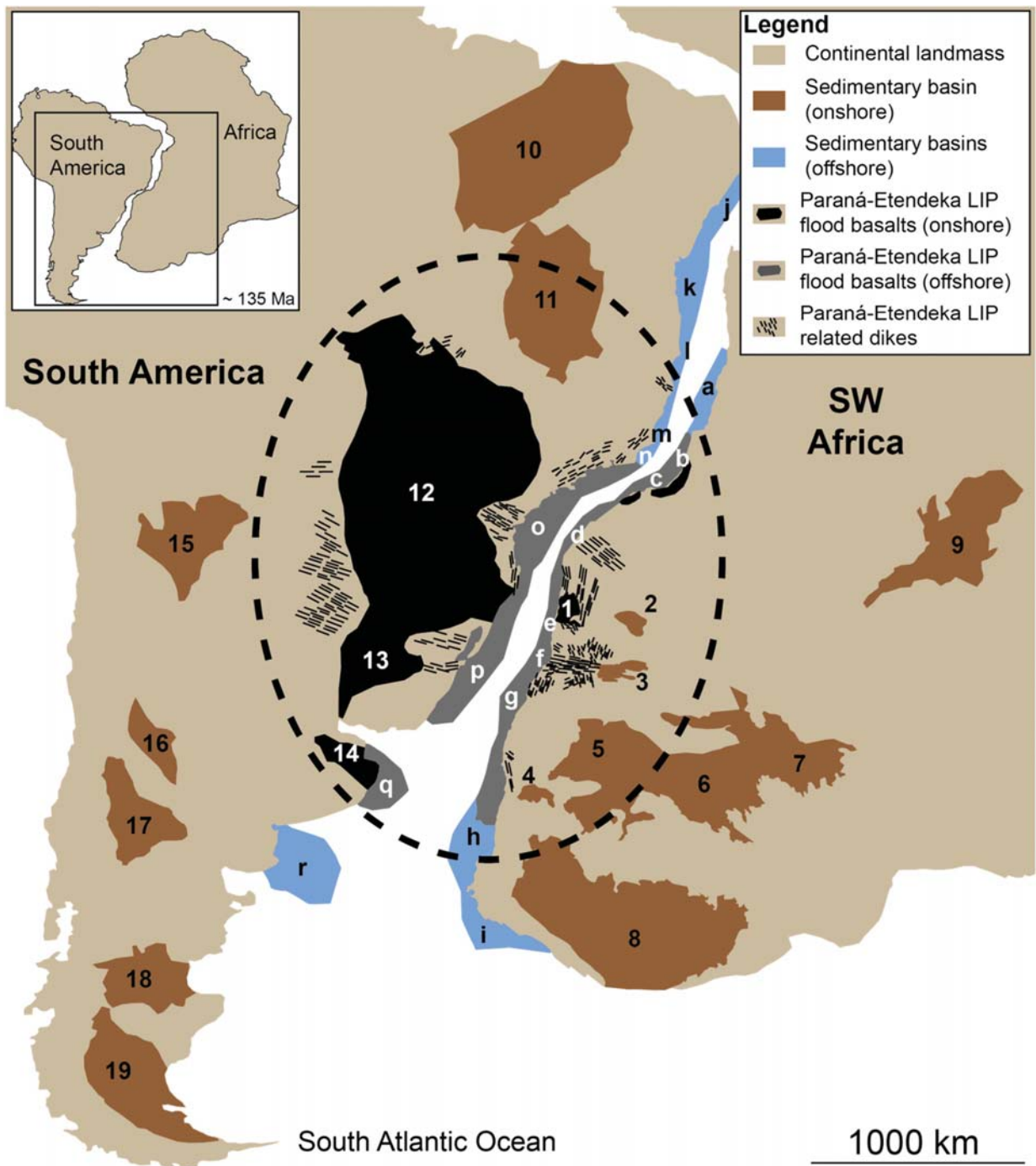


**Fig. 1.** Simplified overview showing the geological archives of the Mesozoic SW Gondwana intraplate environment along the contemporary SAPCMs from NW Angola to South Africa in SW Africa and from NE Brazil to SE Argentina in South America. The figure includes all major Paleozoic to Mesozoic, continental (brown) and marine (blue), sedimentary basins (numbers and letters) surrounding the Paraná-Etendeka Large Igneous Province (LIP) (dashed circle, Franke, 2013), and on- and offshore Paraná-Etendeka flood basalt depositions (black) and Paraná-Etendeka related dike swarm locations (thin black lines) (Following numbers in square brackets refer back to the references accordingly to their order constraint within the reference list of the publication and additional references in the supplementary material [Sxx]. [1]; [66]; [84]; [85]; see supplementary material: [S13]; [S14]; [S18]; [S31]; [S32]; [S44]; [S50]; [S72]; [S81]; [S96]; [S97]; [S100]; [S102]; [S103]). Paleogeographic reconstructions were taken from Torsvik et al. (2006, 2009, 2013). Onshore basins: SW Africa: 1: Huab; 2: Owambo; 3: Waterberg; 4: Karasburg; 5: Aranos; 6: Central Kalahari; 7: Mid-Zambezi; 8: Central Karoo; 9: Congo; South America: 10: Paranaíba; 11: São Francisco; 12: Paraná (Brazil), 13: Paraná (Uruguay); 14: Salado; 15: NE Paleo/Cretaceous; 16: Cuyana; 17: Neuquén; 18: San Jorge; 19: Austral-Magallanes; offshore basins: SW Africa: a: Lower Congo; b: Kwanza; c: Benguela; d: Namibe; e: Walvis Ridge; f: Walvis; g: Luderitz; h: Orange; i: Cape; South America: j: Sergipe; k: Central basins; l: Mucurri; m: Espírito Santo; n: Campos; o: Santos; p: Pelotas; q: Salado offshore; r: Colorado. For further information see Figs. 3a, b, c. (For interpretation of the references to colour in this figure legend, the reader is referred to the web version of this article.)

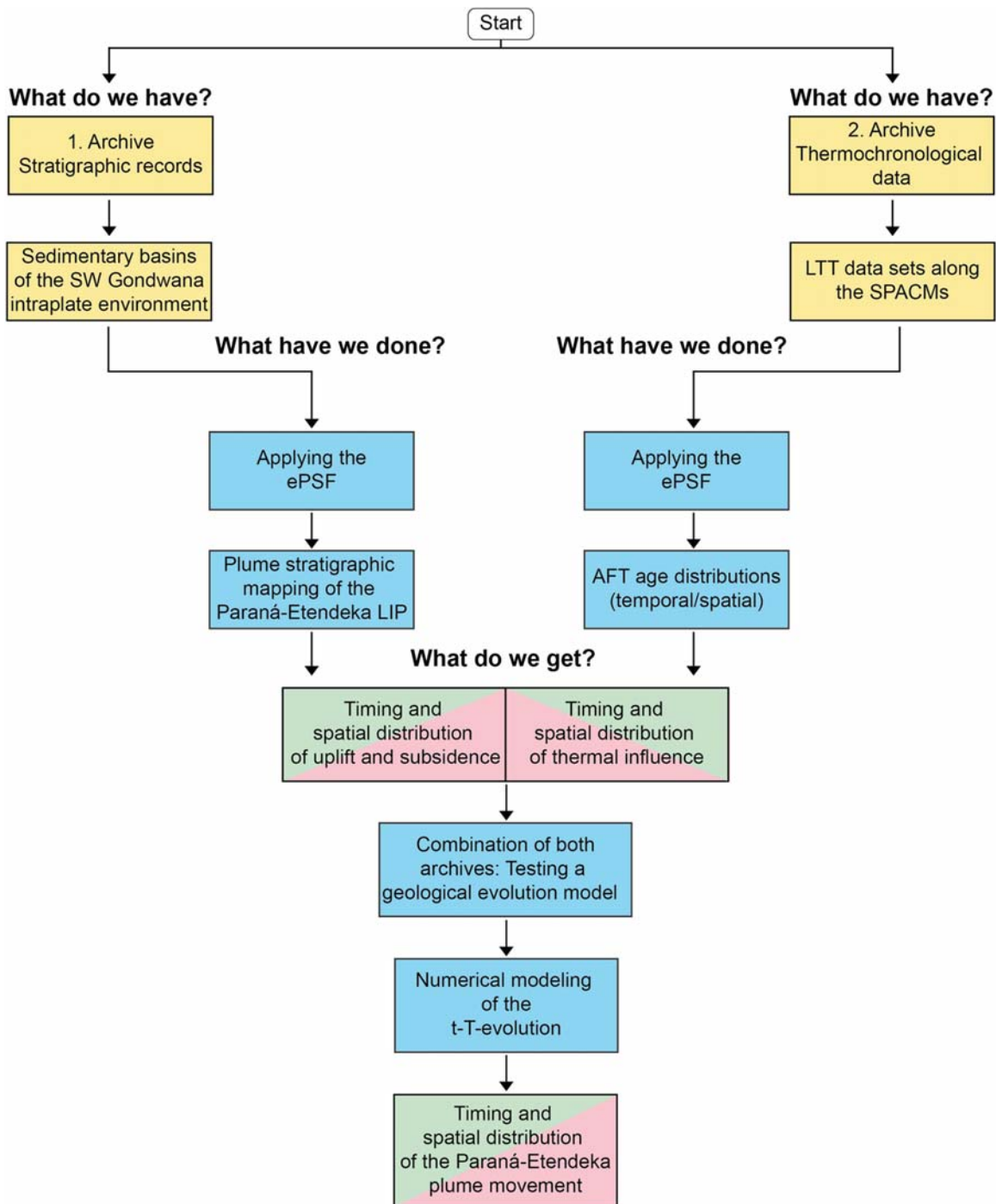


**Fig. 2.** Schematic workflow showing the approach of this research study. First archive (left panel): We compiled published stratigraphic records of the major continental and offshore basins in SW Africa and NE-SE South America and tested the event-based plume stratigraphic framework (ePSF, Friedrich et al., 2018) to retrieve the timing of uplift and subsidence and propose spatial distributions on the Earth's surface affected by the rising Paraná-Etendeka plume. Second archive (right panel): We used published thermochronological data sets along the contemporary South Atlantic passive continental margins (SPACM) from NW Angola to South Africa and Zimbabwe, and NE Brazil to NE Argentina (for references, see supplementary material, Tables S1, S2, S3) and integrated our latest thermochronological data in NW Namibia (Krob et al., 2020; Eldracher (former Menges), pers. comm.) and SE Brazil (Karl et al., 2013; Krob et al., 2019) to retrieve the thermal influence of the ascending Paraná-Etendeka plume. The combination of both archives (middle panel) permits the inverse numerical modeling of our thermochronological data to test them (Karl et al., 2013; Krob et al., 2019; Krob et al., 2020; Eldracher, pers. comm.) against a geological evolution model (GEM) that has been derived from field observations, published stratigraphic records, tectonic evolution, and timing of events described within the ePSF. For further information and references, see Figs. S5 and S6. Explanation of coloured boxes: yellow: data compilation and explanation; blue: methods and approach; green: results; red: discussion. (For interpretation of the references to colour in this figure legend, the reader is referred to the web version of this article.)

### 3. First archive: stratigraphic records of the Paleozoic to Mesozoic SW Gondwana intraplate sedimentary basins

#### 3.1. Pre plume-event evolution of the major continental basins surrounding the Early Cretaceous Paraná-Etendeka LIP

Intraplate environments occur within continental and oceanic plates. Moreover, the amalgamation of converging continental plates, oceanic crust, and smaller crustal to large-scale supercontinents can produce complex lithological and structural inhomogeneous environments (Santosh et al., 2009; Nance et al., 2014; Pirajno and Santosh, 2015). Preparatory to the Mesozoic SW Gondwana intraplate environment, the Pan African/Brasiliano orogeny (~650–490 Ma) led to the formation of the Gondwana supercontinent (e.g. Frimmel et al., 2011). These convergent processes were followed by a long period of post-collisional rock cooling, tectonic and surface uplift, and erosion of the Neoproterozoic igneous, metamorphic, and sedimentary rocks. Early to Late Paleozoic collapse and denudation, as well as Mesozoic denudation of the Neoproterozoic mobile belts supplied enormous amounts of sediments to ensure the Late Paleozoic to Mesozoic evolution of the major sedimentary basins (Figs. 1, #1–19 and #a–r; 3a, #1–9; 3b, #10–19; 3c, #a–r). Extensive intraplate foreland basins, such as the Karoo (#8) and the Paraná (#12) basins formed in front of the northward-moving Cape Fold Belt (Stollhofen, 1999).

The Paleozoic to Mesozoic geological evolution in the later center of the Paraná-Etendeka LIP along the contemporary SAPCMs of NW Namibia and SE Brazil is dominated by deposition of sediments, subsidence, and diagenesis. In NW Namibia (Figs. 1, 3a; S2), the Huab (#1), Owambo (#2), and Waterberg (#3) basins possibly mirror its sedimentary evolution. Subsidence of the Neoproterozoic basement set in with the onset of Karoo sedimentation during the Late Carboniferous. All three basins provide evidence of siliciclastic deposition of the Dwyka, Ecca, and Beaufort groups (Johnson et al., 1996; Stollhofen et al., 2000; Catuneanu et al., 2005). In the Owambo and Waterberg basins, siliciclastic and volcanic deposition of the Etjo and Rundu/Rooivall formations discordantly overlie earlier Karoo sedimentary rocks (Mountey and Howell, 2000). The volcanic rocks are correlated to the Karoo igneous event (~180 Ma; Johnson et al., 1996; Duncan et al., 1997; Catuneanu et al., 2005; Jourdan et al., 2005). Flood basalt deposits of Paraná-Etendeka age (~135 Ma; Renne et al., 1992; Renne et al., 1996; Torsvik et al., 2006) are lacking, although Paraná-Etendeka related dike swarms can be found in proximity to the basin (Turner et al., 1994; Trumbull et al., 2004; Trumbull et al., 2007; Thompson et al., 2001; McMaster et al., 2019). In the western Huab Basin, siliciclastic sedimentary rocks of the arid Twyfelfontein Formation and the flood basalts (Tafelberg Formation) of the Etendeka Group correlate with its Brazilian counterparts of the sedimentary Botucatu, and the volcanic Serra Geral Group (Milner, 1986; Stollhofen et al., 2000; Miller, 2008; Rosetti et al., 2018).

On the opposite margin in South America (Figs. 1, 3b; S2), sedimentary rocks of the Paraná Basin (#12) document the geological evolution of the later Paraná-Etendeka LIP central area in SE Brazil. Ordovician to Jurassic, siliciclastic and carbonate rocks overlay the Neoproterozoic basement (Milani et al., 2007). However, mainly marine rocks are related to the lower Paraná Basin supersequences (Rio Ivaí and Paraná) followed discordantly by Late Carboniferous to Triassic sedimentary rocks (Gondwana I and II). From Late Triassic to Late Cretaceous, erosional processes with an unclear onset occurred as no evidence of further sedimentation is recorded. Deposition resumed with overlaying eolian sands of the Botucatu Formation and the occurrence of Paraná-Etendeka flood basalts (Serra Geral Group). The flood basalts of both, NW Namibia and SE Brazil, are coeval with the syn-rift stage of the South Atlantic rift evolution (Renne et al., 1992; Renne et al., 1996; Torsvik et al., 2006).

Several major continental basins surround the Paraná-Etendeka LIP on both continents (Fig. 1). In SW Africa, further to the east and the

south, stratigraphic records of the Karasburg (#4), Aranos (#5), the Central Kalahari (#6), and the Mid Zambezi (#7) basins indicate a similar geological evolution dominated by sedimentary rocks of the Karoo (#8) Supergroup (Fig. 3a) (Johnson et al., 1996; Catuneanu et al., 2005; Haddon et al., 2005; Nxumalo et al., 2011; Berti, 2014; Phiri et al., 2016). Further northeast, the geological evolution of the central African Congo Basin (#9) is characterized by Early Paleozoic, Carboniferous to Triassic, and Jurassic to Cretaceous depositional sequences (Crosby et al., 2010; Kadima et al., 2011).

In South America (Figs. 1, 3b), two large sedimentary basins record the Late Paleozoic to Mesozoic geological evolution in NE Brazil. Whereas the northern Paranaíba Basin (#10) documents almost continuous deposition from the Silurian to the Late Cretaceous, only Carboniferous to Permian, and Cretaceous sedimentary rocks can be found in the stratigraphic record of the São Francisco Basin (#11) further south (Milani et al., 2007).

Sedimentary sections of the Argentine Salado (#14, onshore), Northeastern Paleozoic/Cretaceous (#15), Cuyana (#16), Neuquén (#17), San Jorge (#18), and Austral-Magallanes (#19) basins show a differentiated, younger evolution mostly dominated by Mesozoic sedimentary rocks (Kokogian et al., 1993; Carol et al., 2010; Baristean et al., 2013; Naipauer et al., 2014; Uliana et al., 2014).

#### 3.2. Post-Paraná-Etendeka plume event evolution of the southern-central SAPCM offshore basins

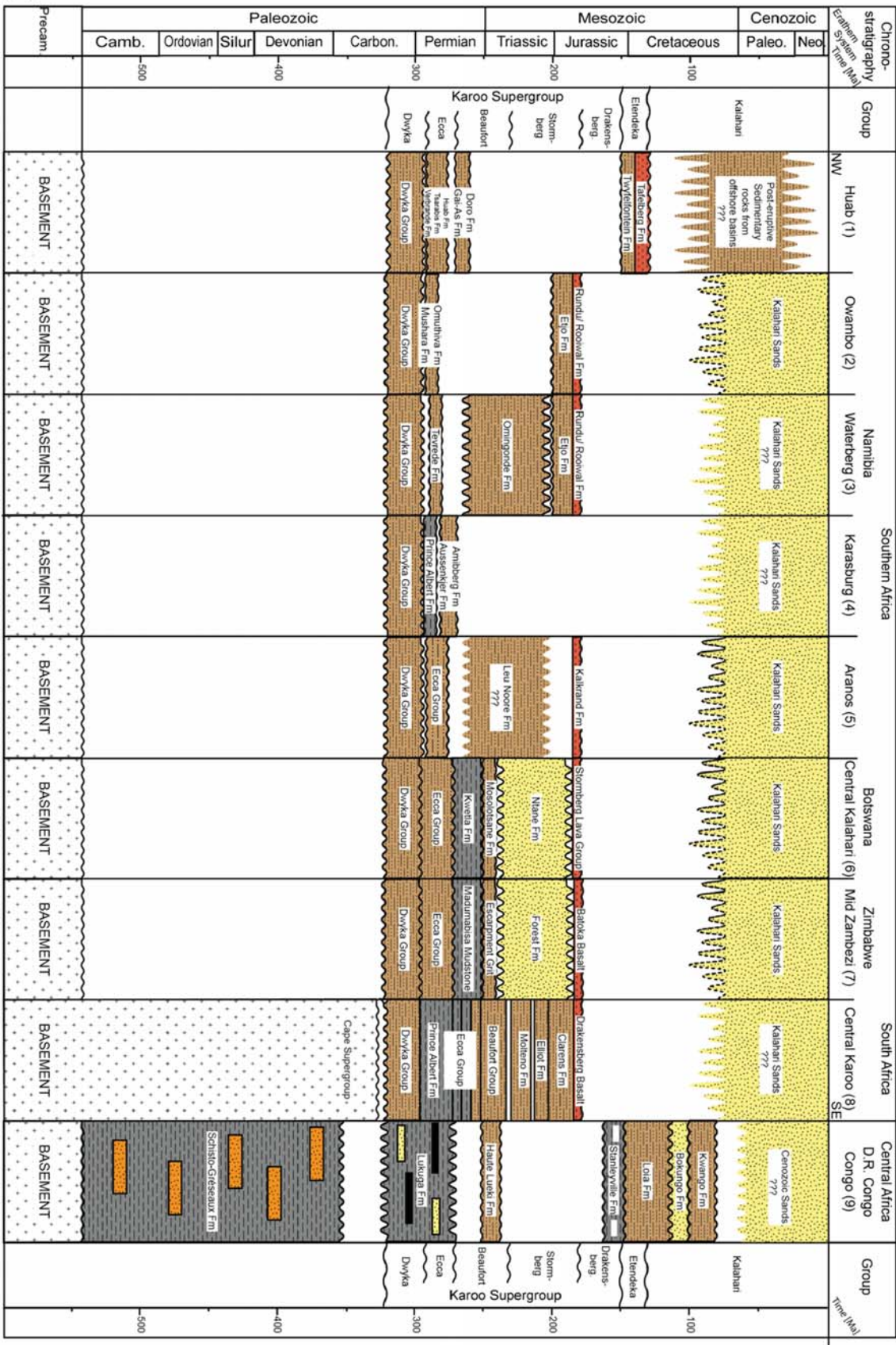
Continuous narrow rifting, the opening of the South Atlantic, and oceanic spreading triggered Gondwana to move further apart leading to the syn- to post-rift evolution of several offshore basins along the SAPCMs (Figs. 1, 3c, #a–r). Along the SW African SAPCM, finer-grained marine sediments dominate the stratigraphic records of the offshore basins from the Congo in the north to South Africa in the south. Paraná-Etendeka volcanic rocks (Etendeka Formation) occur in the Kwanza (#b), and Benguela (#c) basins of Angola, in the Namibian basins of Namibe (#d), Walvis (#f), Luderitz (#g), and along the Walvis Ridge (#e), and partly in the Orange Basin (#h) offshore South Africa (Light et al., 1992; Bray et al., 1998; Marzoli et al., 1999; Schmidt 2004; Luft et al., 2005; de Vera et al., 2010; Guiraud et al., 2010; Nicolai et al., 2013; Schröder et al., 2015; Scarselli et al., 2016) These flood basalt depositions do not extend as far north as the Lower Congo Basin (#a), and as far south as the Cape Basin (#i) (Schmidt, 2004; Shone et al., 2005; Anka et al., 2013; Franke, 2013; Marcano et al., 2013).

The offshore basins of SE Brazil, Uruguay, and NE Argentina are characterized by mostly siliciclastic rocks with interposed depositions of either fine- or coarse-grained material (Milani et al., 2007; Carol et al., 2010; Contreras et al., 2011; Marcano et al., 2013). The Campos (#n), Santos (#o), Pelotas (#p) and Salado (#q, offshore) basins stand out due to the presence of volcanic flood basalt depositions of the Serra Geral Group (Milani et al., 2007; Rosetti et al., 2018).

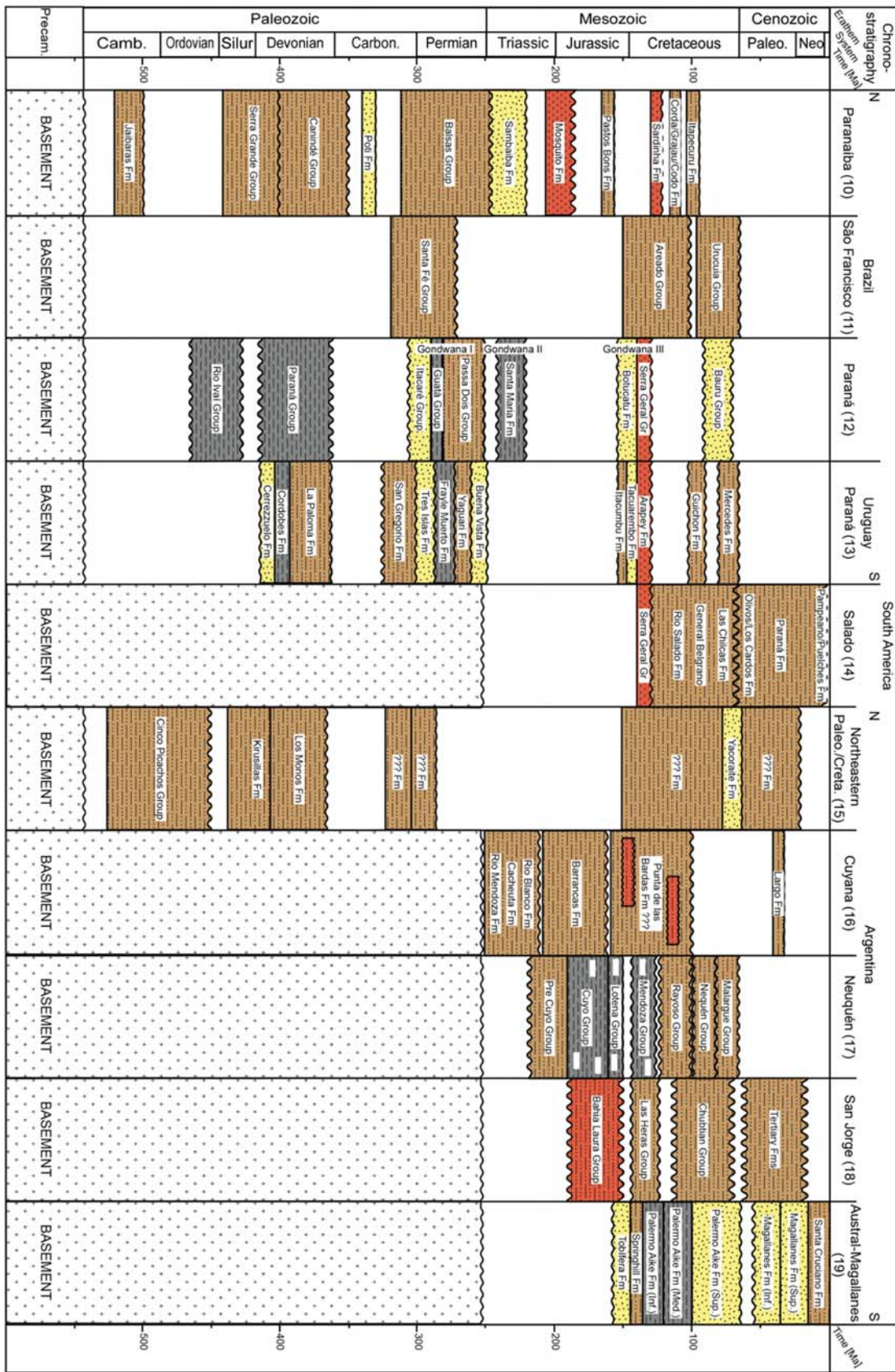
#### 3.3. Plume stratigraphic mapping of the Paraná-Etendeka LIP

We applied the ePSF (Friedrich et al., 2018) to map the full spatial distribution on the Earth's surface that may have been affected by the Paraná-Etendeka plume movement. The ePSF outlines signals and traces triggered by the plume movement that are expressed by distinct patterns in the stratigraphic records, e.g. hiatuses and missing sections prior to (pre-transit time), and following (transit time) the event horizon (initiation of the plume movement at the D<sup>''</sup>) (Fig. 4a). The transit time (depth of the Earth's mantle [km]/ average velocity of plate motion [cm/a]) describes the time of the plume head ascent from the initial plume movement (at time - 1, event horizon) to the event of the flood basalt eruptions (at time 0) (Iaffaldano and Bunge, 2015). The post plume evolution follows the flood basalt eruptions. Following the approach outlined by the ePSF, as an initial guess, the event horizon (-1) was set as ~60 Myr (transit time) prior the

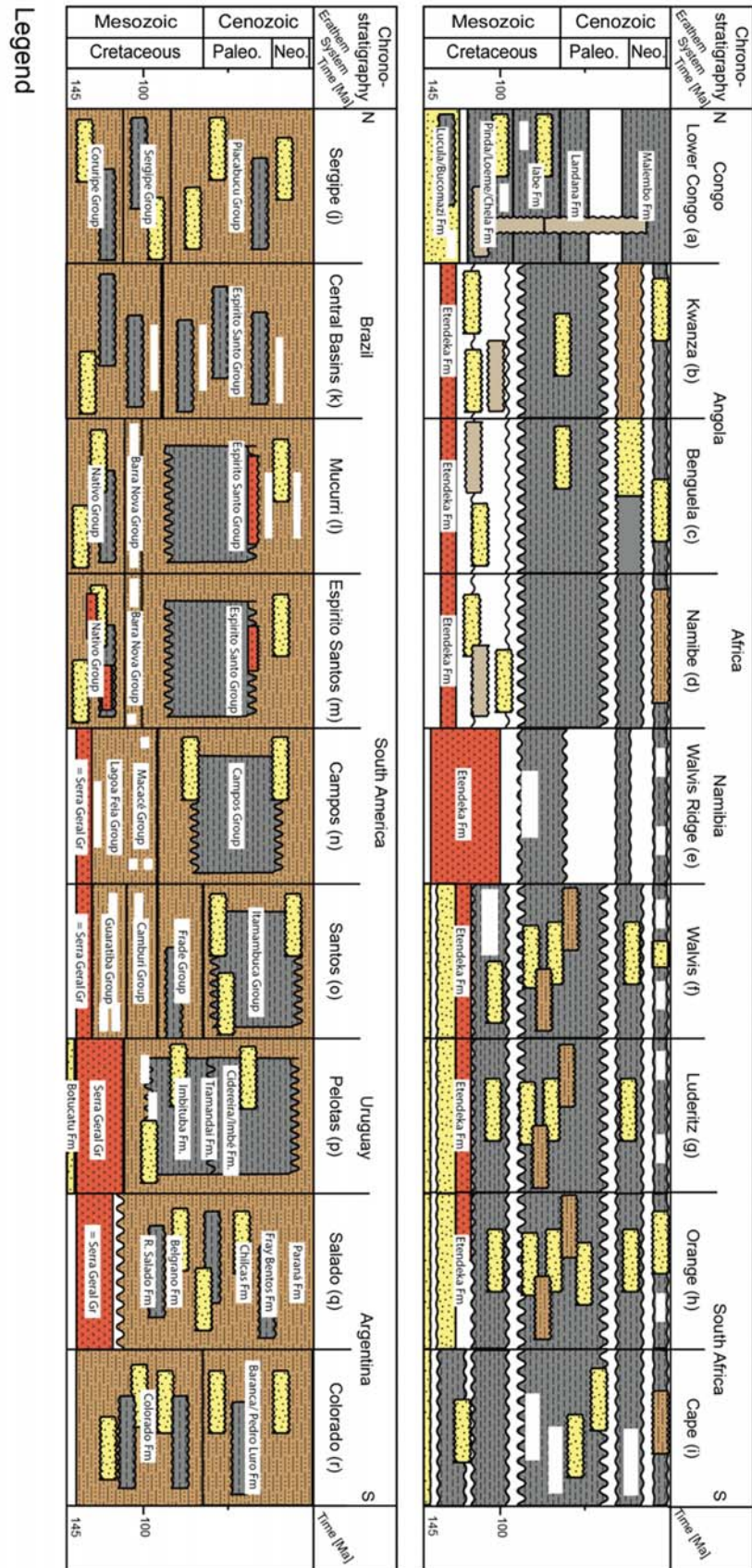
(A)



(B)



(C)



Paraná-Etendeka flood basalt eruptions (0). Then, we grouped the stratigraphic records of the sedimentary basins accordingly to similar patterns as described by the plume stratigraphic mapping approach and defined central, marginal, and distal regions to map and propose a full spatial distribution of the Paraná-Etendeka plume affected area on the Earth's surface (Figs. 4b, c, d; 5).

The ePSF defines the central area above the plume head with the occurrence of dike swarms and flood basalt depositions over stratigraphic unconformities and hiatuses. Characteristic stratigraphic records show hiatuses prior to the event horizon indicating a long continuous phase of rock uplift and erosion during the ascent of the rising mantle plume (Fig. S1). The ePSF expects a collapse of the central dome above the plume head, followed by the inversion and a renewed inward-directed phase of sedimentation. Consequently, the occurrence of (eolian/fine-grained) sedimentary rocks prior to the deposition of the flood basalts is essential for the plume center.

For the plume margin, the ePSF also implies a hiatus prior to, and following the event horizon, as intermediate sedimentary sections undergo initial surface uplift and erosion during the incipient ascent of the plume head correlating with the surface uplift in the plume center. This evolution is followed by a phase of sedimentation (Fig. 4a, unit 2, orange) signaling a first inversion related to the transient narrowing surface uplift of the plume center and accompanied relative subsidence of the margin. Subsequently, sedimentary sections show renewed outward-directed surface uplift and erosion as the plume head collapses and spreads laterally. Ideally, intermediate units (unit 2) are still preserved. However, marginal sedimentary sections are complex, dominated by multiple episodes of transient surface uplift and subsidence, resulting in repeated inversion of the margin region (Friedrich et al., 2018). Flood basalts can occur, though thinner deposits are expected.

Concluding, distal regions are those that hypothetically comprise nearly complete sedimentary sections that did not experience any plume-related surface uplift and erosion, and their geological evolution seems to be clearly disconnected from any plume related impact.

### 3.4. Results and discussion of the stratigraphic mapping of the Paraná-Etendeka LIP

#### 3.4.1. Plume Center

The sedimentary sections of the NW Namibian Huab (#1) and the SE Brazilian (#12), and Uruguayan (#13) Paraná basins (Figs. 4b, c; 5) fulfill all requirements of the plume stratigraphic mapping to define them as part of the plume center. Their stratigraphic records show hiatuses and large missing section for the time before and after the event horizon. Furthermore, a section of eolian or fine-grained siliciclastic rocks is recorded for all three basins interfingering with the overlying Paraná-Etendeka flood basalts. Therefore, their stratigraphic records are consistent with the set of criteria (i.e., hiatus pattern) expected based on the ePSF.

However, the strict compliance to the set of criteria would leave out areas showing expected indications of a potential plume center (e.g., dike swarms and flood basalt depositions, Ernst and Buchan, 1997). Therefore, we decided to extend the set of criteria of the ePSF, to include areas of the combined occurrence of Paraná-Etendeka related dike

swarms and flood basalt depositions to broaden the Paraná-Etendeka LIP central area (Fig. 5). Doing so also allows including the offshore basins showing evidence of flood basalt depositions (Franke, 2013; Stica et al., 2014). This holds from north to south for the African Kwanza (#b), Benguela (#c), Namibe (#d), Walvis (#f), and Luderitz (#g) basins and the Walvis Ridge (#e) (Etendeka Formation) (Fig. 4d). The southernmost Orange Basin (#h) and the Brazilian Espirito Santo Basin (#m) in the north may represent the transition from center to margin partly showing flood basalt deposition. The stratigraphic records of the following Campos (#n), Santos (#o), Pelotas (#p), and Salado (#q) basins display flood basalts of the Serra Geral Group and can be associated with the central area of the Paraná-Etendeka LIP (Franke, 2013).

#### 3.4.2. Plume margin

We suggest the Namibian Owambo (#2), Waterberg (#3) and Karasburg (#4) basins as the marginal regions on the SW African plate (Figs. 4b, c, 5). Their sedimentary sections show large unconformities indicating long and/or intense phases of surface uplift and erosion. However, neither evidence of flood basalt depositions in their stratigraphic records exists, nor are they clearly described in published literature.

Furthermore, there is evidence of siliciclastic sedimentary rocks (Etjo Formation) followed by flood basalts that correlate in age with the Karoo LIP event (Rundu/Rooiwal Formation). Therefore, we assume that the signal of the Paraná-Etendeka plume movement and its predicted stratigraphic patterns on the Earth's surface might have been disturbed by the large-scale effects of the prior Karoo event and its stratigraphic consequences. Nevertheless, due to the clear influence by vertical movement and the proximity to the Paraná-Etendeka related dike swarms these sections were attributed to the marginal region (Fig. 5).

Although, preserved Paraná-Etendeka flood basalt deposits in the NE Argentine Salado Basin (#14) imply a central impact in the stratigraphic record, a section possibly correlated with a unit 4b is missing. Also, there is no evidence of dike swarms related to the Paraná-Etendeka LIP. Therefore, the Argentine Salado Basin (#14) more likely represents the plume margin.

#### 3.4.3. Distal regions

The SW African Aranos (#5), Central Kalahari (#6), Mid Zambezi (#7), and Central Karoo (#8) basins show sedimentary sections rather interrupted or more likely dominated by the earlier Karoo event (Figs. 4b, c, 5) (Duncan et al., 1997). However, they clearly dispose hiatuses and large missing sections for the Late Jurassic to Late Cretaceous indicating long phases of surface uplift and erosion. Nevertheless, their stratigraphic records do not fulfill the requirement of the ePSF to define them as central or marginal regions. The geological evolution of the central African Congo Basin (#9) is clearly disconnected from the geological evolution of the basins located in SW Africa (Kadima et al., 2011) and does not follow any stratigraphic patterns as predicted by the ePSF. This also holds for the stratigraphic records of the Argentine basins (#15–19) that do not show evidence of a possible plume influence when viewed in the frame of the model.

**Fig. 3.** a: Stratigraphic records of the major continental, Paleozoic to Mesozoic, sedimentary basins in SW Africa. For further explanations concerning sedimentology and lithologies, see legend in Fig. 3c. Basins and corresponding references (please see supplementary material): (1) Huab: [S12], [S51]; (2) Owambo: [S12], [S51]; (3) Waterberg: [S12], [S51]; (4) Karasburg: [S3], [S12], [S51]; [S72]; (5) Aranos: Following numbers in square brackets refer back to the references accordingly to their order constraint within the reference list of the publication and additional references in the supplementary material [Sxx]. [S3], [S12], [S51]; [S77]; (6) Central Kalahari: [S12], [S40], [S51], [S77], [S82]; (7) Mid Zambezi: [S12], [S51], [S77], [S82]; (8) Central Karoo: [S3], [S12], [S51]; [S77]; (9) Congo: [S17]; [S52]. b: Stratigraphic records of the major continental, Paleozoic to Mesozoic, sedimentary basins in South America. For further explanations concerning sedimentology and lithologies, see legend in Fig. 3c. Basins and corresponding references (please see supplementary material): (10) Paranaíba: [53]; (11) São Francisco: [53]; (12) Paraná (Brazil): [53]; (13) Paraná (Uruguay): [53]; (14) Salado: [S11]; (15) Northeastern Paleo/Cretaceous: [S105]; (16) Cuyana: [S105]; (17) Neuquén: [S75], [S105]; (18) San Jorge: [S105]; (19) Austral-Magallanes: [S2], [S105]. c: Stratigraphic records of the major marine, Lower Cretaceous to recent, sedimentary basins along the SAPCM of SW Africa and South America. Basins and corresponding references (please see supplementary material): SW African: (a) Lower Congo: [2], [S72]; (b) Kwanza: [S36], [S72], [S76], [S88]; (c) Benguela: [S88], [S89]; (d) Namibe: [S88], [S89]; (e) Walvis Ridge: [S7], [S88]; (f) Walvis: [S7], [S67], [S88]; (g) Luderitz: [S64], [S88]; (h) Orange: [S19], [S64], [S65], [S71], [S87], [S88]; (i) Cape: [S88], [S92]; South American basins: (j) Sergipe: [53]; (k) Central basins: [53]; (l) Mucurri: [53]; (m) Espirito Santos: [53]; (n) Campos: [53]; [S15], [S71], (o) Santos: [53]; [S15], (p) Pelotas: [53]; [S15], (q) Salado: [S11]; (r) Colorado: [S65], [S71], [S80], [S107].

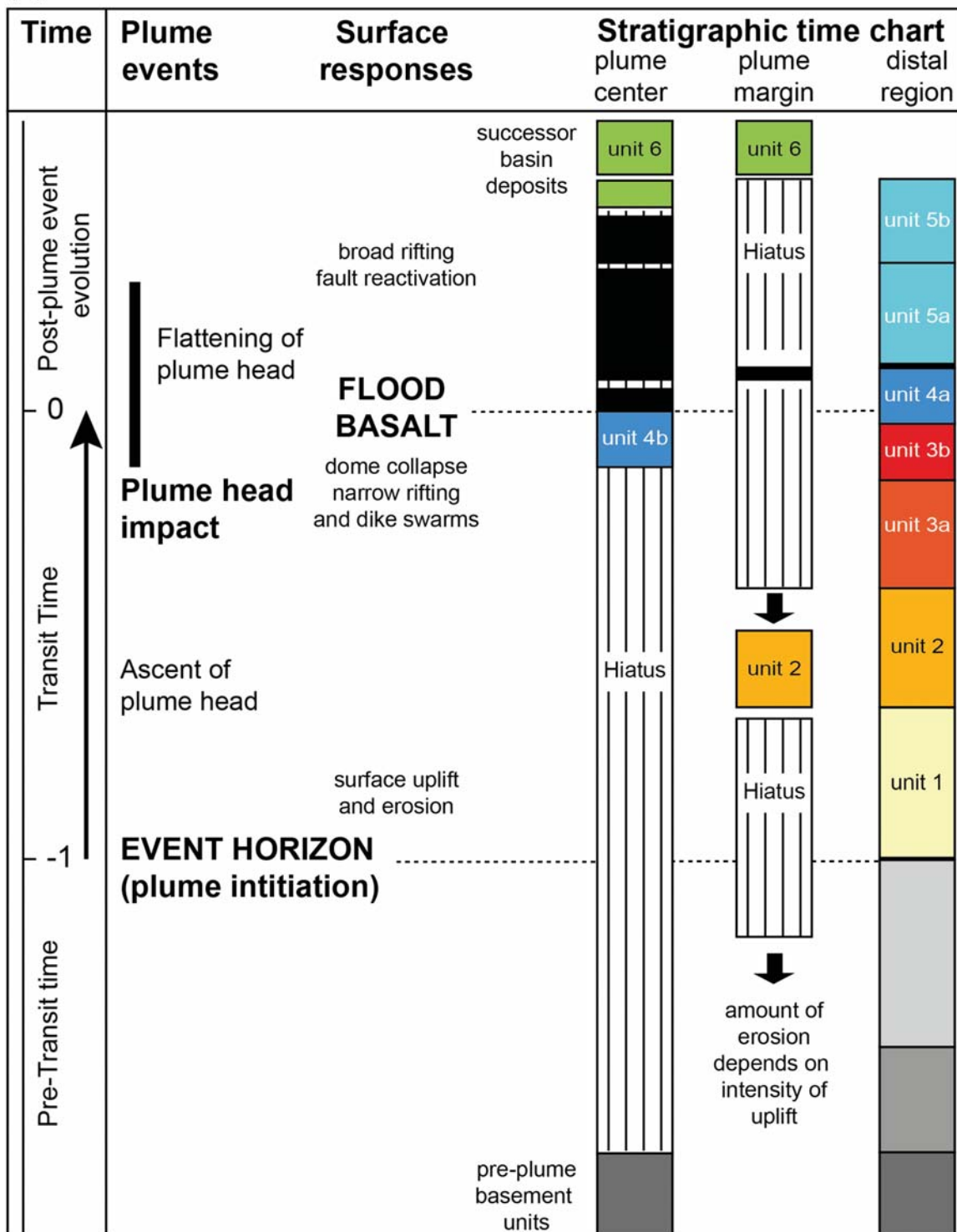
3.4.4. Critical view and uncertainty analysis

This study's approach requires a sincere analysis of appearing uncertainties during the application of the stratigraphic framework outlined by the ePSF, and therefore, we critically reviewed our findings for both, the compiled stratigraphic records and the theoretical model.

Whereas the definition of a plume center proved to be relatively viable, the mapping of the plume margin and the distal areas turn out

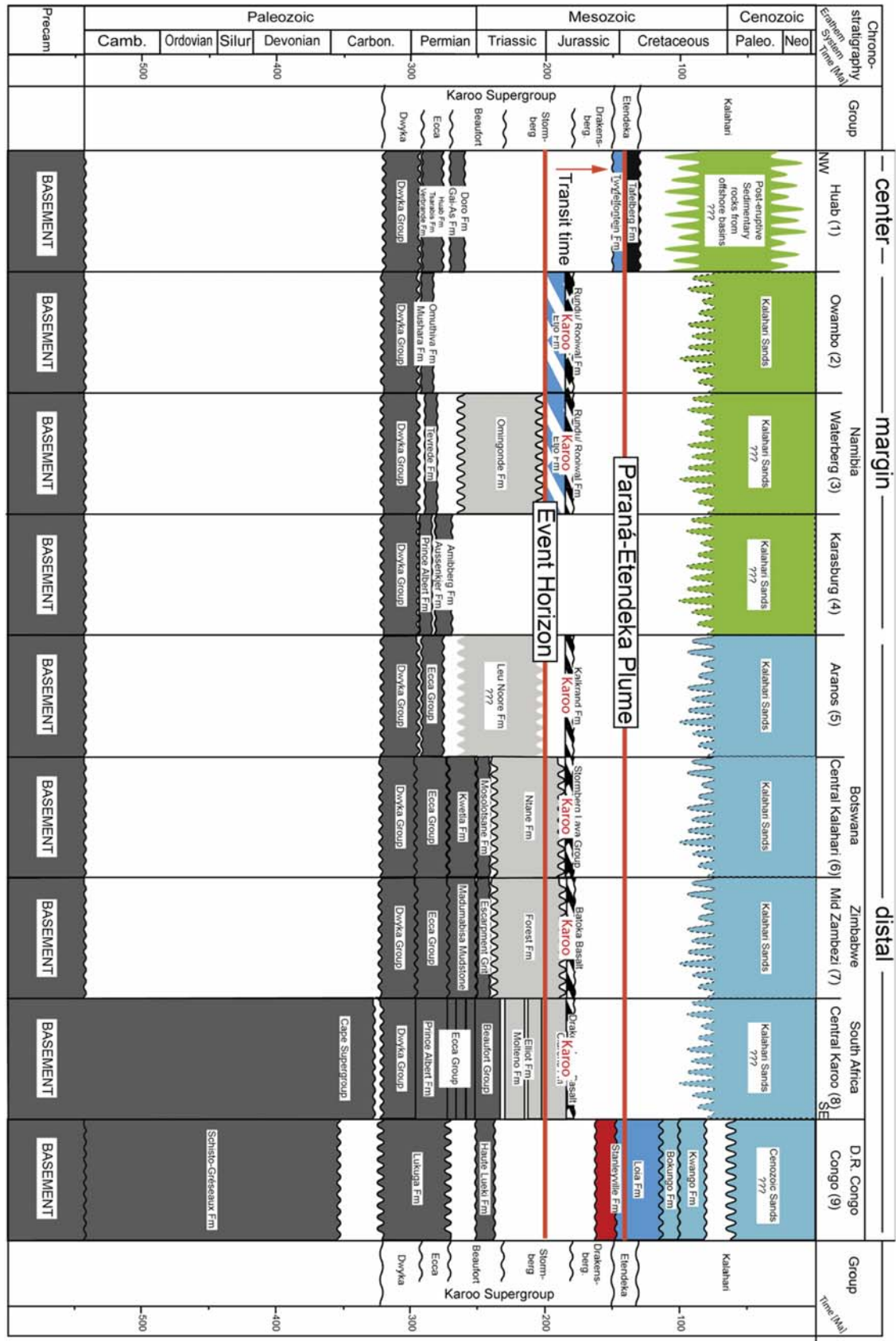
to be possibly flawed. Nevertheless, we the stratigraphic records display signals and traces of the plume movement well when applied to the Paraná-Etendeka LIP within the Mesozoic SW Gondwana intraplate environment. By using the ePSF, we recognize hiatuses and unconformities in the sedimentary sections of the plume center and the margin preceding the Paraná-Etendeka LIP event, and it is viable to map a spatial distribution of the mantle plume affected area within

(A)

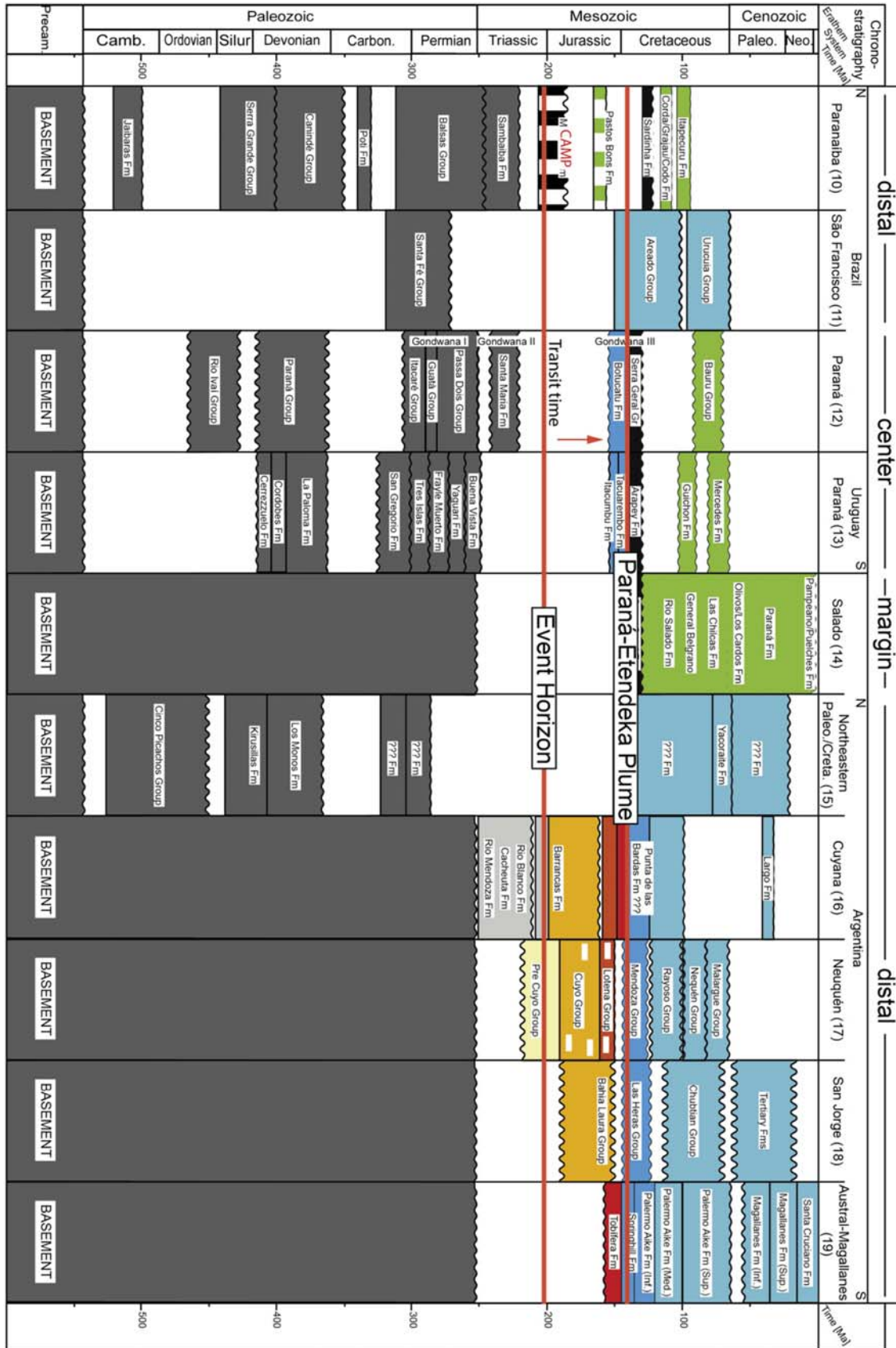




(B)



(C)



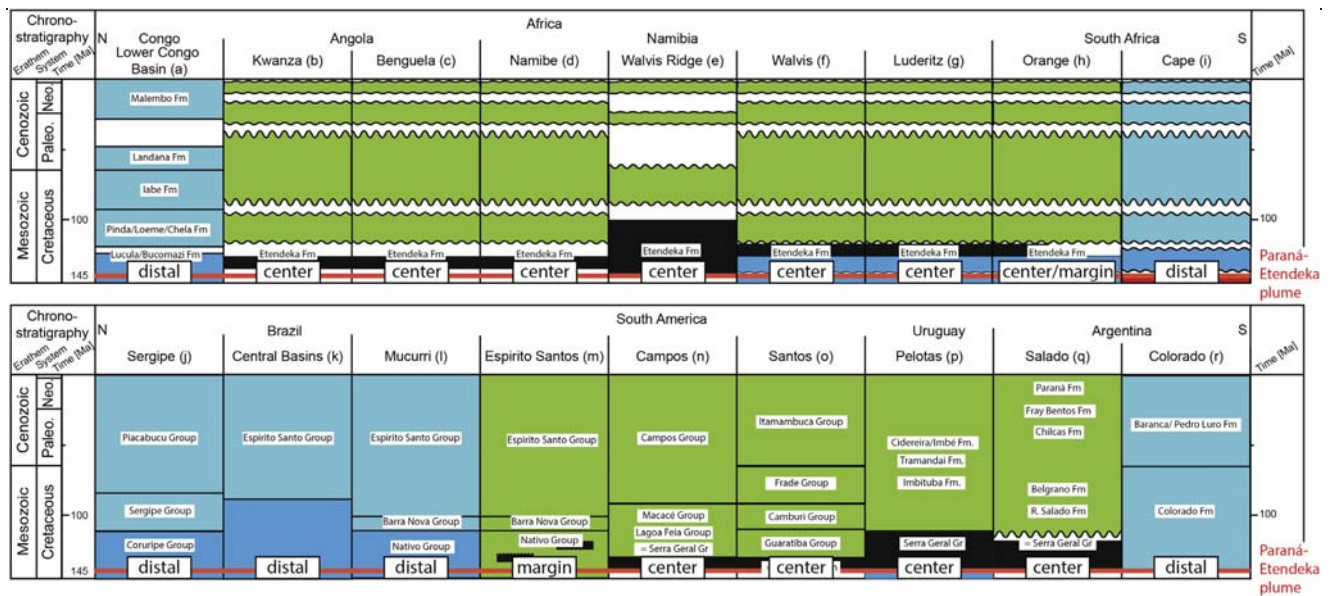


**Fig. 4.** a: Diagram of the plume stratigraphic mapping approach as published within the ePSF (modified after Friedrich et al., 2018). Theoretical time scale and chronostratigraphic chart that would result from a plume-head event that initiated at the core-mantle boundary. Time scale on left is relative to mantle-plume models and shows the plume transit time (Iaffaldano and Bunge, 2015) pinned to the eruption of the flood basalts (at time 0) and the event horizon (at time - 1). Information on chronostratigraphic charts does not account for the thickness of a unit (refer to stratigraphic column), but best represents the formation time b: Plume stratigraphic mapped stratigraphic records of the major continental, Paleozoic to Mesozoic, sedimentary basins in SW Africa. Based on the chronostratigraphic record and the predicted map pattern by Friedrich et al., 2018 (Fig. 4a), we defined the individual sedimentary sections as plume center, a plume margin, or distal region. The lower red line indicates the plume event horizon -60 Myr (transit time) prior to the Paraná-Etendeka LIP event (upper red line). For further information concerning sedimentology and lithologies, please see Fig. 3a and 3c. c: Plume stratigraphic mapped stratigraphic records of the major continental, Paleozoic to Mesozoic, sedimentary basins in South America. Based on the chronostratigraphic record and the predicted map pattern by Friedrich et al., 2018 (Fig. 4a), we defined the individual sedimentary sections as plume center, a plume margin, or distal region. The lower red line indicates the plume event horizon -60 Myr (transit time) prior to the Paraná-Etendeka LIP event (upper red line). For further information concerning sedimentology and lithologies, please see Fig. 3b and 3c. d: Plume stratigraphic mapped stratigraphic records of the major marine, Lower Cretaceous to recent, sedimentary basins along the SAPCM of SW Africa and South America. Based on the chronostratigraphic record and the predicted map pattern by Friedrich et al., 2018 (Fig. 4a), we defined the individual sedimentary sections as plume center, a plume margin, or distal region. The thin red line indicates the Paraná-Etendeka LIP event. For further information concerning sedimentology and lithologies, please see Fig. 3c. (For interpretation of the references to colour in this figure legend, the reader is referred to the web version of this article.)

the Mesozoic SW Gondwana intraplate environment. However, the observed uncertainties allow a range in both, the spatial and the temporal scale.

Several stratigraphic records of the Mesozoic SW Gondwana intraplate environment possibly permit a slightly deviated definition moving away from the strict requirements for the stratigraphic patterns outlined by the ePSF. Particularly, the stratigraphic records of the southern African basins show uncertainties regarding their classifications. The Owambo (#2), Waterberg (#3), and Karasburg (#4) basins provide large hiatuses but lack Etendeka volcanic rocks, though Etendeka related dike swarms occur in the vicinity, and therefore, allow a possible definition as part of the plume center for this area. Nevertheless, they also contain preserved volcanic rocks of the Karoo LIP, and thus, indicate a strong influence by the previous Karoo LIP event. Consequently, the large hiatuses could also stem from the Karoo event.

Beyond the possible plume center, the stratigraphic records permit more possibilities to widen the plume margin. In the north, an inclusion of the Brazilian Paranaíba (#10) and the São Francisco basins (#11) is more likely due to their hiatuses and missing sections. The sedimentary section of the northern most Paranaíba (#10) Basin might also show a potential Central American Magmatic Province (CAMP) signal providing CAMP related flood basalt depositions (Milani et al., 2007). We also recognize a similar timing of the hiatus in the Argentine NE Pale./Cretaceous (#15) Basin that entitles an inclusion to a possible plume margin, though possibly following sections are not preserved.

Towards the south, the plume margin may be wide, as the sedimentary sections of the Argentine San Jorge (#18) and Austral-Magallanes (#19) basins indicate a similar timing of the hiatus correlating with the central basins in the plume center. Nevertheless, an interpretation towards the south and the southwestern areas is highly

complex due to the previous large-scale Karoo LIP event effects and its stratigraphic consequences (Storey et al., 2013; Navarrete et al., 2019). A possible scenario could be a coupled combination of rock and surface uplift signals of both consecutive plume events leading to overlapping long-time uplifted areas expressed by large hiatuses and missing sections as seen in the Sierra Australis and Sierra Septentrionales (Kollenz et al., 2016). This could also yield for the Uruguayan Paraná (#13), Salado (#14), NE Pale./Cretaceous (#15), and Neuquén (#17) basins. However, these areas can be still defined as the Paraná-Etendeka plume margin.

On the African side, an interference of the Karoo plume effects is also highly imminent as the sedimentary sections of the central southern African basins (#5–8) most likely reveal consequences of the large-scale Karoo LIP event (Storey et al., 2013; Navarrete et al., 2019) comprising Karoo-related flood basalt depositions and fine-grained siliciclastic sections. Therefore, we are not able to recognize Paraná-Etendeka plume related stratigraphic signals in those records constraining the western ranges of the plume margin relatively clearly to a minimum on the contemporary African continent.

We assume a highly differentiated predisposition of the mantle rheology concerning upper mantle viscosities and lithosphere rigidities for the SW Mesozoic Gondwana intraplate environment (Richards and Hager, 1984; Mitrovic, 1996; Lithgow-Bertelloni and Gurnis, 1997; Yang and Gurnis, 2016;) that enabled the formation of the displayed basin geometry (Watts et al., 1982; Beaumont, 1978; White and Lovell, 1997; Petersen et al., 2010, 2018), and probably had its role on the ascent of the rising plume head, the direction of lateral deflected asthenospheric material flow (Sleep, 1997; Ebinger and Sleep, 1998) and lastly the spatial distribution of the Paraná-Etendeka flood basalts on the Earth's surface (Sack and Usami et al., 2013). Therefore, we assume that the predisposition of the Karoo LIP may have prevented

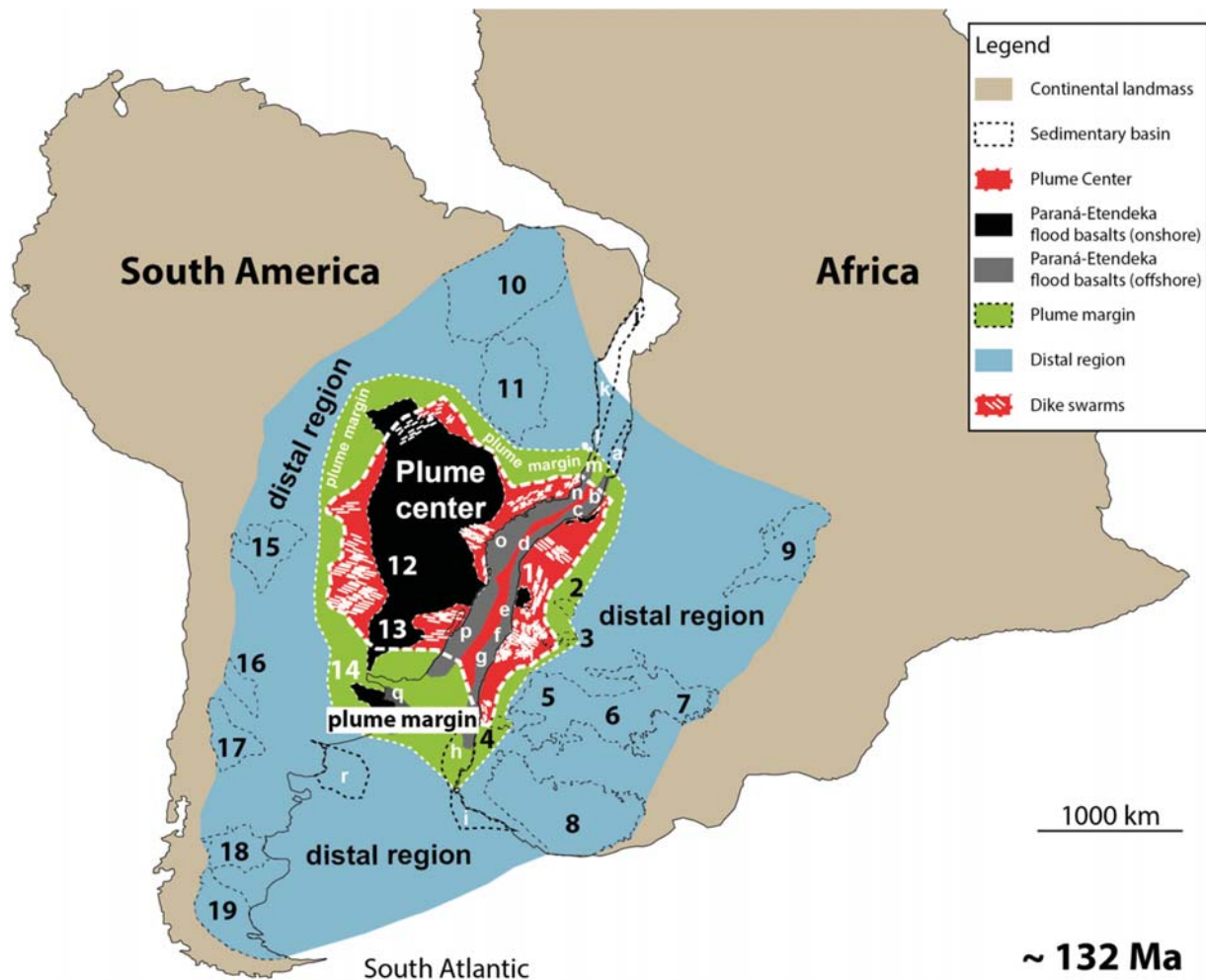


**Fig. 5.** Plume stratigraphic mapped, lateral distribution of the Paraná-Etendeka LIP during the Mesozoic SW Gondwana intraplate environment. Based on the chronostratigraphic record and the predicted map pattern by Friedrich et al., 2018 (Fig. 4a), we defined the individual sedimentary sections as plume center, a plume margin, or distal region. For further information concerning names of basins, reference for paleogeography and location of flood basalt depositions and Paraná-Etendeka related dike swarms, please see Figs. 1, 4b, c, d. Red area: possible plume center; green area: plume margin; blue area: distal regions. For further information, please see Fig. 1. (For interpretation of the references to colour in this figure legend, the reader is referred to the web version of this article.)

the rising Paraná-Etendeka plume head from influencing the present southern African continent during the initial ascent (~Late Triassic/Early Jurassic). Otherwise, the stratigraphic records of the southern-central African basins (#2–8) show hiatuses implying surface uplift and erosion beginning during the Mid Jurassic and may indicate traces of the predominantly uplifted areas during the lateral deflection of asthenospheric mantle flow as the plume head reached the top of the lithosphere (Sleep, 1997; Ebinger and Sleep, 1998).

In the north-western Paraná-Etendeka LIP area, the sedimentary record of the Congo (#9) Basin also leaves room for speculation as we recognize an early hiatus signaling a potential Paraná-Etendeka LIP related surface rock and surface uplift. Sedimentation recommenced during the Late Jurassic that possibly implies the deposition of eastwards transported sediment material indicating the flattening of the plume head at the base of the lithosphere and the horizontal deflection of the initially vertical transported material (Leng and Zhong, 2010). Such a signal can also be recognized in the southern Austral-Magallanes (#19) Basin where deposition is reinstated evidently during the Late Jurassic.

However, we would like to emphasize that overestimation of individual stratigraphic data is as always imminent. Sedimentary sections are often fraught with large uncertainties related to the reliability of the lateral extension, since stratigraphic records are highly

dependent on borehole locations, e.g. this research had to rely on a single stratigraphic profile for the entire Paraná Basin. Therefore, this research often had to cope with single sedimentary sections reflecting the geological evolution of entire basins comprising large areas and different geological regimes. Consequently, this study had to build on to the assumption of homogenous depositions waiving the lateral discrepancies of the sedimentological evolution that should not be ruled out. Further uncertainties that have to be dealt with include erosional unconformities (nonconformities; Fig. 4a; Friedrich et al., 2018) and the temporal interpretation of hiatuses, and unpreserved but potentially originally existing sections. Signals of events can also be disturbed or overprinted by other geological events and, therefore, the accuracy and clarity can be a significant problem. Moreover, rocks get eroded differently and other parameters, such as climate, chemical and physical weathering, and the composition of rocks should be taken into account when analysing stratigraphic records. Whereas the spatial distribution of the Paraná-Etendeka plume influenced area on the Earth's surface can be relatively clearly constrained, a similar interpretation to constrain the temporal range of the plume ascent remains rather uncertain. Whereas, the hiatuses in the stratigraphic records of the central basins (#1, #12, and #13) indicate an upper limit for the event horizon not exceeding the Early Triassic, the data does not provide a similar assumptions towards a lower limit as most

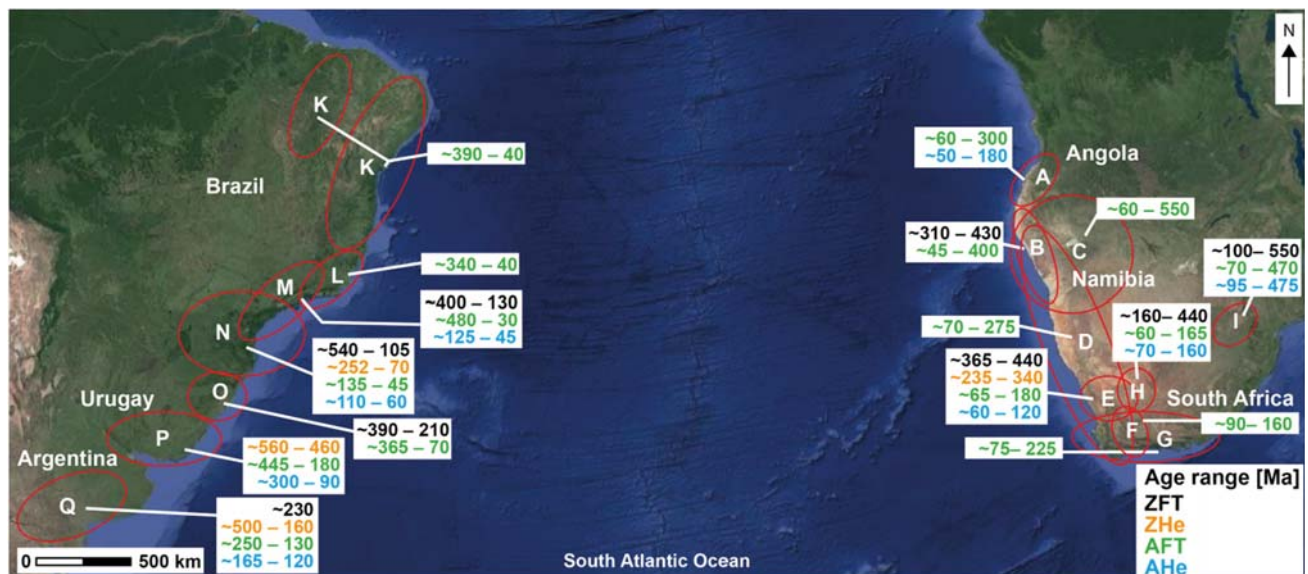


Fig. 6. Simplified Overview of the existing low temperature thermochronology (LTT) data sets along the SAPCMs of SW Africa from NW Angola to South Africa and Zimbabwe, and South America from NE Brazil to NE Argentina (Google Earth). For further information and references, please see supplementary material (Table S1).

of the records lack preserved sedimentary sections to better constrain a possible transit time.

#### 4. Second Archive: thermochronological data sets of the SW African and NE to SE South American SAPCM

##### 4.1. Low-temperature thermochronology (LTT) data sets

Low-temperature thermochronology (LTT) data sets are excellent geological archives to quantify temperature-sensitive processes, such as the cooling and heating of rocks of the upper Earth's crust. While most of the LTT studies along the contemporary SAPCMs from NW Angola to South Africa, and Zimbabwe on the SW African plate and from NE Brazil to NE Argentina on the NE to SE South American plate dispose apatite FT and He data, information about the cooling of rocks from FT and He dating on zircon remains less comprehensive. Nevertheless, compiled data sets of both, FT and He analyses on apatite and zircon provide an excellent overview (Fig. 6; Table S1, for references please see supplementary material) to investigate whether existing LTT data sets are able to retrieve a possible thermal influence of the Paraná-Etendeka plume movement.

On the SW African side, apatite fission track (AFT) ages with youngest values confined to the coastal areas and significant age increase towards the inland range between ~60 Ma and ~550 Ma (Fig. 6, A–G). The trend of younger ages along the coast is also observed on the opposite South American SAPCM with a wide range of AFT ages between ~40 Ma to ~480 Ma (K–Q). Towards the south, data sets from Uruguay (P) and Argentina (Q) indicate older AFT ages reaching from ~200 Ma, and ~130 Ma respectively, to ~325 Ma, or rather ~250 Ma.

Fewer data exists of (U–Th–Sm)/He analyses on apatite (AHe) showing ages between ~50 Ma and ~180 Ma along the Angolan SAPCM, and between ~60 Ma and ~160 Ma in South Africa (Fig. 6, A, E, and H). In Zimbabwe (I) AHe ages correlate with the AFT age range revealing ages between ~95 Ma and ~475 Ma. In SE Brazil, AHe data shows ages between ~45 Ma and ~125 Ma (M, and N). For the Uruguayan (P) and Argentine (Q) SAPCM, AHe data reaches also older ages between ~90 Ma, and ~120 Ma, respectively, and ~300 Ma, or rather ~165 Ma corresponding to the AFT age distribution in these regions.

For both dating techniques using zircon (ZFT and ZHe) few data exists along the SW African SAPCM. However, ZFT data lies between ~310 Ma and ~440 Ma for areas in NW Namibia (Fig. 6, B), and in SW South Africa (E, and H). ZFT Ages of Zimbabwe (I) indicate a wide age spread ranging from younger ages ~100 Ma and reach old ages of up to ~500 Ma. Along the SW African SAPCM only one data set (E) represents the ZHe dating technique with ages between ~235 Ma and ~340 Ma. While ZFT ages on the opposite SAPCM range between ~105 Ma and ~540 Ma for SE Brazil (Fig. 6, M, N, and O), only one published ZFT age of ~230 Ma exists in NE Argentina (Q). The ZHe age distribution in SE Brazil (N) generally corresponds to the ZFT age trend, showing ages between ~70 Ma and ~525 Ma. Whereas ZHe data representing the Uruguayan (P) SAPCM provides the oldest ages between ~460 Ma and ~560 Ma, Argentine (Q) ZHe data correlates with the SE Brazilian data reaching from ~160 Ma to ~500 Ma.

##### 4.2. Visualization of apatite fission-track data sets

The visualization of multiple thermochronological data provides the possibility to investigate data sets related to their lateral age distribution. We decided to work with apatite fission track data solely due to the broad existence of published data, their probable reliability, and comprehensive lateral distribution along the SAPCMs of SW Africa and Zimbabwe, and NE to SE South America. We provide histograms of the AFT data sets showing the temporal correlations and traces to retrieve the Paraná-Etendeka plume movement and plotted the coherent AFT age distribution of the whole study area to investigate the possible spatial dimension of the Paraná-Etendeka plume surface uplift and thermally influenced area. Therefore, we only used (reset) Precambrian basement rock samples and reset sedimentary rock samples (when AFT age < formation age) since detritus ages (AFT age > formation age) would not represent the actual position of one's sample location and most likely lead to a wrong age interpretation.

##### 4.3. Results and discussion: thermochronological data sets in the perspective of the event-based plume stratigraphic framework (ePSF)

The coherent large-scale overview of the AFT age distribution integrates all AFT data sets surrounding the Paraná-Etendeka LIP and

enables the investigation of a large amount of data in the frame of the ePSF (Fig. 7). We compiled altogether 579 (from NW Brazil to Argentina), or rather 741 (SW Africa and Zimbabwe) AFT ages of over 35 research studies (Figs. 7, 8; for further information and references, see supplementary material Figs: S3; S4; Tables S1; S2; S3) to apply the ePSF on the thermochronological data surrounding the Paraná-Etendeka LIP during the Mesozoic SW Gondwana intraplate environment.

The majority of the reset ages (~70–80% (SW Africa) and ~60–70% (South America)) lie around or are younger than the Paraná-Etendeka flood basalt event (1) (Fig. 8; ~135 Ma) and therefore, most likely infer a thermal overprint caused by the Paraná-Etendeka volcanic activity. Post-volcanic cooling and thermal relaxation of the upper Earth's crust as predicted by the ePSF (Fig. 8, blue bar) and Hu et al. (2019) combined with syn- to post-rift rock and surface uplift, and erosion led to the displayed accumulation of AFT ages. Those thermally influenced ages form several well constrained age centers along the SAPCMs from NW Angola to South Africa and from NE Brazil to NE Argentina (Fig. 7, white circles A and B). The two most significant areas are exposed within the (A) Ponta Grossa Arch in SE Brazil and the opposite NW Namibian Damara Belt, and along the (B) Rio de Janeiro state coastal strip and the opposite Angolan SAPCM. Those areas coincide with the Paraná-Etendeka flood basalt depositions and the lateral Paraná-Etendeka related dike swarms distribution on both sides of the continents indicating a highly asymmetric plume central area with possibly two different eruption sources. Whereas we define the Angolan to Namibian and SE Brazilian coastal areas as part of the plume center, the South African region implies a differentiated thermal evolution (Braun et al., 2014).

A second significant smaller peak of accumulated AFT ages is observed between ~220 Ma and ~180 Ma meaning a total of ~5% (SW Africa) and ~8% (South America) of the displayed ages having formed during the Late Triassic/Early Jurassic and may reflect the initial plume movement (2) (Fig. 8; ~195 Ma, ePSF) that caused initial rock and surface uplift, and erosion during the incipient doming on the Earth's surface. Detritus ages (AFT age > formation age) for SW Africa clearly indicate a peak of ages following the first plume movement (2) and the subsequent phase of rock cooling. Though, their source is unknown and therefore their information leaves little room for interpretation.

In general, ages increase from the coastal areas towards the continental inland on both sides. Though, data sets are elusive within the continents and the age distribution is less constrained. However, areas showing ages of ~200 Ma coincide with the plume margin defined by the plume stratigraphic mapping (Fig. 5). The oldest ages are displayed in NE South Africa and Zimbabwe most likely indicating a Paraná-Etendeka plume undisturbed geological evolution (distal regions).

A third accumulation of AFT ages (~12% (SW Africa) and ~18% (South America)) may correspond to erosional processes during and following the Gondwana Ice House period (~350–220 Ma, pre-Transit time; Montañez and Poulsen, 2013).

#### 4.4. Critical view and uncertainty analysis

The application of thermochronological data on the Mesozoic SW Gondwana intraplate environment provide an excellent approach to trace possibly plume-related rock and surface uplift of parts of the upper crust (dynamic topography; Hager et al., 1985; Braun, 2010).

Yet, the interpretation of thermochronological data is complex and requires uncertainty analysis. The thermochronological data are spread over a large region, often lack in comprehensive age information, and are often influenced by the regional geology that impedes assumptions regarding interregional scale forces. Especially along the northern SAPCM of Brazil and along South Africa, non-plume related rifting and tectonic processes have to be considered to explain vertical movement. Braun et al. (2014) suggest Mid Cretaceous rock and surface uplift and increased erosion to be responsible for the rock cooling and therefore, the South African AFT age distribution. This also holds for the NE Brazilian SAPCM that is most likely syn- to post-rift related (e.g., Japsen

et al., 2012) and lacks Paraná-Etendeka flood basalt depositions and Paraná-Etendeka related dike swarms.

As for the SE Brazilian and NW Namibian SAPCM's, we suggest plume induced differentiated rock and surface uplift in the crust together with a strong thermal influence either explained by a temporal higher geothermal gradient derived from the Paraná-Etendeka related dike swarms, and/or the eruption and deposition of the Paraná-Etendeka flood basalts to explain the AFT age distribution. Moreover, the existing flood basalt depositions on- and offshore (Milani et al., 2007; Petrobras unpublished) combined with the geochemical determinations proving mantle plume signature (Trumbull et al., 2007; Keiding et al., 2013; Will et al., 2016; Stroncik et al., 2017; Owen-Smith et al., 2017, 2019; Hartmann et al., 2019) leave little room for interpretation. Although, non-plume-related vertical movement provide an excellent opportunity to explain local geological processes along the SAPCM's, for most of the data in SE Brazil, NW Namibia and also Uruguay a non-plume related evolution does not simply produce an equally good satisfactory explanation (Hueck et al., 2018; Krob et al., 2019). However, these different interpretations of the geological evolution provide the possibility to support a possible plume center, and marginal and distal regions outlined by the plume stratigraphic mapping (Figs. 5, 7).

Nevertheless, another major problem to trace and constrain pre-eruption Paraná-Etendeka plume movement includes the fact that most of the ages have been thermally overprinted during the volcanic activity and/or erupted flood basalts and/or non-plume related pre- to post-rifting processes, and therefore, often no information exists about the geological evolution prior to the Paraná-Etendeka flood basalt event. Therefore, it remains very uncertain to better constrain a possible Paraná-Etendeka plume horizon and verify the initial guess of a transit time of ~60 Ma (Colli et al., 2018). Nevertheless, the LTT data trace a possible signal of the first plume movement expressed by the accumulation of AFT ages that indicates cooling between ~220 and ~180 Ma, and therefore, possibly widens the range of the ePSF event horizon (~195 Ma).

## 5. Combining both archives: stratigraphic records and LTT data sets

### 5.1. Inverse numerical modeling to retrieve the *t*-*T*-evolution of the Paraná-Etendeka plume central area

When combined, both archives, stratigraphic and LTT data allow numerical modeling the *t*-*T*-evolution of the rocks of the Earth's upper crust that contribute to the understanding of long-term landscape evolution processes, such as rock uplift and exhumation (surface uplift and erosion), or rather subsidence and sedimentation of rocks on and near the Earth's surface (Fig. S5). As a formerly connected key area, the present SAPCMs of NW Namibia and SE Brazil are highly suitable to reconstruct the *t*-*T*-evolution of the Neoproterozoic basement under the influence of the vertical Paraná-Etendeka plume movement most likely reflecting the tectono-thermal evolution of the Paraná-Etendeka LIP central area (Torsvik et al., 2009; Franke, 2013).

Inverse numerical modeling of cooling and heating paths (*t*-*T*-history) provides the ability to test thermochronological data by using current fission-track annealing models (Ketcham et al., 2007a, b) and helium diffusion kinetics (Flowers et al., 2009; Guenther et al., 2013) against a constrained possible *t*-*T*-evolution derived from a geological evolution model (GEM). To retrieve the *t*-*T*-evolution under the influence of the vertical plume movement, we applied our thermochronological data set along the SAPCMs of NW Namibia (Krob et al., 2020; Eldracher pers. comm.) and SE Brazil (Karl et al., 2013; Krob et al., 2019) derived solely from metamorphic rocks of the Neoproterozoic basement to the software code HeFTy® (v.1.9.3; Ketcham, 2005; Ketcham et al., 2007a, b, 2009, 2017). For each individual sample the thermochronological data set was applied to HeFTy®. Whereas the thermochronological data set of NW Namibia only provided AFT data, the data set of SE Brazil allowed combining multi-chronometer thermochronological modeling using up

to four different thermochronometers (AFT, AHe, ZFT, and ZHe) for individual samples.

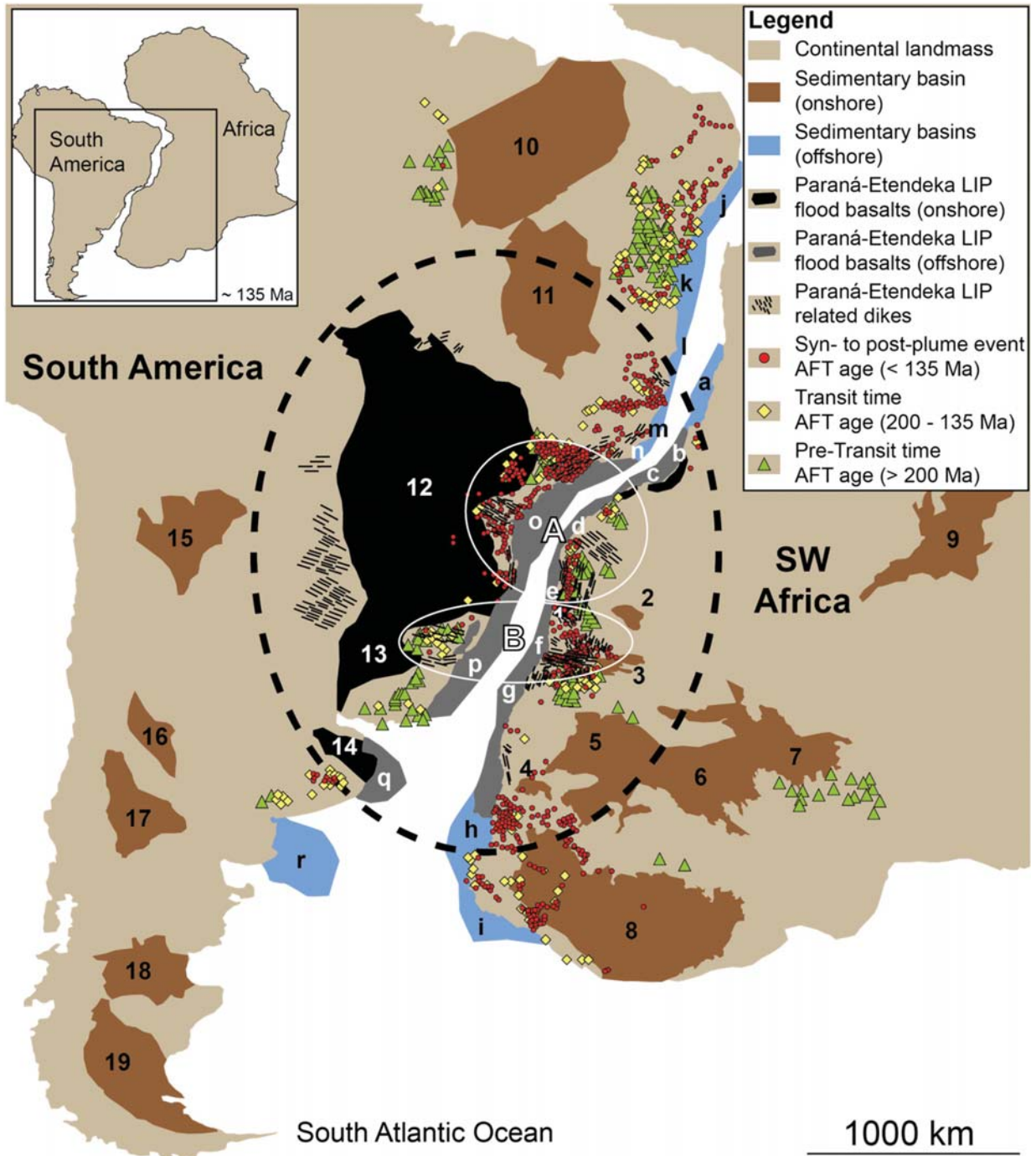


**Fig. 7.** Apatite fission-track (AFT) age distribution showing all AFT data sets along the SAPCMs of SW Africa from NW Angola to South Africa and Zimbabwe, and South America from NE Brazil to NE Argentina. AFT ages were subdivided in three groups: red dot: syn- to post-plume evolution (< 135 Ma); yellow square: Transit time (200–135 Ma); green triangle: pre-Transit time (> 200 Ma). For further information on the AFT data and corresponding references, please see Figs. S3, S4; Tabs: S2, S3). The figure includes all major Paleozoic to Mesozoic, continental (brown) and marine (blue), sedimentary basins (numbers and letters) surrounding the Paraná-Etendeka LIP (dashed circle, Franke, 2013), and on- and offshore Paraná-Etendeka flood basalt depositions (black) and Paraná-Etendeka related dike swarm locations (thin black lines) (Following numbers in square brackets refer back to the references accordingly to their order constraint within the reference list of the publication and additional references in the supplementary material [Sxx],[1]; [66]; [84]; [85]; see supplementary material: [S13]; [S14]; [S18]; [S31]; [S32]; [S44]; [S50]; [S72]; [S81]; [S96]; [S97]; [S100]; [S102]; [S103]). White circles (A and B) indicate possible plume centers showing predominantly AFT ages of the syn- to post-plume event (red) and coincide with Paraná-Etendeka related dike swarm locations. Paleogeographic reconstructions were taken from Torsvik et al. (2006, 2009, 2013). Onshore basins: SW Africa: 1: Huab; 2: Owambo; 3: Waterberg; 4: Karasburg; 5: Aranos; 6: Central Kalahari; 7: Mid-Zambezi; 8: Central Karoo; 9: Congo; South America: 10: Paranaíba; 11: São Francisco; 12: Paraná (Brazil); 13: Paraná (Uruguay); 14: Salado; 15: NE Paleo/Cretaceous; 16: Cuyana; 17: Neuquén; 18: San Jorge; 19: Austral-Magallanes; offshore basins: SW Africa: a: Lower Congo; b: Kwanza; c: Benguela; d: Namibe; e: Walvis Ridge; f: Walvis; g: Luderitz; h: Orange; i: Cape; South America: j: Sergipe; k: Central basins; l: Mucurri; m: Espirito Santo; n: Campos; o: Santos; p: Pelotas; q: Salado offshore; r: Colorado. For further information see Figs. 3a, b, c. (For interpretation of the references to colour in this figure legend, the reader is referred to the web version of this article.)

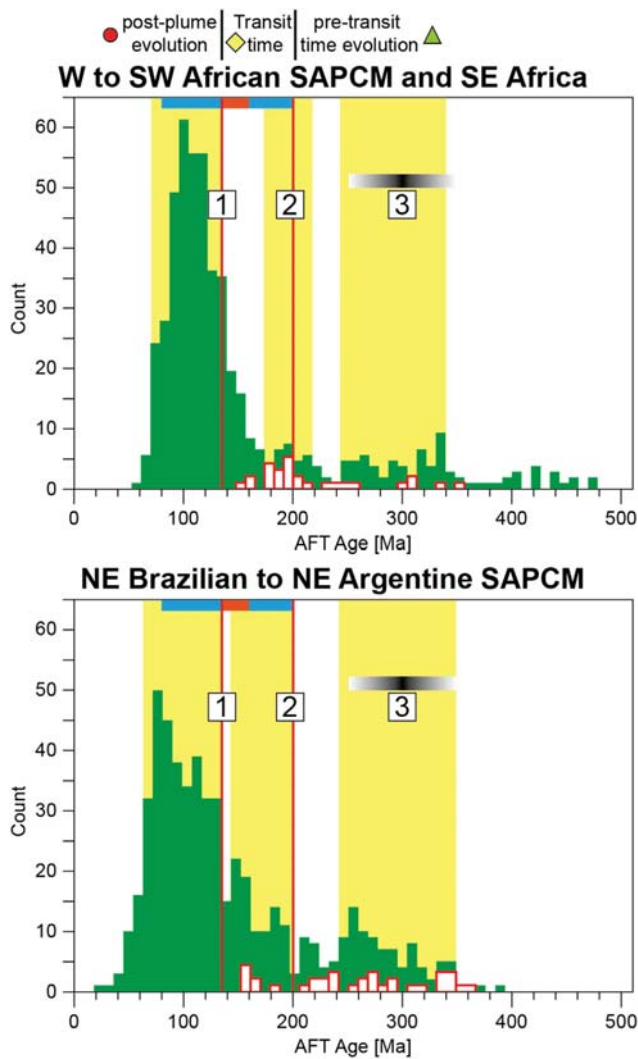


**Fig. 8.** Histograms of the AFT data sets along the SAPCMs of SW Africa from NW Angola to South Africa and Zimbabwe (upper), and South America from NE Brazil to NE Argentina (lower). AFT ages were plotted against their frequency without error. Green: 551 (SW Africa) and 707 (South America) reset AFT ages (AFT age < formation age); white: 27 (SW Africa) and 34 (South America) detritus AFT ages (AFT age > formation age); yellow bars: highlight exposed AFT age peaks; 1: Paraná-Etendeka flood basalt event (~135 Ma; Renne et al., 1992; Renne et al., 1996; Torsvik et al., 2006); 2: initial plume movement as predicted by the ePSF (Friedrich et al., 2018); 3: Gondwana Ice House period (Montañez and Poulsen, 2013). Upper blue (cooling) and red (heating) bars highlight the expected thermal processes as predicted by the ePSF. (For interpretation of the references to colour in this figure legend, the reader is referred to the web version of this article.)

## 5.2. Geological evolution model (GEM)

The GEM pretends a possible geological evolution assuming tectono-thermal processes (t-T-evolution) on the Earth's surface above the ascending plume head (Fig. S1) against the thermochronological data set is tested (Fig. S5). Therefore, it uses field observations and published stratigraphic (Figs. 3 a, b, c; S2), paleo-geographic (Scotese and Golonka, 1992; Scotese et al., 1999; Torsvik et al., 2009), and -climatic knowledge (Wygrala, 1989), the ascending mantle plume model (Campbell and Griffiths, 1990; Colli et al., 2018; Bunge and Glasmacher, 2018), and the ePSF (Fig. S1, Friedrich et al., 2018). Thereafter, the GEM is transferred into specific t-T-constraints (Figs. S6.1-S6.3) and applied to the modeling software.

The GEM mainly supervises the t-T-evolution (<300 °C) from the Triassic to Lower Cretaceous and predicts a first exhumation during the Early to mainly Late Paleozoic (Johnson et al., 1996; Stollhofen et al., 2000; Catuneanu et al., 2005; Milani et al., 2007). During the Triassic, we simulate coherent heating assuming the ongoing subsidence of the Late Paleozoic to Mesozoic basins (Paraná, Huab, Owambo, and Waterberg). From Early Jurassic, t-T-models are constrained by the observations of the stratigraphic records (e.g. occurring hiatuses and unconformities) that correlate with assumptions made by the ePSF and possibly reflect the initial plume movement. Therefore, the GEM simulates cooling assuming transient surface uplift during the plume head rise (Campbell and Griffiths, 1990; Bunge and Glasmacher, 2018). Following, t-T-constraints pretend a reheating during the Early Cretaceous assuming the thermal influence caused by the emplacement of dike swarms and the deposition of the Paraná-Etendeka flood basalts. Concluding, the GEM predicts renewed cooling during the Early Cretaceous that continues throughout the Cenozoic. Individual GEM-derived t-T-constraints may differ between sample locations within the different regions. However, equal t-T-coordinates were applied strictly to samples of the same geological region to guarantee better comparability of the t-T-histories of the modeled samples in their respective areas. Then, HeFTy® performs an inverse model and seeks paths that fit through the t-T-constraints considering the input thermochronological data.

## 5.3. Results of the numerical modeling of the t-T-evolution

The individual results of the inverse numerical modeling of the t-T-evolution of the Neoproterozoic basement are displayed in fig. S7 (NW Namibia) and fig. S8 (SE Brazil) (see supplementary material). For all samples, 50,000 t-T-paths were tested against the thermochronological data set. In general, the numerical modeling yielded high values of the statistic approach "goodness of fit (G.O.F)". The G.O.F. quantifies the probability that a given t-T path generates the thermochronological data set under the assumption of the GEM-generated t-T constraints and therefore, t-T-models passed our requirements when good fits were found. Altogether, all t-T-models reproduced the plume-driven t-T-evolution under the supervision of the given GEM-generated t-T-constraints to our complete satisfaction and the results are discussed together with the 3D visualization of the Neoproterozoic basement thermal structure in chapter 5.5.

## 5.4. 3D-visualization of the t-T-evolution

The sole information of cooling and heating processes of spatially distributed samples urges a better visualization of the t-T-evolution in space, and time to contribute to the understanding of a complex t-T-history. Therefore, 3D-interpolation maps of the projected Neoproterozoic basement thermal structure were generated using the Golden Software Surfer® (Figs. 9a, b, c, d). The maps are based on Paleo-temperatures at specific time steps derived from the "weighted-mean" paths of the modeled t-T-evolution of the individual samples (Figs. S9.1-S9.16). This approach allows transferring local t-T-information from individual samples into space, and time to reconstruct the 3D thermal structure of the intraplate, Neoproterozoic Gondwana basement surface.

The change in temperature is illustrated by the spatial movement and expansion of the green (20–40 °C) and purple (140–160 °C) areas. A regression or vanishing of the green area accompanied by a progressing purple area over subsequent time steps indicates an increase in temperature, whereas a phase of cooling is demonstrated by the progression of the green area accompanied by a regression of the purple area.



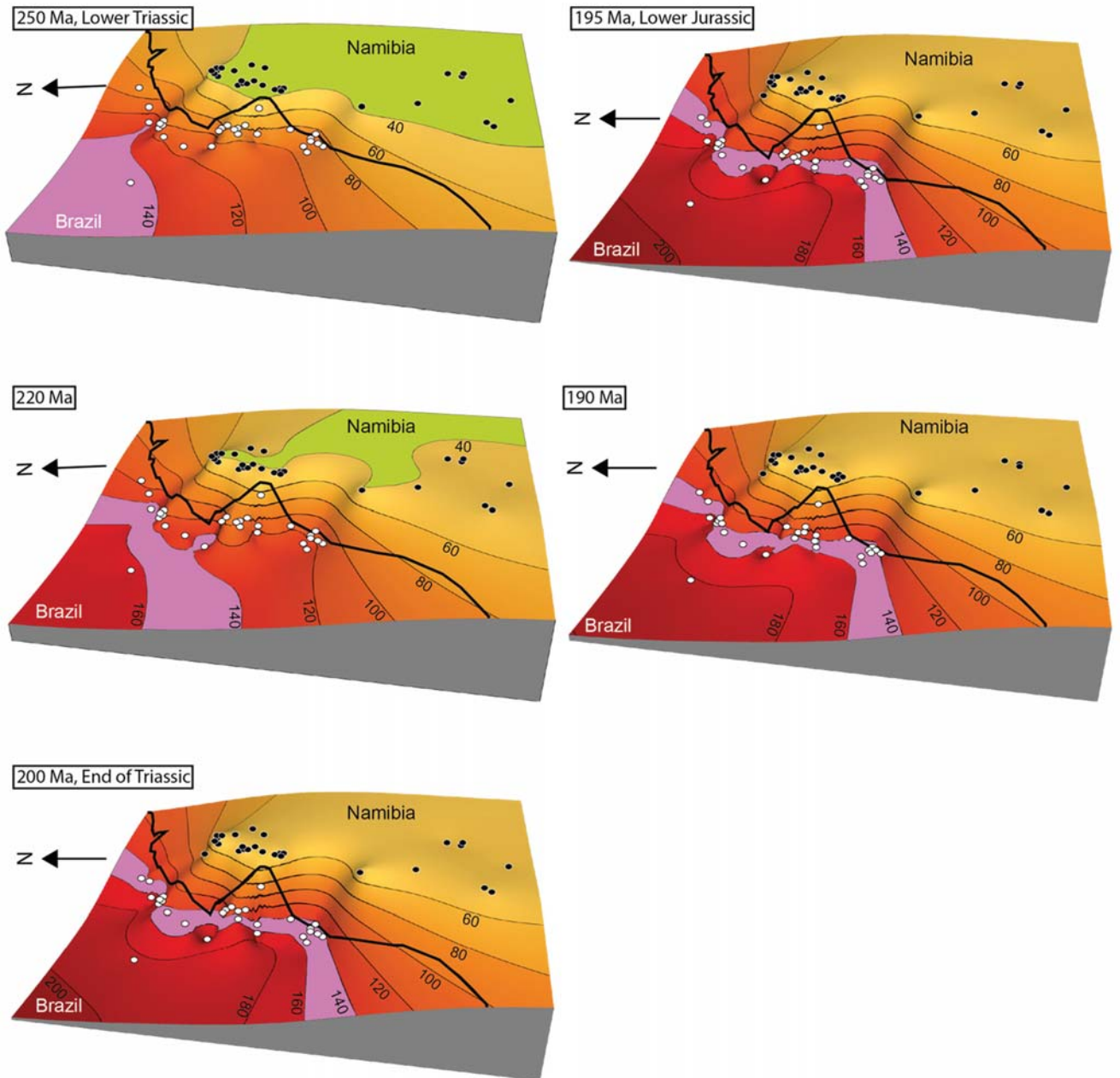
5.5. Results of the 3D-visualization: the thermal structure of the Neoproterozoic, Gondwana basement surface

The Mesozoic t-T- evolution of the 3D thermal structure of the Neoproterozoic surface can be divided into four phases:

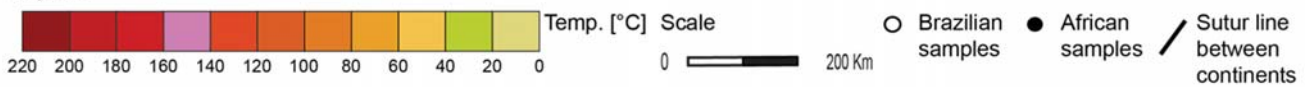
- (1) From the Upper Triassic (~250 Ma) to the Lower Jurassic (~190 Ma) (Fig. 9a), the central plume area (today's NW Namibia

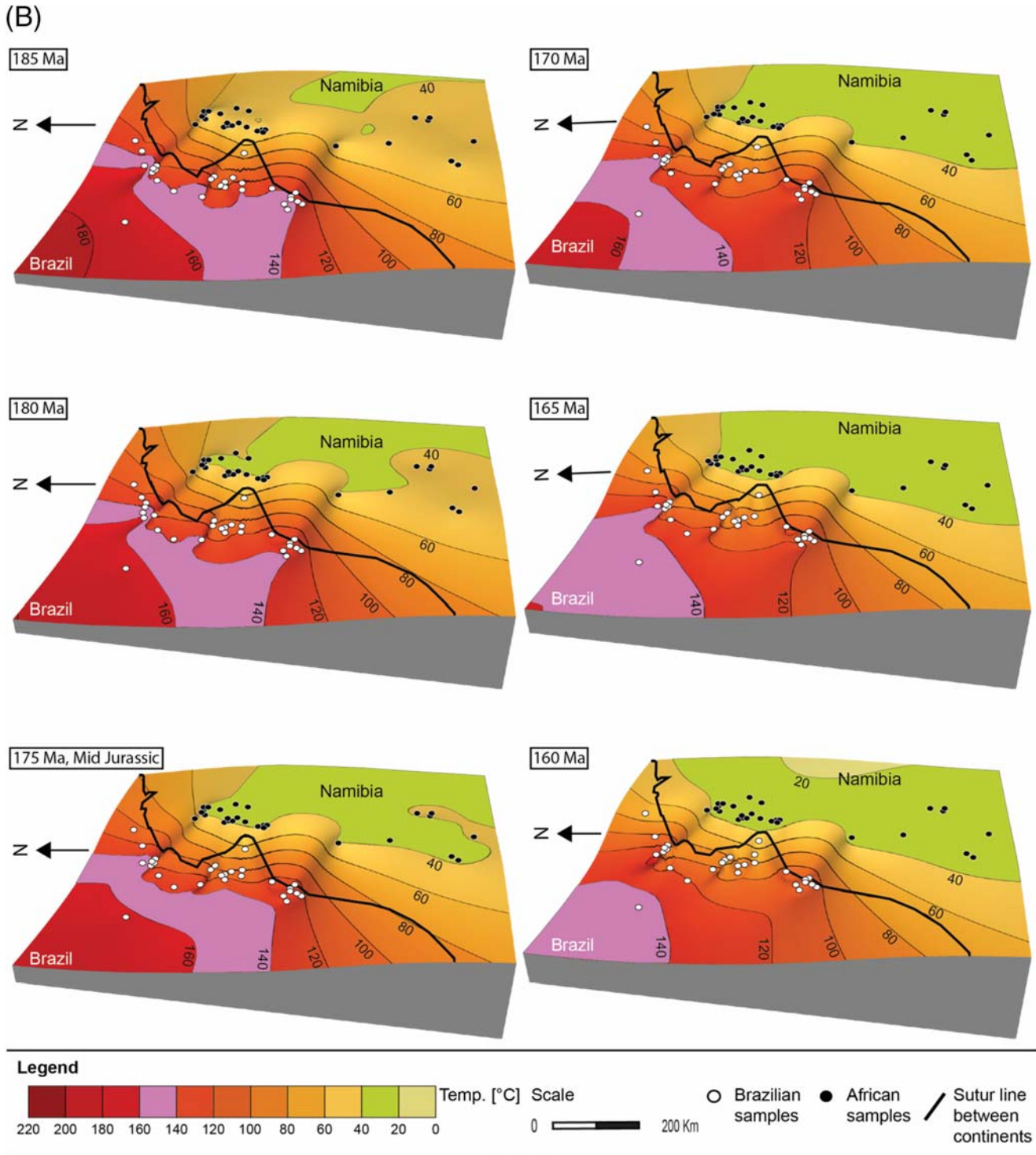
and SE Brazil) is characterized by steady heating. On the Brazilian side, temperatures range from ~80–140 °C (Upper Triassic) and rise to ~100–180 °C (Lower Jurassic), while temperatures in Namibia reach from ~40–60 °C and increase to ~60–100 °C during the same time period. Towards the Lower Jurassic, a tipping point of the t-T-evolution can be observed by less movement of the temperature isolines indicating a slowing down of the ongoing rock heating.

(A)



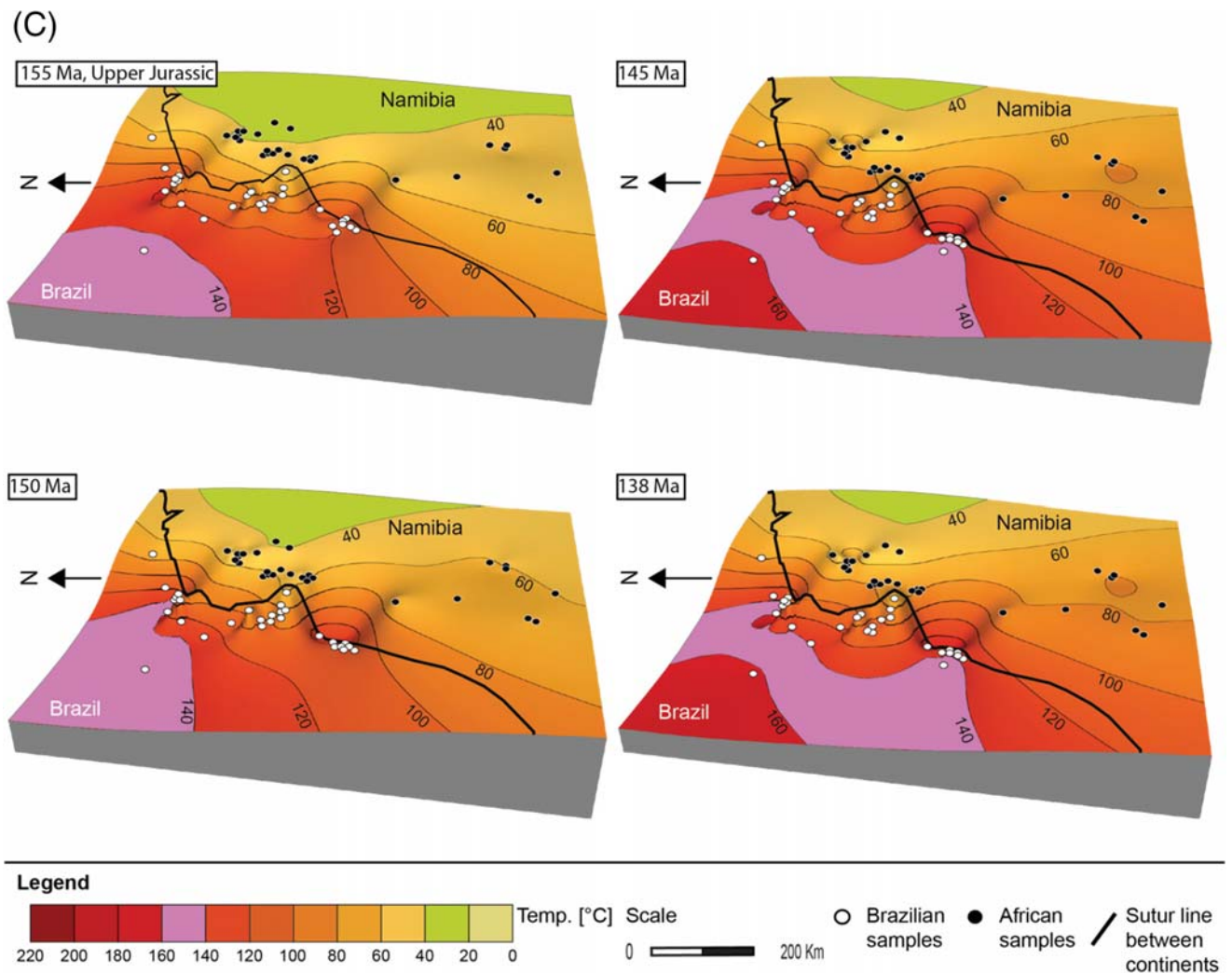
Legend





- (2) Thereafter, a phase of cooling sets in during the Lower Jurassic (~185 Ma) and continues until the Middle Jurassic (~160 Ma) (Fig. 9b). Temperatures decrease from ~100–180 °C to ~80–140 °C on the Brazilian area, and from ~40–80 °C to ~20–60 °C on the Namibia area, respectively.
- (3) This cooling is followed by a second phase of heating from the Upper Jurassic (~155 Ma) to the Lower Cretaceous (~138 Ma)

- (Fig. 9c). During this period, temperatures decrease from 80 to 140 °C to 120–160 °C (SE Brazil) and from 40–80 °C to 40–100 °C (NW Namibia), respectively.
- (4) The last phase (135 Ma to 95 Ma) is marked by slow, steady cooling on both sides (Fig. 9c). On the Brazilian side, maximum temperatures (~80–180 °C) are reached at around 135 Ma and, thereafter, rocks cool down to ~60–120 °C (~95 Ma). The



Namibian side shows temperatures from ~60–120 °C (135–125 Ma) that decrease to temperatures between ~60 °C and ~100 °C.

Summarizing the results of the 3D-visualization, temperatures on the Brazilian side and in the southern part of the central plume area are significantly higher than those for the Namibian counterpart and the northern areas of the central plume area showing a differentiated thermal structure, and t-T-evolution of the intraplate basement surface.

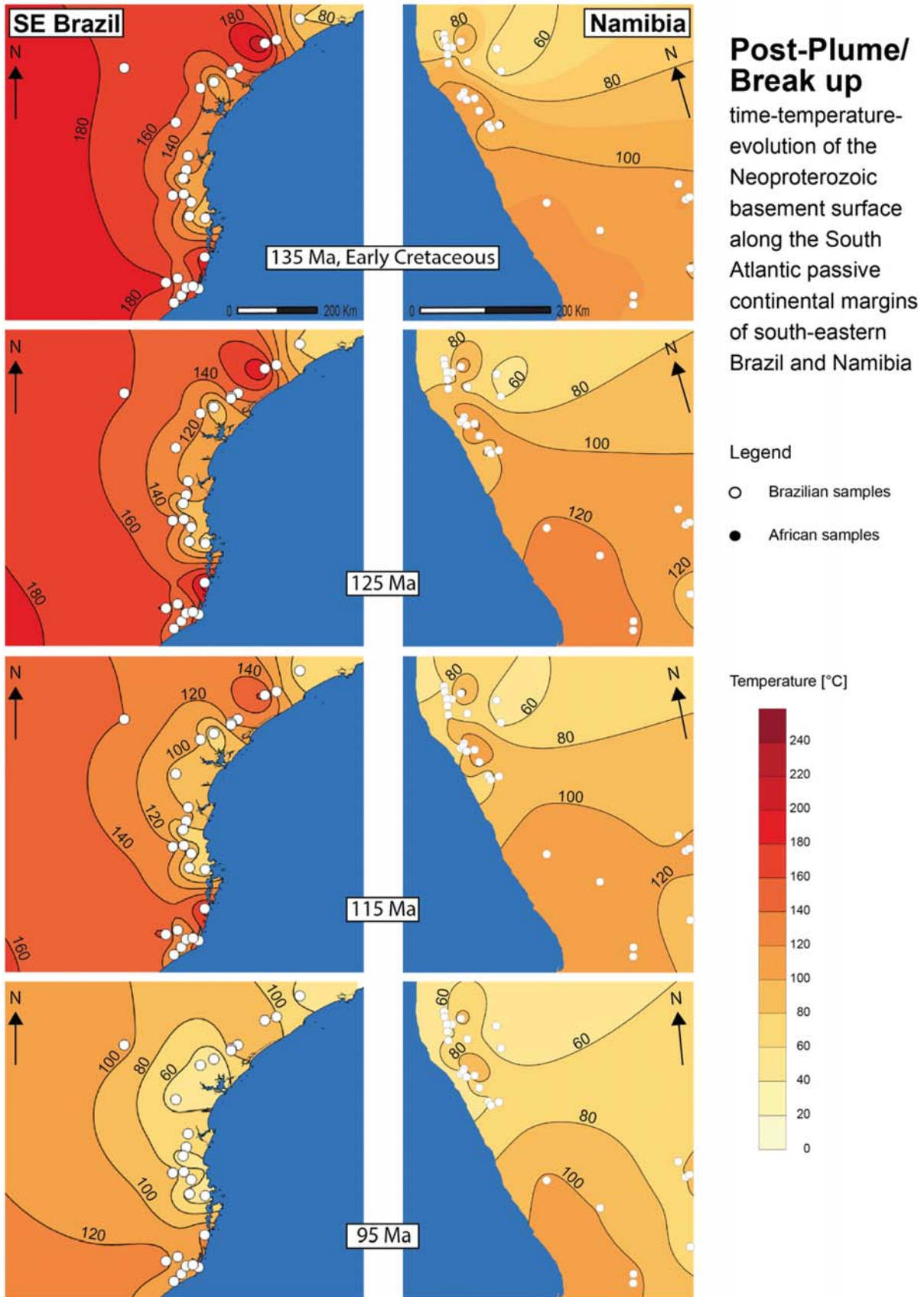
#### 5.6. Discussion: stratigraphic records vs. LTT data sets vs. the ePSF.

Vertical movement of deep mantle material, originating from the CMB has been linked to the dispersal of the Gondwana supercontinent and the Paraná-Etendeka LIP by numerous research studies in the past (Gurnis, 1988; Courtillot et al., 1999; Torsvik et al., 2006, 2014; Maruyama et al., 2007; Trumbull et al., 2007; Santosh et al., 2009; Yoshida and Santosh, 2011; Nance et al., 2014; Pirajno and Santosh, 2015; Torsvik, 2019). Ductile mantle dynamics, such as rapid upwelling of the mantle plume generated significant plume-lithosphere interactions using pre-existing heterogeneities in lithospheric structures (Şengör, 2001; Hu et al., 2018). The ascending mantle plume triggered

cratonic lithosphere modifications, including lithospheric delamination and destabilization, intraplate deformation and crustal thinning, and pre-drift extension, rifting, continental break up, and sea floor spreading (Courtillot et al., 1999; Torsvik et al., 2009; Torsvik and Cocks, 2013; Andrés-Martínez et al., 2019). The t-T-evolution of the Neoproterozoic basement, as a part of the upper crust provides an essential link between the significant cratonic lithosphere modifications and their direct responses to the tectonic, geomorphological, and sedimentological processes near the Earth's surface.

Unfortunately, our modeled thermochronological data only provide information about the t-T-evolution of a narrow zone along the present continental margins of SE Brazil and NW Namibia. Whereas the geological evolution of other areas along both SAPCM's can be also explained by non-plume related rifting events, we favor a plume- and flood basalt eruptions and magmatic activity-influenced t-T-evolution for the area of SE Brazil and NW Namibia (Krob et al., 2019; Krob et al., 2020). Furthermore, the drawn contour lines of the thermal structure on the Neoproterozoic basement are highly dependent on our rather unsystematic distributed sample locations including better constrained areas (e.g. along the present coast) and rather poorly constrained regions (further inland), and therefore, the contour maps illustrate a modeled projection of the data. However, the modeled contour maps permit assumptions of the t-T-evolution of the Neoproterozoic basement thermal structure during the SW Gondwana intraplate environment.

(D)



During the Triassic (Fig. 10a, left column: ~220 Ma), the geological evolution of the plume center on the Earth's surface is characterized by the ongoing, and yet undisturbed Paraná Basin sedimentation (Fig. 10a, middle column). Therefore, the Gondwana intraplate environment experienced subsidence displayed by increasing temperatures of the Neoproterozoic basement rocks during the Early Mesozoic (Fig. 10a, right column, ~220 Ma to ~195 Ma). Generally, the 3D-thermal structure of the basement indicates an inhomogeneous thermal structure most likely caused by lateral differentiated sedimentation. Basement rocks in SE Brazil reached higher temperatures during the Late Paleozoic, and, therefore, are assumed to have been deeper within the upper crust. Maximum temperatures between ~100–200 °C suggest ~2–6 km (~30 °C/km, Brown et al., 1990; Hamza et al., 2005; surface temperature of ~25 °C during the Mesozoic, Wygrala, 1989) of overlying sedimentary rocks prior to the plume initiation, and has been also observed by Milani et al. (2007). In NW Namibia, basement rocks experienced lower temperatures during the Late Paleozoic and, therefore, might have been closer to the Earth's surface. Deposited sediments are assumed to have reached thicknesses of less than ~2 km (<80 °C) until the Lower Jurassic.

As the plume head detached from the CMB ( $D''$ ) and started to rise through the deep non-lithospheric mantle (~195 Ma; ~60 Myr. prior to the Paraná-Etendeka event), the lithosphere reacted with incipient intraplate deformation and rock uplift (Torsvik et al., 2009, 2013; Müller et al., 2019). Hu et al. (2018) also detect destabilization, delamination, and tectonic uplift of intracratonic lithosphere in the Gondwana intraplate environment during the Mesozoic. On the Earth's surface, sedimentation ceased in the center area, and doming and erosion of surface rocks set in (Fig. 10a, middle column, Paraná and Huab Basin) indicating a tipping point for the t-T-evolution of the Neoproterozoic basement. The Lower Jurassic t-T-evolution of the Neoproterozoic basement shows a transition from increasing (Fig. 10a, ~220–195 Ma) up to a threshold (195–190 Ma), and subsequently decreasing temperatures (Fig. 10b, ~190–175 Ma, right column). Concurrently with the transient rise of the plume head, rock uplift and erosion continued to dominate above the plume head (Fig. 10b, left and middle column). Thus, the hiatuses and large missing sections in the sedimentary records of the Paraná and Huab basins perfectly display the evolution of the plume center predicted by the ePSF.

Exhumation processes continued until the Upper Jurassic (Fig. 10b, left column, ~155 Ma) when the plume head reached the base of the lithosphere, and the dome above the plume axis began to collapse. This initialized a second tipping point in the t-T-evolution of the upper crust (Fig. 10b, right column). The inhomogeneous thermal structure remains, though the change of temperature occurs inconsistently on both sides. Exhumation processes led to a decrease in temperature of the basement rocks. On the South American plate, the basement rocks were cooled down more rapidly from ~200–100 °C to ~140–80 °C implying an erosion between ~0.5 km and ~2 km from the Lower to Upper Jurassic. The basement rocks were still kept in depths between ~1.5 km and ~4 km. However, temperatures, or rather depths of basement rocks were generally higher towards the center of the Paraná Basin indicating a trend of lower temperatures towards the suture line between the cratonic plates. Thus, more sediment material was eroded in the Paraná Basin area as compared to the recent SAPCM. The trend

continues on the African side. Temperatures decrease from ~80–60 °C to ~60–40 °C. This means an erosion of ~0.7 km of sedimentary rocks that exhumed the African basement rocks relatively close to the surface.

The impact of the plume head at the base of the lithosphere accompanied by initial lateral spreading of mantle material within the asthenosphere possibly induced the surface uplift of the plume margin (Fig. 10c, left column, ~155 Ma to ~138 Ma). The central dome on the Earth's surface collapsed and the plume center experienced subsidence caused by the inward directed sedimentation of the renewed inverted margin erosion. In the stratigraphic record (Fig. 10c, middle column), this tipping point is displayed by an unconformity section of eolian sediments (Botucatu and Twyfelfontein formations). Consequently, the thermal structure of the upper crust shows a reheating of the Neoproterozoic basement rocks. However, the rapid increase in temperature is more likely related to the concurrent emplacement of the dike swarms than to deposited sediment thickness (<500 m) that would have not been significant for the thermochronological systems. Therefore, the interpretation of the basement depth within the upper crust during the Lower Cretaceous remains uncertain, and higher temperatures are most likely induced by a higher geothermal flux rather than subsidence.

The incipient lateral spreading of the plume head within the asthenosphere reinforced the transient lithospheric intraplate deformation and rapid crustal thinning leading to pre-drift-extension and incipient rifting (Courtilot et al., 1999; Torsvik et al., 2009, 2013; Hu et al., 2018). The climax and collapse is attained during the eruption and deposition of the Lower Cretaceous Paraná-Etendeka flood basalts (Fig. 10d, left, and middle column). The Neoproterozoic basement reached maximum temperatures between ~120 and ~180 °C on the South American side and between ~60 °C and ~120 °C on the African side resetting most of the thermochronological ages during this period (Brown et al., 1990, 2014; Raab et al., 2002, 2005; Krob et al., 2020).

Continuous rifting, continental break up, and sea floor spreading led to a differentiated t-T-evolution of the SAPCM of SW Africa and South America (Courtilot et al., 1999; Torsvik et al., 2009, 2013; Hu et al., 2018; Andrés-Martínez et al., 2019). Continental break up probably occurred along the old Pan African/Brasiliano orogeny suture line (Buiter and Torsvik, 2014) dividing the area, and, therefore, the thermal structures of the Neoproterozoic basement must be considered individually (Fig. 10d, right column). However, thermal structures on both sides show relatively slow, post-eruption thermal recovering and rock cooling indicating a thermally reestablished upper crust during the Lower Cretaceous (Hu et al., 2018). Furthermore, the t-T-evolution of the Neoproterozoic basement thermal structure indicates a similar t-T-history for both, SE Brazil and NW Namibia. However, the temperature distribution remains inhomogeneous showing significantly higher temperatures for southern SE Brazil throughout the entire Mesozoic SW Gondwana intraplate environment (Krob et al., 2019). Moreover, southern regions of the plume central area on both sides, generally, experienced higher temperatures possibly inferring a stronger thermal overprint by the Paraná-Etendeka flood basalts. Therefore, we suggest that pre-plume movement thermal structures and conditions already existed and were not totally reset or overprinted by the effect of the Paraná-Etendeka plume movement (Krob et al., 2019; Krob et al., 2020).

**Fig. 9.** a: Modeled 3D-interpolation maps showing the Neoproterozoic basement, thermal structure of the plume central area during the Mesozoic SW Gondwana intraplate environment from the Early Triassic to Late Jurassic. The maps are based on paleo-temperatures taken at specific time steps and were derived from the “weighted-mean” paths of the modeled t-T-evolution of each modeled sample (black and white dots). Red colors indicate higher temperatures and therefore, are generally assumed to lie deeper within the upper crust. Light colors rather show near surface areas (y-axis shows temperature). During this first period, the Neoproterozoic basement, thermal structure is characterized by continuous heating illustrated by the progression of the purple area (160–140 °C) accompanied by the vanishing of the green area (40–20 °C) over subsequent time steps. The black thick line indicates the former suture line between the continents. The geographical reconstruction and graphical extraction were done after Torsvik et al. (2009, 2013). b: Modeled 3D-interpolation maps showing the Neoproterozoic basement, thermal structure from the Early to Late Jurassic. During this second period, the Neoproterozoic basement, thermal structure is characterized by continuous cooling illustrated by the regression of the purple area (160–140 °C) accompanied by the expansion of the green area (40–20 °C) over subsequent time steps. c: Modeled 3D-interpolation maps showing the Neoproterozoic basement, thermal structure from the Upper Jurassic to Lower Cretaceous. During this third period, the Neoproterozoic basement, thermal structure is characterized by continuous heating illustrated by the progression of the purple area (160–140 °C) accompanied by the regression of the green area (40–20 °C) over subsequent time steps. d: Modeled 2D-interpolation maps showing the Neoproterozoic basement, thermal structure from the Lower to Upper Cretaceous. (For interpretation of the references to colour in this figure legend, the reader is referred to the web version of this article.)

6. Final discussion and interpretation

The analysis of stratigraphic records displaying the sedimentological evolution on the Earth's surface, and the corresponding t-T-evolution of the Neoproterozoic basement rocks derived from thermochronological data sets, as part of the upper crust show the complex patterns and responses between the individual, but connected systems. Geodynamic research implies that vertical material flow in the sublithospheric mantles causing tectonic uplift and exhumation above an ascending mantle plume can occur well in advance to the flood basalt eruptions on the Earth's surface (Campbell and Griffiths, 1990; Davies, 1999; Braun, 2010; Colli et al., 2014, 2013; Bunge and Glasmacher, 2018).

However, quantitative research comprising theoretical models of vertical material flow in the Earth's mantle and the crust remain highly dependent on the properties of the assumed Earth model (Braun, 2010; Bunge and Glasmacher, 2018). Theoretical observations often lacks information about the timing and ranges of dynamic processes and fails to cope with the geology on the Earth's surface. Thus, theoretically calculated parameters, e.g. mantle and lithosphere rheologies were not paramount to our study as such values produce large uncertainties and we focussed on the complex geological observations keeping theoretical knowledge at a minimum. Moreover, this research carries forward the idea of monitoring and attesting geodynamic theories by comparing observations from the upper crust, near, and on the Earth's surface with theoretical models of the Earth's

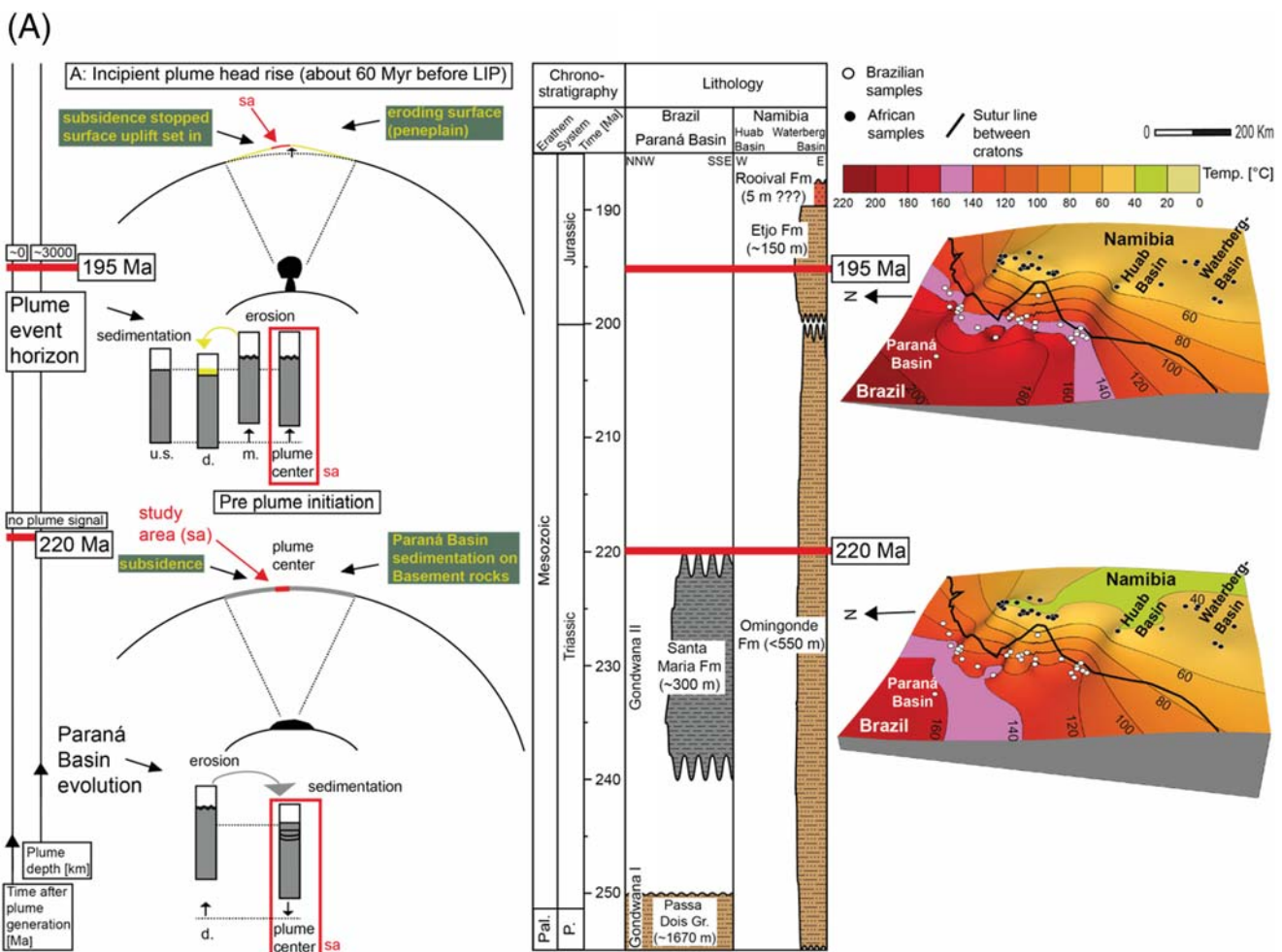


**Fig. 10.** a: Stratigraphic records vs. numerical modeling of LTT data sets vs. ePSF. Diagrams show predicted vertical movement processes during the plume head rise in the non-lithospheric mantle and its direct influence on the asthenosphere, lithosphere and surface processes in the upper crust and on the Earth's surface mirrored in the corresponding stratigraphic records of the central basins of the Paraná-Etendeka LIP and the 3D thermal structure of the Neoproterozoic basement as part of the plume central area. Read from left to right and bottom to top. Left: The plume mode and its stratigraphic record (modified after Friedrich et al., 2018) from pre-plume initiation (~220 Ma) to incipient plume head rise (~195 Ma). Red box shows study area (sa) and its approximate position on the Earth's surface. For further details, see Fig. S1. Middle: Stratigraphic records of the central basins of the Paraná-Etendeka LIP. For a more detailed view, see Fig. S2. Right: 3D structure of the Neoproterozoic basement in the plume central area. For further details, see Figs. 9a, b, c, and d. b: Left: The plume mode and its stratigraphic record (modified after Friedrich et al., 2018) during the ongoing plume head rise (~190 Ma and ~175 Ma). Red box shows study area (sa) and its approximate position on the Earth's surface. For further details, see Fig. S1. Middle: Stratigraphic record of the central basins of the Paraná-Etendeka LIP. For a more detailed view, see Fig. S1. Right: 3D structure of the Neoproterozoic basement of the plume central area. For further details, see Figs. 9a, b, c, and d. c: Left: The plume mode and its stratigraphic record (modified after Friedrich et al., 2018) from plume head impact at the base of the lithosphere (~155 Ma) to the collapse of the plume head (~138 Ma). Red box shows study area (sa) and its approximate position on the Earth's surface. For further details, see Fig. S1. Middle: Stratigraphic record of the central basins of the Paraná-Etendeka LIP. For a more detailed view, see Fig. S1. Right: 3D structure of the Neoproterozoic basement of the plume central area. For further details, see Figs. 9a, b, c, and d. d: Left: The plume mode and its stratigraphic record (modified after Friedrich et al., 2018) from eruption of flood basalts (~135 Ma) to lateral spreading and thermal relaxation (~125 and ~115 Ma). Red box shows study area (sa) and its approximate position on the Earth's surface. For further details, see Fig. S1. Middle: Stratigraphic record of the central basins of the Paraná-Etendeka LIP. For a more detailed view, see Fig. S1. Right: 2D structure of the Neoproterozoic basement of the plume central area. For further details, see Figs. 9a, b, c, and d. (For interpretation of the references to colour in this figure legend, the reader is referred to the web version of this article.)

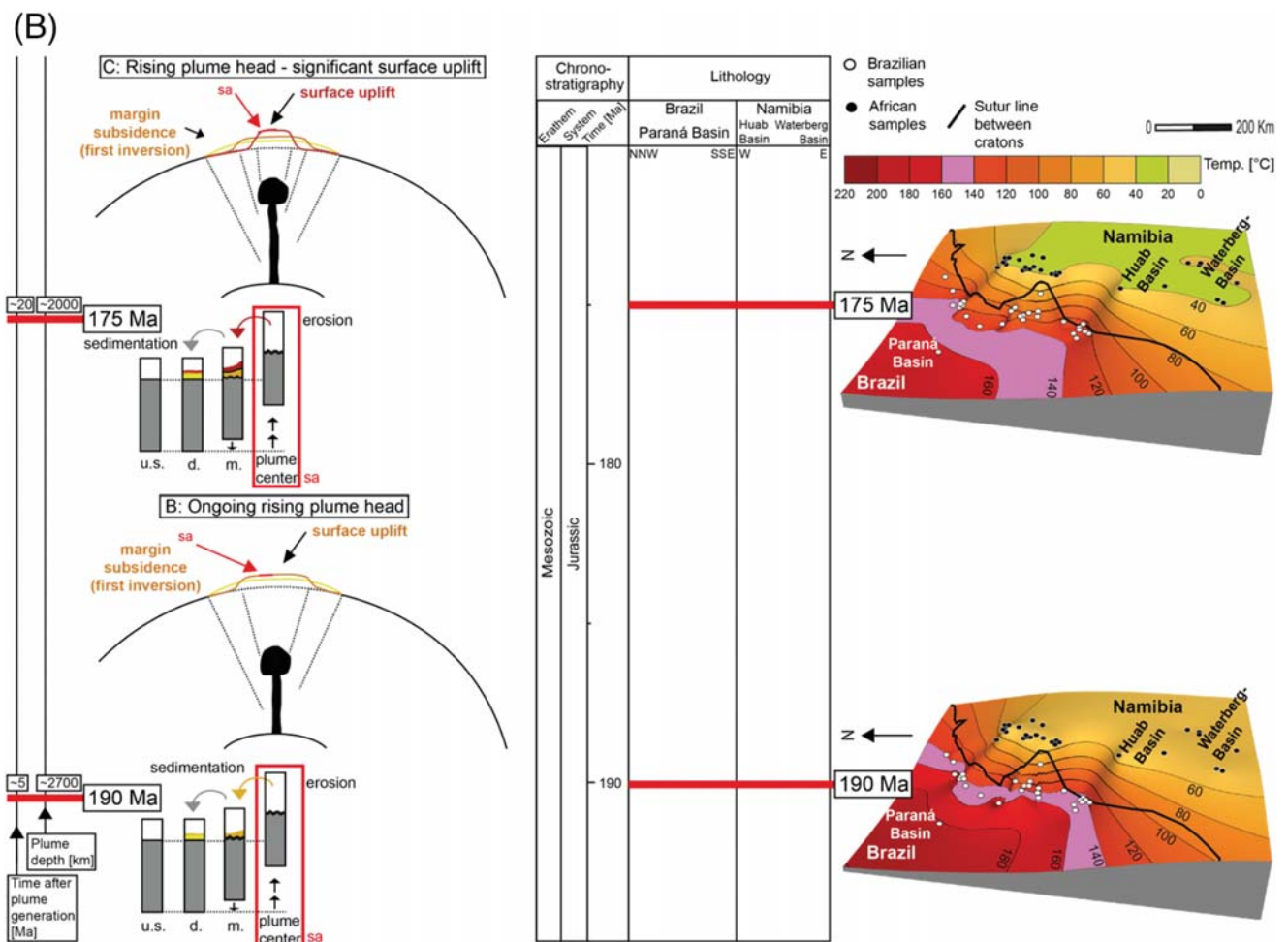


Fig. 10 (continued).

mantle. By this approach, we are able to align and probably even constrain the theoretical research.

The ePSF is designed to compare sole observations on the Earth's surface to the geological evolution predicted by theoretical models. Both geological archives reveal significant signals and traces of flood basalt eruptions preceding rock and surface uplift caused by the Paraná-Etendeka plume movement on the Earth's surface when analysed independently. We recognize rock and surface uplift driven hiatuses and unconformities preceding the Paraná-Etendeka LIP event in the stratigraphic records of the Mesozoic SW Gondwana intraplate environment sedimentary basins. By applying the ePSF, we are able to map a spatial distribution of the mantle plume affected area proposing a possible plume center and a margin region. Furthermore, we perceive the timing of events and distinct temporal patterns in both geological archives as described by the ePSF. Finally, the model provides to probability to combine both archives and test them against a possible t-T-evolution derived from its pretended geological evolution. Thus, we would like to conclude that our combined data succeeds to validate the ePSF displaying a viable t-T-, and geological evolution near, and on the Earth's surface during the Paraná-Etendeka plume movement.

The stratigraphic records seem to confirm the predicted signals and traces of plume movement when applied to the Paraná-Etendeka LIP within the Mesozoic SW Gondwana intraplate environment. Nevertheless, there exist uncertainties related to the reliability of the original lateral extent of sedimentary sections, since stratigraphic

records are highly dependent on borehole locations. Signals of events can also be disturbed or overprinted by other geological events. The erodibility of rocks, and climate and weathering is often uncertain and not considered in the interpretation of stratigraphic records, and, therefore, accuracy and clarity can be a significant problem. Regarding the thermochronological data, this research had to deal with difficulties, such as thermal overprint of most of the data, the consideration of the regional geological evolution, or the lack of comprehensive age information, and interregional scale unsystematically distributed data sets. The applied approach requires critical analysis of temporal and spatial uncertainties of, both, the geological archives and the predicted stratigraphic patterns of the ePSF. Consequently, we would like to introduce possible ranges of both, the spatial distribution and on the temporal scale (Fig. 11).

Whereas the dimensions of the plume center are well constrained by all geological observations, we propose to significantly widen the plume margin, as we recognize a greater range of initial Paraná-Etendeka caused rock and surface uplift. However, especially in the southern and south-western areas, the role and possible interference of the preceding large-scale Karoo LIP event (Storey et al., 2013; Navarrete et al., 2019) and its stratigraphic consequences, most likely leading to overlapping long-time hiatuses in the sedimentary sections, remain uncertain. While the widely distributed thermochronological data are not inconsistent with results from the plume stratigraphic mapping of the Paraná-Etendeka plume, the combined geological data set cannot

(C)

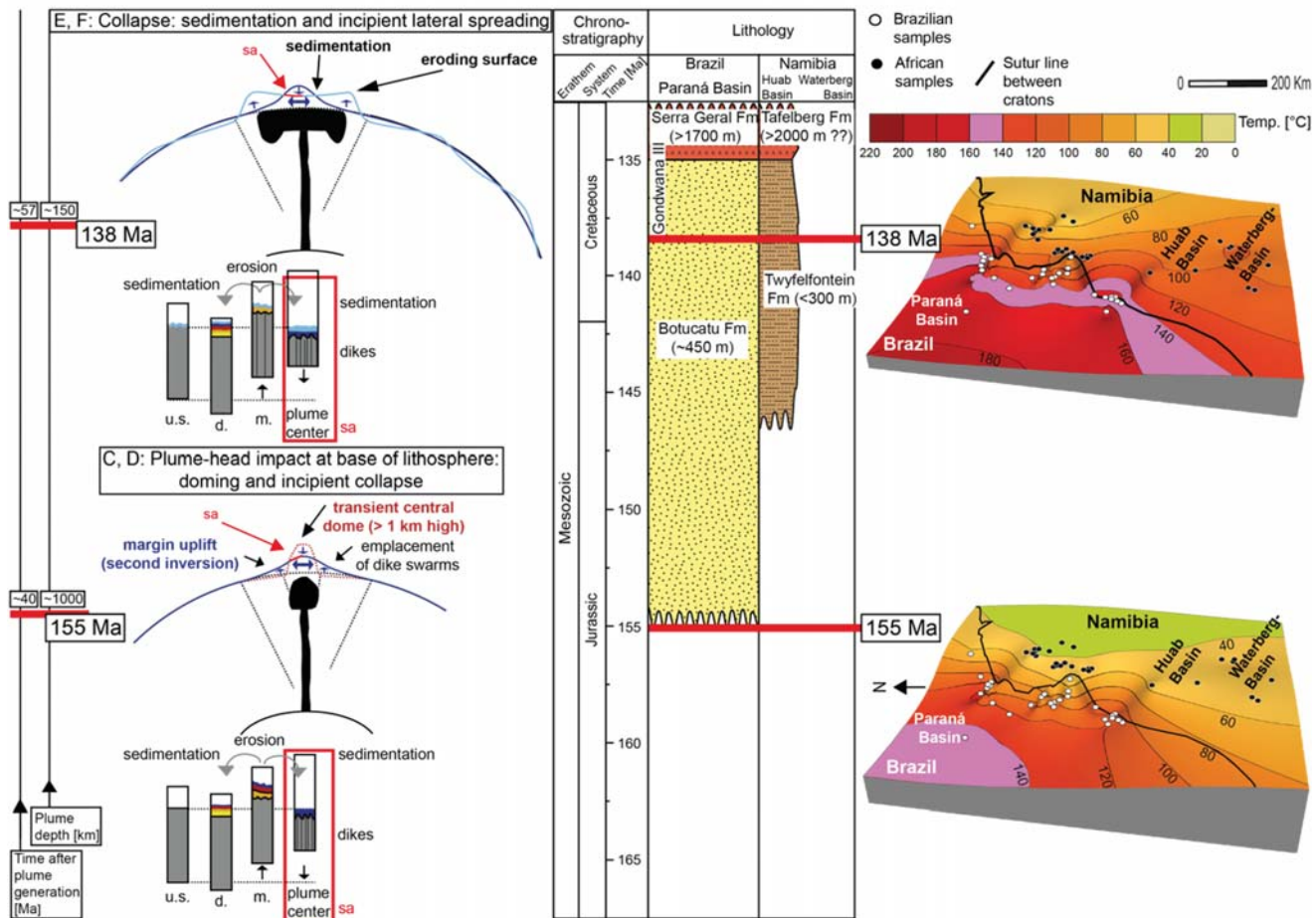


Fig. 10 (continued).

better constrain the spatial range of the Paraná-Etendeka influenced area on the Earth's surface. Furthermore, we do not commit ourselves to propose an exact position of the Paraná-Etendeka plume eruptions but assume that a mantle plume of such size would have influenced large areas of both continental plates. However, the applied plume-stratigraphic mapping shows a highly asymmetric plume center indicating a greater lateral sphere of originally lava covered area (Jackson et al., 2005; Torsvik et al., 2009, 2014; Franke, 2013) (Fig. 11).

Furthermore, we introduce a possible temporal range for the Paraná-Etendeka plume event horizon, and its transit time on the temporal scale (Fig. 11). Though, the probability towards the very poorly constrained upper and lower limits decreases enormously and we assume a smaller range, similar to the temporal predictions of the ePSF, is more likely. Nevertheless, on the base of the combined geological archives, we propose the upper limit of the event horizon does not exceed ~220 Ma, and the lower limit is not <165 Ma permitting a permissible transit time range between ~30 Ma and ~85 Ma. This range would lead to a possible range of ascent velocities of the rising plume head of ~35–100 km/Myr partly overlapping with the transit time range inferred by Colli et al. (2018). Therefore, the limits of the possible temporal range are highly uncertain. Neither geological archive used in this study, presently, is precise enough to determine an exact transit time preceding the Paraná-Etendeka flood basalt eruptions. Nevertheless, our analysis validated the ePSF approach. Thus, the model provides an

excellent fit to retrieve a possible Paraná-Etendeka plume movement when applied to the Mesozoic SW Gondwana intraplate environment.

Eventually, LTT data may also permit to better trace the initial plume movement when assured that samples did not experience thermal overprints afterwards. Therefore, we propose the systematic extension of thermochronological data over wider areas also covering marginal regions, and Paleozoic and Mesozoic sedimentary rocks to better constrain, and therefore, understand the t-T-evolution of the Mesozoic SW Gondwana intraplate environment.

### 7. Conclusions

For the first time, we combined two geological archives, i.e. stratigraphic records and thermochronological data sets, both having stored the sedimentological, magmatic, and thermal evolution surrounding the Paraná-Etendeka LIP and tested the event-based plume stratigraphic framework to retrieve the spatio-temporal patterns that are consistent with geological predictions caused by mantle plume movement.

Both archives show significant signals and traces well in advance of the flood basalt eruptions on the Earth's surface and we recognize the timing of events and distinct patterns of flood basalt event preceding rock and surface uplift consistent with those expected by mantle plume movement. Furthermore, our LTT data combined with



(D)

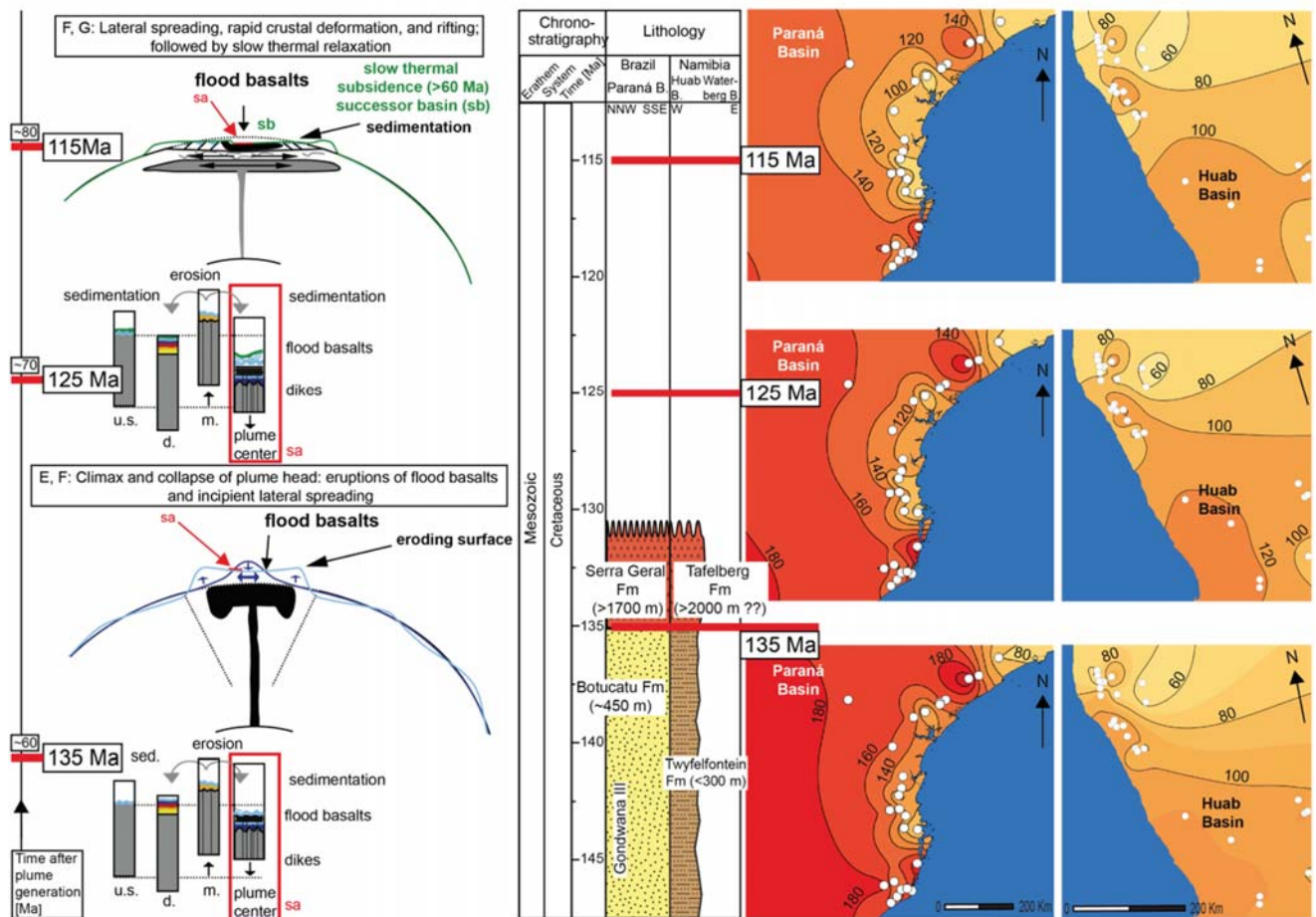


Fig. 10 (continued).

stratigraphic records of the sedimentary basins allow for successful inverse, numerical modeling of a viable mantle plume driven t-T-evolution and therefore, we suggest that thermochronological data, in combination with published stratigraphy records have the potential to retrieve the Paraná-Etendeka plume movement.

The stratigraphic records of the SW Gondwana intraplate environment sedimentary basins provide permissible spatial dimensions of a Paraná-Etendeka plume movement-influenced area. We propose an asymmetric central area that ranges from  $\sim 2.3$  Mio km<sup>2</sup> to  $\sim 2.75$  Mio km<sup>2</sup> showing the predicted geological patterns of a possible plume center. This area permits diameters between  $\sim 2000$  km and  $\sim 2200$  km (horizontally, E-W) and  $\sim 2200$  km (vertically, N-S) providing a plume center extending over both contemporary continental plates. Moreover, we define a possible plume marginal area extending from a minimum of  $\sim 4$  Mio km<sup>2</sup> to a maximum of between  $\sim 9.3$  Mio km<sup>2</sup> and  $\sim 10.6$  Mio km<sup>2</sup> leading to a long-range Paraná-Etendeka plume movement-influenced area in the SW Gondwana intraplate environment with permissible diameters between  $\sim 2200$  km and  $\sim 3000$ – $4100$  km (horizontally, E-W), and between  $\sim 2800$  km and  $\sim 5100$  km (vertically, N-S).

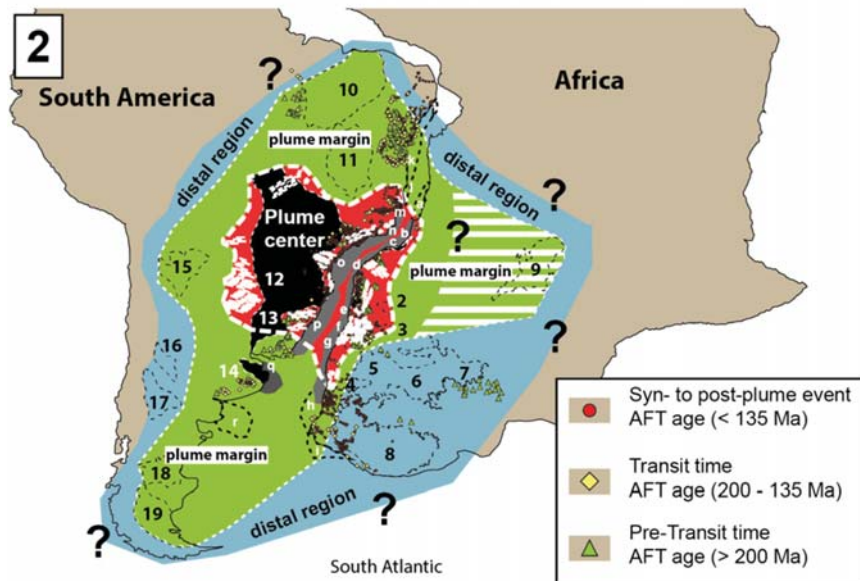
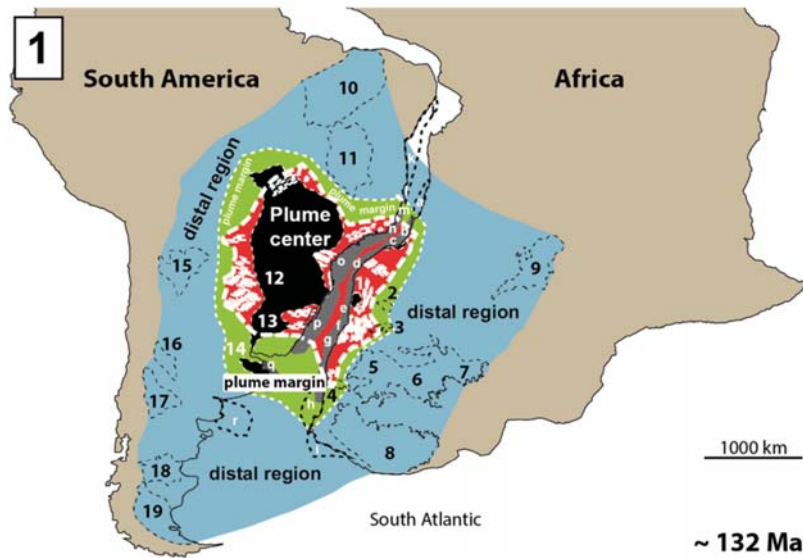
Thermochronological data from the SAPCMs of SW Africa from NW Angola to South Africa, and of South America, from NE Brazil to northern Argentina expose centers of thermally overprinted AFT ages ( $<135$  Ma) that overlap with the Paraná-Etendeka related dike swarms and flood basalt depositions indicating a significant thermal influence by the

volcanic activity of the Paraná-Etendeka LIP. Combined with the timing of hiatuses and unconformities in the stratigraphy records, the AFT data permits to define permissible ranges on the temporal scale. We propose a viable transit time range prior the Paraná-Etendeka LIP event between  $\sim 85$  Ma and  $\sim 30$  Ma leading to a permissible event horizon between  $\sim 220$  Ma and  $\sim 165$  Ma.

However, we critically revealed uncertainties, such as the lateral significance and reliability of stratigraphic records, or the overprint of AFT age information, in both contemporary geological archives, and therefore, conclude that both data sets lack in sensitivity to determine a precise spatial dimension on the Earth's surface, and exact transit time and timing of initial plume movement preceding the Paraná-Etendeka flood basalt eruptions. Consequently, the outer limits of the permissible ranges are highly uncertain. Nevertheless, the analysis validated the ePSF approach and the model provides an excellent fit to retrieve a possible Paraná-Etendeka plume movement when applied to the Mesozoic SW Gondwana intraplate environment. Moreover, we propose the systematic extension of thermochronological data over wider areas also covering marginal regions, and Paleozoic and Mesozoic sedimentary rocks to better constrain, and therefore, understand the t-T-evolution of the Gondwana intraplate environment.

Concluding, this research carries forward the idea of monitoring and attesting geodynamic theories by comparing observations from the upper crust, near, and on the Earth's surface with theoretical models of the Earth's mantle. Size and volume of vertical material flow, the

### Possible ranges of the spatial distribution



**Legend**

- Continental landmass
- Sedimentary basin
- Paraná-Etendeka flood basalts (onshore)
- Paraná-Etendeka flood basalts (offshore)
- Plume Center
- Dike swarms
- Plume margin
- Distal region

### Possible ranges on the temporal scale

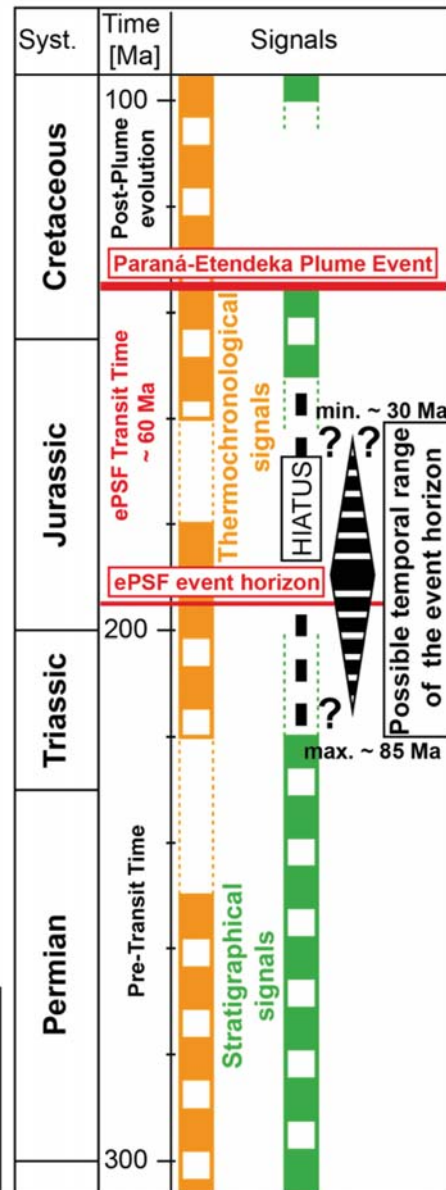


**Fig. 11.** Possible ranges and limits for the spatial distribution of the Paraná-Etendeka LIP influenced area on the Earth's surface and on the temporal scale during a possible plume ascent. Left Panel: Possible ranges of the spatial distribution of the Paraná-Etendeka plume influenced area on the Earth's surface. (1): Possible spatial distribution when followed strictly the outlines of the ePSF (Friedrich et al., 2019). For further details, please see Fig. 5. (2) Spatial distribution showing a possible deviation in the spatial range including a critical uncertainty analysis regarding the geological archives and the ePSF. Right Panel: Possible ranges of the Paraná-Etendeka plume transit time during the plume ascent. The temporal scale includes the Paraná-Etendeka plume event (~135 Ma), and the event horizon (~195 Ma) and transit time (~60 Ma) predicted by the ePSF (red bars). Orange bars illustrate the thermochronological signals indicating the age peaks of all published AFT cooling ages (For further details, please see Fig. 8). Green bars signify the depositional sequences recorded in the stratigraphic records of the central basins (Paraná, Huab, and Waterberg, for further details, please see Figs. 3a, b; and S2). Black dashed line: maximum hiatuses in the stratigraphic records. Black rhombus indicates the possible temporal ranges of the event horizon assuming a decreasing probability towards the poorly constrained upper and lower limits. Both archives leave room for a possible event horizon between ~220 Ma and ~165 Ma, and a Paraná-Etendeka transit time between ~30 Ma and ~85 Ma. (For interpretation of the references to colour in this figure legend, the reader is referred to the web version of this article.)

composition and viscosity of mantle and the Earth's crust, and the nature of the Earth's surface differ from plume ascent to plume ascent and will surely effect the timing of events and spatial distributions, e.g., for the Afar plume in NE Africa (initial uplift ~30 Ma prior to the volcanic activity, Şengör, 2001). Therefore, it would be highly interesting to apply the combined geological archives, stratigraphic records and thermochronological data to other intraplate environments and its large igneous provinces to either validate or better constrain the approach and findings of our research.

#### CRediT authorship contribution statement

**Florian C. Krob:**Methodology, Writing - original draft, Formal analysis, Visualization, Project administration.**Ulrich A. Glasmacher:** Methodology, Writing - review & editing, Supervision, Project administration, Conceptualization, Resources.**Hans-Peter Bunge:** Writing - review & editing, Supervision, Project administration, Conceptualization.**Anke M. Friedrich:**Writing - review & editing, Conceptualization.**Peter C. Hackspacher:**Writing - review & editing.

#### Declaration of competing interest

The authors declare that they have no known competing financial interests or personal relationships that could have appeared to influence the work reported in this paper.

#### Acknowledgements

Special thanks are given to Dipl.-Geol. Daniel Eldrach (former Menges), Dipl.-Geol. Markus Karl and Dr. rer. nat. Sebastian Kollenz for their contribution to this study concerning field work, sample preparation, and dating analyses during their time in our research group. Also we very much appreciate the discussions with members of the SPP-1375 SAMPLE and the discussions and logistic support by the research group of Peter C. Hackspacher and the Geoscience team in Rio Claro, UNESP. Furthermore, we like to thank Danny Stockli's team for the analytical assistance, Richard A. Ketcham and Raymond A. Donelick for providing the computer code HeFTy, Raymond A. Donelick allowing us to use  $D_{\text{par}}$  as a kinetic factor, and István Dunkl for providing the software code TrackKey. We also would like to thank two unknown reviewers for their critical reading and constructive comments on an earlier version of the manuscripts that led to significant improvements. In addition, we very much appreciate the technical support given by the Forschungs-Neutronenquelle FRM II at Garching, TU München, Germany organized by Dr. Gerstenberg. Finally, without the financial support provided with grants to Ulrich A. Glasmacher by the German Research Foundation (Deutsche Forschungsgemeinschaft, DFG, GL182/14-1, 14-2, GL 182/18-1) within the Priority Program 1375 (SAMPLE) and the DAAD (50753850) we would not be able to perform the research.

#### Appendix A. Supplementary data

Supplementary data to this article can be found online at <https://doi.org/10.1016/j.gr.2020.02.010>.

#### References

Andrés-Martínez, M., Gussinyé, M.P., Armitage, J., Morgan, J.P., 2019. Thermomechanical implications of sediment transport for the architecture and evolution of continental rifts and margins. *Tectonics* 38, 641–665.

Anka, Z., Ondrak, R., Kowitz, A., Schodt, N., 2013. Identification and numerical modelling of hydrocarbon leakage in the lower Congo Basin: Implications on the genesis of km-wide seafloor mounded structures. *Tectonophysics* 604, 153–171.

Autin, J., Scheck-Wenderoth, M., Loegering, M.J., Anka, Z., Vallejo, E., Rodriguez, J.F., Dominguez, F., Marchal, D., Reichert, C., di Primio, R., Goetze, H.-J., 2013. Colorado Basin 3D structure and evolution, Argentine passive margin. *Tectonophysics* 604, 264–279. <https://doi.org/10.1016/j.tecto.2013.05.019>.

Beaumont, C., 1978. The evolution of sedimentary basins on a viscoelastic lithosphere: theory and examples. *Geophys. J. R. Astron. Soc.* 55, 471–497.

Braun, J., 2010. The many expressions of mantle dynamics. *Nat. Geosci.* 3, 825–833.

Braun, J., Guillocheau, F., Robin, C., Baby, G., Jelsma, H., 2014. Rapid erosion of the Southern African Plateau as it climbs over a mantle superswell. *Journal of Geophysical Research: Solid Earth* 119, 6093–6112.

Brune, S., Williams, S.E., Butterworth, N.P., Müller, D.R., 2016. Abrupt plate accelerations shape rifted continental margins. *Nature* 536, 201–204.

Buiter, S.J.H., Torsvik, T.H., 2014. A review of Wilson Cycle plate margins: a role for mantle plumes in continental break-up along sutures? *Gondwana Res.* 26, 627–653.

Bunge, H.-P., 2005. Low plume excess temperature and high core heat flux inferred from non-adiabatic geotherms in internally heated mantle circulation models. *Phys. Earth Planet. Inter.* 153 (1–3), 3–10. <https://doi.org/10.1016/j.pepi.2005.03.017>.

Bunge, H.P., Glasmacher, U.A., January 2018. Models and observations of vertical motion (MoveOn) associated with rifting to passive margins: Preface. *Gondwana Res.* 53, 1–8.

Bunge, H.-P., Richards, M.A., Lithgow-Bertelloni, C., Baumgardner, J.R., Grand, S.P., Romanowicz, B.A., 1998. Time scales and heterogeneous structure in geodynamic earth models. *Science* 280:91–95. <https://doi.org/10.1126/science.280.5360.91>.

Burke, K., Dewey, J.F., 1973. Plume-generated triple junctions: key indicators in applying plate tectonics to old rocks. *Journal of Geology* 81:406–433. <https://doi.org/10.1086/627882>.

Burke, K., Wilson, J.T., 1972. Is the African plate stationary? *Nature* 239, 387–390. <https://doi.org/10.1038/239387b0>.

Campbell, I.H., 2007. Testing the plume theory. *Chemical Geology* 241:153–176. <https://doi.org/10.1016/j.chemgeo.2007.01.024>.

Campbell, I.H., Griffiths, R.W., 1990. Implications of mantle plume structure for the evolution of flood basalts. *Earth Planet. Sci. Lett.* 99, 79–93. [https://doi.org/10.1016/0012-821X\(90\)90072-6](https://doi.org/10.1016/0012-821X(90)90072-6).

Colli, L., Fichtner, A., Bunge, H.-P., 2013. Full waveform tomography of the upper mantle in the South Atlantic region: imaging a westward fluxing shallow asthenosphere? *Tectonophysics* 604, 26–40.

Colli, L., Stotz, I., Bunge, H.-P., 2014. Rapid South Atlantic spreading changes and coeval vertical motion in surrounding continents: evidence for temporal changes of pressure-driven upper mantle flow. *Tectonics* 33, 1304–1321.

Colli, L., Ghelichkhan, S., Bunge, H.-P., 2016. On the ratio of dynamic topography and gravity anomalies in a dynamic Earth. *Geophys. Res. Lett.* 43, 2510–2516. <https://doi.org/10.1002/2016gl067929>.

Colli, L., Ghelichkhan, S., Bunge, H.-P., Oeser, J., 2018. Retrodictions of late Paleogene mantle flow and dynamic topography in the Atlantic region from compressible high resolution adjoint mantle convection models: sensitivity to deep mantle viscosity and tomographic input model. *Gondwana Res.* 53, 252–272.

Courtillot, V., Jaupart, C., Manighetti, I., Taponnier, P., Besse, J., 1999. On causal links between flood basalts and continental breakup. *Earth Planet. Sci. Lett.* 166 (3), 177–195. [https://doi.org/10.1016/S0012-821X\(98\)00282-9](https://doi.org/10.1016/S0012-821X(98)00282-9).

Cox, K.G., 1989. The role of mantle plumes in the development of continental drainage patterns. *Nature* 342, 873–877. <https://doi.org/10.1038/342873a0>.

Davies, G.F., 1999. *Dynamic Earth: Plates*. Cambridge University Press, Plumes and Mantle Convection <https://doi.org/10.1017/CBO9780511605802>.

Davies, G.F., Richards, M.A., 1992. Mantle convection. *The Journal of Geology* 100, 151–206. <https://doi.org/10.1086/629582>.

Davies, J.H., Davies, D.R., 2010. Earth's surface heat flux. *Solid Earth* 1, 5–24.

Davies, J.H., Valentine, A.P., Kramer, S.C., Rawlinson, N., Hoggard, M.J., Eakin, C.M., Wilson, C.R., 2019. Earth's multi-scale topographic response to global mantle flow. *Nat. Geosci.* 12, 845–850.

Dressel, I., Scheck-Wenderoth, M., Cacace, M., Lewerenz, B., Gätz, H.-J., Reichert, C., 2015. Reconstruction of the southwestern African continental margin by backward modeling. *Marine and Petroleum Geology* 67, 544–555.

Duncan, R.A., Richards, M.A., 1991. Hotspots, mantle plumes, flood basalts, and true polar wander. *Reviews of Geophysics* 29:31–50. <https://doi.org/10.1029/90RG02372>.

Duncan, R.A., Hooper, P.R., Rehacek, J., Marsh, J.S., Cuncan, A.R., 1997. The timing and duration of the Karoo igneous event, southern Gondwana. *J. Geophys. Res.* 102, 18,127–18,138.

Ebinger, C.J., Sleep, N.H., 1998. Cenozoic magmatism throughout east Africa resulting from impact of a single plume. *Nature* 395, 788–791. <https://doi.org/10.1038/27417>.

Ernst, R.E., Buchan, K.L., 1997. Giant radiating dyke swarms: their use in identifying pre-Mesozoic large igneous provinces and mantle plumes. In: Mahoney, J.J., Coffin, M. (Eds.), *Large Igneous Provinces: Continental, Oceanic, and Planetary Volcanism*. Geophysical Monograph Series. American Geophysical Union vol. 100, 297–333.

Ernst, R.E., Buchan, K.L., 2001. *Mantle Plumes: Their Identification Through Time*. Geological Society of America Special Paper 593 pp.

Franke, D., 2013. Rifting, lithosphere breakup and colcanism: comparison of magma-poor and volcanic rifted margins. *Mar. Pet. Geol.* 43, 63–87.

Friedrich, A.M., Bunge, H.-P., Rieger, S.M., Colli, L., Ghelichkhan, S., Nerlich, R., 2018. Stratigraphic framework for the plume mode of mantle convection and the analysis of interregional unconformities on geological maps. *Gondwana Res.* 53, 159–188. <https://doi.org/10.1016/j.gr.2017.06.003>.

Frimmel, H.E., Basei, M.S., Gaucher, C., 2011. Neoproterozoic geodynamic evolution of SW-Gondwana: a southern African perspective. *Int. J. Earth Sci.* 100, 323–354.

Griffiths, R.W., Campbell, I.H., 1990. Stirring and structure in mantle starting plumes. *Earth and Planetary Science Letters* 99:66–78. [https://doi.org/10.1016/0012-821X\(90\)90071-5](https://doi.org/10.1016/0012-821X(90)90071-5).

Griffiths, R.W., Gurnis, M., Eitelberg, G., 1989. Holographic measurements of surface topography in laboratory models of mantle hotspots. *Geophys. J. Int.* 96, 477–495. <https://doi.org/10.1111/j.1365-246X.1989.tb06009.x>.

- Guillocheau, F., Rouby, D., Robin, C., Helm, C., Rolland, N., Le Carlier de Veslud, C., Braun, J., 2012. Quantification and causes of the terrigenous sediment budget at the scale of a continental margin: a new method applied to the Namibia–South Africa margin. *Basin Research* 24, 3–30. <https://doi.org/10.1111/j.1365-2117.2011.00511.x>.
- Guillocheau, F., Simon, B., Baby, G., Bessin, P., Robin, C., Dauteuil, O., 2018. Planation surfaces as a record of mantle dynamics: the case of example of Africa. *Gondwana Res.* 53, 82–98.
- Gurnis, M., 1988. Large-scale mantle convection and the aggregation and dispersal of supercontinents. *Nature* 332, 695–699.
- Hager, B.H., Clayton, R.W., Richards, M.A., Comer, R.P., Dziewonski, A.M., 1985. Lower mantle heterogeneity, dynamic topography and the geoid. *Nature* 313, 541–545. <https://doi.org/10.1038/313541a0>.
- Hartmann, L.A., Baggio, S.B., Brückmann, M.P., Knijnik, D.B., Lana, C., Masonne, H.J., Opitz, J., Pinto, V.M., Sato, K., Tassinari, C.C.G., Arena, K.R., 2019. U–Pb geochronology of Paraná volcanics combined with trace element geochemistry of the zircon crystals and zircon Hf isotope data. *J. S. Am. Earth Sci.* 89, 219–226.
- Heron, P.J., 2018. Mantle plumes and mantle dynamics in the Wilson cycle. *Geol. Soc. Lond., Spec. Publ.* 470, 18 p.
- Hu, J., Liu, L., Faccenda, M., Zhou, Q., Fischer, K.M., Marshak, S., Lundstrom, C., 2018. Modification of the Western Gondwana craton by plume–lithosphere interaction. *Nat. Geosci.* 11, 203–210.
- Iaffaldano, G., Bunge, H.-P., 2015. Rapid plate motion variations through geological time: observations serving geodynamic interpretation. *Annual Reviews of Earth Planetary Sciences* 43, 571–592.
- Jourdan, F., Féraud, G., Bertrand, H., Kampunzu, A.B., Tshoso, G., Watkeys, M.K., Le Gall, B., 2005. Karoo large igneous province: Brevity, origin, and relation to mass extinction questioned by new  $^{40}\text{Ar}/^{39}\text{Ar}$  age data. *Geological Society of America* 33, 745–748.
- Karl, M., Glasmacher, U.A., Kollenz, S., Franco-Magalhaes, A.O.B., Stockli, D.F., Hackspacher, P.C., 2013. Evolution of the South Atlantic passive continental margin in southern Brazil derived from zircon and apatite (U–Th–Sm)/He and fission-track data. *Tectonophysics* 604, 224–244.
- Keiding, J.K., Frei, O., Renno, A.D., Veksler, I.V., Trumbull, R.B., 2013. Conditions of magma crystallization in the Henties Bay–Outjo dyke swarm, Namibia: implications for the feeder system of continental flood basalts. *Lithos* 179 (2013), 16–27.
- Krob, C., Florian, Eldracher P., Daniel, Glasmacher A., Ulrich, H., Sabine, Salomon, Eric, Hackspacher C., Peter, Titus P., Nortin, et al., 2020. Late Neoproterozoic-to-recent long-term t–t evolution of the Kaoko and Damara belts in NW Namibia. *International Journal of Earth Sciences* <https://doi.org/10.1007/s00531-020-01819-7>.
- Krob, F., Karl, M., Glasmacher, U.A., Perner, M., Hackspacher, P., Stockli, D.F., 2019. Multi-chronometer thermochronological modelling of the Late Neoproterozoic to recent t–t evolution of the SE coastal region of Brazil. *J. S. Am. Earth Sci.* 92, 77–94. <https://doi.org/10.1016/j.jsames.2019.02.012>.
- Leng, W., Zhong, S., 2010. Surface subsidence caused by mantle plumes and volcanic loading in large igneous provinces. *Earth Planet. Sci. Lett.* 291, 207–214.
- Lithgow-Bertelloni, C., Gurnis, M., 1997. Cenozoic subsidence and uplift of continents from time-varying dynamic topography. *Geology* 25, 735–738.
- Maruyama, S., Santosh, M., Zhao, D., 2007. Superplume, supercontinent, and post-perovskite: Mantle dynamics and anti-plate tectonics on the Core–Mantle Boundary. *Gondwana Res.* 11, 7–37.
- Milani, E.J., de Melo, J.H.G., de Souza, P.A., Fernandes, L.A., França, A.B., 2007. Bacia do Paraná. *B. Geociências Petrobras, Rio de Janeiro* 15 (2), 265–287.
- Milner, S.C., 1986. The geological and volcanological features of the quartz latites of the Etendeka Formation. *Community Geological Survey, S.W. Africa/Namibia*, 2, 109–116.
- Miller, R.MacG., Becker, T., 2008. *The geology of Namibia*. Ministry of Mines and Energy, Namibia.
- Mitrovic, J.X., 1996. Haskell [1935] revisited. *J. Geophys. Res.* 101, 555–569.
- Montañez, I.P., Poulsen, C.J., 2013. The Late Paleozoic Ice Age: an evolving paradigm. *Annu. Rev. Earth Planet. Sci.* 41, 629–656.
- Mountey, N., Howell, J., 2000. Aeolian architecture, bedform, climbing and preservation space in the Cretaceous Etjo Formation, NW Namibia. *Sedimentology* 47, 825–849.
- Müller, D.R., Zahirovic, S., Williams, S.E., Cannon, J., Seton, M., Bower, D.J., Tetley, M.G., Heine, C., Le Breton, E., Liu, S., Russell, S.H.J., Yang, T., Leonard, J., Gurnis, M., 2019. A global plate model including lithospheric deformation along Major Rifts and Orogens since the Triassic. *Tectonics* 38, 24 p.
- Nance, R.D., Murphy, J.B., Santosh, M., 2014. The supercontinent cycle: a retrospective essay. *Gondwana Res.* 25, 4–29.
- Navarrete, C., Gianni, G., Encinas, A., Márquez, M., Kamerbeek, Y., Valle, M., Folguera, A., 2019. Triassic to Middle Jurassic geodynamic evolution of southwestern Gondwana: from a large flat-slab to mantle plume suction in a rollback subduction setting. *Earth-Sci. Rev.* 194, 125–159.
- Paton, D.A., van der Spuy, D., di Primio, R., Horsfield, B., 2008. Tectonically induced adjustment of passive-margin accommodation space; influence on the hydrocarbon potential of the Orange Basin. *South Africa: American Association of Petroleum Geologists* 100, 589–609.
- Petersen, K.D., Nielsen, S.B., Clausen, O.R., Stephenson, R., Gerya, T., 2010. Small-scale mantle convection produces stratigraphic sequences in sedimentary basins. *Science* 329, 827–830.
- Petersen, K.D., Schiffer, C., Nagel, T., 2018. LIP formation and protracted lower mantle upwelling induced by rifting and delamination. *Sci. Rep.* 8, 16578.
- Pirajno, F., Santosh, M., 2015. Mantle plumes, supercontinents, intracontinental rifting and mineral systems. *Precambrian Res.* 259, 243–261.
- Renne, P.R., Ernesto, M., Pacca, I.L.G., Coe, R.S., Glen, J.M., Prévot, M., Perrin, M., 1992. The age of Paraná flood volcanism, rifting of Gondwanaland, and the Jurassic–Cretaceous boundary. *Science* 258, 975–979.
- Renne, P.R., Deckart, K., Ernesto, M., Féraud, G., Piccirillo, E.M., 1996. Age of Ponta Grossa dike swarm (Brazil), and implications to Parana flood volcanism. *Earth Planet Science Letter* 144, 199–211.
- Richards, M.A., Hager, B.H., 1984. Geoid Anomalies in a Dynamic Earth. *J. Geophys. Res.* 89, 5987–6002.
- Santosh, M., Maruyama, S., Yamamoto, S., 2009. The making and breaking of supercontinents: some speculations based on superplumes, super downwelling and the role of tectosphere. *Gondwana Res.* 15, 324–341.
- Schuberth, B.S.A., Bunge, H.-P., Steinle-Neumann, G., Moder, C., Oeser, J., 2009. Thermal versus elastic heterogeneity in high-resolution mantle circulation models with pyrolytic composition: High plume excess temperatures in the lowermost mantle. *Geochem. Geophys. Geosyst.* 10 (1). <https://doi.org/10.1029/2008GC002235>.
- Şengör, A.M.C., 1995. Sedimentation and tectonics of fossil rifts. *Tectonics of Sedimentary Basins* 579, 53–118.
- Şengör, A.M.C., 2001. Elevation as indicator of mantle-plume activity. In: Ernst, R.E., Buchan, K.L. (Eds.), *Mantle Plumes: Their Identification Through Time*. Geological Society of America Special Papers Vol. 352:pp. 183–225. <https://doi.org/10.1130/0-8137-2352-3.183>.
- Simmons, N.A., Forte, A.M., Grand, S.P., 2009. Joint seismic, geodynamic and mineral physical constraints on three-dimensional mantle heterogeneity: Implications for the relative importance of thermal versus compositional heterogeneity. *Geophys. J. Int.* 177, 1284–1304.
- Sleep, N.H., 1997. Lateral flow and ponding of starting plume material. *J. Geophys. Res.* 102, 10001–10012.
- Stille, H., 1919. Die Begriffe Orogenese und Epigoronese. *Z. Dtsch. Geol. Ges.* 71, 164–208.
- Stollhofen, H., 1999. Karoo Synrift–Sedimentation und ihre tektonische Kontrolle am entstehenden Kontinentalrand Namibia. *Zeitschrift der deutschen geologischen Gesellschaft* 149, 519–632.
- Stollhofen, H., Stanisstreet, I.G., Bangert, B., Grill, H., 2000. Tuffs, tectonism and glacially related sea-level changes, Carboniferous–Permian, southern Namibia. *Palaeogeogr. Palaeoclimatol. Palaeoecol.* 161, 127–150.
- Stronck, N.A., Trumbull, R.B., Krienitz, M.-S., Niedermann, S., Romer, R.L., Harris, C., Day, J. M.D., 2017. Helium isotope evidence for a deep-seated mantle plume involved in South Atlantic breakup. *Geology* 45, 827–830.
- Torsvik, T.H., 2019. Earth history: a journey in time and space from base to top. *Tectonophysics* 760, 297–313.
- Torsvik, T.H., Smethurst, M.A., Burke, K., Steinberger, B., 2006. Large igneous provinces generated from the margins of the large low velocity provinces in the deep mantle. *Geophysical J. Int.* <https://doi.org/10.1111/j.1365-246X.2006.03158>.
- Torsvik, T.H., Rousse, S., Labails, C., Smethurst, M.A., 2009. A new scheme for the opening of the South Atlantic Ocean and the dissection of an Aptian salt basin. *Geophysical J. Int.* <https://doi.org/10.1111/j.1365-246X.2009.04137.x>.
- Torsvik, T.H., von der Voo, R., Doubrovine, P.V., Burke, K., Steinberger, B., Ashwal, L.D., Trønnes, R.G., Webb, S.J., Bull, A.L., 2014. Deep mantle structures as a reference frame for movements in and on the Earth. *Proc. Natl. Acad. Sci.* 111, 8735–8740.
- Torsvik, T.H., Cocks, L.R.M., 2013. Gondwana from top to base in space and time. *Gondwana Res.* 24, 999–1030.
- Trumbull, R.B., Vietor, T., Hahne, K., Wackerle, R., Ledru, P., 2004. Aeromagnetic mapping and reconnaissance geochemistry of the Early Cretaceous Henties Bay–Outjo dike swarm, Etendeka Igneous Province, Namibia. *J. Afr. Earth Sci.* 40, 17–29.
- Trumbull, R.B., Reid, D.L., de Beer, C., van Acken, D., Romer, R.L., 2007. Magmatism and continental breakup at the west margin of southern Africa: a geochemical comparison of dolerite dikes from northwestern Namibia and the Western Cape. *S. Afr. J. Geol.* 110, 477–502.
- Watts, A.B., Karner, G.D., Steckler, M.S., 1982. Lithospheric flexure and the evolution of sedimentary basins. *Philosophical Transactions of the Royal Society London A* 305, 249–281.
- Wilson, J.T., 1963. A possible origin of the Hawaiian islands. *Can. J. Phys.* 41 (6), 863–870. <https://doi.org/10.1139/p63-094>.
- Wilson, J.T., 1965. A new class of faults and their bearing on continental drift. *Nature* 207, 343–347.
- Yang, T., Gurnis, M., 2016. Dynamic topography, gravity and the role of lateral viscosity variations from inversion of global mantle flow. *Geophys. J. Int.* 207, 1186–1202.
- Yoshida, M., Santosh, M., 2011. Supercontinents, mantle dynamics and plate tectonics: a perspective based on conceptual vs. numerical models. *Earth-Sci. Rev.* 105, 1–24.





# APPENDIX

---

## CONTENTS

A: SUPPLEMENTARY MATERIAL FOR CHAPTER 2	137
B: SUPPLEMENTARY MATERIAL FOR CHAPTER 3	177
C: SUPPLEMENTARY MATERIAL FOR CHAPTER 4	213

---





## A: SUPPLEMENTARY MATERIAL FOR CHAPTER 2

## Supplementary Materials for

### Multi-chronometer thermochronological modelling of the Late Neoproterozoic to recent t-T-evolution of the SE coastal region of Brazil

Florian C. Krob, Ulrich A. Glasmacher, Markus Karl, Melissa Perner, Peter C. Hackspacher, Daniel F. Stockli

**Corresponding author:** Florian Krob, Institute of Earth Sciences, Heidelberg University, Im Neuenheimer Feld 234, 69120 Heidelberg, Germany, E-mail: [florian.krob@geow.uni-heidelberg.de](mailto:florian.krob@geow.uni-heidelberg.de), Telephone: +49-6221-4836.

#### Contents:

- Tables S1 to S8
- Figures S1 to S6
- Additional references

## Tables S1 – S8:

Table A. 1: Sub phases of the syn- to post-rift evolution of the SAPCM, t-t-interval in [Ma], geological events, and sedimentary consequences for the study area. Geological history is based on published work by Hackspacher et al. (2004), Riccomini et al. (2004), Franco-Magalhaes et al. (2010), Hiruma et al. (2010), Cogné et al. (2011, 2012, 2013), Karl et al. (2013), and Engelmann de Oliveira et al. (2016).

Time interval [Ma]	Geological events	Sedimentary consequences for the study area
	Syn- to post-rift	
135-90	- 133±1Ma: Eruptions of Paraná flood basalts	Erosion and Sedimentation in onshore and offshore basins
	Post-rift	
90-65	- ≈90 Ma: Start of Bauru Sedimentation - ≈90-80 Ma: Intrusion and extrusion of alkaline magma	Erosion and Sedimentation in onshore and offshore basins
65-55	Inversion of Paraná Basin	Erosion and Sedimentation in onshore and offshore basins
55-24	- ≈55 Ma: Start of Taubaté Basin subsidence - volcanic activity	Erosion and Subsidence of onshore basins, Sedimentation in onshore and offshore basins
24-0	- ≈24 Ma: Start of surface uplift of Serra do Mar	Erosion and Sedimentation in onshore and offshore basins

Table A. 2: Overview of t-T-constraints derived from the geological model showing t-t-interval, T-T-interval and information/cause behind. Constraint boundaries were implemented in the software code HeFTy® and slightly modified when necessary.

Constraint boundaries		Information behind/ Cause
Time interval [Ma]	Temperature interval [°C]	
700-500	200-300	Rock Formation Age
465-425	5-40	Rio Ivaí Supersequence Sedimentation
405-360	5-80	Paraná Supersequence Sedimentation
305-250	5-205	Gondwana I Supersequence Sedimentation
240-220	5-215	Gondwana II Supersequence Sedimentation
155-133	60-290	Gondwana III Supersequence Sedimentation
66-50	20-40	Inversion of Paraná basin and Start of Taubaté Basin subsidence
24-0	20-50	Uplift of Serra do Mar, uplift to surface, Erosion
Depends on sample age	200-240	ZFT age information
Depends on sample age	160-200	ZHe age information
Depends on sample age	60-110	AFT age information
Depends on sample age	50-75	AHe age information

Table A. 3: All thermochronological samples with corresponding ages, which are shown on map (age < formation age) and were used for modelling (\*). Sample number, L.: Lithology, S: Stratigraphy, E.: Elevation a.s.l. [m], ZFT age, ZHe age, AFT age, AHe age. Gns: gneiss; grt: granite; grd: granodiorite; sch: schist; rhy: rhyolite; s: sandstone; hor: hostrock; cha: chalcosilicate; peb: pebbles; N. Neoproterozoic; P.: Permian; Ca.: Carboniferous; J./C.: Jurassic/Cretaceous; Pa.: Paleogene.

Sample number	L.	S.	E. a.s.l. [m]	ZFT	ZHe	AFT	AHe
<b>Santos Block</b>							
BR10-01*	sch	N.	694			130.7±8.8	95.5±5.7
<b>Peruibe Block</b>							
BR10-02	sch	N.	689	145.5±16.8		80.6±6.6	
BR10-03	gns	N.	55	353.7±48.8		69.5±6.5	
BR10-04*	gns	N.	36		366.5±1.7	89.6±6.5	
BR10-05*	gns	N.	29	188.8±27.6	119.9±9.6	88.0±6.3	81.5±4.9
<b>Ilha Comprida Block</b>							
BR10-07*	gns	N.	56	292.4±51.7	288.2±23.1 303.8±24.3	73.0±8.4	
BR10-08*	gns	N.	193	262.8±32.4	207.3±16.6		
BR10-09*	gns	N.	218	362.6±51.1	368.3±29.5	69.0±8.4	58.9±3.5 46.9±2.8
BR10-10	grd	N.	547			102.9±9.8	47.9±2.9
BR10-11*	gns	N.	728	387.8±57.0	414.2±33.1 392.9±31.4	67.8±7.1	83.1±5.0 93.8±5.6 91.8±5.5
<b>Curitiba Block</b>							
BR09-01*	rhy	N.	990		129.7±10.4		
BR09-02	rhy	N.	1046	255.1±33.3			
BR09-05B	peb	Pa.	751			63.0±6.1	59.5±2.0
BR10-12*	cha	N.	693	349.5±52.9	323.4±25.9	85.0±6.8	78.3±4.7
BR10-15*	grt	N.	913		355.9±28.5	70.9±7.4	75.0±4.5
BR10-17	hor	N.	777	300.0±33.8	295.9±23.7	78.0±5.4	82.2±4.9
BR10-18	grt	N.	102	300.0±44.3	281.5±22.5		
<b>Florianopolis Block</b>							
BR09-16	s	J./C.	945			93.2±8.1	
BR09-24	s	P.	797			125.8±9.6	
BR09-26	peb	P./Ca.	895			118.9±7.8	92.0±1.9
BR09-27	gns	N.	903			120.6±8.9	
BR09-28	grt	N.	830	539.9±68.4		101.9±11.9	
BR10-16	grt	N.	897			93.5±8.7	
BR10-20*	gns	N.	129	314.1±39.8	203.3±16.3 182.5±14.6 191.6±15.3	98.5±6.9	43.0±2.6

Sample number	L.	S.	E. a.s.l. [m]	ZFT	ZHe	AFT	AHe
BR10-21*	gns	N.	37	467.1±64.7	299.1±23.9 310.9±24.9	106.3±10.	52.4±3.1
BR10-22*	gns	N.	25	432.5±64.2	391.3±31.3	104.4±8.4	85.2±5.1
BR10-23*	gns	N.	51		459.9±36.8	102.9±7.0	
BR10-24*	grd	N.	151		411.0±32.9	105.5±6.3	61.9±3.7 78.6±4.7
BR10-25*	grd	N.	66	481.1±68.7	453.5±36.3 435.0±34.8	104.5±7.5	45.4±2.7
BR10-26*	grt	N.	51		306.1±24.5 299.1±23.9	125.8±8.9	107.3±8.6
BR10-27*	grt	N.	211	414.3±64.3	398.6±31.9	85.2±5.3	78.3±6.3
BR10-29*	grt	N.	13		375.4±30.0		
<b>Laguna Block</b>							
BR09-35	s	J.	931			79.7±10.9	
BR09-42	s	P.	760	108.4±15.0		59.5±5.2	
BR09-43	s	J./C.	630		124.9±0.6	-	54.8±0.5
BR09-45*	grd	N.	194	125.6±16.5	106.2±8.5	76.4±5.9	63.2±1.0
BR09-46*	grt	N.	133			69.8±5.6	87.2±7.0 78.2±6.3 72.9±5.8
BR09-47*	grt	N.	0	230.8±32.1	124.2±9.9		
BR09-50*	grt	N.	27	217.3±64.3		76.2±6.6	
BR09-51*	grt	N.	7			76.7±6.1	
BR09-52*	grt	N.	13			73.4±5.6	
BR09-53*	grt	N.	20			70.7±4.6	
BR10-32*	grt	N.	17	106.4±13.9	98.5±7.9 115.3±9.2 117.5±9.4	78.0±5.8	
BR10-34	grt	N.	20			68.4±5.2	

Table A. 4.1: Summary of the dated samples in SE Brazil with corresponding sample numbers, coordinates, block, lithology, stratigraphic age, and elevation ([m] a.s.l.). \*: Samples were used for modeling. The samples of the Tables 6.1-6.6 were taken, prepared, processes, and dated by Dipl. Geol. Markus Karl, Dr. Melissa Perner, Dr. Sebastian Kollenz and myself, and analysed and modeled within this thesis.

Sample number	Longitude	Latitude	Block	Lithology	Stratigraphic Age	Elevation [m a.s.l.]
BR10-01*	-47.066167	-23.937014	Santos	shist	Neoprot.	694
BR10-02	-47.197786	-24.047448	Peruibe	mica shist	Neoprot.	689
BR10-03	-47.371101	-24.209567	Peruibe	gneiss	Neoprot.	55
BR10-04*	-47.453992	-24.287623	Peruibe	gneiss	Neoprot.	36
BR10-05*	-47.655567	-24.351499	Peruibe	mafic gneiss	Neoprot.	29
BR10-07*	-48.107322	-24.756174	Ilha Comprida	mafic gneiss	Neoprot.	56
BR10-08*	-48.214800	-24.819181	Ilha Comprida	gneiss	Neoprot.	193
BR10-09*	-48.216107	-24.854436	Ilha Comprida	gneiss	Neoprot.	218
BR10-10	-48.405987	-24.969814	Ilha Comprida	mafic	Neoprot.	547
BR10-11*	-48.508220	-24.994649	Ilha Comprida	mafic gneiss	Neoprot.	728
BR09-01*	-50.002778	-24.756028	Curitiba	rhyolite	Neoprot.	990
BR09-02	-50.028222	-24.851139	Curitiba	rhyolite	Neoprot.	1046
BR09-05B	-50.349556	-25.105528	Curitiba	pebbles	Paleocene	751
BR10-12*	-48.728815	-25.100749	Curitiba	calcosilicate	Neoprot.	693
BR10-15*	-49.141517	-25.670478	Curitiba	granite	Neoprot.	913
BR10-17	-48.955296	-25.854945	Curitiba	hostrock	Neoprot.	777
BR10-18	-48.892551	-25.970910	Curitiba	granite	Neoprot.	102
BR09-16	-51.578528	-25.858500	Florianópolis	sandstone	Jurassic	1219
BR09-24	-50.067056	-25.868167	Florianópolis	sandstone	Permian	959
BR09-26	-49.746028	-25.770167	Florianópolis	pebbles	Carbon./ Permian	895
BR09-27	-49.526917	-25.683500	Florianópolis	gneiss	Neoprot.	903
BR09-28	-49.786389	-26.116667	Florianópolis	granite	Neoprot.	830
BR10-16	-48.084813	-25.846006	Florianópolis	granite	Neoprot.	897
BR10-20*	-48.933681	-26.235959	Florianópolis	gneiss	Neoprot.	129
BR10-21*	-48.972989	-26.464876	Florianópolis	gneiss	Neoprot.	37
BR10-22*	-49.017046	-26.608871	Florianópolis	gneiss	Neoprot.	25
BR10-23*	-49.199346	-26.890775	Florianópolis	gneiss	Neoprot.	51
BR10-24*	-49.013877	-26.874146	Florianópolis	granodiorite	Neoprot.	151
BR10-25*	-48.890703	-27.007167	Florianópolis	granodiorite	Neoprot.	66
BR10-26*	-48.921248	-27.245727	Florianópolis	granite	Neoprot.	51
BR10-27*	-48.812697	-27.277589	Florianópolis	granite	Neoprot.	211
BR10-29*	-48.646658	-27.277321	Florianópolis	granite	Neoprot.	13
BR09-17	-51.521611	-26.200972	Laguna	andesite	Cretacious	903
BR09-35	-50.193083	-27.866528	Laguna	sandstone	Jurassic	931
BR09-42	-49.527083	-28.394194	Laguna	sandstone	Jurassic	760
BR09-43	-49.508361	-28.388083	Laguna	sandstone	Permian	630
BR09-45*	-49.306389	-28.360639	Laguna	granodiorite	Neoprot.	194
BR09-46*	-49.114694	-28.294778	Laguna	granite	Neoprot.	133
BR09-47*	-48.766278	-28.469722	Laguna	granite	Neoprot.	0
BR09-50*	-49.178583	-28.697250	Laguna	granite	Neoprot.	27
BR09-51*	-49.051778	-28.580389	Laguna	granite	Neoprot.	7
BR09-52*	-48.968083	-28.446528	Laguna	granite	Neoprot.	13
BR09-53*	-48.858167	-28.425528	Laguna	granite	Neoprot.	20
BR10-32*	-48.660976	-27.931087	Laguna	granite	Neoprot.	17
BR10-34	-48.702006	-28.251693	Laguna	granite	Neoprot.	20

Table A 4. 1: Summary of zircon fission-track data. Sample number, \*: Sample were used for modeling, L.: Lithology, F.a.: Formation age, U: uranium concentration in  $\mu\text{g/g}$ , n: number of counted grains,  $\rho_s$ : density of spontaneous tracks ( $\times 10^5/\text{cm}^2$ ),  $N_s$ : number of spontaneous tracks,  $\rho_i$ : density of induced tracks ( $\times 10^5/\text{cm}^2$ ),  $N_i$ : number of induced tracks, P ( $\chi^2$ ) is the probability that single grain ages are consistent and belong to the same population. Test is passed if P ( $\chi^2$ ) > 5% (Galbraith 1981). Ages calculated using a  $\zeta$ -value of  $113.43 \pm 7.86 \text{ a/cm}^2$  for zircon. Gns: gneiss; grd: granodiorite; grt: granite; ms: mica schist; cal: calcosilicate; s: sandstone; rhy: rhyolite. For further descriptions see Table A. 4.1.

Sample number	L.	F.A.	U (std) [ $\mu\text{g/g}$ ]	n	$\rho_s$ [ $\times 10^5/\text{cm}^2$ ]	$N_s$	$\rho_i$ [ $\times 10^5/\text{cm}^2$ ]	$N_i$	$\chi^2$ [%]	Central age [Ma]	$\pm(1\sigma)$ [Ma]
<b>Peruibe Block</b>											
BR10-02	ms	Neoprot	320.9 (89.8)	20	246.8	757	46.9	144	100.0	145.5	16.8
BR10-04*	gns	Neoprot	153.5 (47.6)	20	296.6	994	22.7	76	100.0	353.7	48.8
BR10-05*	ms	Neoprot	271.0 (70.5)	12	274.3	486	39.5	70	100.0	188.8	27.6
<b>Ilha Comprida Block</b>											
BR10-07*	gns	Neoprot	182.6 (38.3)	11	291.0	365	33.5	42	99.7	292.4	51.7
BR10-08*	gns	Neoprot	126.4 (40.4)	20	178.2	839	22.7	107	99.2	262.8	32.4
BR10-09*	gns	Neoprot	115.9 (51.0)	18	201.0	790	18.3	72	100.0	362.6	51.1
BR10-11*	gns	Neoprot	63.5 (16.5)	19	139.0	770	11.6	64	100.0	387.8	57.0
<b>Curitiba Block</b>											
BR09-02	rhy	Neoprot	50.3 (16.1)	19	61.1	587	8.1	78	100.0	255.1	33.3
BR10-12*	cha	Neoprot	138.85 (45.8)	16	255.1	646	23.7	60	100.0	349.5	52.9
BR10-17	grt	Neoprot	132.9 (49.2)	20	215.9	1332	22.9	141	100.0	300.0	33.8
BR10-18	grt	Neoprot	158.5 (31.7)	12	265.2	622	27.7	65	100.0	300.0	44.3
<b>Florianopolis Block</b>											
BR09-28	grt	Neoprot	1.05 (0.4)	21	311.2	1866	16.0	96	100.0	539.9	68.4
BR10-20*	gns	Neoprot	170.3 (44.3)	16	282.5	1003	27.6	98	100.0	314.1	39.8
BR10-21*	gns	Neoprot	77.2 (22.4)	19	191.0	1153	12.3	74	100.0	467.1	64.7
BR10-22*	gns	Neoprot	106.8 (31.0)	19	246.6	905	16.9	62	100.0	432.5	64.2
BR10-25*	grd	Neoprot	82.1 (25.4)	20	208.1	1136	12.5	68	100.0	481.1	68.7
BR10-27*	grt	Neoprot	139.1 (44.5)	20	306.5	791	21.3	55	100.0	414.3	64.3
<b>Laguna Block</b>											
BR09-42	s	Neoprot.	396.72 (111.1)	8	230.2	383	76.3	127	13.5	108.4	15.0
BR09-45*	grd	Neoprot	487.21 (389.8)	7	252.8	409	69.8	113	23.9	125.6	16.5
BR09-47*	grt	Neoprot	2.45 (1.1)	13	2.8	533	0.4	79	100.0	230.8	32.1
BR09-50*	grt	Neoprot	2.64 (0.8)	3	2.9	89	0.5	14	98.1	217.3	64.3
BR10-32*	grt	Neoprot	232.2 (90.5)	11	126.8	377	34.6	103	99.9	106.4	13.9

Table A 4. 2: Summary of zircon (U-Th-(Sm))/He data. Grains were only used when ZHe age < formation age and when ZFT > ZHe Age < AFT. Sample number, \*: Grains were used for modeling, L.: Lithology, M: mass, Contributing U, Th, Sm, and He concentration, eU = [U] + 0.235 [Th] (concentration in weight %), Ft:  $\alpha$ -ejection factor for apatite and zircon calculated after Farley et al. (1996), Uncorrected (Uncorr.) ages and  $\pm 1\sigma$  error are corrected (corr.) for  $\alpha$ -ejection with accordant  $\pm 1\sigma$  error. Gns: gneiss; grd: granodiorite; grt: granite; ms: mica schist; cal: calcosilicate; s: sandstone; rhy: rhyolite. For further descriptions see Table A. 4.1.

Sample number	L.	M [μg]	U [μg/g]	Th [μg/g]	Sm [μg/g]	He [nmol/g]	Th/U	eU [μg/g]	Ft	Uncorr. age	$\pm(1\sigma)$ [Ma]	Corr. age [Ma]	$\pm(1\sigma)$ [Ma]
<b>Peruibe Block</b>													
BR10-04-3*	gns	20.80	39.8	16.7	0.60	75.18	0.42	43.7	0.84	307.9	1.4	366.5	1.7
BR10-05-1*	gns	14.21	574.6	108.00	7.80	319.60	0.19	599.5	0.82	98.3	7.9	119.9	9.6
<b>Ilha Comprida Block</b>													
BR10-07-1*	gns	5.65	128.4	53.10	0.80	166.20	0.41	140.6	0.74	213.3	17.1	288.2	23.1
BR10-07-2*	gns	9.17	115.1	71.55	1.58	174.65	0.62	131.6	0.79	240.2	19.2	303.8	24.3
BR10-08-1*	gns	5.75	289.4	82.60	1.30	266.40	0.29	308.4	0.76	157.5	12.6	207.3	16.6
BR10-09-1*	gns	18.60	86.80	21.40	1.70	154.80	0.25	91.8	0.82	302.0	24.2	368.3	29.5
BR10-11-1*	gns	10.00	35.94	18.35	0.88	73.51	0.51	40.1	0.79	328.5	26.3	414.2	33.1
BR10-11-2*	gns	5.75	46.23	12.23	0.61	81.08	0.26	49.1	0.76	297.8	23.8	392.9	31.4
<b>Curitiba Block</b>													
BR09-01-1*	rhy	4.74	35.5	52.70	3.71	25.12	1.48	47.8	0.74	96.0	7.7	129.7	10.4
BR10-12-2*	cal	4.95	249.6	41.80	22.50	68.20	0.37	271.1	0.74	239.3	19.1	323.4	25.9
BR10-15-1*	grt	15.63	80.31	35.66	0.53	143.30	0.44	88.5	0.82	291.7	23.3	355.9	28.5
BR10-17-1	grt	11.53	140.6	161.23	0.63	232.08	1.15	177.7	0.80	236.2	18.9	295.9	23.7
BR10-18-2	grt	4.18	263.6	372.49	3.85	387.20	1.41	349.4	0.71	200.9	16.1	281.5	22.5
<b>Florianopolis Block</b>													
BR10-20-1*	gns	9.58	769.9	153.00	1.00	701.00	0.20	805.1	0.78	159.1	12.7	203.3	16.3
BR10-20-2*	gns	10.13	474.7	101.80	0.70	394.80	0.21	498.2	0.79	144.2	11.5	182.5	14.6
BR10-20-3*	gns	8.34	653.0	140.42	1.01	562.67	0.22	685.4	0.78	150.1	12.0	191.6	15.3
BR10-21-1*	gns	6.95	107.1	64.90	0.60	154.60	0.61	122.0	0.77	230.3	18.4	299.1	23.9
BR10-21-3*	gns	9.58	128.6	102.14	0.72	200.46	0.79	152.1	0.77	238.4	19.1	310.9	24.9
BR10-22-3*	gns	10.12	159.3	90.30	0.90	312.30	0.57	180.1	0.80	313.0	25.0	391.3	31.3
BR10-23-3*	gns	12.74	79.13	53.96	0.26	190.19	0.68	91.55	0.81	371.3	29.7	459.9	36.8
BR10-24-1*	grd	8.74	175.6	136.30	2.10	367.00	0.78	207.0	0.78	320.6	25.6	411.0	32.9
BR10-25-1*	grd	16.81	72.90	74.89	1.16	184.50	1.03	90.15	0.81	365.9	29.3	453.5	36.3
BR10-25-3*	grd	19.76	88.20	73.80	0.30	207.00	0.84	105.2	0.81	352.4	28.2	435.0	34.8
BR10-26-1*	grt	11.86	164.6	58.19	1.13	242.08	0.35	178.0	0.80	246.1	19.7	306.1	24.5
BR10-26-2*	grt	34.06	166.1	43.91	0.42	249.94	0.26	176.2	0.86	256.6	20.5	299.1	23.9
BR10-27-3*	grt	10.20	63.70	36.10	0.40	126.90	0.57	72.00	0.79	314.9	25.2	398.6	31.9
BR10-29-3*	grt	13.78	0.60	0.40	0.00	1.10	0.66	0.70	0.80	300.3	24.0	375.4	30.0
<b>Laguna Block</b>													
BR09-43-1*	s	8.2	102.3	52.36	11.76	60.94	0.51	114.6	0.78	97.7	0.5	124.9	0.6
BR09-45-2*	grt	4.86	568.0	200.49	4.83	313.05	0.35	615.2	0.74	93.6	7.5	126.5	10.1
BR09-46-1*	grt	15.15	878.3	259.58	39.25	366.23	0.3	939.3	0.82	71.5	5.7	87.2	7
BR09-46-2*	grt	11.69	762.3	375.65	22.71	293.58	0.49	850.5	0.81	63.4	5.1	78.2	6.3
BR09-46-3*	grt	4.28	663.0	437.52	25.26	223.41	0.66	765.8	0.74	54	4.3	72.9	5.8
BR09-47-3*	grt	9.3	659.2	817.45	26.59	458.92	1.24	851.3	0.80	99.4	8.0	124.2	9.9
BR10-32-1*	grt	6.13	487.2	143.30	4.20	211.60	0.29	520.2	0.76	74.9	6.0	98.5	7.9
BR10-32-2*	grt	4.09	643.0	234.36	2.41	316.93	0.36	697.0	0.73	83.6	6.7	115.3	9.2
BR10-32-3*	grt	2.60	266.5	87.50	0.97	123.74	0.33	286.6	0.68	79.4	6.4	117.5	9.4

Table A 4. 3: Summary of apatite fission-track data. L.: Lithology; F.a.: Formation age; U: uranium concentration in  $\mu\text{g/g}$ ; n: number of counted grains,  $\rho_s$ : density of spontaneous tracks ( $\times 10^5/\text{cm}^2$ ),  $N_s$ : number of spontaneous tracks,  $\rho_i$ : density of induced tracks ( $\times 10^5/\text{cm}^2$ ),  $N_i$ : number of induced tracks,  $P(\chi^2)$  is the probability that single grain ages are consistent and belong to the same population. Test is passed if  $P(\chi^2) > 5\%$  (Galbraith 1981). Ages calculated using a  $\zeta$ -value of  $349.07 \pm 15.53 \text{ a/cm}^2$  for apatite. Gns: gneiss; grd: granodiorite; grt: granite; ms: mica schist; cal: calcosilicate; s: sandstone; and: andesite; rhy: rhyolite; ba: basalt. For further descriptions see Table A. 4.1.

Sample number	L.	F.a.	U (std) [ $\mu\text{g/g}$ ]	n	$\rho_s$ [ $\times 10^5/\text{cm}^2$ ]	$N_s$	$\rho_i$ [ $\times 10^5/\text{cm}^2$ ]	$N_i$	$c^2$ [%]	Central age [Ma]	$\pm(1\sigma)$ [Ma]
<b>Santos Block</b>											
BR10-01*	mst	Neoprot.	21.5 (12.0)	25	12.3	626	22.6	1146	99.7	130.7	8.8
<b>Peruibe Block</b>											
BR10-02*	ms	Neoprot.	10.7 (7.5)	22	3.8	283	11.4	848	99.8	80.6	6.6
BR10-03*	gns	Neoprot.	2.8 (1.5)	25	0.9	189	3.3	660	99.6	69.5	6.5
BR10-04*	gns	Neoprot.	9.0 (6.9)	21	3.9	416	10.6	1132	100.0	89.6	6.5
BR10-05	gns	Neoprot.	18.5 (7.4)	21	7.4	706	17.2	1647	99.2	88.0	6.3
<b>Ilha Combrida Block</b>											
BR10-07	gns	Neoprot.	7.7 (6.6)	12	2.3	133	6.3	375	80.2	73.0	8.4
BR10-09	gns	Neoprot.	3.4 (2.1)	20	1.1	118	3.3	353	76.3	69.0	8.4
BR10-10	gns	Neoprot.	5.8 (1.8)	21	2.8	255	5.6	510	97.7	102.9	9.8
BR10-11	gns	Neoprot.	4.8 (2.7)	20	1.5	166	4.6	506	100.0	67.8	7.1
<b>Curitiba Block</b>											
BR09-05B	peb	Paleogene	7.6 (4.1)	20	2.2	274	7.4	922	5.2	63.0	6.1
BR10-12	cal	Neoprot.	19.1 (12.8)	18	7.0	420	16.9	1021	89.8	85.0	6.8
BR10-15	grt	Neoprot.	4.2 (2.6)	24	1.3	175	3.9	511	100.0	70.9	7.4
BR10-17	grt	Neoprot.	47.4 (18.5)	20	18.5	902	49.1	2393	75.0	78.0	5.4
<b>Florianopolis Block</b>											
BR09-16	and	Creta.	4.55 (0.9)	20	2.2	295	3.5	462	90.3	93.2	8.1
BR09-24	s	Carb./Per.	14.02 (13.0)	30	5.7	439	10.6	819	78.0	125.8	9.6
BR09-26	peb	Carb./Per	18.96 (15.0)	57	8.8	1940	18.3	4046		118.9	7.8
BR09-27	gns	Neoprot.	11.55 (3.9)	20	6.7	549	8.1	670	99.8	120.6	8.9
BR09-28	grt	Neoprot.	3.4 (3.0)	27	1.6	141	2.5	218	100.0	101.9	11.9
BR10-16	grt	Neoprot.	7.6 (3.8)	22	3.2	264	7.1	584	99.8	93.5	8.7
BR10-20	gns	Neoprot.	25.8 (11.9)	22	11.7	818	24.7	1719	96.5	98.5	6.9
BR10-21	gns	Neoprot.	3.8 (1.7)	25	1.9	223	3.7	443	100.0	106.3	10.0
BR10-22	gns	Neoprot.	3.0 (1.8)	25	1.5	334	3.1	689	99.3	104.4	8.4
BR10-23	gns	Neoprot.	17.0 (10.7)	23	7.6	573	16.2	1221	92.1	102.9	7.0
BR10-24	grd	Neoprot.	20.4 (9.2)	20	9.7	966	20.6	2046	99.4	105.5	6.3
BR10-25	grd	Neoprot.	9.8 (3.5)	20	4.8	461	10.3	995	98.4	104.5	7.5
BR10-26	grt	Neoprot.	6.4 (1.9)	22	4.0	532	7.2	961	98.0	125.8	8.9
BR10-27	grt	Neoprot.	27.1 (10.3)	19	10.9	737	29.6	1991	76.4	85.2	5.3
<b>Laguna Block</b>											
BR09-17	ba	Creta.	8.67 (4.4)	5	1.9	24	8.6	107	91.4	47.7	11.0
BR09-35	s	Jurassic	9.84 (3.4)	5	3.6	90	7.1	178	89.8	79.7	10.9
BR09-42	s	Jurassic	28.05 (10.9)	19	8.6	495	21.3	1235	1.0	59.5	5.2
BR09-45	grd	Neoprot.	12.36 (6.6)	20	4.6	304	13.8	919	58.7	76.4	5.9
BR09-46	grt	Neoprot.	9.93 (6.6)	23	3.3	269	10.9	888	99.9	69.8	5.6
BR09-50	grt	Neoprot.	17.4 (7.3)	21	6.6	226	19.7	678	99.29	76.2	6.6
BR09-51	grt	Neoprot.	23.98 (10.1)	25	9.1	282	26.6	824	100.0	76.7	6.1
BR09-52	grt	Neoprot.	15.18 (6.4)	21	5.4	307	16.7	949	99.69	73.4	5.6
BR09-53	grt	Neoprot.	16.99 (7.3)	24	5.9	483	18.6	1523	98.92	70.7	4.6
BR10-32	grt	Neoprot.	12.0 (6.9)	23	4.1	381	12.3	1145	98.5	78.0	5.8
BR10-34	grt	Neoprot.	14.4 (7.5)	18	4.6	350	16.0	1210	76.7	68.4	5.2



Table A 4. 4: Summary of apatite fission-track length and Dpar data. Sample number, \*: Data were used for modeling, n CT: number of measured confined tracks, CT mean: mean confined track length, std: standard deviation, skew: skewness of distribution relative to the mean value (measure of asymmetry of the distribution), Lc mean: mean track length after c-axis correction, n Dpar: number of etch pit diameters measured, Dpar mean: mean etch pit diameter. For further descriptions see Table A. 4.1.

Sample number	n CT	CT mean [μm]	CT std [μm]	CT skew	Lc mean [μm]	Lc std [μm]	Lc skew	n Dpar	Dpar mean [μm]	Dpar std [μm]	Dpar skew
<b>Santos Block</b>											
BR10-01*	84	12.6	1.8	-0.793	13.9	1.2	-0.769	125	1.8	0.3	-0.519
<b>Peruibe Block</b>											
BR10-02*	13	12.5	2	-1.828	14.2	1	-1.535	108	1.4	0.2	0.382
BR10-03	1	15.8	-	-	16.3	-	-	125	1.2	0.2	0.949
BR10-04*	59	12.8	1.4	-0.188	14.0	1.1	-0.529	193	1.3	0.2	0.316
BR10-05*	52	13.2	1.1	-0.904	14.4	0.7	-0.807	170	1.5	0.2	0.100
<b>Ilha Comprida Block</b>											
BR10-07	3	14.2	1.1	-1.668	15.0	0.5	0.662	54	1.8	0.3	0.897
BR10-09	-	-	-	-	-	-	-	96	1.6	0.2	0.398
BR10-10	6	14.2	0.4	0.737	15.4	0.3	0.855	106	1.8	0.4	0.403
BR10-11	-	-	-	-	-	-	-	100	1.1	0.2	0.276
<b>Curitiba Block</b>											
BR09-05B	-	-	-	-	-	-	-	181	1.1	0.2	0.570
BR10-12	8	13.3	1.3	0.255	14.6	0.9	0.081	88	1.4	0.2	0.071
BR10-15	3	9.4	2.3	1.110	11.3	3.1	-1.530	121	1.4	0.3	0.370
BR10-17	54	11.7	1.8	-0.941	13.6	1	-0.061	116	1.6	0.2	0.293
<b>Florianopolis Block</b>											
BR09-24	84	11.0	1.9	0.800	13.0	1.5	0.200	30	1.4	0.1	-0.100
BR09-26	91	11.5	1.7	-0.100	14.4	1.4	-0.600	57	1.4	0.1	1.700
BR09-27	9	10.5	1.8	-0.700	12.4	1.3	0.020	50	1.4	0.2	0.210
BR09-28	2	9.3	2.1	-	9.8	2.6	-	26	1.3	0.2	-0.220
BR10-16	1	12.1	-	-	13.9	-	-	108	1.2	0.2	-0.058
BR10-20*	67	12.6	1.9	0.319	14.0	1.3	0.493	135	1.5	0.3	0.542
BR10-21	12	12.5	1.9	0.177	13.9	1.1	0.348	143	1.8	0.3	0.196
BR10-22	3	12.8	1.5	-0.508	13.8	1.4	0.894	125	1.6	0.2	-0.339
BR10-23*	72	13.5	1.4	-0.417	14.6	0.9	-0.316	196	1.9	0.3	0.213
BR10-24*	71	12.9	1.6	-0.766	14.1	1.2	-1.343	161	1.6	0.2	0.301
BR10-25*	66	13.1	1.4	0.219	14.3	1.1	-0.328	230	2.1	0.3	0.299
BR10-26*	55	13.2	1.6	-0.661	14.4	1.2	-1.462	220	1.4	0.2	0.101
BR10-27*	76	13.1	1.4	-0.331	14.4	0.9	-0.544	318	1.6	0.2	0.269
<b>Laguna Block</b>											
BR09-17	-	-	-	-	-	-	-	12	1.0	0.3	0.450
BR09-35	-	-	-	-	-	-	-	5	1.2	0.1	0.200
BR09-45*	95	10.7	1.8	0.174	12.9	1.2	-0.016	140	1.4	0.1	1.5
BR09-46*	93	10.7	1.8	0.478	12.1	1.7	-0.331	165	1.4	0.2	1.6
BR09-50*	80	11.7	1.7	-0.404	13	1.7	-1.184	160	1.3	0.1	1.5
BR09-51*	101	12.2	1.6	-0.402	13.7	1.2	-1.235	175	1.4	0.1	1.7
BR09-52*	78	11.8	1.7	-0.465	12.9	2.1	-1.549	145	1.3	0.1	1.6
BR09-52*	100	11.5	1.9	-0.121	13.1	1.8	-1.068	165	1.3	0.1	1.5
BR10-32*	55	12.5	1.9	-0.057	14.0	1.3	-0.388	243	1.3	0.2	0.232
BR10-34	10	11.6	1.5	-0.100	13.4	1.3	-1.454	90	1.5	0.2	-0.215

Table A 4. 5: Summary of apatite (U-Th-(Sm))/He data. Grains were only used when AHe age < formation age and when AFT > AHe Age. Sample number, \*: Grains were used for modeling, M: mass, contributing U, Th, Sm, and He concentration, eU = [U] + 0.235 [Th] (concentration in weight %), Ft:  $\alpha$ -ejection factor for apatite and zircon calculated after Farley et al. (1996), Uncorrected (Uncorr.) ages and  $\pm 1\sigma$  error are corrected (corr.) for  $\alpha$ -ejection with accordant  $\pm 1\sigma$  error. For further descriptions see Table A. 4.1.

Sample number	M [ $\mu$ g]	U [ $\mu$ g/g]	Th [ $\mu$ g/g]	Sm [ $\mu$ g/g]	He [nmol/g]	Th/U	eU [ $\mu$ g/g]	Ft	Uncorr. age [Ma]	$\pm(1\sigma)$ [Ma]	Corr. age [Ma]	$\pm(1\sigma)$ [Ma]
<b>Santos Block</b>												
BR10-01-3*	1.30	4.59	5.62	4.77	1.91	1.22	5.90	0.62	59.4	3.6	95.5	5.7
<b>Peruibe Block</b>												
BR10-05-3*	13.7	4.09	5.08	29.29	1.99	1.24	5.41	0.82	66.4	4.0	81.5	4.9
<b>Ilha Comprida Block</b>												
BR10-09-2*	3.79	1.68	0.14	13.77	0.43	0.09	1.78	0.74	43.6	2.6	58.9	3.5
BR10-09-3*	2.74	0.88	0.71	5.92	0.19	0.81	1.08	0.70	32.7	2.0	46.9	2.8
BR10-10-3	0.74	5.34	10.24	63.94	1.17	1.92	8.02	0.55	26.1	1.6	47.9	2.9
BR10-11-1*	2.85	1.05	3.64	25.42	0.65	3.47	2.02	0.68	56.5	3.4	83.1	5.0
BR10-11-2*	1.36	3.60	14.51	42.93	2.27	4.03	7.15	0.60	56.7	3.4	93.8	5.6
BR10-11-3*	2.41	2.00	8.27	36.96	1.43	4.13	4.09	0.67	61.7	3.7	91.8	5.5
<b>Curitiba Block</b>												
BR09-05B-3	0.56	18.3	27.56	24.39	4.13	1.51	24.76	0.51	30.3	1.0	59.5	2.0
BR10-12-1*	1.38	8.71	4.60	6.00	2.62	0.53	9.80	0.63	49.3	3.0	78.3	4.7
BR10-15-2*	4.09	1.60	3.70	50.20	0.80	2.41	1.90	0.72	54.0	3.2	75.0	4.5
BR10-17-1	3.21	47.1	72.00	48.10	20.10	1.53	30.40	0.70	57.5	3.5	82.2	4.9
<b>Florianopolis Block</b>												
BR09-26-1	3.88	12.5	21.3	39.68	6.21	1.7	17.54	0.7	64.1	1.3	92	1.9
BR10-20-3*	1.26	6.73	0.24	25.47	1.04	0.04	6.23	0.64	27.6	1.7	43.0	2.6
BR10-21-3*	3.22	1.54	0.11	23.55	0.36	0.07	1.68	0.73	38.2	2.3	52.4	3.1
BR10-22-2*	3.43	1.22	0.92	45.80	0.59	0.75	1.66	0.70	59.5	3.6	85.2	5.1
BR10-24-1*	8.13	7.92	1.48	10.05	2.21	0.19	8.31	0.79	48.9	2.9	61.9	3.7
BR10-24-3*	2.28	19.4	14.39	36.55	6.67	0.74	22.89	0.68	53.4	3.2	78.6	4.7
BR10-25-2*	0.92	5.71	0.96	52.54	0.93	0.17	6.19	0.60	27.1	1.6	45.4	2.7
BR10-26-2*	1.56	4.03	10.83	12.78	2.34	2.69	6.58	0.60	64.6	5.2	107.3	8.6
BR10-27-3	3.48	24.3	36.80	119.2	10.10	1.52	33.40	0.70	54.8	4.4	78.3	6.3
<b>Laguna Block</b>												
BR09-43-1	1.0	43.8	126.2	46.5	12.71	2.88	73.47	0.58	31.8	0.3	54.8	0.5
BR09-45-1	3.94	19.4	15.25	40.47	5.8	0.78	23.04	0.73	45.8	0.7	63.2	1

Table A. 5: Overview of sample data which was used for modelling. Sample number, Block (S.: Santos; P.: Peruibe; I.C.: Ilha Comprida; C.: Curitiba; F.: Florianopolis; L.: Laguna), ZFT Constraint: x when implemented in HeFTy<sup>\*</sup>; ZHe: number of grains implemented for the ZHe system (x); AFT lengths: x when implemented in HeFTy; AHe: number of grains implemented for the AHe system (x).

Sample number	Block	ZFT const.	ZHe	AFT age $\pm$ length	AHe
BR10-01	S.			x	x
BR10-04	P.		x	x	
BR10-05	P.		x	x	x
BR10-07	I. C.		2 x		
BR10-08	I. C.	x	x		
BR10-09	I. C.	x	x		2 x
BR10-11	I. C.	x	2 x		3 x
BR09-01	C.		x		
BR10-12	C.	x	x		x
BR10-15	C.		x		x
BR10-20	F.	x	3 x	x	x
BR10-21	F.	x	2 x		x
BR10-22	F.	x	x		x
BR10-23	F.		x	x	
BR10-24	F.		x	x	2 x
BR10-25	F.	x	2 x	x	x
BR10-26	F.		2 x	x	x
BR10-27	F.	x	x	x	
BR10-29	F.		x		
BR09-45	L.	x	x	x	
BR09-46	L.			x	3 x
BR09-47	L.		x		
BR09-50	L.	x		x	
BR09-51	L.			x	
BR09-52	L.			x	
BR09-53	L.			x	
BR10-32	L.		3 x	x	

Table A. 6: Paraná Basin deposition sequences and corresponding assumed sediment thicknesses (Milani et al., 2007) and expected temperatures. Sequence: Name of depositional sequence, Formation, Period, Time [Ma]: occurrence in [Ma], Time  $\Delta$  [Ma]: time interval in [Ma], col [m]: accumulated sediments for  $\Delta t$ ; Total Col. [m]: accumulated sediment columns of each time interval, assumable deposited on top of the basement, Temp. [°C]: expected temperatures, calculated from total column with corresponding surface temperatures and geothermal gradient including an error ( $\pm 10^\circ\text{C}$ ).

Sequence	Formation	Period	Time [Ma]	Time $\Delta$ [Ma]	Col. [m]	Total Col. [m]	Temp. [°C]
<b>Bauru</b>	<b>Total</b>	<b>Cretaceous</b>	<b>90-70</b>	<b>20</b>	<b>260</b>	<b>7888</b>	<b>300-280</b>
<b>Gondwana</b>	<b>Total</b>	<b>Jurassic/ Cretaceous</b>	<b>155-130</b>	<b>25</b>	<b>215</b>	<b>7628</b>	<b>290-265</b>
Gondwana	Serra Geral	Cretaceous	140-130	10	170	7628	-
Gondwana	Botucatu	Jurassic/ Cretaceous	155-140	15	450	5928	-
<b>Gondwana II</b>	<b>Santa Maria</b>	<b>Triassic</b>	<b>240-220</b>	<b>20</b>	<b>300</b>	<b>5478</b>	<b>215-190</b>
<b>Gondwana I</b>	<b>Total</b>	<b>Carb./ Permian.</b>	<b>305-250</b>	<b>55</b>	<b>382</b>	<b>5178</b>	<b>205-185</b>
Gondwana I	Passa Dois	Permian	280-250	30	167	5178	-
Gondwana I	Guatá	Permian	290-280	10	650	3508	-
Gondwana I	Itararé	Carb./ Permian	305-290	15	150	2858	-
<b>Paraná</b>	<b>Total</b>	<b>Devonian</b>	<b>415-360</b>	<b>55</b>	<b>997</b>	<b>1358</b>	<b>80-40</b>
Paraná	Ponta Grossa	Devonian	405-360	45	660	1358	-
Paraná	Furnas	Devonian	415-405	10	337	698	-
<b>Rio Ivaí</b>	<b>Total</b>	<b>Ordovician/ Silurian</b>	<b>465-445</b>	<b>40</b>	<b>361</b>	<b>361</b>	<b>-</b>
Rio Ivaí	Vila Maria	Silurian	440-425	15	38	361	40-10
Rio Ivaí	Iapó	Ordovician	445-440	5	70	323	-
Rio Ivaí	Alto Gracas	Ordovician	465-445	20	253	253	-

Table A. 7: Compiled published geochronological data for the Southern Ribeira and Dom Feliciano belts in south-eastern Brazil. Data is presented blockwise and organised according to the dating method and closing temperature. Location, Rock type, Age [Ma],  $\pm$ Error [Ma], Primary reference, Secondary reference (where data was found).

<b>Santos Block</b>					
<b>Location</b>	<b>Rock type</b>	<b>Age [Ma]</b>	<b><math>\pm</math> Error [Ma]</b>	<b>Primary reference</b>	<b>Secondary reference</b>
<b>U-Pb (SHRIMP), zircon, T(c): <math>\approx</math>700-800° C</b>					
Complexo	charnockite	571.0	20.0	Tassinari (2008)	Basei et al. (2010)
Complexo	granite	576.0	16.0	Tassinari (2008)	Basei et al. (2010)
Complexo	aplite	584.0	13.0	Tassinari (2008)	Basei et al. (2010)
Complexo	charnockite	577.0	32.0	Tassinari (2008)	Basei et al. (2010)
Complexo	granitoid	567.0	27.0	Tassinari (2008)	Basei et al. (2010)
Complexo	granodiorite	620.0	11.0	Tassinari (2008)	Basei et al. (2010)
<b>U-Pb (LA-ICP-MS), zircon, T(c): <math>\approx</math>700-800° C</b>					
Lagoinha	bt-granite	581.0	4.9	Alves et al. (2013)	
Caucaia	bt-granite	583.2	3.6	Alves et al. (2013)	
Itapeti	bt-granite	578.6	5.1	Alves et al. (2013)	
Sabaúna	bt-granite	577.3	4.8	Alves et al. (2013)	
Santa Catarina	bt-granite	631.8	5.4	Alves et al. (2013)	
Mongaguá	n/a	590-630	n/a	Passarelli et al. (2008)	
Cubatão SZ (CSZ)	n/a	600.0	n/a	Passarelli et al. (2008)	
Mongaguá	amph-bt-monzogranite	612.4	3.1	Passarelli et al. (2004)	
Mongaguá	bt-monzogranite	579.0	11.0	Passarelli et al. (2004)	
Mongaguá	bt-monzogranite	578.0	12.0	Passarelli et al. (2004)	
Mongaguá	bt-tonalite	647.0	8.6	Passarelli et al. (2004)	
Complexo	metasediment	571.0	10.0	Dias Neto (2001)	
Complexo	metagabbro	577.0	23.0	Dias Neto (2001)	
Complexo	metagabbro	593.0	10.0	Dias Neto (2001)	
Complexo	gneiss	571.0	50.0	Dias Neto (2001)	
Complexo	amphibolite	580.0	n/a	Dias Neto (2001)	
Complexo	amphibolite	608.0	n/a	Dias Neto (2001)	
North of São	metavolcanic	628.0	9.0	Hackspacher et al. (2000)	
<b>U-Pb (LA-ICP-MS), monazite, T(c): <math>\approx</math>500-650° C</b>					
North of São	paragneiss	607.0	3.0	Hackspacher et al. (2004)	
North of São	paragneiss	625.0	3.0	Hackspacher et al. (2004)	
North of São	paragneiss	598.0	7.0	Hackspacher et al. (2004)	
North of São	paragneiss	608.0	9.0	Hackspacher et al. (2004)	
<b>U-Pb (TIMS), monazite, T(c): <math>\approx</math>500-650° C</b>					
Serra Q. Cangalha	mus-bt-granite	664.1	1.3	Alves et al. (2013)	
Santa Branca	mus-bt-granite	594.7	1.2	Alves et al. (2013)	
Guacuri	mus-bt-granite	589.8	7.7	Alves et al. (2013)	
Mauá	bt-granite	588.0	2.0	Alves et al. (2013)	
<b>Sm-Nd, isochron, whole rock, T(c): <math>\approx</math>650° C</b>					
Complexo	paragneiss	519.0	13.0	Dias Neto (2001)	
Complexo	paragneiss	482.0	9.5	Dias Neto (2001)	
Complexo	paragneiss	469.0	24.0	Dias Neto (2001)	

Location	Rock type	Age [Ma]	± Error [Ma]	Primary reference	Secondary reference
<b>Sm-Nd, isochron, garnet-RT, T(c): ≈600° C</b>					
Complexo Costeiro	gneiss	529.0	n/a	Dias Neto (2001)	
Complexo Costeiro	gneiss	559.0	n/a	Dias Neto (2001)	
Complexo Costeiro	pegmatite	528.0	17.0	Dias Neto (2001)	
Complexo Costeiro	pegmatite	562.0	n/a	Dias Neto (2001)	
<b>Rb-Sr, isochron, whole rock, T(c): ≈500-750° C</b>					
Complexo Costeiro	paragneiss	547.0	32.0	Dias Neto (2001)	
Complexo Costeiro	paragneiss	463.0	190.0	Dias Neto (2001)	
<b>Rb-Sr, isochron, plag-RT, T(c): ≈550° C</b>					
Complexo Costeiro	gneiss	508.0	n/a	Dias Neto (2001)	
Complexo Costeiro	gneiss	518.0	n/a	Dias Neto (2001)	
Complexo Costeiro	gneiss	507.0	n/a	Dias Neto (2001)	
Complexo Costeiro	gneiss	521.0	n/a	Dias Neto (2001)	
Complexo Costeiro	gneiss	487.0	3.8	Dias Neto (2001)	
<b>Rb-Sr, isochron, plag-muscovite, T(c): ≈500° C</b>					
Complexo Costeiro	gneiss	509.0	n/a	Dias Neto (2001)	
Complexo Costeiro	pegmatite	481.0	190.0	Dias Neto (2001)	
<b>Rb-Sr, isochron, apatite-biotite, T(c): ≈450° C</b>					
Complexo Costeiro	apatite	488.0	8.5	Dias Neto (2001)	
<b>Rb-Sr, isochron, plag-biotite, T(c): ≈400° C</b>					
Complexo Costeiro	gneiss	469.0	n/a	Dias Neto (2001)	
Complexo Costeiro	gneiss	483.0	7.3	Dias Neto (2001)	
Complexo Costeiro	amphibolite	467.0	8.9	Dias Neto (2001)	
Complexo Costeiro	amphibolite	464.0	3.2	Dias Neto (2001)	
<b>K-Ar, hbl-biotite, T(c): ≈300-450° C</b>					
North of São Paulo	paragneiss	580-600	n/a	Hackspacher et al. (2001b)	
<b>K-Ar, muscovite, T(c): ≈350° C</b>					
Complexo Costeiro	paragneiss	475.0	11.6	Dias Neto (2001)	
Complexo Costeiro	paragneiss	419.0	9.9	Dias Neto (2001)	
Complexo Costeiro	paragneiss	491.0	10.4	Dias Neto (2001)	
Complexo Costeiro	paragneiss	486.0	9.4	Dias Neto (2001)	
Complexo Costeiro	paragneiss	506.0	14.7	Dias Neto (2001)	
Complexo Costeiro	gneiss	473.0	14.0	Tassinari (1988)	Dias Neto (2001)
Complexo Costeiro	migmatite	470.0	14.0	Tassinari (1988)	Dias Neto (2001)
<b>K-Ar, biotite, T(c): ≈300° C</b>					
Cubatão Shear Zone	n/a	500.0	n/a	Pasarelli et al. (2008)	
Complexo Costeiro	paragneiss	470.0	10.7	Dias Neto (2001)	
Complexo Costeiro	leptinite	462.0	13.0	Tassinari (1988)	Dias Neto (2001)
Complexo Costeiro	gneiss	443.0	13.0	Tassinari (1988)	Dias Neto (2001)
Complexo Costeiro	migmatite	483.0	14.0	Tassinari (1988)	Dias Neto (2001)
Complexo Costeiro	migmatite	475.0	14.0	Tassinari (1988)	Dias Neto (2001)
Complexo Costeiro	migmatite	496.0	14.0	Tassinari (1988)	Dias Neto (2001)
Complexo Costeiro	gneiss	460.0	14.0	Tassinari (1988)	Dias Neto (2001)
Complexo Costeiro	gneiss	480.0	16.0	Tassinari (1988)	Dias Neto (2001)
<b>K-Ar, amphibole, T(c): ≈200° C</b>					
Complexo Costeiro	paragneiss	491.0	17.5	Dias Neto (2001)	
Complexo Costeiro	paragneiss	465.0	8.7	Dias Neto (2001)	
Complexo Costeiro	paragneiss	428.0	41.0	Dias Neto (2001)	
Complexo Costeiro	leptinite	480.0	14.0	Tassinari (1988)	Dias Neto (2001)
<b>K-Ar, feldspar, T(c): ≈200° C</b>					
Complexo Costeiro	leptinite	455.0	13.0	Tassinari (1988)	Dias Neto (2001)

Peruibe Block					
Domain	Rock type	Age (Ma)	± Error [Ma]	Primary reference	Secondary reference
<b>U-Pb (LA-ICP-MS), zircon, T(cl): ≈700-800° C</b>					
Registro	n/a	590-610	n/a	Pasarelli et al. (2008)	
Embu	n/a	750-800	n/a	Pasarelli et al. (2008)	
Registro	bt-monzogranite	580.0	23.0	Passarelli et al. (2004)	
<b>U-Pb (LA-ICP-MS), monazite, T(cl): ≈500-650° C</b>					
Embu	n/a	580-610	n/a	Pasarelli et al. (2008)	
Juréia Massif	paragneiss	741.0	7.0	Passarelli et al. (2006)	
Juréia Massif	gneiss	752.3	4.3	Passarelli et al. (2004)	
Juquiá	granite	598.0	8.8	Passarelli et al. (2004)	
<b>Sm-Nd, isochron, whole rock, T(cl): ≈650° C</b>					
Itatins Massif, Sp	granulite	607.0	13.6	Picanço (1994)	Passarelli et al. (2018)
Itatins Massif, Sp	gneiss	582.0	22.0	Picanço (1994)	Passarelli et al. (2018)
<b>Rb-Sr, isochron, whole rock, T(cl): ≈500-750° C</b>					
Itatins Massif, Sp	gneiss	601.0	32.0	Picanço (1994)	Passarelli et al. (2018)
<b>K-Ar, hornblende, T(cl): ≈500-550° C</b>					
Itatins Massif, Sp	granulite	656.0	n/a	Picanço (1994)	Passarelli et al. (2018)
<b>K-Ar, muscovite, T(cl): ≈350° C</b>					
Embu	n/a	550.0	n/a	Pasarelli et al. (2008)	
<b>K-Ar, biotite, T(cl): ≈300° C</b>					
Registro	n/a	490-510	n/a	Pasarelli et al. (2008)	
Embu	n/a	500.0	n/a	Pasarelli et al. (2008)	
Embu	mylonite	492.7	13.9	Passarelli (2001)	
Embu	mylonite	413.0	8.8	Passarelli (2001)	
Embu	mylonite	496.7	9.3	Passarelli (2001)	
Embu	mylonite	367.7	7.3	Passarelli (2001)	
Miracatu, Sp	biotite gneiss	504.0	9.0	Passarelli (2001)	Passarelli et al. (2018)
Itatins Massif, Sp	granulite	590-580	n/a	Picanço (1994)	Passarelli et al. (2018)

Ilha Comprida Block					
Domain	Rock type	Age (Ma)	± Error [Ma]	Primary reference	Secondary reference
<b>U-Pb (SHRIMP), zircon, T(cl): ≈700-800° C</b>					
Iporanga Sequeunce	metavolcanic	573.0	34.0	Campanha et al. (2008b)	Siga Jr. et al. (2011)
Iporanga Sequeunce	granite clasts	593.0	15.0	Campanha et al. (2008b)	Siga Jr. et al. (2011)
<b>U-Pb (TIMS), zircon, T(cl): ≈700-800° C</b>					
Varginha Granite	granite	604.0	n/a	Siga Jr. et al. (2011)	
Varginha Granite	granite	616.0	n/a	Siga Jr. et al. (2011)	
Varginha Granite	granite	650.0	n/a	Siga Jr. et al. (2011)	
Varginha Granite	granite	631.0	n/a	Siga Jr. et al. (2011)	
<b>U-Pb (LA-ICP-MS), zircon, T(cl): ≈700-800° C</b>					
Iguape	n/a	580-600	n/a	Pasarelli et al. (2008)	
Iguape	bt-monzogranite	599.0	15.0	Passarelli et al. (2004)	
Serra do Cordeiro	bt-monzogranite	581.6	3.8	Passarelli et al. (2004)	
Votupoca	bt-monzogranite	582.5	8.7	Passarelli et al. (2004)	

Domain	Rock type	Age (Ma)	± Error [Ma]	Primary reference	Secondary reference
Tres	hbl-bt-	605.1	2.0	Prazeres Filho et al.	
Tres	granite	610.0	3.0	Prazeres Filho et al.	
Tres	hbl-bt-gneiss	608.0	5.0	Prazeres Filho et al.	
<b>U-Pb (LA-ICP-MS), monazite, T(cl): ≈500-650° C</b>					
Sete Barras	granite	631.0	23.0	Passarelli et al. (2004)	
<b>Rb-Sr, isochron, whole rock, T(cl): ≈500-750° C</b>					
Tres Córregos	granite	605.0	n/a	Prazeres Filho et al. (2000)	Prazeres Filho et al. (2000)
<b>K-Ar, muscovite, T(cl): ≈350° C</b>					
Serrinha	mylonite	575.0	16.0	Passarelli et al. (2006)	
Iguape	mylonite	575.2	15.7	Passarelli (2001)	
<b>K-Ar, biotite, T(cl): ≈300° C</b>					
Serrinha	mylonite	482.0	12.0	Passarelli et al. (2006)	Passarelli et al. (2006)
Serrinha	mylonite	493.0	9.0	Passarelli et al. (2006)	Passarelli et al. (2006)
Iguape	granite	505.0	15.7	Passarelli (2001)	Passarelli (2001)
Iguape	mylonite	481.5	12.1	Passarelli (2001)	Passarelli (2001)
Iguape	mylonite	493.4	9.2	Passarelli (2001)	Passarelli (2001)

<b>Curitiba Block</b>					
Domain	Rock type	Age (Ma)	± Error [Ma]	Primary reference	Secondary reference
<b>U-Pb (SHRIMP), zircon, T(cl): ≈700-800° C</b>					
Abapã Sequence	metavolcanic	645.0	30.0	Siga Jr. et al. (2009)	Siga Jr. et al. (2011)
Abapã Sequence	metavolcanic	641.0	11.0	Siga Jr. et al. (2009)	Siga Jr. et al. (2011)
Abapã Sequence	metavolcanic	628.0	18.0	Siga Jr. et al. (2009)	Siga Jr. et al. (2011)
Tres Córregos	granite	601.0	13.0	Tassinari (2008)	Basei et al. (2010)
Itaoca pluton	monzogranite	623.0	10.0	Salazar et al. (2008)	
Cunhaporanga	monzogranite	627.0	8.0	Prazeres Filho et al. (2005)	Santos et al. (2015)
Tres Córregos	monzogranite	616.0	11.0	Prazeres Filho et al. (2005)	Santos et al. (2015)
Tres Córregos	monzogranite	608.0	11.0	Prazeres Filho et al. (2005)	Santos et al. (2015)
Tres Córregos	diorite	608.0	24.0	Prazeres Filho et al. (2005)	Santos et al. (2015)
Cunhaporanga	monzogranite	603.0	9.0	Prazeres Filho et al. (2005)	Santos et al. (2015)
Tres Córregos	granodiorite	601.0	13.0	Prazeres Filho et al. (2005)	Santos et al. (2015)
Tres Córregos	qtz-monzogranite	601.0	22.0	Prazeres Filho et al. (2005)	Santos et al. (2015)
Cunhaporanga	granodiorite	601.0	7.0	Prazeres Filho et al. (2005)	Santos et al. (2015)
Cunhaporanga	granite	533.0	15.0	Prazeres Filho et al. (2005)	Basei et al. (2010)
Tres Córregos	granite	645.0	10.0	Prazeres Filho et al. (2005)	Basei et al. (2010)
Tres Córregos	granite	582.0	14.0	Prazeres Filho et al. (2005)	Basei et al. (2010)
Itaicoca Belt	metavolcanic	628.0	18.0	Siga Jr. et al. (2003)	
Itaicoca Belt	metavolcanic	636.0	30.0	Siga Jr. et al. (2003)	
<b>U-Pb (TIMS), zircon, T(cl): ≈700-800° C</b>					
Abapã Sequence	metavolcanic	636.0	30.0	Siga Jr. et al. (2009)	Siga Jr. et al. (2011)
Curitiba	gneiss	595.0	n/a	Siga Junior et al. (1995)	Passarelli et al. (2018)
Curitiba	gneiss	577-617	n/a	Siga Junior et al. (1995)	Passarelli et al. (2018)



Domain	Rock type	Age (Ma)	± Error [Ma]	Primary reference	Secondary reference
<b>U-Pb (LA-ICP-MS), zircon, T(cl): ≈700-800° C</b>					
Itaicoca Belt	metavolcanic	628-	n/a	Siga Jr. et al. (2009)	Siga Jr. et al.
Núcleo Setuva	gneiss	570.0	45.0	Siga Jr. et al. (2007)	
Cunhaporanga	granodiorite	625.0	10.0	Prazeres Filho et al.	
Cunhaporanga	bt-monzogranite	588.0	70.0	Prazeres Filho et al.	
Tres Córregos	hbl-bt-granodiorite	633.0	3.0	Prazeres Filho et al.	
Tres Córregos	hbl-bt-granodiorite	628.0	16.0	Prazeres Filho et al.	
Tres Córregos	hbl-bt-qtz-	604.0	4.0	Prazeres Filho et al.	
<b>U-Pb (EPMA), monazite, T(cl): ≈500-650° C</b>					
Cajati	feldspar	589.0	12.0	Faleiros (2008)	Faleiros (2011)
Cajati	feldspar	575-600	n/a	Faleiros (2008)	Faleiros (2011)
<b>Sm-Nd, isochron, whole rock, T(cl): ≈650° C</b>					
Curitiba	gneiss	595.0	30.0	Siga Jr. et al. (1995)	Passarelli et al.
Mandirituba	amph-gneiss	585.0	30.0	Siga Jr. et al. (1995)	Passarelli et al.
<b>Rb-Sr, isochron, whole rock, T(cl): ≈500-750° C</b>					
Atuba Quarry	bt-amph-gneiss	598.0	48.0	Siga Jr. et al. (1995)	Passarelli et al.
Atuba Quarry	bt-amph-gneiss	617.0	14.0	Siga Jr. et al. (1995)	Passarelli et al.
<b>Ar-Ar, amphib-hbl, T(cl): ≈500-550° C</b>					
Atuba Complex	n/a	570-580	n/a	Machado et al. (2007)	Faleiros (2011)
Tigre Nuclei	qtz-monzodiorite	598.0	1.2	Kaulfuss (2011)	Siga Jr. et al. (2011)
<b>K-Ar, amphib-hbl, T(cl): ≈500-550° C</b>					
Tigre Nuclei	qtz-monzodiorite	618.0	36.0	Kaulfuss (2011)	Siga Jr. et al. (2011)
<b>Ar-Ar, muscovite, T(cl): ≈350° C</b>					
Betara	quartzite	614.0	2.0	Kaulfuss (2011)	Siga Jr. et al. (2011)
Atuba Complex	n/a	560-570	n/a	Machado et al. (2007)	Faleiros (2011)
<b>K-Ar, muscovite, T(cl): ≈350° C</b>					
Betara	quartzite	604.0	11.0	Kaulfuss (2011)	Siga Jr. et al. (2011)
<b>Ar-Ar, biotite, T(cl): ≈300° C</b>					
Cajati	paragneiss	555.0	4.0	Faleiros (2008)	Faleiros (2011)
Núcleo Setuva	orthogneiss	588.0	1.0	Siga Jr. et al. (1995)	Passarelli et al.
<b>K-Ar, biotite, T(cl): ≈300° C</b>					
Atuba Complex	n/a	500-550	n/a	Campagnoli (1996)	Faleiros (2011)
Atuba Complex	gneiss	600.0	20.0	Siga Jr. et al. (1995)	Passarelli et al.

Florianópolis Block					
Domain	Rock type	Age (Ma)	± Error	Primary reference	Secondary reference
<b>U-Pb (SHRIMP), zircon, T(c): ≈700-800° C</b>					
Camboriú Complex	granodiorite	590-630	n/a	Silva et al. (2005),	Florisbal et al.
Rio Pequeno Granite	bt-monzogranite	626.0	7.0	Chemale Jr. et al. (2003), Lopes (2008), Florisbal et al. (2010)	Florisbal et al. (2012)
Itapema granite	bt-monzogranite	640.0	n/a	Chemale Jr. et al. (2003), Lopes	Florisbal et al. (2012)
Itajaí Basin	syenogranite	560.0	9.0	Basei et al. (2008)	Basei et al. (2010)
Itajaí Basin	granite	529.0	16.0	Basei et al. (2008)	Basei et al. (2010)
Itapema Granite	monzogranite	590-630	n/a	Hartmann et al. (2003)	)
Vargem Grande	Flo. Batholith	611.0	3.0	Silva et al. (2002)	Jelinek et al. (2005)
Alto Varginha	Flo. Batholith	579.0	8.0	Silva et al. (2002)	Jelinek et al. (2005)
Rancho Queimado-	Flo. Batholith	608.0	7.0	Silva et al. (2002)	Jelinek et al. (2005)
Águas Mornas	gneiss	595.0	n/a	Silva et al. (2000)	
Camboriú Complex	monzogranite	611.0	5.0	Silva et al. (unpubl.)	Hartmann et al.
Valsungana Granite	monzogranite	596.0	9.0	Silva et al. (unpubl.)	Hartmann et al.
Maruim tonalite	tonalite	610.0	6.0	Silva et al. (unpubl.)	Hartmann et al.
Camboriú Complex	bt-	593.0	9.0	Silva et al. (1999)	Hartmann et al.
Itajaí Basin	syenogranite	563.0	12.0	Cordani et al. (1999)	Basei et al. (2010)
<b>U-Pb (TIMS), zircon, T(c): ≈700-800° C</b>					
Mariscal Granite	metatonalite	646.	15.0	Chemale et al. (2012)	Santos et al. (2015)
Quatro Ilhas Granitoid	felsic volcanic	615.	7.0	Chemale et al. (2012)	Santos et al. (2015)
Morro dos Macacos, Sp	granite	588.	3.0	Chemale et al. (2012)	Santos et al. (2015)
Morro dos Macacos	bt-monzogranite	590.	3.3	Chemale Jr. et al.	Florisbal et al.
Estaleiro Granite Complex	hbl-bt-	602.	3.4	Chemale Jr. et al.	Florisbal et al.
Porto Belo Complex	orthogneiss	646.	15.0	Chemale Jr. et al.	Florisbal et al.
Santa Luzia Granite	Flo. Batholith	600.	7.0	Basei (unpubl.)	Jelinek et al. (2005)
Guabiruba Granite	Flo. Batholith	478.	14.0	Basei (unpubl.)	Jelinek et al. (2005)
Valsungana Granite	Flo. Batholith	647.	12.0	Basei (unpubl.)	Jelinek et al. (2005)
Major Gercino Suite	Flo. Batholith	640.	n/a	Basei et al. (1995)	Jelinek et al. (2005)
<b>U-Pb (LA-ICP-MS), zircon, T(c): ≈700-800° C</b>					
Quatro Ilhas Granitoid	metatonalite	649.	10.0	Chemale et al. (2012)	Santos et al.
Brusque Group	granite	623.	6.0	Chemale et al. (2012)	Santos et al.
Quatro Ilhas Granitoid	felsic volcanic	617.	6.0	Chemale et al. (2012)	Santos et al.
Zimbros Granite	granite	587.	8.0	Chemale et al. (2012)	Santos et al.
Serra dos Macacos Granite	monzogranite	611.0	9.0	Chemale Jr. et al. (2003), Lopes (2008),	Florisbal et al. (2012)
Rio Pequeno Granite	bt-monzogranite	622.0	15.0	Chemale Jr. et al. (2003), Lopes (2008),	Florisbal et al. (2012)
Mariscal Granite	mus-bt-syenogranite	609.0	8.0	Chemale Jr. et al. (2003), Florisbal et al.	Florisbal et al. (2012)
Quatro Ilhas Granitoid	bt-monzogranite	625.0	7.0	Chemale Jr. et al. (2003), Florisbal et al.	Florisbal et al. (2012)
Quatro Ilhas Granitoid	bt-monzogranite	614.0	4.0	Chemale Jr. et al. (2003), Florisbal et al.	Florisbal et al. (2012)
Major Gercino Suite	bt-monzogranite	609.	16.0	Passarelli et al. (2010)	
Major Gercino Suite	bt-monzogranite	614.	2.0	Passarelli et al. (2010)	
Camboriú Complex	bt-monzogranite	638.	32.0	Basei et al. (2000)	Hartmann et al.
Camboriú Complex	bt-monzogranite	628.	7.0	Silva et al. (1999)	Hartmann et al.

Domain	Rock type	Age (Ma)	± Error [Ma]	Primary reference	Secondary reference
<b>Rb-Sr, isochron, whole rock, T(cl): ≈500-750° C</b>					
Quitandinha	bt-amph-gneiss	595.0	41.0	Siga Jr. et al. (1995)	Passarelli et al. (2018)
Quitandinha	bt-amph-gneiss	577.0	17.0	Siga Jr. et al. (1995)	Passarelli et al. (2018)
<b>K-Ar, muscovite, T(cl): ≈350° C</b>					
Major Gercino Suite	mylonite	569.0	14.0	Passarelli et al. (2010)	
Major Gercino Suite	mylonite	539.0	13.0	Passarelli et al. (2010)	
<b>K-Ar, biotite, T(cl): ≈300° C</b>					
Major Gercino Suite	monzogranite	575.0	12.0	Passarelli et al. (2010)	
Major Gercino Suite	syenogranite	584.0	25.0	Passarelli et al. (2010)	
Major Gercino Suite	monzogranite	561.0	18.0	Passarelli et al. (2010)	
Major Gercino Suite	syenogranite	572.0	10.0	Passarelli et al. (2010)	
Major Gercino Suite	mylonite	569.0	10.0	Passarelli et al. (2010)	

<b>Laguna Block</b>					
Domain	Rock type	Age (Ma)	± Error [Ma]	Primary reference	Secondary reference
<b>U-Pb (SHRIMP), zircon, T(cl): ≈700-800° C</b>					
Pedra Grande Suite	granodiorite	613.0	5.0	Jelinek et al. (2005)	
Pedra Grande Suite	monzogranite	595.0	5.0	Jelinek et al. (2005)	
Serra do Tabuleiro Granite	Flo. Batholith	594.0	8.0	Silva et al. (1997)	Jelinek et al. (2005)
Tabuleiro Granite	Flo. Batholith	617.0	9.0	Silva et al. (unpubl.)	Jelinek et al. (2005)
Paulo Lopes Granite	Flo. Batholith	626.0	8.0	Silva et al. (unpubl.)	Jelinek et al. (2005)
Paulo Lopes Granite	monzogranite	628.0	8.0	Silva et al. (unpubl.)	Hartmann et al. (2003)
Pedras Grandes Suite	monzogranite	613.0	5.0	Silva et al. (unpubl.)	Hartmann et al. (2003)

Table A. 8: Calculated cooling and heating rates, respectively, taken from numerical modeling and converted into exhumation and subsidence rates, respectively. Paleo-surface temperatures are  $\approx 10^{\circ}\text{C}$  for pre-Mesozoic time and  $\approx 25^{\circ}\text{C}$  from Mesozoic to recent time. Block, Description: cooling or heating, t-t-segment [Ma],  $\Delta t$ , T-T-segment [ $^{\circ}\text{C}$ ],  $\Delta T$ , Cooling/ Heating rate [ $^{\circ}\text{C}/\text{km}$ ], exhumation/ subsidence rate [ $\text{mm}/\text{a}$ ].

Block	Description	t-t Segment [Ma]	$\Delta t$	T-T Segment [ $^{\circ}\text{C}$ ]	$\Delta T$	Cooling rate [ $^{\circ}\text{C}/\text{Ma}$ ]	Exhumation rate [ $\text{mm}/\text{a}$ ]
Santos	Cooling	640-510	130	750-650	100	0.77	0.026
	Cooling	510-500	10	650-280	370	37.00	1.233
	Cooling	500-380	120	280-15	265	2.21	0.074
	Heating	380-150	230	15-110	95	0.41	0.014
	Cooling	150-55	95	110-25	80	0.84	0.028
	Heating	55-24	31	25-35	10	0.32	0.011
	Cooling	24-0	24	35-20	15	0.63	0.021
Peruibe	Cooling	600-550	50	750-350	400	8.00	0.267
	Cooling	550-400	150	350-280	70	0.47	0.016
	Cooling	400-360	40	280-15	265	6.63	0.221
	Heating	360-135	225	15-140	125	0.556	0.019
	Cooling	135-55	80	140-25	115	1.44	0.048
	Heating	55-24	31	25-36	11	0.36	0.012
	Cooling	24-0	24	36-20	16	0.67	0.022
Ilha Comprida	Cooling	620-560	60	750-340	410	6.83	0.228
	Cooling	560-430	130	340-290	50	0.39	0.013
	Cooling	430-330	100	290-15	275	2.75	0.092
	Heating	330-135	195	15-150	135	0.69	0.023
	Cooling	135-55	80	150-26	124	1.55	0.052
	Heating	55-24	31	26-37	11	0.36	0.012
	Cooling	24-0	24	37-20	17	0.71	0.024
Curitiba (Ponta Grossa area)	Cooling	640-580	60	760-310	450	7.50	0.250
	Cooling	580-430	150	310-15	295	1.97	0.066
	Heating	430-135	295	15-200	185	0.63	0.021
	Cooling	135-55	80	200-27	173	2.14	0.072
	Heating	55-24	31	27-34	7	0.23	0.008
	Cooling	24-0	24	34-20	14	0.59	0.019
Curitiba (coastal)	Cooling	600-560	40	750-350	400	10.00	0.333
	Cooling	560-370	190	350-260	90	0.47	0.016
	Cooling	370-300	70	260-15	245	3.50	0.117
	Heating	300-135	165	15-100	85	0.52	0.017
	Cooling	135-55	80	100-25	75	0.94	0.031
	Heating	55-24	31	25-33	8	0.26	0.009
	Cooling	24-0	24	33-20	13	0.54	0.018

Block	Description	t-t Segment [Ma]	$\Delta t$	T-T Segment [°C]	$\Delta T$	Cooling rate [°C/Ma]	Exhumation rate [mm/a]
Florianopolis	Cooling	600-560	40	750-310	440	11.00	0.367
	Cooling	560-460	100	310-270	40	0.40	0.013
	Cooling	460-310	150	270-15	255	1.70	0.057
	Heating	310-135	175	15-120	105	0.60	0.020
	Cooling	135-55	80	120-25	95	1.19	0.040
	Heating	55-24	31	25-34	9	0.29	0.010
	Cooling	24-0	24	34-20	14	0.58	0.019
Laguna	Cooling	620-530	90	760-420	340	3.78	0.126
	Cooling	530-330	200	420-15	405	2.03	0.068
	Heating	330-145	185	15-170	155	0.8	0.028
	Heating	145-120	25	170-210	40	1.60	0.053
	Cooling	120-70	50	210-95	115	2.30	0.077
	Cooling	70-24	46	95-60	35	0.76	0.025
	Cooling	24-0	24	60-20	40	1.67	0.056

Figures S1-6:

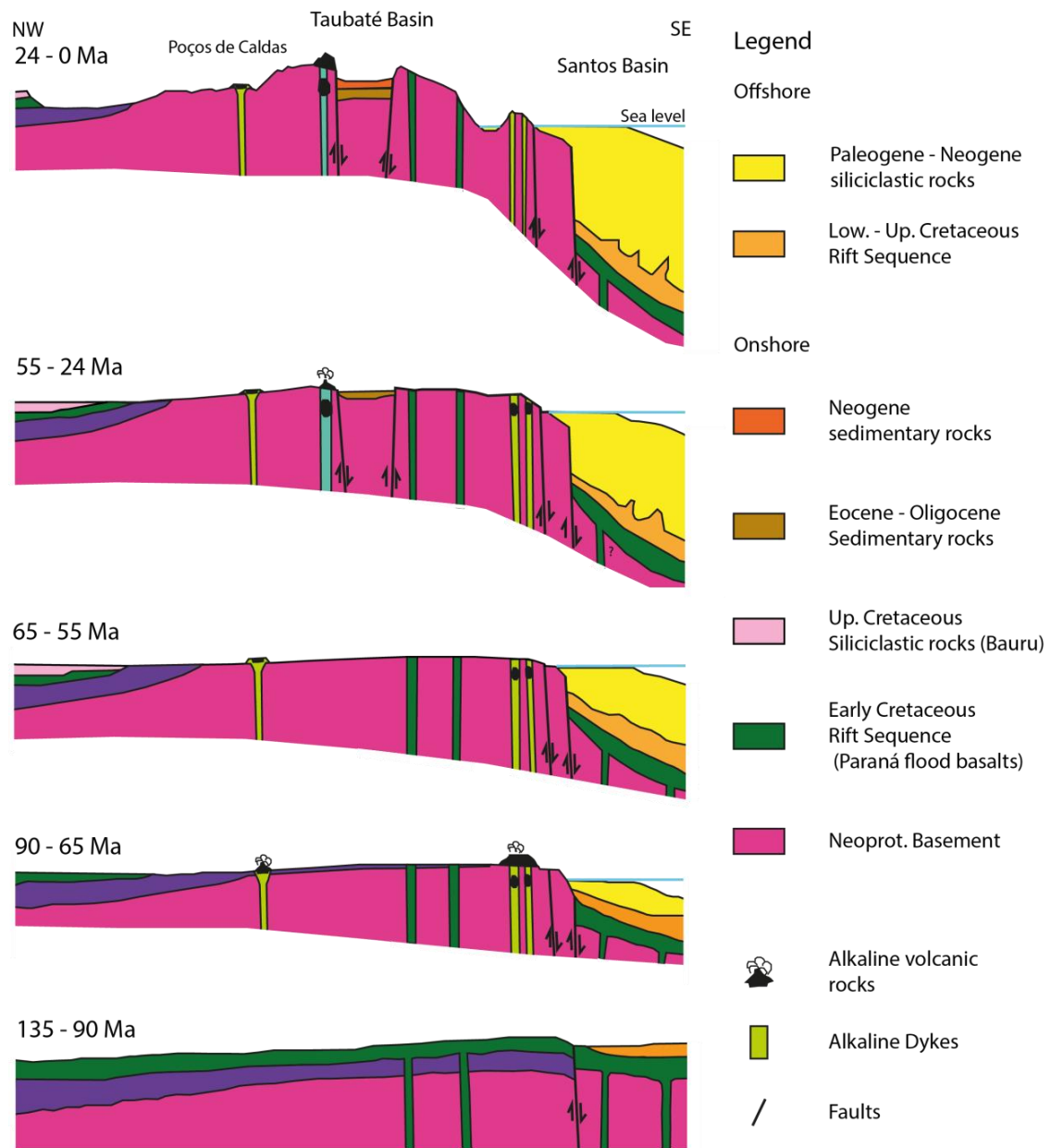


Figure A. 1: 2D-transects of the post-rift- Early Cretaceous to recent geological evolution of the SAPCM in SE Brazil showing onshore graben system activity of the Taubaté Basin (modified after Almeida et al., 1998). Schematic sections and geological evolution are based on published work by: Hackspacher et al., 2004; Riccomini et al., 2004; Franco-Magalhaes et al., 2010; Hiruma et al., 2010; Cogné et al., 2011, 2012, 2013; Karl et al., 2013; Engelmann de Oliveira et al., 2016. Time intervals of this figure correspond with Table A. 1.

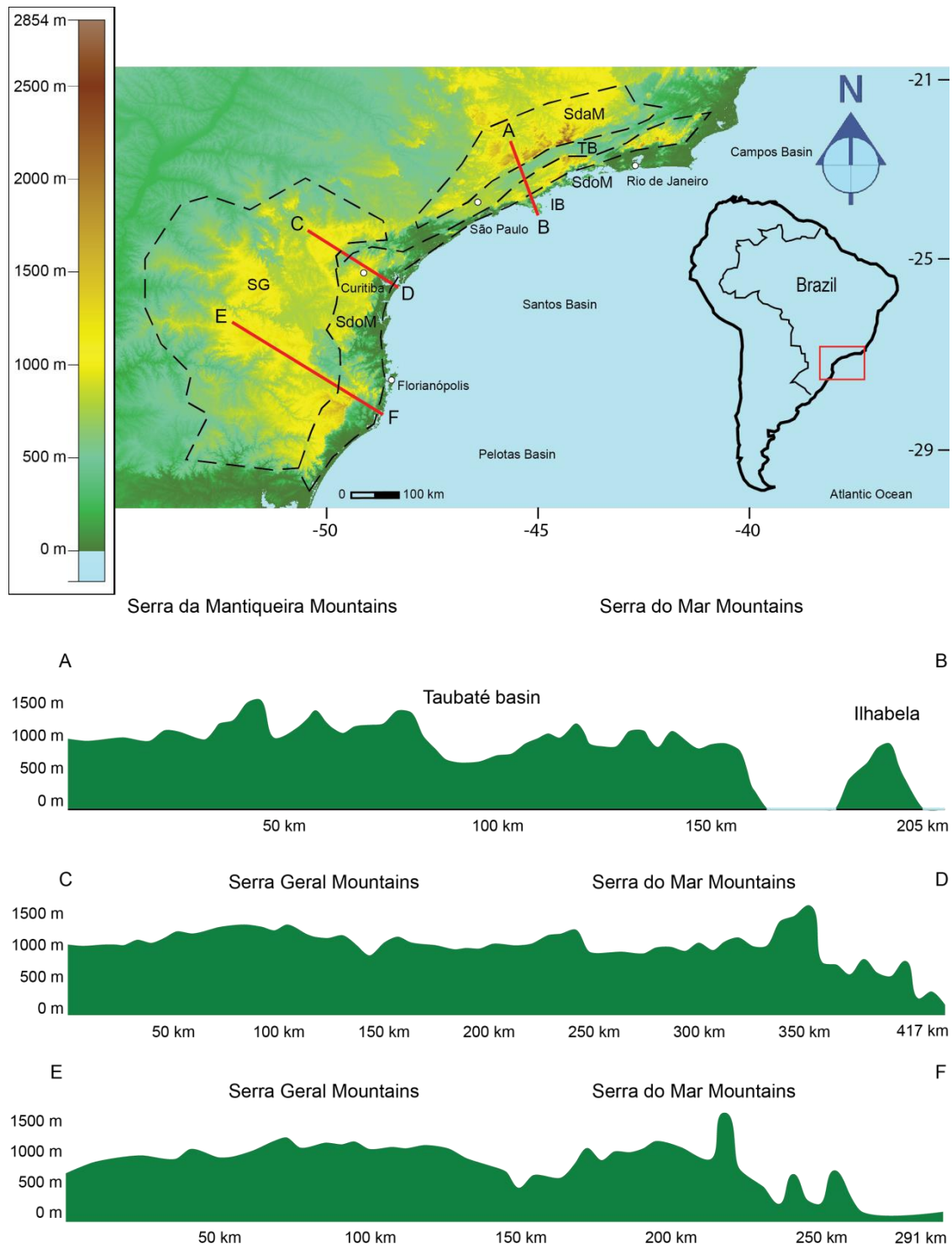


Figure A. 2: Area of research in south-eastern Brazil, showing topographic transects (A-B,C-D,E-F). SG: Serra Geral, SdoM: Serra do Mar, SdaM: Serra da Mantiqueira, TB: Taubaté Basin, IB: Ilhabela (São Sebastião Island) (Stippich, In prep, 2018).

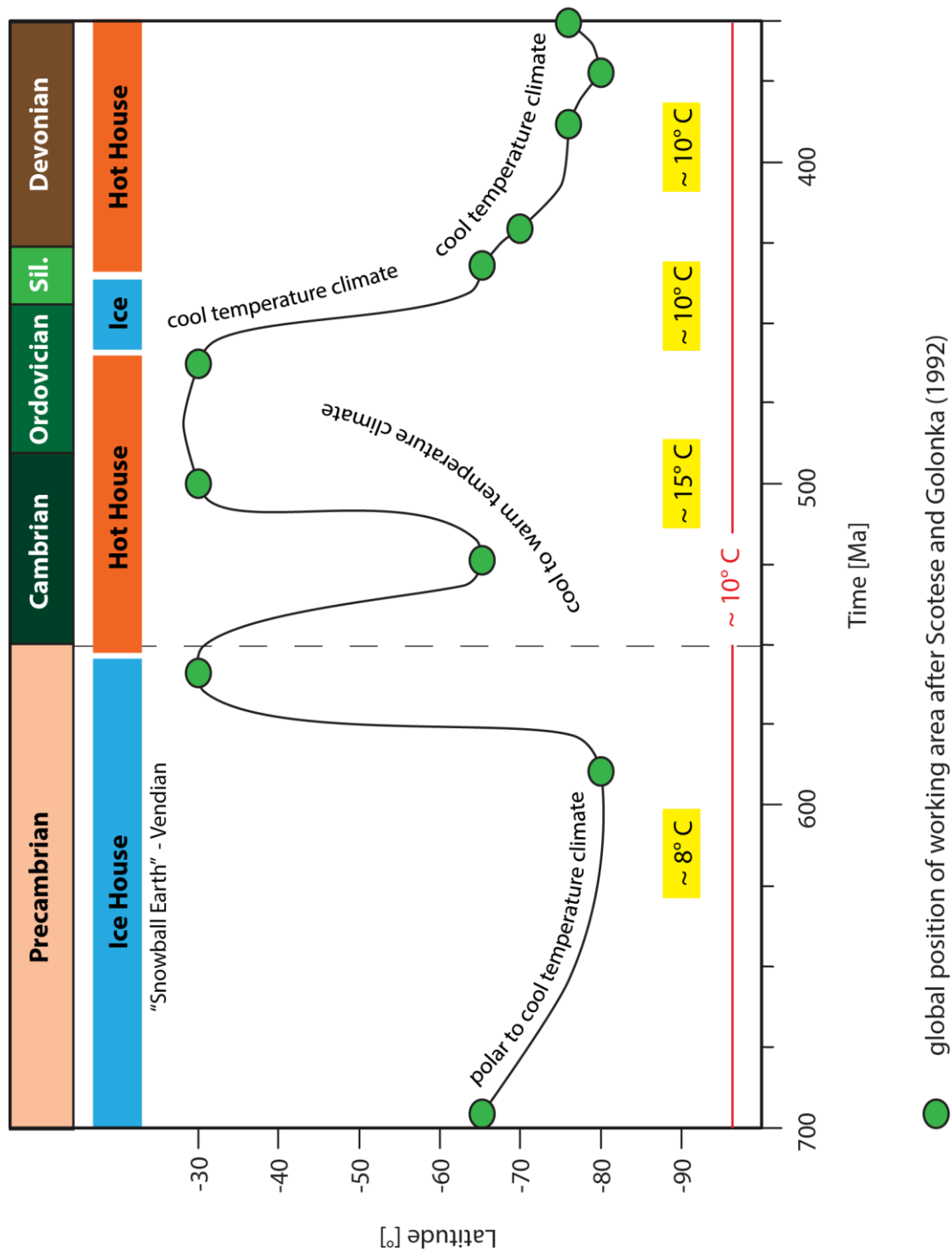


Figure A. 3: Reconstruction of global position of the research area undergoing different climates for Precambrian to Late Paleozoic time, assuming an average surface temperature of  $\approx 10^{\circ}\text{C}$ . Climate record and global position of working area were taken from Scotese and Golonka (1992).



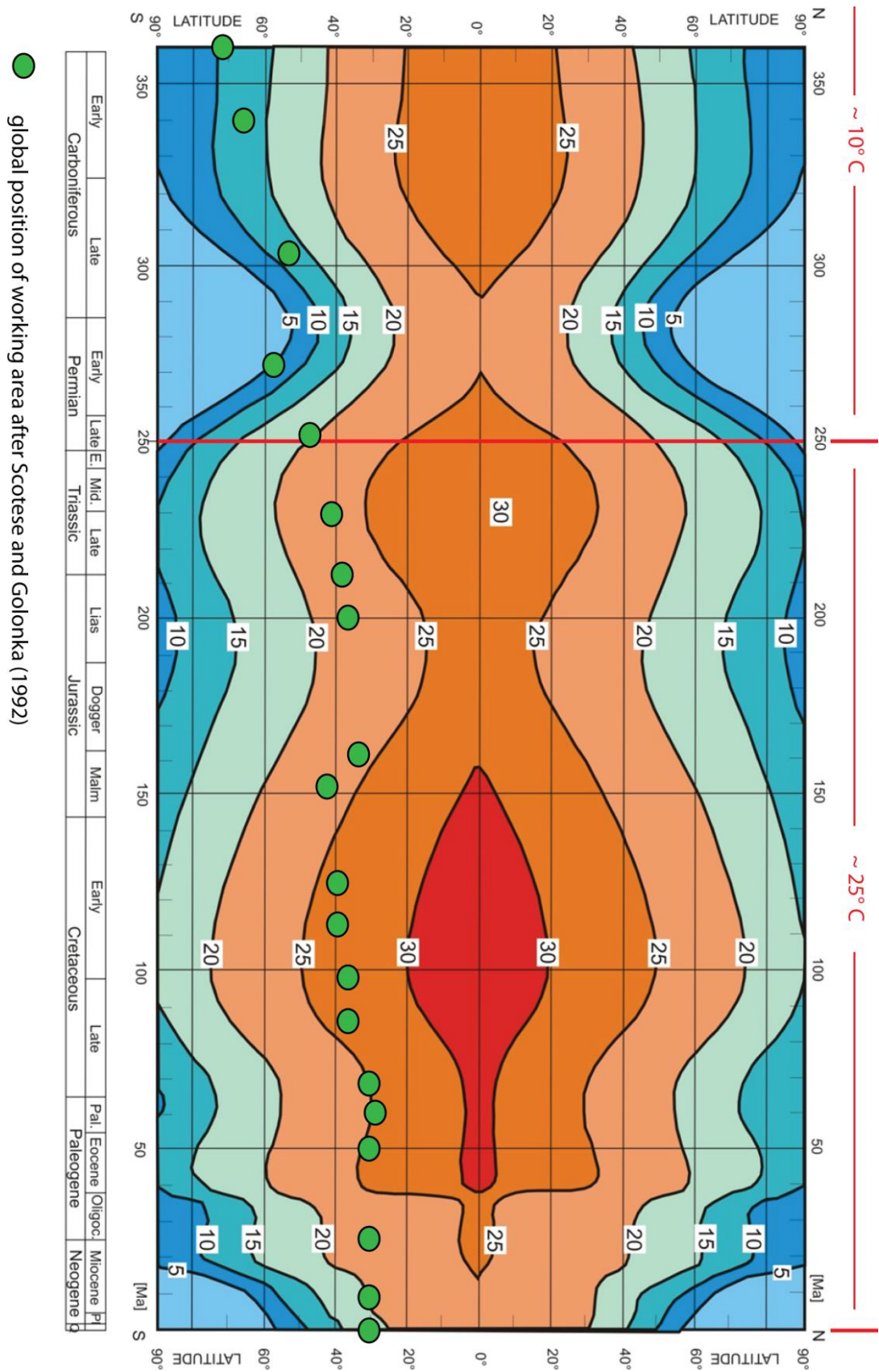


Figure A. 4: Reconstruction of global, average surface temperatures since Carboniferous (Wygrala, 1989). Includes global position of working area after Scotese and Golonka (1992), assuming an average surface temperatures of  $\approx 10^{\circ}\text{C}$  before Mesozoic and  $\approx 25^{\circ}\text{C}$  since Mesozoic.

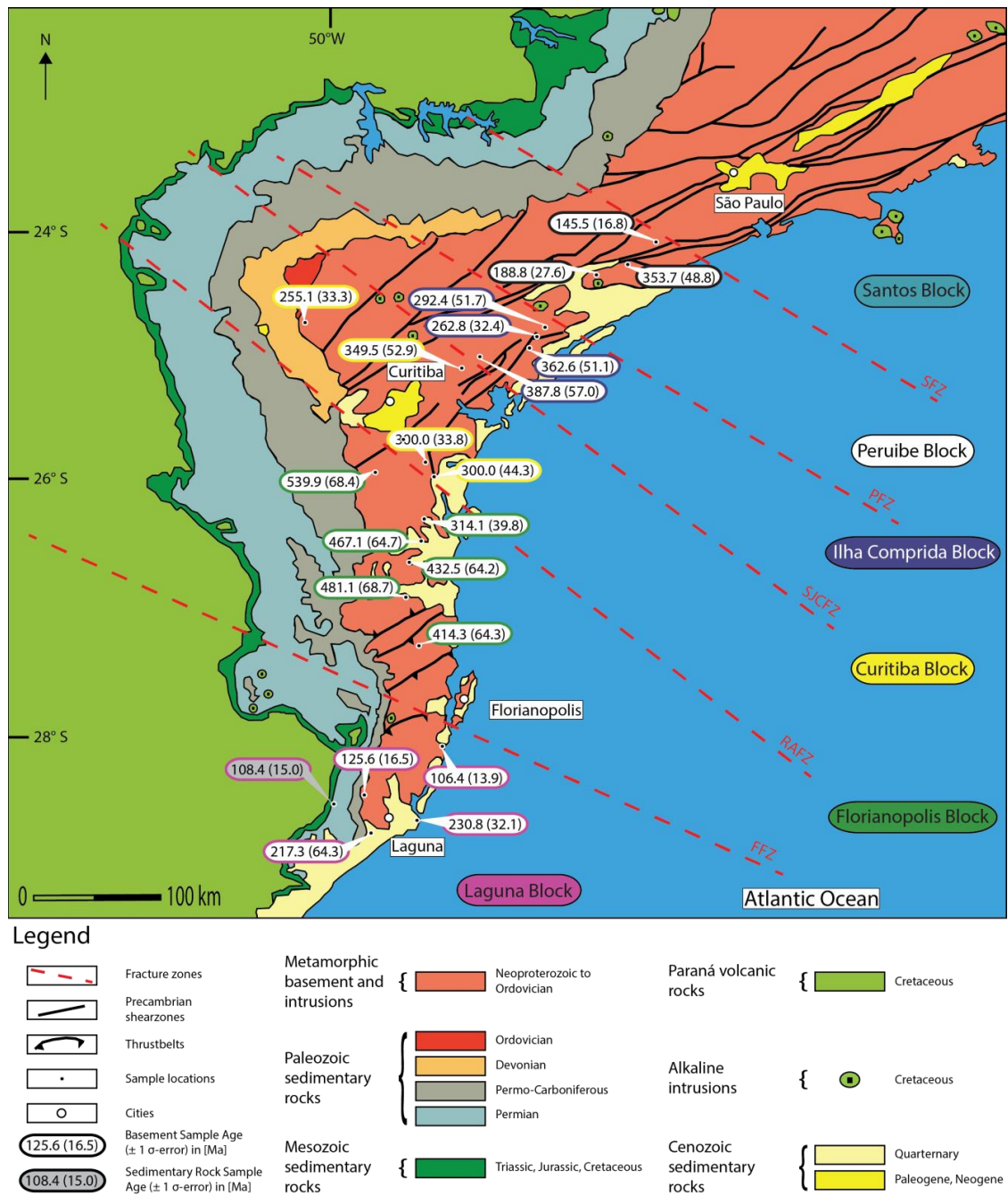


Figure A. 5. 1: Central zircon fission-track (ZFT) ages [Ma] plotted including 1σ-error [Ma]. Positions and directions of fracture zones were taken from Cobbold et al. (2001), Meisling et al. (2001), Riccomini et al. (2005), Strugale et al. (2007), Franco-Magalhaes et al. (2010), and Karl et al. (2013). Onshore extensions only show tendencies and are not confirmed trends.

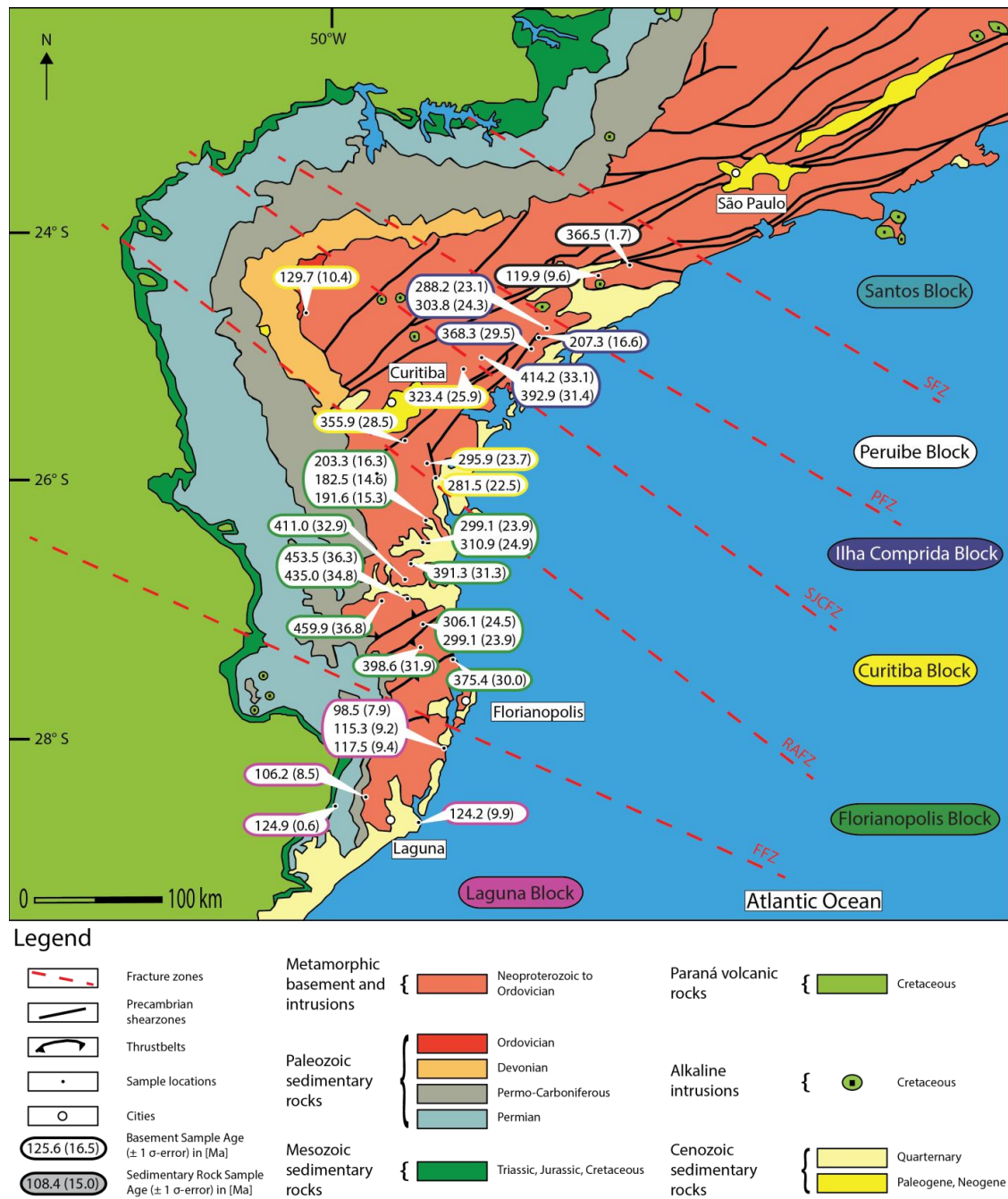


Figure A. 5. 1: Zircon (U-Th-(Sm))/He (ZHe) ages [Ma] plotted including 1σ-error [Ma]. Positions and directions of fracture zones were taken from Cobbold et al. (2001), Meisling et al. (2001), Riccomini et al. (2005), Strugale et al. (2007), Franco-Magalhaes et al. (2010), and Karl et al. (2013). Onshore extensions only show tendencies and are not confirmed trends

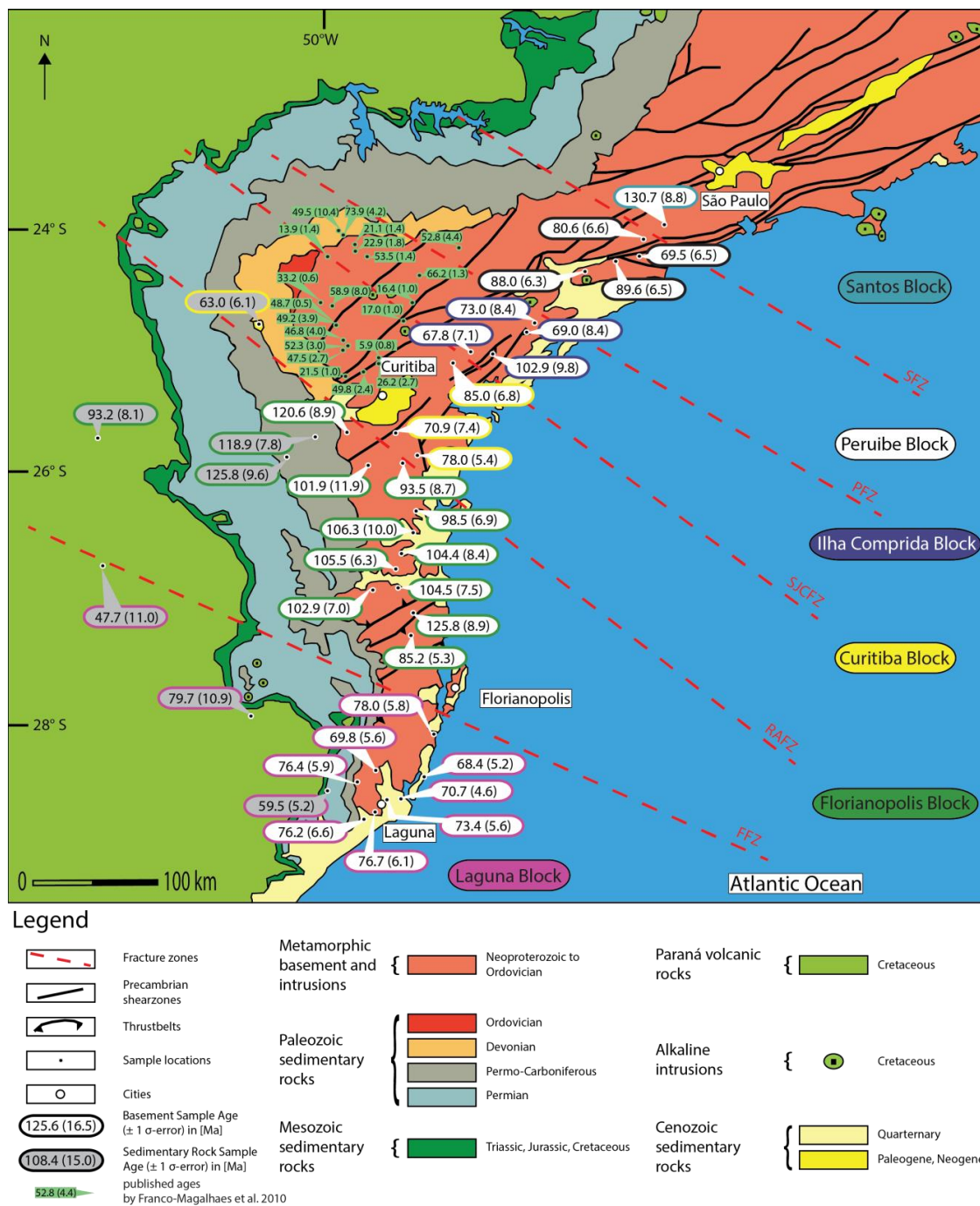


Figure A. 5. 2: Central apatite fission-track (AFT) ages [Ma] plotted including  $1\sigma$ -error [Ma]. Positions and directions of fracture zones were taken from Cobbold et al. (2001), Meisling et al. (2001), Riccomini et al. (2005), Strugale et al. (2007), Franco-Magalhaes et al. (2010), and Karl et al. (2013). Onshore extensions only show tendencies and are not confirmed trends.

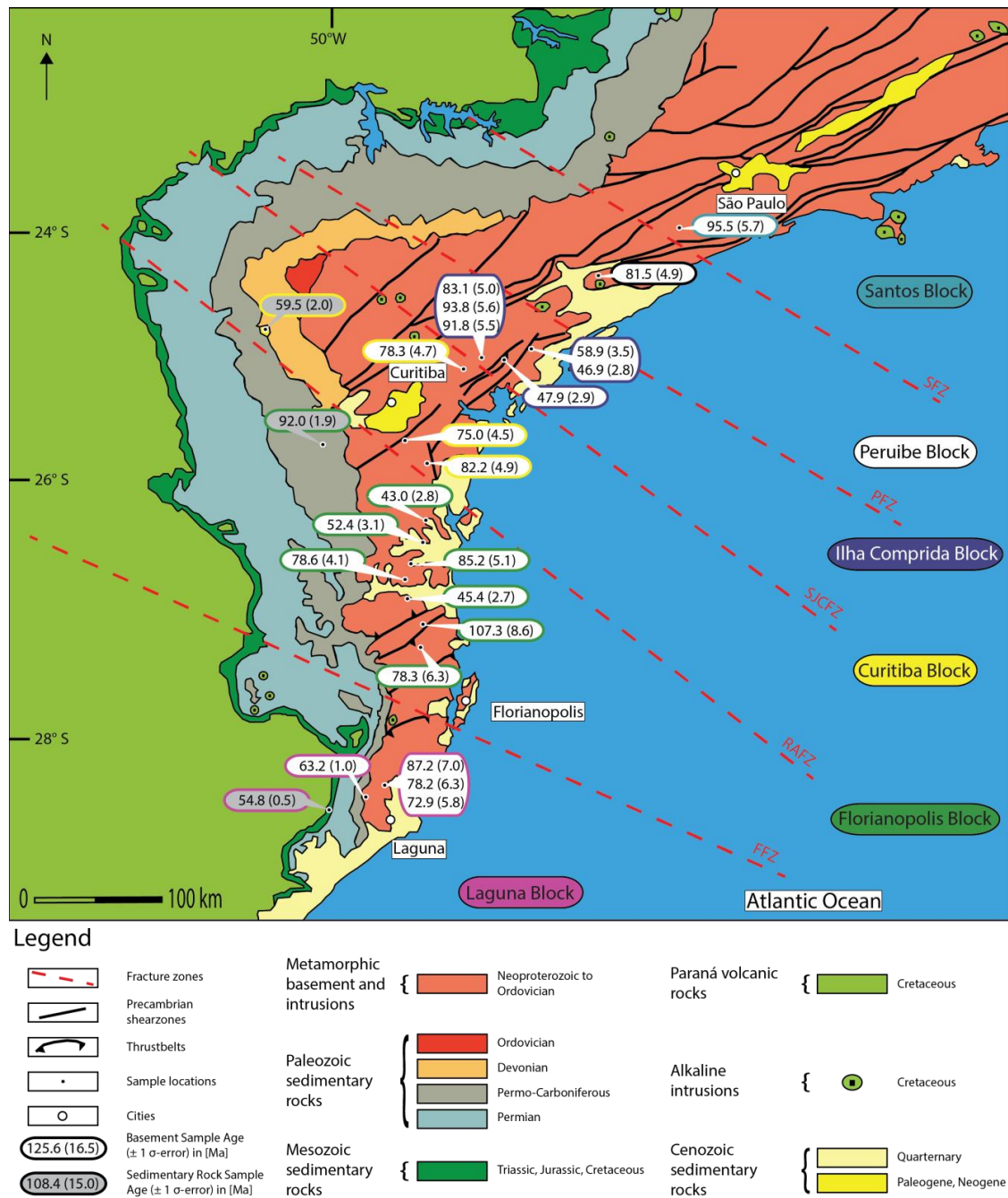
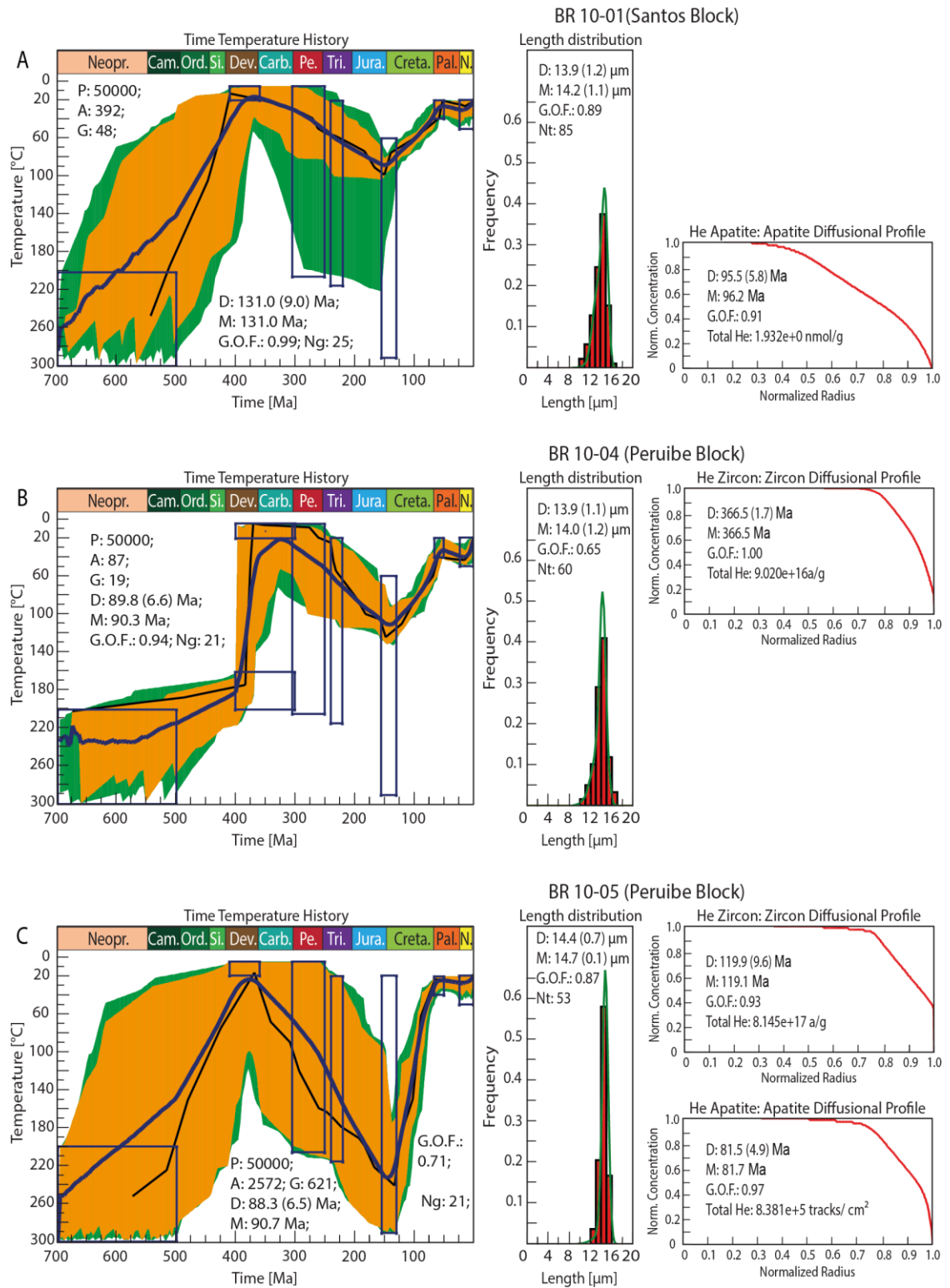


Figure A. 5. 3: Apatite (U-Th-(Sm))/He (AHe) ages [Ma] plotted including 1σ-error [Ma]. Positions and directions of fracture zones were taken from Cobbold et al. (2001), Meisling et al. (2001), Riccomini et al. (2005), Strugale et al. (2007), Franco-Magalhaes et al. (2010), and Karl et al. (2013). Onshore extensions only show tendencies and are not confirmed trends.

Figure A. 6. 1: (Next page) A) BR10-01, B) BR10-04, C) BR10-05. Time (t)-Temperature (T)-evolution paths with corresponding corrected confined spontaneous fission-track length-distribution (Lc) using the numerical software code HeFty® (Richard A. Ketcham). For every sample a standard amount of 50 000 paths were modeled. A: Accepted paths (green); G: Good paths (yellow); D: Dated age (with error); M: Modeled age; G.O.F.: Goodness of fit; Ng: Number of grains counted; Nt: Number of confined spontaneous fission-track lengths measured. The thin black path shows the “best-fit-path”, the thick blue path the “weighted-mean-path”.



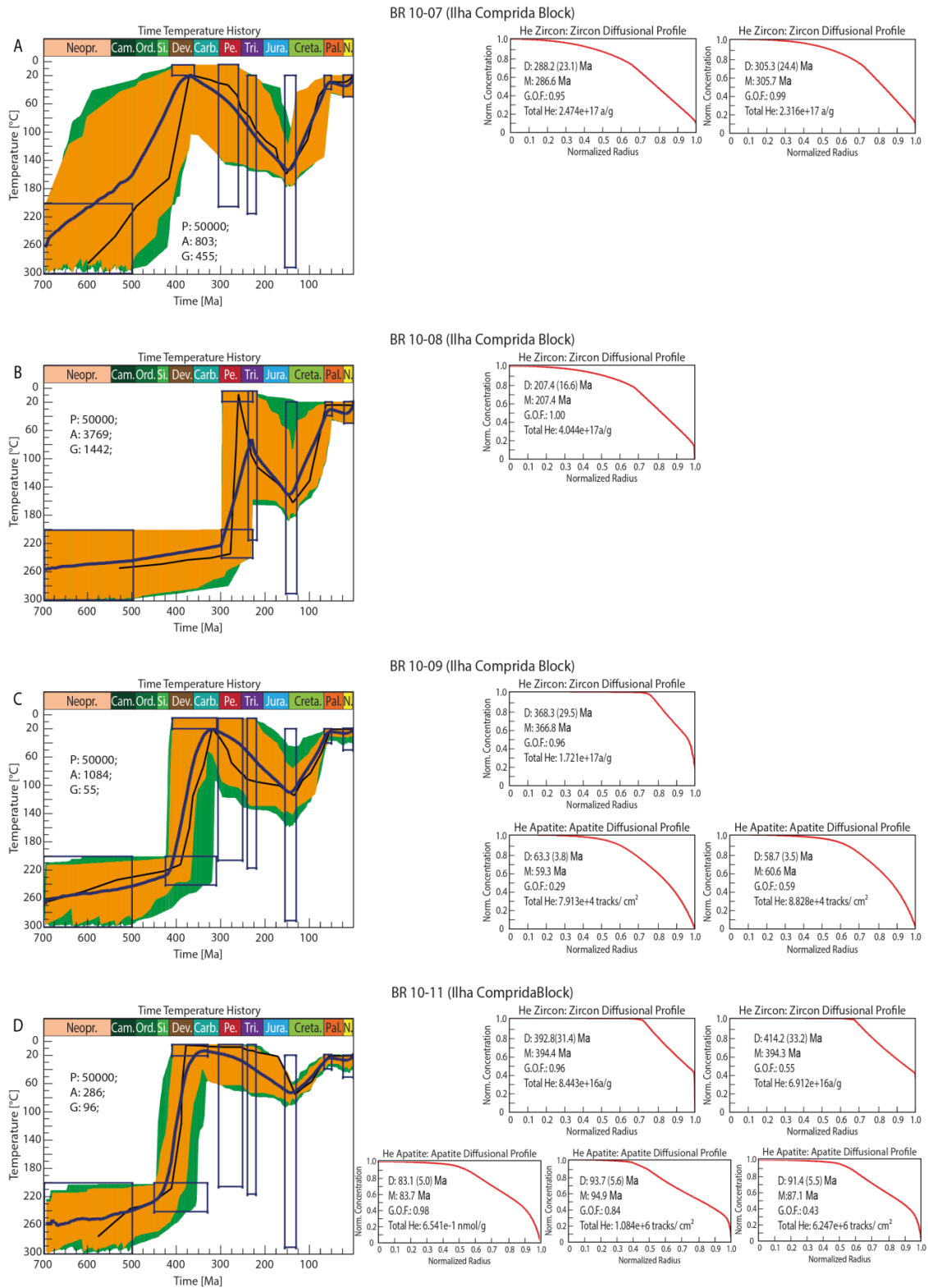
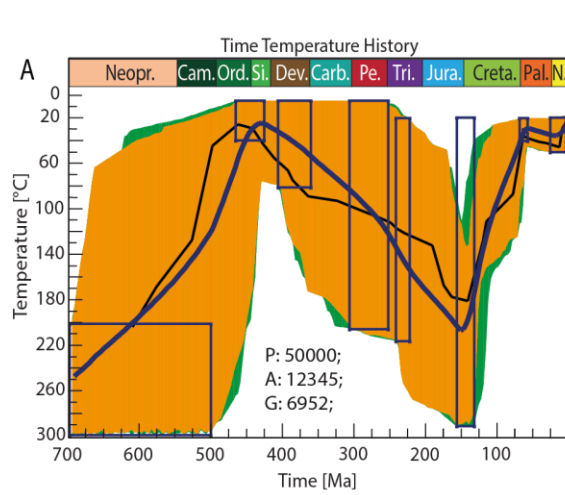
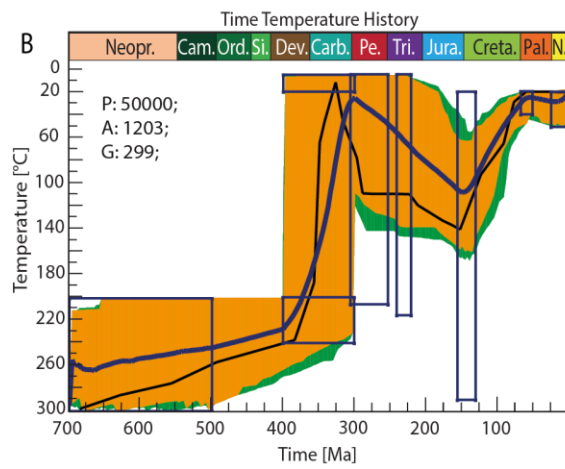
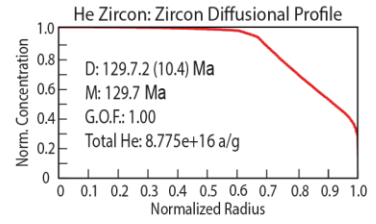


Figure A. 6. 2: A) BR10-07, B) BR10-08, C) BR10-09, D) BR10-11. For further information, please see Figure 6.1.

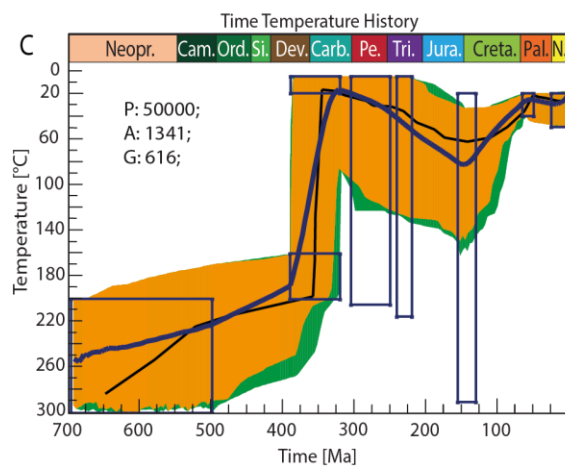
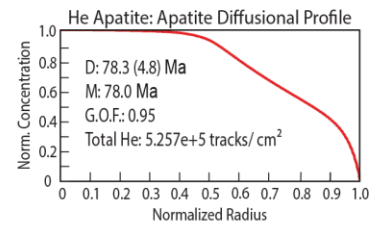
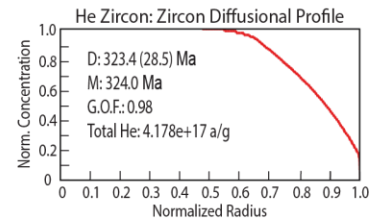




BR 09-01 (Curitiba Block)



BR 10-12 (Curitiba Block)



BR 10-15 (Curitiba Block)

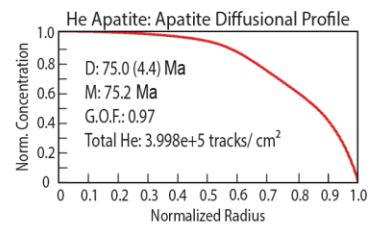
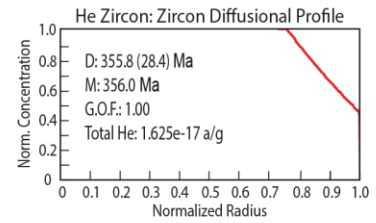


Figure A. 6. 3: A) BR09-01, B) BR10-12, C) BR10-15. For further information, please see Figure 6.1.

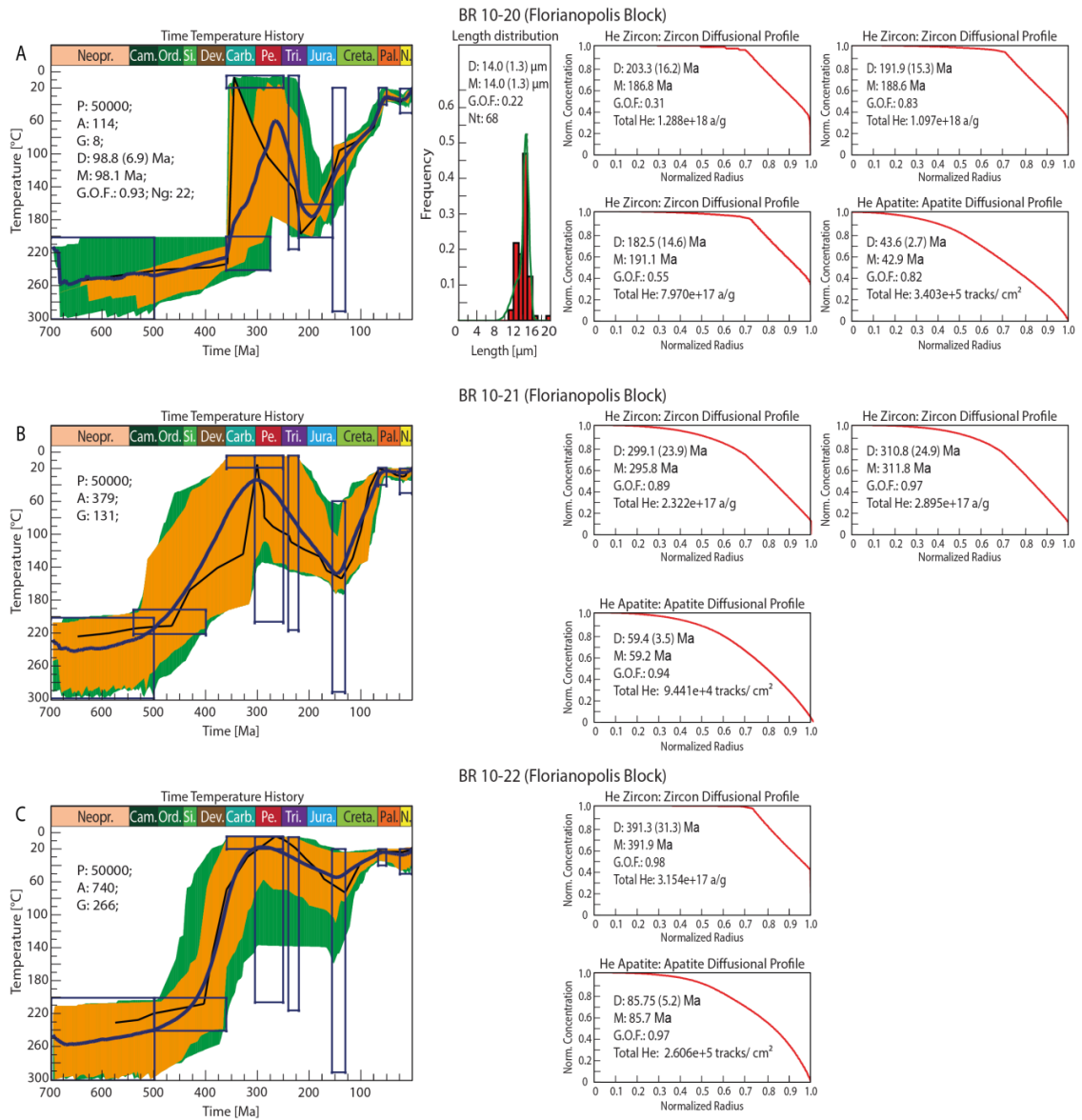


Figure A. 4: A) BR10-20, B) BR10-21, C) BR10-22. For further information, please see Figure 6.1.

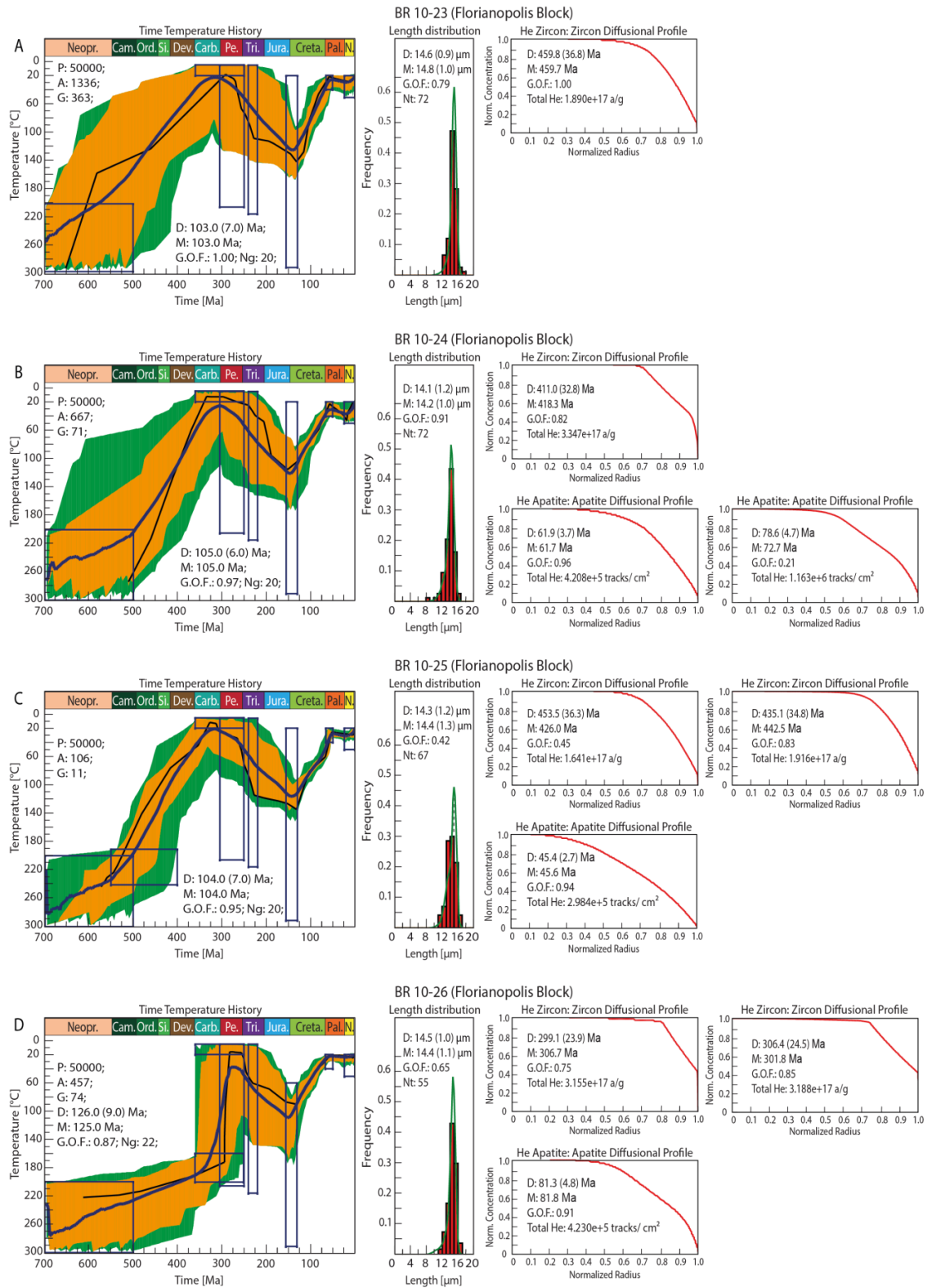


Figure A. 6. 5: A) BR10-23, B) BR10-24, C) BR10-25, D) BR10-26. For further information, please see Figure 6.1.

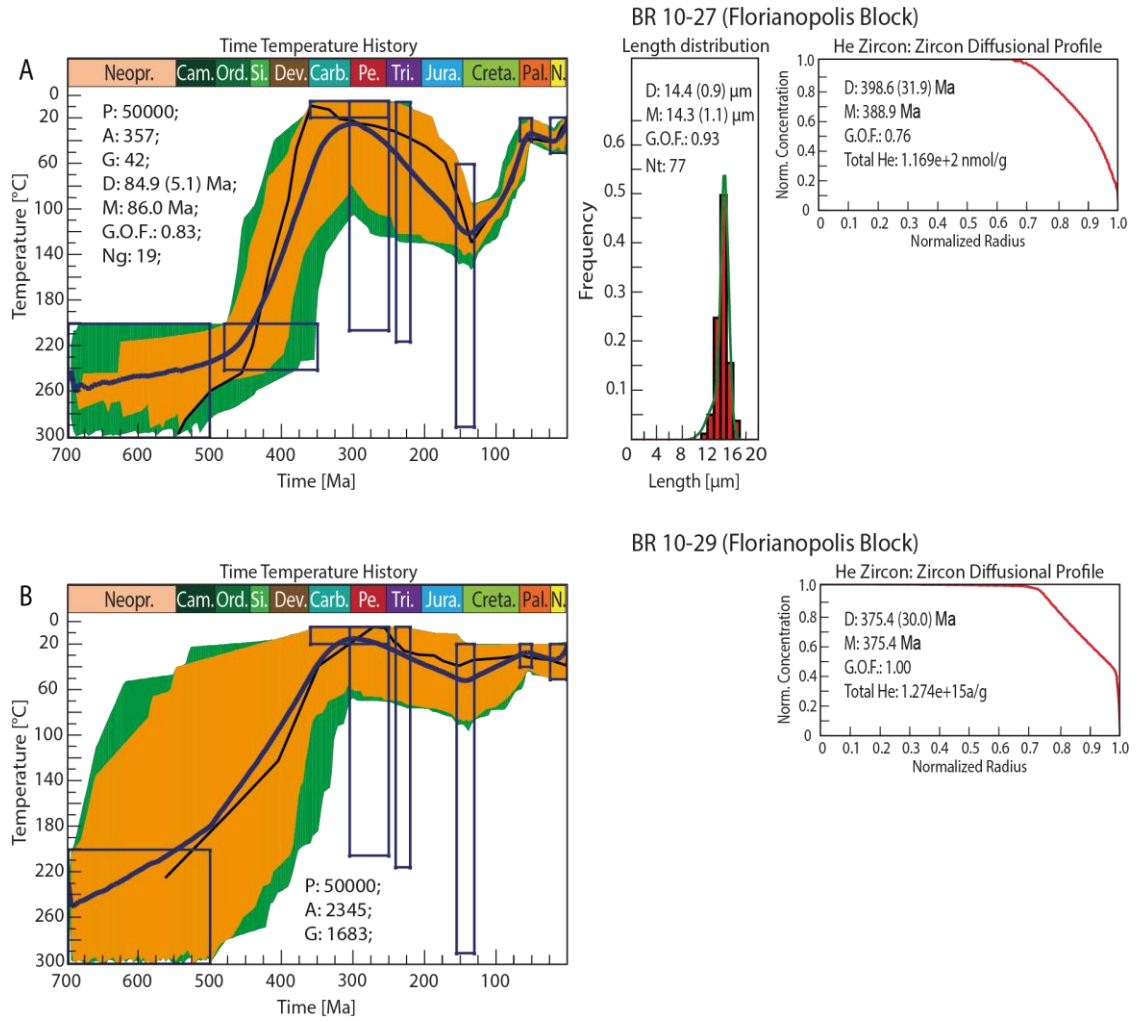


Figure A. 6. 6: A) BR10-27, B) BR10-29. For further information, please see Figure 6.1.

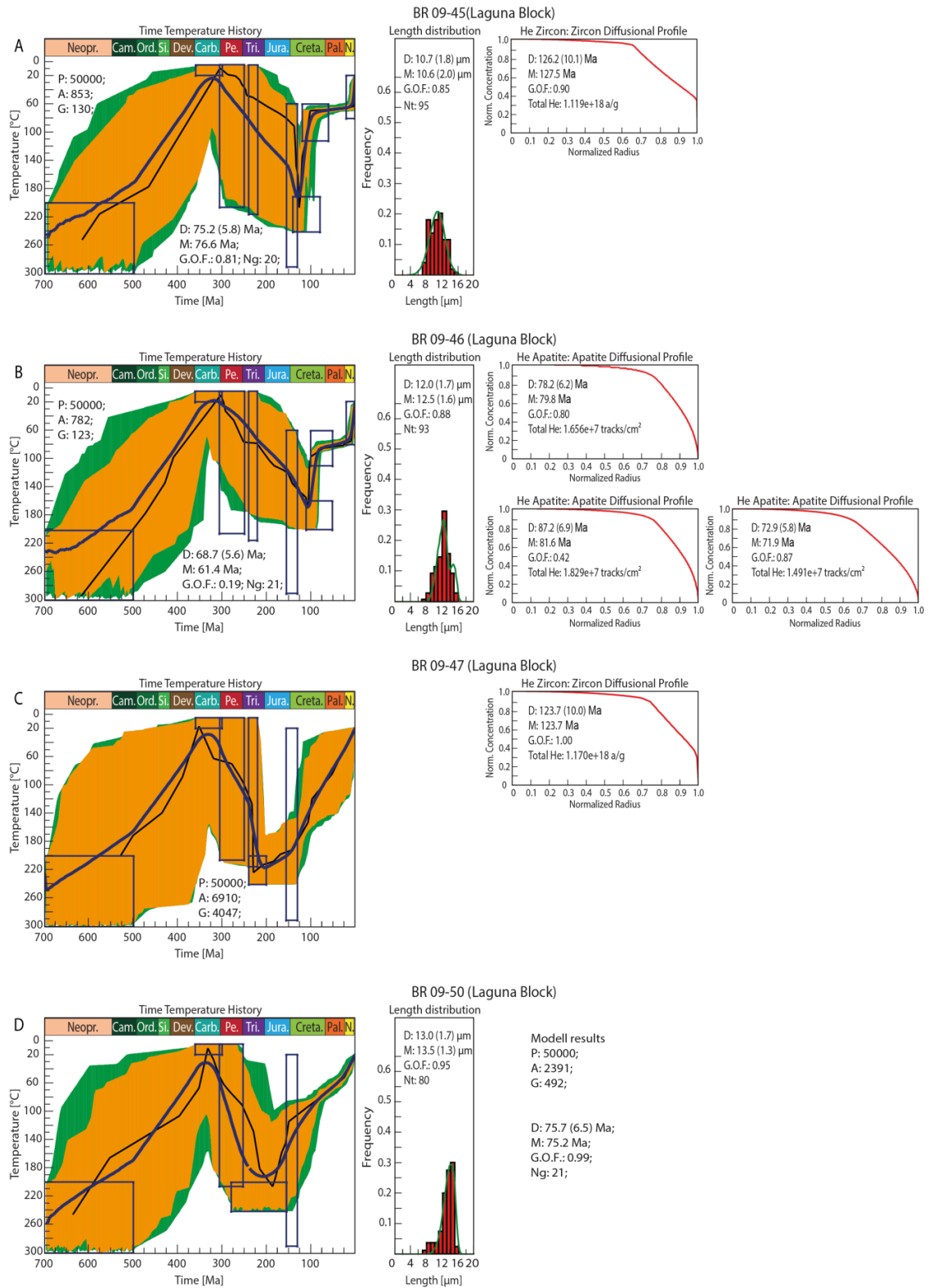


Figure A. 6. 7: A) BR09-45, B) BR09-46, C) BR09-47, D) BR09-50. For further information, please see Figure 6.1.

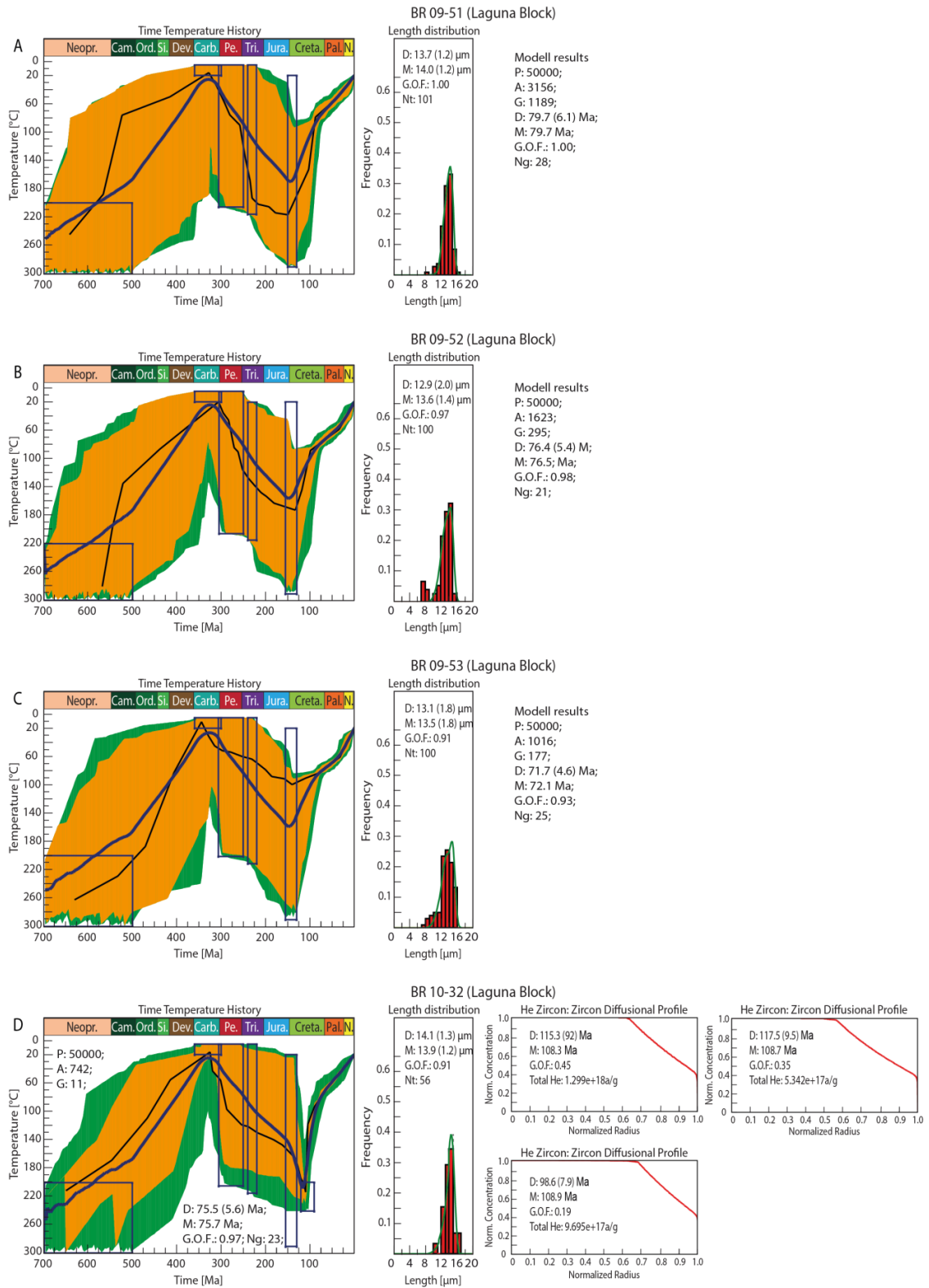


Figure A. 6. 8: A) BR09-51, B) BR09-52, C) BR09-53, D) BR10-32. For further information, please see Figure 6.1.

**Additional references:**

- Campanha**, G. A. C.; Basei, M. A. S.; Tassinari, C. C. G.; Nutman, A. P.; Faleiros, F. M., 2008b. U-Pb SHRIMP and Sm-Nd Analysis for Ribeira Belt Mesoproterozoic and Neoproterozoic Terranes. In: South American Symposium on Isotope 6, Bariloche. Bariloche: INGEIS - Instituto de Geocronología y Geología Isotópica.
- Chemale Jr.**, F., Mallmann, G., Bitencourt, M.F., Kawashita, K., 2003. Isotope geology of syntectonic magmatism along the Major Gercino Shear Zone, southern Brazil: Implications for the timing of deformation events. In: South American Symposium on Isotope Geology 2, Short Papers, 516-519.
- Chemale Jr.**, F., Mallmann, G., Bitencourt, M.F., Kawashita, k., 2012. Time constraints on magmatism along the Major Gercino Shear Zone, southern Brazil; Implications for West Gondwana reconstruction. *Gondwana Research* 22, 184-199.  
<https://doi.org/10.1016/j.gr.2011.08.018>
- Cordani**, U.G., Sato, K., 1999. Crustal evolution of the South American Platform, based on Nd isotopic systematics on Granitoid rocks. *Journal of International Geoscience* 22, 167-173.
- Dunkl**, I., 2002. Trackkey: a Windows program for calculation and graphical presentation of fission-track data. *Computer. Geosciences*. 28, 3-12.  
[https://doi.org/10.1016/S0098-3004\(01\)00024-3](https://doi.org/10.1016/S0098-3004(01)00024-3)
- Florisbal**, L.M., Janasi, V.A., Bitencourt, M.F., Du Frane, A., Heaman, L., 2010. Pb isotope in feldspars by LA-ICP-MS: tracking the isotope signatures in the Neoproterozoic granites from the Florianopolis Batholith, Santa Catarina Shield, Brazil. In: Simpósio Sul Americano de Geologia Isotópica, 2010, Brasília. Short Papers of VII SSAGI, CD, Brasília.
- Lopes**, A.P., 2008. Geologia do Complexo Camboriú (SC). Ph.D. Thesis. Curso de Pós-Graduação em Geoquímica e Geotectônica, University of São Paulo, São Paulo, 102 p.
- Passarelli**, C.R., Basei, M.A.S., Campos Neto, M., Siga Jr., O., Prazeres Filho, H.J., 2004. Geochronologia e Geologia dos Terrenos Pré-Cambrianos da Porção Sul-Oriental do Estado de São Paulo. *Revista do Instituto de Geociências – University of São Paulo* 4, 55-74.  
<http://dx.doi.org/10.5327/s1519-874x2004000100004>
- Picanço**, J.L., 1994. Aplicação das sistemáticas Sm/Nd e Rb/Sr no Maciço de Itatins (SP). MSc Dissertation, Institute of Geosciences, University of São Paulo, 140 p.  
[10.11606/D.44.1994.tde-11062015-101017](https://doi.org/10.11606/D.44.1994.tde-11062015-101017)
- Prazeres Filho**, H.J., 2000. Litogeoquímica, geochronologia U-Pb, e geologia isotópica dos complexos graníticos Cunhaporanga e Três, Estado de Paraná, São Paulo, Dissertation (Mestrado), Instituto de Geociências – University of São Paulo, 180 p.  
[10.11606/D.44.2000.tde-28092015-155909](https://doi.org/10.11606/D.44.2000.tde-28092015-155909)
- Siga Jr.**, O., Basei, M.A.S., Nutman, A.P., Sato, K., McReath, I., 2011. Extensional and collisional magmatic records in the Apiai Terrane, south-south-eastern Brazil: Integration of geochronological U-Pb zircon ages. *Geologia of the University of São Paulo, Serie Científica* 11, 149-175.
- Silva**, L.C., 1999. Geocronologia U–Pb SHRIMP e Sm–Nd na Província Mantiqueira Meridional, no Cinturão Saldania (África do Sul) e a evolução do Ciclo Brasileiro/Pan-Africano. PhD thesis, Curso de Pós-Graduação em Geociências, Universidade Federal do Rio Grande do Sul. Porto Alegre, 243 p.
- Silva**, L.C., Armstrong, R., Pimentel, M.M., Scandola, J., Ramgrab, G., Wildner, W., Angelim, L.A.A., Vasconcelos, A.M., Rizzoto, G., Quadros, M.L.E.S., Sander, A., Rosa, A.L.Z., 2002. Reavaliação da evolução geológica em terrenos Pré-Cambrianos brasileiros com base em novos dados U-Pb SHRIMP, Parte III: Províncias Borborema, Mantiqueira Meridional e Rio Negro-Juruena. *Revista Brasileira de Geociências* 32, 529–544





## B: SUPPLEMENTARY MATERIAL FOR CHAPTER 3

## Supplementary Materials for

### Late Neoproterozoic to recent long-term t-T-evolution of the Kaoko and Damara belts in NW Namibia

Florian C. Krob, Daniel P. Eldracher, Ulrich A. Glasmacher, Sabine Husche, Eric Salomon, Peter C. Hackspacher, Nordin P. Titus.

**Corresponding author:** Florian Krob, Institute of Earth Sciences, Heidelberg University, Im Neuenheimer Feld 234, 69120 Heidelberg, Germany, E-mail: [florian.krob@geow.uni-heidelberg.de](mailto:florian.krob@geow.uni-heidelberg.de), Telephone: +49-6221-4836.

#### Contents:

- Tables S1 to S5
- Figures S1 to S7

## Tables S1 – S5

Table B. 1: Summary of all samples of the NW Namibian Kaoko and Damara belts that were prepared to perform fission-track analysis with corresponding sample number, longitude, latitude, altitude [m a.s.l.], formation age, and lithology. The samples of the Tables B. 1-4 were taken by Dipl. Geol. Markus Karl, Dr. Melissa Perner and Dr. Eric Salomon, prepared, processes and dated by Dipl. Geol. Daniel Eldracher, and analysed and modeled within this thesis.

Sample number	Longitude	Latitude	Altitude [m a.s.l.]	Formation age	Lithology
<b>Kaoko Belt</b>					
<b>Damara Group</b>					
NA11-30	-20.392289	13.301956	39	Neoproterozoic	granite
NA11-53	-19.554694	13.345450	725	Neoproterozoic	granite
NA11-54	-19.635436	13.417022	695	Neoproterozoic	mylonite
NA11-62	-19.159192	13.579175	533	Neoproterozoic	schist
NA11-63	-18.891556	13.293833	542	Neoproterozoic	mica-schist
NA11-65	-18.791708	13.009433	320	Neoproterozoic	gneiss
NA11-66	-18.789156	12.959639	299	Neoproterozoic	granite
NA11-71	-17.839308	13.271531	1114	Neoproterozoic	amphibolite
NA11-72	-17.804728	12.992364	1255	Neoproterozoic	gneiss
NA11-73	-17.794233	12.846425	1307	Neoproterozoic	gneiss
NA11-74	-17.995858	12.864108	1094	Neoproterozoic	gneiss-migmatite
NA11-76	-18.089633	12.713514	975	Neoproterozoic	gneiss (mylonitic)
NA11-79	-18.089061	12.691958	982	Neoproterozoic	Gneiss (mylonitic)
NA11-80	-17.793156	12.526672	926	Neoproterozoic	granite
NA11-81	-17.788792	12.532692	894	Neoproterozoic	gneiss
NA11-83	-17.666531	12.666386	657	Neoproterozoic	gneiss (biotitic)
NA11-84	-17.704611	12.595108	669	Neoproterozoic	gneiss (biotitic)
NA11-85	-17.804144	12.470272	879	Neoproterozoic	mica schist
NA11-86	-17.813089	12.428350	838	Neoproterozoic	mica schist
NA11-87	-17.209811	12.152289	340	Neoproterozoic	gneiss
NA11-88	-17.384933	12.245839	647	Neoproterozoic	orthogneiss
NA11-89	-17.568189	12.277094	791	Neoproterozoic	granitic gneiss
NA11-90	-17.568189	12.277094	791	Neoproterozoic	granite
NA11-91	-17.568189	12.277094	791	Neoproterozoic	pseudotachylite
NA11-92	-17.672206	12.288231	765	Neoproterozoic	gneiss
NA11-93	-17.808339	12.326717	778	Neoproterozoic	amphibolite
NA11-94	-17.808339	12.326717	778	Neoproterozoic	granitic gneiss
NA11-95	-17.950972	12.343394	822	Neoproterozoic	amphibolite
NA11-96	-18.120242	12.357022	636	Neoproterozoic	syenite
NA11-98	-18.242386	12.409581	628	Neoproterozoic	granite
NA11-99	-18.381311	12.437658	502	Neoproterozoic	amphibolite
NA11-103	-18.656747	12.655008	402	Neoproterozoic	meta-sediment
NA11-104	-18.665383	12.639292	388	Neoproterozoic	meta-sediment
NA11-105	-18.718394	12.606869	332	Neoproterozoic	migmatite
NA11-106	-18.750561	12.593106	303	Neoproterozoic	granite
NA11-107	-18.710933	12.637306	431	Neoproterozoic	migmatite
NA11-109	-18.808625	12.702703	471	Neoproterozoic	granite (mylonitic)
NA11-110	-18.874200	12.794758	310	Neoproterozoic	granite (mylonitic)
NA11-111	-18.904069	12.817533	198	Neoproterozoic	gneiss
NA11-115	-18.924064	12.838800	301	Neoproterozoic	mica-schist
NA11-116	-18.960664	12.884222	479	Neoproterozoic	granite (mylonitic)
NA11-117	-19.011994	12.942311	639	Neoproterozoic	granite

Sample number	Longitude	Latitude	Altitude [m a.s.l.]	Formation age	Lithology
NA11-120	-19.195336	13.088344	556	Neoproterozoic	granite (mylonitic)
NA11-121	-19.274056	13.115306	408	Neoproterozoic	gneiss
NA11-122	-19.311103	13.142667	334	Neoproterozoic	syenite
NA11-123	-19.347044	13.163833	264	Neoproterozoic	gneiss
NA11-124	-19.322533	13.240483	309	Neoproterozoic	gneiss (amphibolitic)
NA11-125	-19.307553	13.267697	325	Neoproterozoic	gneiss
NA11-126	-19.294422	13.299956	333	Neoproterozoic	gneiss (mylonitic)
NA11-127	-19.284894	13.314850	332	Neoproterozoic	gneiss-migmatite
NA11-128	-19.248922	13.335022	354	Neoproterozoic	gneiss (mylonitic)
NA11-129	-19.239797	13.366950	366	Neoproterozoic	gneiss
NA11-130	-18.779078	12.854967	511	Neoproterozoic	mylonite
NA11-131	-18.731756	12.735617	573	Neoproterozoic	gneiss
NA11-132	-18.744322	12.693667	519	Neoproterozoic	gneiss
NA11-133	-18.489925	12.793136	626	Neoproterozoic	ultramylonite
NA11-136	-18.236072	12.659786	882	Neoproterozoic	mylonite
NA11-140	-18.265325	13.351917	825	Neoproterozoic	mica-schist
<b>Karoo Supergroup</b>					
NA11-75	-18.078361	12.737281	972	Carbon. /Permian	sandstone
NA11-77	-18.091417	12.737281	960	Carbon. /Permian	sandstone
NA11-78	-18.089675	12.737281	985	Carbon. /Permian	sandstone
NA11-112	-18.905228	12.825367	217	Carbon. /Permian	sandstone
NA11-113	-18.905228	12.825367	217	Carbon. /Permian	sandstone
NA11-118	-18.905228	12.986700	679	Carbon. /Permian	sandstone
NA11-134	-18.492128	12.791442	632	Carbon. /Permian	sandstone
NA11-135	-18.499800	12.80565	590	Carbon. /Permian	conglomerate
NA11-137	-18.499800	12.741256	862	Carbon. /Permian	sandstone
<b>Etendeka Group</b>					
NA11-21	-20.334036	14.108358	781	L. Cretaceous	basalt
NA11-24	-20.271061	13.744697	902	L. Cretaceous	basalt
NA11-55	-19.831058	13.492444	686	L. Cretaceous	basalt
NA11-108	-18.708089	12.636653	424	L. Cretaceous	basalt-dike
NA11-114	-18.905289	12.825203	217	L. Cretaceous	basalt
<b>Damara Belt</b>					
<b>Damara Group</b>					
NA11-09	-20.399178	16.707472	1486	Precambrian	granodiorite
NA11-10	-20.694008	16.846731	1637	Precambrian	granodiorite
NA11-11	-20.648031	16.917344	1590	Precambrian	granite
NA11-14	-20.503921	17.243085	559	Precambrian	granite
NA11-20	-20.564395	14.531667	572	Precambrian	granite
NA11-40	-22.843796	15.384432	755	Precambrian	granite
NA11-42	-22.693578	15.852794	1254	Precambrian	granite
NA11-43	-22.517992	15.857761	964	Precambrian	granite
NA11-44	-22.177083	15.606714	836	Precambrian	granite
NA11-46	-21.982679	15.422987	1172	Precambrian	granite
NA11-49	-21.277386	15.225139	938	Precambrian	granite
NA11-52	-20.754594	14.218636	553	Precambrian	granite
NA11-69A	-21.529778	16.858241	1483	Precambrian	gabbro
NA11-69B	-21.529778	16.858241	1483	Precambrian	granite
NA11-70	-22.004200	16.930392	1297	Precambrian	granite
<b>Karoo and Etendeka groups</b>					
NA11-68	-21.067064	16.384592	1505	Carbon. /Permian	conglomerate
NA11-50	-21.087121	14.680067	939	L. Cretaceous	granite

Table B. 2: Apatite fission-track (AFT) data of Kaoko and Damara belt samples with corresponding sample number, L.: Lithology, E.: Elevation [m a.s.l.], n: number of counted grains, U: uranium concentration in  $\mu\text{g/g}$ ,  $\rho_s$ : density of spontaneous tracks ( $\times 10^5/\text{cm}^2$ ),  $N_s$ : number of spontaneous tracks,  $\rho_i$ : density of induced tracks ( $\times 10^5/\text{cm}^2$ ),  $N_i$ : number of induced tracks, P ( $\chi^2$ ) is the probability that single grain ages are consistent and belong to the same population. Test is passed if P ( $\chi^2$ ) > 5% (Galbraith 1981). Ages calculated using a  $\zeta$ -value of  $344.47 \pm 13.83$  a/cm<sup>2</sup> for apatite. For further descriptions see Table B. 1.

Sample number	Alt. [m a.s.l.]	n	U (std) [ $\mu\text{g/g}$ ]	$\rho_s$ [ $\times 10^5/\text{cm}^2$ ]	$N_s$	$\rho_i$ [ $\times 10^5/\text{cm}^2$ ]	$N_i$	$c^2$ [%]	Central age [Ma]	$\pm(1\sigma)$ [Ma]
<b>Kaoko Belt</b>										
<b>Damara Group</b>										
NA11-30	39	7	46.0 (33.5)	16.3	377	40.5	936	37.16	82.1	6.0
NA11-53	725	20	13.4 (6.6)	15.8	1669	13.7	1446	99.59	234.1	12.7
NA11-54	695	20	22.4 (19.3)	10.6	775	20.3	1490	84.33	107.2	6.5
NA11-62	533	20	27.5 (17.6)	26.0	1660	25.5	1625	82.57	210.8	11.3
NA11-63	542	20	6.6 (3.2)	6.9	1020	6.7	999	71.88	211.5	12.8
NA11-65	320	23	8.9 (3.0)	3.9	855	9.3	2072	98.48	87.0	5.0
NA11-66	299	20	50.0 (26.0)	22.8	1748	50.2	3860	33.75	95.7	4.8
NA11-71	1114	29	20.9 (7.9)	40.6	6835	26.0	4366	5.28	390.9	17.9
NA11-72	1255	20	6.3 (2.1)	9.9	2049	6.7	1395	89.68	308.2	16.5
NA11-73	1307	22	9.2 (3.4)	12.4	2138	11.1	1641	7.51	326.7	18.1
NA11-74	1094	20	22.2 (10.4)	23.0	1273	24.7	1363	35.92	198.9	11.8
NA11-76	975	21	7.7 (2.0)	12.4	1488	9.5	1145	77.16	324.0	18.1
NA11-79	982	22	13.2 (8.0)	7.1	1135	15.9	2554	66.88	112.5	6.0
NA11-80	926	20	8.2 (7.5)	10.6	1429	10.5	1419	0.00	309.8	36.7
NA11-81	894	21	35.9 (11.1)	15.6	1181	48.2	3639	47.33	85.7	4.5
NA11-83	657	21	5.4 (3.7)	5.3	264	6.6	327	99.29	210.9	19.5
NA11-84	669	23	28.4 (8.8)	13.1	2178	35.4	5910	16.32	96.7	4.8
NA11-85	879	4	21.9 (7.0)	21.6	261	25.9	314	0.00	208.8	69.2
NA11-86	838	26	19.4 (4.0)	23.8	4569	24.5	4715	8.08	242.1	11.3
NA11-87	340	22	24.2 (6.0)	11.0	1606	28.9	4196	10.57	93.0	4.9
NA11-88	647	23	26.9 (8.3)	17.6	1368	36.5	2839	57.96	125.3	6.6
NA11-89	791	18	81.3 (19.5)	64.5	3114	98.4	4750	5.48	168.3	8.4
NA11-90	791	17	57.7 (32.9)	47.4	1061	51.2	1148	8.83	192.6	13.0
NA11-91	791	22	32.5 (7.1)	36.7	4380	40.1	4796	0.00	221.2	13.8
NA11-92	765	21	30.0(6.9)	27.5	2374	37.1	3199	48.13	185.3	8.9
NA11-93	778	29	4.0 (2.8)	6.6	787	5.1	602	74.88	331.9	23.2
NA11-94	778	26	25.9 (9.9)	24.3	3307	34.3	4661	7.44	176.6	8.5
NA11-95	822	20	29.3 (10.0)	37.7	5540	30.9	4537	0.00	262.3	14.7
NA11-96	636	21	56.3 (16.3)	28.7	1792	67.9	4244	25.54	107.9	5.4
NA11-98	628	8	24.1 (7.7)	11.2	189	34.0	572	73.29	83.0	7.0
NA11-99	502	22	30.1 (7.8)	14.8	737	37.7	1877	22.38	98.6	6.2
NA11-103	402	21	55.4 (31.6)	18.4	1742	56.3	5333	10.06	81.3	4.2
NA11-104	388	20	17.5 (8.6)	8.1	1042	21.9	2799	36.04	93.3	5.1
NA11-105	332	16	38.2 (21.4)	16.0	670	42.8	1795	37.02	93.9	5.8
NA11-106	303	21	46.5 (17.7)	26.3	1228	55.8	2604	92.86	119.1	6.4
NA11-107	431	20	47.1 (15.6)	27.5	2995	60.0	6540	32.28	116.2	5.4
NA11-109	471	20	68.6 (15.1)	37.0	3461	87.5	8187	92.65	108.3	4.9
NA11-110	310	20	16.6 (7.9)	8.3	1021	23.3	2861	63.37	95.7	5.2
NA11-111	198	20	15.2 (11.5)	7.0	364	18.0	936	57.74	99.0	7.3
NA11-115	301	14	33.7 (9.1)	17.5	446	39.6	1008	45.10	111.4	7.8
NA11-116	479	22	28.0 (15.1)	14.3	1510	31.1	3285	0.00	118.0	10.2
NA11-117	639	20	38.9 (9.3)	18.4	2131	42.8	4962	97.97	93.3	4.5

Sample number	Alt. [m a.s.l.]	n	U (std) [ $\mu\text{g/g}$ ]	$\rho_s$ [ $\times 10^5/\text{cm}^2$ ]	$N_s$	$\rho_l$ [ $\times 10^5/\text{cm}^2$ ]	$N_l$	$c^2$ [%]	Central age [Ma]	$\pm(1\sigma)$ [Ma]
NA11-120	556	20	25.3 (7.8)	19.1	1262	30.5	2017	0.00	148.9	11.9
NA11-121	408	20	43.8 (9.6)	24.6	1516	52.8	3256	40.65	115.4	5.9
NA11-122	334	21	24.8 (6.9)	14.2	1426	30.1	3026	38.72	116.3	6.1
NA11-123	264	20	23.4 (10.1)	13.6	2253	29.9	4948	80.51	121.2	5.8
NA11-124	309	28	6.8 (3.0)	3.6	1100	9.2	2773	4.52	106.0	6.3
NA11-125	325	22	13.9 (5.7)	8.2	1449	18.1	3183	60.62	120.8	6.3
NA11-126	333	20	24.7 (14.6)	10.4	1587	26.9	4101	52.98	84.3	4.3
NA11-127	332	20	27.8 (14.7)	13.2	1843	29.1	4078	45.30	98.5	4.9
NA11-128	354	20	27.5 (17.9)	12.9	885	25.1	1730	60.44	111.6	6.5
NA11-129	366	14	5.5 (4.3)	4.0	428	5.6	592	73.28	190.6	14.4
NA11-130	511	20	24.3 (12.4)	9.5	1423	25.2	3750	73.35	83.2	4.3
NA11-131	573	21	22.7 (7.7)	11.2	670	28.7	1721	11.16	96.2	6.4
NA11-132	519	20	29.4	13.2	882	37.2	2484	20.95	94.7	5.7
NA11-133	626	22	3.8 (3.1)	3.1	483	4.3	680	96.77	181.8	13.1
NA11-136	882	19	2.9 (2.1)	3.1	368	2.9	353	19.54	253.5	22.6
NA11-140	825	20	15.7 (10.4)	21.7	1278	16.6	979	93.99	282.8	16.7
<b>Karoo Supergroup</b>										
NA11-75	972	24	22.4 (13.0)	38.4	2794	23.7	1724	14.02	342.2	18.3
NA11-77	960	23	15.4 (14.5)	18.8	2020	16.0	1716	0.00	327.9	28.8
NA11-78	985	20	17.9 (12.0)	25.3	1916	17.5	1327	89.87	305.0	16.6
NA11-112	217	18	24.7 (13.3)	19.8	697	31.8	1120	0.00	179.3	20.2
NA11-113	217	9	46.6 (21.4)	20.6	577	56.1	1572	0.52	96.5	8.4
NA11-118	679	21	20.4 (5.3)	24.4	2711	25.6	2841	30.64	236.7	11.6
NA11-134	632	9	17.4 (11.1)	12.8	114	22.8	203	30.87	145.1	18.5
NA11-135	590	19	15.4 (14.3)	9.5	639	14.2	949	14.09	174.2	12.1
NA11-137	862	22	3.4 (3.7)	4.4	452	3.5	365	7.73	302.8	27.6
<b>Etendeka Group</b>										
NA11-21	781	10	25.2 (20.9)	11.9	410	22.5	777	60.35	103.5	7.6
NA11-24	902	20	95.1 (79.9)	36.3	2807	71.0	5492	99.97	103.5	4.9
NA11-55	686	3	8.0 (7.7)	5.4	48	8.8	79	61.43	125.6	23.6
NA11-108	424	21	55.4 (17.2)	28.1	2758	67.6	6645	16.07	106.0	5.1
NA11-114	217	23	28.7 (18.4)	14.4	1421	35.5	3512	58.69	108.0	5.6
<b>Damara Belt</b>										
<b>Damara Group</b>										
NA11-09	1486	21	38.3 (16.5)	19.6	936	44.6	2127	5.76	97.5	6.3
NA11-10	1637	24	28.4 (18.4)	13.1	698	31.7	1692	13.53	91.2	6.4
NA11-11	1590	20	51.7 (20.7)	20.8	1028	56.6	2792	85.5	80.5	4.5
NA11-14	559	24	19.0 (3.8)	9.5	1736	23.8	4354	5.99	86.8	4.7
NA11-20	572	20	20.1 (7.4)	9.5	1150	20.5	2465	95.97	94.1	5.1
NA11-40	755	15	16.6 (5.0)	5.5	353	16.9	1078	99.97	63.8	4.8
NA11-42	1254	20	27.6 (5.8)	9.5	965	28.0	2851	99.92	66.1	3.7
NA11-43	964	20	49.6 (9.4)	18.7	1535	49.7	4085	90.88	73.5	3.8
NA11-44	836	20	10.4 (2.3)	3.5	506	10.5	1514	99.58	65.6	4.4
NA11-46	1172	20	22.9 (12.1)	6.9	880	20.9	2647	95.32	65.5	3.8
NA11-49	938	20	21.4 (8.8)	7.7	951	20.6	2552	19.13	73.7	4.4
NA11-52	553	20	21.8 (4.6)	7.2	1160	22.4	3591	90.13	65.5	3.5
NA11-69A	1483	15	6.2 (2.7)	4.3	76	6.3	111	98.68	129.2	20.0
NA11-69B	1483	5	17.1 (26.1)	6.3	55	8.6	75	51.95	138.5	25.3
NA11-70	1297	16	88.0 (78.3)	38.7	400	69.4	718	20.22	104.7	8.5
<b>Karoo and Etendeka groups</b>										
NA11-68	1505	22	29.2 (16.3)	12.7	310	27.1	663	59.34	88.4	7.2
NA11-50	939	16	22.9 (11.2)	7.3	392	20.5	1095	98.17	71.6	5.2

Table B. 3: Apatite fission-track (AFT) length and Dpar<sup>®</sup> data of the Kaoko and Damara belt samples with corresponding sample number, n CT: number of measured confined tracks, CT mean: mean confined track length, std: standard deviation, skew: skewness of distribution relative to the mean value (measure of asymmetry of the distribution), Lc mean: mean track length after c-axis correction, n Dpar<sup>®</sup>: number of etch pit diameters measured, and Dpar<sup>®</sup> mean: mean etch pit diameter. Samples with >50 confined track lengths were used for numerical modeling. For further descriptions see Tables B. 1and B. 2.

Sample number	n CT	CT mean [µm]	CT std [µm]	CT skew	Lc mean [µm]	Lc std [µm]	Lc skew	n Dpar	Dpar mean [µm]	Dpar std [µm]	Dpar skew
<b>Kaoko Belt</b>											
<b>Damara Group</b>											
NA11-30	5	12.4	1.2	-0.43	14.0	1.0	-0.78	35	1.4	0,2	0.71
NA11-53	24	12.0	1.5	-0.54	13.5	1.1	-0.44	120	1.2	0.2	-0.29
NA11-54	4	13.2	0.6	-1.87	14.5	0.2	-1.17	100	1.3	0.2	-0.15
NA11-62	19	11.2	2.1	-0.73	13.1	1.3	-0.15	105	1.2	0.2	0.55
NA11-63	2	10.5	0.3	-	11.7	1.4	-	100	1.3	0.1	-0.24
NA11-65	1	10.7	-	-	13.1	-	-	115	1.1	0.2	0.60
NA11-66	13	12.1	1.2	0.70	13.7	0.8	0.09	110	1.1	0.1	0.30
NA11-71	94	11.9	1.4	-0.65	13.5	0.9	-0.13	145	1.6	0.2	0.43
NA11-72	8	12.7	0.9	0.93	14.1	0.7	-0.15	105	1.5	0.2	0.03
NA11-73	7	7.9	3.4	1.76	11.3	2.5	-0.17	110	1.1	0.3	0.47
NA11-74	10	10.4	1.9	1.28	12.6	1.1	1.61	115	1.3	0.1	0.14
NA11-76	50	8.3	2.3	-0.40	11.6	1.1	-0.98	185	1.2	0.2	0.19
NA11-79	12	9.4	2.5	-0.03	11.7	2.1	-0.72	110	1.2	0.3	0.35
NA11-80	22	11.0	1.4	1.43	13.0	0.8	0.79	100	1.8	0.4	-0.57
NA11-81	8	10.8	1.0	0.13	12.8	1.1	-0.46	110	1.2	0.1	0.12
NA11-83	0	-	-	-	-	-	-	105	1.2	0.1	0.05
NA11-84	92	12.0	1.3	-0.14	13.6	1.0	-0.55	285	1.2	0.1	0.24
NA11-85	8	7.9	2.9	0.52	9.8	2.9	0.08	20	1.3	0.2	-0.21
NA11-86	74	9.7	2.2	0.12	12.2	1.4	-0.69	130	1.3	0.3	0.35
NA11-87	11	12.5	1.6	0.20	14.0	1.1	-0.04	109	1.2	0.2	0.47
NA11-88	2	10.6	2.3	-	11.7	2.9	-	115	1.2	0.2	-0.15
NA11-89	151	11.6	1.6	-0.85	13.3	1.1	-0.69	165	1.0	0.1	0.06
NA11-90	51	11.2	1.8	-0.22	13.0	1.2	-0.09	90	1.0	0.1	0.60
NA11-91	72	10.2	2.4	-0.46	12.5	1.4	0.01	110	1.3	0.2	0.22
NA11-92	51	10.8	2.0	-0.46	12.8	1.4	-0.40	110	1.6	0.4	0.17
NA11-93	3	13.1	1.4	-1.11	14.3	1.1	0.35	145	1.4	0.2	0.10
NA11-94	152	9.5	2.4	-0.13	12.2	1.4	-0.32	130	1.2	0.2	0.68
NA11-95	111	11.2	2.2	-0.03	13.3	1.5	-0.06	110	1.5	0.2	0.04
NA11-96	63	11.9	1.8	-1.16	13.7	0.9	-0.29	160	1.4	0.2	-0.06
NA11-98	3	14.8	0.3	1.55	15.4	0.6	-0.70	40	1.4	0.3	-0.04
NA11-99	14	9.6	2.4	-0.32	12.6	1.1	0.48	110	1.3	0.2	-0.48
NA11-103	82	12.8	1.0	0.04	14.1	0.7	0.12	150	1.4	0.2	0.29
NA11-104	22	12.7	1.1	-0.36	14.2	0.8	-0.21	140	1.2	0.2	0.05
NA11-105	14	12.7	1.1	0.67	14.2	0.8	-0.88	95	1.2	0.1	-0.17
NA11-106	63	12.7	1.0	-0.91	14.1	0.7	-0.87	160	1.3	0.2	0.05
NA11-107	112	12.8	1.1	-0.36	14.2	0.7	-0.36	155	1.3	0.2	0.36
NA11-109	104	13.1	1.0	-0.35	14.4	0.7	-0.19	170	1.3	0.1	-0.77
NA11-110	8	11.2	1.6	0.26	13.1	1.4	-1.21	115	1.2	0.2	0.27
NA11-111	0	-	-	-	-	-	-	100	1.1	0.1	0.08
NA11-115	2	12.0	0.5	-	13.3	1.0	-	70	1.1	0.1	0.62
NA11-116	34	12.0	1.4	-0.30	13.6	1.0	-0.29	140	1.2	0.2	0.26
NA11-117	92	12.8	0.9	-0.40	14.2	0.6	-0.58	245	1.2	0.1	0.00

Sample number	n CT	CT mean [µm]	CT std [µm]	CT skew	Lc mean [µm]	Lc std [µm]	Lc skew	n Dpar	Dpar mean [µm]	Dpar std [µm]	Dpar skew
NA11-120	10	13.0	1.1	0.68	14.5	0.6	0.80	100	1.1	0.1	-0.16
NA11-121	116	11.8	1.3	-0.11	13.5	0.8	-0.14	245	1.1	0.2	1.63
NA11-122	24	12.3	1.5	-0.84	13.9	0.9	-0.31	160	1.2	0.1	-0.41
NA11-123	93	11.7	1.9	-0.67	13.6	1.1	-0.12	190	1.2	0.1	-0.06
NA11-124	2	11.9	2.3	-	13.8	1.3	-	140	1.2	0.2	0.10
NA11-125	6	13.1	1.1	0.53	14.3	0.6	-0.17	110	1.2	0.2	-0.15
NA11-126	37	12.8	0.7	-0.04	14.2	0.5	-0.73	165	1.3	0.2	0.08
NA11-127	98	12.5	1.2	-0.17	14.0	0.8	-0.40	245	1.4	0.2	-0.12
NA11-128	11	11.9	1.9	0.23	13.7	1.2	0.32	105	1.4	0.2	1.18
NA11-129	0	-	-	-	-	-	-	70	1.3	0.2	-0.26
NA11-130	53	12.9	1.0	0.02	14.3	0.7	-0.49	205	1.3	0.2	0.25
NA11-131	6	11.5	2.0	-0.40	13.2	1.5	-0.97	105	1.0	0.1	0.04
NA11-132	28	11.3	1.8	-0.71	13.3	1.0	-0.38	100	1.0	0.1	-0.27
NA11-133	0	-	-	-	-	-	-	110	1.1	0.2	0.57
NA11-136	0	-	-	-	-	-	-	95	1.0	0.1	0.08
NA11-140	53	11.8	1.2	0.10	13.3	1.0	-0.23	125	1.4	0.2	0.04
<b>Karoo Supergroup</b>											
NA11-75	32	11.1	1.7	-0.13	13.2	1.0	0.66	140	1.5	0.2	0.48
NA11-77	58	9.7	1.7	-0.07	12.2	1.2	0.25	120	1.3	0.2	1.69
NA11-78	20	11.3	1.7	-0.32	13.2	1.1	0.00	115	1.4	0.2	-0.09
NA11-112	5	11.4	1.4	1.71	13.6	0.9	1.61	90	1.2	0.2	0.49
NA11-113	2	12.3	1.3	-	13.6	1.4	-	45	1.1	0.2	0.39
NA11-118	34	10.9	2.3	0.06	13.0	1.4	0.18	115	1.1	0.1	0.33
NA11-134	0	-	-	-	-	-	-	45	1.1	0.2	0.85
NA11-135	3	10.8	0.8	0.00	12.8	1.1	-1.61	95	1.2	0.1	0.07
NA11-137	0	-	-	-	-	-	-	109	1.2	0.2	0.07
<b>Etendeka Group</b>											
NA11-21	16	11.7	1.4	-0.61	13.4	0.9	0.06	65	1.0	0.1	0.70
NA11-24	93	12.4	1.2	0.00	13.9	0.8	-0.38	110	1.3	0.1	-0.39
NA11-55	0	-	-	-	-	-	-	15	0.8	0.1	-0.54
NA11-108	52	12.9	1.0	-0.62	14.3	0.6	-0.28	125	1.3	0.1	0.04
NA11-114	7	10.4	2.1	0.05	12.6	1.4	-0.64	120	1.2	0.2	0.56
<b>Damara Belt</b>											
<b>Damara Group</b>											
NA11-09	111	12.4	1.2	-0.83	13.7	0.9	-0.70	105	1.6	0.2	0.14
NA11-10	101	12.1	1.2	-0.13	13.7	0.9	-0.59	140	1.4	0.2	0.41
NA11-11	101	12.2	1.2	0.48	13.6	0.9	0.40	105	1.5	0.2	0.07
NA11-14	28	11.7	1.4	0.12	13.2	1.1	-0.03	135	1.4	0.2	-0.17
NA11-20	18	12.2	1.2	0.13	13.8	0.8	0.38	120	1.1	0.2	0.26
NA11-40	7	11.9	1.7	1.67	13.5	0.7	-0.87	75	1.3	0.2	0.16
NA11-42	53	12.0	1.2	-0.74	13.5	1.0	-0.70	175	1.3	0.2	0.70
NA11-43	102	12.6	1.3	-0.46	14.0	0.9	-0.62	155	1.4	0.2	0.84
NA11-44	3	12.7	0.9	-1.39	13.9	0.3	1.53	105	1.3	0.2	0.13
NA11-46	8	13.5	1.3	-0.35	14.5	1.0	-0.98	100	1.3	0.2	0.68
NA11-49	51	12.0	1.4	-0.22	13.6	0.9	-0.23	170	1.3	0.2	0.04
NA11-52	51	11.9	1.4	-1.02	13.4	1.0	-0.43	175	1.4	0.2	0.41
NA11-69A	0	-	-	-	-	-	-	73	1.2	0.2	0.22
NA11-69B	0	-	-	-	-	-	-	25	1.2	0.3	0.74
NA11-70	51	11.3	1.2	0.34	13.0	1.0	-0.41	85	1.2	0.2	0.06
<b>Karoo Supergroup</b>											
NA11-68	43	10.8	1.5	-0.01	12.8	1.1	-0.54	140	1.3	0.2	0.39
<b>Etendeka Group</b>											
NA11-50	8	8.6	2.1	-0.25	11.9	1.3	-0.68	80	1.3	0.2	-0.03

Table B. 4: Zircon fission-track (ZFT) data of the Kaoko Belt samples with corresponding sample number, lithology, altitude [m a.s.l.], n: number of counted grains, U: uranium concentration in  $\mu\text{g/g}$ ,  $\rho_s$ : density of spontaneous tracks ( $\times 10^5/\text{cm}^2$ ),  $N_s$ : number of spontaneous tracks,  $\rho_i$ : density of induced tracks ( $\times 10^5/\text{cm}^2$ ),  $N_i$ : number of induced tracks,  $P$  ( $\chi^2$ ) is the probability that single grain ages are consistent and belong to the same population. Test is passed if  $P$  ( $\chi^2$ ) > 5% (Galbraith 1981). Ages calculated using a  $\zeta$ -value of  $122.41 \pm 5.25$  a/cm<sup>2</sup> for zircon. Gn: gneiss; sch: schist; amp: amphibolite; sed: sediment; mig: migmatite; rhy: rhyolite; myl: mylonite; con: conglomerate; gr: granite. For further descriptions see Table B. 1.

Sample number	L.	Alt. [m a.s.l.]	n	U (std) [ $\mu\text{g/g}$ ]	$\rho_s$ [ $\times 10^5/\text{cm}^2$ ]	$N_s$	$\rho_i$ [ $\times 10^5/\text{cm}^2$ ]	$N_i$	$c^2$ [%]	Central age [Ma]	$\pm(1\sigma)$ [Ma]
<b>Kaoko Belt</b>											
<b>Damara Group</b>											
NA11-84	gn	669	20	167.8 (65.4)	356.8	4768	31.2	417	46.85	388.2	26.3
NA11-86	sch	838	8	187.0 (86.0)	306.2	1127	30.4	112	79.63	338.3	36.6
NA11-89G	gn	791	2	713.5 (321.1)	410.8	102	120.8	30	64.98	118.2	25.1
NA11-91	pta	791	2	277.1 (41.6)	334.8	239	49.0	35	89.28	233.5	43.5
NA11-95	amp	822	22	168.1 (50.4)	283.3	2748	29.5	286	83.33	334.0	25.4
NA11-99	amp	502	14	192.3 (103.7)	321.8	2291	27.0	192	54.10	413.0	35.9
NA11-103	sed	402	21	175.3 (47.3)	323.3	3005	30.2	281	99.69	362.7	27.6
NA11-105	mig	332	3	228.5 (38.9)	470.0	1118	40.4	96	96.86	401.4	46.1
NA11-106	gr	303	20	145.4 (53.8)	325.7	4039	23.8	295	0.01	436.8	45.9
NA11-109	gr	471	4	197.2 (86.8)	376.6	319	31.9	27	15.96	385.6	87.7
NA11-110	gr	310	21	127.0 (38.1)	256.1	2438	22.3	212	85.14	391.1	32.9
NA11-111	gn	198	22	133.5 (65.4)	228.7	3184	21.5	300	61.26	359.4	26.8
NA11-116	gr	479	6	195.7 (35.2)	361.8	593	31.1	51	95.06	390.0	59.4
NA11-117	gr	639	5	234.3 (56.2)	420.9	553	42.6	56	84.70	338.5	49.7
NA11-120	gr	556	19	214.8 (55.9)	325.9	2336	35.0	251	99.71	322.2	25.6
NA11-122	rhy	334	21	208.1 (49.9)	359.8	2849	36.2	287	99.93	341.4	25.9
NA11-124	gn	309	7	259.7 (57.1)	426.1	378	46.2	41	99.00	313.9	53.4
NA11-125	gn	325	12	143.4 (40.2)	312.9	1246	25.4	101	70.80	413.1	46.4
NA11-126	gn	333	3	291.3 (67.0)	450.8	216	48.0	23	96.09	316.3	70.7
NA11-128	gn	354	9	213.2 (53.3)	422.0	1165	36.2	100	99.04	392.1	44.3
NA11-129	gn	366	9	218.0 (65.4)	360.2	790	35.1	77	90.08	352.5	44.8
NA11-131	gn	573	16	177.5 (55.0)	297.0	2985	29.8	299	76.85	344.4	25.7
NA11-133	myl	626	15	152.4 (50.3)	309.7	1221	26.1	103	99.98	402.2	44.8
NA11-136	myl	882	7	129.7 (44.1)	211.9	585	17.0	47	98.04	429.5	67.8
NA11-140	sch	825	17	128.2 (44.9)	236.0	1215	21.6	111	100.0	378.6	41.0
<b>Karoo Supergroup</b>											
NA11-118	sst	679	21	142.3 (59.8)	248.0	2934	21.9	259	65.66	377.2	30.4
NA11-135GO	con	590	11	120.8 (20.5)	263.7	1640	22.3	139	98.56	396.3	39.0
NA11-135R	con	590	16	158.7 (34.9)	293.3	2286	27.6	215	100.0	365.6	30.6



Table B. 5. 1: Western Kaoko Zone – northern area (green). Compiled published geochronological data for the NW Namibian Kaoko and Damara belts. Data is organised according to the geological region/domain and dating method (closing temperature) with corresponding rock type, age [Ma],  $\pm$ error [Ma], primary reference, and secondary reference (where data was found).

Western Kaoko Zone - northern area (green)						
Rock type	Analysis	Age [Ma]	$\pm$ Er. [Ma]	Interpret.	Primary Reference	Secondary Reference
<b>Western Kaoko Zone, northern Orogen Core</b>						
meta-quartz arenite	U-Pb (SHRIMP), zircon	572.4	5.1	metamorph.	Goscombe et al. (2005)	Goscombe et al. (2005)
Late-M2, pre-SZ peg	U-Pb (SHRIMP), zircon	561.8	4.9	crystal.	Goscombe et al. (2005)	Goscombe et al. (2005)
Late-M2, pre-SZ peg.	U-Pb (SHRIMP), zircon	549.0	5.8	crystal.	Goscombe et al. (2005)	Goscombe et al. (2005)
Post-kinematic peg.	U-Pb (SHRIMP), zircon	507.6	5.3	crystal.	Goscombe et al. (2005)	Goscombe et al. (2005)
quartz-pelite mylonite	Sm-Nd isochron, garnet	506.5	5.4	metamorph.	Goscombe et al. (2005)	Goscombe et al. (2005)
mafic gneiss	$^{40}\text{Ar}/^{39}\text{Ar}$ , hornblende	533.0	4.0	cooling	Gray et al. (2006)	Gray et al. (2006)
amphibolite	$^{40}\text{Ar}/^{39}\text{Ar}$ , hornblende	525.0	7.0	cooling	Hackspacher et al. (2004)	Hackspacher et al. (2004)
mylonitic orthogneiss	$^{40}\text{Ar}/^{39}\text{Ar}$ , muscovite	481.0	3.0	cooling	Gray et al. (2006)	Gray et al. (2006)
mylonitic orthogneiss	$^{40}\text{Ar}/^{39}\text{Ar}$ , biotite	509.0	3.0	cooling	Gray et al. (2006)	Gray et al. (2006)
amphibolite	zircon fission-track	413.0	35.9	cooling	this study	-
schist	zircon fission-track	338.3	36.6	cooling	this study	-
amphibolite	zircon fission-track	334.0	25.4	cooling	this study	-
amphibolite	apatite fission-track	262.3	14.7	cooling	this study	-
schist	apatite fission-track	242.1	11.3	cooling	this study	-
pseudotachylite	apatite fission-track	221.2	13.8	cooling	this study	-
granite	apatite fission-track	192.6	13.0	cooling	this study	-
gneiss	apatite fission-track	168.3	8.4	cooling	this study	-
amphibolite	apatite fission-track	98.6	6.2	cooling	this study	-

Table B. 5. 2: Central Kaoko Zone – northern central area (blue). For further information, please see Table B. 5. 1.

Central Kaoko Zone - northern central area (blue)						
Rock type	Analysis	Age [Ma]	$\pm$ Er. [Ma]	Interpret.	Primary Reference	Secondary Reference
<b>Central Kaoko Zone - Escape Zone/Epupa Complex</b>						
n/a	U-Pb (SHRIMP), zircon	1800-1200	n/a	crystal.	Kröner et al. (2010)	Kröner et al. (2010)
meta-pelite schist	Sm-Nd, garnet	574.3	9.7	metamorph.	Goscombe et al. (2003b)	Goscombe et al. (2005)
schist	$^{40}\text{Ar}/^{39}\text{Ar}$ , whole rock	467.0	3.0	cooling	Gray et al. (2006)	Gray et al. (2006)
mylonite	zircon fission-track	429.5	67.8	cooling	this study	-

Rock type	Analysis	Age [Ma]	± Er. [Ma]	Interpret.	Primary Reference	Secondary Reference
gneiss	zircon fission-track	388.2	26.3	cooling	this study	-
schist	zircon fission-track	378.6	41.0	cooling	this study	-
gneiss	zircon fission-track	348.6	51.1	cooling	this study	-
amphibolite	apatite fission-track	390.9	17.9	cooling	this study	-
n/a	apatite fission-track	360-280	n/a	cooling	Brown et al. (2014)	Brown et al. (2014)
gneiss	apatite fission-track	326.7	18.1	cooling	this study	-
gneiss	apatite fission-track	324.0	18.1	cooling	this study	-
granite	apatite fission-track	309.8	36.7	cooling	this study	-
gneiss	apatite fission-track	308.2	16.5	cooling	this study	-
schist	apatite fission-track	282.8	16.7	cooling	this study	-
schist	apatite fission-track	253.5	22.6	cooling	this study	-
gneiss	apatite fission-track	210.9	19.5	cooling	this study	-
gneiss	apatite fission-track	96.7	4.8	cooling	this study	-

Table B. 5. 3: Western and Central Kaoko Zone – central area (orange). For further information, please see Table B. 5. 1.

Western and Central Kaoko Zone - central area (orange)						
Rock type	Analysis	Age [Ma]	± Er. [Ma]	Interpret.	Primary Reference	Secondary Reference
<b>Western Kaoko Zone, Coastal Terrane</b>						
granitic orthogneiss	U-Pb (TIMS), zircon	703.0	1.0	crystal.	Kröner et al. (2004)	Milani et al. (2015)
granitic orthogneiss	U-Pb (SHRIMP), zircon	694.0	9.0	crystal.	Kröner et al. (2004)	Milani et al. (2015)
granitic orthogneiss	U-Pb (TIMS), zircon	661.0	21.0	crystal.	Kröner et al. (2004)	Milani et al. (2015)
granitic orthogneiss	U-Pb (SHRIMP), zircon	656.0	8.0	crystal.	Seth et al. (1998)	Milani et al. (2015)
granitic orthogneiss	U-Pb (TIMS), zircon	655.0	39.0	crystal.	Kröner et al. (2004)	Milani et al. (2015)
mafic volcanic	U-Pb (SIMS), zircon	650.0	5.0	crystal.	Konopásek et al. (2008)	Milani et al. (2015)
mafic volcanic	U-Pb (LA-ICP-MS), zircon	645.0	5.0	crystal.	Konopásek et al. (2008)	Milani et al. (2015)
meta-pelite gneiss	U-Pb (SHRIMP), zircon	645.0	3.5	crystal.	Franz et al. (1999)	Goscombe et al. (2005)
granite sill	U-Pb (SHRIMP), zircon	~640	n/a	crystal.	Goscombe et al. (2005)	Goscombe et al. (2005)
leucogranite	U-Pb (SHRIMP), zircon	637.7	5.8	crystal.	Goscombe et al. (2005)	Milani et al. (2015)
granitic orthogneiss	U-Pb (SHRIMP), zircon	630.0	8.0	crystal.	Seth et al. (1998)	Milani et al. (2015)
melt patch	U-Pb (SIMS), zircon	630.0	4.0	crystal.	Konopásek et al. (2008)	Milani et al. (2015)
leucogranite	U-Pb (SHRIMP), zircon	625.0	15.0	crystal.	Goscombe et al. (2005)	Milani et al. (2015)
melt patch	U-Pb (LA-ICP-MS), zircon	625.0	10.0	crystal.	Konopásek et al. (2008)	Milani et al. (2015)
leucogranite	U-Pb (SHRIMP), zircon	620.0	18.0	crystal.	Goscombe et al. (2005)	Milani et al. (2015)

Rock type	Analysis	Age[Ma]	± Error [Ma]	Interpr.	Primary Reference	Secondary Reference
gneiss granite	U-Pb (SHRIMP), zircon	576.0	11.0	crystal.	Goscombe et al. (2005)	Milani et al. (2015)
grt-granite	U-Pb (SIMS), zircon	575.0	10.0	crystal.	Konopásek et al. (2008)	Milani et al. (2015)
granite	U-Pb (LA-ICP-MS), zircon	572.0	4.0	crystal.	Konopásek et al. (2008)	Milani et al. (2015)
grt-granite	U-Pb (LA-ICP-MS), zircon	571.0	9.0	crystal.	Konopásek et al. (2008)	Milani et al. (2015)
syenogranite	U-Pb (SHRIMP), zircon	568.0	5.0	crystal.	Goscombe et al. (2005)	Milani et al. (2015)
granite	U-Pb (SHRIMP), zircon	565.0	13.0	crystal.	Seth et al. (1998)	Milani et al. (2015)
granite	U-Pb (SIMS), zircon	562.0	11.0	crystal.	Konopásek et al. (2008)	Milani et al. (2015)
granitic orthogneiss	U-Pb (SHRIMP), zircon	558.6	7.3	crystal.	Franz et al. (1999)	Goscombe et al. (2005)
granitic orthogneiss	U-Pb (SHRIMP), zircon	549.0	4.0	crystal.	Kroner et al. (2004)	Goscombe et al. (2005)
pegmatite	U-Pb (SHRIMP), zircon	530.5	5.3	crystal.	Goscombe et al. (2005)	Milani et al. (2015)
Post-kinematic peg.	U-Pb (SHRIMP), monazite	531.0	6.0	crystal.	Goscombe et al. (2005)	Goscombe et al. (2005)
Post-kinematic peg.	U-Pb (SHRIMP), monazite	514.5	4.9	crystal.	Goscombe et al. (2005)	Goscombe et al. (2005)
granite	Sm-Nd, garnet	534.0	9.0	cooling	Jung et al. (2014)	Jung et al. (2014)
mafic gneiss	$^{40}\text{Ar}/^{39}\text{Ar}$ , hornblende	546.0	5.0	cooling	Foster et al. (2009)	Foster et al. (2009)
paragneiss	$^{40}\text{Ar}/^{39}\text{Ar}$ , muscovite	528.0	6.0	cooling	Foster et al. (2009)	Foster et al. (2009)
granite	zircon fission-track	436.8	45.9	cooling	this study	-
migmatite	zircon fission-track	401.4	46.1	cooling	this study	-
granite	zircon fission-track	391.1	32.9	cooling	this study	-
gneiss	zircon fission-track	359.4	26.8	cooling	this study	-
granite	apatite fission-track	119.1	6.4	cooling	this study	-
schist	apatite fission-track	111.4	7.8	cooling	this study	-
gneiss	apatite fission-track	99.0	7.3	cooling	this study	-
granite	apatite fission-track	95.7	5.2	cooling	this study	-
migmatite	apatite fission-track	93.9	5.8	cooling	this study	-
<b>Western Kaoko Zone, southern Orogen Core</b>						
granitic orthogneiss	U-Pb (SHRIMP), zircon	580.0	3.0	crystal.	Seth et al. (1998)	Goscombe et al. (2005)
granitic orthogneiss	U-Pb (SHRIMP), zircon	578.0	57.0	crystal.	Seth et al. (1998)	Goscombe et al. (2005)
melt segregation	U-Pb (SHRIMP), zircon	573.8	4.0	crystal.	Goscombe et al. (2005)	Goscombe et al. (2005)
pegmatite	U-Pb (SHRIMP), zircon	561.8	4.9	crystal.	Goscombe et al. (2005)	Milani et al. (2015)
Late M2 graniite vein	U-Pb (SHRIMP), zircon	549.2	1.9	crystal.	Goscombe et al. (2005)	Goscombe et al. (2005)
pegmatite	U-Pb (SHRIMP), zircon	539.0	6.0	crystal.	Kroner et al. (2004)	Milani et al. (2015)
metapelite	Sm-Nd, garnet	579.0	16.0	metamorph.	Goscombe et al. (2003)	Goscombe et al. (2003)
meta-pelite gneiss	Sm-Nd, garnet	579.0	15.0	metamorph.	Goscombe et al. (2003b)	Goscombe et al. (2005)

Rock type	Analysis	Age[Ma]	± Error [Ma]	Interpr.	Primary Reference	Secondary Reference
meta-pelite gneiss	Sm-Nd, garnet	571.2	6.1	metamorph.	Goscombe et al. (2003b)	Goscombe et al. (2005)
paragneiss	Sm-Nd, garnet	548.0	5.0	cooling	Jung et al. (2014)	Jung et al. (2014)
orthogneiss	Sm-Nd, garnet	544.0	4.0	cooling	Jung et al. (2014)	Jung et al. (2014)
paragneiss	Sm-Nd, garnet	544.0	5.0	cooling	Jung et al. (2014)	Jung et al. (2014)
granite	Sm-Nd, garnet	536.0	5.0	cooling	Jung et al. (2014)	Jung et al. (2014)
orthogneiss	Sm-Nd, garnet	527.0	8.0	cooling	Jung et al. (2014)	Jung et al. (2014)
calcilicite	Sm-Nd, garnet	527.0	7.0	cooling	Foster et al. (2009)	Foster et al. (2009)
orthogneiss	Sm-Nd, garnet	526.0	15.0	cooling	Jung et al. (2014)	Jung et al. (2014)
paragneiss	Sm-Nd, garnet	521.0	9.0	cooling	Jung et al. (2014)	Jung et al. (2014)
meta-pelite gneiss	Sm-Nd, garnet	504.7	8.0	cooling	Goscombe et al. (2005)	Goscombe et al. (2005)
meta-pelite schist	Sm-Nd, garnet	504.6	4.7	cooling	Goscombe et al. (2005)	Goscombe et al. (2005)
amphibolite gneiss	<sup>40</sup> Ar/ <sup>39</sup> Ar, hornblende	532.9	6.6	cooling	Goscombe et al. (2005)	Goscombe et al. (2005)
psammitic schist	<sup>40</sup> Ar/ <sup>39</sup> Ar, hornblende	528.0	2.0	cooling	Gray et al. (2006)	Gray et al. (2006)
amphibolite gneiss	<sup>40</sup> Ar/ <sup>39</sup> Ar, hornblende	526.5	6.5	cooling	Goscombe et al. (2005)	Goscombe et al. (2005)
granitic mylonite	<sup>40</sup> Ar/ <sup>39</sup> Ar, muscovite	530.0	7.0	cooling	Foster et al. (2009)	Foster et al. (2009)
psemmitite	<sup>40</sup> Ar/ <sup>39</sup> Ar, muscovite	527.0	6.0	cooling	Foster et al. (2009)	Foster et al. (2009)
granitic mylonite	<sup>40</sup> Ar/ <sup>39</sup> Ar, muscovite	524.0	7.0	cooling	Foster et al. (2009)	Foster et al. (2009)
psammitic schist	<sup>40</sup> Ar/ <sup>39</sup> Ar, muscovite	518.0	3.0	cooling	Gray et al. (2006)	Gray et al. (2006)
psammitic schist	<sup>40</sup> Ar/ <sup>39</sup> Ar, muscovite	507.0	3.0	cooling	Gray et al. (2006)	Gray et al. (2006)
mylonitised granite	<sup>40</sup> Ar/ <sup>39</sup> Ar, muscovite	492.0	3.0	cooling	Gray et al. (2006)	Gray et al. (2006)
gneiss	<sup>40</sup> Ar/ <sup>39</sup> Ar, biotite	531.0	5.0	cooling	Gray et al. (2006)	Gray et al. (2006)
psammitic schist	<sup>40</sup> Ar/ <sup>39</sup> Ar, biotite	528.0	2.0	cooling	Gray et al. (2006)	Gray et al. (2006)
granite	zircon fission-track	390.0	59.4	cooling	this study	-
granite	zircon fission-track	385.6	87.7	cooling	this study	-
gneiss	zircon fission-track	344.4	25.7	cooling	this study	-
rhyolite	zircon fission-track	341.4	25.9	cooling	this study	-
granite	zircon fission-track	338.5	49.7	cooling	this study	-
granite	zircon fission-track	322.2	25.6	cooling	this study	-
granite	apatite fission-track	148.9	11.9	cooling	this study	-
gneiss	apatite fission-track	121.2	5.8	cooling	this study	-
granite	apatite fission-track	118.0	10.2	cooling	this study	-
rhyolite	apatite fission-track	116.3	6.1	cooling	this study	-
migmatite	apatite fission-track	116.2	5.4	cooling	this study	-
gneiss	apatite fission-track	115.4	5.9	cooling	this study	-
granite	apatite fission-track	108.3	4.9	cooling	this study	-
gneiss	apatite fission-track	96.2	6.4	cooling	this study	-
gneiss	apatite fission-track	94.7	5.7	cooling	this study	-
meta-sediment	apatite fission-track	93.3	5.1	cooling	this study	-
granite	apatite fission-track	93.3	4.5	cooling	this study	-
mylonite	apatite fission-track	83.2	4.3	cooling	this study	-

Rock type	Analysis	Age[M a]	± Error [Ma]	Interpr.	Primary Reference	Secondary Reference
<b>Central Kaoko Zone, Escape Zone</b>						
meta-pelite schist	Sm-Nd, garnet	574.3	9.7	metamorph	Goscombe et al. (2003b)	Goscombe et al. (2005)
calcsilicate	<sup>40</sup> Ar/ <sup>39</sup> Ar, hornblende	530.0	6.0	cooling	Foster et al. (2009)	Foster et al. (2009)
amphibolite schist	<sup>40</sup> Ar/ <sup>39</sup> Ar, hornblende	526.0	4.0	cooling	Goscombe et al. (2005)	Goscombe et al. (2005)
schist	<sup>40</sup> Ar/ <sup>39</sup> Ar, hornblende	526.0	4.0	cooling	Gray et al. (2006)	Gray et al. (2006)
mafic gneiss	<sup>40</sup> Ar/ <sup>39</sup> Ar, hornblende	524.0	6.0	cooling	Foster et al. (2009)	Foster et al. (2009)
mafic schist	<sup>40</sup> Ar/ <sup>39</sup> Ar, hornblende	521.0	8.0	cooling	Foster et al. (2009)	Foster et al. (2009)
schist	<sup>40</sup> Ar/ <sup>39</sup> Ar, muscovite	527.0	5.0	cooling	Gray et al. (2006)	Gray et al. (2006)
schist	<sup>40</sup> Ar/ <sup>39</sup> Ar, muscovite	525.0	3.0	cooling	Gray et al. (2006)	Gray et al. (2006)
schist	<sup>40</sup> Ar/ <sup>39</sup> Ar, muscovite	524.0	5.0	cooling	Gray et al. (2006)	Gray et al. (2006)
schist	<sup>40</sup> Ar/ <sup>39</sup> Ar, muscovite	522.0	5.0	cooling	Gray et al. (2006)	Gray et al. (2006)
schist	<sup>40</sup> Ar/ <sup>39</sup> Ar, muscovite	518.0	4.0	cooling	Gray et al. (2006)	Gray et al. (2006)
schist	<sup>40</sup> Ar/ <sup>39</sup> Ar, biotite	527.0	5.0	cooling	Gray et al. (2006)	Gray et al. (2006)
gneiss	<sup>40</sup> Ar/ <sup>39</sup> Ar, biotite	519.0	5.0	cooling	Gray et al. (2006)	Gray et al. (2006)
gneiss	zircon fission-track	413.1	46.4	cooling	this study	-
mylonite	zircon fission-track	402.2	44.8	cooling	this study	-
gneiss	zircon fission-track	392.1	44.3	cooling	this study	-
gneiss	zircon fission-track	352.5	44.8	cooling	this study	-
gneiss	zircon fission-track	316.3	70.7	cooling	this study	-
gneiss	zircon fission-track	313.9	53.4	cooling	this study	-
granite	apatite fission-track	234.1	12.7	cooling	this study	-
schist	apatite fission-track	211.5	12.8	cooling	this study	-
schist	apatite fission-track	210.8	11.3	cooling	this study	-
gneiss	apatite fission-track	190.6	14.4	cooling	this study	-
mylonite	apatite fission-track	181.8	13.1	cooling	this study	-
gneiss	apatite fission-track	120.8	6.3	cooling	this study	-
gneiss	apatite fission-track	111.6	6.5	cooling	this study	-
mylonite	apatite fission-track	107.2	6.5	cooling	this study	-
gneiss	apatite fission-track	106.0	6.3	cooling	this study	-
gneiss	apatite fission-track	98.5	4.9	cooling	this study	-
granite	apatite fission-track	95.7	4.8	cooling	this study	-
gneiss	apatite fission-track	87.0	5.0	cooling	this study	-
gneiss	apatite fission-track	84.3	4.3	cooling	this study	-

Table B. 5. 4: Southern Kaoko Belt – Ugab Zone (yellow). For further information, please see Table B. 5. 1.

Southern Kaoko Belt - Ugab Zone (yellow)						
Rock type	Analysis	Age [Ma]	± Error [Ma]	Interpret.	Primary Reference	Secondary Reference
<b>Ugab Zone</b>						
qtz-diorite	U-Pb (TIMS), zircon	540.0	3.0	crystal.	Van de Flierdt et al. (2003)	Milani et al. (2015)
hbl-monozodiorite	U-Pb (SHRIMP), zircon	534.0	4.5	crystal.	Schmitt et al. (2012)	Milani et al. (2015)
granitic vein	U-Pb (SHRIMP), zircon	533.5	6.1	crystal.	Schmitt et al. (2012)	Milani et al. (2015)
Voetspoor intrusion syenite	U-Pb (TIMS), zircon	530.2	3.2	crystal.	Seth et al. (2000)	Seth et al. (2000)
hbl-qtz-monzonite	U-Pb (SHRIMP), zircon	530.0	4.5	crystal.	Schmitt et al. (2012)	Milani et al. (2015)
bt-granite	U-Pb (SHRIMP), zircon	528.0	5.4	crystal.	Schmitt et al. (2012)	Milani et al. (2015)
leucosome	U-Pb (LA-ICP-MS), zircon	513.0	7.0	crystal.	WITS-RTX (2011–2013)	Milani et al. (2015)
southern zone	U-Pb (SHRIMP), monazite	≈505	≈30	crystal.	Goscombe et al. (2017)	Goscombe et al. (2017)
Voetspoor intrusion syenite	U-Pb (TIMS), zircon	456.0	20.0	crystal.	Seth et al. (2000)	Seth et al. (2000)
metapelite gneiss	Sm-Nd isochron, garnet	491.0	33.0	metamorph	Goscombe et al. (2007)	Goscombe et al. (2007)
amphibolite schist	<sup>40</sup> Ar/ <sup>39</sup> Ar, hornblende	513.0	7.5	cooling	Goscombe et al. (2005)	Goscombe et al. (2005)
amphibole schist	<sup>40</sup> Ar/ <sup>39</sup> Ar, hornblende	513.0	5.0	cooling	Gray et al. (2006)	Gray et al. (2006)
southern zone	K/Ar, biotite	≈490	≈40	cooling	Goscombe et al. (2017)	Goscombe et al. (2017)
southern zone	<sup>40</sup> Ar/ <sup>39</sup> Ar, biotite	≈490	≈40	cooling	Goscombe et al. (2017)	Goscombe et al. (2017)
Voetspoor contact aureole schist	<sup>40</sup> Ar/ <sup>39</sup> Ar, biotite	496.0	2.0	cooling	Gray et al. (2006)	Gray et al. (2006)
Voetspoor contact aureole schist	<sup>40</sup> Ar/ <sup>39</sup> Ar, biotite	438.0	2.0	cooling	Gray et al. (2006)	Gray et al. (2006)
mica quartzite	<sup>40</sup> Ar/ <sup>39</sup> Ar, biotite	497.0	1.0	cooling	Gray et al. (2006)	Gray et al. (2006)
granite	apatite fission-track	94.1	5.1	cooling	this study	-

Table B. 5. 5: Damara Belt – Northern Central Zone (red). For further information, please see Table B. 5. 1.

Damara Belt - Northern Central Zone						
Rock type	Analysis	Age [Ma]	± Error [Ma]	Interpret.	Primary Reference	Secondary Reference
<b>Swakop Zone</b>						
Oetmoed granite	U-Pb (TIMS), zircon	589.0	40.0	crystal.	Miller and Burger (1983)	Milani et al. (2015)
Otjiwarongo granite/pegmatite	U-Pb (SHRIMP), zircon	550.0	5.0	crystal.	Lobo-Guerrero Sanz (2005)	Milani et al. (2015)
Oetmoed migmatite	U-Pb (SHRIMP), monazite	538-520	n/a	metamorph.	Jung et al. (2000b)	Goscombe et al. (2005)
Oetmoed granite	U-Pb (SHRIMP), monazite	526-516	n/a	crystal	Jung et al. (2000a)	Goscombe et al. (2005)
Oetmoed granite	U-Pb (SHRIMP), monazite	513-504	n/a	crystal.	Jung et al. (2000a)	Goscombe et al. (2005)
Oetmoed migmatite	U-Pb (SHRIMP), monazite	510-505	n/a	metamorph.	Jung et al. (2000b)	Goscombe et al. (2005)
Oetmoed granite	U-Pb (SHRIMP), monazite	492-488	n/a	crystal.	Jung et al. (2000a)	Goscombe et al. (2005)
Oetmoed migmatite	U-Pb (SHRIMP), monazite	487-470	n/a	metamorph.	Jung et al. (2000b)	Goscombe et al. (2005)
Okombahe Salern granite	Rb-Sr, whole rock	553.0	63.0	intrusion	Haack et al. (1980)	Haack and Martin (1983)
Okombahe diorite	Rb-Sr, whole rock	550.0	22.0	intrusion	Gohn and Haack unpubl.	Haack and Martin (1983)
Okombahe granite	Rb-Sr, whole rock	514.0	22.0	intrusion	Haack et al. (1980)	Haack and Martin (1983)
Sorris-Sorris granite,	Rb-Sr, whole rock	495.0	15.0	intrusion	Hawkesworth et al. (1982)	Haack and Martin (1983)
Okombahe granite	Rb-Sr, whole rock	479.0	16.0	intrusion	Haack et al. (1980)	Haack and Martin (1983)
Okombahe granite	Rb-Sr, whole rock	478.0	27.0	intrusion	Haack et al. (1980)	Haack and Martin (1983)
Okombahe granite	Rb-Sr, whole rock	465.0	31.0	intrusion	Haack et al. (1980)	Haack and Martin (1983)
Oetmoed migmatite	Sm-Nd isochron, garnet	511.0	11.0	metamorph.	Jung et al. (2000b)	Goscombe et al. (2005)
Oetmoed migmatite	Sm-Nd isochron, garnet	508.0	6.0	metamorph.	Jung et al. (2000b)	Goscombe et al. (2005)
leucosome	Sm-Nd isochron, garnet	473.0	3.0	metamorph.	Jung et al. (2000b)	Goscombe et al. (2005)
leucosome	Sm-Nd isochron, garnet	473.0	5.0	metamorph.	Jung et al. (2000b)	Goscombe et al. (2005)
n/a	apatite fission-track	120-80	n/a	cooling	Raab et al (2002)	Raab et al (2002)
granodiorite	apatite fission-track	97.5	6.3	cooling	this study	-
granodiorite	apatite fission-track	91.2	6.4	cooling	this study	-
granite	apatite fission-track	86.8	4.7	cooling	this study	-
granite	apatite fission-track	80.5	4.5	cooling	this study	-
granite	apatite fission-track	73.7	4.4	cooling	this study	-

Table B. 5. 6: Damara Belt – Southern Zone (red). For further information, please see Table B. 5. 1.

Damara Belt - Southern Zone						
Rock type	Analysis	Age [Ma]	± Error [Ma]	Interpret.	Primary Reference	Secondary Reference
<b>Khomas Zone</b>						
Davetsaub migmatite	U-Pb (SHRIMP), monazite	527	n/a	metamorph.	Kukla et al. (1991)	Kukla et al. (1991)
Davetsaub migmatite	U-Pb (SHRIMP), monazite	525	n/a	metamorph.	Kukla et al. (1991)	Kukla et al. (1991)
Davetsaub migmatite	U-Pb (SHRIMP), monazite	524	n/a	metamorph.	Kukla et al. (1991)	Kukla et al. (1991)
Davetsaub migmatite	U-Pb (SHRIMP), monazite	522	n/a	metamorph.	Kukla et al. (1991)	Kukla et al. (1991)
Davetsaub migmatite	U-Pb (SHRIMP), monazite	520	n/a	metamorph.	Kukla et al. (1991)	Kukla et al. (1991)
Kuiseb fm pelite	U-Pb (SHRIMP), monazite	513	n/a	metamorph.	Kukla et al. (1991)	Kukla et al. (1991)
Davetsaub granitic vein	U-Pb (SHRIMP), monazite	507	n/a	crystal.	Kukla et al. (1991)	Kukla et al. (1991)
Otjimbingwe granodiorite	U-Pb (SHRIMP), monazite	507	n/a	crystal.	Kukla et al. (1991)	Kukla et al. (1991)
Donkerhuk granite	U-Pb (SHRIMP), monazite	505	5.0	crystal.	Kukla et al. (1991)	Kukla et al. (1991)
migmatite	Rb-Sr, whole rock	487.9	n/a	cooling	Jung and Mezger (2001)	Jung and Mezger (2001)
migmatite	Rb-Sr, whole rock	469.0	n/a	cooling	Jung and Mezger (2001)	Jung and Mezger (2001)
migmatite	Rb-Sr, whole rock	472.8	n/a	cooling	Jung and Mezger (2001)	Jung and Mezger (2001)
migmatite	Sm-Nd isochron, garnet	543.0	5.0	cooling	Jung and Mezger (2001)	Jung and Mezger (2001)
migmatite	Sm-Nd isochron, garnet	539.0	8.0	cooling	Jung and Mezger (2001)	Jung and Mezger (2001)
migmatite	Sm-Nd isochron, garnet	528.0	11.0	cooling	Jung and Mezger (2001)	Jung and Mezger (2001)
migmatite	Sm-Nd isochron, garnet	511.0	16.0	cooling	Jung and Mezger (2001)	Jung and Mezger (2001)
migmatite	Sm-Nd isochron, garnet	497.0	2.0	cooling	Jung and Mezger (2001)	Jung and Mezger (2001)
migmatite	Sm-Nd isochron, garnet	496.0	10.0	cooling	Jung and Mezger (2001)	Jung and Mezger (2001)



Rock type	Analysis	Age [Ma]	± Error [Ma]	Interpret.	Primary Reference	Secondary Reference
migmatite	Sm-Nd isochron, garnet	492.0	5.0	cooling	Jung and Mezger (2001)	Jung and Mezger (2001)
migmatite	Sm-Nd isochron, garnet	488.0	9.0	cooling	Jung and Mezger (2001)	Jung and Mezger (2001)
Garob mine, shist	<sup>40</sup> Ar/ <sup>39</sup> Ar, hornblende	505.0	2.0	cooling	Gray et al. (2006)	Gray et al. (2006)
Okapuka, mica shist	<sup>40</sup> Ar/ <sup>39</sup> Ar, muscovite	496.0	3.0	cooling	Gray et al. (2006)	Gray et al. (2006)
garnet-biotite schist	<sup>40</sup> Ar/ <sup>39</sup> Ar, muscovite	495.0	3.0	cooling	Gray et al. (2006)	Gray et al. (2006)
biotite schist	<sup>40</sup> Ar/ <sup>39</sup> Ar, muscovite	495.0	3.0	cooling	Gray et al. (2006)	Gray et al. (2006)
Khomas Hochland, mica shist	<sup>40</sup> Ar/ <sup>39</sup> Ar, muscovite	486.0	3.0	cooling	Gray et al. (2006)	Gray et al. (2006)
Kuiseb River, shist	<sup>40</sup> Ar/ <sup>39</sup> Ar, muscovite	477.0	3.0	cooling	Gray et al. (2006)	Gray et al. (2006)
Garob mine, shist	<sup>40</sup> Ar/ <sup>39</sup> Ar, biotite	494.0	5.0	cooling	Gray et al. (2006)	Gray et al. (2006)
Heinitzburg, shist	<sup>40</sup> Ar/ <sup>39</sup> Ar, biotite	488.0	3.0	cooling	Gray et al. (2006)	Gray et al. (2006)
Khomas Hochland, mica shist	<sup>40</sup> Ar/ <sup>39</sup> Ar, biotite	482.0	4.0	cooling	Gray et al. (2006)	Gray et al. (2006)
n/a	apatite fission-track	190-150	n/a	cooling	Brown et al. (2014)	Brown et al. (2014)
n/a	apatite fission-track	120-60	n/a	cooling	Raab et al. (2002)	Raab et al. (2002)
Damara granite	apatite fission-track	104.7	8.5	cooling	this study	-
Damara granite	apatite fission-track	73.5	3.8	cooling	this study	-
Damara granite	apatite fission-track	66.1	3.7	cooling	this study	-

Figures S1 – S7:

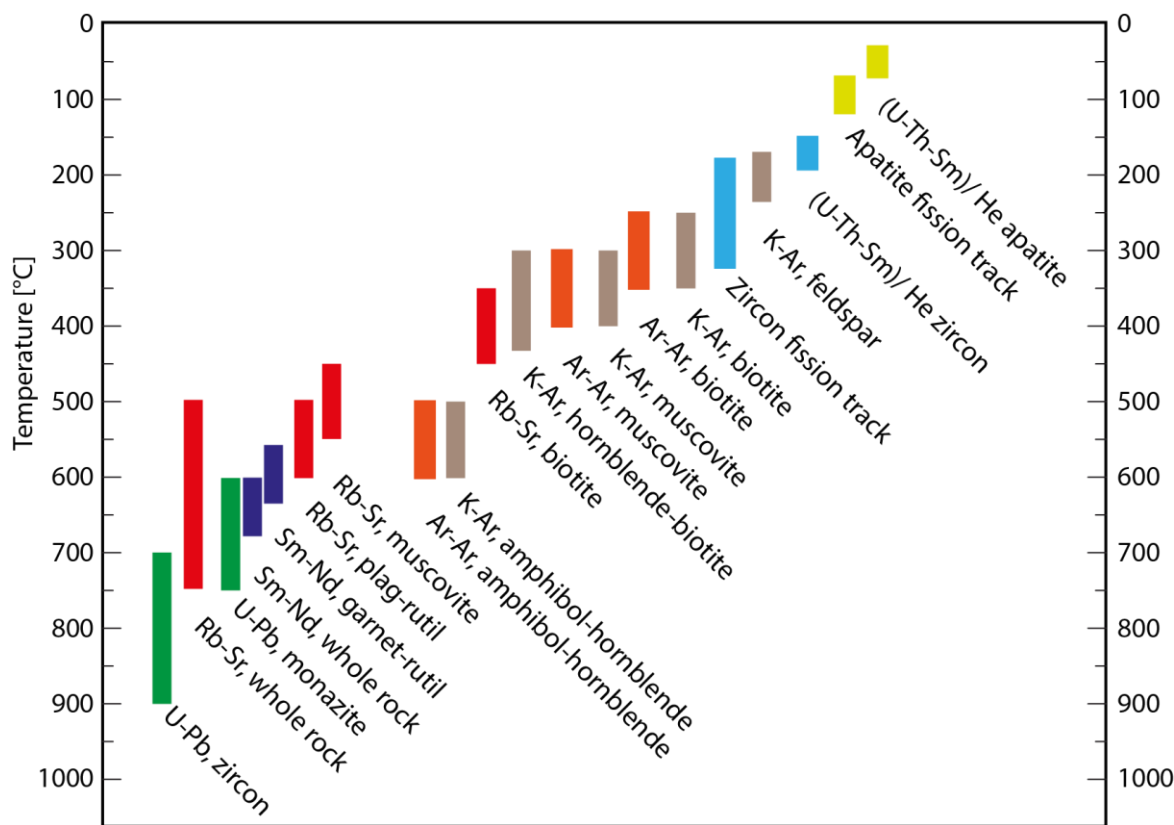
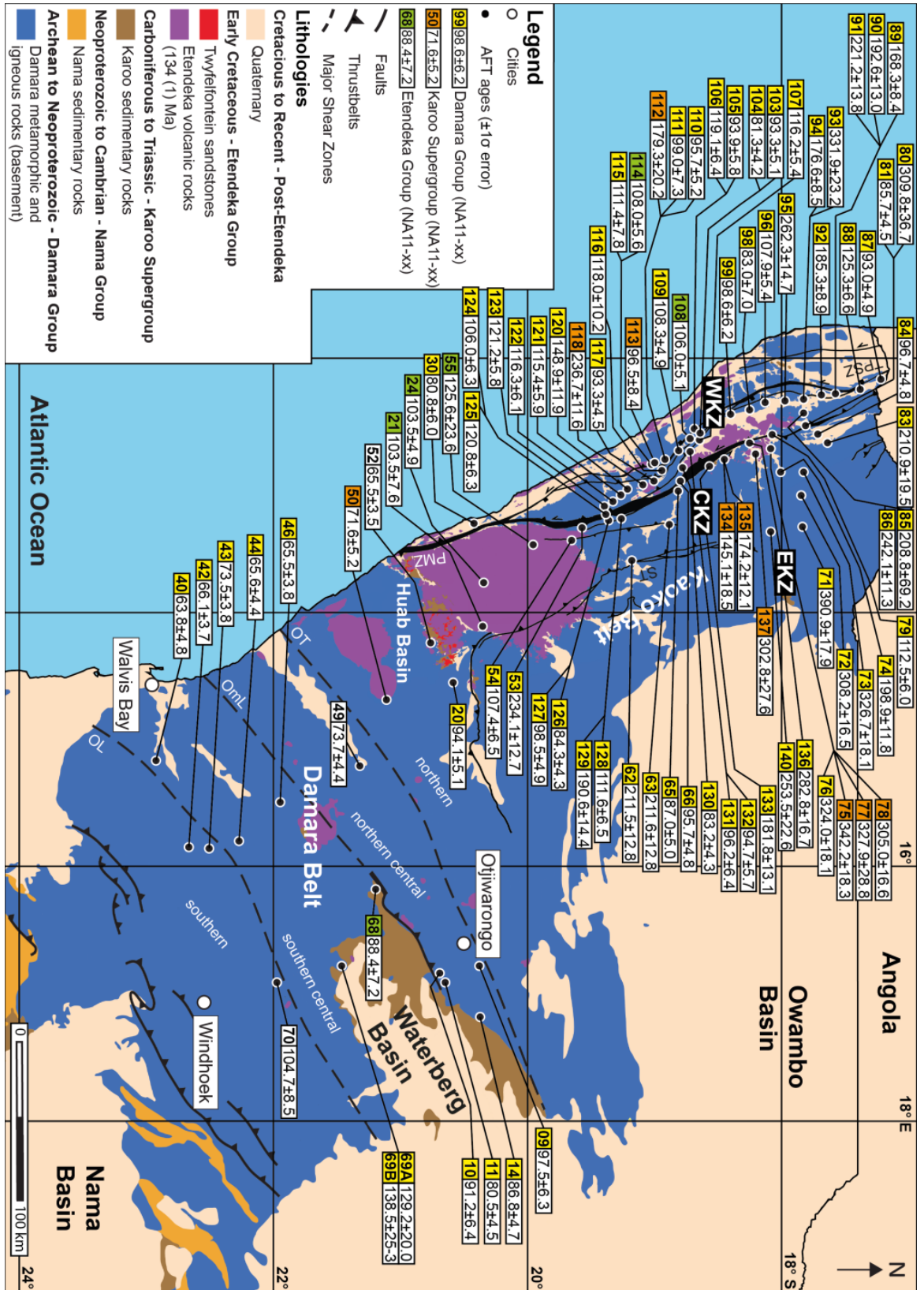


Figure B. 1: Geo- and Thermochronometers that are in current use, and their effective closure temperatures (T<sub>c</sub>) used in this study to reconstruct the t-T-evolution from >800°C to near surface temperatures (modified after Pollard et al., 2002 adapted from P.Fitzgerald, S. Baldwin, G. Gehrels, P.Reiners and M. Ducea).

Figure B. 2: (Next page) Apatite fission-track (AFT) real age distribution in the Kaoko and Damara belts (modified after Frimmel et al., 2011; Location of shear zones after Foster et al., 2009, Salomon, 2015). Boxes show sample number (NA11- xx), Central AFT age ± 1σ-error. WKZ: Western Kaoko Zone; CKZ: Central Kaoko Zone; EKZ: Eastern Kaoko Zone; ST: Sesfontein thrust; PMZ: Purros mylonite zone; TPSZ: Tree palms shear zones; OT: Otjohorong thrust; OML: Omaruru lineament; OL: Okahandja lineament. For further information Tables B. 1 and B. 2.



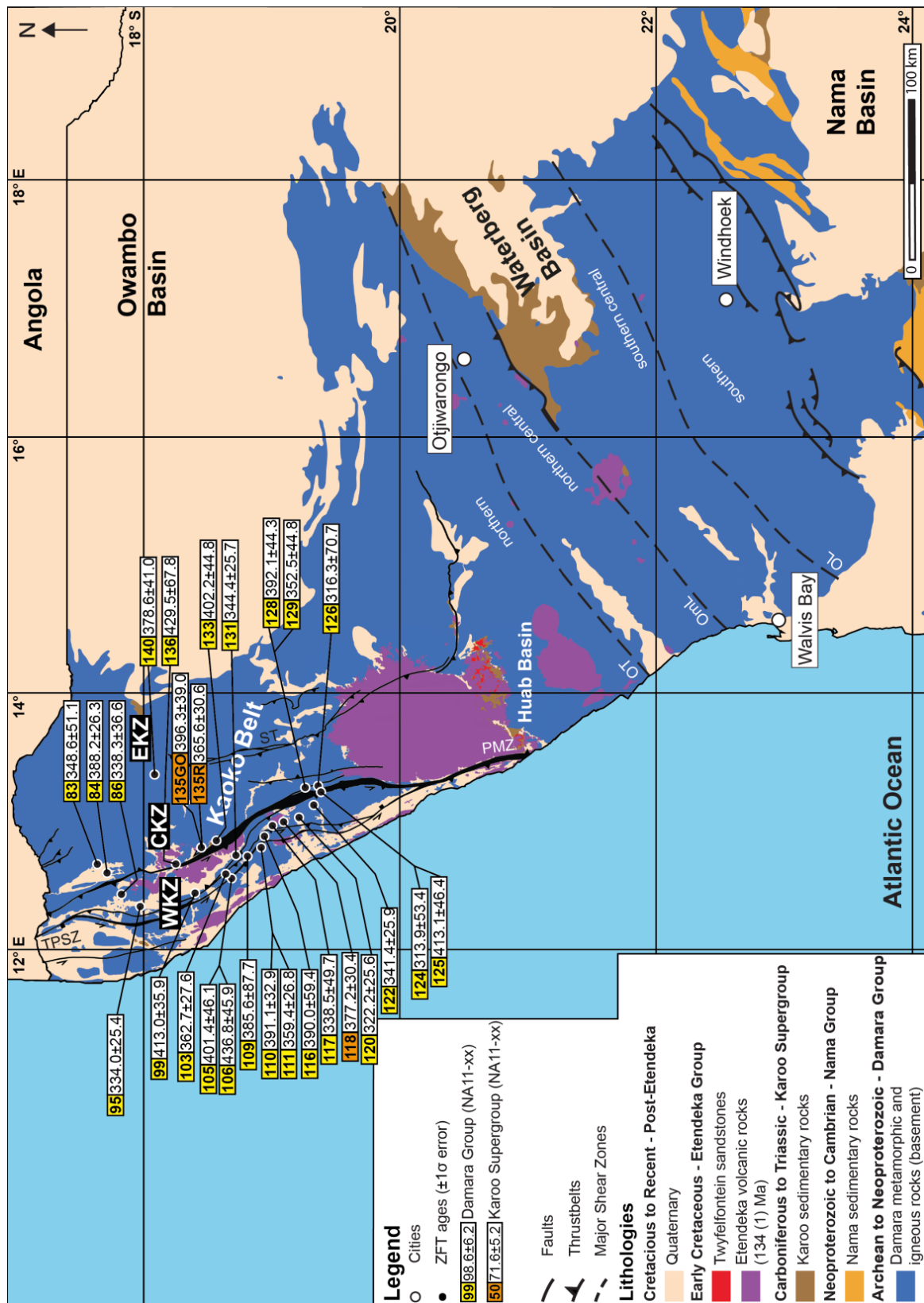
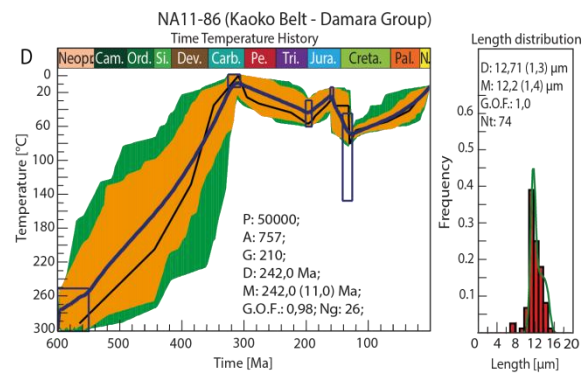
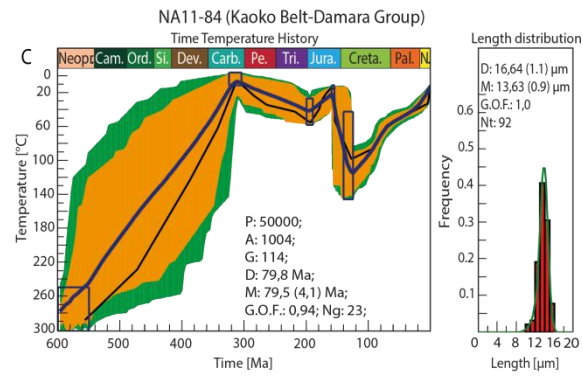
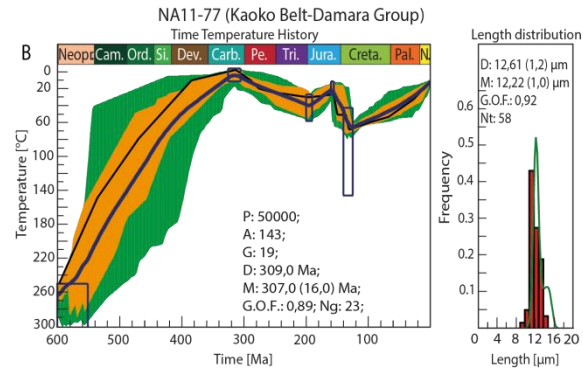
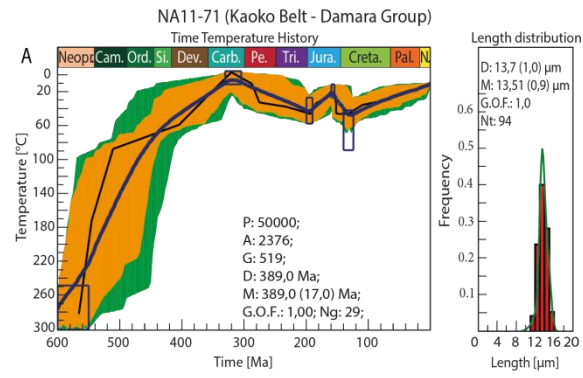


Figure B. 3: (Previous page) Simplified geological map of the study area in NW Namibia showing the regional zircon fission-track (ZFT) real age distribution in the Kaoko Belt (modified after Frimmel et al., 2011; Location of shear zones after Foster et al., 2009, Salomon, 2015). Boxes show sample number (NA11- xx), Central ZFT age  $\pm 1\sigma$ -error. For further information see Tables B. 1 and B. 4.

Figure B. 4. 1: (Next page) A) NA11-71, B) NA11-77, C) NA11-84, D) NA11-86. Time (t)-Temperature (T)-evolution paths with corresponding corrected confined spontaneous fission-track length-distribution ( $L_c$ ) using the numerical software code HeFty® (Richard A. Ketcham). For every sample a standard amount of 50 000 paths were modeled. A: Accepted paths (green); G: Good paths (yellow); D: Dated age (with error); M: Modeled age; G.O.F.: Goodness of fit; Ng: Number of grains counted; Nt: Number of confined spontaneous fission-track lengths measured. The thin black path shows the “best-fit-path”, the thick blue path the “weighted-mean-path”.



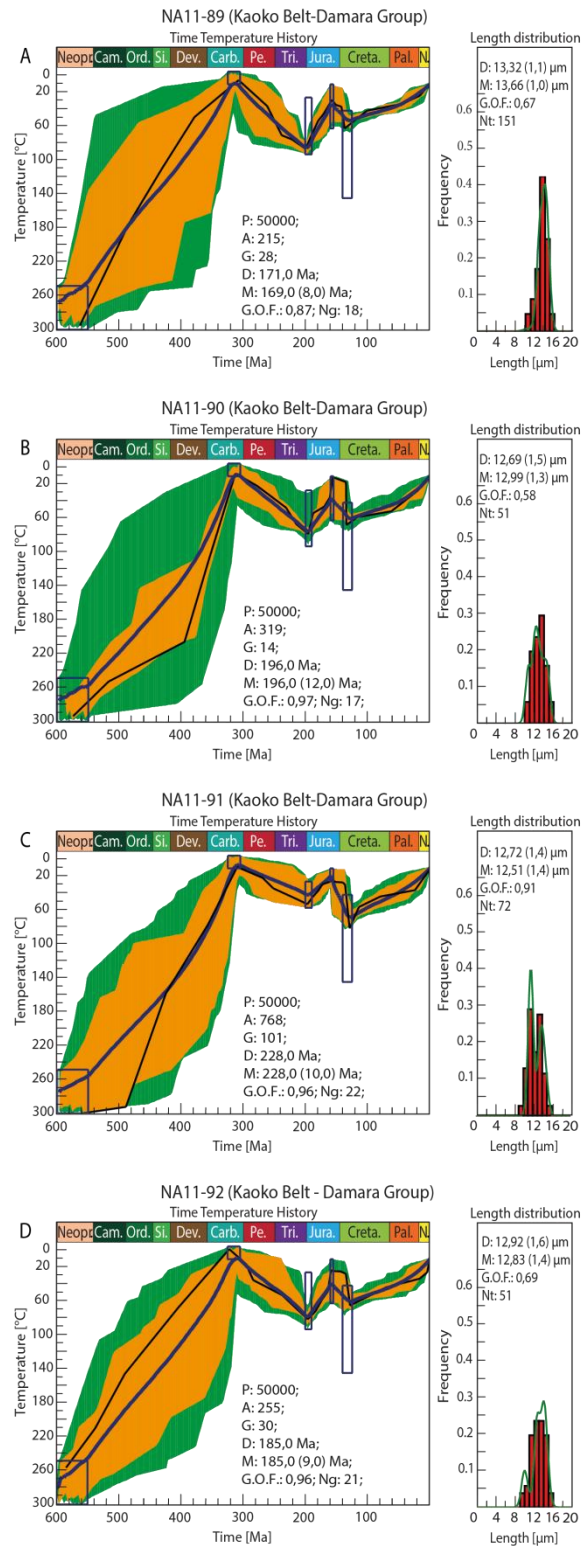


Figure B. 4. 1: Namibia, Kaoko Belt: A) NA11-89, B) NA11-90, C) NA11-91, D) NA11-92. For further information, please see Figure B. 4. 1.

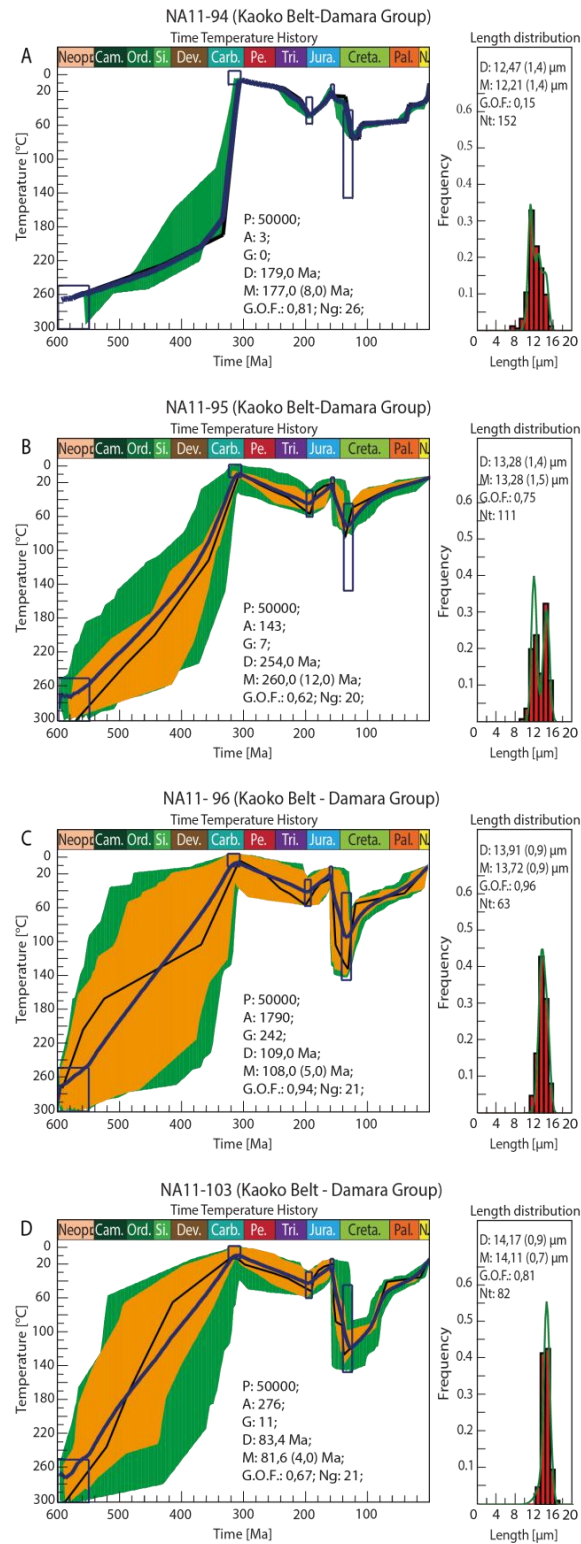


Figure B. 4. 2: Namibia, Kaoko Belt: A) NA11-94, B) NA11-95, C) NA11-96, D) NA11-103. For further information, please see Figure B. 4. 1.



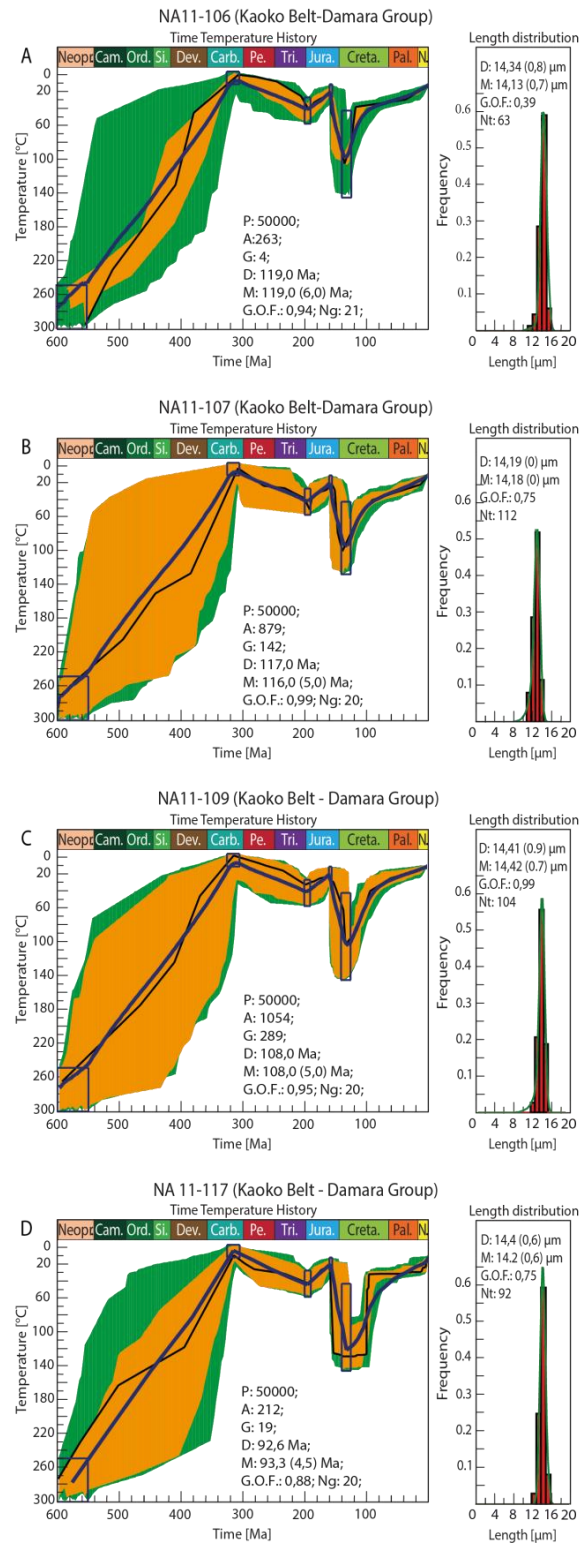


Figure B. 4. 3: Namibia, Kaoko Belt: A) NA11-106, B) NA11-107, C) NA11-109, D) NA11-117. For further information, please see Figure B. 4. 1.

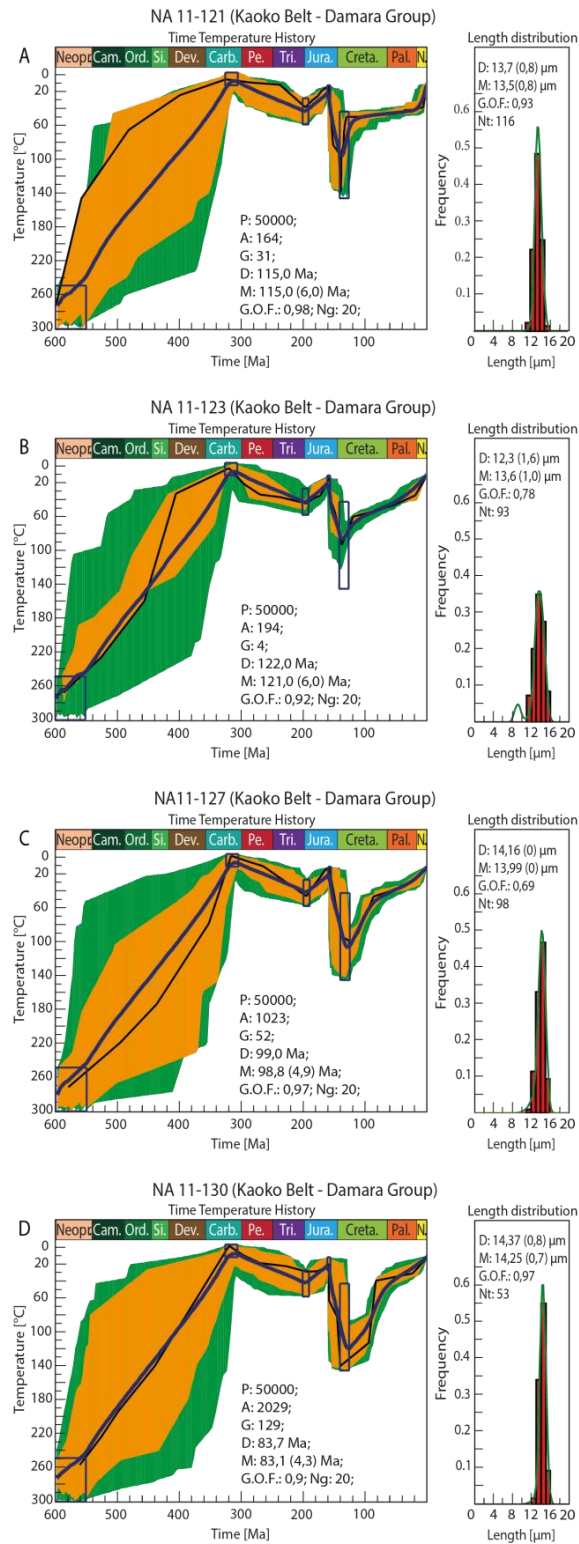


Figure B. 4. 4: Namibia, Kaoko Belt: A) NA11-121, B) NA11-123, C) NA11-127, D) NA11-130. For further information, please see Figure B. 4. 1.

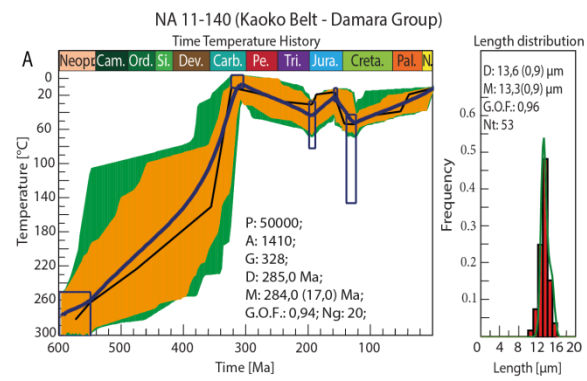


Figure B. 4. 5: Namibia, Kaoko Belt: A) NA11-140. For further information, please see Figure B. 4. 1.

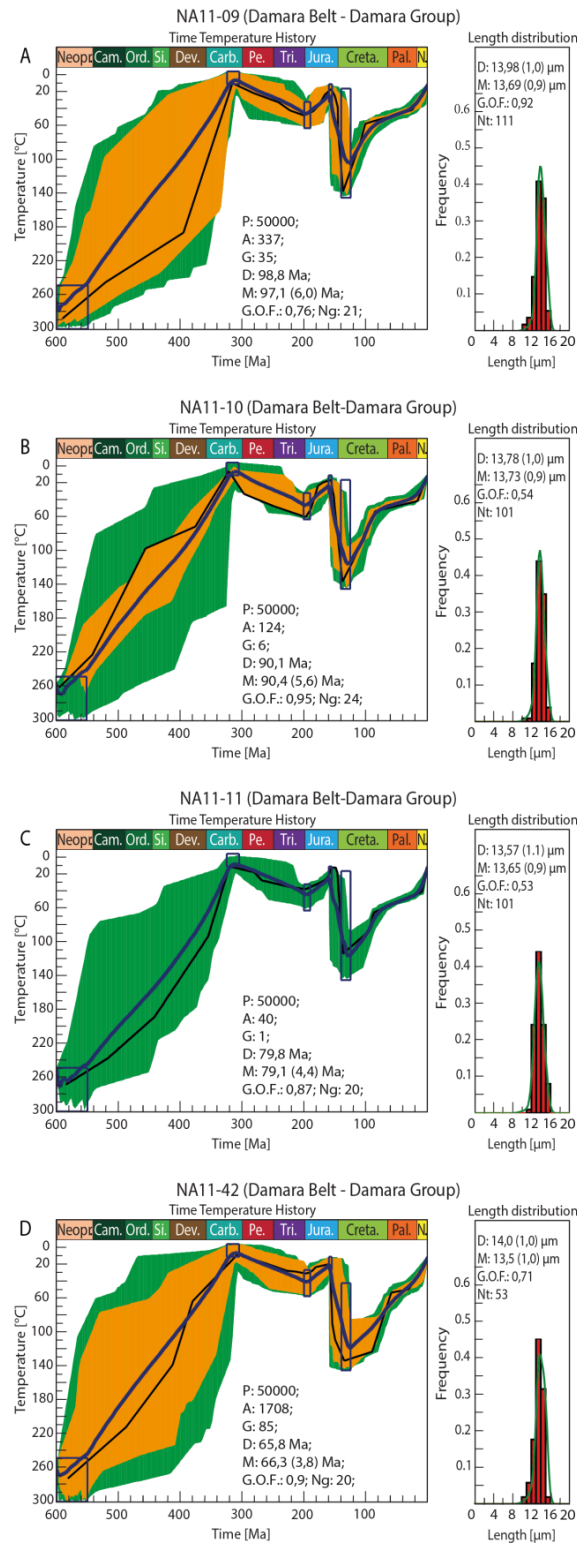


Figure B. 4. 6: Namibia, Damara Belt: A) NA11-09, B) NA11-10, C) NA11-11, D) NA11-42. For further information, please see Figure B. 4. 1.

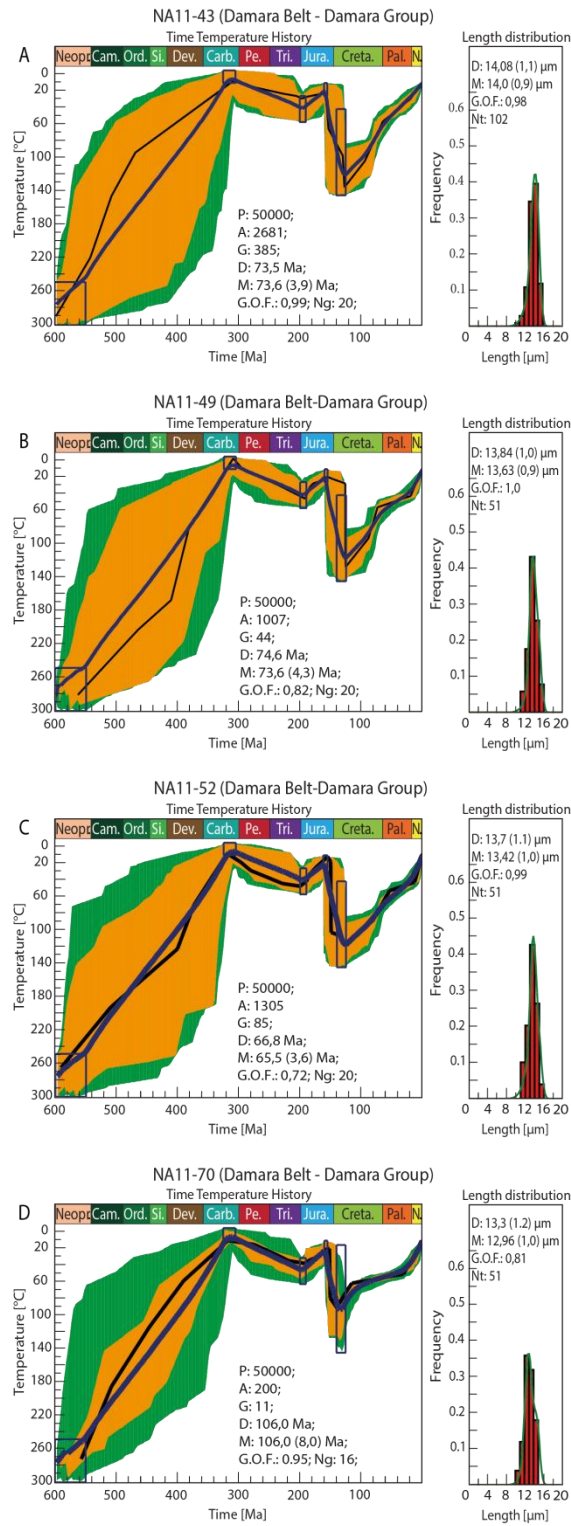


Figure B. 4. 7: Namibia, Damara Belt: A) NA11-43, B) NA11-49, C) NA11-52, D) NA11-70. For further information, please see Figure B. 4. 1.

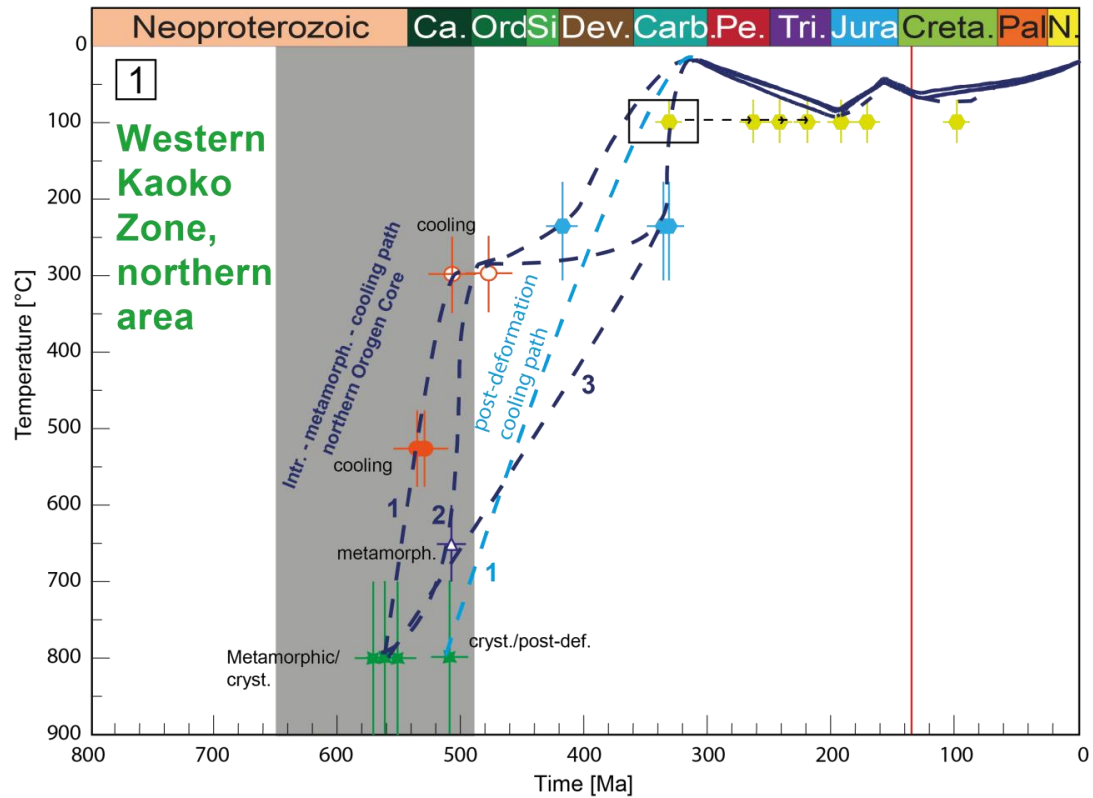
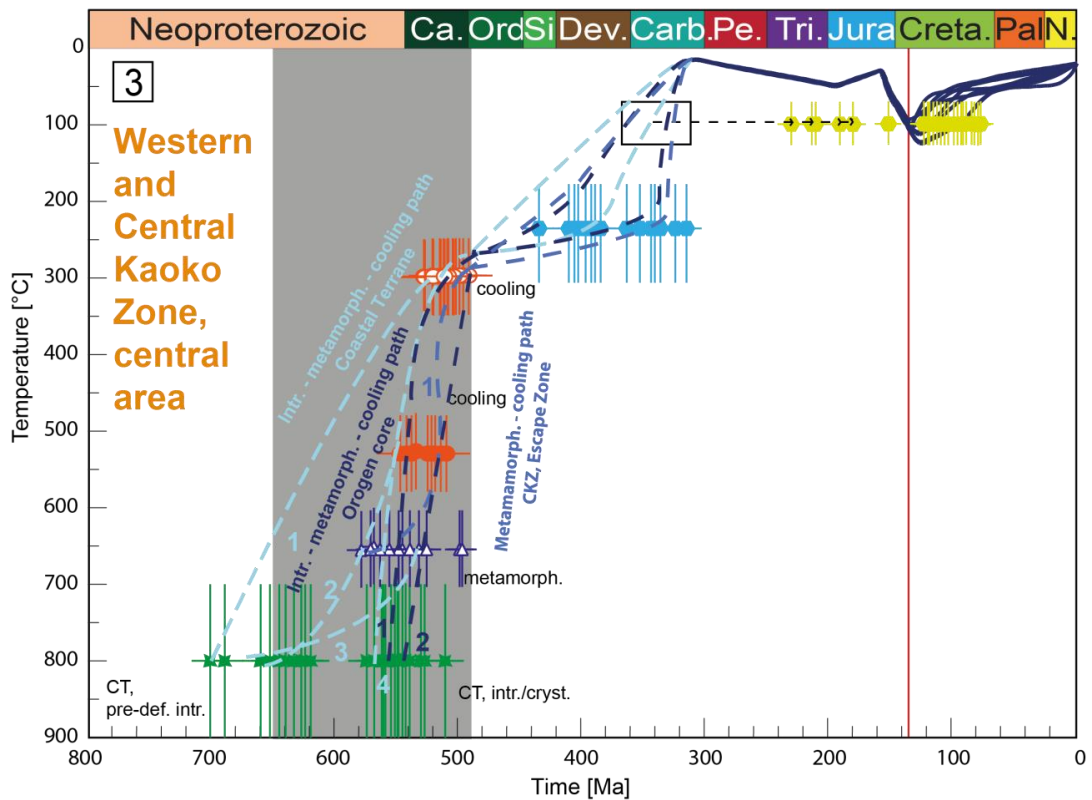
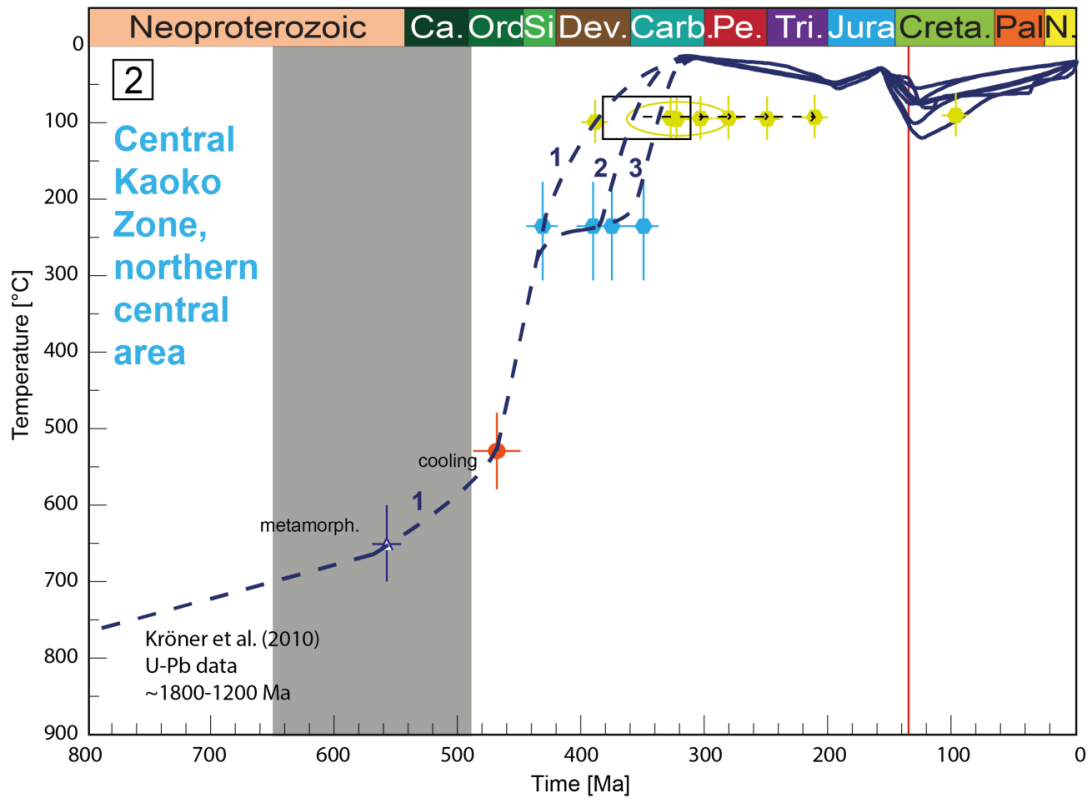


Figure B. 5. 1: Coherent long-term t-T-evolution of the Western Kaoko Zone (WKZ), northern area.. Published geochronological data were directly incorporated into the “weighted-mean” t-T-paths (Fig. 10) of the samples modeled with the software code HeFty<sup>®</sup> (Ketcham et al., 2007) to reconstruct the entire syn-to post- Late Neoproterozoic t-T-evolution of the SAPCM in NW Namibia. Dashed blue lines show possible t-T-paths for the published geochronological data. Grey bar: Pan African/Brasiliano orogeny (e.g., Goscombe and Gray, 2008; Foster et al., 2009; Frimmel et al., 2011; Nascimento et al. 2016); red line: Paraná-Etendeka event Trumbull et al., 2004, 2007; Baksi, 2017). For further information of the geochronological data see Table B. 5. 1.

Figure B. 5. 1: (Next page, upper Figure) Coherent long-term t-T-evolution of the Central Kaoko Zone, northern central area. For further information, see capture of Figure B. 5. 1 and Table B. 5. 2

Figure B. 5. 2: (Next page, lower Figure) Coherent long-term t-T-evolution of the Western and Central Kaoko Zone, central area. For further information, see capture of Figure B. 5. 1 and Table B. 5. 3.



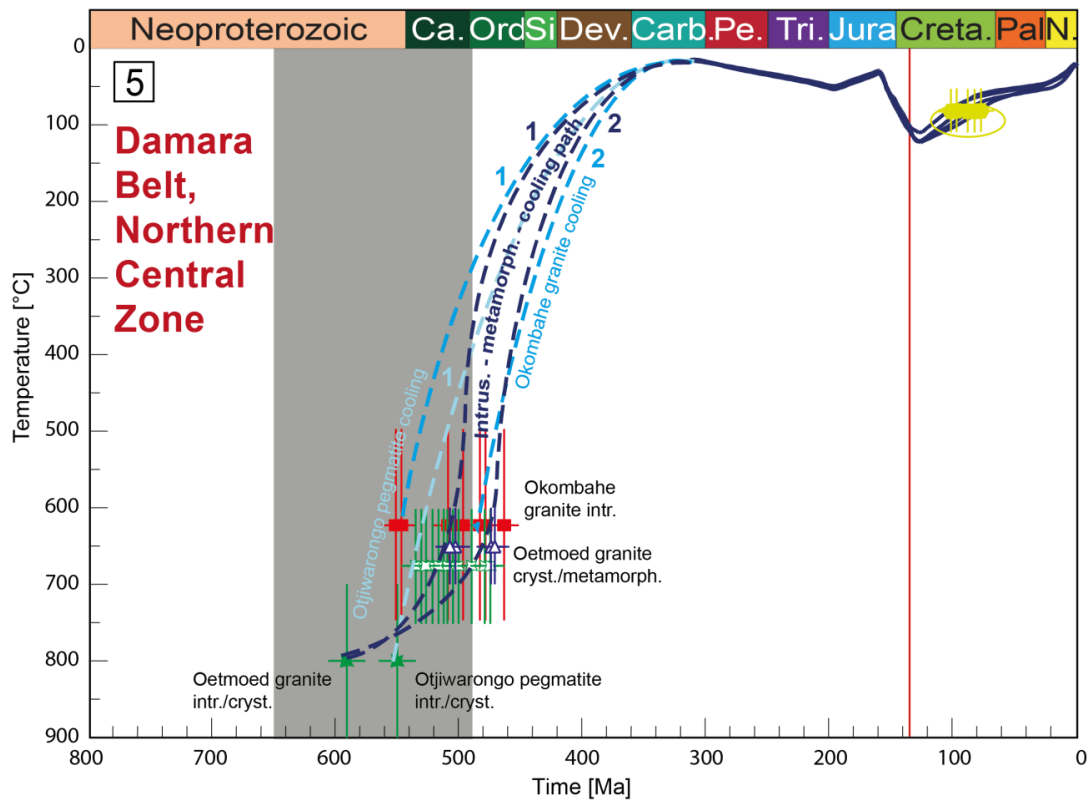
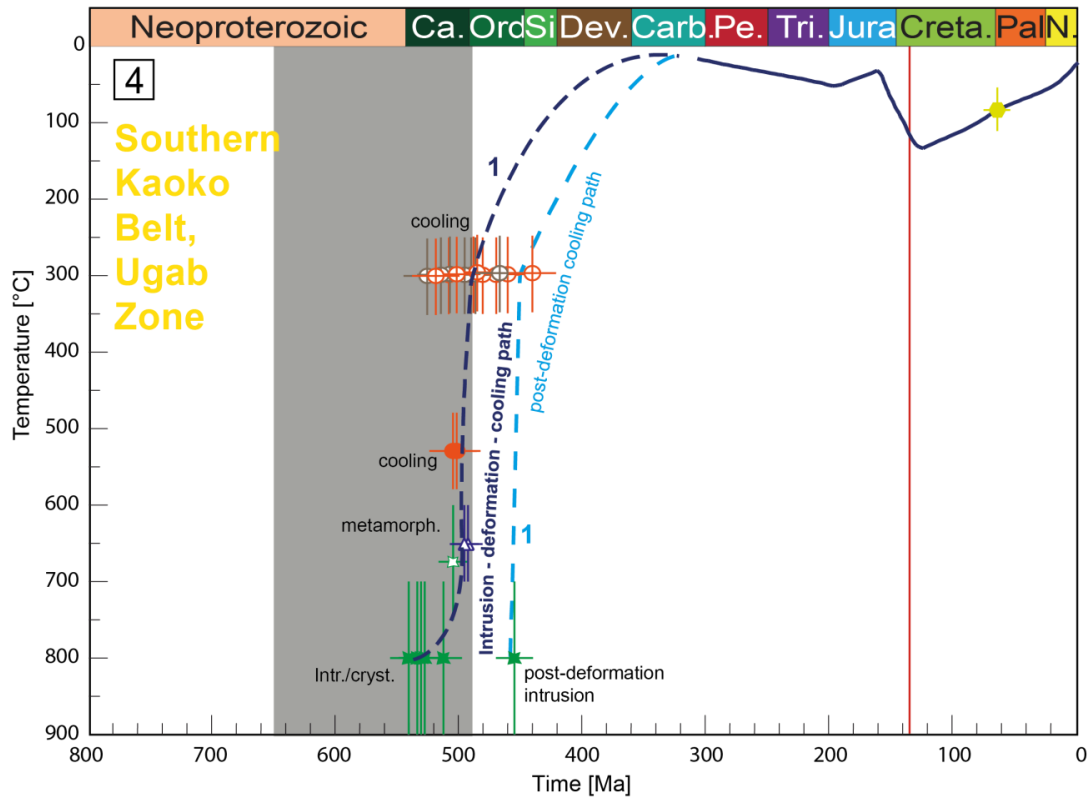




Figure B. 5. 3: (Previous page, upper Figure) Coherent long-term t-T-evolution of the Southern Kaoko Belt, Ugab Zone. For further information, see capture of Figure B. 5. 1 and Table B. 5. 4.

Figure B. 5. 4: (Previous page, lower Figure) Coherent long-term t-T-evolution of the Damara Belt, Northern Central Zone. For further information, see capture of Figure B. 5. 1 and Table B. 5. 5.

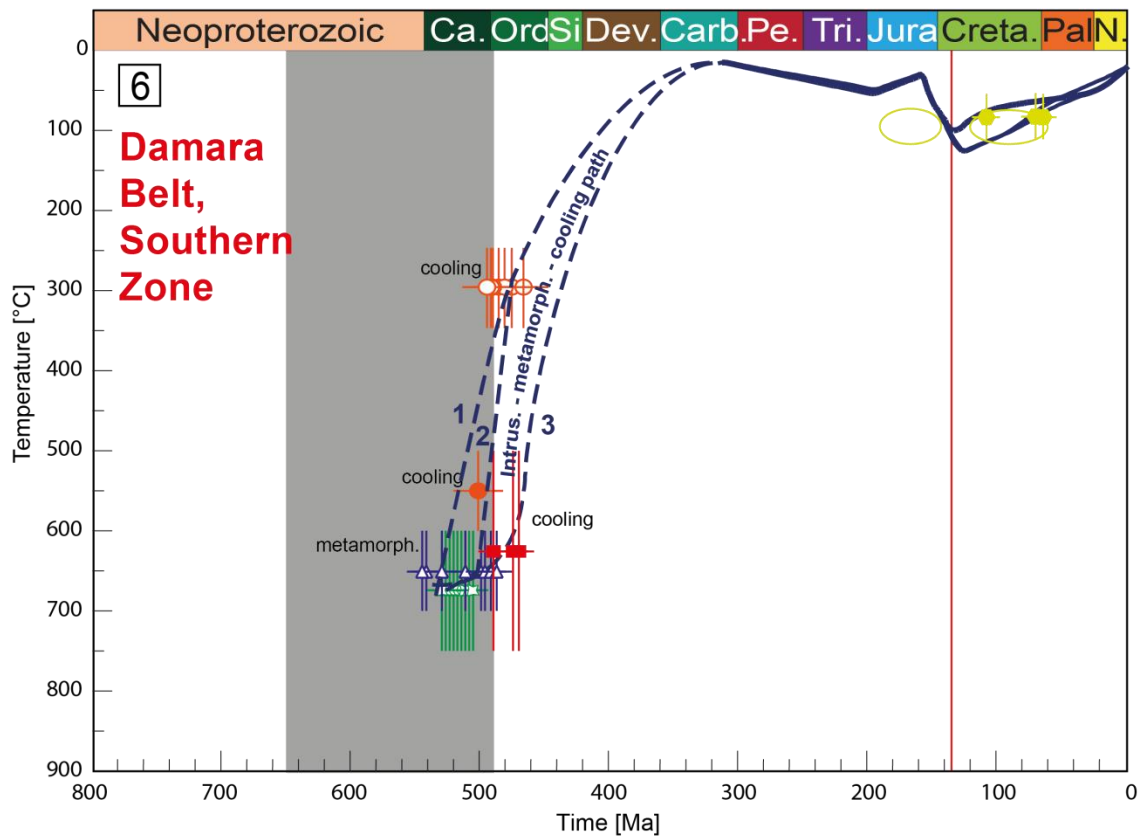


Figure B. 5. 5: Coherent long-term t-T-evolution of the Damara Belt, Southern Zone. For further information, see capture of Figure B. 5. 1 and Table B. 5. 6.

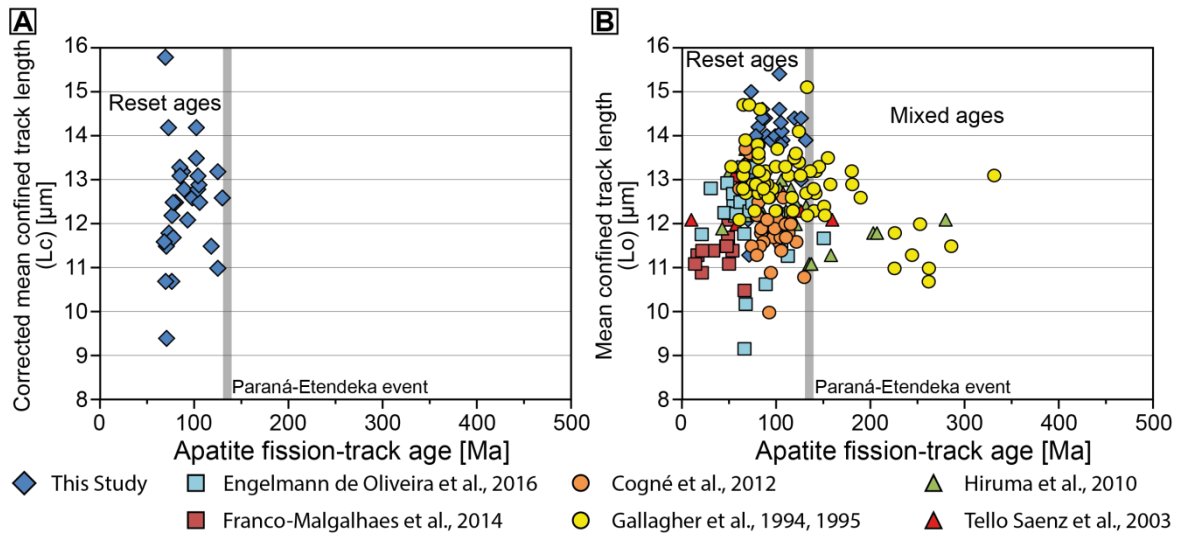


Figure B. 6: Boomerang plots showing the apatite fission-track (AFT) data set (A) of the SE Brazilian data (Krob et al., 2019) plotted against their corrected mean confined track lengths ( $L_c$ ), and (B) the integration of the AFT data to results of previous AFT data from SE Brazil by Tello Saenz et al., 2003; Gallagher et al., 1994, 1995, Franco Magalhaes et al., 2014; Hiruma et al., 2010; Cogné et al., 2012; Engelmann de Oliveira et al., 2016. For the integration the AFT ages were plotted against their (uncorrected) mean confined track lengths ( $L_o$ ). While old ages with long track lengths most likely reflect “source” ages that have not reached high post-depositional annealing temperatures, young ages having long track lengths reflect totally reset cooling ages. Samples showing both intermediate AFT ages and mean confined track lengths possibly represent “mixed” ages having a mixture of pre and post cooling track lengths accumulation (Green, 1986, Lewis et al., 1992; Gallagher et al., 1997, 1998).

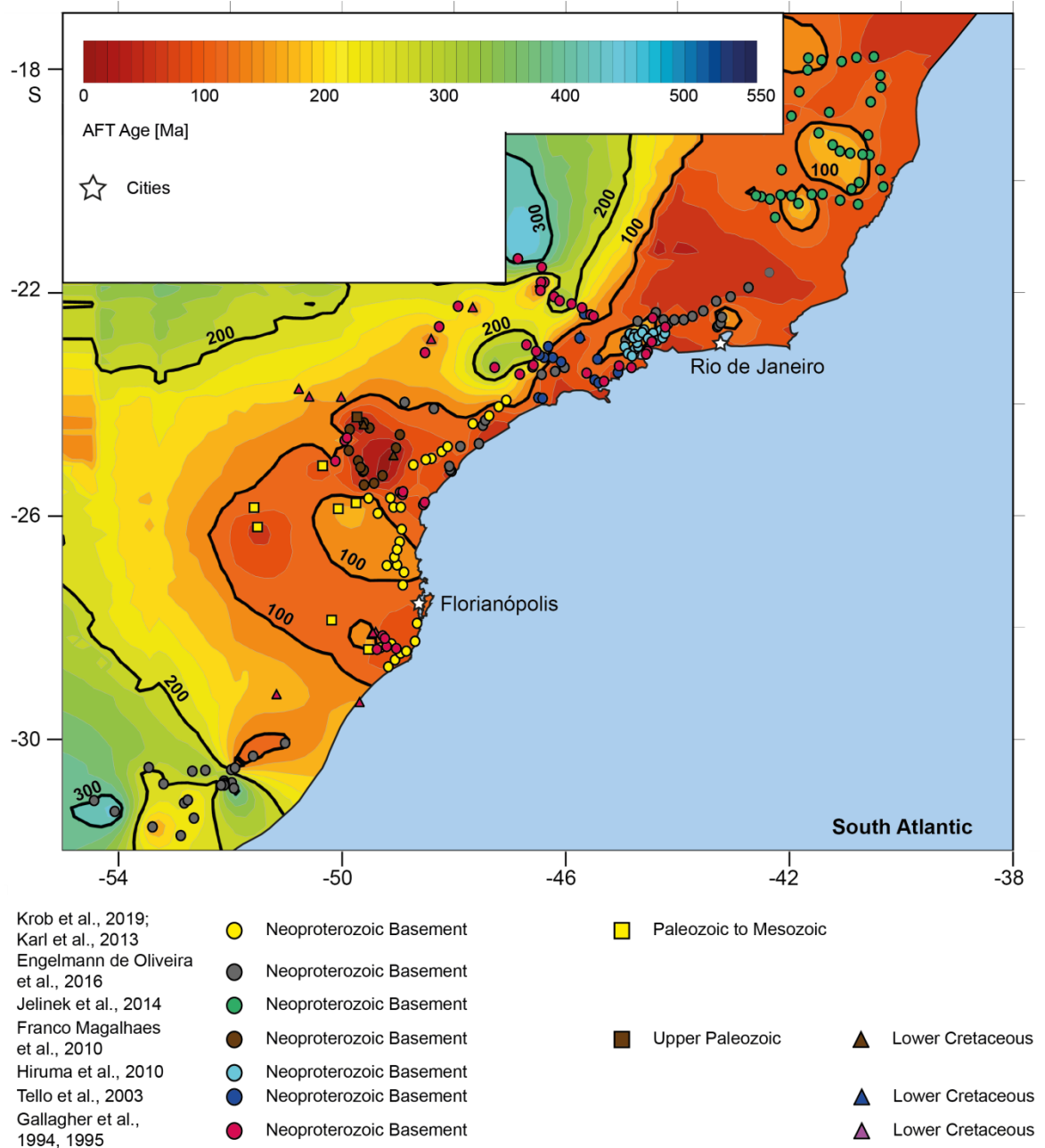


Figure B. 7: Detailed interpolation map showing a possible modeled projection of the AFT age distribution of the major apatite fission-track (AFT) data sets from eastern to south-eastern Brazil using the Golden Software Surfer®. Whereas yellow to red colors indicate younger ages, green to blue colors imply older ages. Isolines show age in [Ma] without error. Colored dots (Neoproterozoic basement rocks), squares (Upper Paleozoic sedimentary rocks) and triangles (Lower Cretaceous sedimentary and volcanic rocks) show sample locations according to the references.



## C: SUPPLEMENTARY MATERIAL FOR CHAPTER 4

## Supplementary Materials for

### Application of stratigraphic frameworks and thermochronological data on the Mesozoic SW Gondwana intraplate environment to retrieve the Paraná-Etendeka plume movement

Florian C. Krob, Ulrich A. Glasmacher, Hans-Peter Bunge, Anke M. Friedrich, Peter C. Hackspacher.

**Corresponding author:** Florian Krob, Institute of Earth Sciences, Heidelberg University, Im Neuenheimer Feld 234, 69120 Heidelberg, Germany, E-mail: [florian.krob@geow.uni-heidelberg.de](mailto:florian.krob@geow.uni-heidelberg.de), Telephone: +49-6221-4836.

#### Contents:

- Tables S1 to S3
- Figures S1 to S7
- Additional references

## Tables S1 – S3:

Table C. 1: Overview of all SAPCM related low temperature thermochronology (LTT) data sets in SW Africa from NW Angola to South Africa and Zimbabwe, and in South America from NE Brazil to NE Argentina. Region, group (circled areas on Figure 6), age spread [Ma] of specific LTT dating technique: ZFT: zircon fission-track, ZHe: zircon (U-Th-(Sm))/He, AFT: apatite fission-track, AHe: apatite (U-Th-(Sm))/He, and reference.

Region	Gr.	Age [Ma] spread of LTT dating technique				Reference
		ZFT	ZHe	AFT	AHe	
<b>African SAPCM</b>						
Angola	A			≈60 – 250		Jackson & Hudec, 2005
Angola	A			≈120 – 275	≈50 – 180	Silva et al., 2019
Angola	A			≈110 – 300		Green & Machado, 2015
Namibia	B	≈310 – 430		≈60 – 400		Krob et al., 2020
Namibia	B			≈45 – 300		Luft et al., 2005
Namibia	C			≈60 – 550		Brown et al., 2014
Namibia	C			≈60 – 550		Raab et al., 2002, 2005
Namibia	C			≈65 – 350		Haack, 1983
South Africa	D			≈70 – 275		Brown et al., 1990
South Africa	E	≈365 – 440	≈235 – 340	≈65 – 180	≈60 – 120	Kounov et al., 2008, 2009, 2012
South Africa	F			≈90 – 160		Tinker et al., 2008
South Africa	G			≈75 – 225		Green et al., 2017
South Africa	H	≈160 – 440		≈60 – 165	≈70 – 160	Wildmann et al., 2015, 2016
South Africa	H				≈70 – 145	Stanley et al., 2013
<b>SE Africa</b>						
Zimbabwe	I	≈100 – 550		≈300 – 470	≈95 – 475	Mackintosh et al., 2017
Zimbabwe	I			≈70 – 270		Noble et al., 1997
<b>South American SAPCM</b>						
NE Brazil	K			≈40 – 350		Jelinek et al., 2014
NE Brazil	K			≈75 – 390		Japsen et al., 2012
NE Brazil	K			≈50 – 180		Morais Neto et al., 2008, 2009
NE Brazil	K			≈80 – 330		Turner et al., 2008
NE Brazil	K			≈75 – 310		Harman et al., 1998
NE Brazil	K			≈210 – 265		Amaral et al., 1997
CE Brazil	L			≈60 – 145		Van Ranst et al., 2019
CE Brazil	L			≈75 – 340		Engelmann de Oliveira et al., 2016
CE Brazil	L			≈40 – 280		Hiruma et al., 2010
CE Brazil	L			≈40 – 180		Carmo, 2005
SE Brazil	M			≈100 – 360		Poços de Caldas, unpublished.
SE Brazil	M			≈40 – 340		Doranti-Tiritan et al., 2014
SE Brazil	M			≈50 – 240		Souza et al., 2014
SE Brazil	M			≈30 – 80		Franco Magalhaes, et al., 2014
SE Brazil	M	≈130 – 390				Curvo et al., 2013
SE Brazil	M			≈60 – 330	≈45 – 125	Cogné et al., 2011, 2012
SE Brazil	M	≈240 – 400		≈50 – 480		Hackspacher et al., 2004, 2006, 2007

Region	Gr.	Age [Ma] spread of LTT dating technique				Reference
		ZFT	ZHe	AFT	AHe	
SE Brazil	M			≈55 – 160		Tello Saenz et al., 2003
SE Brazil	M			≈50 – 330		Gallagher et al., 1994, 1995
SE Brazil	N	≈255 – 390	≈200 – 415	≈65 – 130	≈60 – 110	Krob et al., 2019
SE Brazil	N	≈105 – 540	≈70 – 525	≈45 – 135	≈30 – 95	Karl et al., 2013
SE Brazil	N			≈6 – 60		Franco Magalhaes, et al., 2010
SE Brazil	O	≈210 – 390		≈75 – 340		Engelmann de Oliveira et al., 2016
SE Brazil	O			≈130 – 365		Bicca et al., 2013
SE Brazil	O			≈70 – 290		Borba et al., 2002, 2003
Uruguay	P		≈460 – 560		≈90 – 300	Hueck et al., 2018
Uruguay	P			≈180 – 445		Uruguay, unpublished.
Uruguay	P			≈200 – 325		Kollenz, 2015
Argentina	Q	≈230	≈160 – 500	≈130 – 250	≈120 -165	Kollenz et al., 2016

Table C. 2: All published apatite fission-track (AFT) ages of SW Africa and Zimbabwe that were used for histograms and maps of the AFT age distribution with corresponding coordinates and references sorted by circled areas in Figure 4.14 and Table C. 1. Reference/sample number, Longitude, Latitude, Age [Ma], 1 $\sigma$ -error [Ma], formation age, AFT age < formation age (reset age information).

Reference/ S. -no.	Lon.	Lat.	Age [Ma]	1 $\sigma$ -error [Ma]	Formation age	AFT age < formation age
<b>SW Africa</b>						
<b>Angola</b>						
<b>Silva et al., 2019 (Group A)</b>						
Ang-08	12.2924	-15.0593	128.6	11.5	Lower Cretaceous	Yes
Ang-17	12.3981	-14.9103	167.0	18.8	Lower Cretaceous	No
Ang-09	12.4439	-15.0106	120.5	8.9	Neoproterozoic	Yes
Ang-10	12.7379	-15.0262	141.3	10.2	Neoproterozoic	Yes
Ang-11	13.2086	-15.0387	207.2	16.1	Paleoproterozoic	Yes
Ang-12	13.2213	-15.0525	272.9	21.5	Paleoproterozoic	Yes
<b>Green &amp; Machado, 2015 (Group A)</b>						
1	12.5030	-14.1077	155.9	19.7	Lower Cretaceous	No
3	12.4994	-14.1053	231.5	18.9	Lower Cretaceous	No
4	12.4936	-14.0959	294.2	30.2	Lower Cretaceous	No
5	12.5068	-14.0130	242.1	20.0	Lower Cretaceous	No
7	12.3947	-14.6063	147.9	18.3	Lower Cretaceous	No
10	12.6571	-14.8851	140.2	14.4	Lower Cretaceous	Yes
11	12.2738	-15.2146	137.1	18.8	Lower Cretaceous	Yes
2	12.5030	-14.1077	155.8	11.8	Neoproterozoic	Yes
8	12.4810	-14.6350	251.6	33.7	Neoproterozoic	Yes
9	12.3086	-15.1601	113.6	22.3	Neoproterozoic	Yes
12	12.3693	-14.9856	180.2	61.7	Neoproterozoic	Yes
13	12.4443	-15.0198	206.8	9.4	Neoproterozoic	Yes
14	12.7980	-15.0312	242.9	21.8	Neoproterozoic	Yes
15	13.1085	-15.0552	282.9	25.9	Neoproterozoic	Yes
16	13.2269	-15.0476	247.7	23.9	Neoproterozoic	Yes

Reference/ S. -no.	Lon.	Lat.	Age [Ma]	1 $\sigma$ -error [Ma]	Formation age	AFT age < formation age
17	13.2364	-15.0526	219.9	15.1	Neoproterozoic	Yes
18	13.2331	-15.0768	260.0	36.6	Neoproterozoic	Yes
<b>Jackson &amp; Hudec, 2005 (Group A)</b>						
75	13.4400	-9.3800	116.3	11.7	Lower Cretaceous	Yes
76	13.9500	-9.4900	154.1	20.9	Lower Cretaceous	No
78	13.2900	-9.3200	249.5	27.8	Lower Cretaceous	No
173	14.2200	-10.6900	58.1	20.0	Paleoproterozoic	Yes
174	13.6900	-9.4800	138.4	8.8	Neoproterozoic	Yes
175	13.8600	-9.6100	135.6	7.7	Neoproterozoic	Yes
176	13.1700	-8.7700	116.0	12.3	Paleoproterozoic	Yes
<b>Namibia</b>						
<b>Krob et al., 2020 (Group B)</b>						
NA11-21	14.1084	-20.3340	103.5	7.6	Lower Cretaceous	yes
NA11-24	13.7447	-20.2711	103.5	4.9	Lower Cretaceous	yes
NA11-55	13.4924	-19.8311	125.6	23.6	Lower Cretaceous	yes
NA11-108	12.6367	-18.7081	106.0	5.1	Lower Cretaceous	yes
NA11-114	12.8252	-18.9053	108.0	5.6	Lower Cretaceous	yes
NA11-50	14.6801	-21.0871	98.2	71.6	Lower Cretaceous	yes
NA11-75	12.7373	-18.0784	342.2	18.3	Upper Paleozoic	no
NA11-77	12.7373	-18.0914	327.9	28.8	Upper Paleozoic	no
NA11-78	12.7373	-18.0897	305.0	16.6	Upper Paleozoic	no
NA11-112	12.8254	-18.9052	179.3	20.2	Upper Paleozoic	yes
NA11-113	12.8254	-18.9052	96.5	8.4	Upper Paleozoic	yes
NA11-118	12.9867	-18.9052	236.7	11.6	Upper Paleozoic	yes
NA11-134	12.7914	-18.4921	145.1	18.5	Upper Paleozoic	yes
NA11-135	12.8057	-18.4998	174.2	12.1	Upper Paleozoic	yes
NA11-137	12.7413	-18.4998	302.8	27.6	Upper Paleozoic	no
NA11-68	16.3846	-21.0671	88.4	7.2	Upper Paleozoic	yes
NA11-30	13.3020	-20.3923	82.1	6.0	Neoproterozoic	yes
NA11-53	13.3455	-19.5547	234.1	12.7	Neoproterozoic	yes
NA11-54	13.4170	-19.6354	107.2	6.5	Neoproterozoic	yes
NA11-62	13.5792	-19.1592	210.8	11.3	Neoproterozoic	yes
NA11-63	13.2938	-18.8916	211.5	12.8	Neoproterozoic	yes
NA11-65	13.0094	-18.7917	87.0	5.0	Neoproterozoic	yes
NA11-66	12.9596	-18.7892	95.7	4.8	Neoproterozoic	yes
NA11-71	13.2715	-17.8393	390.9	17.9	Neoproterozoic	yes
NA11-72	12.9924	-17.8047	308.2	16.5	Neoproterozoic	yes
NA11-73	12.8464	-17.7942	326.7	18.1	Neoproterozoic	yes
NA11-74	12.8641	-17.9959	198.9	11.8	Neoproterozoic	yes
NA11-76	12.7135	-18.0896	324.0	18.1	Neoproterozoic	yes
NA11-79	12.6920	-18.0891	112.5	6.0	Neoproterozoic	yes
NA11-80	12.5264	-17.7932	309.8	36.7	Neoproterozoic	yes
NA11-81	12.5327	-17.7888	85.7	4.5	Neoproterozoic	yes
NA11-83	12.6664	-17.6665	210.9	19.5	Neoproterozoic	yes
NA11-84	12.5951	-17.7046	96.7	4.8	Neoproterozoic	yes
NA11-85	12.4703	-17.8041	208.8	69.2	Neoproterozoic	yes
NA11-86	12.4284	-17.8131	242.1	11.3	Neoproterozoic	yes
NA11-87	12.1523	-17.2098	93.0	4.9	Neoproterozoic	yes



Reference/ S. -no.	Lon.	Lat.	Age [Ma]	1 $\sigma$ -error [Ma]	Formation age	AFT age < formation age
NA11-88	12.2458	-17.3849	125.3	6.6	Neoproterozoic	yes
NA11-89	12.2771	-17.5682	168.3	8.4	Neoproterozoic	yes
NA11-90	12.2771	-17.5682	192.6	13.0	Neoproterozoic	yes
NA11-93	12.3267	-17.8083	331.9	23.2	Neoproterozoic	yes
NA11-91	12.2771	-17.5682	221.2	13.8	Neoproterozoic	yes
NA11-92	12.2882	-17.6722	185.3	8.9	Neoproterozoic	yes
NA11-94	12.3267	-17.8083	176.6	8.5	Neoproterozoic	yes
NA11-95	12.3434	-17.9510	262.3	14.7	Neoproterozoic	yes
NA11-96	12.3570	-18.1202	107.9	5.4	Neoproterozoic	yes
NA11-98	12.4096	-18.2424	83.0	7.0	Neoproterozoic	yes
NA11-99	12.4377	-18.3813	98.6	6.2	Neoproterozoic	yes
NA11-103	12.6550	-18.6567	81.3	4.2	Neoproterozoic	yes
NA11-104	12.6393	-18.6654	93.3	5.1	Neoproterozoic	yes
NA11-105	12.6069	-18.7184	93.9	5.8	Neoproterozoic	yes
NA11-106	12.5931	-18.7506	119.1	6.4	Neoproterozoic	yes
NA11-107	12.6373	-18.7109	116.2	5.4	Neoproterozoic	yes
NA11-109	12.7027	-18.8086	108.3	4.9	Neoproterozoic	yes
NA11-110	12.7948	-18.8742	95.7	5.2	Neoproterozoic	yes
NA11-111	12.8175	-18.9041	99.0	7.3	Neoproterozoic	yes
NA11-115	12.8388	-18.9241	111.4	7.8	Neoproterozoic	yes
NA11-116	12.8842	-18.9607	118.0	10.2	Neoproterozoic	yes
NA11-117	12.9423	-19.0120	93.3	4.5	Neoproterozoic	yes
NA11-120	13.0883	-19.1953	148.9	11.9	Neoproterozoic	yes
NA11-121	13.1153	-19.2741	115.4	5.9	Neoproterozoic	yes
NA11-122	13.1427	-19.3111	116.3	6.1	Neoproterozoic	yes
NA11-123	13.1638	-19.3470	121.2	5.8	Neoproterozoic	yes
NA11-124	13.2405	-19.3225	106.0	6.3	Neoproterozoic	yes
NA11-125	13.2677	-19.3076	120.8	6.3	Neoproterozoic	yes
NA11-126	13.3000	-19.2944	84.3	4.3	Neoproterozoic	yes
NA11-127	13.3149	-19.2849	98.5	4.9	Neoproterozoic	yes
NA11-128	13.3350	-19.2489	111.6	6.5	Neoproterozoic	yes
NA11-129	13.3670	-19.2398	190.6	14.4	Neoproterozoic	yes
NA11-130	12.8550	-18.7791	83.2	4.3	Neoproterozoic	yes
NA11-131	12.7356	-18.7318	96.2	6.4	Neoproterozoic	yes
NA11-132	12.6937	-18.7443	94.7	5.7	Neoproterozoic	yes
NA11-133	12.7931	-18.4899	181.8	13.1	Neoproterozoic	yes
NA11-136	12.6598	-18.2361	253.5	22.6	Neoproterozoic	yes
NA11-140	13.3519	-18.2653	282.8	16.7	Neoproterozoic	yes
NA11-09	16.7075	-20.3992	97.5	6.3	Neoproterozoic	yes
NA11-10	16.8467	-20.6940	91.2	6.4	Neoproterozoic	yes
NA11-11	16.9173	-20.6480	80.5	4.5	Neoproterozoic	yes
NA11-14	17.2431	-20.5039	86.8	4.7	Neoproterozoic	yes
NA11-20	14.5317	-20.5644	94.1	5.1	Neoproterozoic	yes
NA11-40	15.3844	-22.8438	63.8	4.8	Neoproterozoic	yes
NA11-42	15.8528	-22.6936	66.1	3.7	Neoproterozoic	yes
NA11-43	15.8578	-22.5180	73.5	3.8	Neoproterozoic	yes
NA11-44	15.6067	-22.1771	65.6	4.4	Neoproterozoic	yes
NA11-46	15.4230	-21.9827	65.5	3.8	Neoproterozoic	yes
NA11-49	15.2251	-21.2774	73.7	4.4	Neoproterozoic	yes
NA11-52	14.2186	-20.7546	65.5	3.5	Neoproterozoic	yes
NA11-69A	16.8582	-21.5298	129.2	20.0	Neoproterozoic	yes

Reference/ S. -no.	Lon.	Lat.	Age [Ma]	1 $\sigma$ -error [Ma]	Formation age	AFT age < formation age
NA11-69B	16.8582	-21.5298	138.5	25.3	Neoproterozoic	yes
NA11-70	16.9304	-22.0042	104.7	8.5	Neoproterozoic	yes
<b>Luft et al., 2005 (Group B)</b>						
PKB-01	12.8500	-18.7800	79.7	6.1	Proterozoic	yes
PKB-03B	13.0100	-18.7900	74.4	6.4	Proterozoic	yes
PKB-16	14.2800	-19.7600	296.7	26.1	Proterozoic	yes
PZ-01	13.1400	-19.3600	99.4	8.6	Proterozoic	yes
PZ-12A	13.2200	-19.3200	46.9	3.8	Proterozoic	yes
PZ-18A	13.2800	-19.2900	170.6	12.2	Proterozoic	yes
PZ-66A	13.1900	-19.3200	74.0	5.5	Proterozoic	yes
PK-01	13.4000	-19.1500	71.4	5.3	Proterozoic	yes
PK-06	13.2600	-19.2500	55.5	5.1	Proterozoic	yes
<b>Brown et al., 2014 (Group C)</b>						
8732-57	16.8330	-21.9670	164.0	8.0	Precambrian	yes
8732-58	16.5000	-21.9500	95.0	5.0	Precambrian	yes
8732-62	15.0500	-22.2830	70.0	4.0	Precambrian	yes
8732-63	14.8500	-22.5000	79.0	3.0	Precambrian	yes
8732-64	14.7500	-22.5830	78.0	3.0	Precambrian	yes
8732-65	14.5170	-22.6330	76.0	4.0	Precambrian	yes
8732-71	13.2500	-20.2500	111.0	4.0	Precambrian	yes
8732-72	13.6670	-21.1670	108.0	4.0	Precambrian	yes
8732-73	13.9670	-21.4170	92.0	4.0	Precambrian	yes
8732-74	14.0830	-21.0830	92.0	3.0	Precambrian	yes
8732-75	14.5000	-21.3330	102.0	6.0	Precambrian	yes
8732-80	16.6670	-20.5000	92.0	4.0	Precambrian	yes
8832-137	11.9500	-17.6670	74.0	3.0	Precambrian	yes
8832-138	11.9000	-17.3500	59.0	3.0	Precambrian	yes
8832-139	12.0170	-17.2170	69.0	4.0	Precambrian	yes
8832-151	17.1830	-22.5670	184.0	25.0	Precambrian	yes
8832-152	18.9500	-22.4330	277.0	52.0	Precambrian	yes
8832-153	19.7830	-22.3830	289.0	21.0	Precambrian	yes
MD-008	14.5000	-21.1800	111.0	9.0	Precambrian	yes
MD-012	14.5000	-21.1800	109.0	14.0	Precambrian	yes
MD-104	14.5000	-21.1800	83.0	5.0	Precambrian	yes
RB 2543	15.5300	-22.2000	84.0	4.0	Precambrian	yes
RM1423	17.1170	-21.9500	449.0	20.0	Precambrian	yes
93-099	16.9170	-21.9920	239.0	17.0	Precambrian	yes
93-100	16.8750	-21.7570	250.0	8.0	Precambrian	yes
93-101	16.7800	-20.6880	101.0	5.0	Precambrian	yes
93-104	16.7880	-20.6780	107.0	4.0	Precambrian	yes
93-105	16.7430	-20.5730	91.0	6.0	Precambrian	yes
93-114	13.3920	-17.9330	315.0	19.0	Precambrian	yes
93-115	13.1670	-17.8500	329.0	21.0	Precambrian	yes
93-116	13.0750	-17.8670	296.0	15.0	Precambrian	yes
93-117	12.9650	-17.7820	310.0	27.0	Precambrian	yes
93-118	12.9920	-17.8040	329.0	23.0	Precambrian	yes
93-120	14.2250	-17.3920	269.0	11.0	Precambrian	yes
93-121	14.2270	-17.4080	262.0	13.0	Precambrian	yes
93-122	14.2900	-17.4020	305.0	29.0	Precambrian	yes

Reference/ S. -no.	Lon.	Lat.	Age [Ma]	1 $\sigma$ -error [Ma]	Formation age	AFT age < formation age
93-125	15.6780	-24.6710	83.0	10.0	Precambrian	yes
<b>Raab et al., 2005 (Group C)</b>						
BB-1	14.5770	-21.1500	98.0	9.0	Lower Cretaceous	yes
BB-2	14.5710	-21.1490	94.0	9.0	Lower Cretaceous	yes
BB-3	14.5750	-21.1600	81.0	10.0	Lower Cretaceous	yes
BB-4	14.5740	-21.1730	79.0	9.0	Lower Cretaceous	yes
BB-5	14.5420	-21.1680	77.0	15.0	Lower Cretaceous	yes
BB-6	14.5320	-21.1910	70.0	10.0	Lower Cretaceous	yes
BB-7	14.5410	-21.1850	68.0	12.0	Lower Cretaceous	yes
BB-8	14.5290	-21.1930	67.0	8.0	Lower Cretaceous	yes
BB-9	14.5270	-21.1950	66.0	11.0	Lower Cretaceous	yes
BB-10	14.5170	-21.2220	68.0	3.0	Lower Cretaceous	yes
BB-11	14.5170	-21.2220	69.0	4.0	Lower Cretaceous	yes
OK-1	15.3270	-20.8380	103.0	9.0	Lower Cretaceous	yes
OK-2	15.3220	-20.8380	104.0	8.0	Lower Cretaceous	yes
OK-3	15.3230	-20.8400	88.0	5.0	Lower Cretaceous	yes
OK-4	15.3230	-20.8400	83.0	6.0	Lower Cretaceous	yes
OK-5	15.3230	-20.8430	79.0	16.0	Lower Cretaceous	yes
OK-6	15.3230	-20.8430	73.0	10.0	Lower Cretaceous	yes
OK-7	15.3220	-20.8470	73.0	11.0	Lower Cretaceous	yes
OK-8	15.3220	-20.8470	66.0	10.0	Lower Cretaceous	yes
OK-9	15.2930	-20.8630	68.0	9.0	Lower Cretaceous	yes
<b>Raab et al., 2002 (Group C)</b>						
1-5-96-2	14.1333	-19.8167	107.0	8.0	Lower Cretaceous	yes
3-10-97-2	15.8500	-22.4167	86.0	7.0	Lower Cretaceous	yes
6-10-97-5	15.3333	-21.8833	72.0	3.0	Lower Cretaceous	yes
6-10-97-10	15.4667	-21.5333	90.0	6.0	Lower Cretaceous	yes
7-10-97-1	15.8833	-21.4500	112.0	8.0	Lower Cretaceous	yes
7-10-97-2	15.8000	-21.4667	105.0	10.0	Lower Cretaceous	yes
1-4-96-3	16.2667	-23.6167	287.0	32.0	Precambrian	yes
1-5-96-1	14.3000	-20.4167	108.0	7.0	Precambrian	yes
1-5-96-3	14.2833	-19.7500	417.0	16.0	Precambrian	yes
1-5-96-4	14.6500	-19.5833	399.0	31.0	Precambrian	yes
3-4-96-2	15.7500	-23.4667	76.0	5.0	Precambrian	yes
3-4-96-3	15.7667	-23.4667	114.0	10.0	Precambrian	yes
3-4-96-5	15.7667	-23.3000	206.0	14.0	Precambrian	yes
3-10-97-1	15.8500	-22.7000	74.0	3.0	Precambrian	yes
4-10-97-1	15.5167	-22.0833	71.0	3.0	Precambrian	yes
4-10-97-2	15.5500	-22.1667	71.0	5.0	Precambrian	yes
4-10-97-3	15.5833	-22.3500	62.0	3.0	Precambrian	yes
4-10-97-4	15.6000	-22.3667	63.0	4.0	Precambrian	yes
4-10-97-5	15.6167	-22.4333	88.0	4.0	Precambrian	yes
5-4-96-8	15.5833	-22.5000	76.0	4.0	Precambrian	yes
5-10-97-5	15.6000	-21.7500	92.0	4.0	Precambrian	yes
6-10-97-2	15.6000	-21.8167	73.0	4.0	Precambrian	yes
6-10-97-4	15.4167	-21.9667	70.0	4.0	Precambrian	yes
6-10-97-6	15.3500	-21.8500	65.0	3.0	Precambrian	yes
6-10-97-7	15.4167	-21.7667	77.0	4.0	Precambrian	yes
6-10-97-9	15.4667	-21.6833	79.0	3.0	Precambrian	yes

Reference/ S. -no.	Lon.	Lat.	Age [Ma]	1 $\sigma$ -error [Ma]	Formation age	AFT age < formation age
6-10-97-12	15.6500	-21.4833	84.0	5.0	Precambrian	yes
7-10-97-3	15.7500	-21.4500	92.0	3.0	Precambrian	yes
7-10-97-4	15.8167	-21.3167	91.0	4.0	Precambrian	yes
7-10-97-5	15.7333	-21.2333	97.0	5.0	Precambrian	yes
7-10-97-6	15.6667	-21.1667	93.0	4.0	Precambrian	yes
7-10-97-7	15.6000	-21.1000	90.0	6.0	Precambrian	yes
7-10-97-8	15.4000	-21.2167	81.0	4.0	Precambrian	yes
7-10-97-9	14.8333	-20.7333	93.0	5.0	Precambrian	yes
24-9-97-3	15.5833	-23.3500	450.0	50.0	Precambrian	yes
24-9-97-4	16.6500	-23.3500	547.0	95.0	Precambrian	yes
24-9-97-7	16.7167	-23.5167	372.0	68.0	Precambrian	yes
24-9-97-8	16.6833	-23.6000	267.0	20.0	Precambrian	yes
24-9-97-9	16.6833	-23.6833	258.0	15.0	Precambrian	yes
28-4-96-1	15.7333	-21.4833	79.0	6.0	Precambrian	yes
28-4-96-4	15.4167	-21.3500	102.0	4.0	Precambrian	yes
28-4-96-5	15.2167	-21.2667	94.0	4.0	Precambrian	yes
28-4-96-6	15.0500	-21.2167	101.0	7.0	Precambrian	yes
30-4-96-1	14.9000	-21.0167	117.0	9.0	Precambrian	yes
30-4-96-2	14.9833	-20.8667	116.0	9.0	Precambrian	yes
30-4-96-3	14.8333	-20.7333	93.0	8.0	Precambrian	yes
31-3-96-1	16.4000	-23.5167	326.0	1.0	Precambrian	yes
8732-59	16.1667	-21.9667	88.0	5.0	Precambrian	yes
8732-60	15.6333	-21.9667	70.0	2.0	Precambrian	yes
8732-61	15.2000	-22.0333	68.0	3.0	Precambrian	yes
8732-76	14.8333	-21.0667	81.0	3.0	Precambrian	yes
8732-77	15.0000	-20.9500	78.0	3.0	Precambrian	yes
8732-78	15.0500	-20.0833	433.0	22.0	Precambrian	yes
8732-79	15.0500	-20.0500	417.0	28.0	Precambrian	yes
8832-107	15.0500	-23.4667	90.0	6.0	Precambrian	yes
8832-108	15.0500	-23.3833	120.0	19.0	Precambrian	yes
8832-110	16.2833	-23.2333	215.0	15.0	Precambrian	yes
8832-111	16.3000	-23.2500	317.0	44.0	Precambrian	yes
8832-114	16.2500	-23.3333	252.0	16.0	Precambrian	yes
8832-116	16.2500	-23.3167	198.0	13.0	Precambrian	yes
8832-119	16.3000	-23.3667	129.0	19.0	Precambrian	yes
93-106	15.3667	-19.8000	329.0	27.0	Precambrian	yes
93-107	15.1833	-19.7167	321.0	18.0	Precambrian	yes
93-108	14.8500	-19.6167	293.0	18.0	Precambrian	yes
93-110	14.3167	-19.7000	311.0	16.0	Precambrian	yes
PH-2	16.3667	-23.8333	288.0	12.0	Precambrian	yes
<b>Haack, 1983 (Group C)</b>						
295	17.3944	-22.6098	185.0	37.0	Precambrian	yes
584	16.7135	-22.2986	207.0	54.0	Precambrian	yes
608	16.7466	-22.1303	152.0	31.0	Precambrian	yes
646	16.4048	-22.2680	88.0	5.0	Precambrian	yes
698	17.3663	-22.0207	199.0	15.0	Precambrian	yes
790 A	16.2824	-22.5077	334.0	20.0	Precambrian	yes
C 4	14.5432	-22.7424	84.0	7.0	Precambrian	yes
C 15	15.1093	-22.3068	65.0	6.0	Precambrian	yes
C 30	16.2286	-22.4695	262.0	30.0	Precambrian	yes
C 32	16.0938	-22.4312	192.0	20.0	Precambrian	yes

Reference/ S. -no.	Lon.	Lat.	Age [Ma]	1 $\sigma$ -error [Ma]	Formation age	AFT age < formation age
C 37	15.8846	-22.6486	100.0	10.0	Precambrian	yes
C 55	15.6500	-21.4166	146.0	19.0	Precambrian	yes
C 59	15.9666	-21.1333	125.0	15.0	Precambrian	yes
D 67	16.2000	-20.8000	117.0	17.0	Precambrian	yes
C 68	15.7551	-23.4870	115.0	16.0	Precambrian	yes
C 69	15.8999	-22.1583	125.0	14.0	Precambrian	yes
D 1	15.7444	-22.6608	138.0	15.0	Precambrian	yes
D 3	15.7166	-20.9333	103.0	16.0	Precambrian	yes
D 5	15.8489	-22.6811	98.0	10.0	Precambrian	yes
D 6	15.6867	-22.9591	132.0	15.0	Precambrian	yes
H 11	15.8208	-22.7398	197.0	12.0	Precambrian	yes
H 12	15.7596	-22.8137	169.0	15.0	Precambrian	yes
H 77	17.0909	-21.8830	315.0	25.0	Precambrian	yes
H 98 A	16.7109	-22.0487	265.0	28.0	Precambrian	yes
H 100	16.6217	-22.1915	107.0	7.0	Precambrian	yes
H 101	16.5401	-22.1328	189.0	19.0	Precambrian	yes
H 104	16.3870	-22.2476	107.0	14.0	Precambrian	yes
H 106	16.2340	-22.2505	142.0	13.0	Precambrian	yes
H 110	16.1957	-22.4007	266.0	35.0	Precambrian	yes
H 111	16.2060	-22.4287	282.0	25.0	Precambrian	yes
H 120	16.1167	-22.4822	333.0	34.0	Precambrian	yes
H 122	16.0503	-22.3853	142.0	12.0	Precambrian	yes
H 133	15.1374	-22.3470	90.0	12.0	Precambrian	yes
H 134	15.1501	-22.3802	116.0	11.0	Precambrian	yes
H 211	15.3822	-23.1428	102.0	13.0	Precambrian	yes
H 212	15.3899	-23.1683	125.0	8.0	Precambrian	yes
H 237	15.5658	-21.9135	133.0	20.0	Precambrian	yes
H 262	14.8314	-22.4363	79.0	7.0	Precambrian	yes
H 271	16.8562	-21.6305	87.0	11.0	Precambrian	yes
H 323	15.8948	-22.1045	131.0	19.0	Precambrian	yes
H 336	15.6423	-22.2068	74.0	6.0	Precambrian	yes
H 341	15.5968	-22.2680	77.0	10.0	Precambrian	yes
H 375	15.3899	-22.4236	151.0	8.0	Precambrian	yes
H 382	14.8518	-22.7169	94.0	6.0	Precambrian	yes
H 495	15.8285	-22.4261	75.0	9.0	Precambrian	yes
H 525	15.5531	-22.4900	86.0	7.0	Precambrian	yes
K 1	16.9889	-22.6582	102.0	18.0	Precambrian	yes
K 2	16.6063	-23.1836	346.0	60.0	Precambrian	yes
K 3	16.4533	-22.9846	324.0	40.0	Precambrian	yes
K 4	15.9356	-23.0612	305.0	34.0	Precambrian	yes
K 9	15.5103	-23.5686	113.0	9.0	Precambrian	yes
K 15	16.3029	-23.2397	240.0	55.0	Precambrian	yes
K 17	16.9073	-22.5685	176.0	45.0	Precambrian	yes
K 18	16.6981	-22.5686	144.0	42.0	Precambrian	yes
K 22	17.4173	-22.6506	165.0	22.0	Precambrian	yes
K 24	17.4607	-22.7806	97.0	21.0	Precambrian	yes
K 28	17.3612	-22.3701	256.0	37.0	Precambrian	yes
K 32	16.8971	-21.9034	331.0	25.0	Precambrian	yes
K 37	15.8412	-22.0155	115.0	16.0	Precambrian	yes
K 38	16.1703	-23.6400	210.0	23.0	Precambrian	yes
K 40	16.8435	-22.8877	166.0	45.0	Precambrian	yes

Reference/ S. -no.	Lon.	Lat.	Age [Ma]	1 $\sigma$ -error [Ma]	Formation age	AFT age < formation age
<b>South Africa</b>						
<b>Brown et al., 1990 (Group D)</b>						
8732-34	19.4700	-33.6500	155.0	4.0	Lower Paleozoic	yes
8732-35	18.9600	-33.7300	129.0	5.0	Lower Paleozoic	yes
8732-36	18.3700	-34.0500	124.0	4.0	Lower Paleozoic	yes
8732-39	20.0200	-32.8800	142.0	12.0	Lower Paleozoic	yes
8732-40	20.2700	-32.7300	160.0	11.0	Lower Paleozoic	yes
8732-41	20.4300	-32.5500	178.0	12.0	Lower Paleozoic	yes
8732-42	18.2500	-31.0000	100.0	5.0	Lower Paleozoic	yes
8732-43	18.2200	-30.9300	120.0	5.0	Lower Paleozoic	yes
8732-44	18.0300	-31.0700	108.0	3.0	Lower Paleozoic	yes
8732-45	17.8500	-31.2500	110.0	5.0	Lower Paleozoic	yes
732-46	17.8700	-30.2400	153.0	7.0	Lower Paleozoic	yes
8732-51	17.7300	-29.2300	116.0	6.0	Lower Paleozoic	yes
8732-52	17.6500	-28.7500	107.0	7.0	Lower Paleozoic	yes
8732-50	17.5000	-29.7000	115.0	6.0	Lower Paleozoic	yes
8732-55	17.6800	-27.9000	72.0	3.0	Lower Paleozoic	yes
8732-56	17.9500	-27.3000	127.0	9.0	Lower Paleozoic	yes
8732-81	15.1000	-26.6500	100.0	5.0	Lower Paleozoic	yes
8732-82	15.3800	-26.7000	95.0	3.0	Lower Paleozoic	yes
8732-83	15.6200	-26.5800	102.0	4.0	Lower Paleozoic	yes
8732-84	16.3300	-26.6800	138.0	8.0	Lower Paleozoic	yes
8732-85	17.7300	-26.8200	83.0	3.0	Lower Paleozoic	yes
8732-86	19.3000	-28.8000	114.0	7.0	Lower Paleozoic	yes
8732-87	19.1000	-29.2000	105.0	6.0	Lower Paleozoic	yes
8732-88	19.4000	-29.1000	104.0	4.0	Lower Paleozoic	yes
8732-93	21.1000	-28.6000	91.0	4.0	Lower Paleozoic	yes
8832-62	18.9000	-33.7000	119.0	9.0	Lower Paleozoic	yes
8832-63	18.9000	-33.7000	93.0	6.0	Lower Paleozoic	yes
8832-65	18.9000	-33.7000	89.0	6.0	Lower Paleozoic	yes
8832-66	19.0000	-33.7000	86.0	7.0	Lower Paleozoic	yes
8832-68	18.8000	-33.5000	90.0	6.0	Lower Paleozoic	yes
8832-54	20.6000	-32.6000	126.0	6.0	Lower Paleozoic	yes
8832-55	20.6000	-32.5000	127.0	6.0	Lower Paleozoic	yes
8832-56	20.6000	-32.5000	142.0	8.0	Lower Paleozoic	yes
8832-57	20.6000	-32.6000	131.0	8.0	Lower Paleozoic	yes
8832-58	20.6000	-32.6000	111.0	7.0	Lower Paleozoic	yes
8832-59	20.5000	-32.6000	126.0	8.0	Lower Paleozoic	yes
8832-60	20.5000	-32.6000	120.0	7.0	Lower Paleozoic	yes
8832-61	19.4000	-33.6000	104.0	7.0	Lower Paleozoic	yes
8832-71	18.1000	-32.8000	102.0	6.0	Lower Paleozoic	yes
8832-72	18.4000	-30.5000	88.0	3.0	Lower Paleozoic	yes
8832-73	18.4000	-30.5000	83.0	4.0	Lower Paleozoic	yes
8832-74	18.3000	-30.5000	118.0	6.0	Lower Paleozoic	yes
8832-75	18.5000	-30.3000	95.0	4.0	Lower Paleozoic	yes
8832-78	18.1000	-30.5000	89.0	4.0	Lower Paleozoic	yes
8832-79	18.1000	-30.5000	90.0	4.0	Lower Paleozoic	yes
NF-008	19.8000	-29.3000	92.0	9.0	Lower Paleozoic	yes
S-19	21.5000	-31.2000	163.0	9.0	Lower Paleozoic	yes
S-20	21.1000	-29.5000	99.0	5.0	Lower Paleozoic	yes
S-21	21.1000	-29.5000	104.0	9.0	Lower Paleozoic	yes

Reference/ S. -no.	Lon.	Lat.	Age [Ma]	1 $\sigma$ -error [Ma]	Formation age	AFT age < formation age
DR3	21.0000	-33.0000	138.0	6.0	Lower Paleozoic	yes
FTCG 4	18.9000	-33.7000	119.0	9.0	Lower Paleozoic	yes
FTCG 5	18.9000	-34.0000	130.0	4.0	Lower Paleozoic	yes
FTCG 6	18.8000	-34.0000	151.0	6.0	Lower Paleozoic	yes
FTCG 8	18.5000	-33.6000	160.0	7.0	Lower Paleozoic	yes
FTCG 9	18.0000	-33.1000	147.0	10.0	Lower Paleozoic	yes
FTCG 11	17.9000	-33.0000	147.0	5.0	Lower Paleozoic	yes
FTCG 14	18.0000	-32.8000	157.0	12.0	Lower Paleozoic	yes
FTCG 16	18.8000	-33.5000	120.0	5.0	Lower Paleozoic	yes
FTCG 17	18.7000	-33.5000	132.0	4.0	Lower Paleozoic	yes
FTCG 18	18.4000	-33.5000	142.0	4.0	Lower Paleozoic	yes
MDW-01	17.0500	-29.6500	119.0	9.0	Lower Paleozoic	yes
MDW-04	17.5700	-29.6300	111.0	12.0	Lower Paleozoic	yes
MDW-02	17.1800	-29.6300	108.0	4.0	Lower Paleozoic	yes
MDW-03	17.3700	-29.5800	123.0	7.0	Lower Paleozoic	yes
MDW-05	17.7300	-29.6800	129.0	6.0	Lower Paleozoic	yes
MDW-06	17.9000	-29.6700	125.0	26.0	Lower Paleozoic	yes
MDW-07	18.1200	-29.5700	125.0	4.0	Lower Paleozoic	yes
MDW-08	18.3800	-29.4800	126.0	6.0	Lower Paleozoic	yes
MDW-09	18.6800	-29.1300	111.0	5.0	Lower Paleozoic	yes
MDW-10	19.3800	-29.1300	107.0	6.0	Lower Paleozoic	yes
MDW-11	20.2500	-28.8300	70.0	5.0	Lower Paleozoic	yes
MDW-12	21.1500	-29.3000	73.0	4.0	Lower Paleozoic	yes
<b>Kounov et al., 2013 (Group E)</b>						
FRC03	17.6167	-27.6434	80.5	9.6	Precambrian	yes
FRC04	17.6129	-27.6437	81.2	12.4	Precambrian	yes
FRC05	17.6089	-27.6435	83.5	17.4	Precambrian	yes
FRC06	17.6086	-27.6462	70.0	11.4	Precambrian	yes
FRC09	17.6083	-27.6471	66.8	26.2	Precambrian	yes
AG01	20.1852	-28.8476	93.0	9.8	Precambrian	yes
AG04	20.5521	-28.5277	87.6	12.0	Precambrian	yes
AG05	20.5677	-28.2787	87.3	8.6	Precambrian	yes
AG06	20.4026	-28.2380	91.3	13.4	Precambrian	yes
AG07	20.8899	-28.6441	87.2	11.6	Precambrian	yes
AG08	20.2862	-28.5465	76.0	6.6	Precambrian	yes
AG09	20.2842	-28.5548	82.7	7.4	Precambrian	yes
AG10	20.2738	-28.5713	82.6	7.4	Precambrian	yes
AG11	20.2536	-28.5780	83.5	12.8	Precambrian	yes
AG12	20.0396	-28.8634	91.6	10.8	Precambrian	yes
<b>Kounov et al. 2009 (Group E)</b>						
CA04/04	19.9200	-31.3200	136.6	9.2	Jurassic	yes
CA04/15	19.1900	-31.3900	122.9	10.5	Jurassic	yes
CA04/16	19.2600	-31.4300	94.2	4.9	Jurassic	yes
CA04/19	20.5900	-31.3800	128.7	15.6	Jurassic	yes
CA04/23	20.9900	-31.2900	131.8	9.2	Jurassic	yes
CA04/18	20.3100	-31.4300	103.1	6.7	Upper Paleozoic	yes
CA04/21	20.8000	-31.3600	128.7	9.4	Upper Paleozoic	yes

Reference/ S. -no.	Lon.	Lat.	Age [Ma]	1 $\sigma$ -error [Ma]	Formation age	AFT age < formation age
CA04/22	21.0800	-31.2700	127.7	8.1	Upper Paleozoic	yes
CA04/05	19.0200	-31.3700	123.9	7.3	Lower Paleozoic	yes
CA04/06	18.4100	-31.6300	98.0	7.3	Lower Paleozoic	yes
CA04/08	18.2400	-31.8100	131.6	10.3	Lower Paleozoic	yes
CA04/10	18.7100	-31.6100	86.0	4.9	Lower Paleozoic	yes
CA04/11	18.9200	-31.4800	94.7	6.0	Lower Paleozoic	yes
VA04/05	18.0500	-30.1900	125.9	6.1	Precambrian	yes
VA04/06	18.2100	-30.1500	136.8	8.5	Precambrian	yes
VA04/08	18.4100	-29.9400	148.3	7.1	Precambrian	yes
VA04/16	18.9400	-29.5200	111.5	6.0	Precambrian	yes
VA04/34	17.5800	-30.8600	103.3	6.8	Precambrian	yes
VA04/31	17.8900	-30.7700	106.8	9.2	Precambrian	yes
VA04/13	18.0100	-30.5900	114.0	5.1	Precambrian	yes
VA04/12	18.0600	-30.4800	103.4	7.4	Precambrian	yes
<b>Kounov et al., 2008 (Group E)</b>						
VA04/26	18.7300	-30.6700	146.4	7.2	Basement	yes
VA04/27	18.9000	-30.7600	115.3	6.4	Basement	yes
VA04/29	19.1000	-30.8500	117.7	5.5	Basement	yes
CA04/25	19.2400	-30.9200	109.0	4.8	Basement	yes
<b>Tinker et al., 2008 (Group F)</b>						
JT02-01	22.2007	-33.3973	89.0	6.0	Upper Paleozoic	yes
JT02-02	22.2519	-33.4291	108.0	12.0	Upper Paleozoic	yes
JT02-04	22.2539	-33.4642	92.0	15.0	Upper Paleozoic	yes
JT02-05	22.2413	-33.4215	114.0	7.0	Upper Paleozoic	yes
JT02-14	22.5525	-34.0047	107.0	9.0	Upper Paleozoic	yes
JT02-19	22.3420	-33.7813	131.0	10.0	Upper Paleozoic	yes
JT02-20	22.2712	-33.6915	143.0	9.0	Upper Paleozoic	yes
JT02-26	21.7499	-33.3487	119.0	10.0	Upper Paleozoic	yes
JT02-30	22.0256	-33.2208	102.0	6.0	Upper Paleozoic	yes
JT02-31	22.0330	-33.1691	112.0	7.0	Upper Paleozoic	yes
JT02-32	22.0492	-33.1137	115.0	8.0	Upper Paleozoic	yes
JT02-33	22.0009	-33.0271	108.0	7.0	Upper Paleozoic	yes
JT02-34	21.9861	-32.9630	114.0	9.0	Upper Paleozoic	yes
JT02-35	21.9623	-32.8756	134.0	10.0	Upper Paleozoic	yes
JT02-36	21.9784	-32.7696	104.0	7.0	Upper Paleozoic	yes
JT02-37	22.1173	-32.6513	126.0	8.0	Upper Paleozoic	yes
JT02-38	22.2990	-32.5101	106.0	8.0	Upper Paleozoic	yes
JT02-39	22.5717	-32.3087	103.0	6.0	Upper Paleozoic	yes
JT02-41	22.5581	-32.2075	111.0	12.0	Upper Paleozoic	yes
JT02-42	22.5495	-32.1859	137.0	20.0	Upper Paleozoic	yes
JT02-44	22.3585	-31.6817	157.0	14.0	Upper Paleozoic	yes
JT02-45	22.2631	-31.2258	127.0	9.0	Upper Paleozoic	yes
JT02-46	22.1662	-30.7997	138.0	18.0	Upper Paleozoic	yes
JT02-48	22.6143	-30.0814	128.0	7.0	Upper Paleozoic	yes
JT02-51	22.3313	-29.5277	93.0	11.0	Upper Paleozoic	yes
<b>Green et al., 2017 (Group G)</b>						
GC1070-2	19.3873	-33.6353	95.4	8.5	Late J./Lower C.	yes
GC1070-3	19.5915	-33.6906	134.9	9.7	Late J./Lower C.	yes
GC1070-4	20.0645	-33.8288	130.1	14.0	Late J./Lower C.	yes



Reference/ S. -no.	Lon.	Lat.	Age [Ma]	1 $\sigma$ -error [Ma]	Formation age	AFT age < formation age
GC1070-5	20.0953	-33.8029	106.5	7.5	Late J./Lower C	yes
GC1070-6	20.0009	-33.8349	126.3	9.7	Late J./Lower C	yes
GC1070-10	21.8780	-33.5020	143.2	14.6	Late J./Lower C	yes
GC1070-11	22.0306	-33.5963	188.8	13.2	Late J./Lower C	no
GC1070-13	22.1970	-33.6452	171.8	9.8	Late J./Lower C	no
GC1070-14	22.2077	-33.5780	190.0	12.4	Late J./Lower C	no
GC1070-16	22.2534	-33.4489	180.3	21.5	Late J./Lower C	no
GC1070-17	22.6887	-33.5011	209.3	13.5	Late J./Lower C	no
GC1070-23	23.4256	-34.0041	142.9	10.3	Late J./Lower C	yes
GC1070-46	22.1750	-33.6549	94.9	13.9	Late J./Lower C	yes
GC1070-35	22.5712	-32.2571	99.0	12.8	Late J./Lower C	yes
GC1059-60	25.6542	-33.5906	189.7	16.9	Late J./Lower C	no
GC1059-61	25.6542	-33.5906	172.7	11.2	Late J./Lower C	no
GC1059-62	25.5416	-33.4631	192.0	19.4	Late J./Lower C	no
GC1059-63	25.4389	-33.4350	198.9	16.6	Late J./Lower C	no
GC1059-64	25.7459	-33.4394	223.0	20.8	Late J./Lower C	no
GC1059-65	25.6058	-33.8411	172.2	14.2	Late J./Lower C	no
GC1059-66	25.4814	-33.8069	200.8	12.2	Late J./Lower C	no
GC1059-67	25.4289	-33.7542	189.6	11.7	Late J./Lower C	no
GC1059-69	25.3356	-33.4836	178.8	11.4	Late J./Lower C	no
GC1059-70	25.4553	-33.6572	177.7	16.9	Late J./Lower C	no
GC1070-33	22.5719	-32.3090	96.4	6.3	Triassic	yes
GC1070-34	22.5663	-32.2631	96.5	5.8	Triassic	yes
GC1070-36	22.5579	-32.2129	109.8	14.2	Triassic	yes
GC1070-37	22.5480	-32.1760	100.9	7.0	Triassic	yes
GC1070-38	22.4477	-32.1227	116.3	15.6	Triassic	yes
GC1070-39	22.5290	-32.3824	90.9	7.5	Triassic	yes
GC1070-40	22.5347	-33.0598	107.5	9.4	Triassic	yes
GC1070-18	26.6347	-33.2267	137.7	7.7	Upper Paleozoic	yes
GC1070-19	26.5762	-33.3075	121.8	11.4	Upper Paleozoic	yes
GC1070-32	21.9630	-33.1475	101.2	9.3	Upper Paleozoic	yes
GC1070-41	22.5460	-33.2429	92.9	6.9	Upper Paleozoic	yes
GC1070-42	22.4775	-33.3032	129.7	11.5	Upper Paleozoic	yes
GC1070-47	22.1503	-33.6892	162.6	11.5	Upper Paleozoic	yes
GC1059-71	25.7096	-33.3828	182.7	13.0	Upper Paleozoic	yes
GC1070-1	19.2088	-33.6995	82.3	9.1	Lower Paleozoic	yes
GC1070-7	21.4038	-33.4153	106.0	14.3	Lower Paleozoic	yes
GC1070-8	21.5700	-33.4886	139.1	8.5	Lower Paleozoic	yes
GC1070-9	21.8763	-33.4976	113.4	8.7	Lower Paleozoic	yes
GC1070-15	22.2447	-33.5352	126.8	6.8	Lower Paleozoic	yes
GC1070-25	22.2411	-33.4210	113.6	14.5	Lower Paleozoic	yes
GC1070-27	22.0656	-33.3636	92.5	7.3	Lower Paleozoic	yes
GC1070-28	22.0543	-33.3586	84.8	25.9	Lower Paleozoic	yes
GC1070-29	22.0474	-33.3521	109.1	10.7	Lower Paleozoic	yes
GC1070-30	22.0430	-33.3288	81.2	9.2	Lower Paleozoic	yes
GC1070-43	22.5600	-33.3868	106.4	11.3	Lower Paleozoic	yes
GC1070-44	22.5498	-33.4219	101.1	7.2	Lower Paleozoic	yes
GC1070-45	22.5600	-33.4571	74.8	5.2	Lower Paleozoic	yes
GC1059-58	24.8495	-34.0267	184.9	13.4	Lower Paleozoic	yes

Reference/ S. -no.	Lon.	Lat.	Age [Ma]	1 $\sigma$ -error [Ma]	Formation age	AFT age < formation age
GC1059-68	25.4292	-33.5706	189.6	11.7	Upper Paleozoic	yes
<b>Wildman et al., 2017 (Group H)</b>						
FS1605	22.2000	-29.2200	122.8	7.5	Precambrian	yes
GGO2	20.3000	-28.3600	96.6	3.6	Precambrian	yes
PRU	19.5200	-28.4800	106.0	78.1	Precambrian	yes
S-25	26.0800	-29.5200	128.7	6.3	Precambrian	yes
SA12-05	23.7000	-29.1500	83.9	6.7	Precambrian	yes
SA12-06b	23.1400	-29.5400	97.7	6.5	Precambrian	yes
SA12-08	22.3100	-29.5200	102.1	8.7	Precambrian	yes
SA12-09	22.1200	-29.4000	112.5	5.9	Precambrian	yes
SA12-10	21.9400	-29.3600	89.0	10.0	Precambrian	yes
SA12-11	21.9400	-29.2400	58.9	5.9	Precambrian	yes
SA12-12	21.6300	-29.3000	85.4	3.8	Precambrian	yes
SA12-13a	21.4700	-29.2800	85.7	4.4	Precambrian	yes
SA12-19b	19.5300	-29.3400	97.0	4.6	Precambrian	yes
SA12-14	21.1500	-29.3500	93.4	5.5	Precambrian	yes
SA12-15	20.9800	-29.4200	64.5	4.1	Precambrian	yes
SR-17	25.2500	-27.1300	331.0	11.0	Precambrian	yes
V-10	26.4200	-26.6300	379.0	23.0	Precambrian	yes
<b>Wildman et al., 2006 (Group H)</b>						
SA12-27	18.7000	-30.2300	60.9	3.7	Upper Paleozoic	yes
JN2	18.0500	-30.6800	132.2	3.6	Precambrian	yes
JN3	17.3800	-29.9000	116.8	3.2	Precambrian	yes
NQ12-01	17.9900	-30.5500	85.4	3.4	Precambrian	yes
NQ12-03	17.9500	-30.4600	86.0	3.0	Precambrian	yes
NQ12-04	17.9300	-30.4000	89.6	4.1	Precambrian	yes
NQ12-06	17.8600	-30.3400	90.2	2.4	Precambrian	yes
NQ12-07	17.8200	-30.3200	96.0	2.6	Precambrian	yes
NQ12-08	17.8000	-30.3400	98.7	3.0	Precambrian	yes
NQ12-09	17.7700	-30.3400	106.6	3.8	Precambrian	yes
NQ12-10	17.7500	-30.3600	79.7	6.3	Precambrian	yes
NQ12-11	17.7200	-30.3700	110.4	6.0	Precambrian	yes
NQ12-12	17.6800	-30.3600	83.7	2.7	Precambrian	yes
NQ12-13	17.6200	-30.3600	84.0	4.1	Precambrian	yes
NQ12-15	17.3000	-30.3200	91.5	6.3	Precambrian	yes
NQ12-16	17.2700	-30.2900	93.5	6.1	Precambrian	yes
NQ12-17	17.2900	-30.3600	104.9	4.6	Precambrian	yes
NQ12-18	17.2800	-30.3400	108.4	4.9	Precambrian	yes
NQ12-19	17.6400	-30.2800	105.8	4.6	Precambrian	yes
NQ12-20	17.7200	-30.2000	102.5	3.6	Precambrian	yes
NQ12-21	17.7700	-30.2100	83.2	4.0	Precambrian	yes
NQ12-23	18.5200	-31.2300	58.3	2.6	Precambrian	yes
NQ12-24	18.3500	-31.1300	92.7	3.2	Precambrian	yes
NQ12-25	17.9300	-30.2100	112.6	4.9	Precambrian	yes
NQ12-26	17.9300	-30.1300	107.2	2.7	Precambrian	yes
NQ12-27	17.8800	-30.0300	105.8	2.7	Precambrian	yes
NQ12-28	17.9000	-30.1700	102.1	2.5	Precambrian	yes
NQ12-29	17.7800	-30.0900	99.1	5.6	Precambrian	yes

Reference/ S. -no.	Lon.	Lat.	Age [Ma]	1 $\sigma$ -error [Ma]	Formation age	AFT age < formation age
NQ12-30	17.8300	-30.1500	108.5	2.6	Precambrian	yes
NQ12-33	18.0800	-30.1700	105.8	4.5	Precambrian	yes
NQ12-34	18.1600	-30.1800	110.0	5.3	Precambrian	yes
SA12-22	19.0800	-29.9300	97.2	3.1	Precambrian	yes
SA12-30	18.0000	-30.5300	73.2	3.3	Precambrian	yes
SA12-32	18.0600	-30.5300	75.1	8.3	Precambrian	yes
SA12-33	18.0600	-30.4900	110.0	7.0	Precambrian	yes
SA12-35	18.0600	-30.4500	119.0	10.0	Precambrian	yes
SA12-36	18.0600	-30.4500	91.4	6.3	Precambrian	yes
SA12-37	18.0600	-30.4300	85.0	4.8	Precambrian	yes
SA12-38	18.0700	-30.4000	74.4	3.0	Precambrian	yes
SA12-47	18.2300	-30.3900	100.8	5.9	Precambrian	yes
SA12-51	18.4200	-30.3200	107.7	3.8	Precambrian	yes
SA12-52	18.4600	-30.3200	102.8	8.6	Precambrian	yes
<b>Zimbabwe</b>						
<b>Mackintosh et al., 2017 (Group I)</b>						
96Z-01	30.7970	-18.8960	443.0	22.0	Archean	yes
96Z-02	30.8960	-18.6510	415.0	57.0	Archean	yes
96Z-14	29.3680	-18.4020	466.0	20.0	Archean	yes
96Z-18	30.1680	-17.9060	418.0	27.0	Archean	yes
96Z-22	29.8690	-18.9440	433.0	18.0	Archean	yes
96Z-26	30.8040	-17.6730	391.0	8.0	Archean	yes
96Z-29	30.9410	-17.3900	319.0	13.0	Archean	yes
96Z-38	31.3890	-17.6480	345.0	17.0	Archean	yes
96Z-61	31.3700	-18.1000	311.0	16.0	Archean	yes
96Z-65	32.1540	-18.6330	320.0	15.0	Archean	yes
96Z-101	32.0310	-17.9120	335.0	26.0	Archean	yes
96Z-104	29.5100	-19.7090	470.0	23.0	Archean	yes
96Z-105	28.8220	-20.0550	434.0	15.0	Archean	yes
96Z-106	28.3820	-20.3280	397.0	12.0	Archean	yes
96Z-109	27.5510	-20.3510	358.0	18.0	Archean	yes
96Z-110	28.9890	-20.4020	396.0	17.0	Archean	yes
96Z-111	29.0240	-20.6560	361.0	9.0	Archean	yes

Table C. 3: All published apatite fission-track (AFT) ages of the South American SAPCM that were used for histograms and maps of the AFT age distribution with corresponding coordinates and references sorted by circled areas in Figure 6 and Table C. 1. Reference/sample number, Longitude, Latitude, Age [Ma], 1 $\sigma$ -error [Ma], formation age, AFT age < formation age (reset age information).

Reference/ S. -no.	Lon.	Lat.	Age [Ma]	1 $\sigma$ -error [Ma]	Formation age	AFT age < formation age
<b>South America</b>						
<b>NE Brazil</b>						
<b>Jelinek et al., 2014 (Group K)</b>						
PTAM 10	-38.8600	-10.9200	150.0	21.0	Late J./ Lower C.	yes
PTAM 15	-38.7500	-10.5900	175.0	26.0	Late J./ Lower C.	no
PTAM 16	-38.9500	-10.5100	119.0	15.0	Late J./ Lower C.	yes
PTAM 34	-38.8400	-10.8900	119.0	18.0	Late J./ Lower C.	yes
ES-01	-42.6000	-20.2600	109.0	11.0	Neoproterozoic	yes
ES-02	-42.5000	-20.2900	60.0	3.0	Neoproterozoic	yes
ES-03	-42.3500	-20.3300	82.0	5.0	Neoproterozoic	yes
ES-04	-42.1500	-20.2500	106.0	7.0	Neoproterozoic	yes
ES-05	-41.9700	-20.2800	90.0	6.0	Neoproterozoic	yes
ES-06	-41.8400	-20.4100	171.0	43.0	Neoproterozoic	yes
ES-07	-41.6000	-20.2600	97.0	6.0	Neoproterozoic	yes
ES-08	-41.4100	-20.2400	80.0	6.0	Neoproterozoic	yes
ES-09	-41.0900	-20.3500	64.0	5.0	Neoproterozoic	yes
ES-10	-40.7700	-20.4200	69.0	7.0	Neoproterozoic	yes
ES-13	-40.3200	-20.1100	75.0	7.0	Neoproterozoic	yes
ES-14	-40.3700	-19.8000	72.0	7.0	Neoproterozoic	yes
ES-15	-40.5700	-19.5400	97.0	10.0	Neoproterozoic	yes
ES-16	-40.5900	-19.1900	87.0	8.0	Neoproterozoic	yes
ES-18	-40.5500	-18.5900	88.0	8.0	Neoproterozoic	yes
ES-19	-40.3600	-18.3300	78.0	4.0	Neoproterozoic	yes
ES-20	-40.3700	-18.1200	95.0	7.0	Neoproterozoic	yes
ES-22	-40.4900	-17.7800	39.0	4.0	Neoproterozoic	yes
ES-23	-40.8000	-17.7900	68.0	7.0	Neoproterozoic	yes
ES-24	-41.0600	-17.8700	71.0	6.0	Neoproterozoic	yes
ES-25	-41.4200	-17.8400	112.0	8.0	Neoproterozoic	yes
ES-26	-41.6600	-17.8100	117.0	15.0	Neoproterozoic	yes
ES-27	-41.6700	-18.0300	98.0	8.0	Neoproterozoic	yes
ES-28	-41.8200	-18.4000	93.0	7.0	Neoproterozoic	yes
ES-29	-41.9700	-18.8400	71.0	6.0	Neoproterozoic	yes
ES-31	-41.2900	-18.7800	56.0	4.0	Neoproterozoic	yes
ES-33	-42.1400	-19.8000	77.0	6.0	Neoproterozoic	yes
ES-34	-42.2600	-20.6600	77.0	6.0	Neoproterozoic	yes
MG-63	-41.4678	-19.1378	136.0	8.0	Neoproterozoic	yes
MG-65	-41.2278	-19.3594	149.0	16.0	Neoproterozoic	yes
MG-66	-41.0989	-19.4708	127.0	10.0	Neoproterozoic	yes
MG-67	-40.9089	-19.5172	153.0	14.0	Neoproterozoic	yes
MG-68	-40.6947	-19.5289	116.0	13.0	Neoproterozoic	yes
MG-71	-40.7481	-20.0339	118.0	6.0	Neoproterozoic	yes
MG-72	-40.8853	-20.1494	126.0	12.0	Neoproterozoic	yes
PTAM 2	-38.0400	-11.0700	99.0	14.0	Neoproterozoic	yes
PTAM 4	-38.0900	-10.1200	69.0	7.0	Neoproterozoic	yes
PTAM 7	-39.1600	-10.1700	63.0	5.0	Neoproterozoic	yes

Reference/ S. -no.	Lon.	Lat.	Age [Ma]	1 $\sigma$ -error [Ma]	Formation age	AFT age < formation age
PTAM 8	-39.1600	-10.3500	120.0	40.0	Neoproterozoic	yes
PTAM 9	-38.9700	-10.9400	80.0	8.0	Neoproterozoic	yes
PTAM 11	-39.1700	-10.7200	102.0	14.0	Neoproterozoic	yes
BA 06	-39.0000	-12.2800	142.0	11.0	Neoproterozoic	yes
BA 08	-39.0600	-12.2700	202.0	12.0	Neoproterozoic	yes
BA 10	-39.7400	-12.1700	247.0	27.0	Neoproterozoic	yes
BA 11	-40.1700	-11.9600	231.0	18.0	Neoproterozoic	yes
BA 12	-40.2400	-11.9600	236.0	14.0	Neoproterozoic	yes
BA 13	-40.2700	-11.9600	326.0	41.0	Neoproterozoic	yes
BA 15	-40.3600	-11.9300	296.0	22.0	Neoproterozoic	yes
BA 16	-40.4000	-11.8800	300.0	71.0	Neoproterozoic	yes
BA 27	-40.3700	-11.2100	265.0	32.0	Neoproterozoic	yes
BA 29	-39.8200	-11.4500	295.0	34.0	Neoproterozoic	yes
BA 30	-39.7800	-11.4800	250.0	46.0	Neoproterozoic	yes
BA 31	-39.6800	-11.5600	249.0	19.0	Neoproterozoic	yes
BA 32	-39.6000	-11.6300	274.0	30.0	Neoproterozoic	yes
BA 34	-39.5700	-11.6600	299.0	56.0	Neoproterozoic	yes
BA 35	-38.9700	-12.0600	180.0	19.0	Neoproterozoic	yes
BA 36	-38.9100	-12.0500	264.0	21.0	Neoproterozoic	yes
BA 37	-38.9000	-12.0500	253.0	17.0	Neoproterozoic	yes
BA 39	-38.8000	-12.0100	299.0	30.0	Neoproterozoic	yes
BA 41	-38.9900	-11.5800	319.0	48.0	Neoproterozoic	yes
BA 64	-39.5000	-10.6600	233.0	60.0	Neoproterozoic	yes
BA 65A	-39.6800	-10.6600	350.0	57.0	Neoproterozoic	yes
BA 65B	-39.6800	-10.6600	237.0	19.0	Neoproterozoic	yes
BA 67	-40.1300	-10.6200	215.0	15.0	Neoproterozoic	yes
BA71	-40.2900	-9.8600	250.0	25.0	Neoproterozoic	yes
BA 72	-40.4600	-9.5100	187.0	19.0	Neoproterozoic	yes
BA 75	-40.4800	-9.5100	203.0	46.0	Neoproterozoic	yes
BA 77	-39.8700	-9.6000	209.0	33.0	Neoproterozoic	yes
BA 80	-39.5600	-9.8000	214.0	27.0	Neoproterozoic	yes
BA 81B	-39.4700	-9.8500	313.0	53.0	Neoproterozoic	yes
BA 85A	-39.3600	-12.9700	242.0	20.0	Neoproterozoic	yes
BA 87A	-39.8600	-12.8600	260.0	22.0	Neoproterozoic	yes
BA 92	-39.8700	-13.3500	218.0	21.0	Neoproterozoic	yes
BA 94	-39.0100	-13.1100	274.0	25.0	Neoproterozoic	yes
BA 104	-38.9900	-12.5900	276.0	25.0	Neoproterozoic	yes
BA 110	-39.4200	-14.2400	270.0	38.0	Neoproterozoic	yes
BA 111	-39.5300	-14.2100	273.0	41.0	Neoproterozoic	yes
BA 112	-39.6200	-14.2000	202.0	27.0	Neoproterozoic	yes
BA 114	-39.9600	-13.9800	251.0	30.0	Neoproterozoic	yes
BA 144	-40.1000	-12.5200	282.0	31.0	Neoproterozoic	yes
BA 86	-39.6700	-12.9700	183.0	38.0	Neoproterozoic	yes
BA 90	-40.6000	-13.5300	122.0	19.0	Neoproterozoic	yes
BA 93	-40.4400	-13.1900	211.0	31.0	Neoproterozoic	yes
BA 117A	-40.9900	-14.7800	172.0	36.0	Neoproterozoic	yes
BA 118	-40.7500	-15.0600	120.0	8.0	Neoproterozoic	yes
BA 120A	-40.6200	-15.1000	145.0	15.0	Neoproterozoic	yes
BA 122	-39.9200	-14.9900	137.0	18.0	Neoproterozoic	yes

Reference/ S. -no.	Lon.	Lat.	Age [Ma]	1 $\sigma$ -error [Ma]	Formation age	AFT age < formation age
BA 123A	-39.6700	-14.8600	118.0	14.0	Neoproterozoic	yes
BA 125	-39.4700	-14.8900	135.0	26.0	Neoproterozoic	yes
BA 132	-39.4400	-15.2100	137.0	16.0	Neoproterozoic	yes
BA 160B	-40.7500	-15.0600	145.0	59.0	Neoproterozoic	yes
BA 161B	-40.2900	-15.3600	171.0	34.0	Neoproterozoic	yes
BA 01	-38.4700	-12.9500	128.0	12.0	Neoproterozoic	yes
BA 05A	-38.4700	-12.9500	144.0	7.0	Neoproterozoic	yes
BA 97A	-38.5000	-13.0100	309.0	61.0	Neoproterozoic	yes
BA 97B	-38.5000	-13.0100	202.0	26.0	Neoproterozoic	yes
BA 98A	-40.4900	-13.0200	239.0	32.0	Neoproterozoic	yes
BA 100A	-37.9700	-12.5000	142.0	14.0	Neoproterozoic	yes
BA 101A	-37.6300	-11.8100	168.0	27.0	Neoproterozoic	yes
BA 102	-37.5700	-11.5400	147.0	25.0	Neoproterozoic	yes
BA 107	-39.1500	-13.7300	263.0	28.0	Neoproterozoic	yes
BA 108	-39.2100	-14.0700	304.0	36.0	Neoproterozoic	yes
BA 130	-39.2400	-15.3700	147.0	15.0	Neoproterozoic	yes
AFT Seal-1	-37.8400	-11.3800	109.0	14.0	Neoproterozoic	yes
AFT Seal-2B	-37.6700	-11.1800	92.0	12.0	Neoproterozoic	yes
AFT Seal-3	-37.8100	-10.7300	140.0	37.0	Neoproterozoic	yes
AFT Seal-4	-37.4300	-10.7600	113.0	15.0	Neoproterozoic	yes
AFT Seal-5	-37.3600	-10.6200	156.0	21.0	Neoproterozoic	yes
AFT Seal-7	-36.9400	-10.1500	91.0	22.0	Neoproterozoic	yes
AFT Seal-10	-37.4000	-9.6900	120.0	12.0	Neoproterozoic	yes
AFT Seal-11	-37.2800	-9.4700	102.0	12.0	Neoproterozoic	yes
AFT Seal-12	-36.8200	-9.8900	96.0	19.0	Neoproterozoic	yes
AFT Seal-13	-36.4400	-8.8100	122.0	15.0	Neoproterozoic	yes
AFT Seal-14	-35.9300	-8.4700	109.0	11.0	Neoproterozoic	yes
AFT Seal-15	-35.5200	-8.9600	109.0	11.0	Neoproterozoic	yes
AFT Seal-16	-35.6800	-8.9800	102.0	13.0	Neoproterozoic	yes
AFT Seal-17	-35.7600	-9.2500	91.0	9.0	Neoproterozoic	yes
AFT Seal-18	-36.9100	-10.3900	108.0	13.0	Neoproterozoic	yes
<b>Japsen et al., 2012 (Group K)</b>						
GC990-40	-37.9700	-11.7500	348.8	21.5	Cenozoic	no
GC990-24	-38.8200	-11.0800	331.4	31.6	Lower Cretaceous	no
GC990-25	-38.5700	-10.8000	254.0	30.7	Lower Cretaceous	no
GC990-26	-38.4300	-10.6300	150.0	26.1	Lower Cretaceous	no
GC990-27	-38.4200	-10.3700	213.4	19.9	Lower Cretaceous	no
GC990-28	-38.3800	-10.3800	228.6	25.5	Lower Cretaceous	no
GC990-29	-38.3300	-10.2500	208.7	13.2	Lower Cretaceous	no
GC990-36	-38.6700	-11.5700	263.6	57.2	Lower Cretaceous	no
GC990-37	-38.6000	-11.5700	222.5	37.5	Lower Cretaceous	no
GC990-38	-38.3700	-11.7500	255.2	14.6	Lower Cretaceous	no
GC990-42	-38.5000	-12.8700	339.9	37.4	Lower Cretaceous	no
GC990-43	-38.6300	-12.9000	152.1	18.8	Lower Cretaceous	no
GC990-48	-38.3200	-12.3300	102.2	9.5	Lower Cretaceous	yes
GC990-49	-38.3800	-12.6300	129.0	17.1	Lower Cretaceous	yes
GC990-108	-39.1300	-13.9500	341.7	26.8	Lower Cretaceous	no
GC990-111	-39.1000	-13.6700	308.1	34.3	Lower Cretaceous	no
GC990-113	-39.0700	-13.4200	327.8	41.9	Lower Cretaceous	no
GC990-116	-39.0000	-13.1500	285.8	24.0	Lower Cretaceous	no

Reference/ S. -no.	Lon.	Lat.	Age [Ma]	1 $\sigma$ -error [Ma]	Formation age	AFT age < formation age
GC990-123	-38.4300	-9.3800	231.9	32.2	Lower Cretaceous	no
GC990-18	-38.7200	-12.4000	271.6	25.3	Late Jurassic	no
GC990-20	-38.7200	-12.2500	232.1	17.0	Late Jurassic	no
GC990-30	-38.3200	-10.0800	199.2	25.6	Late Jurassic	no
GC990-31	-38.2500	-10.0800	357.2	37.7	Late Jurassic	no
GC990-35	-38.8500	-11.5800	110.8	25.4	Late Jurassic	yes
GC990-45	-38.8000	-13.0300	86.3	9.5	Late Jurassic	yes
GC990-15	-38.2000	-12.7000	285.1	27.0	Jurassic	no
GC990-21	-38.6800	-12.2700	251.6	25.3	Permian	yes
GC990-32	-38.2200	-10.0800	186.3	25.3	Upper Paleozoic	yes
GC990-33	-38.1800	-10.0800	246.3	29.5	Upper Paleozoic	yes
GC990-125	-37.8300	-9.5000	338.3	25.8	Lower Paleozoic	no
GC990-22	-38.6300	-12.2700	386.2	23.8	Proterozoic	yes
GC990-23	-38.9700	-11.5500	336.3	30.0	Proterozoic	yes
GC990-34	-38.1300	-10.0800	213.9	27.9	Proterozoic	yes
GC990-46	-38.9700	-13.0000	188.0	14.7	Proterozoic	yes
GC990-47	-38.9700	-12.5300	255.7	12.1	Proterozoic	yes
GC990-57	-39.0000	-12.2300	191.7	17.3	Proterozoic	yes
GC990-58	-39.5300	-12.5200	202.4	16.1	Proterozoic	yes
GC990-60	-40.2000	-12.5000	235.1	36.4	Proterozoic	yes
GC990-61	-40.8700	-12.4200	214.7	31.7	Proterozoic	yes
GC990-62	-41.3200	-12.7000	172.7	42.7	Proterozoic	yes
GC990-64	-41.2300	-12.7500	301.6	33.7	Proterozoic	yes
GC990-66	-41.3300	-12.9500	75.3	28.2	Proterozoic	yes
GC990-68	-41.3700	-13.0000	137.9	25.7	Proterozoic	yes
GC990-72	-41.2800	-13.2800	133.2	26.3	Proterozoic	yes
GC990-73	-41.4800	-13.4500	283.7	51.4	Proterozoic	yes
GC990-74	-41.5300	-13.4300	150.7	23.2	Proterozoic	yes
GC990-75	-41.5700	-13.4300	102.0	8.9	Proterozoic	yes
GC990-76	-41.5700	-13.5000	102.4	7.8	Proterozoic	yes
GC990-78	-41.8200	-13.4800	248.5	42.9	Proterozoic	yes
GC990-79	-41.8700	-13.4800	311.1	21.7	Proterozoic	yes
GC990-80	-41.8200	-13.5700	144.1	16.3	Proterozoic	yes
GC990-81	-41.8000	-13.5800	127.2	21.2	Proterozoic	yes
GC990-82	-41.7000	-13.9200	121.1	15.4	Proterozoic	yes
GC990-84	-41.4700	-14.4000	131.7	14.4	Proterozoic	yes
GC990-85	-41.1300	-14.4800	139.9	11.2	Proterozoic	yes
GC990-86	-41.0500	-14.5800	107.9	10.0	Proterozoic	yes
GC990-87	-41.0000	-14.6800	105.5	11.9	Proterozoic	yes
GC990-88	-40.8300	-14.8000	159.8	15.8	Proterozoic	yes
GC990-93	-40.7300	-15.0500	80.3	7.3	Proterozoic	yes
GC990-94	-40.7200	-15.0700	103.7	7.7	Proterozoic	yes
GC990-95	-40.6500	-15.1700	145.6	17.0	Proterozoic	yes
GC990-97	-40.2500	-15.2500	75.8	4.7	Proterozoic	yes
GC990-99	-39.7300	-14.8700	99.7	8.3	Proterozoic	yes
GC990-101	-39.3000	-14.6300	114.6	9.4	Proterozoic	yes
GC990-103	-39.0700	-15.3000	176.2	14.9	Proterozoic	yes
GC990-105	-39.0200	-14.7500	340.1	22.0	Proterozoic	yes
GC990-106	-39.3000	-14.5500	163.8	0.6	Proterozoic	yes

Reference/ S. -no.	Lon.	Lat.	Age [Ma]	1 $\sigma$ -error [Ma]	Formation age	AFT age < formation age
GC990-107	-39.3200	-14.2700	225.4	12.7	Proterozoic	yes
GC990-109	-39.1300	-13.8700	365.2	16.7	Proterozoic	yes
GC990-110	-39.1300	-13.7000	333.2	21.8	Proterozoic	yes
GC990-115	-39.0300	-13.0700	324.2	19.3	Proterozoic	yes
GC990-119	-37.6300	-9.9200	87.8	8.1	Proterozoic	yes
GC990-120	-37.8000	-9.6200	140.3	15.7	Proterozoic	yes
GC990-122	-38.0000	-9.3300	121.6	7.5	Proterozoic	yes
GC990-126	-37.5300	-10.1300	109.6	7.4	Proterozoic	yes
GC990-128	-37.4700	-10.6800	119.0	8.7	Proterozoic	yes
GC990-5	-38.5300	-12.9700	274.7	26.1	Archean	yes
GC990-14	-38.3800	-12.9200	117.6	6.8	Archean	yes
GC990-16	-37.9700	-12.4700	122.1	5.9	Archean	yes
GC990-17	-38.4500	-12.9700	261.5	15.5	Archean	yes
GC990-39	-38.1300	-11.6700	120.4	7.4	Archean	yes
GC990-41	-37.8000	-11.7000	242.9	13.3	Archean	yes
<b>Morais Neto et al., 2008, 2009 (Group K)</b>						
RD57-4	-36.6000	-5.6500	98.9	8.4	Neoproterozoic	yes
RD57-9a	-36.5300	-6.1800	102.1	13.1	Neoproterozoic	yes
RD57-11	-36.6200	-6.5200	108.5	7.1	Neoproterozoic	yes
RD57-15	-37.1100	-6.9800	102.0	6.2	Neoproterozoic	yes
RD57-17	-37.2900	-7.2000	93.6	12.0	Neoproterozoic	yes
RD57-18	-37.3900	-7.3300	71.1	5.9	Neoproterozoic	yes
RD57-21	-37.8600	-7.6200	82.2	7.0	Neoproterozoic	yes
RD57-23	-38.1200	-7.8700	173.3	24.1	Neoproterozoic	yes
RD57-24	-38.2500	-7.9500	123.5	9.0	Neoproterozoic	yes
RD57-26	-35.2000	-6.8500	97.2	8.2	Neoproterozoic	yes
RD57-29	-35.6300	-6.7500	66.8	8.1	Neoproterozoic	yes
RD57-31	-35.9500	-6.6800	52.1	4.4	Neoproterozoic	yes
RD57-33	-36.2300	-6.5100	85.9	6.8	Neoproterozoic	yes
RD57-36	-36.9200	-6.0300	97.3	6.6	Neoproterozoic	yes
<b>Turner et al., 2008 (Group K)</b>						
JT4	-38.3200	-10.1200	264.0	20.0	Lower Cretaceous	no
JT5	-38.3200	-10.1700	267.0	21.0	Lower Cretaceous	no
JT9	-38.3500	-11.3500	221.0	12.0	Lower Cretaceous	no
JT11	-38.3800	-11.4700	152.0	8.0	Lower Cretaceous	no
JT13	-38.8300	-11.0300	306.0	29.0	Lower Cretaceous	no
GC854-7	-38.5700	-10.0200	244.0	21.7	Lower Cretaceous	no
GC854-11	-38.3700	-10.1200	328.0	41.7	Lower Cretaceous	no
GC854-1	-38.8800	-12.0500	235.6	14.5	Neoproterozoic	yes
GC854-2	-38.8800	-12.0500	274.8	13.8	Neoproterozoic	yes
GC854-5	-39.0000	-11.5200	283.5	20.3	Neoproterozoic	yes
GC854-14	-36.8200	-9.8800	81.3	6.8	Neoproterozoic	yes
GC854-16	-36.7000	-9.7200	140.7	22.6	Neoproterozoic	yes
GC854-17	-36.8800	-9.6700	97.1	13.9	Neoproterozoic	yes
GC854-19	-36.4200	-9.5800	108.4	7.7	Neoproterozoic	yes
GC854-20	-36.2700	-9.5700	86.5	6.0	Neoproterozoic	yes



Reference/ S. -no.	Lon.	Lat.	Age [Ma]	1 $\sigma$ -error [Ma]	Formation age	AFT age < formation age
<b>Harman et al., 1998</b>						
94/85	-49.5250	-6.1383	266.0	23.0	Archean	yes
94/86	-49.7406	-6.9772	225.0	18.0	Archean	yes
94/87	-50.1456	-7.0061	259.0	9.0	Archean	yes
94/89	-50.5844	-6.8150	258.0	11.0	Archean	yes
94/92	-51.5850	-6.7247	291.0	21.0	Archean	yes
94/94	-49.9436	-7.1208	145.0	9.0	Archean	yes
94/95	-50.0375	-6.4547	261.0	10.0	Archean	yes
94/97	-50.0819	-8.0342	294.0	21.0	Archean	yes
94/98	-50.2436	-8.1669	180.0	9.0	Archean	yes
94/99	-50.4142	-8.5533	302.0	10.0	Archean	yes
94/100	-50.4964	-8.7944	286.0	22.0	Archean	yes
94/102	-50.6972	-8.6250	309.0	11.0	Archean	yes
94/103	-50.8772	-8.6083	266.0	10.0	Archean	yes
94/104	-51.0172	-8.4172	284.0	12.0	Archean	yes
94/105	-51.1522	-8.3186	301.0	15.0	Archean	yes
94/106	-51.2994	-8.3239	288.0	12.0	Archean	yes
94/107	-51.3086	-8.4447	268.0	15.0	Archean	yes
94/109	-49.5928	-4.7736	137.0	8.0	Archean	yes
94/110	-49.8358	-4.5236	159.0	9.0	Archean	yes
94/113	-50.3897	-3.8925	146.0	8.0	Archean	yes
94/1	-38.0400	-12.5900	83.0	5.0	Archean	yes
94/3	-37.7000	-11.7900	94.0	7.0	Archean	yes
94/4	-37.8000	-11.5200	95.0	1.0	Archean	yes
94/7	-37.4500	-10.6600	104.0	6.0	Archean	yes
94/15	-38.9400	-10.6800	167.0	9.0	Archean	yes
94/18	-39.0400	-10.5100	187.0	20.0	Archean	yes
94/19	-39.1600	-10.4600	130.0	19.0	Archean	yes
94/20	-39.2400	-10.4700	186.0	25.0	Archean	yes
94/22	-39.4900	-10.6600	244.0	15.0	Archean	yes
94/24	-39.7500	-10.6700	187.0	19.0	Archean	yes
94/74	-39.3300	-8.0800	85.0	12.0	Archean	yes
94/75	-39.4600	-8.0800	76.0	0.0	Archean	yes
94/76	-39.6400	-8.1100	260.0	0.0	Archean	yes
94/77	-39.7300	-8.1800	143.0	25.0	Archean	yes
94/78	-39.8300	-8.2600	173.0	17.0	Archean	yes
94/79	-40.0100	-8.5500	182.0	8.0	Archean	yes
94/80	-40.3900	-9.2000	107.0	11.0	Archean	yes
94/81	-40.1800	-10.4000	172.0	9.0	Archean	yes
94/83	-40.2500	-9.9800	167.0	11.0	Archean	yes
94/84	-40.4600	-9.5100	193.0	19.0	Archean	yes
<b>Amaral et al., 1997 (Group K)</b>						
K-1	-39.9200	-11.2700	261.0	29.0	Proterozoic	yes
A-1	-40.5500	-15.1800	210.0	23.0	Proterozoic	yes
E-1	-39.8700	-9.8700	250.0	28.0	Proterozoic	yes

Reference/ S. -no.	Lon.	Lat.	Age [Ma]	1 $\sigma$ -error [Ma]	Formation age	AFT age < formation age
<b>CE Brazil</b>						
<b>Van Ranst et al., 2019 (Group L)</b>						
BR-01	-41.8366	-20.4106	145.3	32.8	Neoproterozoic	yes
BR-03	-41.8546	-20.4226	83.9	4.8	Neoproterozoic	yes
BR-05	-41.9078	-20.4437	63.6	2.3	Neoproterozoic	yes
BR-07	-41.7770	-20.2614	63.1	2.5	Neoproterozoic	yes
BR-08	-41.4419	-20.2183	76.8	3.5	Neoproterozoic	yes
BR-09	-41.2583	-20.2840	71.0	2.7	Neoproterozoic	yes
BR-10	-41.0911	-20.3521	61.8	2.5	Neoproterozoic	yes
BR-11	-41.0174	-20.3873	68.2	2.7	Neoproterozoic	yes
BR-12	-40.8597	-20.4123	61.7	3.4	Neoproterozoic	yes
BR-13	-40.2731	-20.3339	80.9	4.5	Neoproterozoic	yes
BR-14	-40.3215	-20.1138	81.3	3.5	Neoproterozoic	yes
BR-16	-40.4096	-19.9324	71.7	2.1	Neoproterozoic	yes
BR-17	-40.4989	-19.9352	78.8	4.1	Neoproterozoic	yes
BR-19	-40.6787	-19.8146	73.1	3.5	Neoproterozoic	yes
BR-20	-40.6223	-19.5311	63.7	5.6	Neoproterozoic	yes
BR-22	-40.6809	-19.4084	78.2	3.2	Neoproterozoic	yes
BR-23	-40.8080	-19.2362	78.1	3.5	Neoproterozoic	yes
BR-24	-40.8664	-19.2295	89.9	5.5	Neoproterozoic	yes
BR-25	-40.9089	-19.2184	80.6	3.9	Neoproterozoic	yes
BR-26	-40.9669	-19.0807	80.9	3.1	Neoproterozoic	yes
BR-27	-41.1081	-18.8674	67.2	2.1	Neoproterozoic	yes
BR-28	-41.2654	-18.7963	88.4	4.0	Neoproterozoic	yes
BR-29	-41.4108	-18.7506	83.6	3.8	Neoproterozoic	yes
BR-30	-41.9624	-18.8355	70.4	4.5	Neoproterozoic	yes
<b>Engelmann de Oliveira et al., 2016 (Group L)</b>						
TR7RJ4	-43.2100	-22.4500	157.0	35.0	Neoproterozoic	yes
TR7RJ5	-43.2300	-22.5500	101.8	6.6	Neoproterozoic	yes
TR7RJ6	-43.2700	-22.5900	73.1	5.5	Neoproterozoic	yes
TR7RJ7	-43.2900	-22.6200	76.2	5.8	Neoproterozoic	yes
TR8RJ8	-44.3900	-22.3600	30.5	1.6	Neoproterozoic	yes
TR8RJ10	-44.2500	-22.4900	70.4	5.0	Neoproterozoic	yes
TR11RJ1	-42.3600	-21.6500	48.7	5.1	Neoproterozoic	yes
TR11RJ2	-42.7300	-21.9100	48.0	2.9	Neoproterozoic	yes
TR11RJ3	-43.0500	-22.0800	56.1	3.8	Neoproterozoic	yes
TR11RJ4	-43.3100	-22.1600	57.7	3.9	Neoproterozoic	yes
TR11RJ5	-43.5400	-22.3300	54.5	4.1	Neoproterozoic	yes
TR11RJ6	-43.7400	-22.4300	54.1	4.5	Neoproterozoic	yes
TR11RJ7	-43.8900	-22.4800	67.5	5.2	Neoproterozoic	yes
TR11RJ8	-44.0600	-22.4900	100.8	8.0	Neoproterozoic	yes
TR11RJ9	-44.1700	-22.5600	88.6	5.3	Neoproterozoic	yes
TR11RJ10	-44.7100	-22.5200	66.2	6.5	Neoproterozoic	yes
TR9SP4	-48.3600	-24.0800	89.6	6.9	Neoproterozoic	yes
TR9SP7	-47.5500	-24.7100	44.9	2.8	Neoproterozoic	yes
TR10SP1	-48.8800	-23.9700	112.0	23.0	Neoproterozoic	yes
TR10SP14	-47.8900	-24.7600	105.0	14.0	Neoproterozoic	yes
TR10SP16	-48.0800	-25.1200	65.8	6.1	Neoproterozoic	yes
TR10SP17	-48.0500	-25.2100	57.4	4.2	Neoproterozoic	yes

Reference/ S. -no.	Lon.	Lat.	Age [Ma]	1 $\sigma$ -error [Ma]	Formation age	AFT age < formation age
TR10SP18	-48.0700	-25.1800	21.0	1.8	Neoproterozoic	yes
TR11SP11	-44.9300	-22.8600	150.0	12.0	Neoproterozoic	yes
TR11SP12	-46.0200	-23.3500	61.9	5.1	Neoproterozoic	yes
TR11SP13	-46.1900	-23.4100	64.3	4.8	Neoproterozoic	yes
TR11SP14	-46.4300	-23.4700	71.4	4.5	Neoproterozoic	yes
TR11SP15	-47.4900	-24.3800	64.6	4.4	Neoproterozoic	yes
TR11SP19	-47.4400	-24.2900	74.4	8.1	Neoproterozoic	yes
<b>Hiruma et al., 2010 (Group L)</b>						
BOC-2	-44.3790	-22.7986	50.6	4.4	Neoproterozoic	yes
BOC-17	-44.5243	-22.8324	115.3	9.9	Neoproterozoic	yes
BOC-29	-44.4484	-22.7874	53.9	6.8	Neoproterozoic	yes
BOC-35	-44.7953	-22.8131	120.3	14.3	Neoproterozoic	yes
BOC-46	-44.6455	-22.7325	131.2	26.8	Neoproterozoic	yes
BOC-61	-44.7190	-22.9346	202.3	21.6	Neoproterozoic	yes
BOC-75	-44.4693	-22.8672	77.1	7.9	Neoproterozoic	yes
BOC-79	-44.3695	-22.8132	67.5	6.7	Neoproterozoic	yes
BOC-84	-44.6129	-22.6740	278.9	36.0	Neoproterozoic	yes
BOC-94	-44.2267	-22.7338	55.9	15.1	Neoproterozoic	yes
BOC-100	-44.2771	-22.8103	42.5	3.9	Neoproterozoic	yes
BOC-127	-44.7644	-22.7895	206.2	27.4	Neoproterozoic	yes
BOC-134	-44.7099	-22.7963	119.6	10.6	Neoproterozoic	yes
BOC-148	-44.8853	-23.0941	105.0	7.9	Neoproterozoic	yes
BOC-152	-44.4340	-22.7344	134.7	61.7	Neoproterozoic	yes
BOC-154	-44.4472	-22.8749	67.2	6.3	Neoproterozoic	yes
BOC-156	-44.3737	-22.8612	84.3	7.5	Neoproterozoic	yes
BOC-161	-44.7270	-22.8908	157.5	22.4	Neoproterozoic	yes
BOC-172	-44.7019	-22.9728	117.6	22.9	Neoproterozoic	yes
BOC-174	-44.7633	-23.0134	104.6	9.6	Neoproterozoic	yes
BOC-178	-44.7700	-22.7485	243.7	65.5	Neoproterozoic	yes
BOC-188	-44.5954	-22.6766	136.8	18.3	Neoproterozoic	yes
BOC-190	-44.9432	-22.9725	103.4	10.5	Neoproterozoic	yes
BOC-191	-44.8152	-23.1400	70.3	6.1	Neoproterozoic	yes
BOC-197	-44.3065	-22.6725	65.2	5.3	Neoproterozoic	yes
BOC-198	-44.8488	-22.7329	99.4	9.8	Neoproterozoic	yes
BOC-199	-44.8652	-22.7593	109.9	9.7	Neoproterozoic	yes
<b>Carmo, 2005 (Group L)</b>						
FTSEB-01b	-41.4600	-21.8200	39.0	n/a	Neoproterozoic	yes
FTSEB-02	-41.7200	-21.6500	56.0	n/a	Neoproterozoic	yes
FTSEB-04	-41.1500	-21.6000	58.0	n/a	Neoproterozoic	yes
FTSEB-07a	-42.6000	-21.5000	73.0	n/a	Neoproterozoic	yes
FTSEB-08	-42.7800	-21.3400	96.0	n/a	Neoproterozoic	yes
FTSEB-11	-43.6100	-21.2400	96.0	n/a	Neoproterozoic	yes
FTSEB-12	-43.6100	-21.2700	118.0	n/a	Neoproterozoic	yes
FTSEB-16	-43.7500	-21.2800	131.0	n/a	Neoproterozoic	yes
FTSEB-18	-44.3200	-21.0800	178.0	n/a	Neoproterozoic	yes
FTSEB-20	-44.0400	-20.3200	153.0	n/a	Neoproterozoic	yes
FTSEB-21	-43.9700	-20.2900	142.0	n/a	Neoproterozoic	yes

Reference/ S. -no.	Lon.	Lat.	Age [Ma]	1 $\sigma$ -error [Ma]	Formation age	AFT age < formation age
FTSEB-22	-43.9600	-20.2900	167.0	n/a	Neoproterozoic	yes
FTSEB-24	-43.6900	-20.3200	175.0	n/a	Neoproterozoic	yes
FTSEB-29	-43.3000	-20.1500	162.0	n/a	Neoproterozoic	yes
FTSEB-30	-43.2700	-20.1400	114.0	n/a	Neoproterozoic	yes
FTSEB-31	-43.0900	-20.1300	109.0	n/a	Neoproterozoic	yes
FTSEB-32	-42.9700	-20.1100	87.0	n/a	Neoproterozoic	yes
FTSEB-34	-42.7800	-20.0500	67.0	n/a	Neoproterozoic	yes
FTSEB-47	-40.4000	-20.3000	81.0	n/a	Neoproterozoic	yes
FTSEB-49	-41.0200	-20.3800	69.0	n/a	Neoproterozoic	yes
FTSEB-50	-41.2300	-20.3000	59.0	n/a	Neoproterozoic	yes
FTSEB-51	-41.7800	-20.2600	77.0	n/a	Neoproterozoic	yes
FTSEB-52	-42.0700	-20.2700	95.0	n/a	Neoproterozoic	yes
<b>SE Brazil</b>						
<b>Poços de Caldas, unpublished (Group M)</b>						
JM01	-46.4005	-22.2552	170.6	13.1	Neoproterozoic	yes
JM02	-46.4143	-22.2314	157.5	10.1	Neoproterozoic	yes
JM03	-46.4364	-22.2098	167.9	12.6	Neoproterozoic	yes
JM05	-46.4241	-22.1921	226.3	18.1	Neoproterozoic	yes
JM07	-46.4146	-22.1783	130.7	8.3	Neoproterozoic	yes
JM08	-46.4377	-22.1665	192.8	14.8	Neoproterozoic	yes
JM09	-46.4419	-22.1558	157.0	11.3	Neoproterozoic	yes
JM13	-46.5046	-22.0788	117.1	7.3	Neoproterozoic	yes
JM14	-46.4696	-22.0691	101.2	6.5	Neoproterozoic	yes
JM15	-46.4071	-22.0548	105.1	7.0	Neoproterozoic	yes
JM16	-46.3666	-22.0540	105.5	7.9	Neoproterozoic	yes
JM17	-46.3174	-22.0211	107.7	7.7	Neoproterozoic	yes
JM18	-46.2886	-22.0487	211.3	13.5	Neoproterozoic	yes
JM19	-46.2399	-22.0808	248.0	18.8	Neoproterozoic	yes
JM20	-46.1993	-22.0916	210.4	13.0	Neoproterozoic	yes
JM21	-46.1827	-22.1301	237.0	15.4	Neoproterozoic	yes
JM22	-46.1562	-22.1323	224.4	16.5	Neoproterozoic	yes
JM26	-45.8851	-22.0419	195.7	18.1	Neoproterozoic	yes
JM30	-45.9700	-22.2512	117.1	7.3	Neoproterozoic	yes
JM32	-46.3455	-22.4039	280.0	18.3	Neoproterozoic	yes
JM33	-46.3390	-22.3585	362.6	23.8	Neoproterozoic	yes
<b>Doranti-Tiritan et al., 2014 (Group M)</b>						
TF 1204	-46.7576	-21.9763	101.3	5.4	Lower Cretaceous	yes
TF 1207	-46.6749	-21.9387	42.7	3.4	Lower Cretaceous	yes
TF 1208	-46.6635	-21.9380	60.3	3.7	Lower Cretaceous	yes
TF 1209	-46.6693	-21.9021	69.0	4.4	Lower Cretaceous	yes
TF 1211	-46.5618	-21.8040	61.9	3.1	Lower Cretaceous	yes
TF 1212	-46.6187	-21.8418	63.5	4.3	Lower Cretaceous	yes
TF-313	-46.4003	-21.9350	61.8	9.6	Lower Cretaceous	yes
TF-1074	-46.5666	-22.0552	48.7	10.7	Lower Cretaceous	yes
TF-1076	-46.5717	-21.8890	51.7	5.2	Lower Cretaceous	yes
TF-1077	-46.5511	-21.8216	60.9	10.1	Lower Cretaceous	yes
TF-134	-46.6243	-21.5367	337.3	27.6	Neoproterozoic	yes
TF-135	-46.6425	-21.5638	256.7	25.4	Neoproterozoic	yes
TF-556	-46.8885	-21.8292	248.7	29.8	Neoproterozoic	yes

Reference/ S. -no.	Lon.	Lat.	Age [Ma]	1 $\sigma$ -error [Ma]	Formation age	AFT age < formation age
TF-557	-46.8005	-21.8225	159.3	42.3	Neoproterozoic	yes
TF-559	-46.3416	-21.7216	175.6	20.1	Neoproterozoic	yes
TF-667	-46.9166	-21.6597	324.5	46.0	Neoproterozoic	yes
TF-668	-46.8143	-21.5279	299.6	27.6	Neoproterozoic	yes
TF-700	-46.6938	-21.4995	330.7	46.8	Neoproterozoic	yes
TF-702	-46.6369	-21.4608	242.1	21.1	Neoproterozoic	yes
TF-703	-46.6401	-21.4507	205.6	25.3	Neoproterozoic	yes
TF-714	-46.4070	-21.6482	323.6	38.5	Neoproterozoic	yes
TF-1079	-46.6557	-21.6999	94.0	13.7	Neoproterozoic	yes
TF-1080	-46.7557	-21.6557	151.6	13.0	Neoproterozoic	yes
<b>Souza et al., 2014 (Group M)</b>						
A-1	-46.1200	-21.7700	167.7	10.1	Neoproterozoic	yes
A-2	-46.1300	-21.8100	125.0	7.5	Neoproterozoic	yes
A-3	-45.8800	-22.0800	113.0	7.7	Neoproterozoic	yes
A-4a	-45.9800	-22.0500	240.0	15.0	Neoproterozoic	yes
A-5a	-45.9900	-21.9800	205.0	14.5	Neoproterozoic	yes
A-5b	-45.9900	-21.9800	211.0	13.1	Neoproterozoic	yes
A-4b	-45.9800	-22.0500	220.0	12.5	Neoproterozoic	yes
A-6	-45.9300	-21.7100	162.0	11.3	Neoproterozoic	yes
A-7	-46.3200	-22.0600	70.0	6.2	Neoproterozoic	yes
A-9	-46.2500	-21.8100	153.0	16.2	Neoproterozoic	yes
TF-311	-46.5700	-21.7600	60.0	16.7	Neoproterozoic	yes
TF-315	-46.4300	-21.9300	51.0	6.0	Neoproterozoic	yes
TF-503	-46.7000	-21.6500	59.0	4.0	Neoproterozoic	yes
TF-558	-46.6700	-21.8400	105.0	13.0	Neoproterozoic	yes
<b>Franco-Magalhaes et al., 2014 (Group M)</b>						
TF-118	-45.1800	-22.5900	52.0	6.0	Neoproterozoic	yes
TF-612	-45.6000	-22.8800	61.0	7.0	Neoproterozoic	yes
TF-746	-45.7800	-22.8600	51.0	5.0	Neoproterozoic	yes
TF-748	-45.8800	-23.3100	81.0	8.0	Neoproterozoic	yes
TF-176	-45.3500	-23.7400	50.0	3.0	Neoproterozoic	yes
TF-498	-44.8500	-22.8300	33.0	11.0	Neoproterozoic	yes
TF-729	-45.8700	-23.4700	62.0	4.0	Neoproterozoic	yes
TF-1133	-45.5900	-23.5500	70.0	5.0	Neoproterozoic	yes
TF-122	-44.9400	-23.1200	52.0	5.0	Neoproterozoic	yes
TF-125	-44.8400	-23.2000	42.0	4.0	Neoproterozoic	yes
TF-661	-45.7400	-23.5700	49.0	23.0	Neoproterozoic	yes
<b>Cogné et al., 2012 (Group M)</b>						
Br 1	-45.7700	-22.7900	97.5	5.9	Neoproterozoic	yes
Br 2	-45.4600	-22.6600	108.5	2.9	Neoproterozoic	yes
Br 3	-45.4300	-22.6700	102.7	3.7	Neoproterozoic	yes
Br 5	-45.4000	-22.7100	83.7	6.3	Neoproterozoic	yes
Br 6	-45.4400	-23.2000	107.1	4.1	Neoproterozoic	yes
Br 7	-45.3600	-23.2000	92.3	3.3	Neoproterozoic	yes
Br 8	-45.2900	-23.3100	96.9	4.1	Neoproterozoic	yes
Br 9	-45.1900	-23.4000	102.7	3.3	Neoproterozoic	yes

Reference/ S. -no.	Lon.	Lat.	Age [Ma]	1 $\sigma$ -error [Ma]	Formation age	AFT age < formation age
Br 10	-45.0300	-23.4100	86.2	3.5	Neoproterozoic	yes
Br 11	-44.7800	-23.3700	81.0	2.8	Neoproterozoic	yes
Br 12	-44.7100	-23.2300	89.7	2.8	Neoproterozoic	yes
Br 13	-45.2500	-23.1400	99.7	4.2	Neoproterozoic	yes
Br 15	-45.1500	-23.0000	82.6	3.7	Neoproterozoic	yes
Br 17	-44.8700	-23.1600	100.2	4.5	Neoproterozoic	yes
Br 18	-44.9500	-23.1200	101.1	4.3	Neoproterozoic	yes
Br 19	-45.0300	-23.0300	112.8	3.6	Neoproterozoic	yes
Br 21	-45.2600	-22.8500	104.4	6.9	Neoproterozoic	yes
Br 22	-44.9200	-22.5400	80.5	4.5	Neoproterozoic	yes
Br 23	-44.9000	-22.5600	79.5	4.5	Neoproterozoic	yes
Br 24	-44.0800	-22.5100	121.1	6.8	Neoproterozoic	yes
Br 25	-44.6000	-22.4900	84.0	5.2	Neoproterozoic	yes
Br 27	-45.1600	-22.5900	73.8	4.0	Neoproterozoic	yes
Br 28	-45.2100	-22.5200	105.1	3.7	Neoproterozoic	yes
Br 29	-45.1700	-22.5500	79.2	2.9	Neoproterozoic	yes
Br 31	-45.2900	-22.4500	129.3	4.3	Neoproterozoic	yes
Br 32	-45.3500	-22.4300	110.1	4.6	Neoproterozoic	yes
Br 33	-45.4300	-22.3100	98.1	5.4	Neoproterozoic	yes
Br 34	-45.3600	-22.2600	109.5	4.6	Neoproterozoic	yes
Br 35	-45.2500	-22.0700	115.1	4.3	Neoproterozoic	yes
Br 38	-44.8900	-22.1900	90.2	4.5	Neoproterozoic	yes
Br 40	-44.7400	-22.2800	71.7	4.6	Neoproterozoic	yes
Br 41	-44.7600	-22.3400	67.4	2.6	Neoproterozoic	yes
Br 42	-44.7600	-22.3800	91.9	7.6	Neoproterozoic	yes
Br 43	-44.7500	-22.4000	94.1	7.5	Neoproterozoic	yes
Br 46	-44.7500	-22.4300	60.7	1.9	Neoproterozoic	yes
<b>Hackspacher et al., 2007 (Group M)</b>						
TF-93	-45.8200	-22.2000	115.0	13.0	Neoproterozoic	yes
TF-95	-46.5200	-22.1600	107.0	13.0	Neoproterozoic	yes
TF-96	-45.8700	-22.2000	110.0	12.0	Neoproterozoic	yes
TF-136	-46.6400	-21.5500	143.0	24.0	Neoproterozoic	yes
TF-311	-46.5800	-21.7600	76.0	10.0	Neoproterozoic	yes
TF-366	-45.8500	-22.5400	185.0	16.0	Neoproterozoic	yes
TF-377	-45.9100	-21.9600	89.0	6.0	Neoproterozoic	yes
TF-381	-46.9600	-21.3800	115.0	20.0	Neoproterozoic	yes
TF-485	-45.1200	-21.9100	139.0	17.0	Neoproterozoic	yes
TF-488	-45.0300	-22.1300	124.0	7.0	Neoproterozoic	yes
TF-493b	-44.7600	-22.4300	66.0	8.0	Neoproterozoic	yes
TF-502	-46.6100	-21.7600	63.0	9.0	Neoproterozoic	yes
TF-503	-46.7000	-21.6500	71.0	8.0	Neoproterozoic	yes
TF-505	-46.3900	-21.8800	52.0	7.0	Neoproterozoic	yes
TF506	-46.3800	-21.9500	74.0	7.0	Neoproterozoic	yes
TF-507	-46.3900	-21.9300	74.0	8.0	Neoproterozoic	yes
TF-509	-46.3700	-21.8600	65.0	6.0	Neoproterozoic	yes
TF-511	-46.7000	-21.2400	334.0	42.0	Neoproterozoic	yes
TF-556	-46.8900	-21.8200	194.0	22.0	Neoproterozoic	yes
TF-559	-46.3500	-21.7100	180.0	21.0	Neoproterozoic	yes
TF-560	-46.0700	-21.6300	180.0	20.0	Neoproterozoic	yes

Reference/ S. -no.	Lon.	Lat.	Age [Ma]	1 $\sigma$ -error [Ma]	Formation age	AFT age < formation age
<b>Hackspacher et al., 2004</b>						
TF-101	-48.6400	-23.1400	355.0	64.0	Neoproterozoic	yes
TF-99	-48.5300	-23.2200	77.0	9.0	Neoproterozoic	yes
TF-100	-48.6500	-23.3300	100.0	12.0	Neoproterozoic	yes
TF-96	-48.1600	-22.5000	62.0	7.0	Neoproterozoic	yes
TF-95	-48.1800	-22.7300	79.0	9.0	Neoproterozoic	yes
TF-94	-48.0200	-22.6700	88.0	7.0	Neoproterozoic	yes
TF-108	-48.0000	-22.8300	45.0	5.0	Neoproterozoic	yes
TF-92	-48.2000	-23.0400	49.0	6.0	Neoproterozoic	yes
TF-107	-48.2600	-23.1400	43.0	4.0	Neoproterozoic	yes
TF-120	-47.8700	-23.1200	68.0	4.0	Neoproterozoic	yes
TF-5	-47.6500	-23.0500	42.0	9.0	Neoproterozoic	yes
TF-128	-47.6200	-23.1400	31.0	5.0	Neoproterozoic	yes
TF-121	-47.8800	-23.2800	76.0	4.0	Neoproterozoic	yes
TF-123	-47.9000	-23.4100	61.0	2.0	Neoproterozoic	yes
TF-173	-47.7900	-23.5600	58.0	4.0	Neoproterozoic	yes
TF-42	-47.7700	-23.6300	39.0	9.0	Neoproterozoic	yes
<b>Tello Saenz et al., 2003 (Group M)</b>						
TF-4	-45.7361	-22.7859	67.2	9.4	Lower Cretaceous	yes
TF-11	-46.3846	-23.1674	159.0	25.4	Cambrian	yes
TF-12	-46.2351	-23.1675	58.9	7.7	Cambrian	yes
TF-20	-45.0691	-23.4359	9.9	1.3	Cambrian	yes
TF-1	-45.6684	-22.3851	107.0	12.8	Neoproterozoic	yes
TF-9	-46.3174	-22.9692	115.0	17.3	Neoproterozoic	yes
TF-10	-46.4675	-23.1177	126.0	16.4	Neoproterozoic	yes
TF-5	-45.7520	-22.8174	55.1	7.2	Neoproterozoic	yes
TF-13	-46.0854	-23.2504	68.5	11.0	Neoproterozoic	yes
TF-17	-45.4334	-23.2004	108.9	18.5	Neoproterozoic	yes
TF-22	-45.4835	-23.5668	78.7	11.0	Neoproterozoic	yes
TF-29	-46.4850	-23.8845	88.2	14.1	Neoproterozoic	yes
TF-30	-46.4187	-23.9002	71.0	11.4	Neoproterozoic	yes
TF-21	-45.4190	-23.6169	57.4	2.3	Neoproterozoic	yes
<b>Gallagher et al., 1994, 1995 (Group M)</b>						
32a-BRA808	-47.6700	-22.2700	117.3	9.0	Lower Cretaceous	yes
32b-BRA810	-47.6700	-22.2700	120.5	10.0	Lower Cretaceous	yes
30-BRA804	-48.4000	-22.8400	96.6	8.0	Lower Cretaceous	yes
26-BRA442	-50.5900	-23.8800	118.9	5.0	Lower Cretaceous	yes
27-BRA443	-50.7800	-23.7300	154.4	15.0	Lower Cretaceous	no
28-BRA447	-50.0200	-23.8700	131.5	6.0	Lower Cretaceous	yes
7-BRA413	-49.4900	-28.3800	150.3	16.0	Lower Cretaceous	no
8-BRA414	-49.4900	-28.3800	157.0	14.0	Lower Cretaceous	no
9-BRA415	-49.5100	-28.3800	141.2	13.0	Lower Cretaceous	yes
10a-BRA417	-49.5400	-28.3900	88.6	5.0	Lower Cretaceous	yes
10b-BRA417	-49.5400	-28.3900	95.4	4.0	Lower Cretaceous	yes
10c-BRA878	-49.5400	-28.3900	92.3	7.0	Lower Cretaceous	yes
10d-BRA879	-49.5400	-28.3900	81.0	6.0	Lower Cretaceous	yes
10e-BRA880	-49.5400	-28.3900	74.8	4.0	Lower Cretaceous	yes

Reference/ S. -no.	Lon.	Lat.	Age [Ma]	1 $\sigma$ -error [Ma]	Formation age	AFT age < formation age
10f-BRA881	-49.5400	-28.3900	88.0	7.0	Lower Cretaceous	yes
11-BRA419	-49.4800	-28.1200	123.7	6.0	Lower Cretaceous	yes
12-LFT5/24	-49.4800	-28.1200	132.3	5.0	Lower Cretaceous	yes
13-BRA885	-49.4500	-28.1000	95.7	6.0	Lower Cretaceous	yes
14-BRA420	-49.4400	-28.0900	99.4	8.0	Lower Cretaceous	yes
15-BRA424	-49.4000	-28.0800	90.1	10.0	Lower Cretaceous	yes
1-BRA866	-51.1700	-29.2000	139.8	10.0	Lower Cretaceous	yes
2a-BRA872	-49.6900	-29.3400	123.7	7.0	Lower Cretaceous	yes
2b-BRA874	-49.6900	-29.3400	121.2	27.0	Lower Cretaceous	yes
2c-BRA875	-49.6900	-29.3400	101.0	10.0	Lower Cretaceous	yes
3-BRA405	-49.0300	-28.3800	52.2	5.0	Neoproterozoic	yes
4-BRA406	-49.2000	-28.3400	64.7	6.0	Neoproterozoic	yes
5-BRA408	-49.3300	-28.3600	67.5	3.0	Neoproterozoic	yes
6-BRA410	-49.3800	-28.3900	82.3	4.0	Neoproterozoic	yes
16-BRA429	-49.2700	-28.1400	60.7	4.0	Neoproterozoic	yes
17-BRA430	-49.2300	-28.1900	77.0	8.0	Neoproterozoic	yes
18-BRA431	-48.5500	-25.8000	65.1	4.0	Neoproterozoic	yes
19-BRA432	-48.5300	-25.7600	87.0	4.0	Neoproterozoic	yes
20-BRA433	-48.9600	-25.5800	82.7	7.0	Neoproterozoic	yes
21-BRA434	-48.9400	-25.5800	86.8	4.0	Neoproterozoic	yes
22-BRA435	-48.9200	-25.5700	81.1	7.0	Neoproterozoic	yes
23-BRA438	-50.1200	-25.0200	112.7	10.0	Neoproterozoic	yes
24-BRA440	-49.9500	-24.6500	141.7	43.0	Neoproterozoic	yes
25-BRA441	-49.9200	-24.6000	144.6	5.0	Neoproterozoic	yes
29-BRA802	-48.5200	-23.0800	135.8	7.0	Neoproterozoic	yes
31-BRA805	-48.2700	-22.6100	151.2	39.0	Neoproterozoic	yes
33-BRA813	-47.9300	-22.2500	180.2	32.0	Neoproterozoic	yes
34-BRA794	-46.7000	-22.9400	224.9	11.0	Neoproterozoic	yes
35-BRA796	-46.5300	-23.0600	243.4	19.0	Neoproterozoic	yes
36-BRA797	-46.5800	-23.3000	189.0	14.0	Neoproterozoic	yes
37-BRA798	-46.5900	-23.3300	179.6	11.0	Neoproterozoic	yes
38-BRA799	-46.8200	-23.4700	139.4	8.0	Neoproterozoic	yes
39-BRA800	-47.2700	-23.3400	261.2	37.0	Neoproterozoic	yes
40-BRA824	-46.8600	-21.4000	330.3	22.0	Neoproterozoic	yes
41-BRA827	-46.4300	-21.5500	284.9	10.0	Neoproterozoic	yes
42a-BRA829	-46.3800	-21.8100	80.1	5.0	Neoproterozoic	yes
42b-BRA831	-46.4400	-21.8200	81.0	6.0	Neoproterozoic	yes
42c-BRA832	-46.4400	-21.8200	81.0	3.0	Neoproterozoic	yes
43-BRA834	-46.4500	-21.9600	71.1	5.0	Neoproterozoic	yes
44-BRA836	-46.2100	-22.0800	261.0	14.0	Neoproterozoic	yes
45-BRA837	-46.1100	-22.1500	251.9	9.0	Neoproterozoic	yes
46-BRA838	-45.9000	-22.2100	225.2	12.0	Neoproterozoic	yes
47-BRA839	-45.7100	-22.2800	116.3	13.0	Neoproterozoic	yes
48-BRA841	-45.5700	-22.4000	132.6	6.0	Neoproterozoic	yes
49-BRA843	-45.5100	-22.4300	109.4	5.0	Neoproterozoic	yes
50-BRA849	-44.4500	-22.4600	125.4	12.0	Neoproterozoic	yes
51-BRA850	-44.2200	-22.6200	67.2	3.0	Neoproterozoic	yes
52-BRA853	-44.4600	-22.8900	78.3	3.0	Neoproterozoic	yes
53-BRA854	-44.5400	-23.0500	64.5	3.0	Neoproterozoic	yes
54-BRA855	-44.5600	-23.1100	66.2	4.0	Neoproterozoic	yes
55-BRA858	-44.8200	-23.3500	91.6	4.0	Neoproterozoic	yes

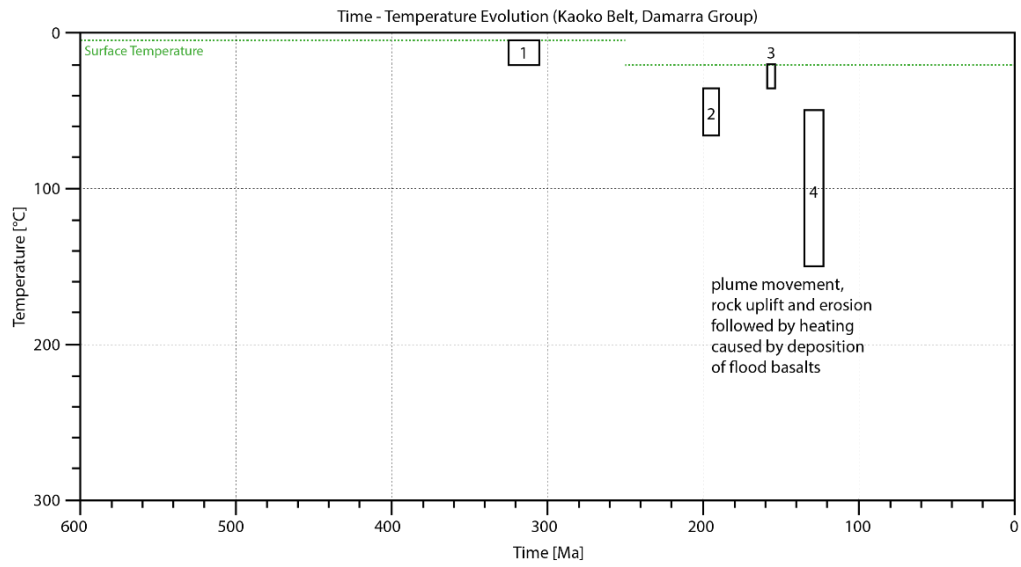


Reference/ S. -no.	Lon.	Lat.	Age [Ma]	1 $\sigma$ -error [Ma]	Formation age	AFT age < formation age
56-BRA859	-45.0500	-23.3200	81.4	14.0	Neoproterozoic	yes
57-BRA860	-45.3200	-23.6000	86.1	6.0	Neoproterozoic	yes
58-BRA861	-45.6300	-23.4400	99.1	3.0	Neoproterozoic	yes
<b>Krob et al., 2019; Karl et al., 2013 (Group N)</b>						
BR09-16	-51.5785	-25.8585	93.2	8.1	Lower Cretaceous	yes
BR09-17	-51.5216	-26.2010	47.7	11.0	Lower Cretaceous	yes
BR09-42	-49.5271	-28.3942	59.5	5.2	Lower Cretaceous	yes
BR09-24	-50.0671	-25.8682	125.8	9.6	Upper Paleozoic	yes
BR09-26	-49.7460	-25.7702	118.9	7.8	Upper Paleozoic	yes
BR09-35	-50.1931	-27.8665	79.7	10.9	Upper Paleozoic	yes
BR09-45	-49.3064	-28.3606	76.4	5.9	Neoproterozoic	yes
BR09-46	-49.1147	-28.2948	69.8	5.6	Neoproterozoic	yes
BR09-50	-49.1786	-28.6973	76.2	6.6	Neoproterozoic	yes
BR09-51	-49.0518	-28.5804	76.7	6.1	Neoproterozoic	yes
BR09-52	-48.9681	-28.4465	73.4	5.6	Neoproterozoic	yes
BR09-53	-48.8582	-28.4255	70.7	4.6	Neoproterozoic	yes
BR09-27	-49.5269	-25.6835	120.6	8.9	Neoproterozoic	yes
BR09-28	-49.3589	-25.9597	101.9	11.9	Neoproterozoic	yes
BR10-01	-47.0662	-23.9370	130.7	8.8	Neoproterozoic	yes
BR10-02	-47.1978	-24.0474	80.6	6.6	Neoproterozoic	yes
BR10-03	-47.3711	-24.2096	69.5	6.5	Neoproterozoic	yes
BR10-04	-47.4540	-24.2876	89.6	6.5	Neoproterozoic	yes
BR10-05	-47.6556	-24.3515	88.0	6.3	Neoproterozoic	yes
BR10-07	-48.1073	-24.7562	73.0	8.4	Neoproterozoic	yes
BR10-09	-48.2161	-24.8544	69.0	8.4	Neoproterozoic	yes
BR10-10	-48.4060	-24.9698	102.9	9.8	Neoproterozoic	yes
BR10-11	-48.5082	-24.9946	67.8	7.1	Neoproterozoic	yes
BR10-12	-48.7288	-25.1007	85.0	6.8	Neoproterozoic	yes
BR10-15	-49.1415	-25.6705	70.9	7.4	Neoproterozoic	yes
BR10-16A	-49.0848	-25.8460	93.5	8.7	Neoproterozoic	yes
BR10-17A	-48.9553	-25.8549	78.0	5.4	Neoproterozoic	yes
BR10-20	-48.9337	-26.2360	98.5	6.9	Neoproterozoic	yes
BR10-21	-48.9730	-26.4649	106.3	10.0	Neoproterozoic	yes
BR10-22	-49.0170	-26.6089	104.4	8.4	Neoproterozoic	yes
BR10-23A	-49.1993	-26.8908	110.5	7.1	Neoproterozoic	yes
BR10-23B	-49.1993	-26.8908	102.9	7.0	Neoproterozoic	yes
BR10-24	-49.0692	-26.7461	105.5	6.3	Neoproterozoic	yes
BR10-25	-49.0139	-26.8741	104.5	7.5	Neoproterozoic	yes
BR10-26	-48.8907	-27.0072	125.8	8.9	Neoproterozoic	yes
BR10-27	-48.9212	-27.2457	85.2	5.3	Neoproterozoic	yes
BR10-32	-48.6610	-27.9311	78.0	5.8	Neoproterozoic	yes
BR10-34	-48.7020	-28.2517	68.4	5.2	Neoproterozoic	yes
<b>Franco Magalhaes et al., 2010 (Group N)</b>						
TF-619	-49.5167	-24.4333	53.5	1.4	Neoproterozoic	yes
TF-1007	-48.9667	-24.5500	66.2	1.3	Neoproterozoic	yes
TF-934	-49.0333	-24.7833	16.4	1.0	Neoproterozoic	yes
TF-621	-49.6167	-24.3333	21.1	1.4	Neoproterozoic	yes

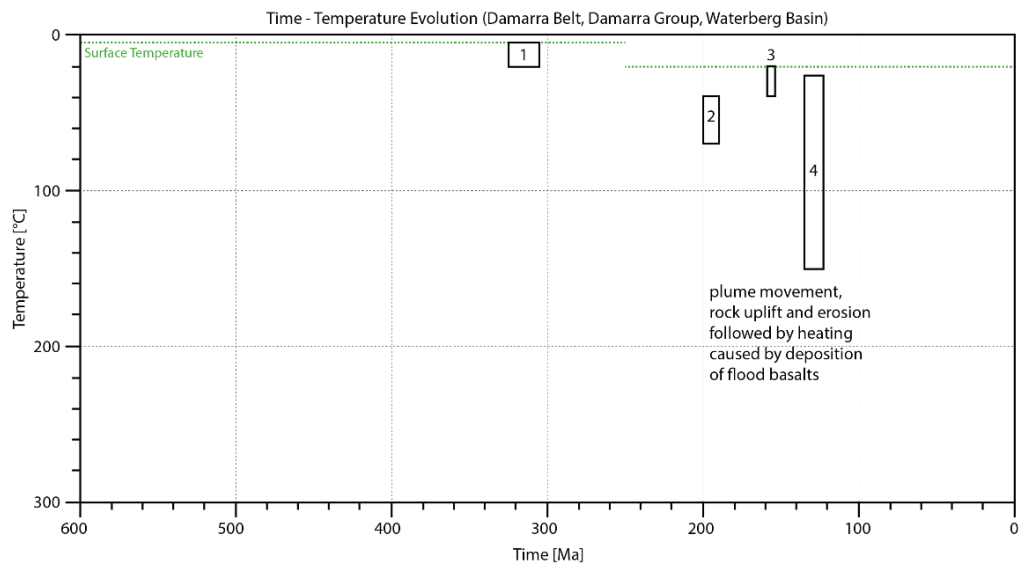
Reference/ S. -no.	Lon.	Lat.	Age [Ma]	1 $\sigma$ -error [Ma]	Formation age	AFT age < formation age
TF-785	-49.8667	-24.4500	13.9	1.4	Neoproterozoic	yes
TF-1073	-49.8833	-24.8333	33.2	0.6	Neoproterozoic	yes
TF-1072	-49.7167	-25.0167	48.7	0.5	Neoproterozoic	yes
TF-1070	-49.6667	-25.1333	46.8	4.0	Neoproterozoic	yes
TF-1069	-49.6167	-25.1833	52.3	3.0	Neoproterozoic	yes
TF-1068	-49.6333	-25.2000	47.5	2.7	Neoproterozoic	yes
TF1065	-49.7167	-25.0167	49.2	3.9	Neoproterozoic	yes
TF-1061	-49.4333	-25.4167	49.8	2.4	Neoproterozoic	yes
TF-929	-49.6167	-25.4500	21.5	1.0	Neoproterozoic	yes
TF-619	-49.5167	-24.4333	53.5	1.4	Neoproterozoic	yes
TF-1007	-48.9667	-24.5500	66.2	1.3	Neoproterozoic	yes
TF-934	-49.0333	-24.7833	16.4	1.0	Neoproterozoic	yes
TF-621	-49.6167	-24.3333	21.1	1.4	Neoproterozoic	yes
TF-785	-49.8667	-24.4500	13.9	1.4	Neoproterozoic	yes
TF-1073	-49.8833	-24.8333	33.2	0.6	Neoproterozoic	yes
TF-1072	-49.7167	-25.0167	48.7	0.5	Neoproterozoic	yes
TF-1070	-49.6667	-25.1333	46.8	4.0	Neoproterozoic	yes
TF-1069	-49.6167	-25.1833	52.3	3.0	Neoproterozoic	yes
TF-1068	-49.6333	-25.2000	47.5	2.7	Neoproterozoic	yes
TF1065	-49.7167	-25.0167	49.2	3.9	Neoproterozoic	yes
TF-1061	-49.4333	-25.4167	49.8	2.4	Neoproterozoic	yes
TF-929	-49.6167	-25.4500	21.5	1.0	Neoproterozoic	yes
<b>Engelmann de Oliveira et al., 2016 (Group O)</b>						
TFRS-05	-54.4400	-31.1000	298.0	26.0	Neoproterozoic	yes
TFRS-06	-54.0600	-31.2900	340.0	33.0	Neoproterozoic	yes
TFRS-12	-53.4600	-30.5000	234.0	14.0	Neoproterozoic	yes
PRD-02	-53.4600	-30.5100	161.0	16.0	Neoproterozoic	yes
PJV-07	-51.9200	-30.5100	77.3	5.8	Neoproterozoic	yes
PJV-11	-51.0200	-30.0700	95.4	4.5	Neoproterozoic	yes
PJV-14	-51.6000	-30.3100	91.0	16.0	Neoproterozoic	yes
TFRS-07	-53.3900	-31.5700	110.4	8.0	Neoproterozoic	yes
PRD-04	-52.8300	-31.1500	197.0	14.0	Neoproterozoic	yes
PRD-05	-52.7700	-31.0800	138.0	14.0	Neoproterozoic	yes
PJV-17	-52.6500	-31.4100	160.8	8.6	Neoproterozoic	yes
PRD-10	-52.6800	-30.5700	241.0	19.0	Neoproterozoic	yes
PRD-12	-52.4500	-30.5600	243.0	28.0	Neoproterozoic	yes
TFRS-08	-52.8900	-31.7200	175.2	8.4	Neoproterozoic	yes
PJV-02	-52.1700	-30.8200	183.0	15.0	Neoproterozoic	yes
PJV-03b	-53.1900	-30.8000	203.0	11.0	Neoproterozoic	yes
PJV-03c	-52.1100	-30.8200	250.0	20.0	Neoproterozoic	yes
PJV-04	-52.1100	-30.7900	240.0	17.0	Neoproterozoic	yes
PJV-05	-52.1100	-30.7500	252.0	22.0	Neoproterozoic	yes
PJV-06	-51.9900	-30.5500	219.0	9.9	Neoproterozoic	yes
PRD-18	-51.9800	-30.7800	298.0	25.0	Neoproterozoic	yes
PRD-19	-51.9400	-30.8700	334.0	44.0	Neoproterozoic	yes
TFRS-11	-53.1900	-30.8000	176.4	9.4	Neoproterozoic	yes

Reference/ S. -no.	Lon.	Lat.	Age [Ma]	1 $\sigma$ -error [Ma]	Formation age	AFT age < formation age
<b>Bicca et al., 2013 (Group O)</b>						
MA-MS-110	-53.4200	-30.9000	311.0	24.2	Lower Paleozoic	yes
MA-UC-89	-53.4400	-30.9100	274.0	15.7	Lower Paleozoic	yes
MA-Ryt-54	-53.4100	-30.9000	133.0	8.3	Lower Paleozoic	yes
MA-LC-109	-53.4200	-30.9000	362.0	34.9	Lower Paleozoic	yes
MA-US-44	-53.4200	-30.8900	355.0	30.5	Lower Paleozoic	yes
MA-LS-106	-53.4200	-30.9000	361.0	31.0	Lower Paleozoic	yes
<b>Borba et al., 2002, 2003 (Group O)</b>						
NR	-53.4078	-30.5675	250.2	12.0	Neoproterozoic	yes
GS-1	-53.5139	-30.6169	247.5	13.2	Neoproterozoic	yes
GS-3	-53.4647	-30.5547	245.5	12.3	Neoproterozoic	yes
GN-1	-53.4900	-30.4511	274.8	14.1	Neoproterozoic	yes
GN-2	-53.4475	-30.4997	193.5	13.9	Neoproterozoic	yes
GN-3	-53.4192	-30.4314	73.7	4.5	Neoproterozoic	yes
EN-26	-53.7700	-30.7300	290.0	14.6	Neoproterozoic	yes
EN-27	-53.8000	-30.7400	278.0	14.8	Neoproterozoic	yes
EN-193	-53.8200	-30.7600	287.0	13.3	Neoproterozoic	yes
EN-216	-53.8500	-30.7600	280.0	13.3	Neoproterozoic	yes
<b>Uruguay</b>						
<b>Uruguay, unpublished (Group P)</b>						
U14-01	-55.5892	-33.9263	388.4	-22.5	Precambrian	yes
U14-02	-55.4910	-33.8376	314.4	-24.5	Proterozoic	yes
U14-03	-55.4025	-33.6796	282.6	-19.6	Precambrian	yes
U14-05	-55.1800	-33.4904	328.0	-19.1	Precambrian	yes
U14-06	-55.0822	-33.5267	324.7	-23.2	Precambrian	yes
U14-07	-54.9367	-33.5345	445.7	-26.7	Archean	yes
U14-08	-54.4620	-32.9994	223.9	-25.7	Cambrian	yes
U14-12	-54.1246	-32.5126	298.3	-24.5	Precambrian	yes
U14-13	-54.2959	-32.9279	293.3	-27.1	Precambrian	yes
U14-14	-54.7896	-33.9513	182.6	-18.9	Precambrian	yes
U14-15	-54.6449	-34.3056	288.5	-35.7	Precambrian	yes
U14-16	-54.1526	-34.6684	206.5	-13.8	Precambrian	yes
U14-17	-54.1216	-34.5920	202.0	-12.0	Precambrian	yes
U14-19	-54.2053	-34.5455	189.0	-18.1	Precambrian	yes
U14-20	-54.2297	-34.5714	220.0	-25.4	Precambrian	yes
<b>Kollenz, 2015 (Group P)</b>						
U 6	-56.9881	-34.0422	325.7	24.8	Precambrian	yes
U 10	-56.2378	-33.9582	200.2	19.3	Precambrian	yes
U 11	-56.2030	-34.1001	298.3	22.4	Precambrian	yes
U 37	-54.2346	-32.8060	238.8	20.3	Precambrian	yes
U 42	-54.9521	-34.9735	219.1	25.3	Precambrian	yes
U 43	-56.1689	-34.9206	245.0	24.3	Precambrian	yes
U 47	-56.1586	-34.9314	227.3	43.1	Precambrian	yes

Reference/ S. -no.	Lon.	Lat.	Age [Ma]	1 $\sigma$ -error [Ma]	Formation age	AFT age < formation age
<b>Argentina</b>						
<b>Kollenz et al., 2016; Kollenz, 2015 (Group Q)</b>						
ARG 04	-60.0656	-38.0555	157.8	10.7	Upper Paleozoic	yes
ARG 05	-62.7102	-38.1322	233.5	17.0	Upper Paleozoic	yes
ARG 09	-61.8708	-38.0660	190.9	14.8	Upper Paleozoic	yes
ARG 12	-61.7296	-38.1226	141.9	10.7	Upper Paleozoic	yes
ARG 15	-61.4844	-38.2105	169.8	13.1	Upper Paleozoic	yes
ARG 16	-61.8674	-38.0048	156.0	11.7	Upper Paleozoic	yes
ARG 17	-61.8598	-37.8869	161.4	12.3	Upper Paleozoic	yes
ARG 01	-59.9489	-37.0709	129.2	9.3	Precambrian	yes
ARG 02	-59.4150	-37.5941	186.7	14.5	Precambrian	yes
ARG 08	-62.1718	-37.9396	242.7	17.1	Precambrian	yes
ARG 12-01	-59.0655	-37.3371	138.0	15.3	Proterozoic	yes
ARG 12-02	-58.9981	-37.3882	104.8	7.5	Proterozoic	yes
ARG 12-03	-58.9682	-37.4178	124.5	11.8	Proterozoic	yes
ARG 12-04	-58.9576	-37.3447	157.1	13.7	Proterozoic	yes
ARG 12-05	-58.9346	-37.3490	189.1	13.7	Proterozoic	yes
ARG 12-06	-59.1028	-37.3783	108.1	10.1	Proterozoic	yes
ARG 12-07	-59.1128	-37.3977	162.0	13.5	Proterozoic	yes
ARG 12-08	-59.9724	-37.2960	101.6	9.4	Proterozoic	yes
ARG 12-09	-59.9508	-37.1821	104.0	7.1	Proterozoic	yes
ARG 12-10	-60.0581	-37.0821	140.8	9.4	Proterozoic	yes
ARG 12-11	-59.7569	-37.0619	116.7	11.5	Proterozoic	yes
ARG 12-12	-59.2339	-37.2957	116.1	8.4	Proterozoic	yes
ARG 12-13	-59.1917	-37.4263	228.9	22.3	Proterozoic	yes
ARG 12-14	-59.4593	-37.4444	135.0	9.3	Proterozoic	yes
ARG 12-16	-58.9238	-37.4601	138.1	9.8	Proterozoic	yes
ARG 12-17	-58.6217	-37.6272	164.9	32.5	Proterozoic	yes
ARG 12-18	-58.6217	-37.7538	141.3	9.9	Proterozoic	yes



No.	Time [Ma]	Temperature [°C]	Event
1	325 - 305	20 - 5	Onset of Paraná Basin sedimentation
2	200 - 190	65 - 35	Possible initial plume rise and surface uplift based on stratigraphic records
3	160 - 155	35 - 20	Possible climax and collapse of plume head based on renewed sedimentation
4	140 - 125	150 - 50	Twyfelfontein Sedimentation, Paraná-Etendeka flood basalts (Tafelberg Fm)



No.	Time [Ma]	Temperature [°C]	Event
1	325 - 305	20 - 5	Onset of sedimentation
2	200 - 190	70 - 40	Possible Initial plume rise and surface uplift based on stratigraphic records
3	160 - 155	40 - 20	Possible climax and collapse of plume head based on renewed sedimentation
4	140 - 125	150 - 25	Deposition of Paraná-Etendeka flood basalts (Etjo Formation, Rooiwal Fm)

Figure C 1: The geological evolution model (GEM) for the samples of the Namibian Damara Group located in the Kaoko Belt (upper) and Damara Belt (lower).

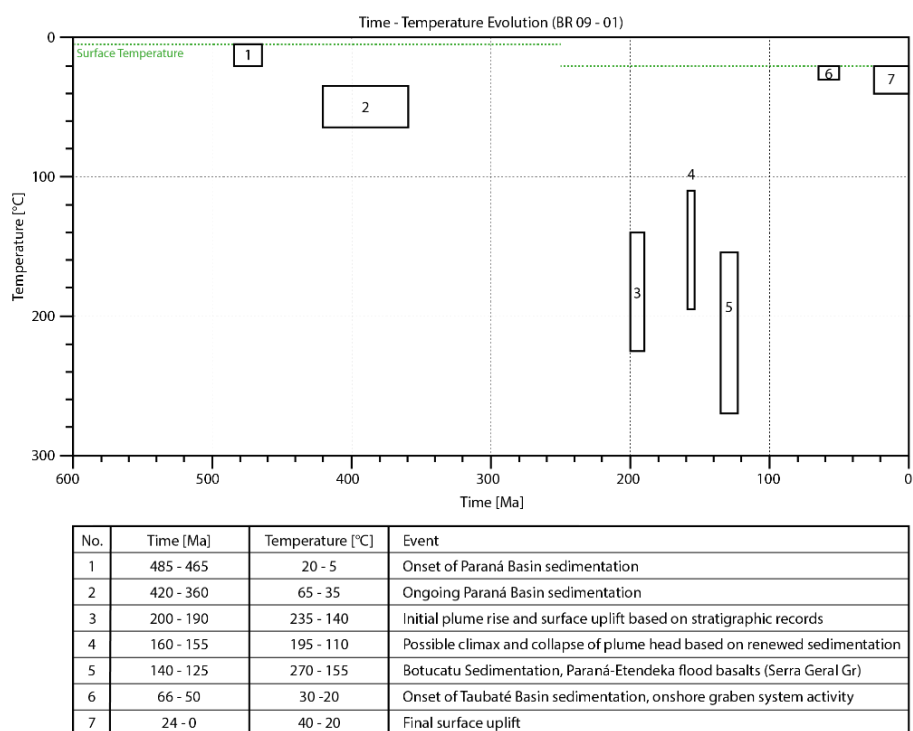
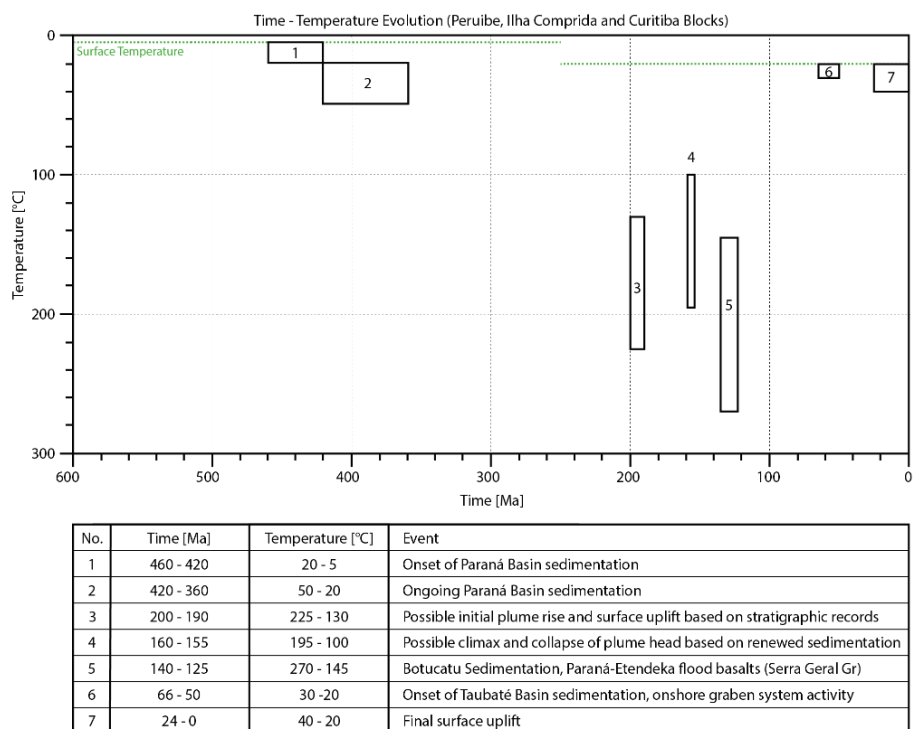
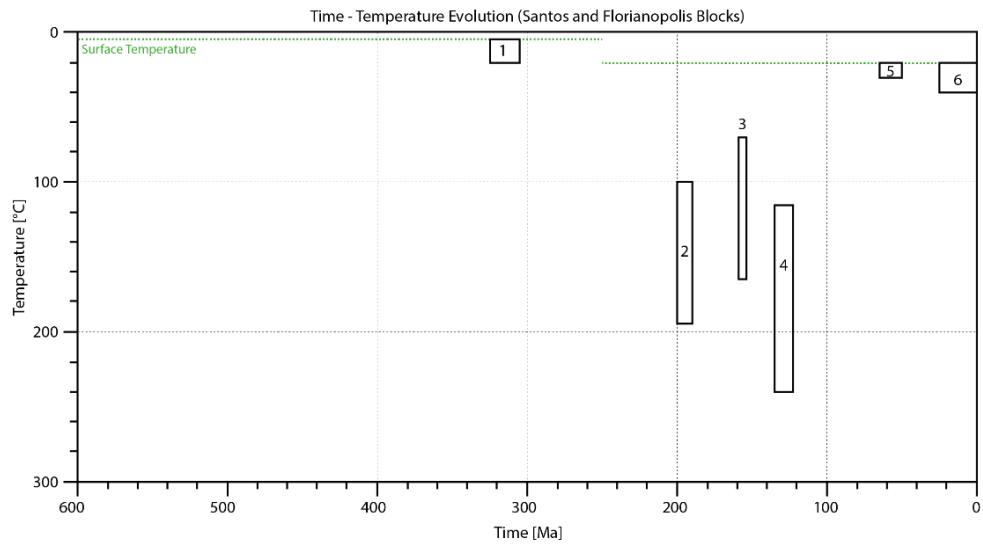
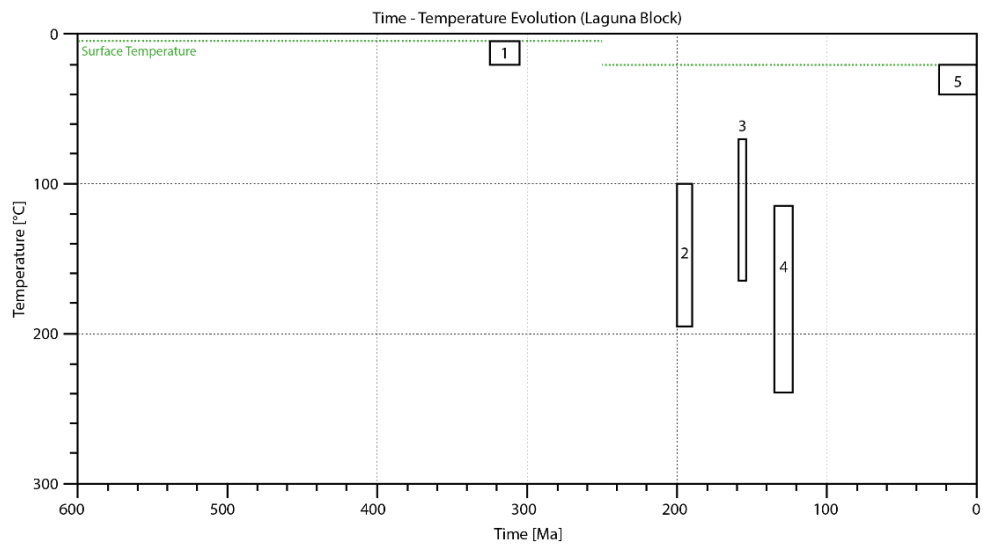


Figure C 2: The geological evolution model (GEM) for samples of the Brazilian Neoproterozoic basement for the northern Peruibe, Ilha Comprida and Curitiba blocks (upper) and the sample BR09-01 in the Ponta Grossa Arc area (lower).



No.	Time [Ma]	Temperature [°C]	Event
1	325 - 305	20 - 5	Onset of Paraná Basin sedimentation
2	200 - 190	195 - 100	Possible initial plume rise and surface uplift based on stratigraphic records
3	160 - 155	165 - 70	Possible climax and collapse of plume head based on renewed sedimentation
4	140 - 125	240 - 115	Botucatu Sedimentation, Paraná-Etendeka flood basalts (Serra Geral Gr)
5	66 - 50	30 - 20	Onset of Taubaté Basin sedimentation, onshore graben system activity
6	24 - 0	40 - 20	Final surface uplift



No.	Time [Ma]	Temperature [°C]	Event
1	325 - 305	20 - 5	Onset of Paraná Basin sedimentation
2	200 - 190	195 - 100	Possible initial plume rise and surface uplift based on stratigraphic records
3	160 - 155	165 - 70	Possible climax and collapse of plume head based on renewed sedimentation
4	140 - 125	240 - 115	Botucatu Sedimentation, Paraná-Etendeka flood basalts (Serra Geral Gr)
5	24 - 0	40 - 20	Final surface uplift

Figure C 3: The geological evolution model (GEM) for samples of the Brazilian Neoproterozoic basement for the northern Santos and central Florianopolis (upper), and the southern Laguna blocks (lower).

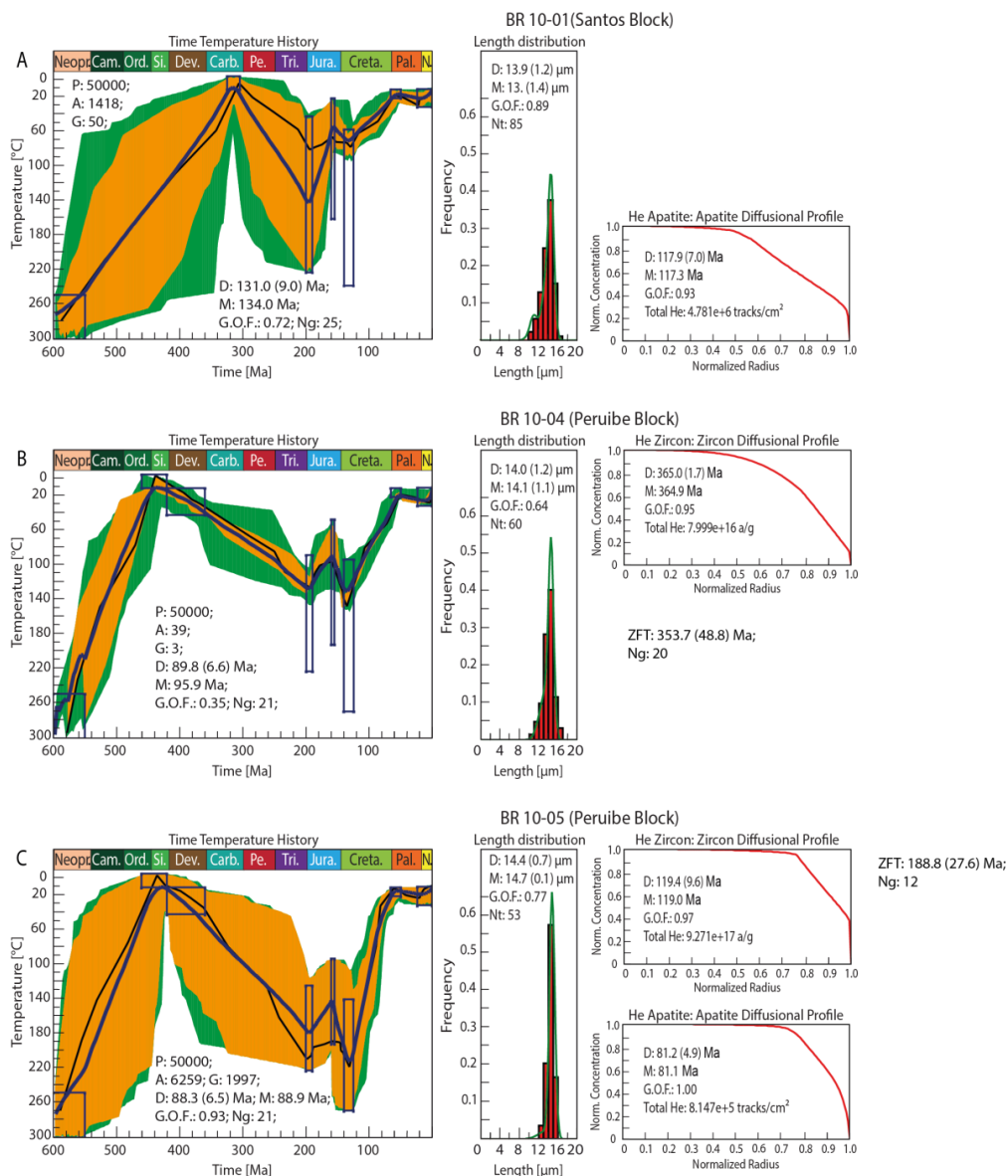
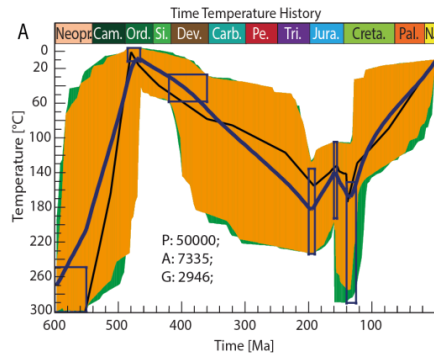
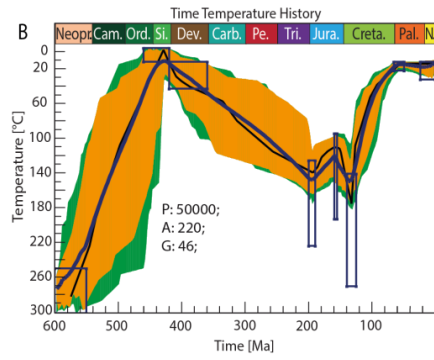
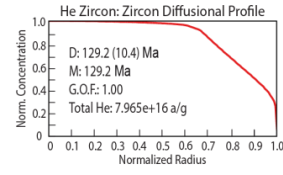


Figure C 4. 1: A) BR10-01, B) BR10-04, C) BR10-05. Time (t)-Temperature (T)-evolution paths with corresponding corrected confined spontaneous fission-track length-distribution (Lc) using the numerical software code HeFty® (Richard A. Ketcham). For every sample a standard amount of 50 000 paths were modeled. A: Accepted paths (green); G: Good paths (yellow); D: Dated age (with error); M: Modeled age; G.O.F.: Goodness of fit; Ng: Number of grains counted; Nt: Number of confined spontaneous fission-track lengths measured. The thin black path shows the “best-fit-path”, the thick blue path the “weighted-mean-path”.

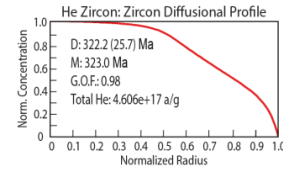




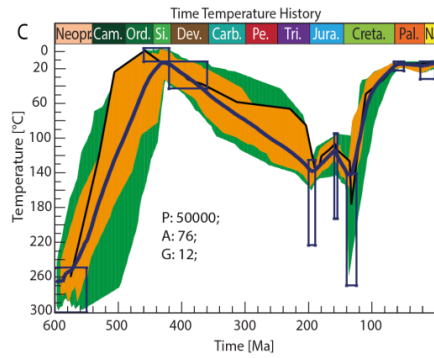
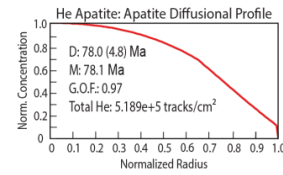
BR 09-01(Curitiba Block)



BR 10-12 (Curitiba Block)



ZFT: 349.5 (52.9) Ma;  
Ng: 16



BR 10-15 (Curitiba Block)

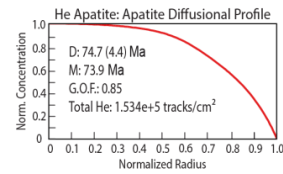
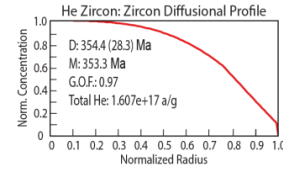
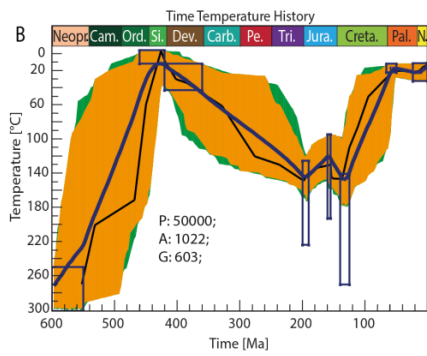
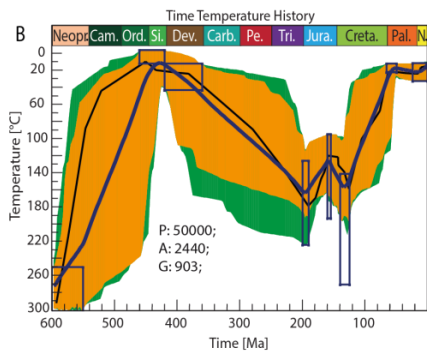
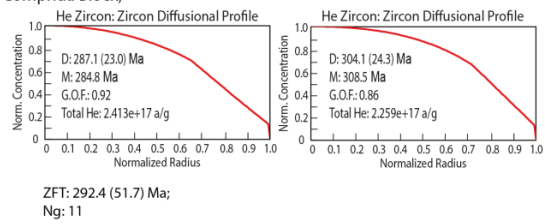


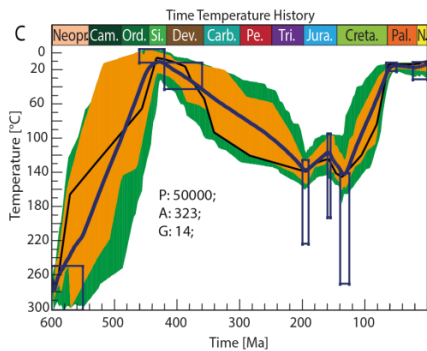
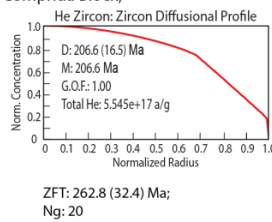
Figure C 4. 2: A) BR10-07, B) BR10-08, C) BR10-09, D) BR10-11. For further information, please see Figure C 4. 1.



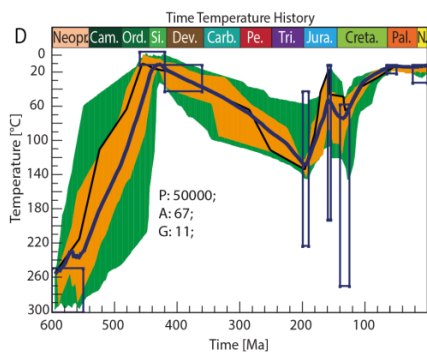
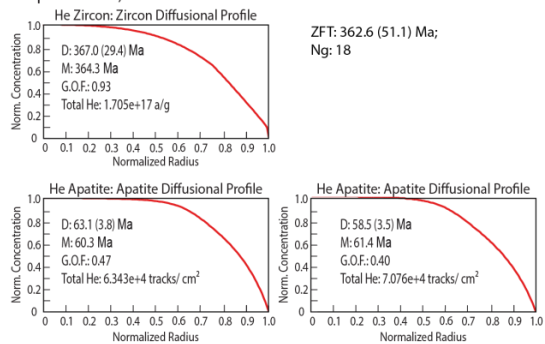
BR 10-07 (Ilha Comprida Block)



BR 10-08 (Ilha Comprida Block)



BR 10-09 (Ilha Comprida Block)



BR 10-11 (Ilha Comprida Block)

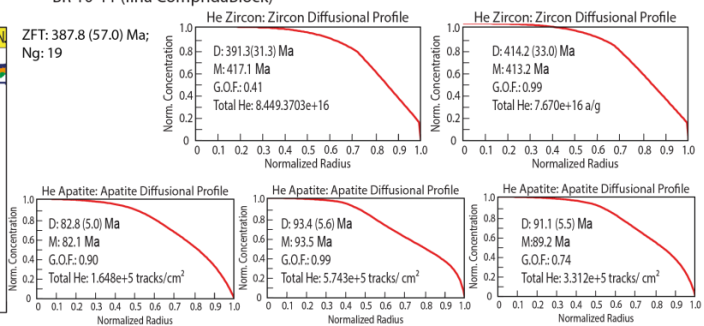


Figure C 4. 3: A) BR09-01, B) BR10-12, C) BR10-15. For further information, please see Figure C 4. 1.

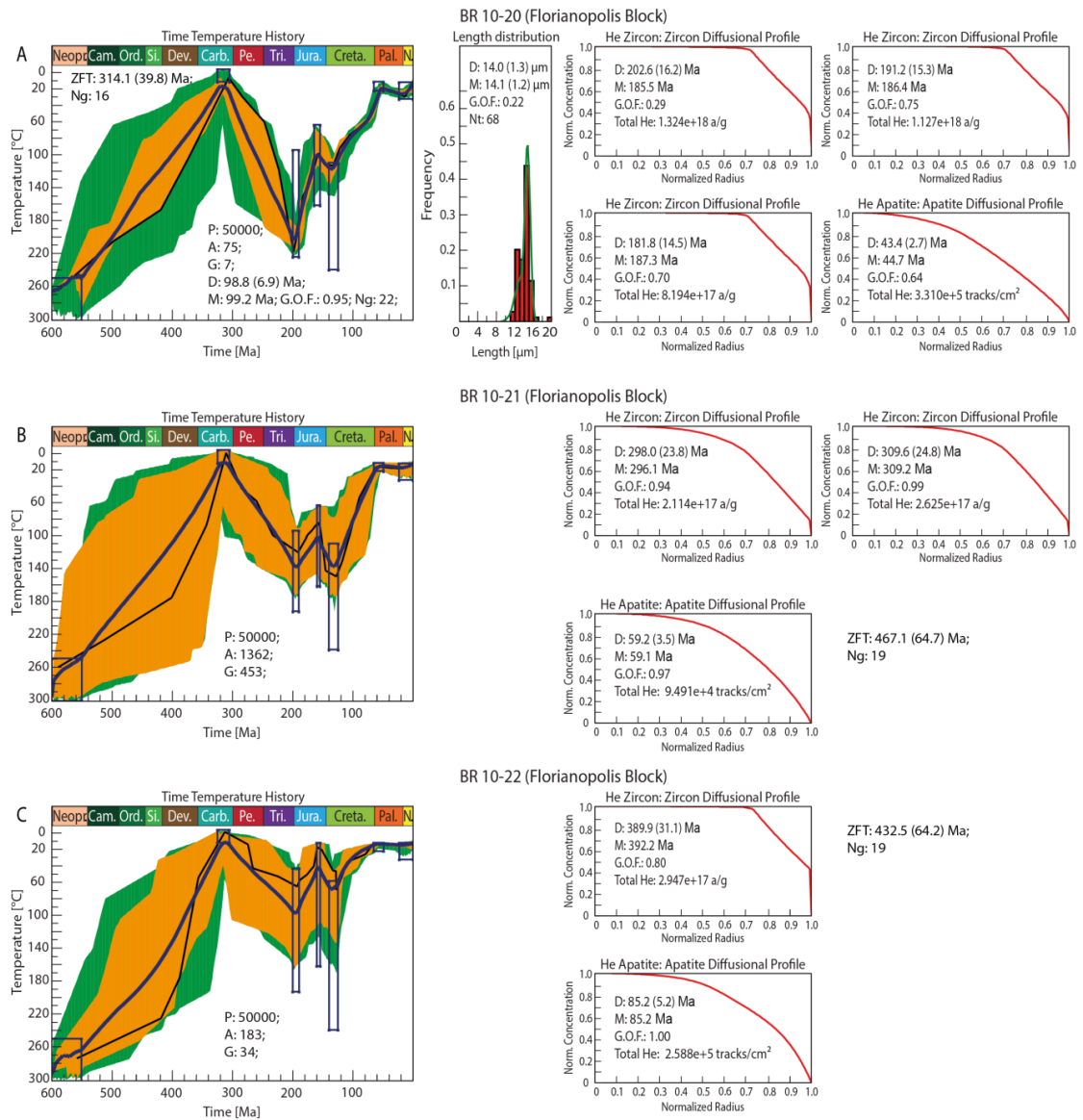


Figure C 4. 4: A) BR10-20, B) BR10-21, C) BR10-22. For further information, please see Figure C 4. 1.

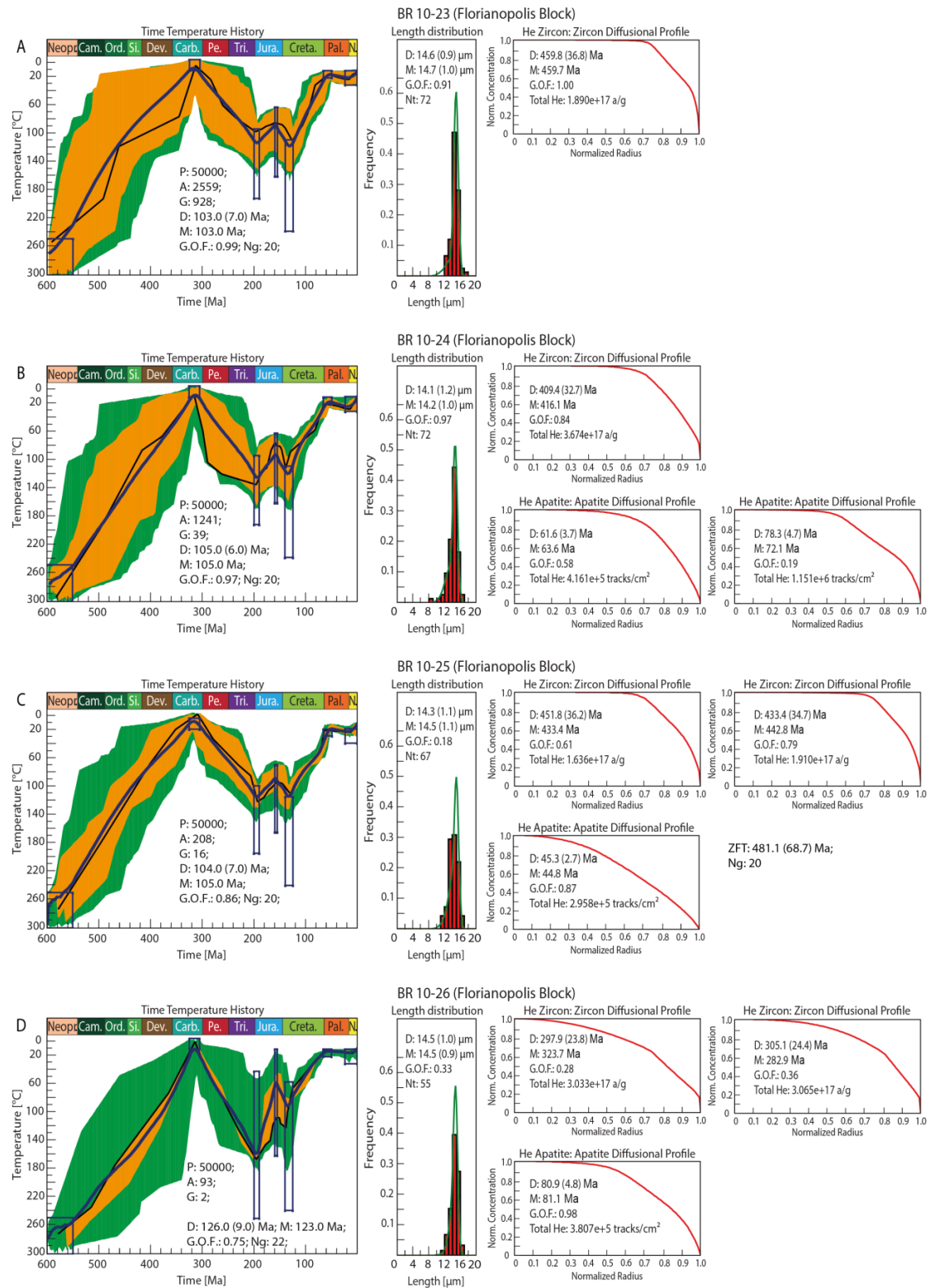


Figure C 4. 5: A) BR10-23, B) BR10-24, C) BR10-25, D) BR10-26. For further information, please see Figure C 4. 1.

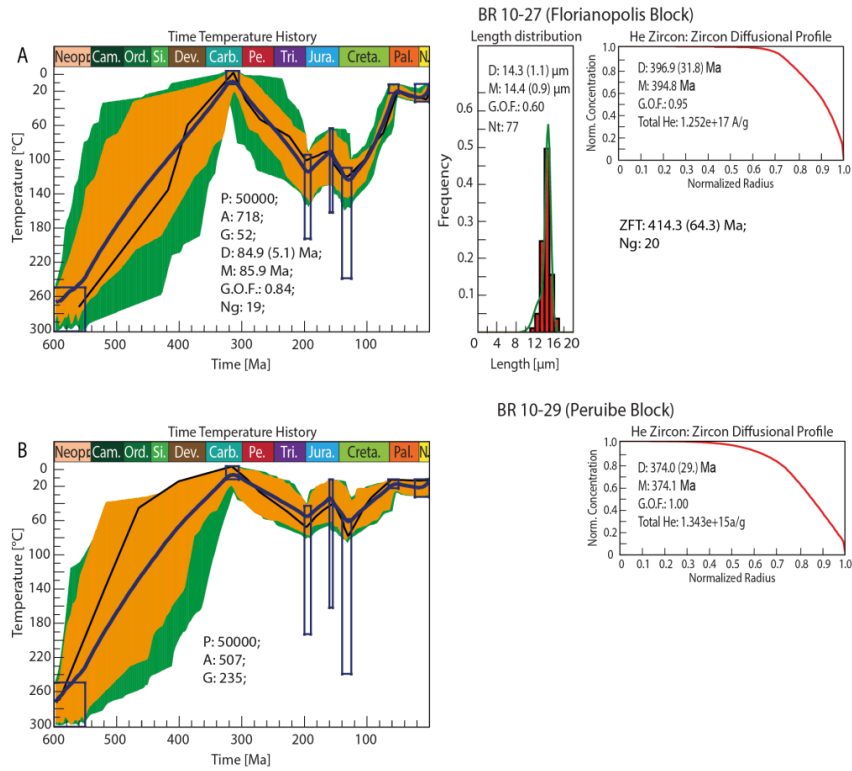


Figure C 4. 6: A) BR10-27, B) BR10-29. For further information, please see Figure C 4. 1.

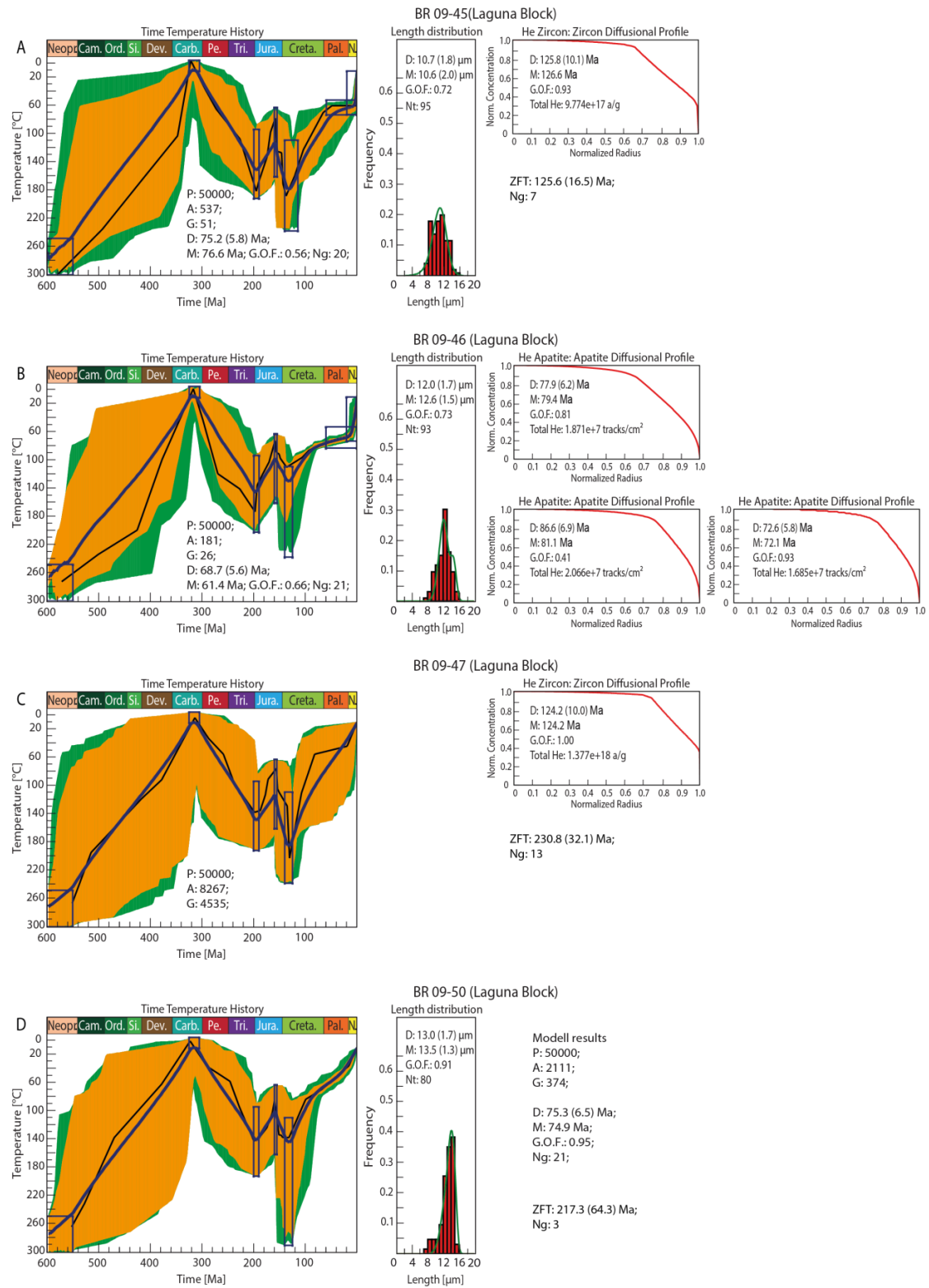


Figure C 4. 7: A) BR09-45, B) BR09-46, C) BR09-47, D) BR09-50. For further information, please see Figure C 4. 1.

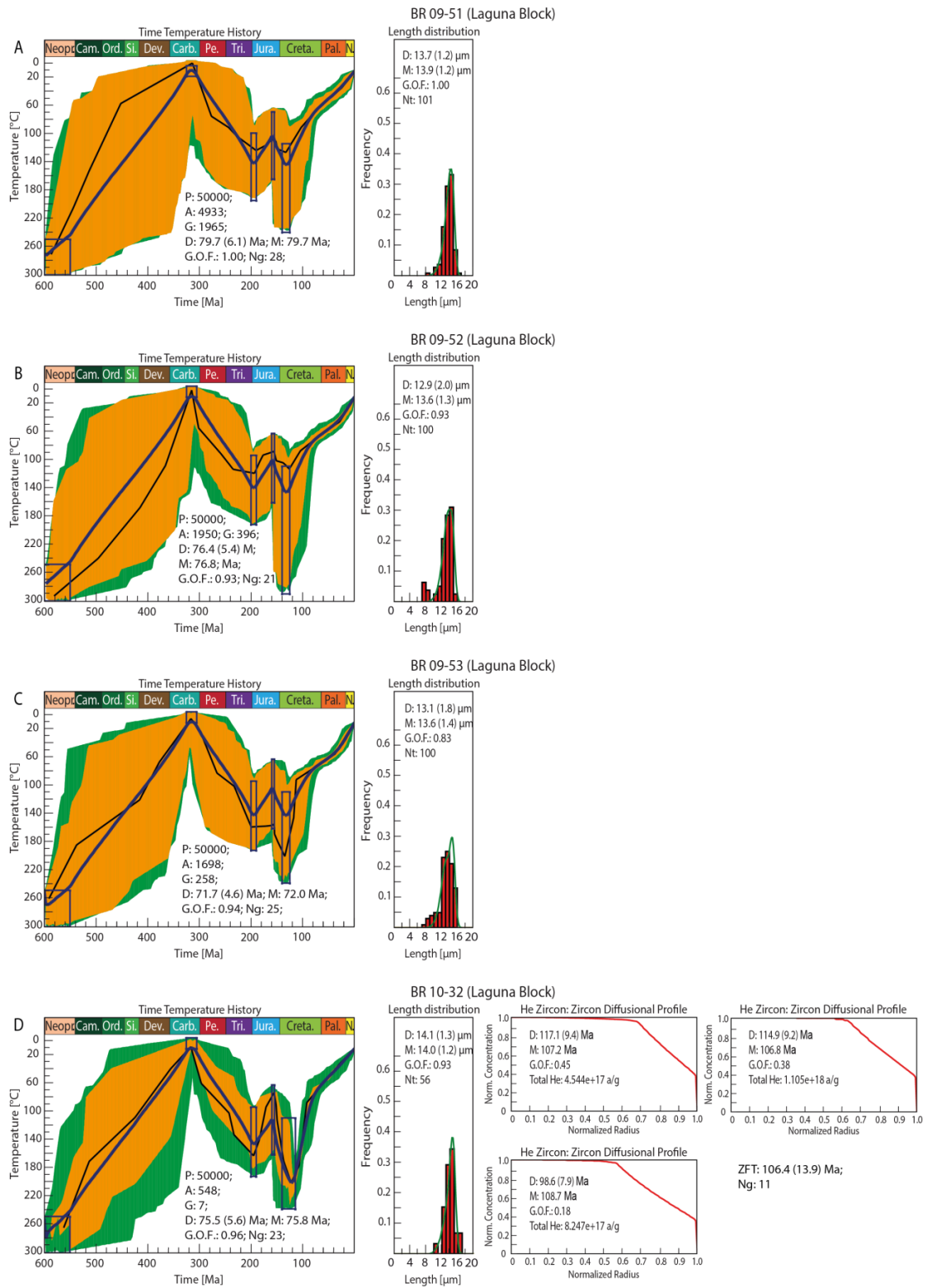


Figure C 4. 8: A) BR09-51, B) BR09-52, C) BR09-53, D) BR10-32. For further information, please see Figure C 4. 1.

## Additional references:

- Amaral**, G., Born, H., Hadler, J.C., Iunes, P.J., Kawashita, K., Machado Jr., D.L., Oliveira, E.P., Paulo, S.R., Tellos S., C.A., 1997. Fission-track analysis of apatite from São Francisco craton and Mesozoic alkaline-carbonatite complexes from central and south eastern Brazil. *Journal of South American Earth Sciences* 10, 285-294.  
[https://doi.org/10.1016/S0895-9811\(97\)00020-5](https://doi.org/10.1016/S0895-9811(97)00020-5)
- Baristeads**, N., Anka, Z., di Primio, R., Rodriguez, J.F., Marchal, D., Dominguez, F., 2013. New insights into the tectono-stratigraphic evolution of the Malvinas Basin offshore of the southernmost Argentinean continental margin. *Tectonophysics* 604, 280-295.  
<https://doi.org/10.1016/j.tecto.2013.06.009>
- Berti**, M., 2014. The evolution of marginal-marine systems of the Gamibberg formation, Karasburg Basin, Southern Namibia: Implications for Early-Middle Permian palaeogeography in South Western Gondwana. (MSc.) Dissertation. University of the Witwatersrand, Johannesburg, South Africa.
- Bicca**, M.M., Chemale Jr., F.F., Jelinek, A.R., Engelmann de Oliveira, C.H., Guadagnin, F., Armstrong, R., 2013. Tectonic evolution and provenance of the Santa Bárbara Group, Camaquã Mines region, Rio Grande do Sul, Brazil. *Journal of South American Earth Sciences* 48, 173-192.  
<https://doi.org/10.1016/j.jsames.2013.09.006>
- Borba**, A.W., Lima, E.F., Vignol-Lelarge, M.L.M., Mizusaki, A.M.P., 2002. Uplift and denudation of the Caçapava do Sul granitoids (southern Brazil) during the late Paleozoic and Mesozoic: constraints from apatite fission-track data. *Journal of South American Earth Sciences* 15, 683-692.  
[https://doi.org/10.1016/S0895-9811\(02\)00086-X](https://doi.org/10.1016/S0895-9811(02)00086-X)
- Borba**, A.W., Lima, E.F., Vignol-Lelarge, M.L.M., Mizusaki, A.M.P., Sparrenberg, I., Barros, C.E., 2003. Significance of Late Paleozoic Fission-track Ages in Volcanic Rocks from the Lavras Do Sul Region, Southernmost Brazil. *Gondwana Research* 6, 79-88.  
[https://doi.org/10.1016/S1342-937X\(05\)70645-6](https://doi.org/10.1016/S1342-937X(05)70645-6)
- Bray**, R., Lawrence, S., Swart, R., 1998. Source rock, maturity data indicates potential off Namibia. *Oil & Gas Journal* 1, 1-10.
- Brown**, R.W., Rust, D.J., Summerfield, M.A., Gleadow, A.J.W., de Wittm M.C.J., 1990. An early Cretaceous phase of accelerated erosion on the south-western margin of Africa: Evidence from apatite fission track analysis and the offshore sedimentary record. *Nuclear Tracks and Radiation Measurements* 17, 339-350.  
[https://doi.org/10.1016/1359-0189\(90\)90056-4](https://doi.org/10.1016/1359-0189(90)90056-4)
- Carmo**, I.O., 2005. Geocronological do intemperismo cenozoico no sudeste do Brasil. Ph.D. thesis. Instituto de Geociências, University of Rio de Janeiro.
- Carol**, E.S., Kurse, E.E., Pousa, J.L., 2010. Eco-hydrological role of deep aquifers in the Salado sedimentary basin in the Province of Buenos Aires, Argentina. *Environmental Earth Sciences* 60, 749-756.  
<https://doi.org/10.1007/s12665-009-0212-4>
- Catuneanu**, O., Wopfner, H., Eriksson, P.G., Cairncross, B., Rubidge, B.S., Smith, R.M.H., Hancox, P.J., 2005. The Karoo basins of south-central Africa. *Journal of African Earth Sciences* 43, 211-253.  
<https://doi.org/10.1016/j.jafrearsci.2005.07.007>
- Cogné**, N., Gallagher, K., Cobbold, P.R., 2011. Post-rift reactivation of the onshore margin of southeast Brazil: Evidence from apatite (U–Th)/He and fission-track data. *Earth and Planetary Science Letters* 309, 118-130.  
<https://doi.org/10.1016/j.epsl.2011.06.025>
- Cogné**, N., Gallagher, K., Cobbold, P.R., Riccomini, C., Gautheron, C., 2012. Post break-up tectonics in southeast Brazil from thermochronological data and combined inverse forward thermal history modelling. *Journal of Geophysical Research* 117, B 11413.  
<https://doi.org/10.1029/2012JB009340>



- Contreras, J., Zühlke, R., Bowman, S., Bechstädt, T.,** 2010. Seismic stratigraphy and subsidence analysis of the southern Brazilian margin (Campos, Santos and Pelotas basins). *Marine and Petroleum Geology* 27, 1952-1980.  
<https://doi.org/10.1016/j.marpetgeo.2010.06.007>
- Curvo, E.A.C., Tello S., C.A., Carter, A., Dias, A.N.C., Soares, C.J., Nakasuga, W.M., Resende, R.S., Gomes, M.R., Alencar, I., Hadler, J.C.,** 2013. Zircon fission track and U-Pb dating methods applied to São Paulo and Taubaté Basins located in the southeast Brazil. *Radiation Measurements* 50, 172-180.  
<https://doi.org/10.1016/j.radmeas.2012.07.015>
- Crosby, A.G., Fishwick, S., White, N.,** 2010. Structure and evolution of the intracratonic Congo Basin. *Geochemistry, Geophysics, Geosystems* 11, No. 6, 22 p.  
<https://doi.org/10.1029/2009GC003014>
- Daniels, K.A., Bastow, I.D., Keir, D., Sparks, R.S.J., Menand, T.,** 2014. Thermal models of dyke intrusion during development of continent-ocean transition. *Earth and Planetary Sciences Letters* 385, 145-153.  
<https://doi.org/10.1016/j.epsl.2013.09.018>
- De Vera, J., Granado, P., McClay, K.,** 2010. Structural evolution of the Orange Basin gravity-driven system, offshore Namibia. *Marine and Petroleum Geology* 27, 223-237.  
<https://doi.org/10.1016/j.marpetgeo.2009.02.003>
- Doranto-Tiritan, C., Hackspacher, P.C., Ribeiro, M.C.S., Glasmacher, U.A., de Souza, D.H.,** 2014. Evolução do relevo da região do planalto de Poços de Caldas (SP/MG) baseado em dados de termocronológica de baixa temperatura e modelagem termocinematica 3D. *Revista Brasileira de Geomorfologia* 15, 291-310.
- Eldracher (former Menges), D.** Long-term subsidence, cooling and exhumation history along the South Atlantic passive margin in NW-Namibia. Ph.D. thesis, Heidelberg University (in prep.).
- Engelmann de Oliveira, C.H., Jelinek, A.R., Chemale Jr., F., Bernet, M.,** 2016. Evidence of post-Gondwana breakup in Southern Brazilian Shield: Insights from apatite and zircon fission track thermochronology. *Tectonophysics* 666, 173-187.  
<https://doi.org/10.1016/j.tecto.2015.11.005>
- Engelmann de Oliveira, C.H., Jelinek, A.R., Chemale Jr., Cupertino, J.A.,** 2016. Thermotectonic history of the southeastern Brazilian margin: Evidence from apatite fission track data of the offshore Santos Basin and continental basement. *Tectonophysics* 685, 21-34.  
<https://doi.org/10.1016/j.tecto.2016.07.012>
- Ernesto, M., Raposo, M.I.B., Marques, L.S., Renne, P.R., Diogo, L.A., de Min, A.,** 1999. Paleomagnetism, geochemistry and  $^{40}\text{Ar}/^{39}\text{Ar}$  dating of the North-eastern Paraná Magmatic Province: tectonic implications. *Journal of Geodynamics* 28, 321-340.  
[https://doi.org/10.1016/S0264-3707\(99\)00013-7](https://doi.org/10.1016/S0264-3707(99)00013-7)
- Florisbal, L.M., Heaman, L.M., de Assis Janasi, V., Bitencourt, M.F.,** 2014. Tectonic significance of the Florianópolis Dyke Swarm, Paraná-Etendeka Magmatic Province: A reappraisal based on precise U-Pb dating. *Journal of Volcanology and Geothermal Res.* 289, 140-150.  
<https://doi.org/10.1016/j.jvolgeores.2014.11.007>
- Flowers, R.M., Bowring, S.A., Reiners, P.W.,** 2009. Low long-term erosion rates and extreme continental stability documented by ancient (U-Th)/He dates. *Geology* 34, 925-928.  
<https://doi.org/10.1130/G22670A.1>
- Franco-Magalhães, A. O. B., Hackspacher, P. C., Glasmacher, U. A., Saad, A. R.,** 2010. Rift to post-rift evolution of a "passive" continental margin: The Ponta Grossa Arch, SE Brazil. *International Journal of Earth Sciences (Geologische Rundschau)* 99, 1599-1613.  
<https://doi.org/10.1007/s00531-010-0556-8>
- Franco-Magalhães, A. O. B., Cuglieri, M.A.A., Hackspacher, P. C., Saad, A. R.,** 2014. Long-term landscape evolution and post-rift reactivation in the southeastern Brazilian passive continental margin: Taubaté basin. *International Journal of Earth Sciences (Geologische Rundschau)* 103, 441-453.  
<https://doi.org/10.1007/s00531-013-0967-4>

- Gallagher**, K., Hawkesworth, C.J., Mantovani, M.S.M., 1994. The denudation history of the offshore continental margin of SE Brazil inferred from apatite fission-track data. *Journal of Geophysical Research* 99, 18117-18145.  
<https://doi.org/10.1029/94JB00661>
- Gallagher**, K., Hawkesworth, C.J., Mantovani, M.S.M., 1995. Denudation, fission track analysis and the long-term evolution of passive margin topography: application to the southeast Brazilian margin. *Journal of South American Earth Sciences* 8, 65-77.  
[https://doi.org/10.1016/0895-9811\(94\)00042-Z](https://doi.org/10.1016/0895-9811(94)00042-Z)
- Gibson**, S.A., Thompson, R.N., Day, J.A., 2006. Timescales and mechanism of plume-lithosphere interactions:  $^{40}\text{Ar}/^{39}\text{Ar}$  geochronology and geochemistry of alkaline igneous rocks from the Paraná-Etendeka large igneous province. *Earth and Planetary Science Letters* 251, 1-17.  
<https://doi.org/10.1016/j.epsl.2006.08.004>
- Guedes**, E., Heilbron, M., Valeriano, C. M., Almeida, J.C.H., Szatmari, P., 2016. Evidence of Gondwana early rifting process recorded by Resende-Ilha Grande Dike Swarm, southern Rio de Janeiro, Brazil. *Journal of South American Earth Sciences* 67, 11-24.  
<https://doi.org/10.1016/j.jsames.2016.01.004>
- Guenther**, W.R., Reiners, P.W., Ketcham, R.A., Nasdala, L., Giester, G., 2013. Helium diffusion in natural zircon: Radiation damage, anisotropy, and the interpretation of zircon (U-Th)/He thermochronology: *American Journal of Science* 313, 145-198. 10.2475/03.2013.01
- Green**, P.F., Machado, V., 2015. Pre-rift and syn-rift exhumation. Post-rift subsidence and exhumation of the onshore Namibe Margin of Angola revealed from apatite fission track analysis. Geological Society, London, Special Publications 438, 20 p.  
<https://doi.org/10.1144/SP438.2>
- Green**, P.F., Duddy, I.R., Japsen, P., Bonow, J.M., Malan, J.A., 2017. Post-breakup burial and exhumation of the southern margin of Africa. *Basin Research* 29, 96-127.  
<https://doi.org/10.1016/j.gr.2017.03.007>
- Guiraud**, M., Buta-Neto, A., Quesne, D., 2010. Segmentation and differential post-rift uplift at the Angola margin as recorded by the transform-rifted Benguela and oblique-to-orthogonal-rifted Kwanza basins. *Marine and Petroleum Geology* 27, 1040-1068.  
<https://doi.org/10.1016/j.marpetgeo.2010.01.017>
- Haack**, U., Martin, H., 1983. Geochronology of the Damara Orogen - A review. *Intracontinental Fold Belts*, ed. by Martin, H. and Eder, F.W., Berlin, Heidelberg, Springer.  
[https://doi.org/10.1007/978-3-642-69124-9\\_36](https://doi.org/10.1007/978-3-642-69124-9_36)
- Hackspacher**, P.C., Ribeiro, L.F.B., Ribeiro, M.C.S., Fetter, A.H., Hadler, N.J.C., Tello Saenz, C.A., Dantas, E.L., 2004. Consolidation and break-up of the South American Platform in south-eastern Brazil: tectono-thermal and denudation histories. *Gondwana Res* 1, 91-101.
- Hackspacher**, P.C., Tello S., S.C., 2006. Thermal History at the Mantiqueira Province, Southeastern Brasil: Modeling with fission track on zircon. *South American Symposium on Isotope Geology*, V. Punta del Este, Uruguay, Short Papers, 105-107.
- Hackspacher**, P.C., Godoy, D.F., Ribeiro, L.F.B., Hadler, N.J.C., Franco, A.O.B., 2007. Modelagem térmica e geomorfologia da borda sul do cráton do São Francisco: termocronologia por traços de fissão em apatita. *Revista Brasileira de Geociências* 37, 928-938.
- Haddon**, I.G., 2005. The sub-Kalahari geology and tectonic evolution of the Kalahari Basin, Southern Africa. Dissertation. University of the Witwatersrand, Johannesburg, South Africa.
- Hamza**, V.M., Cardoso, R.A., Gomes, A.J.L., 2005. Gradiente e fluxo geotérmico na região sudeste: indícios de calor residual do magmatismo alcalino e implicações para maturação térmica de sedimentos na plataforma continental. 3rd Simpósio de Vulcanismo e Ambientes Associados, Cabo Frio, SBG, Anais, 1, 319-324.

- Harman**, R., Gallagher, K., 1998. Accelerated denudation and tectonic/geomorphic reactivation of the cratons of northeastern Brazil during the Late Cretaceous. *Journal of Geophysical Research* 103, NO. B11, 27,091-27,105.  
<https://doi.org/10.1029/98JB02524>
- Hartmann**, L.A., Lopes, W.R., Savian, J.F., 2016a. Integrated evaluation of the geology, aerogammaspectrometry and aeromagnetometry of the Sul-Riograndense Shield, southernmost Brazil. *Anais da Academia Brasileira de Ciencias* 88, 75-92.  
<http://dx.doi.org/10.1590/0001-3765201520140495>
- Hartmann**, L.A., Savian, J.F., Lopes, W.R., 2016b. Airborne geophysical characterization of geotectonic relationships in the southern Ribeira Belt, Luís Alves Craton, and northern Dom Feliciano Belt, Brazilian Shield. *International Geology Review* 58, 471-488.  
<https://doi.org/10.1080/00206814.2015.1089424>
- Hiruma**, S.T., Riccomini, C., Modenesi-Gauttieri, M.C., Hackspacher, P.C., Neto, J.C.H., Franco-Magalhaes, A.O.B., 2010. Denudation history of the Bocaina Plateau, Serra do Mar, southeastern Brazil: Relationships to Gondwana break-up and passive margin development. *Gondwana Research* 18, 674-687.  
<https://doi.org/10.1016/j.gr.2010.03.001>
- Hueck**, M., Dunkl, I., Heller, B., Basei, M.A.S., Siegesmund, S., 2018. (U-Th)/He Thermochronology and Zircon Radiation Damage in the South American Passive Margin: Thermal Overprint of the Paraná LIP? *Tectonics* 37, 18 p.  
<https://doi.org/10.1029/2018TC005041>
- Jackson**, M.P.A., Hudec, M.R., 2005. The great West African Tertiary coastal uplift: Fact or fiction? A perspective from the Angolan divergent margin. *Tectonics*, 24, 23 p.  
<https://doi.org/10.1029/2005TC001836>
- Jelinek**, A.R., Chemale Jr., F., van der Beek, P.A., Guadagnin, F., Cupertino, J.A., Viana, A., 2014. Denudation history and landscape evolution of the northern East-Brazilian continental margin from apatite fission-track thermochronology. *Journal of South American Earth Sciences* 54, 158-181.  
<https://doi.org/10.1016/j.jsames.2014.06.001>
- Jerram**, D.A., Sharp, I.R., Torsvik, T.H., Poulsen, R., Watton, T., Freitag, U., Halton, A., Sherlock, S.C., Malley, J.A.S., Finley, A., Roberge, J., Swart, R., Puigdefabregas, C., Ferreira, C.H., Machado, V., 2019. Volcanic constraints on the unzipping of Africa from South America: Insights from new geochronological controls along the Angola margin. *Tectonophysics* 760, 252-266.  
<https://doi.org/10.1016/j.tecto.2018.07.027>
- Johnson**, M.R., Van Vuuren, C.J., Hegenberger, W.F., Key, R., Shoko, U., 1996. Stratigraphy of the Karoo Supergroup in southern Africa: an overview. *Journal of African Earth Sciences* 23, 3.15.  
[https://doi.org/10.1016/S0899-5362\(96\)00048-6](https://doi.org/10.1016/S0899-5362(96)00048-6)
- Kadima**, R., Delvaux, D., Sebagenzi, N.S., Tack, L., Kabeya, S.M., 2011. Structure and geological history of the Congo Basin: an integrated interpretation of gravity, magnetic and reflection seismic data. *Basin Research* 23, 449-527.  
<https://doi.org/10.1111/j.1365-2117.2011.00500.x>
- Ketcham**, R.A., 2005. Forward and Inverse Modelling of low-temperature thermochronometry data. *Rev. Min. Geoch.* 58, 275-314.  
<https://doi.org/10.2138/rmg.2005.58.11>
- Ketcham**, R.A., Carter, A., Donelick, R.A., Barbarand, J., Hurford, A.J., 2007 a. Improved measurements of fission-track annealing in apatite. *Am. Mineral* 92, 789-798.  
<https://doi.org/10.2138/am.2007.2280>
- Ketcham**, R.A., Carter, A., Donelick, R.A., Barbarand, J., Hurford, A.J., 2007 b. Improved modelling of fission-track annealing in apatite. *Am. Mineral* 92, 799-810.  
<https://doi.org/10.2138/am.2007.2281>

- Ketcham, R.A., Donelick, R.A., Balestrieri, M.L., Zattin, M., 2009.** Reproducibility of apatite fission-track length data and thermal history reconstruction. *Earth Planet Science Letter* 284, 504-515. <https://doi.org/10.1016/j.epsl.2009.05.015>
- Ketcham, R.A., 2017.** HeFTy version 1.9.3, Manual.
- Kokogían, D.A., Fernández Seveso, F., Mosquere, A., 1993.** Las secuencias sedimentarias triásicas. *Geología y Recursos Naturales de Mendoza, XII Congreso Geológico Argentino y II Congreso de Exploración de Hidrocarburos (Mendoza), Relatorio I*, 65-78.
- Kollenz, S., 2015.** Long-term landscape evolution, cooling and exhumation history of the South American passive continental margin in NE Argentina & SW Uruguay. Ph.D. thesis, Institute of Earth Sciences, Heidelberg University.
- Kollenz, S., Glasmacher, U.A., Rosello, E.A., Stockli, D.F., Schad, S., Pereyra, R.E., 2016.** Thermochronological constraints on the Cambrian to recent geological evolution of the Argentine passive continental margin. *Tectonophysics* 716, 182-203. <https://doi.org/10.1016/j.tecto.2016.11.019>
- Kounov, A., Viola, G., de Wit, M.J., Andreoli, M., 2009.** Denudation along the Atlantic passive margin: New insights from apatite fission-track analysis on the western coast of South Africa. *Geological Society London Special Publications* 324, 287-306. <https://doi.org/10.1144/SP324.19>
- Kounov, A., Viola, G., de Wit, M.J., Andreoli, M., 2008.** A Mid Cretaceous paleo-Karoo River valley across the Knersvlakte plain (northwestern coast of South Africa): Evidence from apatite fission-track analysis. *Southern African Journal of Geology* 111, 409-420. <https://doi.org/10.2113/gssajg.111.4.409>
- Kounov, A., Viola, G., Dunkl, I., Frimmel, H.E., 2013.** Southern African perspectives on the long-term morpho-tectonic evolution of cratonic interiors. *Tectonophysics* 601, 177-191. <https://doi.org/10.1016/j.tecto.2013.05.009>
- Light, M.P.R., Maslanyj, M.P., Banks, N.L., 1992.** Neo geophysical evidence for extensional tectonics on the divergent margin offshore Namibia. *Geological Society, London, Special Publications* 68, 257-270. <https://doi.org/10.1144/GSL.SP.1992.068.01.16>
- Light, M.P.R., Maslanyj, M.P., Greenwood, R.J., Banks, N.L., 1993.** Seismic sequence stratigraphy and tectonics offshore Namibia. *Tectonics and Seismic Sequence Stratigraphy. Geological Society Special Publications* 71, 163-191. <https://doi.org/10.1144/GSL.SP.1993.071.01.08>
- Luft, F.F., Chemale Jr., F., Lelarge, M.L.M.V., Luft Jr, J.L., 2005.** Phanerozoic thermo-tectonic evolution of NW Namibia and implications on Walvis Basin. *Short Papers - IV South American Symposium on Isotope Geology*.
- Mackintosh, V., Kohn, B., Gleadow, A., Tian, Y., 2017.** Phanerozoic morphotectonic evolution of the Zimbabwe Craton: Unexpected outcomes from a multiple low-temperature thermochronology study. *Tectonics* 36, 2044-2067. <https://doi.org/10.1002/2017TC004703>
- McMaster, M., Almeida, J., Heilbron, M., Guedes, E., Mane, M.A., Linus, J.H., 2019.** Characterisation and tectonic implications of the Early Cretaceous, Skeleton Coast dyke Swarm, NW Namibia. *Journal of African Earth Sciences* 150, 319-336. <https://doi.org/10.1016/j.jafrearsci.2018.11.010>
- Marcano, G., Anka, Z., di Primio, R., 2013.** Major controlling factors on hydrocarbon generation and leakage in South Atlantic conjugate margins: A comparative study of Colorado, Orange, Campos, Lower Congo basins. *Tectonophysics* 133, 19 p. <https://doi.org/10.1016/j.tecto.2013.02.004>
- Marzioli, A., Melluso, V. M., Renne, P.R., Sgrosso, I., D'Antonio, M., Morais, L.D., Morais, E.A.A., Ricci, G., 1999.** Geochronology and petrology of Cretaceous basaltic magmatism in the Kwanza basin (western Angola), and relationships with the Paraná-Etendeka continental flood basalt province. *Journal of Geodynamics* 28, 341-356. [https://doi.org/10.1016/S0264-3707\(99\)00014-9](https://doi.org/10.1016/S0264-3707(99)00014-9)

- Morais Neto**, J.M., Green, P.F., Karner, G.D., Alkmim, F.F., 2008. Age of the Serra do Martin Formation, Borborema Plateau, northeastern Brazil: constraints from apatite and zircon fission track analysis. *B. Geoci. Petrobras*, Rio de Janeiro 16, 23-52.
- Morais Neto**, J.M., Hegarty, K.A., Karner, G.D., Alkmim, F.F., 2009. Timing and mechanisms for the generation and modification of the anomalous topography of the Borborema Province, northeastern Brazil. *Marine and Petroleum Geology* 26, 1070-1086.  
<https://doi.org/10.1016/j.marpetgeo.2008.07.002>
- Naipauer**, M., Tunik, M., Marques, J.C., Vera, E.A.R., Vujovich, G.I., Pimentel, M.M., Ramos, V.A., 2014. U-Pb detrital zircon ages of Upper Jurassic continental successions: implications for the provenance and absolute age of the Jurassic-Cretaceous boundary in the Neuquén Basin. *Geological Society, London, Special Publications* 399, 131-154.  
<https://doi.org/10.1144/SP399.1>
- Nicolai**, C. von, Scheck-Wunderoth, M., Warsitzka, M., Schodt, N., Andersen, J., 2013. The deep structure of the South Atlantic Kwanza Basin - Insights from 3D structural and gravimetric modelling. *Tectonophysics* 604, 139-152.  
<https://doi.org/10.1016/j.tecto.2013.06.016>
- Noble**, W. P. (1997), Post Pan African tectonic evolution of eastern Africa: An apatite fission track study, (PhD thesis). Melbourne, Australia: La Trobe University.
- Nxumalo**, V., 2011. Stratigraphy and basin modelling of the Gemsbok sub-basin (Karoo supergroup) of Botswana and Namibia. (MSc.) Dissertation. University of the Witwatersrand, Johannesburg, South Africa.
- Owen-Smith**, T.M., Ashwal, L.D., Sudo, M., Trumbull, R.B., 2017. Age and Petrogenesis of the Doros Complex, Namibia, and implications for Early Plume-derived Melts in the Paraná-Etendeka LIP. *Journal of Petrology* 58, 423-442.  
<https://doi.org/10.1093/petrology/egx021>
- Owen-Smith**, T.M., Ganerod, M., van Hinsbergen, D.J.J., Gaina, C., Ashwal, L.D., Torsvik, T.H., 2019. Testing Early Cretaceous Africa-South America fits with new paleomagnetic data from the Etendeka Magmatic Province (Namibia). *Tectonophysics* 760, 23-35.  
<https://doi.org/10.1016/j.tecto.2017.11.010>
- Pangaro**, F., Ramos, V.A., 2012. Paleozoic crustal blocks of onshore and offshore central Argentina: New pieces of the southwestern Gondwana collage and their role in the accretion of Patagonia and the evolution of Mesozoic south Atlantic sedimentary basins. *Marine and Petroleum Geology* 37, 162-183.  
<https://doi.org/10.1016/j.marpetgeo.2012.05.010>
- Peate**, D.W., 1997. The Paraná-Etendeka Province. Large Igneous Provinces: Continental, Oceanic, and Planetary Flood Volcanism, pp. 217.
- Phiri**, C., Wang, P., Nyambe, I.A., 2016. Geology and potential hydrocarbon play system of Lower Karoo Group in the Maamba Coalfield Basin, southern Zambia. *Journal of African Earth Sciences* 118, 245-262.  
<https://doi.org/10.1016/j.jafrearsci.2016.03.006>
- Raab**, M.J., Brown, R.W., Gallagher, K., Carter, A., Weber, K., 2002. Late Cretaceous reactivation of major crustal shear zones in northern Namibia: constraints from apatite fission track analysis. *Tectonophysics* 349, 75-92.  
[https://doi.org/10.1016/S0040-1951\(02\)00047-1](https://doi.org/10.1016/S0040-1951(02)00047-1)
- Raab**, M.J., Brown, R.W., Gallagher, K., Weber, K., Gleadow, A.J.W., 2005. Denudational and thermal history of the Early Cretaceous Brandberg and Kenyena igneous complexes on Namibia's Atlantic passive margin. *Tectonics* 24, 15 p.  
<https://doi.org/10.1029/2004TC001688>
- Rosetti**, L., Lima, E.F., Waichel, B.L., Hole, M.J., Simões, M.S., Scherer, C.M.S., 2018. Lithostratigraphy and volcanology of the Serra Geral Group, Paraná-Etendeka Igneous Province in Southern Brazil: Towards a formal stratigraphical framework. *Journal of Volcanology and Geothermal Research* 355, 98-114.  
<https://doi.org/10.1016/j.jvolgeores.2017.05.008>

- Sacek**, V., and Ussami, N., 2013. Upper mantle viscosity and dynamic subsidence of curved continental margins. *Nature Communications* 4:2036, 6 p.  
<https://doi.org/10.1038/ncomms3036>
- Scarselli**, N., McClay, K., Elders, C., 2016. Seismic geomorphology of cretaceous megaslides offshore Namibia (Orange Basin): Insights into segmentation and degradation of gravity-driven linked systems. *Marine and Petroleum Geology* 75, 151-180.  
<https://doi.org/10.1016/j.marpetgeo.2016.03.012>
- Schmidt**, S., 2004. The Petroleum Potential of the Passive Continental Margin of South-Western Africa - A Basin Modelling Study. Dissertation, RWTH Aachen, Germany, 182 p.
- Schröder**, S., Ibekwe, A., Saunders, M., Dixon, R., Fisher, A., 2015. Algal-microbial carbonates of the Namibe Basin (Albian, Angola): Implications for microbial carbonate mound development in the South Atlantic. *Petroleum Geosciences* 22, 2014-083. <https://doi.org/10.1144/petgeo2014-083>
- Scotese**, C.R., Golonka, J., 1992. Paleogeographic Atlas. Paleomap Projekt. Department of Geology, U. Texas at Arlington.  
[https://doi.org/10.1016/S0899-5362\(98\)00084-0](https://doi.org/10.1016/S0899-5362(98)00084-0)
- Scotese**, C.R., Boucot, A.J., McKerrow, W.S., 1999. Gondwanan paleogeography and paleoclimatology. *Journal of African Earth Sciences* 28 (1), 99-114.  
[https://doi.org/10.1016/S0899-5362\(98\)00084-0](https://doi.org/10.1016/S0899-5362(98)00084-0)
- Shone**, R.W., Booth, P.W.K., 2005. The Cape Basin, South Africa: A review. *Journal of African Earth Sciences* 43, 196-210.  
<https://doi.org/10.1016/j.jafrearsci.2005.07.013>
- Silva**, B.V., Hackspacher, P.C., Ribeiro, M.C.S., Glasmacher, U.A., Gonçalves, A.O., Doranti-Tiritan, C., Godoy, D.F., Constantino, R.R., 2019. Evolution of the Southwestern Angolan Margin: episodic burial and exhumation is more realistic than long-term denudation. *International Journal of Earth Sciences* 108, 89-113.  
<https://doi.org/10.1007/s00531-018-1644-4>
- Souza de**, D.H., Hackspacher, P.C., Doranti-Tiritan, C., Godoy, D.F., 2014. Comparação da dinâmica evolutiva em longo e curto prazo, entre o planalto de Poços de Caldas e o planalto de São Pedro de Caldas plateau. *Revista Brasileira de Geomorfologia* 16, 251-272.
- Stanley**, J.R., Flowers, R.M., Bell, D.R., 2013. Kimberlite (U-Th)/He dating links surface erosion with lithospheric heating, thinning, and metasomatism in the southern African Plateau. *Geology* 41, 1243-1246.  
[https://doi.org/10.1016/0899-5362\(91\)90048-4](https://doi.org/10.1016/0899-5362(91)90048-4)
- Stewart**, K., Turner, S., Kelley, S., Hawkesworth, C., Kirsteins, Linda, Mantovani, M., 1996. 3-D, <sup>40</sup>Ar-<sup>39</sup>Ar geochronology in the Paraná continental flood basalt province. *Earth and Planetary Science Letter* 143, 95-109.  
[https://doi.org/10.1016/0012-821X\(96\)00132-X](https://doi.org/10.1016/0012-821X(96)00132-X)
- Stica**, J.M., Zalan, P.V., Ferrari, A.L., 2014. The evolution of rifting on the volcanic margin of the Pelotas Basin and the contextualization of the Paraná-Etendeka LIP in the separation of Gondwana in the South Atlantic. *Marine and Petroleum Geology* 50, 1-21.  
<https://doi.org/10.1016/j.marpetgeo.2013.10.015>
- Tello Saenz**, C.A., Hackspacher, P.C., Hadler Neto, J.C., Lunes, P.J., Guedes, S., Ribeiro, L.F.B., Paulo, S.R., 2003. Recognition of Cretaceous, Paleocene, and Neogene tectonic reactivation through apatite fission-track analysis in Precambrian areas of southeast Brazil: association with the opening of the south Atlantic Ocean. *Journal of South American Earth Sciences* 15, 765-774.  
[https://doi.org/10.1016/S0895-9811\(02\)00131-1](https://doi.org/10.1016/S0895-9811(02)00131-1)
- Thompson**, R.N., Gibson, S.A., Dicking, A.P., Smith, P.M., 2001. Early Cretaceous Basalt and Picrite Dykes of the Southern Etendeka Region, NW Namibia: Windows into the Role of the Tristan Mantle Plume in Paraná-Etendeka Magmatism. *Journal of Petrology* 42, 2049-2081.  
<https://doi.org/10.1093/petrology/42.11.2049>
- Tinker**, J., de Wit, M., Brown, R., 2008. Mesozoic exhumation of the southern Cape, South Africa, quantified using apatite fission track thermochronology. *Tectonophysics* 455, 77-93.  
<https://doi.org/10.1016/j.tecto.2007.10.009>

- Travassos**, R.P., 2014. Interpretação estrutural regional do escudo Sul-Rio-Grandense -Rio Grande do Sul, Brasil, com base em aeromagnetometria. Dissertação de Mestrado. Instituto de Geociencias. Universidade de Brasilia, Brazil.
- Turner**, S., Regelous, M., Kelley, S., Hawkesworth, C., Mantovani, M., 1994. Magmatism and continental break-up in the South Atlantic high precision  $^{40}\text{Ar}$ - $^{40}\text{Ar}$  geochronology. *Earth and Planetary Science Letters* 121, 333-348. [https://doi.org/10.1016/0012-821X\(94\)90076-0](https://doi.org/10.1016/0012-821X(94)90076-0)
- Turner**, J.P., Green, P.F., Holford, S.P., Lawrence, S.R., 2008. Thermal history of the Rio Muni (West Africa) - NE Brazil margins during continental breakup. *Earth and Planetary Science Letters* 270, 354-367. <https://doi.org/10.1016/j.epsl.2008.04.002>
- Uliana**, M.A., Legarreta, L., Laffitte, G.A., Villar, H.J., 2014. Estratigrafía y Geoquímica de la facies generadoras de hidrocarburos en la cuencas petrolíferas de Argentina. IV Congreso de Exploración y Desarrollo de Hidrocarburos (Mar del Plata), Actas. 1, 1-63.
- Van Ranst**, G., Pedrosa-Soares, A.C., Novo, T., Vermeesch, P., De Grave, J., 2019. New insights from low-temperature thermochronology into the tectonic and geomorphology evolution of the south-eastern Brazilian highlands and passive margin. *Geoscience Frontiers* 11, 303-324. <https://doi.org/10.1016/j.gsf.2019.05.011>
- Vayssaire**, A., Prayitno, W., Figueroa, D. Quesada, S., 2008. Petroleum system of deep water Argentina: Malvinas and Colorado basins. In: Cruz, C. E., Rodríguez, J.F., Hechem, J.J. y Villar, H.J. (editores): *Sistemas Petroleros de las cuencas andinas*. VII Congreso de Exploración y Desarrollo de Hidrocarburos. Imaginando un nuevo siglo, 33-51. <https://doi.org/10.3997/2214-4609-pdb.266.3>
- White**, N. and Lovell, B., 1997. Measuring the pulse of a plume with the sedimentary record. *Nature* 387, 888-891. <https://doi.org/10.1038/43151>
- Wildman**, M., Brown, R., Beucher, R., Persano, C., Stuart, F.M., Gallagher, K., Schwanethal, J., Carter, A., 2016. The chronology and tectonic style of landscape evolution along the elevated Atlantic continental margin of South Africa resolved by joint apatite fission track and (U-Th-Sm)/He thermochronology. *Tectonics* 35, 511-545. <https://doi.org/10.1002/2015TC004042>
- Wildman**, M., Brown, R., Persano, C., Beucher, R., Stuart, F.M., Mackintosh, V., Gallagher, K., Schwanethal, J., Carter, A., 2017. Contrasting Mesozoic evolution across the boundary between on and off craton regions of the South Africa plateau inferred from apatite fission track and (U-Th-Sm)/He thermochronology. *Journal of Geophysical Research: Solid Earth* 122, 1517-1547. <https://doi.org/10.1002/2016JB013478>
- Will**, T.M., Frimmel, H.E., Pfänder, J.A., 2016. Möwe Bay Dykes, Northwestern Namibia: Geochemical and geochronological evidence for different mantle source regions during the Cretaceous opening of the South Atlantic. *Chemical Geology* 444, 141-157. <https://doi.org/10.1016/j.chemgeo.2016.08.040>
- Wygrala**, B.P., 1989. Integrated Study of an oil field in the southern Po Basin, northern Italy. KFA-Jülich, 2313, 217 p. <http://hdl.handle.net/2128/6740>





# CURRICULUM VITAE

Name: Florian Krob  
 Birthday: 05.09.1988  
 Birthplace: Freiburg im Breisgau  
 Nationality: german  
 E-Mail: [florian\\_krob@web.de](mailto:florian_krob@web.de)  
[Florian.krob@geow.uni-heidelberg.de](mailto:Florian.krob@geow.uni-heidelberg.de)



## Education

---

**Since November 2016**

**Expected July, 2020**

Ph.D. Candidate at Heidelberg University  
 Research Group: Thermochronology and Archaeometry

Topic:

“THE NEOPROTEROZOIC TO RECENT EVOLUTION OF SW GONDWANA – FROM AN OROGEN TO A PASSIVE CONTINENTAL MARGIN ENVIRONMENT INDUCED BY THE “PLATE” AND “PLUME MODE”

Special emphasis on the influence of vertical plume movement on the long-term landscape evolution of the South Atlantic passive continental margins of Namibia, SW Africa and SE Brazil, South America derived from stratigraphic frameworks and thermochronological data

Supervisor: Prof. Dr. Ulrich A. Glasmacher

**August 2018 - February 2019**

Research associate (project management) at the Heidelberg University to co-assist the initiative to establish the DFG priority program (Beyond Plate Tectonics)

**April 2016 - October 2016**

Student assistant at Heidelberg University  
 Research Group: Thermochronology and Archaeometry

**October 2013 - March 2016**

Heidelberg University, Studies of Earth Sciences

Major Fields of studies: Geology of sedimentary rocks

Master of Science, final degree: 1.5

Master thesis:

“Influence of subsidence and inversion of the Paraná Basin on the thermochronological evolution of SE Brazil”

Supervisor: Prof. Dr. Ulrich A. Glasmacher

### **October 2009 - July 2013**

Heidelberg University, Studies of Earth Sciences

Major Fields of studies: Geology

Including:

DAAD Exchange Program (1 semester)

at the "Universidade estadual paulista Julio de Mesquita Filho" (UNESP), University of Rio Claro, São Paulo, Brazil

Bachelor of Science, final degree: 1.8

Bachelor thesis:

"Thermochronological analyses of rocks, south of Florianópolis, SE Brazil on the basis of apatite fission-track dating."

Supervisor: Prof. Dr. Ulrich A. Glasmacher

### **September 1999 - July 2008**

Erasmus Gymnasium, Denzlingen

General qualification for university entrance

Abitur (A-level), final degree: 2.3

### **Scientific experience**

---

Geological scientific methods:

Optical microscopy, radiometric apatite fission-track dating, preparation of samples for optical microscopy, computer modeling of thermochronological history paths using numerical modeling (HeFTy)

August - September 2011

### **Internships**

---

Transvaal Gold Mining Estates, in cooperation with the University of KwaZulu Natal, Durban, South Africa,

Research Program of the Pilgrims Rest Goldfield

## Supervisions

---

Master theses (Niklas Brachmann, Maria Zimmermann, Stephen Katzenberger, Denis Fath)  
 Bachelor theses (Sabine Husch, Marcel Hefner, Sebastian Rieger)  
 Bachelor projects (2016, 2017)

Tutoring and temporary lecturing on substitutional behalf  
 Organisation, planning and assistance of educational field trips for students

### Short Courses:

Numerical Modeling (February 2017) at the  
 LA.TE.ANDES laboratory in Salta, Argentina

## LIST OF PUBLICATIONS

### Peer review publications

---

**Krob**, F.C., Glasmacher, U.A., Friedrich, A.M., Bunge, H.P., Hackspacher, P.C, 2020. Application of stratigraphic frameworks and thermochronological data on the Mesozoic SW Gondwana intraplate environment to retrieve the Paraná-Etendeka plume movement. *Gondwana Research* 84, 81-110. <https://doi.org/10.1016/j.gr.2020.02.010>

**Krob**, F.C., Eldracher, D.P., Glasmacher, U.A., Husch, S., Salomon, E., Hackspacher, P.C., Titus, N.P., 2020. Late Neoproterozoic-to-recent long- t-T-evolution of the Kaoko and Damara belts in NW Namibia. *International Journal of Earth Sciences (Geologische Rundschau)*. <https://doi.org/10.1007/s00531-020-01819-7>

**Krob**, F. C., Glasmacher, U.A., Karl, M., Perner, M., Hackspacher, P., Stockli, D.F., 2019. Multi-chronometer thermochronological modelling of the Late Neoproterozoic to recent t-T-evolution of the SE coastal region of Brazil. *Journal of South American Earth Sciences* 92, 77-94, <https://doi.org/10.1016/j.jsames.2019.02.012>.

### Conference contributions

---

#### European Geosciences Union (EGU) General Assembly 2020, Vienna, Austria

Application of stratigraphic frameworks and thermochronological data on the Mesozoic SW Gondwana intraplate environment to retrieve the Paraná-Etendeka plume movement.  
 Florian C. Krob, Ulrich A. Glasmacher, Hans-Peter Bunge, Peter C. Hackspacher (Abstract and poster).

#### GeoBonn 2018, Annual Meeting of the DGGV and DMG, Bonn, Germany

Do stratigraphic records and thermochronological data store the Paraná-Etendeka plume movement? Florian C. Krob, Ulrich A. Glasmacher, Hans-Peter Bunge, Peter C. Hackspacher (Abstract and poster).

## LIST OF PUBLICATIONS

### **European Geosciences Union (EGU) General Assembly 2018**, Vienna, Austria

Do thermochronological data and stratigraphic records store the Paraná-Etendeka plume movement? Florian Krob, Ulrich A. Glasmacher, Hans-Peter Bunge, Peter C. Hackspacher (Abstract and poster).

### **GeoBremen 2017**, Annual Meeting of the DGGV and DMG, Bremen, Germany

New insights on the geological evolution of the continental margin in South-eastern Brazil derived from zircon and apatite (U-Th-Sm)/He fission-track data. Florian C. Krob, Christian Stippich, Ulrich A. Glasmacher, Peter C. Hackspacher (Abstract and oral).

### **European Geosciences Union (EGU) General Assembly 2017**, Vienna, Austria

New insights on the geological evolution of the continental margin in South-eastern Brazil derived from zircon and apatite (U-Th-Sm)/He fission-track data. Florian C. Krob, Christian Stippich, Ulrich A. Glasmacher, Peter C. Hackspacher (Abstract and poster).

### **LAK 2017 - 24rd Latin American Colloquium**, Heidelberg, Germany

New insights on the geological evolution of the continental margin in South-eastern Brazil derived from zircon and apatite (U-Th-Sm)/He fission-track data. Florian C. Krob, Christian Stippich, Ulrich A. Glasmacher, Peter C. Hackspacher (Abstract and oral).

### **Thermo 2016 - 15th International Conference on Thermochronology**, Maresias, SP, Brazil

Evolution of the South Atlantic passive continental margin and lithosphere dynamic movement in Southern Brazil derived from zircon and apatite (U-Th-Sm)/He and fission-track dating. Florian C. Krob, Christian Stippich, Ulrich A. Glasmacher, Peter C. Hackspacher (Abstract and poster).

### **European Geosciences Union (EGU) General Assembly 2016**, Vienna, Austria

Evolution of the South Atlantic passive continental margin and lithosphere dynamic movement in Southern Brazil derived from zircon and apatite (U-Th-Sm)/He and fission-track dating. Florian C. Krob, Christian Stippich, Ulrich A. Glasmacher, Peter C. Hackspacher (Abstract and poster).